REVIEW OF THE VKI DOCTORAL RESEARCH

2014 - 2015



von Karman Institute for Fluid Dynamics

Covert art
Front: Ablation experiment in the VKI Plasmatron of a composite material used for the heat shield of spacecraft entering a Planet's atmosphere. The hot plasma free-stream (~10,000 K) combusts with the hydrocarbons ejected by the high-heated and pyrolyzing material.
Back cover: Scanning Electron Micrographs of tested carbon-phenolic ablators. Soot formation on the material's surface in nitrogen plasma (left), oxidation (needle shape) of carbon fibers in air plasma (right).

©2015 by the von Karman Institute for Fluid Dynamics
Waterloosesteenweg 72, B-1640 Sint-Genesius-Rode
To order: https://www.vki.ac.be

ISBN 978-2-87516-091-1

D/2015/0238/658, T. Magin, Editor-in-Chief

The contents of this book are the property of the von Karman Institute for Fluid Dynamics. No part of this book may be reproduced or distributed in any form of by any means, or stored in a database or retrieval system, without the prior written permission from the Publisher.

PREFACE

The sixth symposium on the doctoral research of the von Karman Institute for Fluid Dynamics took place during the period March 11 to 13, 2015. The doctoral students have presented the progress of their research work carried out in the three departments: Aeronautics and Aerospace, Environmental and Applied Fluid Dynamics, Turbomachinery and Propulsion. The first year students have presented a poster on their research plans and some preliminary results, while the most advanced students have proposed a presentation followed by a session of questions.

This event was attended by the faculty of the von Karman Institute as well as by colleagues from universities and industrial partners. The Symposium was open to external attendees free of charge. In addition to the presentations of the PhD candidates, we had the pleasure to welcome two prominent keynote lecturers who have opened each day the Symposium:

- Xavier Ottavy, CNRS, LMFA, "*Unsteadiness and instabilities in aeronautical compressors,*"
- Sebastian Karl, DLR, Germany, *"Design, testing and assessment of a subscale scramjet vehicle."*

This year a special IFAR virtual conference (International Forum for Aviation Research http://www.ifar.aero) was organized in collaboration with NASA. This virtual conference was broadcasted among the IFAR members and associated universities with interaction during the question session. Three PhD members were selected this year to present their work related to IFAR activities: Sara González Ruiz, Gabriele Grasso and Cis de Maesschalck. Dr. Jaiwon Shin, Associate Administrator for Aeronautics Research Mission Directorate at NASA opened the IFAR session with a speech emphasizing the importance of international collaboration.

This year, the best presentation award has been attributed to Bernd Helber for his research on "*Ablation radiation measurements of ablation products in the boundary layer of carbon based ablators*." We would like to congratulate him on this achievement. The illustrated cover art of these proceedings is based on his research results.

This proceedings volume contains 37 papers which are divided into the following topics: "*Aero-Thermal Investigations in Turbomachinery*," "*Multiphase Flows*," "*Development of Advanced CFD and Optimization*," "*Numerical Approach for Hypersonic and Plasma Flows*," "*Uncertainty Quantification*," "*Ablation*," "*Noise and Aeroacoustics*," "*Ground and Flight Experiments,*" "*Numerical Modelling for Aerothermodynamics.*"

We would like to emphasize that this publication serves as a tool for communication and aims to enhance exchange between the doctoral candidates, the faculty and external attendees. The annual publication of their results in proceedings is of crucial importance to the VKI research providing a thorough review of the different activities within the three departments.

As such, the doctoral candidate students play a key role in strengthening the expertise in experimental research, computational methods, and physical modelling. In addition to basic research, works carried out at the von Karman Institute often leads to implementation of real life industrial applications critical to the fluid dynamics community.

Clara Garcia Sánchez Jérôme Sans Phd Representatives	Thierry Magin Mario Rosaria Vetrano Professors	Christelle Debeer Organizer	Jean Muylaert VKI Director

The contribution of all VKI members who helped with this event is deeply acknowledged in particular the faculty, library and printing office staff.

TABLE OF CONTENTS

Editorial notes i

Table of contents iii

AEROTHERMAL INVESTIGATIONS IN TURBOMACHINERY

Julien CLINCKEMAILLIE 3
Analysis and consequences of the separation/transition mechanisms of the flow on a modern low-pressure gas turbine airfoil

Giulia DELL'ERA 13
Experimental and numerical investigation of the three dimensional unsteady flow field in a high speed axial compressor

Gian Luca GORI (first year PhD) 27
Determination and modelling of the aero-thermal behaviour of a cooling channel

Gabriele GRASSO 31
A rotor wake- rotor tonal interaction noise computation procedure for contra-rotating fans

Sebastian SCHOLL 39
Conjugate heat transfer of an internal rib-roughened cooling channel using large eddy simulations

Roberto TOMASSINI 51
Blade tip timing and blade tip clearance measurement system based on magnetoresistive sensors

MULTIPHASE FLOWS

Alejandro ÁLVAREZ LAGUNA 61
Multi-fluid modelling of magnetic reconnection in astrophysical and laboratory plasmas

Nicolas DE COCK 71
Splash plate nozzle design optimisation

Sara GONZÁLEZ RUIZ 79
Development of a remote sensing technique for airborne droplets and particles using the glory and speckle pattern

Imre HORVÁTH 87
Particle characterization on a liquid-gas interface

Miguel Alfonso MENDEZ 91
Dynamics of gas jet impingement on vertical falling liquid films

Alessia SIMONINI 105
Topographic reconstruction of free surface motion due to harmonic sloshing

Orkun TEMEL (first year PhD) 115
Multiscale modelling of atmospheric dispersion

Agustin VILLA ORTIZ (first year PhD) 121
Turbulent heat transfer on at different Prandtl number fluids in natural convection boundary layer on a vertical plate

DEVELOPMENT OF ADVANCED CFD AND OPTIMIZATION

Hassanine Mohamed AISSA 125
A GPU-accelerated Navier-Stokes solver for steady turbomachinery simulations

Christopher CHAHINE 133
Multidisciplinary optimization of aero-engine fan blades

Cis DE MAESSCHALCK 141
Turbine tip flow optimization for modern aero-engines

Aude LAHALLE (first year PhD) 153
Experimentally and numerically driven optimization of high performance instrumentation for real engine testing

Lasse MÜLLER 155
Development of gradient-based optimization framework for turbomachinery using CAD-based Discrete Adjoint Method

Jorge FERNANDES LOPES DE SOUSA 169
One-dimensional assessment of supersonic inlet turbines

Nikolaos STERGIANNIS (first year PhD) 177
Full rotor CFD simulations of the MEXICO wind turbine including the nacelle in OpenFOAM

Stefano VAGNOLI 179
CFD analysis of the mutual effect different components of a turboengine: application to the combustor – high pressure turbine and to the inlet duct – compressor interaction

NUMERICAL APPROACH FOR HYPERSONIC AND PLASMA FLOWS

Georgios BELLAS CHATZIGEORGIS 195
Development of advanced gas surface interaction models for reusable materials

Aurélie BELLEMANS 205
SPARK: Simplified PlasmA models based on Reduced Kinetics

Bruno Ricardo DIAS BARROS (first year PhD) 217
Simulation of the atmospheric entry of meteors with application to radio detection

Koen GROOT 223
Non-linear extensions of global flow stability theory

Alan VILADEGUT 235
Assessment of gas-surface interaction modelling for lifting body re-entry flight design

UNCERTAINTY QUANTIFICATION

Clara GARCÍA SÁNCHEZ 245
Quantifying inflow uncertainties for CFD simulations of dispersion in the atmospheric boundary layer

NOISE AND AEROACOUSTICS

Daniel GUARIGLIA 255
Design of a facility shock-cell noise investigation on a subsonic / supersonic coaxial jet

Ugur KARBAN 269
Numerical investigation of the noise produced by a tandem diaphragm in a cylindrical duct using LES data

ABLATION

Bernd HELBER 279
Absolute radiation measurements of ablation products in the boundary layer of carbon based ablators

Pierre SCHROOYEN 291
Development of a numerical simulation tool for the aerothermal flow through an ablative thermal protection system for atmospheric entry

James B. SCOGGINS 303
Fast hybrid statistical narrow band model for radiative transfer in atmospheric entry flows

Pedro Milheiro SANTOS DUARTE 313
A hybrid method for coupled spallation-radiation physics for ablating heat shields under re-entry conditions

GROUND AND FLIGHT EXPERIMENTS

İşil ŞAKRAKER 321
In-flight experiment design and ground testing of a re-entry CubeSat

Thorsten SCHOLZ 335
Efficient trajectory simulation for optimization of the simultaneous deployment of a network of CubeSats

Bart VAN HOVE 345
Simulation and reconstruction tools for atmospheric entry probes to Mars

Who's who 351

AEROTHERMAL INVESTIGATIONS IN TURBOMACHINERY

Analysis and Consequences of the Separation/Transition Mechanisms of the Flow on a Modern Low-Pressure Gas Turbine Airfoil

Julien Clinckemaillie

Turbomachinery and Propulsion Department, von Karman Institute for Fluid Dynamics, Belgium, julien.clinckemaillie@vki.ac.be

Supervisor: Tony Arts

Professor and Head of Department, Turbomachinery and Propulsion Department, von Karman Institute for Fluid Dynamics, Belgium, tony.arts@vki.ac.be

University Supervisor: Hervé Jeanmart

Professor, Institute of Mechanics, Materials and Civil Engineering, Université Catholique de Louvain, Belgium, herve.jeanmart@uclouvain.be

Abstract

A detailed analysis of the effect of incoming periodic wakes on the aerodynamic performance of a very-high-lift, mid-loaded low-pressure turbine airfoil (T106C) is presented. This experimental study was performed on a large scale linear cascade in the S-1/C transonic wind tunnel, operating at a fixed exit isentropic Mach number equal to 0.65, covering a range of exit isentropic Reynolds numbers (90,000 – 200,000 based on chord length) and at low inlet free-stream turbulence intensity (0.8%). The simulation of incoming periodic wakes was realized by means of a disc equipped with bars rotating at high speed upstream of the leading edge plane, allowing an engine representative simulation of the operating conditions (flow coefficient, reduced frequency, wake width and depth) encountered in low-pressure turbines of modern aero-engines. Some features of the multi-mode transition germane to unsteady wake-boundary layer interactions in a low-pressure turbine environment are also discussed for specific cases.

Keywords: Turbomachinery, low-pressure turbine, transition, multi-mode transition, separation, bursting, unsteady wake-boundary layer interaction, blade-row interference

Nomenclature

c	Chord
E	Hot-film voltage
f	Frequency
FSTI	Free-stream turbulence intensity
g	Pitch
h	Span
LE	Leading edge
LPT	Low-pressure turbine
M	Mach number
P	Pressure
PS	Pressure side
PSDI	Power spectral density integral
Re	Reynolds number
s	Curvilinear coordinate
SS	Suction side
t	Time
TE	Trailing edge
U	Peripheral speed
V	Velocity
x	Axial coordinate
y	Pitch-wise coordinate

Greek symbols

β	Flow angle
γ	Intermittency

	Isentropic exponent
ϕ	Flow coefficient
τ	Pseudo-wall shear stress
ζ	Kinetic energy loss coefficient

Subscripts

0	Reference length
	Total condition
	Zero-flow condition
1	Upstream condition
2	Downstream condition
ax	Axial
bar	Referring to the bars
is	Isentropic
L	Laminar
m	Mid-span
r	Reduced
T	Turbulent
w	Wall

1. Introduction

The actual design trend for modern state-of-the-art commercial aero-engines is characterized by an ever-increasing bypass ratio. This, in turn, requires the low pressure turbine (LPT) to provide an increasingly higher power output in order to drive the large fan, without any efficiency penalty. At the same time, the current need to save weight and to reduce production and maintenance costs translates itself into a reduction of the blade count per row and thus increased pitch-to-chord ratios. The combined effect of those design requirements on the low-pressure turbine implies an increased aerodynamic loading per blade, and has led to the development of very-high-lift and even ultra-high-lift airfoils. They are characterized by an increased velocity peak level on the suction side, followed by a significant diffusion of the flow along the rear part of the suction side until the trailing edge. The resulting strong adverse pressure gradient can lead to a separation of the boundary layer, particularly under the low Reynolds number conditions which are germane to low pressure turbines of commercial jet engines operating at cruising altitude. These separation bubbles cause a significant degradation of the engine efficiency, particularly open separation bubbles that fail to reattach, resulting in a major loss in aerodynamic efficiency, thrust and flow turning [1]. For large commercial aero-engines, a component efficiency drop of 2 percent can occur between sea-level take-off conditions, where the Reynolds number is of the order of 5 10^5, and high-altitude cruising conditions where the Reynolds number drops by a factor of 3 to 4 [2; 3]. This drop in efficiency can even become as large as 7 percent for smaller engines operating at even higher cruising altitudes (e.g. Unmanned Aerial Vehicles [3]). Due to the low Reynolds numbers typical of high-altitude cruising conditions, a large part of the boundary layer developing on the suction surface of a very-high-lift LPT blade may still be laminar until past the velocity peak, even with significant background free-stream turbulence intensity levels. If the subsequent diffusion is strong enough, the boundary layer is not able to withstand the adverse pressure gradient and separates from the surface. If transition from laminar to turbulent occurs soon enough in the separated free shear layer, the flow will reattach to the surface and a separation bubble is formed. The separation and transition of the boundary layer are thus closely linked, and the accurate prediction of transition onset and development under relevant conditions is essential to the design of efficient LPT airfoils.

A considerable wealth of information on transition can be found in the literature. Mayle [1] discerned three modes of transition and considered that none of them is more crucial to low-pressure turbines than the separated-flow transition mode. A classification of the separated-flow transition based on the type of separation bubble, long or short, and its effect on the overall pressure distribution along the suction surface was also proposed. Short bubbles have only a local displacement effect, with the pressure distribution before and after the bubble remaining very close to that of the flow without separation, whereas long bubbles interact with the outer flow to such an extent that the overall pressure distribution is extremely modified, a phenomenon typically associated with drastically increased losses and significantly reduced outlet flow angle. The change from a short bubble type to a long one is called bursting, and can be triggered by small changes in either Reynolds number or angle of attack. Mayle's study has since then been critically discussed, reviewed and extended by other research groups [4; 5; 2]. The transition processes described here above can also be strongly affected by the periodic unsteady nature of the flow in gas turbines. Although the periodic unsteadiness can take multiple forms, the present paper focuses entirely on the unsteady blade-wake interactions, as discussed by Halstead et al. [6] and Mayle [1].

A great amount of state-of-the-art studies concerning the aerodynamic performance of very-high-lift low-pressure turbine airfoils under uniform and periodic

inflow conditions can be found in the literature. However, most studies have been performed in low-speed wind tunnels [2; 7; 8] or in high-speed wind tunnels with an unrealistically high flow coefficient [9]. The aim of the present praper is to contribute to the available literature by discussing the aerodynamic performance of a very-high-lift mid-loaded low-pressure turbine airfoil (T106C) under engine representative conditions in terms of exit Mach and Reynolds number, and including the effects of unsteady blade row interference phenomena on the behavior of the boundary layer along the suction surface of the airfoil providing a realistic reduced frequency and flow coefficient. The background free-stream turbulence intensity was kept at a low level (0.8%) in order to better highlight the effects of the periodic unsteady blade-wake interactions.

2. Experimental Setup

2.1. Experimental facility

The measurement campaign was performed in the high speed S-1/C wind tunnel of the von Karman Institute (Fig. 1). This continuous closed-loop wind tunnel is driven by a 615 kW axial flow compressor. A cooler maintains the temperature close to atmospheric conditions (~290 K) and dry air is maintained at all conditions. The mass flow can further be regulated with a by-pass valve, while the absolute pressure level inside the test section can be lowered down to ~10,000 Pa by means of a vacuum pump. This implies that the flow through a linear cascade of two-dimensional LPT airfoils can be aerodynamically investigated over a large range of independently adjusted exit isentropic Mach ($M_{2,is}$ = 0.5 - 0.8) and Reynolds numbers ($Re_{2,is}$ = 2 10^4 – 3 10^5 based on a chord c ranging between 0.02 and 0.10 m), allowing to cover a wide range of engine representative operating conditions.

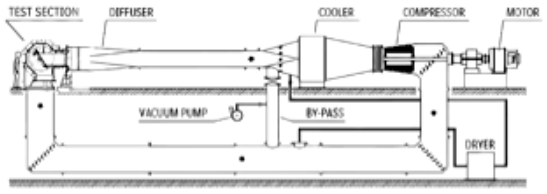

Figure 1: The S-1/C high speed, variable density wind tunnel

The test section consists of a linear cascade of six up-scaled T106C high-lift, mid-loaded low-pressure turbine blades and two end-blocks (effectively forming 7 blade passages) with a span of 225 mm. This guarantees a sufficiently high aspect ratio (above 2.30) and therewith limits the impact of the end-wall boundary layers at mid-span of the inlet duct. The main characteristics of the test cascade are listed in Tab. 1 [10]. Located in a plane 0.67 x/c_{ax} upstream of the cascade, a spoke-wheel type wake generator equipped with bars and driven by a 30 kW electric motor generates periodically incoming wakes in order to simulate unsteady blade row interference effects. The wake generator consists of a solid brass disk with a diameter of 625 mm on which 32 equally spaced cylindrical molybdenum bars with a diameter of 2 mm and a length of 215 mm are mounted. The rotating bars are only parallel to the blade leading edge when passing in front of the central instrumented blade, extending over the entire blade span except for a clearance of 30 mm for safety reasons. The rotational speed of the disk (adjustable by means of a variable frequency controller) as well as the amount of bars were carefully determined in order to match conditions representative of a modern commercial aero-engine in terms of reduced frequency and flow coefficient. For this experimental campaign, a rotational speed of 2,665 RPM was chosen. In this configuration, a flow coefficient $\phi = V_{1,ax}/U_m$ of 0.75 and a reduced frequency $f_r = (f_{bar}c)/V_{2,is}$ of 0.62 were achieved. In the following presentation of the results, both cases – uniform (without periodic incoming wakes) and periodic inflow conditions – will be discussed.

Table 1: T106C cascade characteristics

Chord	c	mm	93.01
Pitch-to-chord ratio	g/c	-	0.95
Aspect ratio	h/c	-	2.4:1
Blade stagger angle	ϕ	deg	30.7
Inlet flow angle	β_1	deg	32.7

2.2. Instrumentation

The third airfoil from the top of the cascade can be alternatively replaced by an instrumented blade with pneumatic wall static pressure taps or with wall hot-film gauges (for pseudo-wall shear stress measurements). In both cases, the sensors are located at blade mid-span and deployed along the suction side length, with a higher concentration of sensors in the region where the boundary layer is expected to separate at low Reynolds numbers. A fixed Pitot probe allows

measuring the total pressure upstream of the cascade, while the upstream total temperature is quantified by means of a bare type-K thermocouple (without flow velocity correction since the thermocouple is located in a stagnation region). The inlet (P_{01}, T_{01} and β_1) and outlet (P_2) boundary conditions are accurately quantified in measurement planes located at an axial distance of 0.67 x/c_{ax} upstream of the LE and 0.55 x/c_{ax} downstream of the TE respectively. In the presence of the wake generator used to simulate the periodic inflow conditions, the upstream boundary conditions P_{01} and β_1 cannot be measured but are determined using hot-wire data previously obtained in identical flow conditions [11] and based on the total pressure measured by a Pitot probe located upstream of the wake generator. The pitch-wise distributions of flow angle and total pressure upstream and downstream of the cascade were quantified by means of wall static pressure taps, a 3-hole and a 5-hole probe respectively. A Pitot probe with a flattened head was also traversed upstream of the cascade in the spanwise direction in order to characterize the inlet endwall boundary layer. The latter was quantified as fully turbulent (shape factor = 1.4) with a boundary layer thickness equal to 13% of the inlet duct width and a displacement thickness ranging between 3 and 5 mm for the Reynolds numbers investigated. All pneumatic measurements were sampled at 400 Hz before being subsequently time-averaged, with the exception of the continuous probe traverses which were sampled at 1 kHz with a sufficiently slow carriage speed in order to take into account their relatively low time response. Since a quantitative calibration of the hot-films array is not possible, the raw output signal of the hot-film gauges was processed in a semi-quantitative manner [12] using Eq. 1, where the value of the pseudo-wall shear stress is proportional to the associated bridge voltage reading E during the experiment, and the voltage reading E_0 under zero-flow conditions. The hot-film signals were sampled at 60 kHz and low-pass filtered at 25 kHz. The (measured) frequency response of the hot-film gauges was ~10 kHz.

$$\tau_w = \left(\frac{E^2 - E_0^2}{E_0^2} \right)^3 \quad (1)$$

2.3. Uncertainty

The reader should realize that the tests were performed at very low absolute pressure (~10,000 Pa), and that the ambient pressure was used as the main reference pressure for all pneumatic measurements. The application of a rigorous error propagation will therefore lead to higher uncertainties, especially at the lowest Reynolds numbers. However, the obtained results proved to be very repeatable, not only during the measurement campaign, but also when compared to previous measurement campaigns performed in similar flow conditions [10; 11]. The following uncertainty values were estimated for the lowest Reynolds number, the most critical one for the uncertainty estimation. The relative uncertainties on isentropic Mach and Reynolds number are 2.2% and 2.5% respectively, while the absolute uncertainty for the kinetic energy losses and exit flow angle are 0.034 and 1.5 deg respectively.

3. Results and Discussion

3.1. Time-averaged pneumatic results

Fig. 2 shows the blade velocity evolution (isentropic Mach number evolution) along the suction side of the T106C blade for four exit isentropic Reynolds numbers (90,000 – 200,000), at nominal exit isentropic Mach number (0.65), at low free-stream turbulence intensity (FSTI = 0.8%) and with uniform inflow conditions. The fully turbulent 2D Navier-Stokes numerical computation TRAF2D (using the algebraic Baldwin-Lomax turbulence model, and with uniform inflow boundary conditions) is used as a reference velocity distribution, characterized by a fully attached boundary layer along the entire surface of the airfoil. The reader is referred to Arnone [13] for more information on the numerical code.

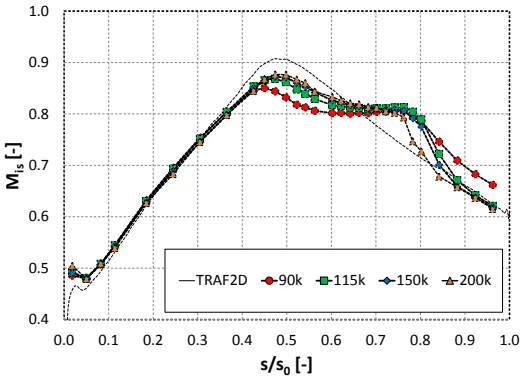

Figure 2: Isentropic Mach number evolution along the suction side of the T106C blade for four different Reynolds numbers; uniform inflow conditions

For all the investigated cases, the results show a significant deviation from the numerical prediction due

to the presence of a separation bubble along the diffusing part of the suction side downstream of the velocity peak. For the highest Reynolds number ($Re_{2,is}$ = 200,000), the separated shear layer is reattaching to the blade surface before the trailing edge, resulting only in a locally perturbed aerodynamic loading of the blade in the region of the separation bubble, caused by the displacement effect of the latter. However, the velocity distribution is significantly altered for the lowest Reynolds number ($Re_{2,is}$ = 90,000) as the separated shear layer is unable to reattach before the trailing edge, resulting in an open separation bubble. Between these two extreme cases, the bursting of the separation bubble from a short type ($Re_{2,is}$ = 150,000) to a long type ($Re_{2,is}$ = 115,000) takes place, corroborating the results obtained by Michálek et al. [10] which identified a critical Reynolds number of 140,000 at which bubble-bursting takes place.

The mass-averaged kinetic energy losses (Eq. 2) and exit flow angle are presented in Fig. 3 and 4 respectively, showing the progressive augmentation of losses as well as the reduction in turning angle as the exit isentropic Reynolds number is lowered, culminating in a significant deterioration of the aerodynamic performances for the lowest Reynolds number investigated.

$$\zeta = 1 - \frac{1 - (\overline{P_2}/\overline{P_{02}})^{\gamma-1/\gamma}}{1 - (\overline{P_2}/\overline{P_{01}})^{\gamma-1/\gamma}} \tag{2}$$

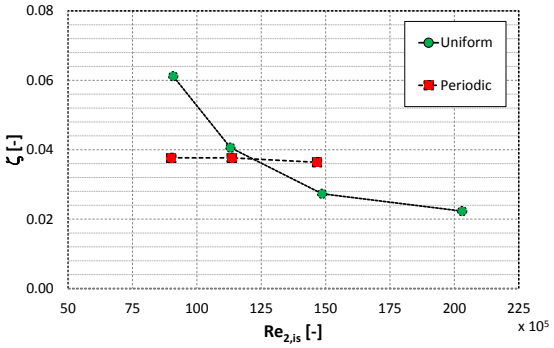

Figure 3: Mass-averaged kinetic energy losses as a function of $Re_{2,is}$; comparison between uniform and periodic inflow conditions

In the presence of periodic incoming wakes generated upstream of the cascade, several conclusions can be drawn from the time-averaged blade velocity distribution alone (Fig. 5) when compared to the steady state results for the lowest Reynolds numbers (90,000 and 115,000). The most striking difference compared to the steady state case is the significant decrease of the separation bubble size even for the lowest Reynolds number. This is due to the reenergizing effect that the convected turbulent wake has on the unstable boundary layer downstream of the velocity peak. A time-averaged reduction of the aerodynamic loading on the front part of the suction surface is also observed, due to the periodically altered inlet velocity triangle in the presence of a wake, resulting therefore in periodic pressure disturbances on the blade surface [14].

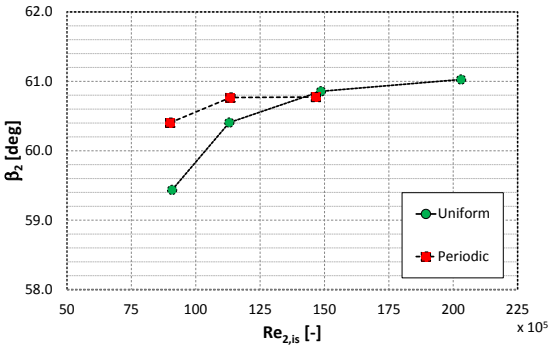

Figure 4: Mass-averaged outlet flow angle β_2 as a function of $Re_{2,is}$; comparison between uniform and periodic inflow conditions

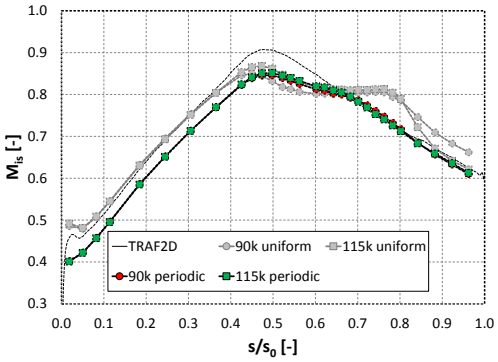

Figure 5: Isentropic Mach number evolution along the suction side of the T106C blade for two different Reynolds numbers; comparison between uniform and periodic inflow conditions

Fig. 6 and 7 present the downstream pitchwise traverses through the wake for uniform and periodic inflow conditions respectively. From the uniform case, it is clearly visible that the main source of losses emanates from the suction side of the airfoil since that part of the wake grows wider and deeper with decreasing Reynolds number. Under periodic inflow conditions however, the wake profiles, where P_{01} is an accurate estimation of the inlet total pressure downstream of the wake generator based on previously obtained data [11], remain nominally unaltered for different Reynolds numbers, a conclusion that is supported by the relatively constant kinetic energy losses with re-

spect to $Re_{2,is}$ (Fig. 3). Interestingly, for Reynolds numbers bigger than 125,000, the losses in the periodic case are greater than in the uniform case, an observation that can be attributed to a bigger surface being covered by turbulent flow in the periodic case, thereby increasing the profile losses [3].

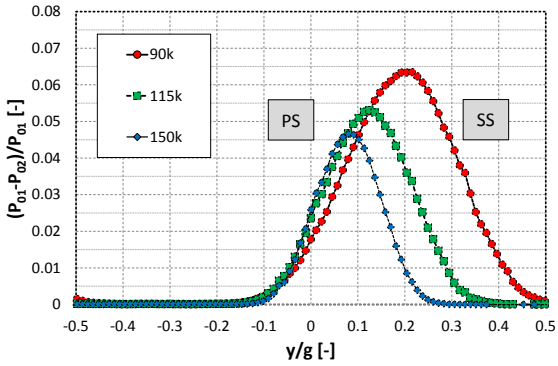

Figure 6: Pitchwise wake profiles for three different Reynolds numbers with uniform inflow conditions

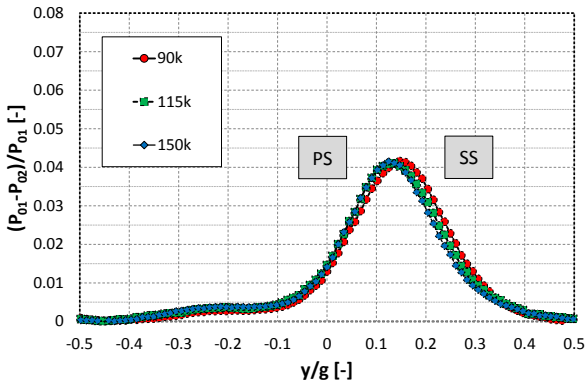

Figure 7: Pitchwise wake profiles for three different Reynolds numbers with periodic inflow conditions

3.2. Time-resolved hot-films anemometry results

The status of the boundary layer developing on the suction surface of the airfoil can further be investigated using the output signals of hot-film gauges, albeit qualitatively rather than quantitatively (Eq. 1). Fig. 8 presents the evolution of the mean pseudo-wall shear stress, the rms normalized by the local mean value and the local intermittency factor for one Reynolds number ($Re_{2,is} = 115,000$) with uniform inflow conditions. The local intermittency factor is computed following Eq. 3 [15] and is based on the progressively increasing power spectral density integral ($PSDI$) throughout the transition process as the boundary layer goes from laminar ($PSDI_L$, $\gamma_{PSDI} = 0$) to turbulent ($PSDI_T$, $\gamma_{PSDI} = 1$).

$$\gamma_{PSDI(s)} = \frac{PSDI(s) - PSDI_L}{PSDI_T - PSDI_L} \tag{3}$$

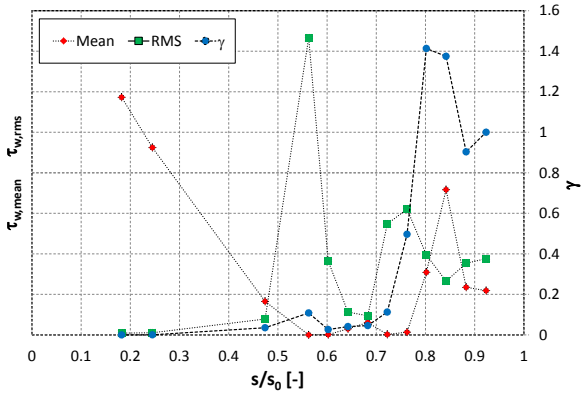

Figure 8: Mean pseudo-wall shear stress, rms and intermittency factor evolution along the suction side; $Re_{2,is} = 115,000$; uniform inflow conditions

Upstream of the velocity peak ($s/s_0 < 0.5$), the pseudo time-averaged wall shear stress values are all above zero with low rms values and a low energy content (Fig. 9), as expected for an accelerating laminar boundary layer. The spectral peak at ~170 Hz and its first harmonic are believed to be linked to large periodic flow structures generated upstream of the cascade [10]. The separation point ($s/s_0 = 0.56$) is characterized by a zero value for the wall shear stress and a first peak in the rms value as well as a global increase of the energy content, especially in the lower frequency range (1,000 – 2,000 Hz). An explanation for the first peak in rms was proposed by Michálek et al. [10] who linked it with the periodic ejection of flow from the near-wall region into the shear layer, as described by Hatman and Wang [5]. The high value of the first rms peak can also partly stem from the near-zero mean value of the pseudo-wall shear stress with which the rms is normalized.

In the separation region ($s/s_0 = 0.64 - 0.68$), a slight increase of the wall shear stress can be observed, suggesting the back flow caused by the vortical structure inside the bubble. The transition onset takes place at $s/s_0 = 0.68$, marked by the gradual increase of both the rms and the local intermittency. The second peak in rms ($s/s_0 = 0.76$) corresponds to the mid-transition point and the maximum displacement point from the pneumatic measurements. Finally, the end of transition takes place at $s/s_0 = 0.84$ (just before reattachment), aft of which a fully turbulent boundary layer develops until the trailing edge.

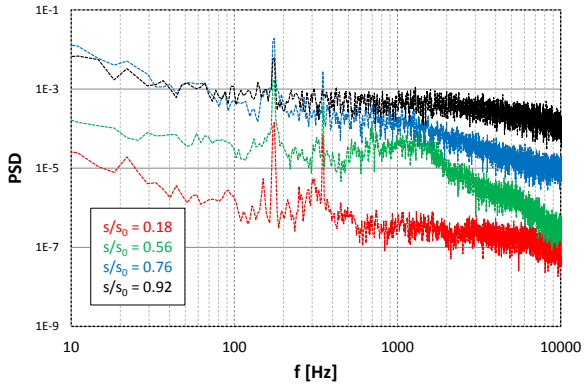

Figure 9: Power spectral density of four hot-film sensors along the suction side; $Re_{2,is} = 115,000$; uniform inflow conditions

Fig. 10 and 11 present the space-time diagrams of the phase-locked averaged pseudo-wall shear stress and its rms respectively normalized by the maximum value at the same sensor location, thus emphasizing the periodic fluctuation of the signal at the expense of its absolute value, for one Reynolds number ($Re_{2,is} = 115,000$) and with periodic inflow conditions. Three wake passing events are shown in order to provide a better interpretation of the results. The following discussion concentrates mainly on the diffusing region of the blade ($s/s_0 > 0.5$), where the unsteady wake-boundary layer interaction effects are the most critical.

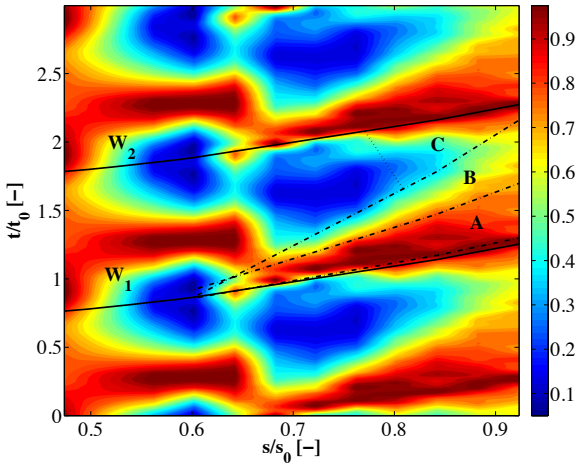

Figure 10: Space-time diagram of the phase-locked averaged mean pseudo-wall shear stress for $Re_{2,is} = 115,000$ with periodic inflow conditions

As described by Halstead et al. [6], the unsteady boundary layers are developing along two separate but coupled paths: the wake-induced path (lying under the wake trajectory, or lagging slightly behind the

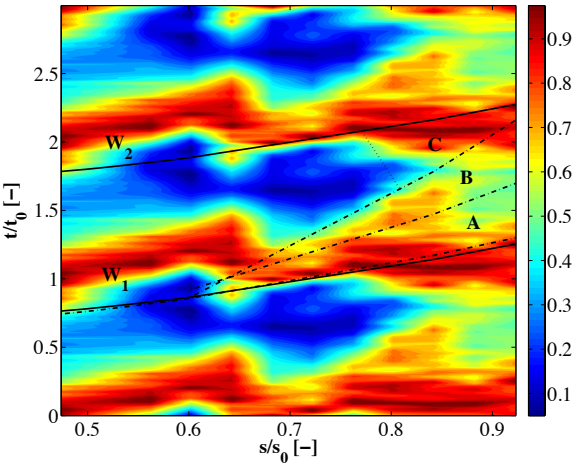

Figure 11: Space-time diagram of the phase-locked averaged pseudo-wall shear stress rms for $Re_{2,is} = 115,000$ with periodic inflow conditions

latter) and the path between two consecutive wakes. The first path W_1 induced by the presence of the wake can be clearly observed in the obtained results, with the typical wedge-shaped wake-induced transitional strip (zone A) and the associated calmed region (zone B) starting at the location $s/s_0 = 0.62$, well into the diffusing part of the blade. The shape of the wedge is related to the different convection velocities of the leading and trailing edges of turbulent spots (0.5 V_{is} and 0.88 V_{is} respectively) as well as the convection velocity of the calmed region (0.3 V_{is}). This transitional region is characterized by an abrupt increase of the wall shear stress coupled with high rms values, followed by a gradual decay of both in the calmed region, an observation that was confirmed by analyzing the hot-film time traces (not shown). In the path between two consecutive wakes, a region of attached (non-zero wall shear stress) transitional (high rms) flow can be observed where the calmed region becomes weaker (zone C), eventually merging with the following wake-induced transitional strip W_2 until the trailing edge. Finally, after analyzing the signal of the most aft hot film sensor, the calmed region could not be discerned anymore, thus assuming that the boundary layer is fully turbulent and attached when reaching the trailing edge of the blade. This is a typical case of multi-mode transition where, at a fixed moment in time, transition can take place at different locations on the blade and be triggered by different mechanisms. As a final remark, it should be noted that separation, characterized by near-zero wall shear stress and rms values, only seems to take place intermittently between two consecutive wake passing

events, an observation that was confirmed after analyzing the time traces of the processed hot-film signals. This demonstrates the overall suppressing effect that incoming wakes have on the separation bubble. The earliest point of separation ($s/s_0 = 0.56$) also coincides with the separation location under uniform inflow conditions (Fig. 8).

4. Conclusions and future work

4.1. Conclusions

A rigorous investigation of the aerodynamic performance of the very-high-lift mid-loaded T106C LPT blade was performed at high isentropic exit Mach number (0.65) and for a range of engine representative isentropic exit Reynolds numbers (90,000 – 200,000), covering the bursting of the separation bubble from a short type to a long or even fully open one. In the case of uniform inflow conditions, the Reynolds number has a significant influence on the physical size of the separation bubble, and therefore on the aerodynamic losses and loading of the airfoil. A significant deterioration of the aerodynamic performance was observed as the Reynolds number decreases, culminating in a fully open separation bubble at the lowest Reynolds number investigated. In the case of periodic inflow conditions, a beneficial effect of the unsteady wake-boundary layer interactions was observed at the lower Reynolds numbers (90,000 – 115,000), as the impinging turbulent wakes are periodically suppressing the separation bubble. An analysis of the boundary layer evolution along the diffusing part of the suction surface showed that its development occurs along two distinct paths for one wake-passing event: the wake-induced transitional strip, characterized by its wedge shape and the calmed region, and the path between two consecutive wakes, characterized by attached transitional flow. Furthermore, at higher Reynolds numbers ($Re_{2,is} > 125,000$), an inversion of the loss evolution occurs: the aerodynamic losses under periodic inflow conditions become more significant than under uniform inflow conditions due to an increased surface being covered by turbulent flow, therefore increasing the profile losses.

4.2. Future work

The aerodynamic performance of low-pressure turbine airfoils in the S-1/C wind tunnel has so far mainly been analyzed based on time-averaged data acquired by means of pneumatic probes with a (very) low frequency response. However, in order to obtain more information and physical insight into the inherently unsteady nature of the separation/transition process, time-resolved data are obviously required. To this end, a calibration methodology for constant temperature hot-wire anemometry in a compressible non-isothermal low-density flow (such as in the S-1/C wind tunnel) will be applied in order to perform accurate time-resolved velocity measurements in the wake region directly downstream of the trailing edge, or across the boundary layer developing along the rear part of the suction surface of the blade. The obtained data will also be invaluable for the validation of models dealing with boundary layer separation/transition in a low-pressure turbine environment.

Finally, as described in the introduction of this paper, reducing the weight of the low-pressure turbine is one of the main current trends in aeroengine design. Recent developments in material technology allow the use of lighter materials in parallel with the common practice of reducing the blade count per row. However, the manufacturing process of the blade using these lighter materials can result in a rougher finish of the blade surface. Investigating the effect of the resulting surface roughness on the aerodynamic performance of a LPT airfoil forms the other point of definite interest for this doctoral research project.

5. Acknowledgments

The funding of this work by the Fonds pour la Formation à la Recherche dans l'Industrie et dans l'Agriculture (FRIA - FNRS) is gratefully acknowledged by the first author. The author also wishes to acknowledge the permission to have access to previous experimental results obtained within the framework of the European research projects UTAT (GRD1-2001-40192) and TATMo (AST5-2006-030939) performed at the von Karman Institute.

References

[1] Mayle, R. E., The role of laminar-turbulent transition in gas turbine engines, Journal of Turbomachinery 113 (1991) 509–537.

[2] Volino, R. J. and Hultgren, L. S., Measurements in separated and transitional boundary layers under low-pressure turbine airfoil conditions, Journal of Turbomachinery 123 (2001) 189–197.

[3] Hodson, H. P. and Howell, R. J., The role of transition in high-lift low-pressure turbines for aeroengines, Progress in Aerospace Sciences 41 (2005) 419–454.

[4] Walker, G. J., The role of laminar-turbulent transition in gas turbine engines: a discussion, Journal of Turbomachinery 115 (1993) 207–217.

[5] Hatman, A. and Wang, T., A prediction model for separated-flow transition, Journal of Turbomachinery 121 (1999) 594–602.

[6] Halstead, D. E., Wisler, D. C., Okiishi, T. H., Walker, G. J., Hodson, H. P. and Shin, H.-W., Boundary layer development in axial compressors and turbines: part 1 of 4 - Composite picture, Journal of Turbomachinery 119 (1997) 114–127.

[7] Schobeiri, M. T. and Ozturk, B., Experimental study of the effect of periodic unsteady wake flow on boundary layer development, separation, and re-attachment along the surface of a low pressure turbine blade, in: ASME Turbo Expo 2004: Power for Land, Sea and Air, no. GT2004-53929, Vienna, Austria, 2004.

[8] Stieger, R., Hollis, D. and Hodson, H., Unsteady surface pressures due to wake induced transition in a laminar separation bubble on a LP turbine cascade, in: ASME Turbo Expo 2003: Power for Land, Sea and Air, no. GT2003-38303, Atlanta, USA, 2003.

[9] R. Ciorciari, Kirik, I. and Niehuis, R., Effects of Unsteady Wakes on the Secondary Flows in the Linear T106 Turbine Cascade, Journal of Turbomachinery 136 (2014) 0910101–1 – 11.

[10] Michael, J., Monaldi, M. and Arts, T., Aerodynamic performance of a very high lift low pressure turbine airfoil (T106C) at low Reynolds and high Mach number with effect of free stream turbulence intensity, in: ASME Turbo Expo 2010: Power for Land, Sea and Air, no. GT2010-22884, Glasgow, UK, 2010.

[11] T. Arts, Aerodynamic performance of two very high lift low pressure turbine airfoils (T106C - T2) at low Reynolds and high Mach numbers, in: 5th European Conference for Aerospace Sciences, Munich, Germany, 2013.

[12] Hodson, H. P., Detection of boundary layer transition and separation in high speed turbine cascades, in: Measurement Techniques for Transonic and Supersonic Flow - Proc. 7th Symposium, Aachen, Germany, 1983.

[13] A. Arnone, Viscous Analysis of a Three-Dimensional Rotor Flow Using a Multigrid Method, Journal of Turbomachinery 116 (1994) 435–445.

[14] Dietz, A. J. and Ainsworth, R. W., Unsteady Pressure Measurements on the Rotor of a Model Turbine Stage in a Transient Flow Facility, in: International Gas Turbine and Aeroengine Congress and Exposition, no. ASME-92-GT-156, Cologne, Germany, 1992.

[15] Coton, T., Arts, T., Lefebvre, M. and Liamis, N., Unsteady and calming effects investigation on a very high-lift LP turbine blade - Part I: experimental analysis, Journal of Turbomachinery 125 (2003) 281–289.

Experimental and Numerical Investigation of the Three Dimensional Unsteady Flow Field in a High Speed Axial Compressor

Giulia Dell'Era

Turbomachinery and Propulsion Department, von Karman Institute for Fluid Dynamics, Belgium, dellera@vki.ac.be

Supervisor: Jean-Francois Brouckaert

Associate Professor, Turbomachinery and Propulsion Department, von Karman Institute for Fluid Dynamics, Belgium, brouckaert@vki.ac.be

University Supervisor: Tony Arts, Philippe Chatelain

Professor, Turbomachinery and Propulsion Department, Head of the Department, von Karman Institute of Fluid Dynamics, Belgium, arts@vki.ac.be
Professor, Université Catholique de Louvain, Institute of Mechanics, Materials and Civil Engineering, Belgium, philippe.chatelain@uclouvain.be

Abstract

The topic of this Ph.D. study is unsteady phenomena appearing in high speed axial compressors. The comparison between unsteady experimental data and steady computations has revealed discrepancies in both the determination of the global performance of a compressor stage and the detailed representation of the flow field. The project has two objectives: the first is to determine a numerical strategy in order to provide an accurate representation of the flow physics in a compressor stage, which may be utilized in improving current compressor design tools and approach. The second objective is to employ CFD as a tool for a deeper analysis of the flow-field in axial compressors. Even though the unsteadiness of the flow field has impacts on the aerodynamic, mechanical and acoustic characteristics, the common practice in design is still based on time-averaged quantities and steady simulations.

Keywords: unsteady, axial compressor, rotating stall

Roman Symbols

1	quantity relative to upstream the stage
4	quantity relative to downstream the stage
CR	Cell rotation
Nn	shaft speed [% with respect to design speed]
OSC	Oscillation
P	Pressure [mbar]
PS	Static Pressure [mbar]
ROT	Rotor

1. Introduction

In the often conflicting optimization of the various objectives set by the production, such as the increase of power, efficiency and the reduction of weight, the blading constitutes one of the most important components. Even though the unsteadiness of the flow field impacts on the aerodynamic, mechanical and acoustic characteristics of a compressor stage, not only the design common practice is still based on time averaged quantities, but also employs steady simulations which are characterized by a systematic error due to the assumption of a pitchwise periodic flow at the rotor/stator interaction. On the other hand the simulations that are modelling the unsteady effects require a high computational time.

The compressor remains a critical component, not only in terms of weight (the whole compressing system approximately constitutes 40 % of the weight of the engine) but also regarding the performance and the stability of the machine [1]. A higher efficiency of the compressor stages will lead to a reduction of their number, therefore to a decrease of the overall weight of the engine.

This research program aims at the determination of

a numerical strategy by comparing both steady and unsteady simulations with time-resolved experimental data. The first step is the assessment of the uncertainties and confidence levels on the time-resolved data obtained within this study in the VKI R4 compressor rig at various operating points covering the whole performance map, followed by the analysis of the stall transients. The next step is the comparison of simulation results with the experimental data analyzed, while taking various parameters influencing simulations such as the turbulence model, numerical scheme and type of simulation into account.
An appropriate representation of the unsteady effects is crucial at the design operating point in order to provide a complete prediction of the losses, which are indeed due to secondary flows (such as the tip leakage vortex and the hub corner separation) and endwall effects. In the near stall condition it is even more relevant: a high level of unsteadiness is typical of the operating points close to the stability limit of the machine. Both operating points are taken into account in this study: the aim is to find not only an appropriate description of the unsteady flow feature at the design operating point, but also an accurate determination of the stall margin.
The first part of this article presents the experimental analysis of the stall inception patterns of the compressor stage and their development during the complete flow breakdown and recovery. Rotating stall phenomena appear at the stability limit of a compressor and may constitute the origin of severe consequences on the whole engine. Therefore not only it must be accurately avoided, but also the increase in the stability margin is one of the primary objectives in the compressor design. In order to have a better understanding on the definition of the operating range obtained numerically, the experimental data are used as a reference and analyzed while the numerical simulations will be performed later on. In this part of the article, the facility used, the test section and the instrumentation are described, then the time averaged and the time resolved measurements related to the stall inception are presented. These are followed by the frequency analysis applied to both the stall inception and the transients. The behavior of the stage is then described.
The second part of the article presents the ongoing research about the comparison of different types of simulations with the experimental data. Steady, Nonlinear Harmonic (NLH) method and conventional unsteady computations are compared in terms of determination of global performance and detailed representation of the flow field. Given that the NLH requires the use of Spalart-Allmaras as turbulence model and a centered numerical scheme, the effect of these two parameters is evaluated first in a steady computation with respect to various turbulence models (k-ϵ, k-ω, k-ω SST, Baldwin-Lomax) and an upwind second order scheme. The representation of the performance map and the unsteady fluctuations are then presented.

2. Characterization of stall phenomena

2.1. Aerodynamic design

In an engine, the fan provides the core with a pressure ratio distribution skewed towards the hub. The booster has the function to counterbalance this effect, while not yielding a high pressure ratio. The new design technologies tend to increase the aerodynamic load, imposing high diffusion factors in the low radius region thus making hub critical stages.
The present booster is the first stage of the core and has been scaled to be adapted to the test section of the facility employed for the tests. A fixed stagger inlet guide vane row (IGV) is placed to simulate the spanwise flow distribution provided by the fan root. The rotor blades are characterized by a 0.84 hub/tip ratio and an inlet relative Mach number at the tip of approximately 0.8. The nominal rotational speed is 8750 rpm (100% Nn).

2.2. Experimental set-up

2.2.1. VKI-R4 test rig

The tests are performed in the VKI-R4 compressor rig, shown in Figures 1 and 2. It is a closed-loop configuration used for investigating high speed axial and radial compressors. A throttle valve allows the regulation of the mass flow while the inlet total temperature is maintained using water heat exchangers and the inlet total pressure is regulated by means of a control system connected to pressure and vacuum reservoirs. The shaft with a maximum rotational speed of 9000 rpm is driven by a 450 kW DC motor, via a 1:12 gearbox.

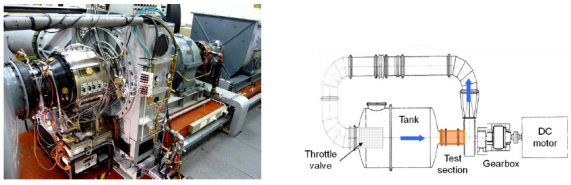

Figure 1: Photo and layout of the VKI-R4 compressor rig test section.

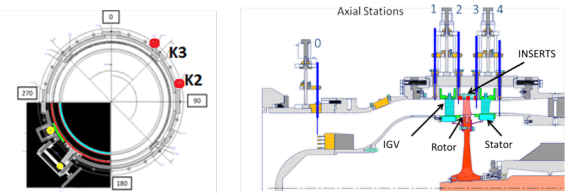

Figure 2: Circumferential and axial cross-section of the VKI-R4 compressor rig.

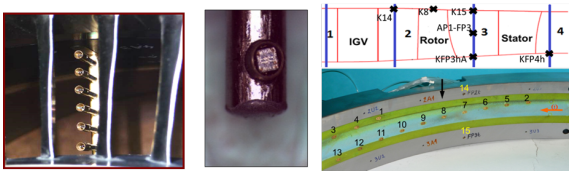

Figure 3: rakes, AP1-FP3 fast-response total pressure probe head and inserts in the casing

The test section, designed to represent the first LP stage of a high bypass ratio turbofan engine consists of an IGV row with 100 blades simulating the effects of a fan, a rotor row with 76 blades followed by a stator row of 100 vanes. Measurements are performed downstream the rotor at 8400 rpm corresponding to 96% of the nominal speed. The signal from an optical once-per-revolution sensor mounted on the shaft is recorded to be used in phase-locked and ensemble averages.

2.2.2. *Instrumentation, data acquisition and uncertainty*

Five axial locations, presented in Figure 2, allow acquisitions along radial traverses: far upstream the IGV (plane 0), at the IGV inlet (plane 1), at the rotor inlet (plane 2), at the rotor outlet (plane 3) and at the stator outlet (plane 4). Probe traverses are available at four circumferential positions (0 deg, 90 deg, 180 deg, 270 deg, Figure 2).
The focus of this study is the understanding of the stall phenomena appearing in the compressor stage considered, therefore both the global performance and the detailed topology of the flow are investigated. Rakes and static pressure taps located in plane 0 and plane 4 provide time averaged measurements of global quantities such as pressure ratio, mass flow and efficiency. Time resolved pressure measurements describe the topology of the flow field on the rotor casing, at the rotor outlet and at the stator outlet. The fast response probe utilized is located at the rotor outlet at midspan at 90 deg (see Figure 3).

2.2.3. *Steady instrumentation*

The steady measurements are sampled continuously in real-time during the experiments at 2 Hz allowing the monitoring of the machine and the evaluation of the global performance.
Each of the four rakes located in plane 0 and in plane 4 consists of six small Kiel heads each one containing a total pressure tap and a T-type thermocouple junction. The corresponding axial position is equipped also with static pressure taps at the hub and in the casing.
The uncertainty associated to the measurements is calculated with the ASME method (proposed by Dieck [2]) and the values are presented for a 95% confidence interval. The uncertainty values retrieved are 0.5 mbar and 0.7 K which result in a 0.00053 uncertainty on the pressure ratio.

2.2.4. *Unsteady instrumentation*

Fifteen piezo-resistive pressure transducers (see Figure 3) monitor the static pressure at the rotor casing by means of time-resolved measurements. These differential sensors have a range of 15 psi and a resonance frequency higher than 200 kHz. They are contained in a metallic insert and protected by a cavity which is limiting the bandwidth to 60 kHz.
The determination of the time resolved pressure levels in both the axial and the circumferential directions is fundamental for the detection of the stall cell(s). The sensors cover an arc of 42 deg (K2 and K3 represent the two extremes and are located respectively at 38 and 80 deg) and are equally spaced by one rotor pitch. The sensors are axially displaced between plane 2 and plane 3 as shown in Figure 3. The static pressure at the hub is retrieved in plane 3 and plane 4 by means of sensors located at 66 deg. The sensors are calibrated in situ by pressurizing the loop.
They are characterized by an uncertainty of 1.2 mbar, computed with the ASME method as for the steady instrumentation.
A fast response aerodynamic pressure probe (AP1-FP3, see Figure 3) is located at midspan at the rotor outlet at 90 deg. This is used together with the static pressure taps at the hub and in the casing to determine the size of the stall cell(s). The probe has an output voltage Vp proportional to the measured pressure and an output voltage Vs proportional to the measured temperature. The probe is characterized by a 3 mm

diameter stem and a flush mounted 25 psi absolute sensor which has a resonance frequency of around 300 kHz.
The probe presents a calibration uncertainty of 1.8 mbar.
All the acquisitions of the time resolved data are performed with a 16 bit data acquisition system for 10 s with a sampling frequency of 1MHz.

2.3. Stall inception

The stall inception behavior of the stage varies according to the rotational speed: at the highest rpm (100% Nn, 96% Nn) the stage abruptly enters into stall, at lower rpm (90% Nn, 85% Nn, 80% Nn) instabilities precede the flow breakdown (see Figure 6). The instabilities present different features at each rotational speed. The performance map, expressed in terms of both static-to-total and total-to-total pressure ratio (Figures 4 and 5), clearly shows this peculiarity of the machine investigated: in the higher speed curves the performance drops instantaneously after reaching the maximum pressure rise point on a speed line, while in the lower speed range the static-to-total pressure ratio still increases after reaching a point with a lower slope. Figures 4 and 5 report the performance map obtained with the steady instrumentation described in the previous paragraph.
All the curves are obtained by continuously closing the throttling valve with slow motion and reopening it instantaneously after the compressor enters into stall.
Different factors are representative of the stall inception: the drop of the static to total pressure ratio, the presence of high amplitude fluctuations in the unsteady signals, the temperature rise in both the averaged value of the rakes at the stator outlet and in the Vs signal provided by the probe in plane 3.

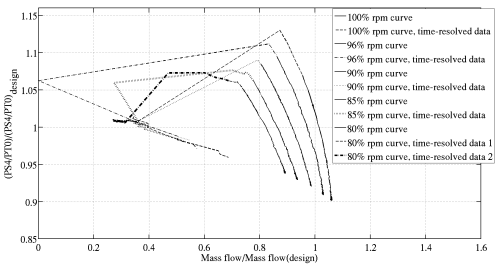

Figure 4: Static to total performance map

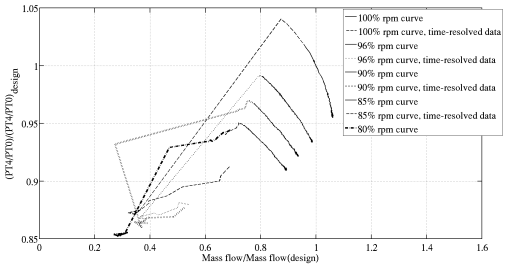

Figure 5: Total to total performance map

Figure 6 presents the time resolved static pressure signal on the casing rotor inlet for various rotational speeds, the raw signal is compared to its low pass filtered component at 50 Hz. The filtering frequency has been chosen to focus on the stall cell phenomena after the frequency analysis has been performed. Instabilities are not visible in any pressure signals recorded at 96% and 100% Nn (both filtered and unfiltered), therefore it is possible to conclude that the compressor stage presents an abrupt stall behavior. These cases are shown in Figure 6, case a and case b.
At 90% Nn fluctuations appear modulated by a lower frequency when the pressure rise curve presents a less negative slope (between points 1 and 2 in Figure 6, case c). The instabilities have a period of approximately five revolutions. The closing of the throttling valve has the effect of starting the fully developed stall transient.
At 85% Nn the fluctuations arise at first as in the case at 90% Nn (points 1 and 2 in Figure 6, case d), then, while closing the throttling valve, the low frequency component disappears and the oscillations increase in amplitude (between points 2 and 3) until the drop of the pressure ratio (point 3). The slope of the pressure rise curve always presents negative values before the stall inception.
At 80% Nn various phenomena are observed while closing the throttling valve. The link between the slope of the pressure rise curve and the oscillations is highlighted by presenting two consecutive parts of the transient: Figure 6, case e and case f. In point 1 (Figure 6, case e) the slope presents lower negative values and the instabilities appear as in the previous case (85% Nn, Figure 6, case d). The progressive reduction of the mass flow corresponds in this case to a decrease in the amplitude of the fluctuations (between points 2 and 3 in Figure 6, case f) before the stage enters into stall.
Figure 7 shows a zoom of the transient recorded at

85% Nn (Figure 6, case d) with different fast response sensors. The instabilities are extended to the full span: their presence is denoted in the pressure signals on the casing, at the hub and at midspan (Figure 7, K15, KFP3hA, AP1-FP3). The fluctuations appear simultaneously in the signals at the rotor inlet and at the stator outlet (Figure 7, K14, KFP4h), therefore occupy the whole stage. The oscillations present also a significant circumferential extension: the pressure varies with a phase shift in the two sensors which are more circumferentially apart (Figure 7, K2 and K3). The stall cell extension is addressed in the last paragraph of this article.

2.4. Discussion on the nature of the instabilities

The nature of the fluctuations appearing during the stall inception requires further discussion. The two "classical" stall inception patterns, shown in the contribution of Day (1998), have been considered at first: spikes and modal waves.
The hypothesis of spikes has been immediately discarded: the fluctuations cover the whole span. The pressure signals recorded at the rotor outlet at the hub, at the shroud and at midspan, presented in Figure 7 together with those at the rotor inlet, midchord and stator outlet, show indeed the presence of synchronized instabilities, while the spikes would be confined to the tip region. Oscillations cover also the whole stage: the time resolved pressure signals recorded at the rotor inlet and at the stator outlet in a corresponding circumferential position are in phase.
On the other hand the length scale of the instabilities may lead to consider them as modal waves: as explained in Day et al. [3] a typical modal wave period is between 3 and 5 rotor revolutions. The oscillations though never occur at the maximum of the pressure rise curve but in a point of less negative slope. This hypothesis is therefore rejected as well. Several cases of stall inception which are not represented by the "classical" patterns are presented in literature. Mailach et al. [4] show a case of rotating instabilities appearing on the pressure rise curve before modal waves arise at the zero slope. Courtiade and Ottavy [5] observed rotating instabilities with a period lower than a revolution localized in the tip region of the rotor inlet of the third stage of a three stage compressor. The analysis of the time resolved signal at various span locations at the rotor outlet may provide a better understanding of the phenomena linked to the rotating instabilities.

Figures 8 and 9 present the evolution along the pressure rise curve at 85% Nn employing the pressure signals at the rotor outlet at midspan, at the hub and on the casing from the choke operating point until reaching the flow breakdown. The choke condition is shown in Figure 8 (left) in terms of ensemble average based on the rotor revolution frequency, detected by a trigger placed on the shaft, and in which 142 revolutions are considered. This acquisition has been obtained by recording the transient from a point in between points 2 and 3 of Figure 6, case d and the reattachment to the pressure rise curve at choke condition due to the opening of the throttling valve. The near stall condition is also presented (Figure 8, right) in terms of ensemble average based on the rotor revolution frequency and for which an equal amount of revolutions are considered. The average has been applied on the signals recorded before point 1 in Figure 6, case d. On the other hand the instabilities and the stall cell are presented in terms of raw signal.
The blade passages are visible in the ensemble average both at choke and at near stall condition. At near stall condition though the wakes appear to occupy a larger part of the blade passage than at choke. This effect is more evident in the hub region and at midspan than on the casing. In the rotating instabilities (part A of Figure 7) this effect is amplified: the raw signals show the blade passages at the tip, though affected by the presence of the instability, but not at the hub (see Figure 10, left). In the fully developed cell the blade passages are not observed at any span location (Figure 10, right).
From this analysis it appears that the flow starts to separate at near stall condition in the hub region partially blocking the blade passage. The separation then extends towards the casing when the instabilities arise creating a full span rotating stall cell of smaller circumferential extension than the fully developed one, while the hub region separates along the whole circumference. A further closing of the throttling valve induces a full span stall cell occupying a larger portion of the annulus. The signals representing the instabilities at the three span locations show a fluctuating component as in the case of the fully developed cell, with a lower amplitude though (Figure 9). Therefore it may be hypothesized that the instabilities constitute full span rotating stall cells of smaller size with respect to those appearing in the transient.

The analysis of the instabilities has been carried out utilizing the Fast Fourier transformation and focusing in the range of the blade passing frequency at 85%Nn. When the instabilities arise the blade passing

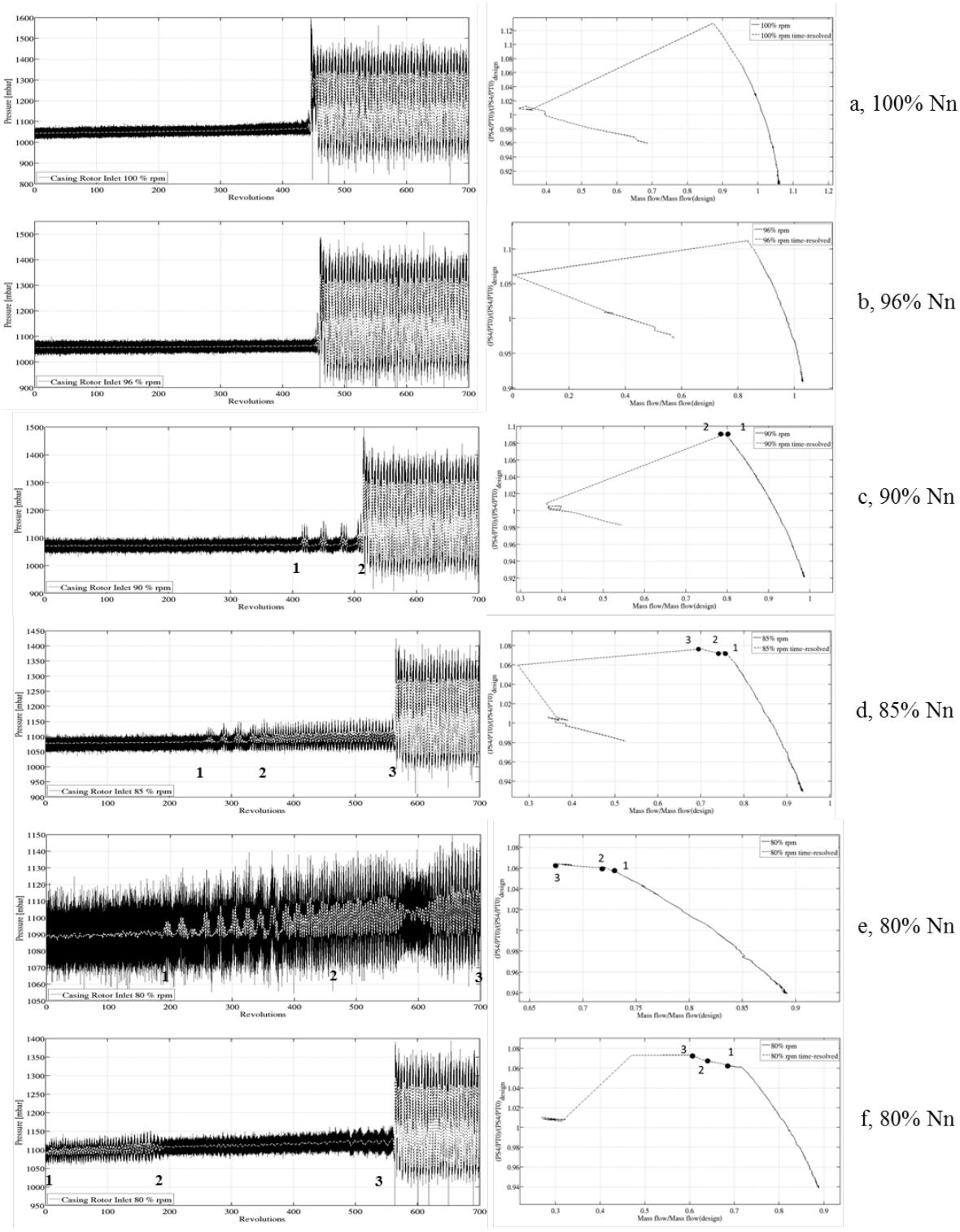

Figure 6: Time-resolved pressure signal at the casing rotor inlet, static-to-total performance map

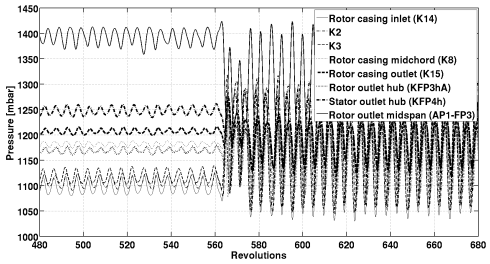

Figure 7: time resolved signals (low-pass filtered at 50 Hz) at 85% Nn

frequency appears as a high peak. The amplitude of the peak is linked to the quantity measured: the total pressure signal retrieved by the probe will provide a higher amplitude peak than the static pressure signal retrieved by the sensors at the casing and the hub.
The blade passing frequency appears as a high peak at midspan and on the casing when the instabilities arise (part A of Figure 7). On the other hand at the hub it is more distributed and presents a lower amplitude (see Figure 11). During the transient, when the rotating cell is fully developed, the peak at the hub almost disappears (see Figure 11, right).
The instabilities fluctuate with a slightly higher frequency than the one of the fully developed stall cell at all the span locations, they appear therefore as a rotating pattern (a more detailed explanation is provided in the next section). This peculiarity is visible in the raw signal, presented in Figure 9 only at the hub and at midspan for clarity reasons, and in the corresponding low pass filtered signal, shown in Figure 7 which presents the low pass filtered signal at 50 Hz before and during the stall inception (part A and part B).
At 80% Nn the fluctuations reduce their amplitude before the stall inception, it appears therefore that the performance curve has a first unstable zone followed by a stable one. A similar case has been presented in N. Diez et al. [6] on a centrifugal compressor in which a first unstable zone exists due to rotating stall, followed by a second stable zone characterized by a recirculation area towards the casing.

2.5. Frequency analysis

The frequency analysis has been performed utilizing both a Fast-Fourier transformation and a wavelet transformation. All the signals considered in the frequency analysis are low pass filtered at 50 Hz. The cutting frequency has been chosen in order to focus on the stall phenomena and to distinguish the stall inception features from the flow breakdown, which are both appearing in the low frequency range. The comparison between the FFT of the filtered and the unfiltered signal has been utilized to determine the cutting frequency.
Given its time-frequency analysis capability, the wavelet transformation is a suitable tool to detect the triggering and the developing of flow instabilities such as those appearing in a stall transient (Lin et al. [7]). The most appropriate mother wavelet was found to be the Morlet wavelet with a centering frequency of 1 Hz and a time window of 0.001 s since it provides the best correlation with the signal. The range of frequency analyzed is from 2 to 60 Hz.
In the case examined the wavelet transformation points out a constant number of stall cells during the transient at all the rotational speeds: a splitting into a higher number of cells would correspond to a sudden increase in frequency. The comparison between the wavelet transformation and the corresponding time-resolved acquisition at the rotor inlet casing (K14) indicates that the stall cell reduces in size along the transient as the throttling valve is reopening. An example is shown in Figure 12 (case a) which represents the case at 100% Nn.
It is also shown that the beginning of the signature of the instabilities always has origin from a 5 Hz component for all the rotational speeds. This low frequency appears as a sharp peak and arises around the blade passing frequency when the instabilities start. As pointed out in Hellmich et al. [8] this may be due to the acoustic resonance of the facility. The calculation of the Helmholtz frequency of the facility provides a resonance frequency f $\approx$ 5 Hz. Therefore the triggering of the instabilities might be attributed to acoustic waves related to the facility itself. Courtiade, Ottavy [5] also retrieved an influence of acoustic waves in a case of rotating instabilities.
The fluctuations are triggered by a frequency of approximately 5 Hz. The instabilities denote at first a higher frequency than the one of the rotating stall cell on the corresponding isospeed curve and a modulation with a 5 Hz component, then the behavior of the machine varies with the rotational speed. At 90% Nn the stage enters into stall after showing this pattern (Figure 12, case b). At 85% Nn the 5 Hz component disappears and the fluctuations show a higher frequency than the one of the stall cell which decreases until reaching a lower frequency than the one of the stall cell (Figure 12, case c). The stage then enters into stall. At 80% Nn the compressor behaves at first as at 85% Nn (Figure 12, case d, left) but presents a time interval (corresponding to a more negative slope

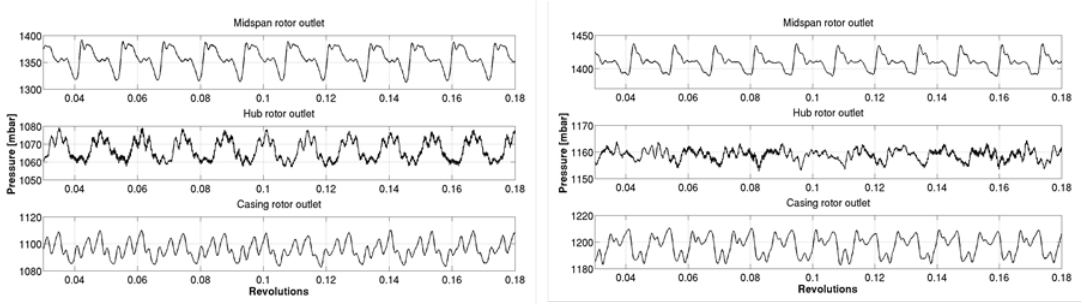

Figure 8: ensemble average of the signal at hub, tip and midspan in choke (left) and near stall (right) condition at 85% Nn

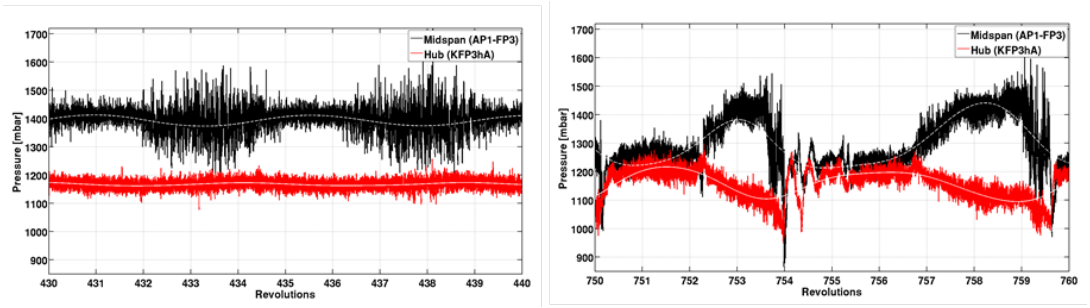

Figure 9: raw signal at hub and midspan corresponding to part A and part B of Figure 7

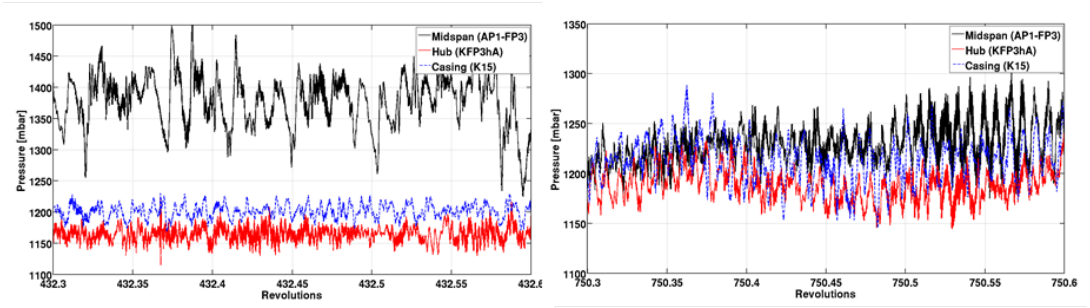

Figure 10: zooms on the rotating instability at hub and midspan corresponding to part A and part B of Figure 7

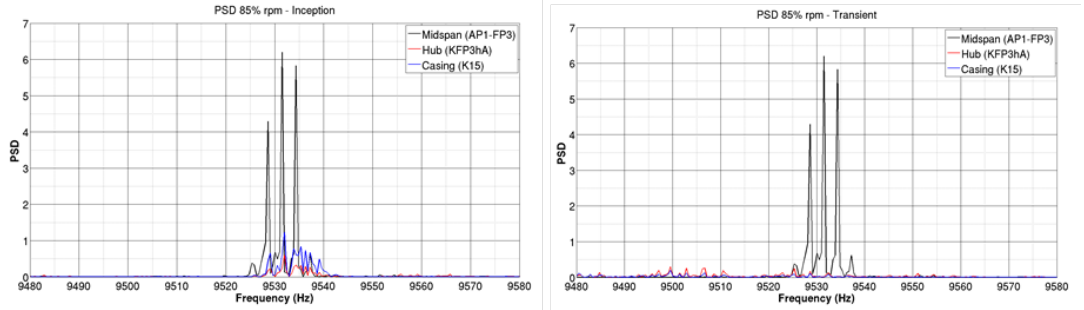

Figure 11: FFT around the blade passing frequency corresponding to part A and part B of Figure 7

of the pressure rise curve) in which the fluctuations disappear before the stall inception starts (Figure 12, case d, right).

2.6. Stall transient

The frequency analysis presented in the previous section points out that the number of stall cells remains constant during the transient. The determination of the number of stall cells, rotating speed and size is presented in this part of the article. The number of stall cells is retrieved with the methodology described by Levy et al. [9]. The pressure signals corresponding to different circumferential locations (not equally spaced in the machine to enable the detection of the stall cells, in case their number is a multiple of the number of sensors) are modeled as sine functions: $p = Bsin(\omega_{OSC}t+\phi)$. The pressure fluctuations in time of the low pass filtered signal retrieved during the stall transient are shifted in space by the angular distance between the inserts considered. The oscillations depend also on the number of stall cells appearing. The number of stall cells appearing in the transient can therefore be determined plotting the signals of two inserts separated by a distance proportional to the angle between them and repeating the first signal, as shown in Figure 13. The signals considered for the calculation of the number of cells are those related to the sensors on the casing that are circumferentially most separated and axially less distant (K2, K3, which are located at the rotor inlet, respectively at 38 deg and 80 deg).
The peaks of the various signals correspond to the same stall cell(s) and are linked by a line of constant phase. Therefore the number of stall cells can be determined: the line of constant phase follows the same stall cell through the different sensors. The time of the complete rotation of the stall cell t_{CR} is defined by the crossing of the constant phase line and the pressure signal of the sensor at 0 deg and 360 deg. The time of a pressure fluctuation is defined as the time between two maxima of the signal. The number of stall cells is determined as: $n = t_{CR}/t_{OSC}$. In all the cases examined, the number of cells has been found to be 1.

Having defined the number of stall cells and the frequency of one pressure fluctuation f_{OSC}, the frequency of the cell rotation is calculated as: $f_{CR} = f_{OSC}/n$ The value obtained corresponds to the peak retrieved in the frequency analysis. This confirms the presence of one stall cell as hypothesized in the previous section. The stall cell has always been found to rotate at approximately 20% of the rotational speed of the machine in all the tests performed.
The percentage circumferential extension of the cell is calculated as: $\phi_{covered} = \Delta t_c ell * f_C R * 100$ where $\Delta t_c ell$ denotes the period of the fluctuation between two maxima, f_{CR} is the frequency of the stall cell. A summary of the values retrieved in all the acquisitions is presented in Table 1, together with the percentage speed of the stall cell and the perturbation frequency to rotor frequency. The latter quantities are approximately constant for all the rotational speeds investigated.
The cell is a full span stall cell: the fluctuations observed in Figure 7 (part B) are extending from the hub to the shroud. The cell occupies the stage from inlet to outlet as shown in Figure 7. These features are also present in the instabilities occurring before the stall inception (Figure 7, part A).

3. Numerical simulations

3.1. Numerical set-up

3.1.1. Geometrical model and mesh

Steady and NLH computations

A complete description of the geometrical model is provided in [10]. The mesh used for the steady and the NLH computations is also presented in [10].

Unsteady computations

The unsteady computation is performed with the Domain Scaling Method. This method allows the use of a reduced domain, with a consequently lower computational time, provided an equal pitch at the interface of two blade rows. The one and a half compressor stage has 100 blades on the IGV and the stator and 76 on the rotor. The domain considered in the simulation consists of 4 IGV blades, 3 rotor blades and 4 stator blades. A blade has indeed been removed on the rotor raw in order to respect the equality condition at the interface.

The mesh employed has 11 million elements. The quality of the mesh is guaranteed by a criterion of minimum skewness of 25, maximum expansion ratio of 1.8 and aspect ratio of 4000. The first cell size is of 1 μ m, ensuring a $Y+ < 1$.

3.1.2. Boundary conditions

The simulations are performed with Numeca FINE/Turbo. The design operating point at 100% rpm is considered in the comparison. The boundary conditions imposed in the unsteady computation are:

- the rotational speed, which at 100% rpm corresponds to 8748 rpm

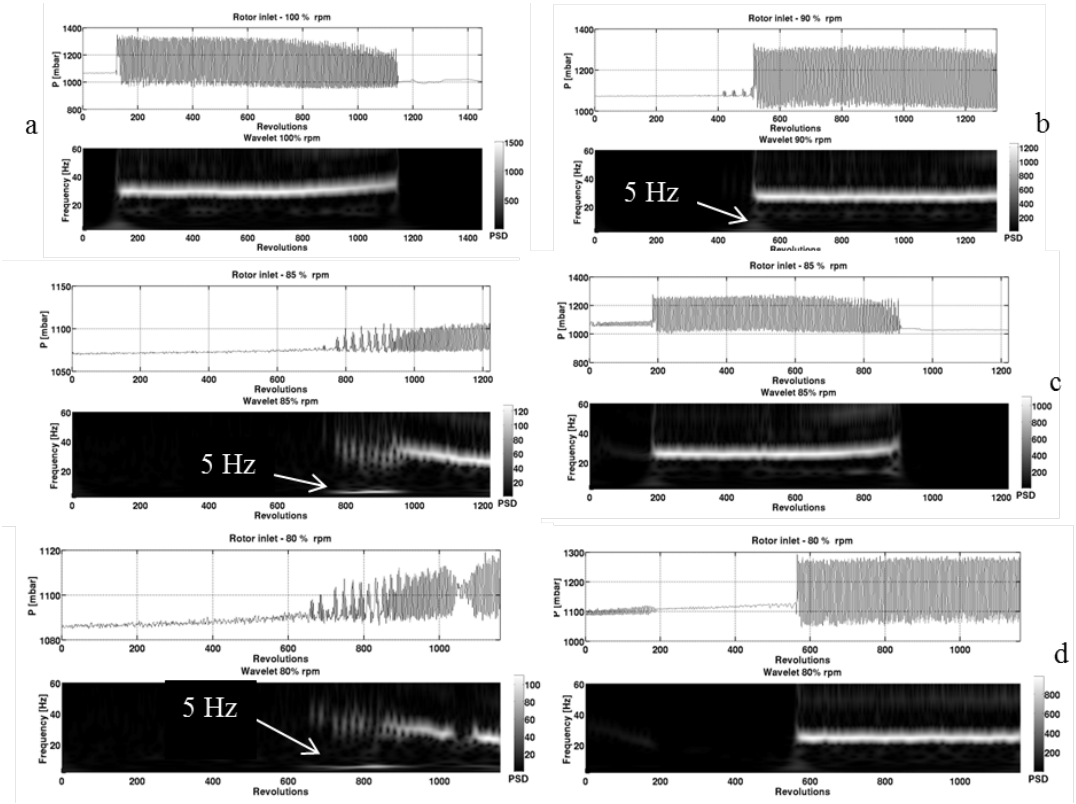

Figure 12: Time-resolved signals (low pass filtered at 50Hz) and corresponding wavelet transformation

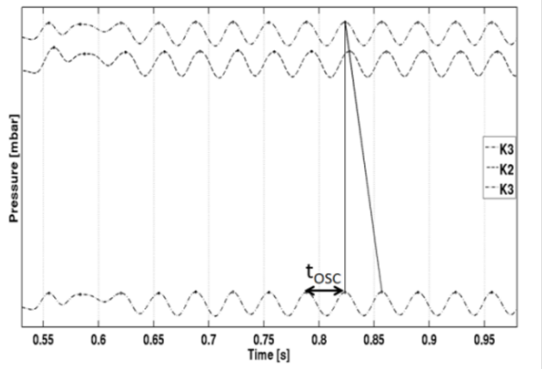

% Rpm	f_{CR} FFT	f_{CR} Levy	φ %	ω %	f_{CR}/f_{ROT}
100%	29.45	29.05	49.86	20.78	0.20192
96%	28.45	28.16	49.87	21.01	0.203214
90%	26.94	25.86	49.74	20.62	0.205257
85%	25.81	24.65	49.49	21.24	0.208212
80%	24.80	21.93	50.96	21.30	0.212584

Figure 13: graphic method to determine the number of cells, Table 1

- the inlet total pressure spanwise distribution derived from the experimental results
- the inlet total temperature spanwise distribution derived from the experimental results
- the inlet tangential velocity component $V_t/V_z = 0$
- the inlet radial velocity component $V_r/V_z = 0$
- the inlet turbulent viscosity spanwise distribution in the case of Spalart-Allmaras model, k and ϵ in case of k-ϵ and k-ω SST, k and ω in case of k-ω
- the outlet static pressure derived from the experimental results in a given radial location and the radial equilibrium

In the steady computations equal boundary conditions are imposed except regarding the inlet turbulent viscosity, for which they are varying according to the turbulence model used.

3.1.3. Spatial discretization scheme

A centered scheme is employed in the unsteady computation in order to maintain a higher number of parameters equal with respect to the steady and the NLH computations. A comparison between the results obtained in the steady case with a centered and an upwind scheme is performed.

3.2. Reference experimental data

The experimental data employed for the calculation of the performance of the stage are time averaged measurements performed at the inlet and at the outlet of the machine. A total pressure pneumatic probe and a thermocouple are traversed along 23 radial positions in plane 1 and 4 (see Figure 2, right).
The data describing the total pressure topology at the stator outlet are obtained by subsequently performing a circumferential traverse along 1.5 stator pitch and a radial traverse along 23 radial locations.

3.3. Effect of the turbulence model and the spatial discretization scheme

The effect of the turbulence model is studied with respect to the representation of the performance map, total pressure and eddy viscosity ratio. The representation of these quantities is also investigated for the understanding of the spatial discretization scheme effect.
Figure 14 shows the performance map retrieved with

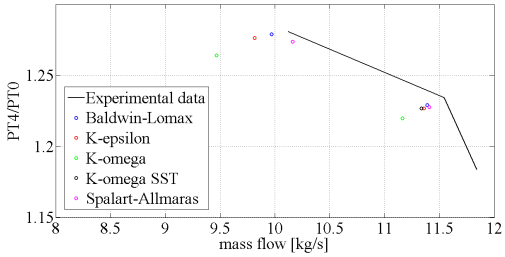

Figure 14: Influence of the turbulence model on the prediction of the global performances

steady computations using various turbulence models at 100% rpm, which are compared to the corresponding experimental data. The computation of mass flow and pressure ratio is performed also for the simulations by applying the experimental post-processing technique, in such a way to have an appropriate comparison with respect to the reference. The various quantities have been extracted in the location of the measurements and averaged in the pitchwise direction in order to obtain the mean spanwise distribution.

The inlet total pressure spanwise distribution is equal for all the cases because is imposed as boundary condition from the experimental data, while the distribution at the stator outlet (Figure 15) shows that the numerical simulations provide a more resolved representation of the boundary layer than the experiments. This may explain the reason of the lower mass flow and pressure ratio predicted by the computations.

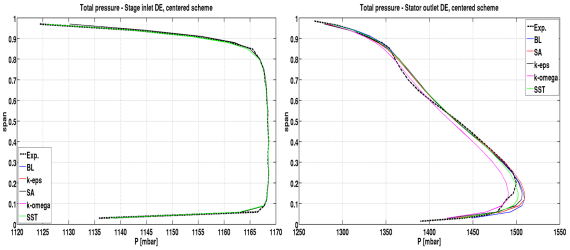

Figure 15: Influence of the turbulence model on the spanwise total pressure distribution at the stage inlet and outlet

The k-ω model presents the most pessimistic prediction in terms of both pressure ratio and mass flow: in the design condition the error on the mass flow is of the order of magnitude of 3%, on the pressure ratio of 1.2%. On the other hand k-ϵ, Baldwin Lomax and Spalart-Allmaras present a more optimistic prediction: the error on the mass flow prediction obtained with Spalart-Allmaras is 1.15%, the one on the pressure ratio 0.5%. A similar trend is obtained in the near

stall condition.

The pitchwise total pressure distribution at 50% of the span at the stator outlet shows that in all the cases the uncertainty on the experimental data does not contain the result obtained numerically. The mixing plane approach employed in the steady computations averages out the rotor wake, which appears in the experimental data as a pressure deficit.

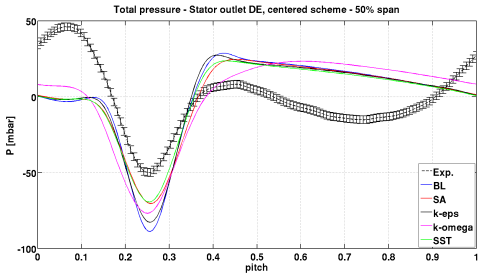

Figure 16: Influence of the turbulence model on the pitchwise total pressure distribution at the stator outlet at 50% of the span

In order to have a better understanding on the representation of the turbulence parameters, the comparison of the Eddy Viscosity Ratio distributions at the stage outlet is presented in Figure 20. In all the profiles it is possible to distinguish the location of the wake which corresponds to an increase in the distribution. The exception is represented by the Baldwin-Lomax model, which imposes $\mu_t = 0$ in this case ([11]).

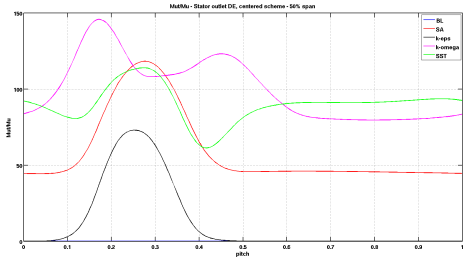

Figure 17: Influence of the turbulence model on the Eddy Viscosity Ratio distribution at the stator outlet at 50% of the span

The effect of the spatial discretization scheme is investigated through the same parameters considered in the effect of the turbulence model and reported in Figures 18, 19, 20 in the case of the Spalart-Allmaras turbulence model. Regarding the representation of the global performance, the mass flow and pressure ratio predictions present a difference with respect to the centered one of respectively 1.16% and 0.55%. The pitchwise distributions of total pressure and Eddy Viscosity Ratio also do not present significant discrepancies with respect to the centered scheme.

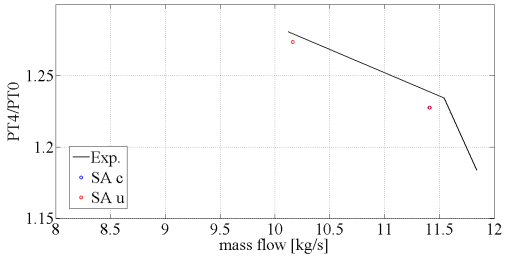

Figure 18: Influence of the spatial discretization scheme on the prediction of the global performances

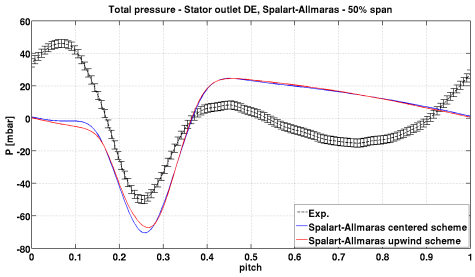

Figure 19: Influence of the spatial discretization scheme on the total pressure fluctuations at the stator outlet at 50% of the span

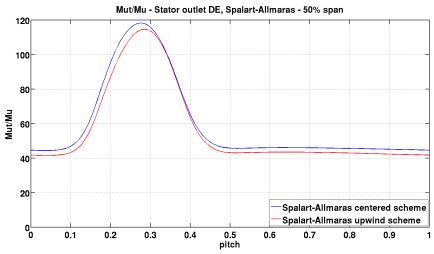

Figure 20: Influence of the spatial discretization scheme on the Eddy Viscosity Ratio distribution at the stator outlet at 50% of the span

3.4. Effect of the simulation type

The effect of the simulation type is presented with respect to the representation of the global performances and the total pressure fluctuations at the stator outlet.

Figure 21 presents the global performance obtained with the steady and the unsteady cases. The steady and the NLH case provide an equal average value at

the different span locations, therefore the mass flow and pressure ratio overlap. On the other hand the unsteady computation yields lower values of both the mass flow and the pressure ratio. The coarser mesh refinement influences the representation of the various quantities with a less accurate representation, therefore the difference in mass flow of 1.5% and in pressure ratio of 0.5% with respect to the experimental data.

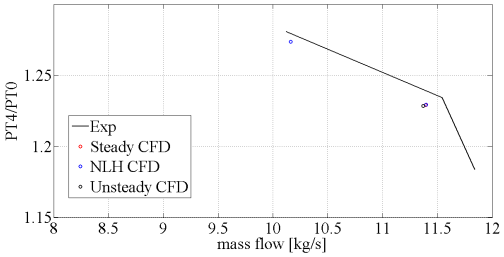

Figure 21: Influence of the simulation type on the prediction of the global performances

On the other hand the unsteady computation provides a more accurate representation of the flow structures. Figures 22 and 23 show the total pressure fluctuations around the pitchwise average at the stator outlet. The pressure deficit due to the rotor wake is captured with both the NLH and the unsteady computations. The shape of the wake retrieved with the unsteady simulation is however more accurate than in the other two cases considered.

The global performance prediction of the unsteady computation results to be affected by a coarser mesh with respect to the steady and the NLH simulations. This is due to a computational time limitation: a more refined mesh would significantly increase the already high CPU time required by the unsteady computation. On the other hand a computation of this kind is able to provide a more accurate representation of the unsteadiness of the flow field, which in this case is presented in terms of total pressure fluctuations around the pitchwise average computed at each span location at the stator outlet.

4. Conclusions

The article presents the experimental characterization of rotating stall phenomena appearing in a high speed low pressure axial compressor stage.
The machine exhibits different stall inception behaviors at different rotational speeds: at higher speed it

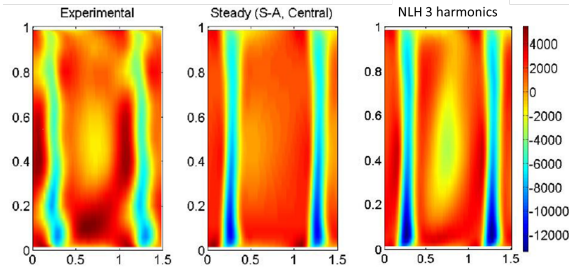

Figure 22: Influence of the simulation type on the total pressure fluctuations at the stator outlet (experimental data, steady simulation, NLH simulation)

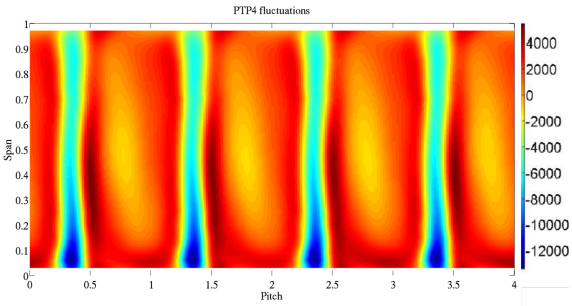

Figure 23: Influence of the simulation type on the total pressure fluctuations at the stator outlet (unsteady simulation)

abruptly enters into stall, at lower speed instabilities dominate the stall inception process.
The instabilities observed are not represented by any of the ”classical” cases shown in the contribution of Day (1998). Spikes are confined to the tip region while the instabilities occupy the whole span and cover the whole stage, modal waves occur at the maximum of the pressure rise curve, while the instabilities appear on a negative slope point. The instabilities are characterized by a period of approximately four revolutions and cover a considerable circumferential extension (as appears from the phase shift between the signals K2 and K3 presented in Figure 7, part A).
The hypothesis of the stall inception mechanism is believed to start with a hub separation in the near stall condition, which extends towards the tip while closing the throttling valve and creating a full span cell of smaller size with respect to the fully developed one, while the hub region separates around the whole annulus. The case at 85% Nn has been thoroughly examined while the cases at 90 and 80 Nn require further investigations.
A further closing of the throttling valve generates the flow breakdown and the appearance of a full span stall cell. The methodology presented by Levy has been

applied to determine the number of stall cells, resulting in one stall cell for all the rotational speeds investigated. This result is consistent with the frequency analysis. The stall cell occupies almost 50% of the annulus and travels at around 20% of the rotational speed.

This article presents also the ongoing research on the comparison between the various type of simulations and the experimental data.

Spalart-Allmaras, despite being a one equation turbulence model, provides comparable predictions with respect to two equation models such as k-ϵ and k-ω SST. The upwind scheme combined with the Spalart-Allmaras turbulence model yields a very small difference in the mass flow and the pressure ratio predictions with respect to the centered scheme. The effect of the spatial discretization scheme results therefore to be negligible in the determination of the global peformance.

Unsteady computations show higher accuracy in the representation of the flow field with respect to NLH and steady cases. Further investigation is though required for the understanding of their potentialities and the simulations will be exploited for the analysis of the flow field and the investigation on the losses distribution.

The near stall operating point will also be considered in this work. The objective is to investigate the influence of the different parameters in the stability limits in order to be able to provide a tool for a better prediction of the stall margin. To this aim unsteady computations performed with both a reduced domain and a full annulus will be compared to experimental data in the near stall condition and in the stall inception process.

References

[1] J. Kurzke, Aeroengine design: from state of art of turbofans towards innovative architectures Preliminary design, LS 2013-04, von Karman Institute for Fluid Dynamics (2013).

[2] R. H. Dieck, Measurement uncertainties methods and applications, ISA, Research Triangle Park, 2007.

[3] T.R. Camp and I. Day, A study of spike and modal stall phenomena in a low speed axial compressor, Journal of Turbomachinery 120 (3) (1998) 393–401.

[4] R. Mailach, I. Lehmann, K. Vogeler, Rotating Instabilities in an Axial Compressor Originating From the Fluctuating Blade Tip Vortex, Journal of Turbomachinery 123 (2008) 453–463.

[5] N. Courtiade and X. Ottavy, Experimental Study of Surge Precursors in a High-speed Multistage Compressor, Journal of Turbomachinery 13 (6).

[6] L. A. S. d. G. L. T. N.G. Diez, J.P.M. Smeulers, Predictability of rotating stall and surge in a centrifugal compressor stage with dynamic simulations, in: Proceedings of the ASME Turbo Expo, ASME GT2014-26712, Dusseldorf, Germany, 2014.

[7] F. Lin, J. Chen, M. Li, Wavelet analysis of rotor-tip disturbances in an axial flow compressor, Journal of Propulsion and Power 20 (2).

[8] B. Hellmich, J. R. Seume, Causes of Acoustic Resonance in a High-Speed Axial Compressor, Journal of Turbomachinery 130 (3).

[9] J. P. Y. Levy, The number of stall cells during rotating stall, in: Proceedings of the ASME Turbo Expo, ASME GT2003-38221, Atlanta, USA, 2003.

[10] N. Pallag, Unsteady numerical analysis of the performance and stability of a low pressure axial compressor, PR 2014-22, von Karman Institute for Fluid Dynamics (2013).

[11] B.S. Baldwin, H. Lomax, Thin layer approximation and algebraic model for separated turbulent flows, AIAAr 78-0257.

Determination and Modeling of the Aero-Thermal Behaviour of a Cooling Channel

Gian Luca Gori

Turbomachinery and Propulsion Department, von Karman Institute for Fluid Dynamics, Belgium, gian.luca.gori@vki.ac.be

Supervisor: Tony Arts

Professor, Head of the Turbomachinery and Propulsion Department, von Karman Institute for Fluid Dynamics, Belgium, arts@vki.ac.be

Abstract

Internal Cooling technology for Gas Turbines, although supported by wide literature, still present possible important improvements. The classical CFD codes, based on constant Pr_t and isotropic turbulence, present a limited fidelity for the convective heat transfer prediction (at best 10-15%). A direct contribution to the causes of the low liability will be given by high detailed and high quality experimental data.

Keywords: turbomachinery, convective heat transfer, internal cooling

1. Introduction

The present research on cooling channels focuses on an aeronautical application (gas turbine), but is of definite interest to many other fields of engineering (oil industry, automotive, nuclear environments). The performance, in terms of thermal efficiency and specific power of a gas turbine cycle, increases with the Turbine Inlet Temperature (TIT). The limits are set by the blades and endwalls material resistance against thermal and mechanical loads. The lifetime of these components increases using efficient cooling techniques, cutting down the high costs for parts replacements. A major contribution to the heat extraction is given by forced convection in internal passages (Fig. 1).

The main objective of internal cooling channels is to maximize the wall heat transfer while keeping the channel pressure drop as low as possible. Initially designed with smooth walls, their surface has rapidly been equipped with various obstacles to increase the thermal exchange area and the local mixing. The resulting flow field is strongly 3D and unsteady; it becomes even more heterogeneous when the channel is put into rotation (rotor blades application). The strong assumptions of isotropic turbulence and constant Pr_t limit the accuracy of the heat transfer prediction (at best 10-15%) by CFD. The lack of experimental data due to the complexity and the availability of representative facilities, certainly, does not help for numerical improvements. Further limitations are set by the investigated geometries, far from the realistic cases, and by the flow conditions which do not cover the entire operating range. The present research wants to contribute at providing high quality and high resolu-

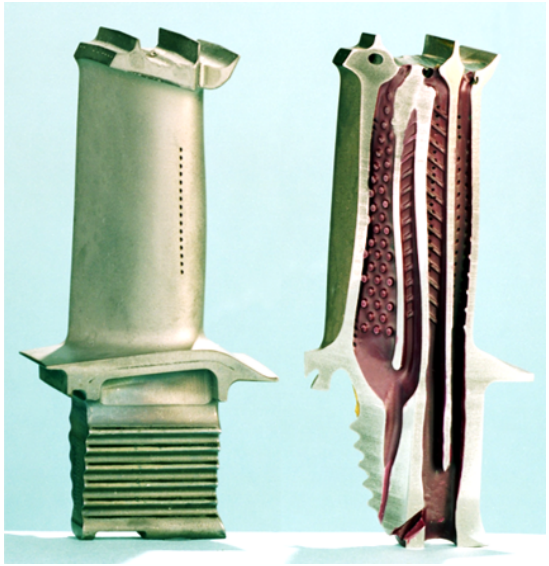

Figure 1: An air-cooled HP turbine blade and its cross-section.

tion experimental data for more representative configurations and operating conditions. Unlike most of the investigations available in literature, not only the wall heat transfer and velocity fields, but also the flow temperature distribution will be object of this experimental study. Although for velocity and surface heat transfer measurements, Particle Image Velocimetry (PIV) and Liquid Crystal Thermography (LCT) are already consolidated and largely used techniques, a few Cold Wire measurements show to affect the flow field [1]. Therefore, Laser-Induced Fluorescence (LIF) has been selected for two dimensional temperature measurements, as it is a non-intrusive optical approach. The technique is a spectroscopic method based on the spontaneous emission of molecules after excitation by a laser pulse. Never applied yet for internal cooling research so far, it will need to be developed for this specific application. Acetone vapor will be used as the fluorescent dye for high signal images as well as its low toxicity and low cost [2]. The absorption between 200 and 350 nm has been shown by Lozano [3] and Thurber [4] whereas the emission occurs between 350 and 550 nm [5]. The investigation will be carried out for a well-mixed acetone-air flow. The corresponding *Pr* variations deviate at most by 5% from the real operating one for an acetone molar concentration below 15%. The two-color LIF technique will be used to avoid a concentration dependence on the measurement output [6].

2. Experimental set-up

The equipment for the measurement set-up is basically composed by a pulsed UV laser, a test section and two CCD cameras. High temperature sensitivity is ensured by a low excitation wavelength (248 nm or 266 nm). The former has a higher dependence on temperature, however, it is characterized by about half the absorption cross-section than the one at 266 nm excitation wavelength. High quantum efficiency detectors are required for the specific emission bandwidth. Further, ref. [6] suggests cameras with low noise and high dynamic range and Sakakibara and Adrian [7] underlined the fact that the major source of temperature uncertainty in two-color PLIF is given by the cameras noise. The test section design will take into account constraints given by the optical accesses for the two cameras and the laser excitation. Thus, it will be equipped by glass and UV quality fused silica or quartz glass windows. The investigated geometry will be the one studied in [8] for the already available heat transfer and aerodynamic experimental data as well as some CFD computations.

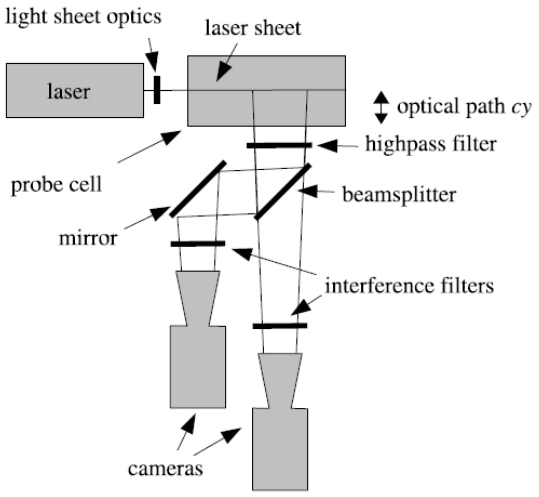

Figure 2: Calibration set-up used for two-color PLIF [7].

A calibration at different temperatures is needed for the measurement campaign. Images were taken for a static reference cell in a constant temperature (monitored by one or more thermocouples) and concentration ambience [9] [10] [7]. A possible calibration set-up is shown in [9] (Fig. 2). The laser sheet is created through a series of lenses. The optical path lines of the two cameras are perpendicular to the plane of measurement. The light ray is split between the two detectors positioned one next to the other. A possible alternative can be represented by the second camera positioned on the opposite side of the probe cell. In this way the LIF emission intensity has not to be split but may be affected by concentration variations along the laser thickness and two optical accesses are required. The two cameras will be provided with some chromatic filters for the maximum temperature sensitivity following the approach in [10]. For the final set-up the probe cell will be replaced by the cooling channel test section.

3. Conclusion

Temperature measurements will be taken in addition to the already available flow and heat transfer fields in a canonical configuration of a cooling channel for a more complete phenomena analysis. The major advantage of them, however, will be to be able to provide high reliable quantitative information of temperature fluctuations for thermal stress modeling.

Even more challenging, the turbulent heat transport term $\overline{v'T'}$, required for the determination of the thermal diffusivity, can be obtained by coupling LIF and PIV measurements. The final output will be a distribution of Pr_t. Measurements will first be conducted in static conditions for canonical configurations. The following step, instead, will extend the study to a realistic geometry covering the whole operating range of such apparatus in static and rotating conditions. In summary, the present investigation will cope with the issues on heat transfer prediction by looking directly at the major causes of the numerical and experimental data discrepancies. The aerodynamic and thermal analysis will provide a physical explanation of the complex phenomena. Finally, the high quality and high resolution data will represent a suitable tool for CFD codes validation and modeling improvements.

Acknowledgments

The funding of this PhD research project through a FRIA grant, delivered by the Fonds de la Recherche Scientifique (FNRS), is gratefully acknowledged.

References

[1] T. Arts, M. T. Abad-Lozano, Y. Kinoue and S. Pierret, The Unsteady Temperature Field in a Turbine Blade Cooling Channel, no. RTO Symposium, Advanced Flow Managment, Loen, Norway, 2001.

[2] M. C. Thurber, F. Grisch, B. J. Kirby and M. Votsmeier, Measurements and modeling of acetone laser induced fluorescence with implication for temperature imaging diagnostics, Applied Optics 37 (21) (1998) 4963–4978.

[3] A. Lozano, Laser-excited luminescent tracers for planar concentration measurements in gaseous jets, Ph.D. thesis, Stanford University (1992).

[4] M. C. Thurber, F. Grisch and R. K. Hanson, Temperature imaging with single- and dual-wavelength acetone planar laser-induced fluorescence, Optics Letters 22 (4) (1996) 251–253.

[5] R. A. Bryant, J. M. Donbar and J. F. Driscoll, Acetone laser induced fluorescence for low pressure/low temperature flow visualization, Experiments in Fluids 28 (2000) 471–476.

[6] F. Mayinger, Optical Measurements: Techniques and Applications, 2nd Edition, Springer-Verlag, 2001.

[7] J. Sakakibara and R. J. Adrian, Measurement of temperature field of a Rayleigh-Benard convection using two-color laser-induced fluorescence, Experiments in Fluids 37 (2004) 331–340.

[8] F. Coletti, T. Maurer, T. Arts and A. Di Sante, Flow Field investigation in rotating rib-roughened channel by means of particle image velocimetry, Experiments in Fluids 52 (2004) 1043–1061.

[9] M. Bruchhausen, F. Guillard and F. Lemoine, Instantaneous measurement of two-dimensional temperature distributions by means of two-color planar laser induced fluorescence (PLIF), Experiments in Fluids 31 (2005) 123–131.

[10] P. Lavieille, F. Lemoine, G. Lavergne and M. Lebouch, Evaporating and combusting droplet temperature measurements using two-color laser-induced fluorescence, Experiments in Fluids 31 (2001) 45–55.

A Rotor Wake - Rotor Tonal Interaction Noise Computation Procedure for Contra-Rotating Fans

Gabriele Grasso

Environmental and Applied Fluid Dynamics Department, von Karman Institute for Fluid Dynamics, Belgium, gabriele.grasso@vki.ac.be

Supervisor: Christophe Schram

Associate Professor, Aeronautics and Aerospace Department & Environmental and Applied Fluid Dynamics Department, von Karman Institute for Fluid Dynamics, Belgium, christophe.schram@vki.ac.be.

Abstract

An analytical method to compute the tonal noise from rotor wake - rotor interaction in contra-rotating fans is presented. The method consists in the generation of a synthetic wake based on empirical correlations, the computation of the unsteady lift on the rear blade surface according to Amiet's theory and the computation of the far-field noise spectrum by means of the Ffowcs Williams and Hawkings analogy. Two contra-rotating fan geometries are thus analysed in order to evaluate the influence of lean and sweep of the blade profiles on the noise prediction.

Keywords: Aeroacoustics, Amiet's theory, contra-rotating fans.

1. Introduction

Contra-rotating open rotors (CRORs) are substantially more efficient than normal propellers. In fact, at low airspeed, the front rotor produces a high amount of tangential air flow whose energy is wasted in single-propeller architectures, but is recuperated, in this case, by the rear rotor. However, the main drawback that limits the commercial diffusion of CRORs is their high noise emission. In order to reduce the environmental impact of this engine architecture, both in terms of fuel consumption and noise emissions, it is important to include an aeroacoustic evaluation procedure in the preliminary design phase, which can lead to a multidisciplinary optimization of the geometry. We need therefore a noise prediction method that takes into account the geometry variations induced by the optimization while keeping a low computational cost. In this paper, such a procedure for the computation of tonal rotor wake - rotor interaction noise is presented, which uses a model of the wake based on empirical correlations. In this way we can focus on analysing the effect of geometry variations on the emitted noise, while leaving for the following step of the project the use of CFD based wake data. The noise prediction model will be applied to two different contra-rotating fan geometries that have the same number of blades, rotational speed and very similar operating points. The first geometry, in the following called the "Baseline", is the 4.2 m diameter contra-rotating fan of the VKI low speed Eiffel-type open-jet wind tunnel L-1. The design of this fan follows relatively simple rules: the blade profiles are stacked in the radial direction without tangential or axial displacement (called "lean" and "sweep", respectively). The second geometry, henceforth called the "Optimised", is the result of an aerodynamic and aeroacoustic optimisation of the Baseline [1] and is characterised by the application of lean and sweep to the blade profiles. In the following, the importance of this geometric features for the objective of noise reduction will be outlined.

2. Prediction of wake interaction noise

Since the flow ingested by a rotor is not homogeneous, each blade segment experiences a variation of both the magnitude and angle of incidence of the velocity while rotating. These variations induce a total instantaneous force $L(t)$, which derives from the integration of the local instantaneous lift forces over the blade surface. The periodic component of

$L(t)$ is responsible for the noise emission at discrete frequencies[2]. The unsteady lift generated by the passage of the rear rotor blades in the wakes shed from the front rotor is believed to be a major source of aerodynamic noise in the present test case.

2.1. A linearized aeroacoustic theory

Figure 1 describes a two-dimensional case in which U is the characteristic convection speed of disturbances along the airfoil chord line, $\vec{u}$ is the velocity fluctuation which would exist if no airfoil were present, with u and w, the streamwise and normal components, respectively.

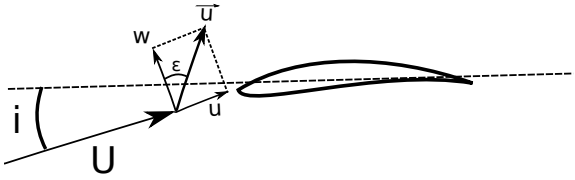

Figure 1: Small disturbances of the flow incident to an airfoil. [2]

In the case of a slightly loaded airfoil, the normal component w of the velocity fluctuations to the airfoil plane is responsible for the major part of the unsteady lift. For this reason, only this component is considered in a linearised unsteady aerodynamic theory and the airfoil is assumed to behave like a flat plate with zero incidence to the flow. Such a theory was used by Fournier [3] to compute the noise generated by helicopter ducted tail rotors. Its principle is that the tonal and broadband spectral components of noise generated by the wake interaction are distinct and hence the related aeroacoustic phenomena are themselves decoupled. For this reason, it is supposed that the tonal noise spectrum is due to the interaction of the blades with the periodic mean velocity deficit of the wakes, while the broadband noise spectrum is due to the turbulence of the wakes, as represented in figure 2. This is then a linear approach to the interaction phenomena, from both an aerodynamic and acoustic viewpoints.

2.2. Modelling the wake - rotor interaction

The simplest way to model the interaction between the blade segments and the incoming wake is to assume that the mean velocity deficit of the wake represents a parallel incompressible gust for the rear rotor. The corresponding formulation[4] for the local instantaneous lift fluctuation, l, is in function of the chord-wise coordinate, x', and of the chord-wise wave number of the incoming gust is, that is $k_x = 2\pi\lambda/(T_{pp}U)$,

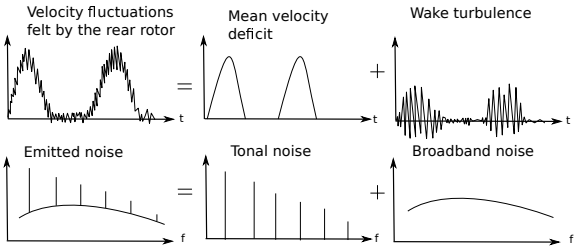

Figure 2: Decomposition of noise spectra and corresponding generation mechanisms [3].

being T_{pp} the blade passing period related to the front rotor and λ the index of the Fourier mode. For a given blade passing frequency harmonic (BPFH) the local unsteady lift is then

$$l(k_x, x', t) = 2\pi\,\rho_0\,U\,\hat{w}(k_x)\,g(k_x, x')\,\exp(-i\,k_x\,U\,t) \tag{1}$$

where $\hat{w}(k_x)$ is the spatial Fourier transform of the velocity fluctuation, and $g(k_x, x')$ is the aerodynamic response function of the profile. The local instantaneous lift fluctuation is then integrated along the chord and the span of the airfoil to get the total unsteady lift in function of the wave number:

$$L(k_x, t) = \pi^2\,\rho_0\,c\,d\,U\,\hat{w}(k_x)\,G(k_x)\exp\Big(-i\,k_x\,U\,t\Big) \tag{2}$$

whose Fourier transform is

$$\hat{L}(k_x, \omega) = \pi^2\,\rho_0\,c\,d\,U\,\hat{w}(k_x)\,G(k_x)\delta\Big(\omega - k_x\,U\Big) \tag{3}$$

$$= \pi^2\,\rho_0\,c\,d\,U\,\hat{w}(K_x)\,G(K_x) \tag{4}$$

The Kronecker delta appearing in Eq.(3) means that a given frequency component of the pressure jump is produced by the $K_x = \omega/U$ value of the chord-wise wave number.

The interaction between the rear rotor and the wakes shed from the front rotor is, however, more likely to be represented by a skew gust - airfoil interaction model. In fact, the incoming wake will sweep the leading edge of the rotor with a finite velocity, giving rise to the existence of a span-wise wave number. Furthermore, whereas in a turbulent gust an ideally infinite set of span-wise wave numbers, k_y, is related to a single value of the chord-wise wave number, K_x, in this case only one K_y value corresponds to a given K_x.

In this context, the relative inclination of the rear blades with respect to the incoming wakes is taken into account by means of a blade segmentation method which allows to reduce the three-dimensional wake - blade interaction phenomenon to a series of

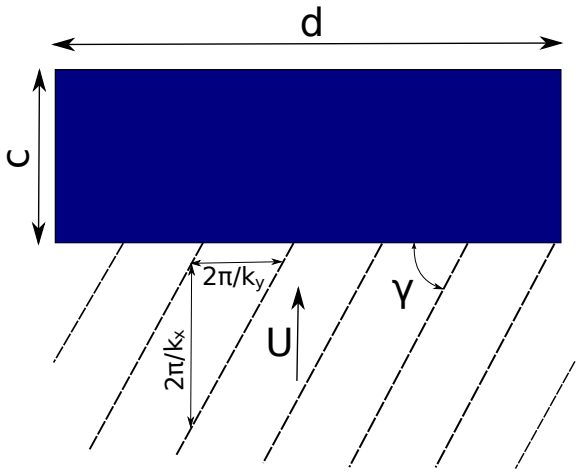

Figure 3: Equivalent bi-dimensional skew gust interaction problem.

skew gust - airfoil interaction problems of known solution, as seen in figure 3.

Generalising the previous formulation for parallel gust, the local unsteady lift can now be expressed in the frequency domain as:

$$\hat{l}(K_x, K_y, x') = 2\,\pi\,\rho_0\,U\hat{\hat{w}}(K_x, K_y)\ldots \\ \ldots g(K_x, K_y, x')\,\exp(-i\,K_y\,y) \qquad (5)$$

where $\hat{\hat{w}}(K_x, K_y)$ is the double spatial Fourier transform of the velocity fluctuation. Integrating Eq.(5) over the blade segment surface yields:

$$\hat{L}(K_x, K_y) = 2\,\pi\,\rho_0\,U\hat{\hat{w}}(K_x, K_y)\ldots \\ \ldots G(K_x, K_y)\,\frac{i}{K_y}\,(\exp(-i\,K_y\,d) - \exp(i\,K_y\,d)). \qquad (6)$$

As for the aerodynamic response function, $g(K_x, K_y, x')$, we have made use of Amiet's theory for leading edge noise[4; 5], which takes into account also the compressibility and non-compactness effects that may be present in the gust - airfoil interaction problem. The response functions for subcritical and supercritical gusts are derived by first solving the scattering of noise from the leading edge of the airfoil with Schwarzschild's technique and then adding a correction term for the back-scattering from the trailing edge, where the Kutta condition holds. The integrated response functions, $G(K_x, K_y)$, appearing in Eq. (6) are reported in appendix Appendix A.

2.3. Noise propagation formulation

The far-field noise has been computed by using the formulation of Ffowcs Williams and Hawkings (FWH) analogy [6] with Bessel functions. The acoustic pressure, p', is computed at locations equally spaced on the surface of a sphere as

$$p'_{nB} \sim -\frac{iBk_{nB}}{4\pi}\frac{e^{-ik_{nB}x}}{x}\sum_{m=-\infty}^{+\infty} e^{-i(nB-m)(\phi-\phi_0-\pi/2)}\ldots \\ \ldots\Big(J_{-nB+m}(-k_{nB}R_0\sin\theta)F_m^{(T)}\cos\theta- \\ -\frac{nB-m}{k_{nB}R_0}J_{-nB+m}(-k_{nB}R_0\sin\theta)F_m^{(D)} \\ -iJ_{-nB+m}(-k_{nB}R_0\sin\theta)\sin\theta\,F_m^{(R)}\Big) \qquad (7)$$

where p'_{nB} is the sound pressure perturbation emitted at a given BPFH of the rear rotor; B is the number of rear blades, so this formula represents a constructive interference for which the total sound emitted by the fan is B times the sound of a single blade; x is the listener's distance from the source; p represents the blade loading harmonics (BLH), so the noise emitted at a given BPFH is the sum over all the BLHs; ϕ and θ are the listener's azimuthal and polar angle, respectively; R_0 is the radius where the force is applied; J_{-nB+m} is a Bessel function of the first kind which modulates the Doppler frequency shift during blade revolution; finally, $F_m^{(T)}$, $F_m^{(R)}$, $F_m^{(D)}$ are the tangential, radial and axial components of the unsteady lift, respectively. The sound pressure perturbation is thus computed for each dipole at every point on the spherical surface and for all the BPFHs up to the ninth. Then the contributions of the different sources are summed and the sound power is integrated over the sphere.

The introduction of lean and sweep generates an azimuthal and axial displacement, respectively, of the center of force of the unsteady lift. The relative azimuthal displacement of the blade strips can be accounted for in the far-field formula with the term ϕ_0, which represents a phase shift, whereas the the axial coordinate of the dipole location is subtracted to that of each point of the sphere.

3. Generation of synthetic wake data

The shape of the wakes shed from the front rotor can be approximated by using a Gaussian function, which is defined by the mean velocity deficit in the wake center-line, μ_c, and by the wake width, Y_S, as outlined in figure 4. As a consequence, the periodic velocity disturbance that sweeps the rear rotor can be modelled by:

$$w\Big(\frac{x'}{U_0}, t\Big) = \overline{w}\sum_n f_s\Big(\frac{x'}{U_0} - t + nTpp\Big) \qquad (8)$$

where $\overline{w}$ is the upwash component of the mean velocity deficit, μ_c, and n is the number of blades of the front rotor. The periodicity is achieved thanks to the choice of a function f_s slightly different from 0 outside the wakes, which is

$$f_s(t) = \exp\Big[-\frac{\chi t^2}{\tau_s^2}\Big] \tag{9}$$

where $2\tau_s = 2Y_S/\Omega R$. The parameter χ has been set equal to 12 by Fournier[3] in agreement with the experimental results of Raj and Lakshminarayana [7], who investigated the development of three-dimensional turbulent wakes behind rotors of axial turbomachinery.

In order to calculate the unsteady lift, the function describing the mean velocity deficit of the wake (Eq. (8)) is decomposed in Fourier series as

$$w(x',t) = \overline{w}\sum_{\lambda} F(\lambda)\exp\Big[i\Big(\frac{2\pi\lambda}{T_{pp}}\Big(\frac{x'}{U_0} - t\Big)\Big)\Big] \tag{10}$$

where $2\pi/T_{pp}$ is the blade passing angular frequency. The Fourier coefficients, F, are

$$F(\lambda) = \frac{\tau_s}{T_{pp}}\sqrt{\frac{\pi}{\chi}}\exp\Big[-i\frac{\pi^2\lambda^2\tau_s^2}{\chi T_{pp}^2}\Big]. \tag{11}$$

The parameters mu_c and Y_S need to be extrapolated in order to provide their value at the leading edge of the rear rotor and this is done by using the empirical correlations of Raj and Lakshminarayana [7]. According to these Authors, the decaying of the defect in mean velocity at the wake centerline is given by

$$\frac{\mu_c}{\overline{U_s}} = \exp\Big[-\frac{\pi^2}{14}\Big(\frac{x}{S}+3.46\Big)\Big] \text{ for } \frac{x}{S} > 0.15 \tag{12}$$

where $\overline{U}_s$ is the mean velocity in the streamwise direction and S is the pitch of the blades. The trend of the wake width variation is in its turn

$$\frac{Y_S}{Y_{S0}} = 1.61\Big(\frac{x}{S}\Big)^{0.23} \tag{13}$$

where Y_{S0} is the wake width taken at the first extraction plane.

Synthetic wake data have been generated for the noise calculations presented in this work. In this case, the shape of the wake is given by Eq.s (8) and (9), whereas the variation of the mean velocity deficit and of the wake width is controlled by Eq.s (12) and (13), respectively. Anyway, there are more complex physical phenomena which are not taken into account in this empirical model, as already remarked by other Authors[8], in particular, no velocity disturbance in the radial direction has been implemented.

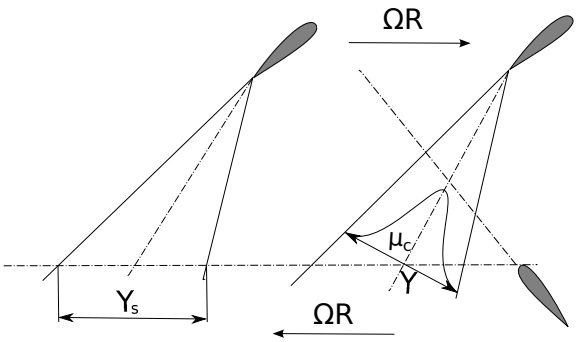

Figure 4: Geometric representation of the wake [3].

Figures 5 and 6 depict the trajectory of the wake center-line (the locus of the maximum velocity deficit at every radius) in the Baseline and in the Optimised configuration, respectively. The velocity disturbance distribution at a fixed radius (mid-span) is depicted as well. Already from this pictures it is possible to notice the fact that the relative inclination of the rear rotor and the incoming gust is significantly bigger in the Optimised configuration than in the Baseline. The effect of this inclination on the noise generation will be quantified in the following paragraphs.

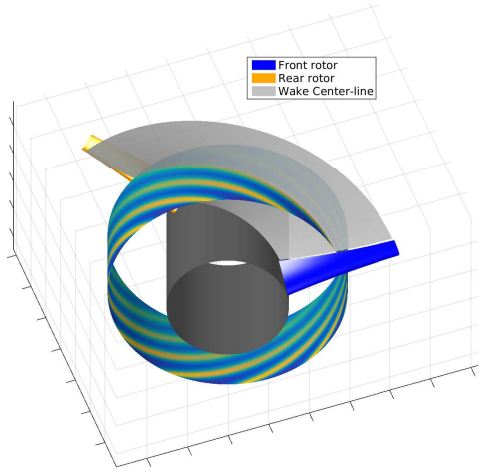

Figure 5: Visualization of the wake - rotor interaction in the Baseline configuration.

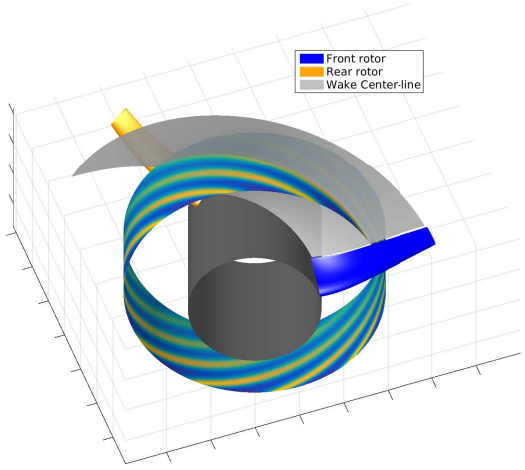

Figure 6: Visualization of the wake - rotor interaction in the Optimised configuration.

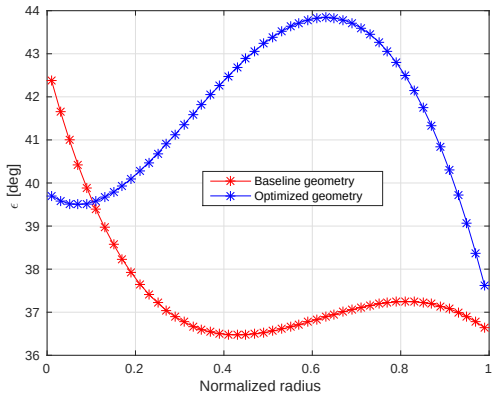

Figure 7: Comparison of the angle between the velocity disturbance vector and the upwash direction.

4. Analysis of the wake -rotor interaction noise results

In this section the main parameters involved in the computation of the unsteady lift on the rear blade surface and in the computation of the far-field noise spectrum will be analysed.

4.1. Projection of the upwash component of the velocity disturbance

First of all, let us go back to figure 1, where the angle ϵ between the velocity disturbance vector and the direction normal to the blade strip surface (upwash) is defined. Clearly, the bigger ϵ the lower will be the upwash component of the velocity disturbance, which is the main cause of tonal noise. Figure 7 shows the value of ϵ for each blade strip along the radial direction for the two geometries of interest, where it is generally higher in the case of the Optimised configuration.

4.2. Computation of the inclination of the incoming gust

As described in section 2.2, the interaction between the rear rotor blade strips and the incoming wake is modelled as a skew gust sweeping a rectangular flat plate. In other published works about wake - rotor interaction noise, the wake is considered aligned with the radial direction and therefore only the inclination of the leading edge of the rear blade is responsible for the gust skewness. This assumption is acceptable in cases where the two rotors are close enough one another that the wake is not distorted by the swirling flow. But, as we have seen in figure 6, especially in the case of the Optimised geometry, the wake is quite inclined with respect to the radial direction when it interacts with the rear rotor. Figure 8 defines β, the angle between the radial direction and the tangent to the wake centerline upstream of the rear rotor at a given radius, while the distribution of β for the two geometries is given in figure 9. From the latter figure we can see that in neither of the geometries the radial inclination of the wake center-line is negligible. This quantity is in its turn necessary to correctly project the wake in the plane of the rectangular strip that approximates the rear blade at a given radius. The result of this projection is the angle γ between the equivalent incoming gust and the leading edge of the blade strip, defined in figure 3. It should also be noted that $K_y/K_x = \tan\gamma$. We can see from figure 10 that in the upper 80% of the span the equivalent incoming gust is more skew in the Optimised configuration than in the Baseline. In order to assess the effect of the gust skewness on the computation of the unsteady lift on a blade strip, we can look at figure 11, where the magnitude of the aerodynamic transfer function (calculated with the flow conditions at mid-span) is plotted with reference to the skewness angle of the gust. In this picture, the maximum skewness found in the Baseline and in the Optimised geometry is also highlighted, showing a difference of around two thirds in the related transfer function magnitude.

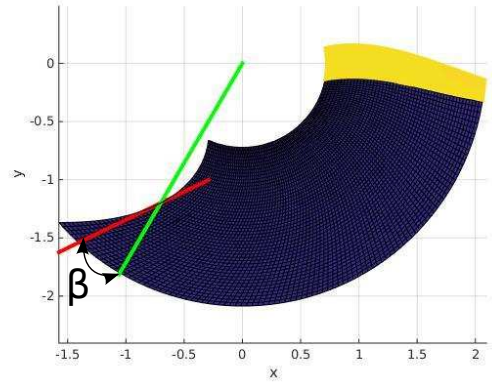

Figure 8: Example of computation of the inclination of the wake center-line (Optimized configuration). The green line represents the radial direction, while the red line is tangent to the wake center-line at mid-span.

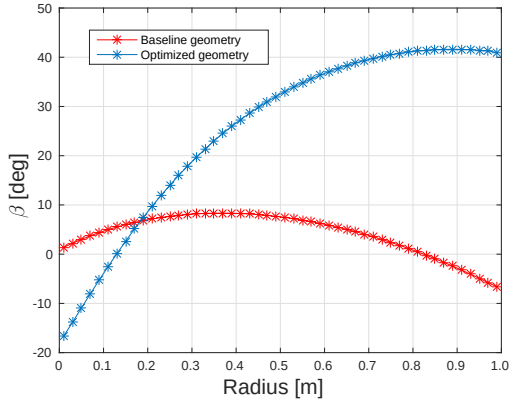

Figure 9: Comparison of the inclination of the wake center-line with respect to the radial direction.

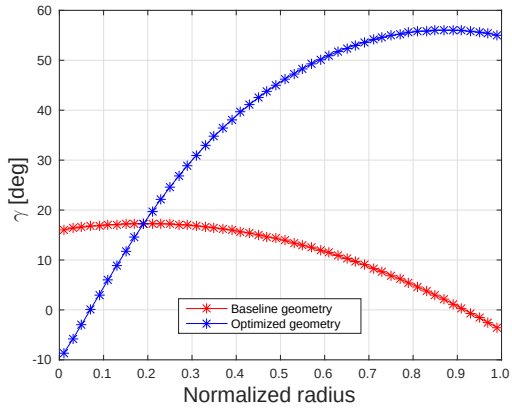

Figure 10: Comparison of the inclination of the equivalent incoming gust with respect to the leading edge of the rear rotor strips.

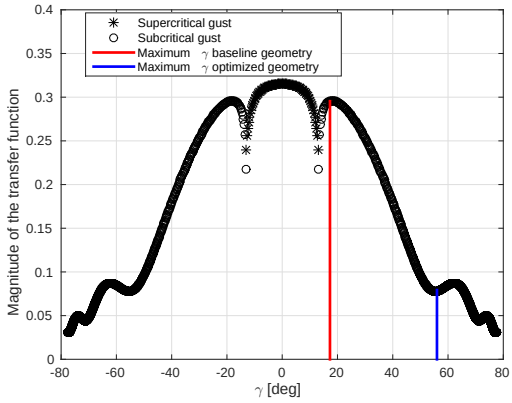

Figure 11: Magnitude of the aerodynamic response function and indication of the maximum skewness angle of the incoming gust for the two geometries under examination.

4.3. Computation of the source of noise and of its propagation

Having observed the effect of the gust skewness on the reduction of the magnitude of the aerodynamic response function, it is not surprising that the amplitude of the unsteady lift on the surface of the Optimised geometry is significantly lower, especially towards the tip of the blade, as shown in figure 12. In this plot, the unsteady lift has been normalized by the product of the reference density of air, $\rho_0 = 1.184$ kg m^{-3}, and the square of the mean flow velocity, $U = 26.2$ m s^{-1}. Each unsteady lift force applied to a blade strip acts as an acoustic dipole. Besides, it must be noticed that the dipoles distributed along the span of the rear blade display a certain phase shift, which is more important in the case of the Optimised geometry, as in figure 13. This phase shift represents a retarded time in the interaction, not to be confused with the retarded time of the emission defined in section 2.3. Finally, figure 14 shows the far-field noise spectrum computed by means of the Ffowcs Williams and Hawkings analogy of equation 7. The formula is applied to every blade strip and, for each blade strip, to a given number of blade loading harmonics (in this case, six). The overall noise is the summation of the contribution from all the strips. As a consequence of the reduction of the strength of the dipoles, due to the increased skewness of the incoming wake, and of their increased phase shift, the noise spectrum of the Optimised geometry is significantly lower than that of the Baseline.

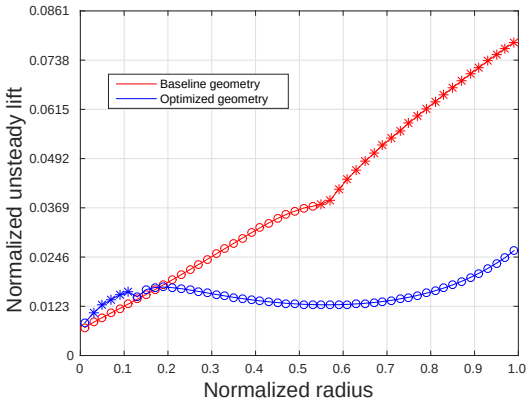

Figure 12: Comparison of the magnitude of the first harmonic of the unsteady lift on the rear blade surface.

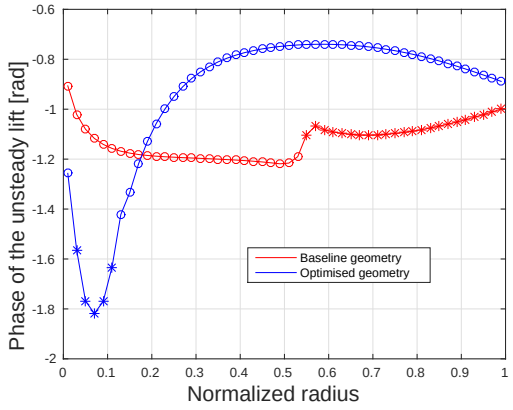

Figure 13: Comparison of the phase of the first harmonic of the unsteady lift on the rear blade surface.

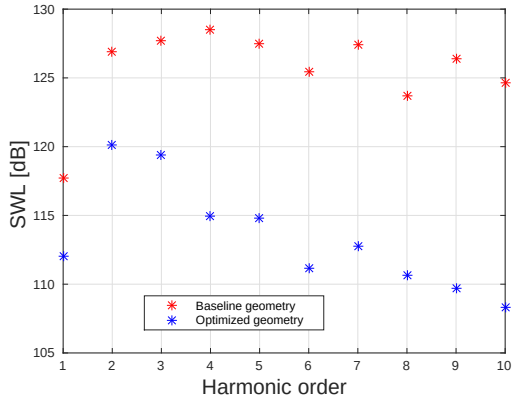

Figure 14: Comparison of the far-field noise spectrum at the BPF and at its first nine harmonics.

5. Conclusions and future work

In this work, a method to compute the rotor wake - rotor interaction tonal noise has been presented. The main focus has been on the parameters describing the geometry of the blades and of the wake and on how the unsteadiness can be reduced by varying them. For this reason, a simplified model of the wake development has been adopted and two contra-rotating fan geometries have been analysed, which differ in terms of lean and sweep, the two geometric features that are generally believed to be significant in wake interaction noise reduction. Thanks to the comparison between the two geometries, the importance of lean and sweep has been elucidated.

The same noise prediction method can be made more effective by applying it to wake data provided by a CFD simulation. In particular, our current research is focussing on the extraction of the variation of the mean flow velocity in the wake from steady state simulations. The main obstacle in this task is that the profile of the wake coming from the front rotor is not available in the computational domain of the rear rotor, but this can be overcome by implementing a numerical procedure of extrapolation of the wake characteristics. Another foreseen development is the extension of this model to the prediction of the broadband noise component generated by the turbulence associated with the wakes.

Acknowledgments

The Authors gratefully acknowledge the support of the EC under the project FlowAirS (Grant Agreement no 289352) and the project RBF4AERO (Grant Agreement no 605396).

Appendix A. Integrated response functions for the skew gust formulation.

In the framework of Amiet's theory, a gust is defined as supercritical or subcritical according to the following relation:

$$(\bar{k_y}/\beta)^2 < (\bar{k_x}^* M)^2 \quad \text{supercritical} \qquad \text{(A.1)}$$

$$(\bar{k_y}/\beta)^2 > (\bar{k_x}^* M)^2 \quad \text{subcritical} \qquad \text{(A.2)}$$

where $M = U/c_0$, $\beta = \sqrt{1 - M^2}$, $\bar{k_x} = k_x\, c/2$, $\bar{k_x}^* = \bar{k_x}/\beta^2$ and $\bar{k_y} = k_y\, c/2$.

The aerodynamic response functions for both supercritical and subcritical regimes are given below,

where the subscript 1 denotes the main leading edge term and 2 denotes the trailing edge back-scattering correction[5].

Appendix A.1. Supercritical gust

Defining the non dimensional chord-wise coordinate as $\bar{x} = x/(c/2)$, the leading edge and trailing edge terms are, respectively

$$G_{1sup}(k_x, k_y) = \frac{c}{2}\int_{-1}^{1} \frac{\exp(-i\,\frac{\pi}{4})}{\pi\,\sqrt{\pi\,(k_x+\beta^2\,\kappa)\,(\bar{x}+1)}}\ldots$$
$$\ldots\exp(-i\,(\kappa - M^2\,\bar{k_x}^*)\,(\bar{x}+1))\,d\bar{x} =$$
$$= \frac{c}{2}\,\frac{(1-i)}{\pi\,\sqrt{(k_x+\beta^2\,\kappa)\,\theta_1}}\,E^*(2\,\theta_1) \qquad \text{(A.3)}$$

and

$$G_{2sup}(k_x, k_y) \approx -\frac{c}{2}\int_{-1}^{1} \frac{\exp(-i\,\frac{\pi}{4})}{\pi\,\sqrt{2\,\pi\,(k_x+\beta^2\,\kappa)}}\ldots$$
$$\ldots[1-(1+i)\,E^*(2\,\kappa\,(1-\bar{x}))]\ldots$$
$$\ldots\exp(-i\,(\kappa - M^2\,\bar{k_x}^*)\,(\bar{x}+1))\,d\bar{x} =$$
$$= \frac{c}{2}\frac{\exp(-i\,\frac{\pi}{4})}{\theta_1\,\pi\,\sqrt{2\,\pi\,(k_x+\beta^2\,\kappa)}}\ldots$$
$$\ldots\{i\,(1-\exp(-2\,i\,\theta_1)) + (1-i)\,[E^*(4\,\kappa) -$$
$$-\sqrt{\frac{2\,\kappa}{2\,\kappa-\theta_1}}\,\exp(-2\,i\,\theta_1)\,E^*(2\,(2\,\kappa-\theta_1))]\} \qquad \text{(A.4)}$$

where $\kappa = \sqrt{(\bar{k_x}^*\,M)^2 - (\bar{k_y}/\beta)^2}$, $\theta_1 = \kappa - \bar{k_x}^*\,M^2$ and $E^*(x) = \int_0^{-x}\frac{\exp(-i\,t)}{\sqrt{2\,\pi\,t}}dt$ is the complex conjugate of the Fresnel integral.

Appendix A.2. Subcritical gust

Defining, as for the supercritical gust, the non dimensional chord-wise coordinate as $\bar{x} = x/(c/2)$, the leading edge and trailing edge terms are, respectively

$$G_{1sub}(k_x, k_y) = \frac{c}{2}\int_{-1}^{1} \frac{\exp(-i\,\frac{\pi}{4})}{\pi\,\sqrt{\pi\,(k_x+i\,\beta^2\,\kappa')\,(\bar{x}+1)}}\ldots$$
$$\ldots\exp(i\,(\kappa' + M^2\,\bar{k_x}^*)\,(\bar{x}+1))\,d\bar{x} =$$
$$= \frac{c}{2}\,\frac{(1-i)}{\pi\,\sqrt{(k_x+i\,\beta^2\,\kappa')\,\theta_2}}\,E(2\,\theta_2) \qquad \text{(A.5)}$$

and

$$G_{2sub}(k_x, k_y) \approx -\frac{c}{2}\int_{-1}^{1} \frac{\exp(-i\,\frac{\pi}{4})}{\pi\,\sqrt{2\,\pi\,(k_x+i\,\beta^2\,\kappa')}}\ldots$$
$$\ldots\left\{1-\mathrm{erf}(\sqrt{2\,\kappa'\,(1-\bar{x})})\right\}\exp(i\,(\kappa' + M^2\,\bar{k_x}^*)\,(\bar{x}+1))\,d\bar{x}$$
$$= -\frac{c}{2}\frac{\exp(-i\,\frac{\pi}{4})}{\theta_2\,\pi\,\sqrt{2\,\pi\,(k_x+i\,\beta^2\,\kappa')}}\ldots$$
$$\ldots\Big(\sqrt{\frac{2\,\kappa'}{2\,\kappa'+i\,\theta_2}}\,\exp(2\,i\,\theta_2)\,\mathrm{erf}(\sqrt{2\,(2\,\kappa'+i\,\theta_2)}) \qquad \text{(A.6)}$$
$$-\mathrm{erf}(\sqrt{4\kappa'}) - (\exp(2\,i\,\theta_2)-1)\Big)$$

where $\kappa' = \sqrt{(\bar{k_y}/\beta)^2 - (\bar{k_x}^*\,M)^2}$, $\theta_2 = \kappa' + \bar{k_x}^*\,M^2$, $E(x) = \int_0^x \frac{\exp(i\,t)}{\sqrt{2\,\pi\,t}}dt$ is the Fresnel integral and $\mathrm{erf}(x) = \frac{1}{\sqrt{\pi}}\int_0^{x^2}\frac{\exp(-t)}{\sqrt{t}}$ is the error function.

From a physical point of view, a smooth transition of the response function from the supercritical to the subcritical regime is expected. However, a discontinuity is observed at $\kappa = 0$, which is due to the fact that an exact analytical solution could be reached only by infinite iterations of Schwarzschild's method[9]. For this reason, a numerical regularization technique has been adopted, matching the values of the response functions on both sides of the discontinuity [**?**].

References

[1] G. Grasso, J. Christophe, C. Schram, T. Verstraete, Aerodynamic, aeroacoustic and structural optimization of a contra-rotating fan, in: 15th International Symposium on Transport Phenomena and Dynamics of Rotating Machinery, 2014.

[2] M. Roger, Noise in turbomachines, in: Lecture Series 2000-02, Von Karman Institute for Fluid Dynamics.

[3] F. Fournier, Mise au point d'une methode de calcul adapte au bruit des fenestrons d'hlicoptres, Ph.D. thesis, Ecole Centrale de Lyon (1988).

[4] R. K. Amiet, Acoustic radiation from an airfoil in a turbulent stream, Journal of Sound and Vibration 41 (4).

[5] J. Christophe, Application of hybrid methods to high frequency aeroacoustics, Ph.D. thesis, Université Libre de Bruxelles - von Karman Institute for Fluid Dynamics (2011).

[6] M. E. Goldstein, Aeroacoustics, McGRAW-HILL International Book Company, 1976.

[7] R. Raj, B. Lakshminarayana, Three dimensional characteristics of turbulent wakes behind rotors of axial flow turbomachinery, Journal of Engineering for Power 98 (2).

[8] A. Carazo, M. Roger, M. Omais, Analytical prediction of wake-interaction noise in counter-rotation open rotors, in: 17th AIAA/CEAS Aeroacoustics Conference (32nd AIAA Aeroacoustics Conference), 2011.

[9] M. Roger, S. Moreau, Back-Scattering Correction and Further Extensions of Amiet's Trailing-Edge Noise Model. Part 1: Theory, Journal of Sound and Vibration 286 (2005) 477–506.

Conjugate Heat Transfer of an Internal Rib-Roughened Cooling Channel using Large Eddy Simulations

Sebastian Scholl

Turbomachinery and Propulsion Department, von Karman Institute for Fluid Dynamics, Belgium, sebastian.scholl@vki.ac.be

Supervisor: Tom Verstraete

Assistant Professor, Turbomachinery and Propulsion Department, von Karman Institute for Fluid Dynamics, Belgium, tom.verstraete@vki.ac.be.

Promotor: Wolfgang Schröder

Professor, RWTH Aachen, Aerodynamisches Institut , office@aia.rwth.de.

Abstract

The following contribution focuses on the conjugate heat transfer computation of a rib-roughened internal turbine blade cooling channel, at a Reynolds number of 40,000, via the coupling of two numerical in-house tools: an LES flow solver (AVBP) and a solid conduction solver (AVTP) developed by CERFACS. The fluid solver has also been compared with steady and unsteady simulations obtained with the open source code OpenFOAM demonstrating the inferiority of steady fluid flow simulations, while LES accurately capture the flow field. Interested in the thermal steady states of such problems, both fluid and solid solvers provide time dependent de-synchronized solutions. A weak coupling strategy for Conjugate Heat Transfer was used: It first computes the fluid domain until it reaches a statistically steady state from which the mean temporal solution is obtained. Then, it solves the solid domain with the mean boundary conditions imposed from the fluid leading to an updated fluid boundary condition. This process is repeated until convergence of the coupled problem. The aerodynamic and heat transfer results were validated against experimental data obtained at the von Karman Institute for Fluid Dynamics.

Keywords: Conjugate Heat Transfer, Coupling, Turbine Blade, Cooling Channel, Large Eddy Simulation

Nomenclature

Latin

c_s	solid heat capacity	$[JK^{-1}]$
D_h	Hydraulic diameter	$[m]$
c_p	fluid heat capacity	$[JK^{-1}]$
Bi	Biot number	
c	speed of sound	$[ms^{-1}]$
EF	enhancement factor	
F	flux tensor	
h	heat transfer coefficient	$[Wm^{-2}K]$
L	characterisitc length scale	$[m]$
Nu	Nusselt number	
P	pitch length in the ribbed channel	$[m]$
p	pressure	$[Nm^{-2}]$
Pr	Prandtl number	
q	heat flux	$[Wm^{-2}]$
Re	Reynolds number	
T	temperature	$[K]$
t	time	$[s]$
u,v,w	velocity components	$[ms^{-1}]$
x,y,z	Cartesian coordinates	$[m]$
y+	non-dimensional wall distance	

Greek

β	relaxation coefficient	
μ	dynamic viscosity	$[Pa^1 s^1]$
ν	kinematic viscosity	$[m^2 s^{-1}]$
ρ	density	$[kg^1 m^{-3}]$

Abbreviations

CFL	Courant-Friedrich-Levy number
LES	large eddy simulation
SGS	Sub-grid Scale

Super- and Subscripts

∞	free stream quantity
f	fluid domain
s	solid domain

1. Introduction

Trying to comply with the claims for environmental awareness and the rising use of energy, the turbomachinery industry is bound to improve the gas turbine efficiency in several regions, one of which consists in increasing the turbine inlet temperature. Since the life of a turbine blade is reduced by half with an increased temperature of 15 Kelvin [1], the prediction of local heat transfer coefficients and temperatures is a crucial step towards the design of turbine blades.
Current numerical methods lack the needed predictive capacity and call for new numerical strategies. Two reasons explain the current status: First, Reynolds averaged Navier-Stokes simulations fail to predict complex flow fields and can lead to wrong thermal predictions. Second, conjugate effects need to be taken into account for reliable thermal predictions, but are often neglected. Conjugate heat transfer describes the interaction between fluid and solid domain. If the temperature distribution would be known at the interface a priori, the problem would reduce to a convective problem, but the temperature distribution (and the heat flux distribution) is unknown a priori and is part of the coupled solution of the fluid and solid energy equations, which is the conjugate heat transfer problem [2]. The coupling of fluid and solid solvers is a demanding task, stability problems can occur and the time scales in the fluid and solid domain vary by orders of magnitude. Large Eddy Simulations (LES) improve the turbulent flow field and heat transfer predictions, but are expensive. Due to those challenges, only few computations of conjugate heat transfer (CHT) with LES have been done and research is still needed for an efficient LES based CHT Strategy.
The following sections subsequently describe the used methods and solvers, a thorough mesh study for the conducted LES, followed by a comparison of two different LES solvers and a comparison of the LES with steady simulation. The flow field predictive capabilities are evaluated, followed by an analysis of the heat transfer. The influence of the imposed thermal boundary condition is demonstrated and finally results of conjugate computations are shown, demonstrating the need for further research on LES based coupling strategies.

2. Numerical Method

The applied method for the conjugate heat transfer in the cooling channel couple a parallel LES solver for the fluid domain with a parallel conduction solver for the solid domain.

2.1. Fluid solver

Two different fluid solvers were used for comparisons. First, the fluid flow was computed by the CERFACS in-house LES solver AVBP (Schönfeld and Poinsot [3]; Mendez and Nicoud [4]. Applying Favre filtering to the unsteady, compressible Navier-Stokes equations Sagaut [5], leads to the following LES equations:

$$\frac{\partial \bar{W}}{\partial t} + \nabla \cdot \bar{F} = 0, \tag{1}$$

with the conservative variables $\bar{W} = (\bar{\rho}, \bar{\rho}\tilde{u}, \bar{\rho}\tilde{v}, \bar{\rho}\tilde{w}, \bar{\rho}\tilde{E})$ the flux tensor $\bar{F}$, the density $\bar{\rho}$, the velocity components $(\tilde{u}, \tilde{v}, \tilde{w})$, and the total Energy $\tilde{E}$. The fluid follows the Favre filtered equation of state $\bar{p} = \bar{\rho} r \tilde{T}$, with the gas constant r. The conductive heat flux is included in the flux tensor and given by Fourier's law of conduction:

$$\bar{q}_i = -\bar{\lambda} \frac{\partial \tilde{T}}{\partial x_i}, \tag{2}$$

with the thermal conductivity

$$\bar{\lambda} = \frac{\bar{\mu}(\bar{T}) c_p(\bar{T})}{Pr}, \tag{3}$$

where c_p is the specific heat at constant pressure, Pr the Prandtl number and $\bar{\mu}$ the dynamic viscosity. The solver uses tabulated values for the temperature dependent specific heat at constant pressure. The fluid viscosity follows a temperature dependent power law. The unknowns appearing in the LES equations, i.e. the subgrid-scale (SGS) quantities, need to be modeled. The Boussinesq eddy viscosity assumption is applied for which a subgrid-scale turbulent viscosity ν_t is modeled via the Wall Adapting Linear Eddy (WALE) model (Nicoud and Ducros 1999). Using the SGS turbulent viscosity, the SGS turbulent conductivity is modeled as $\lambda_t = \bar{\rho} \nu_t c_p / Pr_t$, with the turbulent Prandtl number fixed at $Pr_t = 0.7$. The equations are discretized by centered spatial schemes and explicit time schemes with a Finite-Element based two step Taylor-Galerkin (TTGC) scheme for the convection in a cell-vertex formulation (Colin and Rudgyard [6] and Donea and Huerta [7]). This explicit

scheme is of third order accuracy in space (on hybrid meshes) and time, providing low dissipation, especially suitable for LES. The diffusion term is discretized with a vertex-centered operator closely following the Galerkin method and is of second order, having a $\Delta 2$ stencil. The time step is controlled via the Courant-Friedrich-Lewy (CFL) condition for compressible flows: $CFL = \frac{(U+c)\Delta t}{\Delta x} \simeq 0.7$, with the smallest grid cell size Δx and the minimal Δt in the whole domain, U and c being the local flow and sound speeds. The Navier-Stokes Characteristic Boundary Conditions (NSCBC) of Poinsot and Lele [8], are applied at the inlet and the outlet.
The second fluid solver was an incompressible solver, used from the OpenFOAM® platform. The pressure-velocity coupling was treated with the PISO algorithm, which uses a momentum predictor and a correction loop in which the pressure equation is solved and the momentum equation corrected based on the pressure change. The flow equations are discretized with an explicit Euler scheme in time and a second order central finite-volume discretization scheme in space. The Smagorinsky model was used to compute the subgrid-scale turbulent viscosity.

2.2. Solid solver

The conduction solver AVTP uses a Galerkin diffusion scheme, second order accurate with an explicit time advancement to solve the energy conservation:

$$\rho_s c_s \frac{\partial T(\mathbf{x}, t)}{\partial t} = -\frac{\partial q_i}{\partial x_i}, \tag{4}$$

with the temperature in the solid T, the solid density ρ_s, the heat capacity c_s and the heat flux q, given by Fourier's law of conduction: $q_i = -\lambda_s \frac{\partial T}{\partial x_i}$.

3. Experimental configuration

The applied configuration models the experimental facility of Cukurel, see [9] and [10], which was a simplified model of an internal rib-roughened turbine blade cooling channel. It was scaled up by a factor of 15 with respect to real engine conditions, keeping the Reynolds number constant. Figure 1 and tables 1 2 and 3 show more details of the channel dimensions. The experimental facility consisted of three sections: an inlet, a test and an outlet section from which the test section with its six ribs is fully represented by the configuration for the numerical simulations. The other two sections are represented in parts. The cross section dimensions are 75x75mm and the test section

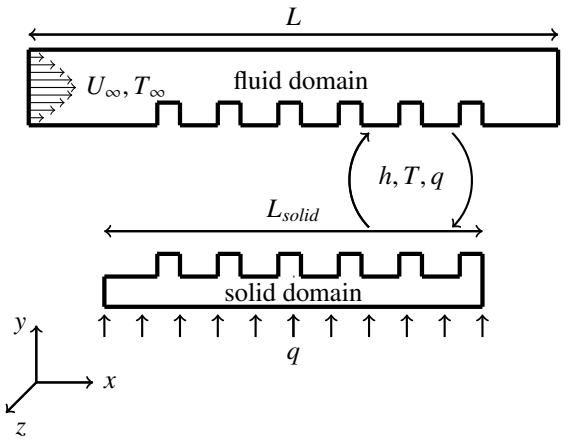

Figure 1: Sketch of the channel geometry.

length is 1260mm. Since a compressible solver is used for the computations, the geometry was scaled down by a factor of 10 to increase the Mach number and reach faster convergence of the simulations.

Parameter	abbr.	Value
length	L	1597.5 mm
height, depth	H, d	75 mm
hydraulic diameter	D_h	75 mm
rib height	h	22.5 mm
pitch	p/h	10
blockage ratio	h/D_h	0.3
angle of attack		90°

Table 1: Channel characteristics.

Parameter	abbr.	Value
length	L_{solid}	1250 mm
height, depth	H_{solid}, d_{solid}	75 mm
thickness	t_{solid}	22.5 mm
material	AISI 304 Steel 1260	
conductivity	k	$16.2 \frac{W}{m^2}$

Table 2: Ribbed slab characteristics.

Parameter	abbr.	Value
flux under slab	q	$1167 W/m^2$
interface flux	q_w	$1153.8 W/m^2$
inflow temperature	T_∞	295.3K
Reynolds number	Re_{D_h}	40000

Table 3: Flow characteristics and boundary conditions.

4. Computational model

Flow and boundary conditions

No-slip conditions were applied at all walls. The inlet and outlet boundaries are positioned far from the actual part of interest avoiding major influences on the flow around the ribs. Adiabatic conditions were applied on the lateral walls and the top wall, while iso-flux boundary conditions were applied to the rib-surrounding surface. Keylock et al. [11] demonstrated on a single rib with a lower blockage ratio (0.15) than in the present study that the rib has such a strong effect on the flow that the precise nature of the inlet condition, with regards to the turbulent fluctuations and length scales, is forgotten and only small differences for the flow separation and reattachment may appear. The reattachment lengths and many flow quantities will be preserved reasonably well, regardless of the inlet profile. Due to the even larger blockage ratio used in this study, a turbulent mean profile without fluctuations for the flow was applied as inlet condition. At the outlet, the static pressure was set. To simulate the exact flow conditions with the small Mach number of the experimental campaign of Cukurel [9] at Ma = 0.02, the computational time (using a compressible solver with explicit time integration) would have been unjustifiably long. Hence, the Mach number was increased to Ma = 0.2, keeping the same Reynolds number, based on the bulk velocity and the hydraulic diameter, at 40,000. This scaling granted a decrease of the computational cost and a re-scaling to more real engine conditions, while maintaining the similarity with the experimental data and keeping the simulated Mach number small enough to avoid compressibility effects.

4.1. Mesh for LES computations with AVBP

With the present wall-resolved approach for the numerical simulations and the ubiquitous presence of walls in the internal cooling passage, the mesh requirements are high, leading to demanding and costly computations. The unstructured LES solver AVBP was designed to deal with hybrid meshes. Therefore, a hybrid mesh (consisting of tetrahedra within the channel and prismatic elements at the walls) has been used for the current application. Figure 2 shows the tetrahedra of the used mesh around two ribs of the channel in the symmetry plane. For reliable results, the closest grid point needs to be within the viscous sublayer, leading to small grid cells at the wall. A prismatic layer in the wall-normal direction provides a good orthogonality and needs less elements for the same resolution than a tetrahedral layer. Fransen [12] recently observed that using one prism layer results in the best mesh quality for a hybrid mesh in such a ribbed geometry, which has been done for the present computations. Increasing the amount of prism layers penalized the quality in the rib to bottom wall corners.

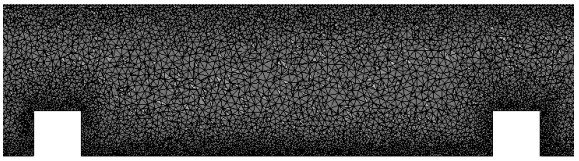

Figure 2: Mesh around two ribs for LES computation with AVBP.

4.2. Mesh for RANS and LES computations with OpenFOAM®

Figure 3 shows the mesh used for the computations with OpenFOAM®. A structured mesh consisting of hexahedra has been used. The y+ value of this mesh was slightly lower than the y+ value of the AVBP mesh, but the order of the spatial numerical scheme one order smaller. Most distances of the first grid cell to the wall remain lower than 5, remaining within the viscous sub-layer. The y+ distribution is penalized by the grid cells at the corners, where a boundary layer is not existent.

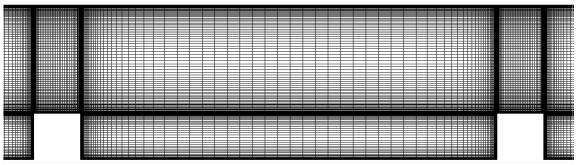

Figure 3: Mesh around two ribs for LES and RANS computation with OpenFOAM®.

	mesh M1	mesh M2	mesh M3	mesh M4	mesh M5	$M_{OpenFOAM®}$
cells	3.53M	8M	10.5M	20.6M	20.3M	3.2M
nodes	0.69M	1.5M	2M	3.86M	3.74M	-
prisms	no	yes	yes	yes	yes	-
mean y+	18.72	8	4.1	4.1	3.4	2.5
x+,z+	~ 1	~ 5	~ 5	~ 5	~ 8	-

Table 4: Used meshes. y+ is defined using the wall-normal distance y, the friction velocity u_τ the wall shear stress τ_w as: $y+ = \frac{u_\tau y}{\nu}$. x+ and z+ are defined with the streamwise and spanwise mesh resolution, determining the aspect ratio of the cell.

5. Results

The following section first presents a mesh convergence study showing five levels of refinement. After assessing the quality of the used mesh and the aerodynamics field, with a comparison of two different LES solvers, two different RANS simulations and two different iso-flux boundary conditions, the section shows the results for the heat transfer comparing the two different tested cases. Both iso-flux cases were done with the finest mesh, resulting from the mesh study, at $12{,}000 W/m^2$ and $120{,}000 W/m^2$ comparing each others heat transfer enhancement to observe the dependency of the heat transfer coefficient on the boundary condition.

5.1. Enhancement Factor and mesh convergence

A comparison of different mesh resolutions resulting in a convergence study, and its effect on the enhancement factor (EF) has been done. The enhancement factor quantifies the increase of heat transfer in comparison with a correlation valid for flow in a smooth pipe at the same Reynolds number. It is defined as:

$$EF = \frac{Nu}{Nu_0}. \tag{5}$$

The Nusselt number is defined as:

$$Nu = \frac{h \cdot D_h}{\lambda(T)}, \tag{6}$$

with the heat transfer coefficient h, the hydraulic diameter D_h and the fluid conductivity λ . The Dittus-Boelter correlation (Dittus and Boelter 1930) gives the denominator for the enhancement factor (valid for $0.7 < Pr < 120$) and is defined as: $Nu_0 = 0.023 Re_{D_h}^{4/5} Pr^{0.4}$. The heat transfer coefficient h is defined as in Eq. (1), while T_∞ is defined as the bulk temperature T_{bulk}. Due to uniform heating and periodical flow conditions, the bulk temperature is assumed to linearly increase inside the channel. Considering the values around ribs, the linear increase of the bulk temperature is further simplified with a sequence of step functions (which results in a constant bulk temperature along the pitch). This assumption allowed a fair comparison with previous results, which used the same data reduction approach (Cakan, 2000[13]). A mass flow average was used for the inlet and outlet temperatures of the simulations. Table 4 summarizes

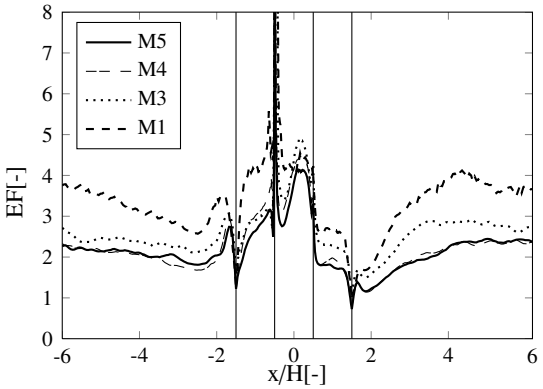

(a) EF around rib n^0 4. View on the bottom surface with the front and back surfaces of the rib unfolded.

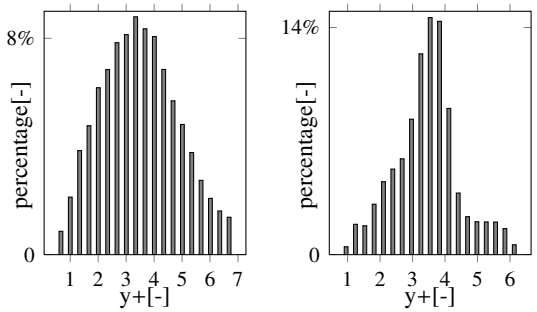

(b) $y+$ distribution for mesh M4.

(c) $y+$ distribution for mesh M5.

Figure 4: EF of used meshes along the unfolded rib and y+ value distribution around the ribs of the meshes. y+ is defined using the wall-normal distance y, the friction velocity u_τ the the wall shear stress τ_w as: $y+ = \frac{u_\tau y}{\nu}$.

the mesh properties. Mesh M1 lacked quality to resolve major flow structures. From mesh M2 on, using a higher resolution and a prism layer in the boundary layer, the aerodynamics were well represented, but till mesh M3 the heat transfer kept increasing (Fig. 3(a)). Mesh M4 had a higher resolution mainly in the channel mid-section. To further improve the heat transfer predictions, mesh M5 used larger cell aspect ratios of wall prisms, while still remaining lower than 8 ($\Delta z \simeq \Delta x \simeq AR \cdot \Delta y$), as Sagaut (2000) suggests. The histograms in Fig. 3(b) and Fig. 3(c) present the y+ distribution around the ribs for the meshes M4 and M5. The smaller wall distance of the first grid point of mesh M5 (and the larger aspect ratios of M5 to keep a reasonable cell count) lead to a beneficial y+ distribution in comparison with M4, keeping the majority of first node distances within the viscous sub-layer and $y+ < 5$. Collado Morata et al. (2012) have recently shown (on a turbine blade) that with the used solver and numerical schemes a y+ value of 4 leads to good predictions for the heat transfer. The mean y+ value for meshes M3 and M4 are around this value while the value for mesh M5 is even smaller. Since the heat transfer changed very little (Fig. 4(a)) from mesh M4 to mesh M5, the result for mesh M5 can be considered grid-converged. Hence, mesh M5 is assumed to deliver reliable results and will be used for the analyses in the following sections.

5.2. Aerodynamic analysis

The following section presents results for time-averaged statistics. The averaging time of the simulations was equivalent to 22 flow throughs, which is the time a fluid particle needs to travel through the whole channel, based on the bulk velocity. Note that the channel contains six ribs, which would translate to 132 flow throughs in a periodic case, ensuring sufficient statistical convergence. The streamlines in Fig. 4 show the four main recirculation zones in streamwise direction. Table 3 compares their lengths with the experimental study of Casarsa [14] as well as Casarsa and Arts [15]. The values of the recirculation lengths are evaluated by applying the criteria defined by Casarsa to assure a direct comparison. The reattachment lengths are therefore measured at a small distance above the wall with a negative streamwise velocity for V1 at $y/H = 0.05$ and for V3 at $y/H = 0.01$, a positive streamwise velocity for V2 at $y/H = 0.05$ and a vertical velocity, exceeding a threshold of 0.05m/s (scaled for LES) at $y/H = 0.05$. Comparing the first LES case with $12{,}000 W/m^2$ iso-flux boundary condition, the separation downstream

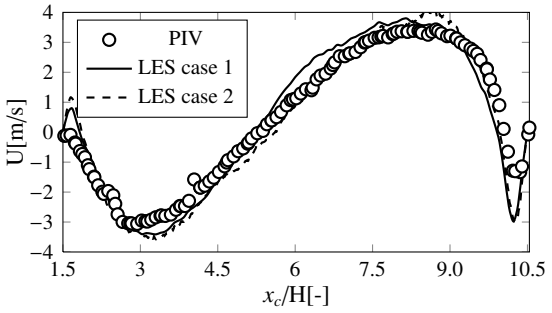

(a) Streamwise velocity at $y/H = 0.05$.

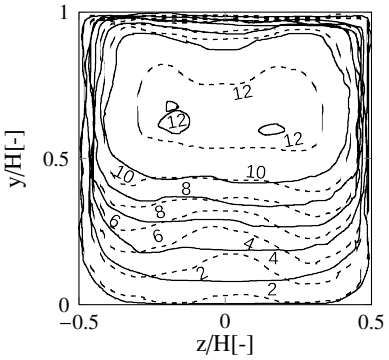

(b) Isotachs, u[m/s] at $x_c = 6$

Figure 6: Streamwise velocity comparisons: (a) between experimental and numerical data along the symmetry plane at $y/H = 0.05$; (b) between the two LES cases. Results for experiments by Casarsa [14]. Note: value for LES results have been divided by the scaling factor for comparison.

of the rib (V1) is in good agreement with the measurement, being close to the range of the experimental uncertainty. The downstream corner region (V2) is only slightly overestimated. The recirculation bubble sizes agree well for the top (V3) and front (V4a) regions. We also found a small recirculation region in the upstream corner (V4b) (using a measurement criterion of $y/H = 0.005$) that has not been observed prior to this study, to our knowledge.

Figure 5 (a) shows the streamwise velocity in the symmetry plane at $y/H = 0.05$, comparing the present LES with the experiment of Casarsa and Arts [15] showing good agreement. More detailed quantitative results with respect to the aerodynamics were compared with the experimental data (iso-thermal) of Casarsa [14][15], which are in good agreement as Fig. 6 shows. The secondary flow structures as shown by time averaged spanwise and vertical velocity components are qualitatively and quantitatively well represented by the simulations. The average pressure drop

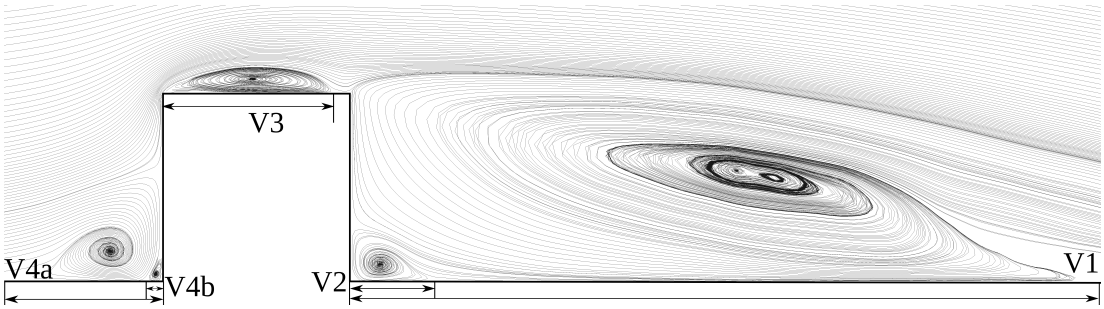

Figure 5: Recirculating zones at rib n^0 4 visualized with streamlines in the center plane.

	V1	V2	V3	V4a	V4b
exp. [14]	3.76H-3.84H	0.225H-0.28H	0.6H-0.9H	1.04H-1.5H	-
simulation, case 1	3.7H	0.31H	0.86H	1.46H	0.07H
simulation, case 2	4.09H	0.36H	0.84H	1.69H	0.03H

Table 5: Sizes of recirculation zones in the symmetry plane in streamwise direction (see Fig. 4).

over one pitch interval is also an important integral parameter to demonstrate the simulation quality (Arts et al. 2007). The pressure drop is expressed using the friction factor:

$$f = \frac{D_h \Delta P}{2L\rho U^2}, \tag{7}$$

with L being the pitch lengths. The rib effect can be demonstrated by normalizing the friction factor with the friction factor for a smooth pipe $f_0 = 0.046Re^{-0.2}$. Table 4 shows the ratio of these friction factors for the simulation compared with an experiment. The difference between the experiment and the simulation is less than 6% which validates the simulations.

	f/f_0
experiment [14]	12.3 ± 0.25
simulation	13.3

Table 6: Normalized friction factor.

5.2.1. Primary recirculation zones

Figure 5 shows the main recirculation zones in streamwise direction obtained from the LES with AVBP. Four major recirculation zones exist: the largest recirculation zone after the rib (V1), a small recirculation zone directly behind the rib (V2), a recirculation zone on the rib top (V3) and another recirculation zone in front of the rib (V4). Figure 6 (a) shows the streamwise velocity at the height of the measurement taken to evaluate the recirculation point. The experiment resulted in a value of $x/H = 5.3$ for the reattachment location. Both LES are in good accordance with this value, with $x/H = 5.2$ for the AVBP LES and $x/H = 5.4$ for the OpenFOAM® LES. The RANS underpredict the reattachment location. Downstream of the reattachment location the LRR Reynolds-stress model is still in satisfactory agreement with the experiment, even though it does not predict the recirculation zone directly in front of the rib (V4). Upstream of the reattachment point the LRR Reynolds stress model is in a bad agreement with the PIV data. The $k - \epsilon$ does neither predict the front rib recirculation zone (V4), nor predict the streamwise velocity upstream and downstream of the reattachment point well. Both LES, on the other hand, give good predictions of the streamwise velocity and also capture all recirculation zones. Figure 7 shows the streamwise velocity profile evolution starting on top of the rib proceeding to the pitch in-between two ribs until the front of the subsequent rib. The velocity profiles are continuously better predicted by the LES. Table 5 shows the sizes for the recirculation zones V1 and V3 of all simulations compared with the available experimental data. The zone sizes are measured in the symmetry plane of the channel and expressed in multiples of the rib height H. The reattachment lengths were measured at a small distance above the wall with a negative streamwise velocity for V1 at $y/H = 0.05$

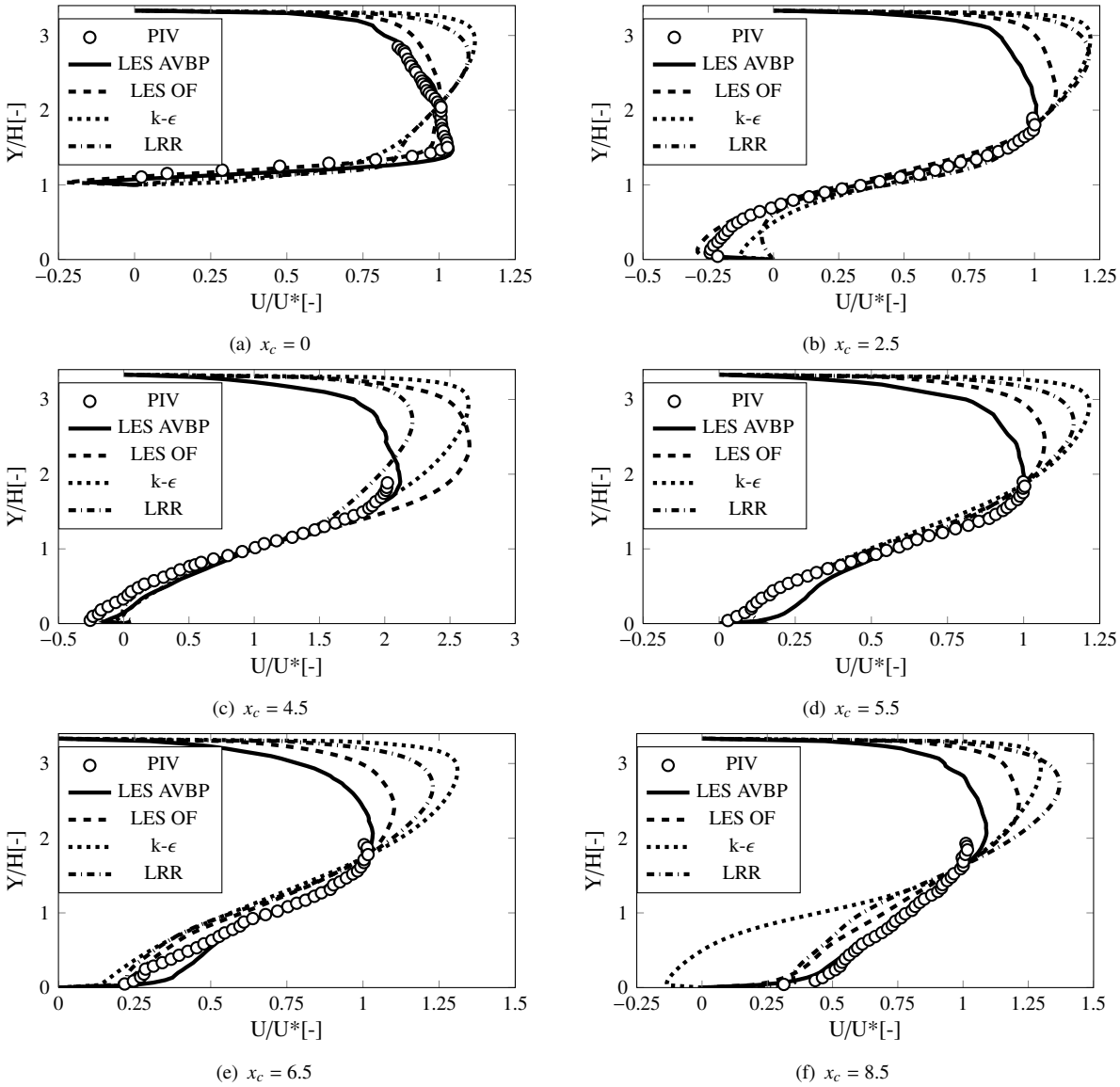

(a) $x_c = 0$ (b) $x_c = 2.5$

(c) $x_c = 4.5$ (d) $x_c = 5.5$

(e) $x_c = 6.5$ (f) $x_c = 8.5$

Figure 7: Streamwise velocity profiles along the rib ad pitch.

and for V3 at $y/H = 0.01$. Both LES show a good agreement with the PIV data, being within or close to the uncertainty of the experiments. The RANS simulations, however, both the $k - \epsilon$ model and the LRR Reynolds-stress model fail to predict realistic sizes of the recirculation zones. The major zone V1 is under predicted by both models, even more by the Reynolds-stress model. The $k - \epsilon$ model, however, completely fails to predict the recirculation zone on the rib top, while it is still by far under predicted by the Reynolds-stress model.

5.2.2. Secondary flow structures

Figures 8 (a) shows the streamlines for the PIV measurement on the rib top at the mid-section of the rib. Figure 8 (d) demonstrates that the three-dimensional flow field is not reproduced by the $k - \epsilon$ model and that it provides only two-dimensional results. Figure 8 (c) shows the streamlines for the LES of the OpenFOAM® computations. The secondary flow structures are well-visible and in a good agreement with the experimental data. Only the center of the secondary flow structure is positioned higher in the channel than in the experiment. In the top corners of

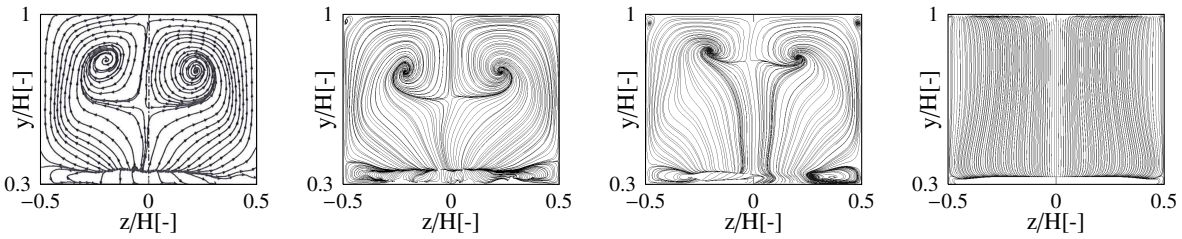

(a) PIV measurement (b) LES AVBP (c) LES OF (d) RANS $k\epsilon$

Figure 8: Streamlines on the rib top.

the channel, above the rib, another, smaller secondary flow structure is visible. It is counter-rotating opposite to the main circulation zones over the rib. Figure 8 (b) shows the streamlines on top of the rib for the LES with AVBP. Again, as for the OpenFOAM® LES, the secondary flow is well reproduced. The agreement with the experiment is very good, also for the position of the circulation zone center and for the magnitude of the circulation. As for the LES with OpenFOAM® and opposed to the experimentally shown streamlines, small counter-rotating circulation zones are visible, even smaller as in the OpenFOAM® case. To summarize the results for the secondary flow structures, only the LES, in particular obtained with AVBP show a good agreement with the experiment.

5.3. Heat transfer analysis

For the convective computations, iso-flux boundary conditions were applied around the ribs. The imposed iso-flux boundary condition for the experiment of Cukurel [9] was scaled as explained in the previous chapter by a factor of 10 and since we want to keep the Nusselt number constant with the same conductivity in the fluid, the characteristic length is now 10 times smaller, such that the heat transfer coefficient will be 10 times larger. To keep the same temperature ratio from inlet to the wall, the flux needs to be increased by a factor of 10 to keep dimensionally similar conditions.

Figure 9 shows the heat transfer on the bottom surface in terms of the enhancement factor around rib n^0 4 of the channel and shows a good agreement with the experimental results of Cukurel [9]. The overall level of the EF in the experiments and simulation is in very good agreement. Moreover, the effect of the secondary vortical structures on the EF is well visible in the EF contour plot. Only at the front and top parts of the rib the EF level differs quantitatively. A reason for parts of this discrepancy could be lateral conduction in the experiment, since it is very difficult to impose iso-flux boundary conditions on the edges without any lateral conduction, thus smoothing temperature peaks

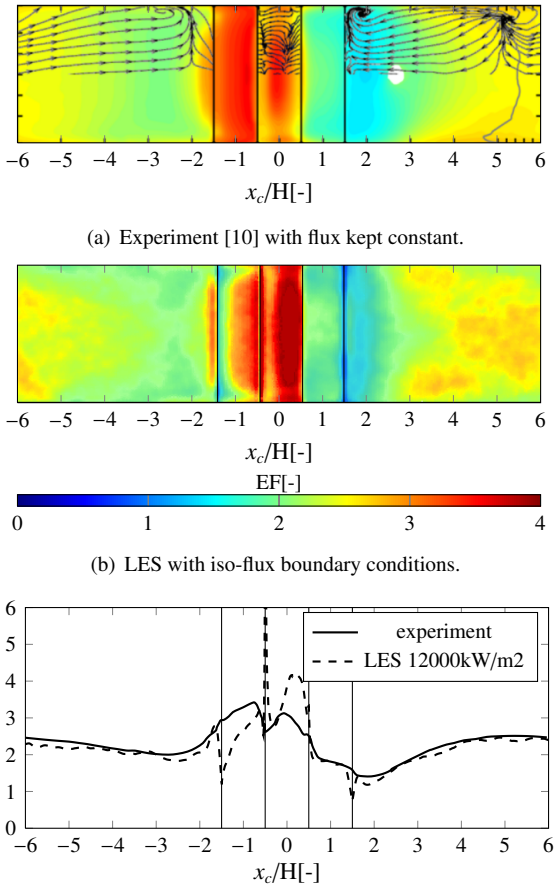

(a) Experiment [10] with flux kept constant.

(b) LES with iso-flux boundary conditions.

(c) EF for LES and experiment around unfolded rib.

Figure 9: EF contour plot over rib n^0 4 for convective computations (b) in comparison with experiment (a). View on the bottom surface with the front and back surfaces of the rib unfolded. Quantitative comparison between LES and experiment EF (c).

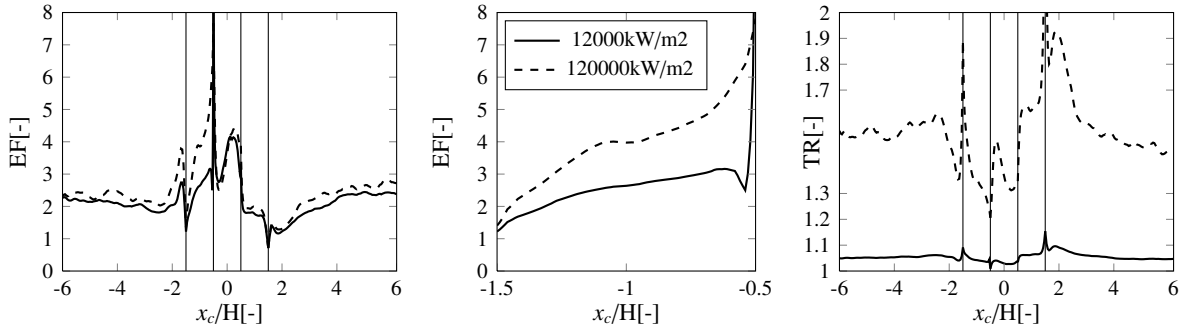

(a) EF around rib $n4$ (b) EF at rib front (c) Temperature ratio (T/T_∞) around rib

Figure 10: EF over rib n^0 4 (a) and the rib front (b) and the temperature around the rib for two different convective computations.

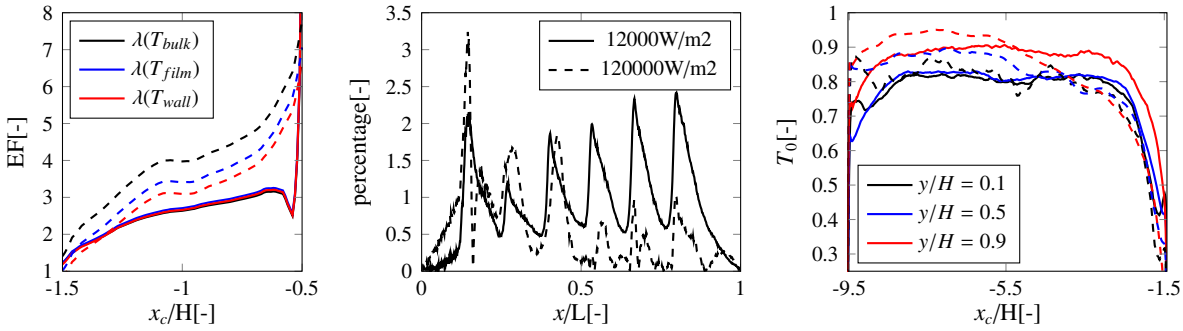

(a) EF at the rib front for different reference temperatures for the fluid conductivity $\lambda(T)$, with $T_{film} = \frac{T_{wall}+T_{bulk}}{2}$.

(b) Used bulk temperature (T_{bulk}) deviation from the centerline temperature ($100 \cdot \frac{T_{center}-T_{bulk}}{T_{bulk}}$) through the whole channel.

(c) Non-dimensionalized temperatures with $T_0 = \frac{T_{wall}-T(x)}{T_{wall}-T_{bulk}}$, perpendicular to rib front at different heights for both cases.

Figure 11: Impacts on the heat transfer coefficient and the EF.

	Rib						
	Upstream	Top	Downstream	Mean	Inter Rib	Average	Increase
experiment*	3.2	2.86	1.89	2.65	2.2	2.31	-
LES 12,000W/m^2	2.65	3.72	1.7	2.7	2.04	2.2	-
LES 120,000W/m^2	3.8	3.68	1.89	3.12	2.35	2.48	13%

Table 7: Enhancement Factor comparison; *experiment by [10].

that occur in the numerical simulations. The relative bulk flow temperature (or temperature ratio) $\frac{T_\infty}{\Delta T}$ was assumed to have only a small effect on the heat transfer in the experiments [10], and it is assumed that the Nusselt number depends only on the Reynolds number, the conductivity ratio between fluid and solid and the Biot number: $Nu = f(Re, K, Bi)$. To investigate the validity of this assumption, a second computation with a iso-flux boundary condition, increased by one order of magnitude in comparison with the first simulation, was done. In contrast to the assumption that the temperature ratio is negligible, Fig. 8 shows that there is indeed an influence of the inlet to wall temperature ratio on the heat transfer coefficient or respectively the enhancement factor. Globally, the enhancement factor varies by 13 % (Table 5 summarizes all values for the enhancement factor). The largest difference between both simulations appears at the rib front (Fig. 8 (b)), where the difference is on average 43 % and locally more than 100%.

The changes of fluid properties (viscosity and density) in the channel, especially close to the walls exposed to

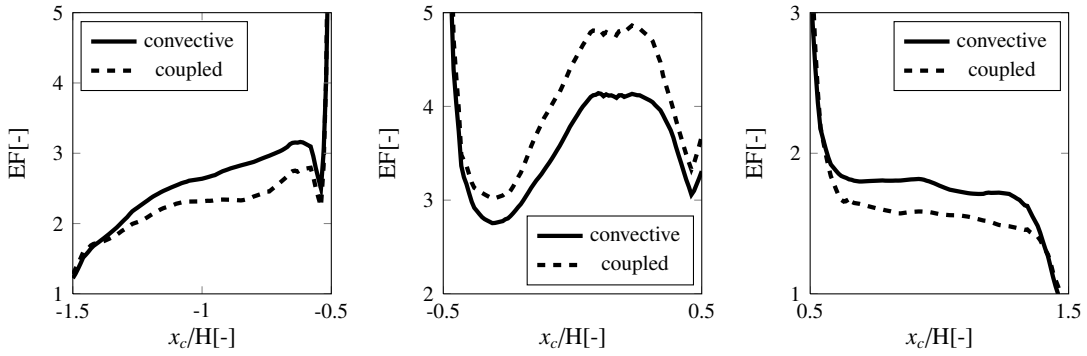

(a) EF around at rib front (b) EF around at rib top (c) EF around at rib back

Figure 12: EF over rib n^0 4 (a) and the rib front (b) and the temperature around the rib for two different convective computations.

the iso-flux boundary conditions lead to changes in the aerodynamics, as Table 3 shows, where the recirculation zones of different vortices are compared between the two cases. The larger recirculation zone V1 leads to an accelerated flow downstream, stronger impacting the next rib (Fig. 5 (a) and (b)), leading to a modified heat transfer. In addition, due to changes of the fluid temperature, the fluid conductivity $\lambda(T)$ changes and thus also alters the heat transfer (Fig. 9(a)). In discussing the differences between both computations, a review of the definition of the heat transfer coefficient (Eqn. 1) with the bulk temperature T_{bulk} is inevitable. The choice of a linearly increasing bulk temperature along the channel introduces errors as Fig. 9 (b) shows, where T_{bulk} is compared with the time-averaged temperature along the centerline for both cases. Moreover, the flow conditions in the channel are far from the assumptions of an ideal thermal boundary layer, as it is found on a heated flat plate, for which Eqn. 1 is more suited. It assumes the temperature reaches a constant value outside of the thermal boundary layer, which is not present in the current investigation as Fig. 9 (c) demonstrates. It shows non-dimensionalized temperatures for both cases starting perpendicular from the rib front at different heights, until reaching upstream the previous rib. Regarding the rectangular geometry of the heated walls, it is apparent that an unambiguous choice for the bulk temperature cannot be made. Also, none of the temperature distribution reaches unity, meaning the bulk flow temperature. Nevertheless, the change in channel aerodynamics, the choice and approximations of the reference output quantities of interest and the change in density, viscosity and fluid conductivity cannot solely explain the large differences for the heat transfer coefficient with the changed thermal boundary condition. It is furthermore assumed that the effect of the upstream history in the boundary layer as Maffulli (2013) describes, may also be important. Moreover, the upper half of the rib front is exposed to the reestablishing flow (Fig. 4) and is therefore particularly sensitive to changes in the operating or boundary conditions. This is where the largest differences between the two simulations appear as well as where differences between both simulations and the experiment occur. For the practical case of a real turbine blade, assuming a coolant temperature of 900K and a metal temperature at the material limit of 1200K (e.g., [10]) and a Biot number of order unity, we obtain a temperature difference in the blade of around 10K. Locally, this value may be larger due to larger local enhancement factor differences. Since the life of a turbine blade is reported to be half for an increased temperature of 30K, this temperature difference demonstrates the severe impact of the applied boundary condition on the design application.

5.4. Conjugate Heat Transfer and LES

Two major problems for conjugate heat transfer computations exist, which amplify in conjunction with LES: First, the large time scale disparity between solid and fluid domain [16] makes a pure strong coupling solution strategy obsolete. Second, it is well-known that for weak coupling strategies, stability problems occur. These stability problems depend on the specific weak coupling strategy (boundary conditions used, rate of exchange and the mesh size) and have been addressed by [17](confirmed by the numerical experiment presented in a previous study), [18] and more recently [19], among others, and are

current subject of research. The applied weak coupling strategy resembles the coupling strategy detailed by Verstraete [17] for RANS computations. Boundary conditions are exchanged from one domain to another, if the solution is considered as converged. Since we apply an unsteady computation (LES) for the fluid part, convergence means a statistically converged state. Knowing the stability properties of this weak coupling procedure for steady state simulation, its validity is assumed also for statistically converged LES. Dealing with a Biot number of order unity, a mixed type boundary condition using the heat transfer coefficient provides the advantage of an accelerated convergence using an appropriate value for the heat transfer coefficient, obtained via convective computations. For the cooling channel application, the hFFB (heat transfer coefficient forward flux backward) method was used. Figure 12 shows the results in terms of the EF around the rib. The EF increased for the coupled computation in comparison with the iso-flux LES and decreased on the rib front and back.

6. Conclusions

This contribution shows the suitability of the applied LES to capture the flow of a rib-roughened cooling channel, which is in good agreement with experimental results. Moreover, the heat transfer predictions for convective cases are also in a good agreement with the experimental results. This study shows that steady simulations are inappropriate to simulate the fluid flow and heat transfer in the channel. A significant influence of the applied thermal boundary condition has been observed demonstrating the importance of conjugate heat transfer. Finally, we applied an LES based weak coupling strategy for the cooling channel demonstrating a significant change in heat transfer.

Acknowledgments

The author is grateful to his Promotor Professor Wolfgang Schröder and supervisor Professor Tom Verstraete for the support and promotion of this doctoral research. The research leading to these results has received funding from the European Community's Seventh Framework Programme (FP7, 2007-2013), PEOPLE programme, under the grant agreement No.FP7-290042(COPAGT project).

References

[1] J. Han, S. Dutta, S. Ekkad, Heat Transfer Cooling Technology, Taylor and Francis, Reading, MA, 2000.

[2] L. Perelmann, On conjugate problems of heat transfer, International Journal of Heat and Mass Transfer 3 (1961) 293–303.

[3] T. Schönfeld, T. Poinsot, Influence of boundary conditions in les of premixed combustion instabilities, Annual Research Briefs. Center for Turbulence Research, NASA Ames and Stanford University, pp. 73-84.

[4] S. Mendez, F. Nicoud, Large eddy simulation of a bi-periodic turbulent flow with effusion, Journal of Fluid Mechanics, 598, pp 27-65.

[5] P. Sagaut, Large eddy simulations for incompressible flows, Scientific computation series. Springer-Verlag.

[6] O. Colin, M. Rudgyard, Development of high-order taylor-galerkin schemes for unsteady calculations, Journal of Computational Physics. 162(2), pp338-371.

[7] O. Colin, A. Benkenida, C. Angelberger, 3d modeling of mixing, ignition and combustion phenomena in highly stratified gasoline engine, Oil and Gas Science Tech. 58, 1 , 47-62, 111.

[8] T. Poinsot, S. Lele, Boundary conditions for direct simulations of compressible viscous flows, J. Comput. Phys., 101(1), pp. 104-129.

[9] B. Cukurel, Conjugate heat transfer investigation of a fixed rib roughened cooling passage., Ph.D. thesis, Purdue University and Von Karman Institute for Fluid Dynamics (2012).

[10] B. Cukurel, T. Arts, Local heat transfer dependency on thermal boundary condition in ribbed cooling channel geometries, ASME Journal of Heat Transfer 135 (2013) 101001–1–101001–11.

[11] C. J. Keylock, T. E. Tokyay, G. Constantinescu, A method for characterizing the sensitivity of turbulent flow fields to the structure of inlet turbulence., Journal of Turbulence.

[12] R. Fransen, - simulation aux grandes echelles pour la modélisation aérothermique des aubages de turbines refroidies, Ph.D. thesis, Université de Toulouse - MeGeP - Dynamique des Fluides (2013).

[13] M. Cakan, Aero-thermal investigation of fixed rib-roughened cooling passages, Ph.D. thesis, Universite Catholique de Louvain and Von Karman Instititue for Fluid Dynamics (2000).

[14] L. Casarsa, Aerodynamic performance investigation of a fixed rib-roughened internal cooling passage, Ph.D. thesis, Universita Degli Studi Udine and Von Karman Instititue for Fluid Dynamics (2003).

[15] L. Casarsa, T. Arts, Experimental investigation of the aerothermal performance of a high blockage rib-roughened cooling channel, ASME Journal of Turbomachinery 127 (2005) 580–588.

[16] L.He, M. Oldfield, Unsteady conjugate heat transfer modeling, ASME Journal of Turbomachinery 133 (2011) 031022–1–12.

[17] T. Verstraete, Multidisciplinary turbomachinery component optimization considering performance, stress and internal heat transfer, Ph.D. thesis, Ghent University and Von Karman Instititue for Fluid Dynamics (2008).

[18] F. Duchaine, A. Corpon, L. Pons, V. Moureau, F. Nicoud, T. Poinsot, Development and assessment of a coupled strategy for conjugate heat transfer with large eddy simulation: Application to a cooled turbine blade, International Journal of Heat and Fluid Flow 30 (2009) 1129–1141.

[19] M. Errera, B.Baque, A quasi-dynamic procedure for coupled thermal simulations, International Journal for Numerical Methods in Fluids 72 (2013) 1183–1206.

Blade Tip Timing and Blade Tip Clearance Measurement System Based on Magnetoresistive Sensors

Roberto Tomassini

Turbomachinery and Propulsion Department, von Karman Institute for Fluid Dynamics, Belgium, roberto.tomassini@vki.ac.be

Supervisor: Jean-Franois Brouckaert

Associate Professor, Turbomachinery and Propulsion Department, von Karman Institute of Fluid Dynamics, Belgium, brouckaert@vki.ac.be

University Supervisor: Gianluca Rossi

Full professor, Mechanical Engineering Department, University of Perugia, Italy, gianluca.rossi@unipg.it

Abstract

A simultaneous Blade Tip Timing (BTT) and Blade Tip Clearance (BTC) measurement system enables the determination of turbomachinery blade vibrations and ensures the monitoring of the existing running gaps between the blade tip and the casing. This contactless instrumentation presents several advantages compared to the well-known telemetry system with strain gauges, at the cost of a more complex data processing procedure. Nevertheless, margins of improvement still exist for different aspects of this measurement technique.

This paper particularly focuses on the results achieved using a novel magnetoresistive sensor for simultaneous BTT and BTC measurements. The sensor measurement principle is described. The sensitivity to gap variation is investigated. In terms of measurement of vibrations, experimental investigations were performed at ITWL (Warsaw - Poland) in a real aeroengine and in the VKI R2 compressor rig. The advantages and limitations of the magnetoresistive probe for turbomachinery testing are highlighted.

Keywords: tip timing, tip clearance, non-contact measurement system, magnetoresistive sensor

1. Introduction

All turbomachinery blades and components experience vibrations during operation due to several sources such as: unbalance, pressure distortions, flutter, stall and surge, mistuning [1]. Unfortunately this undesirable structural motion affects fatigue life, performance and integrity. For more than half a century, vibration measurements have been performed by installing strain gauges on the blades and using telemetry to transmit their signals. Nowadays, the so-called Blade Tip Timing (BTT) technique, is adopted by all manufacturers as a replacement for the classical strain gauge technique because of its non-intrusive character. The main concept behind a BTT system is the determination of the time of arrival (TOA) of the blade tips. Contactless sensors mounted in the casing generate a signal pulse at the blade passage. In absence of any vibration, the TOA of the blade tip depends on the rotational speed only. Nevertheless, when the blade vibrates, blade arrival times will depend on amplitude, frequency and phase of the vibration. Therefore, the blade motion can be measured from time variations.

A fundamental parameter influencing the machine efficiency is the blade tip clearance. During operation the tip gap changes due to mechanical loads and varying temperature and pressure conditions inside the turbomachine. To prevent a fatal damage, an accurate monitoring system is mandatory for optimized and safe operations. The so-called blade tip clearance (BTC) measurement systems are based on non-contact probes sensitive to the distance between the passing blade tip and the casing.

The contactless probes adopted in BTT and BTC systems can be of various types: optical, eddy current, microwave, capacitive, as briefly introduced by Chana [2]. The most used are optical ones, because of the fast rise time, the reliability and the repeatabil-

ity. However, they suffer from low tolerance to debris which makes their application difficult outside of laboratory conditions [3].

Whatever the applied technology is, the instrumentation consists of several sensors mounted at fixed angular positions in the casing of a turbomachine. To excite the vibrations of the blades, different techniques can be adopted. Magnetic exciters were used at NASA [4] and at MTU [5]. A jet impinging on the blade tip was proposed by Sonnichsen et al [6], as well as inlet flow distortions by Meyer et al [7]. The standard approach is to excite the blade vibrations during rotation. Another way reported in literature to test tip-timing systems consists in generating simulated data. For instance, a numerical calibrator, the UTTC, was realized at Siemens by Uwe and Zidorn [8]. Hardware components were used to generate TTL pulses according to simulated tip timing signals and to directly inject them into commercially available BTT systems. A numerical simulator was developed also by Health and Imregun [9] while developing a new post-processing method, as well as in the work of Gallego Garrido et al [10].

This paper focuses on a novel BTT and BTC probe based on magnetoresistive elements [11]. The sensor measurement principle is described. This technology is already used in commercial displacement sensors, but is new for turbomachinery applications. A preliminary characterization showed the main advantages: cheap technology, small size, fast response [12]. This paper reports measurements of blade tip clearance and blade vibrations. An innovative testing approach suggested by Rossi and Brouckaert [13], based on the blade motion decomposition, was adopted to realize an innovative calibration bench [14]. In this case the vibration is imposed to the probe, while non-vibrating blades are kept in rotation. A large part of the development of the measurement system based on magnetoresistive elements was performed in the innovative bench. Advantages and limitations are reported. Finally, a validation test of the whole instrumentation chain was performed in a real engine at ITWL (Warsaw - Poland). The improved measurement system was then installed in the VKI R2 compressor.

2. The magnetoresistive sensor

Magnetoresistivity is the ability of a material, like a Permalloy thin film, to change resistance under the influence of a magnetic field [11]. In particular, a change of direction (θ) of the magnetic field, results in a variation of the output DC voltage. By placing a magnetoresistive element beside a permanent magnet, a system sensitive to the variation of magnetic field is created. Hence, if a ferromagnetic object (like a blade) passes in front of it (Figure 1), there will be a distortion of the magnetic field, therefore a variation in the output signal. During the design and development of the novel probe, different configurations of the two components (sensing element-magnet) were investigated. For the same $\Delta\theta$, the output signal amplitude changes with the magnet position, shape and strength. In order to maximize the Signal to Noise Ratio (SNR), a preliminary optimization of the sensor components layout was performed experimentally and numerically [15]. The first sensor prototype manufactured is shown in Figure 2. It is made of a cylindrical permanent magnet placed beside the magnetoresistive thin film. The casing is a 8 mm outer diameter Brass pipe, with the sensing element placed at the top. A length of 40 mm was the best compromise for the tests reported. Smaller probes can be realized, up to 30 mm length. A characterization of the sensor and a comparison with other types of probes, is reported in [14]. Interesting results were pointed out: fast rise time (about 20 ns), high signal repeatability and uncertainty of ± 22 μm (20:1) in clearance measurements.

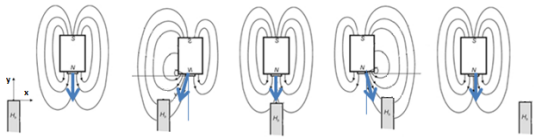

Figure 1: the sensor measurement principle

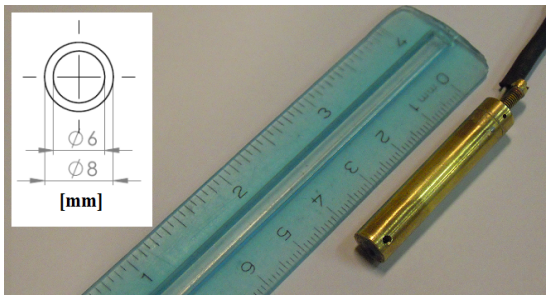

Figure 2: the magnetoresistive sensor

3. Clearance measurements

This paragraph focuses on the experimental investigations of clearance measurements. Every time a

blade is passing in front of the sensor, a pulse is generated. Tests have shown that the amplitude of the output signal is sensitive to variations of the gap between a passing blade tip and the sensor head.

3.1. Test setup and methodology

The passage of a blade in front of the sensor at different gaps was studied in a static test bench. As shown in Figure 3, a blade was mounted in a rotary slider with a resolution of 1°, facing the magnetoresistive sensor installed in a linear slider with a resolution of 10 μm. The sensor axis was aligned with the blade axis at 0° on the rotary slider. The blade passage was discretized and studied in the angular range [-20 + 20]° with an angular step of 2°. The measurements were repeated for different gaps (sensor head-blade tip): [0.5 1 1.5] mm. At every fixed position, the output DC signal was acquired and represents one point of the resulting fitting curves of Figure 4.

3.2. Results

Figure 4 shows the typical pulses observed at the blade passage at different gaps. The variation of the clearance results in a signal amplitude variation: the bigger the gap, the smaller the signal amplitude. An interesting aspect to point out is that, whatever the clearance is, all signals pass through a common point at 0 Volt. This behavior is of fundamental importance for tip timing measurements because the zero volt crossing time does not depend on the clearance. The clearance between a passing blade tip and the new sensor head can be monitored by the maximum peak value or the peak to peak value of the blade pulse. As recently shown by Tomassini et al [14], clearance measurements are possible with an uncertainty of ± 22 μm (20:1).

4. Vibration measurements

The components of the measurement system (sensors, electronics and software) were realized during the on-going collaboration between VKI and the Italian Universities of Perugia and Padova. A large part of the development process was performed in an innovative calibration bench: according to the idea of the blade motion decomposition [13], the new bench was realized and recently presented by Tomassini et al [14]. Instead of having fixed casing sensors and vibrating blades, the innovative approach consist in letting the sensor vibrate while non-vibrating blades are kept in rotation. The biggest advantages of this

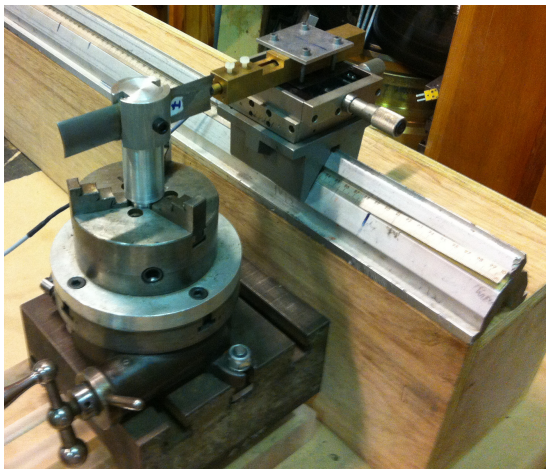

Figure 3: the clearance test bench

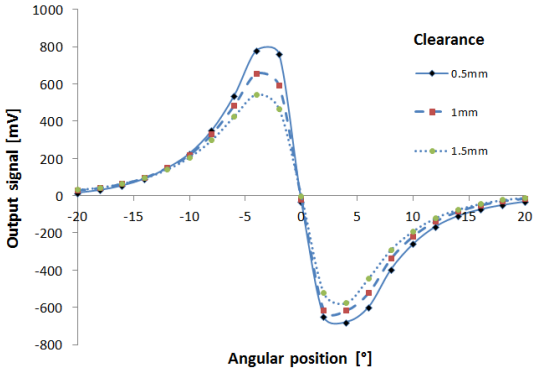

Figure 4: blade passage pulse at different clearances

system are the possibility to know the expected measured vibrations and the flexibility in changing the test conditions. Recently, the whole measurement system (software included) was improved and validated during two external collaborations at Fogale Nanotec (Nimes, France) and at ITWL (Warsaw, Poland) in a real military engine (Figure 5).
This paragraph reports the validation test in Poland and a vibration test performed in the VKI R2 compressor rig (Figure 6) with the improved instrumentation.

4.1. The SO-3 turbojet engine: test setup and methodology

The magnetoresistive sensors were mounted in the military SO-3 turbojet engine of Figure 5. Four sensors were installed in slots prepared in the upper compressor casing in the plane of the second rotor stage of the compressor. The rotor has 41 blades and a tip

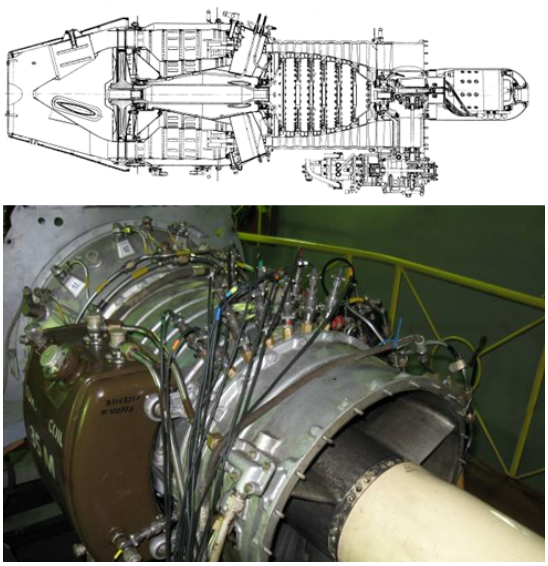

Figure 5: the SO-3 turbojet engine

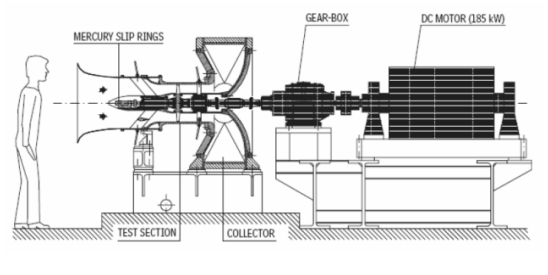

Figure 6: the VKI R2 compressor rig

radius of 207 mm. Tip-timing data were acquired during a speed transient up to 16000 rpm. An inlet obstruction object, namely a piece of felt, was attached to the IGVs to excite the blade resonances. Previous tests performed at ITWL showed two blade resonances around 8000 rpm and 12000 rpm. The objective of the test was to repeat the experiment to validate the diagnostic system based on magnetoresistive elements.

4.2. Results

The magnetoresistive signals were recorded and processed by the ITWL Tip-Timing software. Figures 7 and 8 display the waterfalls of the measured displacements of the first 15 blades. The graph of Figure 7 is related to the test with the ITWL instrumentation, the one of Figure 8 is related to the magnetoresistive probes. Both waterfalls show two resonances around 8000 rpm and 12000 rpm. Some blades were excited at a slightly different speed, which can be due to mistuning. Unfortunately, the measured displacements obtained with the magnetoresistive sensors show a drift. There might be several reasons and further investigations on the single components of the measurement chain are on-going.

From the FEM analysis performed at ITWL on the blade geometry, the two measured resonances correspond to the excitation of the first bending mode calculated at 457Hz. The data must be processed further to have an estimate of the measured vibration frequency. Nevertheless, it is possible to compare the results in a qualitative way. Figure 9 focuses on the measured displacements around 12000 rpm. The peaks of the resonances of the blades in the two tests are in strong agreement, both in amplitude and with respect to the speed. The expected resonances were measured correctly and this confirm the possibility of performing tip-timing measurements with the novel magnetoresistive probes. Moreover, the whole instrumentation chain was successfully working in a real engine for the first time. The VKI sensors were compatible with the ITWL acquisition system and processing software. No damage was reported. Finally, the dedicated electronics developed at VKI was successfully working up to 11KHz blade passing frequency and no particular noise problems were observed.

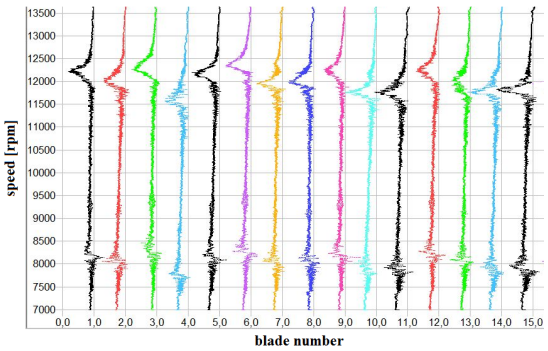

Figure 7: The waterfall of the measured displacements of the first 15 blades - ITWL sensors

4.3. The VKI R2 compressor: test setup and methodology

The validated and improved instrumentation was installed in the VKI R2 compressor. It is a high speed compressor driven by a 185kW DC motor. The rotational speed can vary up to 6000 rpm. It is a single stage axial compressor with a 400 mm tip diameter test section. The rotor is composed of 24 subsonic blades of the NACA 65 family; the hub radius is 100 mm. The stator is composed of 30 blades. The probes

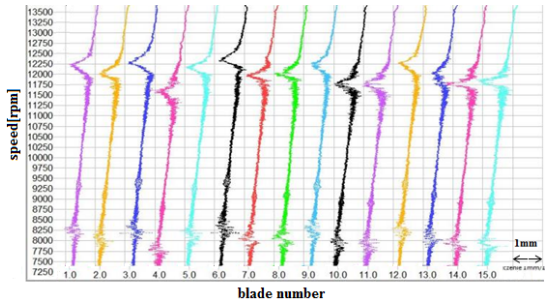

Figure 8: The waterfall of the measured displacements of the first 15 blades - Magnetoresistive sensors

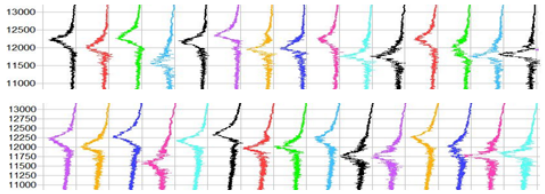

Figure 9: Comparison of the measured displacements around 12000 rpm

can be inserted at four circumferential locations, every 90°. Three sensors were mounted in the casing at [0 90 180]° . Tip-timing signals were acquired along a speed transient from 2000 rpm up to 5500 rpm, with a sampling frequency of 1 MHz per channel. No information was available regarding the expected blade vibration modes and frequencies. For this reason, a hammer test with an accelerometer was performed on the blades to have an estimate of the first bending frequency. It was assessed to be around 480Hz. Considering this and the speed range of the test, it is possible to get the Campbell diagram of figure 10. The red line represents the first bending frequency of the blades. It should account for the contribution of the centrifugal force at different rpm, which increases the blade resonance frequency with the speed, but it could not be estimated at this stage. The Engine Order lines (EO) indicate the multiple integers of the rotor rotational frequency. For instance, the 2EO is the line fitting all the points equal to 2 times the rotational frequency. When a line representing a blade vibration mode crosses an EO line, a synchronous resonance can be excited at the crossing speed. Therefore, during this test, synchronous blade resonances may appear around 2800, 3200, 3600, 4200, 4800 rpm. To let the compressor works in off-design condition, a distortion grid was mounted at the rotor inlet (Figure 11). Moreover, an air injection system at the blade tip was installed to excite asynchronous resonances. Four bent pipes were installed in the casing, two at 0° and two at 180° (figure 11). They blow compressed air at 5 bar against the blade tips during the rotation at about 3500 and 5400 rpm. The air injection was controlled manually by means of a pneumatic valve. It was connected to a collector that sent air to the two couples of casing pipes, as in figure 12.

From the acquired signals, the software provides the measured blade tip displacement samples. The basic concept behind a tip-timing system is to calculate the blade vibrations from the time variations. Indeed, if there is a vibration, the arrival time of the blade tip will be delayed (with a positive or negative sign) with respect to the undisturbed rotation. Therefore, at every revolution, for every blade, the tip velocity is estimated from the successive passages of the blades and the variation of the tip arrival time, due to the vibrations, is calculated (ΔTOA). Finally, the blade displacement samples are obtained as follows:

$$S_{ir} = V_{tip} * \Delta TOA \tag{1}$$

Where:
S_{ir} = the measured displacement sample of the blade i (i = 1...24), at the revolution r;
V_{tip} = the blade tip velocity;
ΔTOA = the measured variation of the time of arrival of the blade pulse;

The measured displacements of all the blades are plotted together in the so-called waterfall graph. Displacement amplitudes are plotted against the rotor speed and shifted along the y axis, according to the blade number, in order to have an ensemble plot. From one sensor, it is possible to calculate one sample per blade per revolution. When a blade is vibrating, it has a frequency higher than the revolution frequency, therefore the measurement of blade vibrations with only one sensor is affected by aliasing. To avoid this, usually 6 to 8 sensors are mounted together in the commercial BTT systems. In this work, three sensors were installed in the compressor, but at this stage, the results are obtained from only one of them.

4.4. Results

Figure 13 shows the waterfall of the measured displacements of the first 4 blades. The measured displacements of blade 2, 3 and 4 were shifted (by adding a DC constant value) to have the waterfall of all the samples on the same graph.

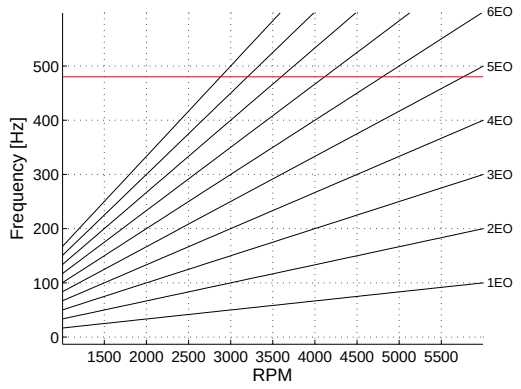

Figure 10: the VKI R2 Campbell diagram

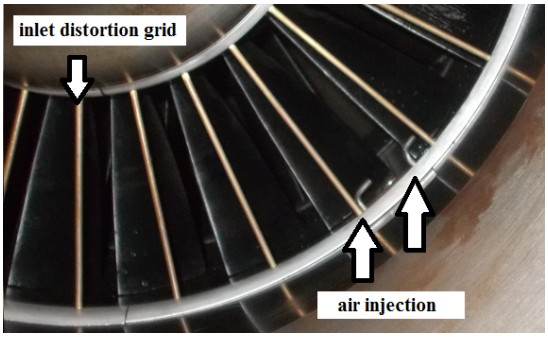

Figure 11: the VKI R2 compressor inlet

The blade vibration frequency can be measured by having several sensors mounted in the casing, at optimized angular positions and by processing the acquired signal with a professional commercial multichannel software. At this stage, it was possible to process the data from only one sensor. Therefore, the samples plotted are correct in terms of amplitude of the measured blade tip displacement, but the frequency is aliased. The synchronous blade resonances appear in the waterfall as a change in the DC component of the measured displacement and the maximum peak value is representative of the vibration amplitude. The asynchronous blade resonances appear as an increase of frequency with respect to the base noise of the system and the maximum peak value is representative of the vibration amplitude.

As shown in Figure 14, a synchronous resonance around 3650 rpm and an asynchronous resonance around 3450 rpm were measured. The latter was excited by the air injection system. Moreover, two synchronous resonances around 4200 and 4900 rpm were measured (Figure 15). The latter was expected to

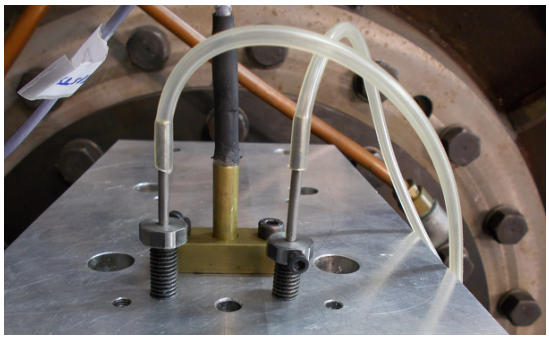

Figure 12: one sensor and the air pipes mounted in the compressor casing

be around 4800 rpm, but the effect of the centrifugal force was not considered. Finally, the asynchronous resonance around 5400 rpm is also present.

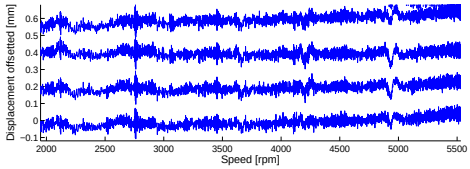

Figure 13: the waterfall of the measured displacements of the first 4 blades

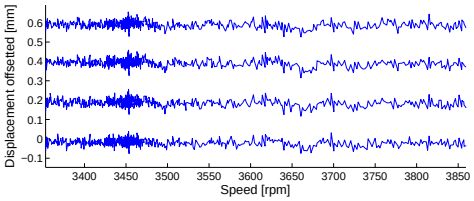

Figure 14: A detail of the measured displacements around 3500 and 3600 rpm

5. Conclusions

A magnetoresistive probe for simultaneous Tip-Timing and Tip-Clearance measurements was realized and tested. The blade tip gap can be monitored by means of the maximum signal amplitude or the peak to peak value. Blade vibration measurements were performed in a real engine at ITWL Poland, and in the VKI R2 compressor. An innovative approach for the testing and the characterization of Tip Timing systems was introduced with the calibration bench. Imposing the vibration to the sensor ensures

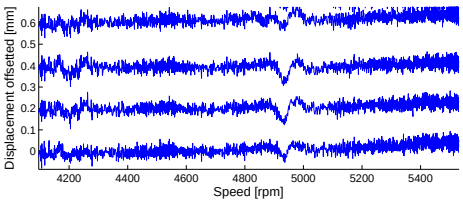

Figure 15: A detail of the measured displacements around 4200 and 4800 rpm

the advantages of knowing the expected results and having more flexibility in the simulation of different vibration cases. Further developments can significantly help in the non-trivial uncertainty analysis of tip-timing data. Regarding the application of the magnetoresistive technology in turbomachinery testing, the main advantages reported are a performance in line with the existing sensors but at lower costs, small sizes and tolerance to debris. Limitations may occur in applications at high temperature (such as turbines), which should be investigated and with non-ferromagnetic blades, which require special expedients.

Acknowledgments

The author would like to acknowledge the professors and technicians of the von Karman Institute, the University of Padova CISAS G. Colombo and the Engineering Department of the University of Perugia. Finally, thanks goes to ITWL (Warsaw - Poland) and Dr. Radoslaw Przysowa for collaborating in this work. The validation test was financed by the Polish National Science Centre (NCN) under the decision DEC-2011/01/D/ST8/07612.

References

[1] J.-F. Brouckaert, Tip timing and tip clearance problems in turbomachinery, Lecture Series VKI-LS-2007, von Karman Institute for Fluid Dynamics (2007).

[2] K. Chana, Fundamentals of tip timing and tip clearance sensors, in Tip timing and tip clearance problems in turbomachinery, Lecture Series VKI-LS-2007, von Karman Institute for Fluid Dynamics (2007).

[3] G. Husler, P. Ettl, M. Schenk, G. Bohn, I. Laszlo, Limits of optical range sensors and how to exploit them, International Trends in Optics and Photonics 74 (1999) 328–342.

[4] J. Dexter, G.V. Brown and O. Mehmed, A magnetic suspension and excitation system for spin vibration testing of turbomachinery blades, National Aeronautics and Space Administration, Lewis Research Center, 1998.

[5] M. Zielinski, Non-contact blade vibration and tip clearance measurements on aero engine compressors with BSSM, in Tip timing and tip clearance problems in turbomachinery, Lecture Series VKI-LS-2007, von Karman Institute for Fluid Dynamics (2007).

[6] H. E. Sonnichsen, P. H. Wawrzonek, R. B. Connell, B. D. Milatovic, Blade vibration test apparatus and method, uS Patent 6,679,121 (Jan. 20 2004).

[7] A. Meyer, H. F. Calvert, C. R. Morse, Effects of obstructions in compressor inlet on blade vibration in 10-stage axial-flow compressor, Tech. Rep. NACA-RM-E9L05, NASA Center (1950).

[8] U. Pfeifer, M. Zidorn, Tip timing measurement chain validation with the universal tip timing calibrator uttc, approach and experience, in: 10th International conference on vibration measurements by laser and noncontact techniques AIVELA 2012, Vol. 1457, AIP Publishing, 2012, pp. 43–51.

[9] S. Heath, M. Imregun, An improved single-parameter tip-timing method for turbomachinery blade vibration measurements using optical laser probes, International journal of mechanical sciences 38 (10) (1996) 1047–1058.

[10] J. Gallego-Garrido, G. Dimitriadis, J. R. Wright, Development of a multiple modes simulator of rotating bladed assemblies for blade tip-timing data analysis, in: 2002 International Conference on Noise and Vibration Engineering, Katholieke Universiteit Leuven, 2002, pp. 1437–1446.

[11] P. Holman, Magnetoresistance (mr) transducers and how to use them as sensors, Honeywell International. July.

[12] J.-F. Brouckaert, R. Marsili, G. Rossi, R. Tomassini, Development and experimental characterization of a new non contact sensor for blade tip timing, in: 10th International conference on vibration measurements by laser and noncontact techniques AIVELA 2012, Vol. 1457, AIP Publishing, 2012, pp. 61–68.

[13] R. G, B. JF, Design of blade tip timing measurements systems based on uncertainty analysis, ISA 58th International Instrumentation Symposium, San Diego, USA.

[14] R. Tomassini, G. Rossi, J. Brouckaert, On the development of a magnetoresistive sensor for blade tip timing and blade tip clearance measurement systems, in: 11th International conference on vibration measurements by laser and noncontact techniques AIVELA 2014: Advances and Applications, Vol. 1600, AIP Publishing, 2014, pp. 65–73.

[15] E. Cardelli, A. Faba, R. Marsili, G. Rossi, R. Tomassini, Magnetic nondestructive testing of rotor blade tips, Journal of Applied Physics 117 (17) (2015) 17A705.

MULTIPHASE FLOWS

Multi-Fluid Modeling of Magnetic Reconnection in Astrophysical and Laboratory Plasmas

Alejandro Alvarez Laguna

von Karman Institute for fluid Dynamics, Aeronautics and Aerospace Department, alejandro.alvarez.laguna@vki.ac.be

Supervisor: Herman Deconinck

Professor, von Karman Institute for fluid Dynamics, Aeronautics and Aerospace Department,deconinck@vki.ac.be

Co-Supervisor: Andrea Lani

von Karman Institute for fluid Dynamics, Aeronautics and Aerospace Department, lani@vki.ac.be

Promoter: Stefaan Poedts

Professor, KU Leuven, Centrum voor mathematische Plasma-Astrofysica, stefaan.poedts@wis.kuleuven.be

Abstract

Improved models for characterizing magnetized partially ionized plasma are essential to understand the phenomena taking place in astrophysical and laboratory plasmas. Particularly, scenarios where dissipative processes and thermo-chemical inequilibrium play an important role are beyond the classical single-fluid Magnetohydrodynamics (MHD) representation. Multi-fluid models that consider each particle species as a separate fluid offer an alternative approach especially suitable for those conditions. In the present work, the magnetic reconnection taking place in the chromosphere is studied using a two-fluid model considering neutrals and charged species. The numerical method solving multi-fluid equations coupled to Maxwell's equations is presented in this work. Also, a finite volume method for solving the radiative transfer equation (RTE) is presented to be used in future studies of magnetic reconnection.

Keywords: Magnetohydrodynamics (MHD), Magnetic Fields, Plasmas, Magnetic Reconnection, Sun: Atmosphere, Radiative Transfer.

1. Introduction

Numerical study of plasma flows continues to be an important area of research in a number of fields ranging from astrophysics to engineering applications. The application of electromagnetic fields to control the dynamics of electrically conducting flows has a long tradition in the aerospace industry that uses different concepts for flight and propulsion including plasma actuators, plasma thrusters or MHD by-pass arrangements in scramjets. In the present work, we will focus in two areas of particular interest for the CFD community, solar physics and laboratory plasmas.

The activity of the Sun has a great impact in our technology and ultimately in today's modern society that strongly depends on communications and satellite operations. From a global socio-economic perspective, the most important manifestations of solar activity are the solar wind and solar eruptions, i.e. solar flares and coronal mass ejection (CMEs). The unsteady but continuous emission of particles at high speed and temperature from the Sun into the space can hinder human activity at different levels. Satellite operations can be seriously affected by plasma ejected during solar storms, producing important damages or the loss of some of them, like the Telstar 401 that was short cut in January 1997. More recently, in 2003, a solar storm caused disruptions in the airplane routes and the CME affected several communication satellites (two were total loss). Also, when

the high energetic charged particles ejected from the Sun reach our atmosphere can produce the so-called Geo-magnetically Induced Currents (GICs) that cause hazards in oil pipelines and power grid outages. An example of the latter is the magnetic storm that burned a $36 million transformer in New Jersey and left 6 million people more than 10 hours without electrical power in Quebec in winter conditions (March 1989). As a matter of fact, the cost of a severe space storm has been estimated to be trillions of dollars for the first year after the storm with recovery times of 4 to 10 years (an order of magnitude more than that of Hurricane Katrina) [1].

It is therefore necessary to improve the understanding and modeling of the phenomena taking place in the Sun for enhancing the tools used for the space weather forecasting and eventually reducing its risk on our technology. Magnetic reconnection is a process especially significant in space weather since it has been long considered as a mechanism for creating transient phenomena in magnetized plasma. It occurs when oppositely directed magnetic field lines in conducting plasma merge due to diffusive processes producing a change of topology. The rearrangement of magnetic field lines produces a change of the magnetic flux that due to the finite conductivity creates a current sheet. In addition, the reconnection process causes a conversion of magnetic energy into kinetic and thermal energy, heating up the flow and accelerating it up to very high speed in very small timescales.

There are a wide variety of astrophysical scenarios in which the magnetic reconnection plays an important role. It is considered to be a likely mechanism to heat the corona to a few million degrees, still one of the biggest mysteries in Heliophysics [2]. Also, in CMEs and solar flares it is considered as a triggering mechanism which is present during the onset and early stages of the ejection [3]. In the Earths magnetosphere it is said to produce the plasma outflow at the magnetotail that is driven by the Earths magnetic field into the atmosphere producing the aurorae borealis and the GICs [4].

Magnetic reconnection also occurs in nuclear fusion and laboratory plasmas producing instabilities such as sawtooth in tokamaks and relaxation processes in reverse field pinch and spheromak devices, causing degradation in energy and particle confinement. A recent experimental study [5] has shown that during reconnection taking place in laboratory plasmas, magnetic energy is transferred differently to ions than electrons. Also, it is shown the different dynamics of ions and electrons due to their different mass and electric charge. The latter is the so-called *two-fluid effects*.

In the present work, we will focus on studying the magnetic reconnection in the Sun chromosphere, following the work presented in [6]. Observational data [7] have unveiled that the magnetic reconnection is the driver mechanism for the chromospheric jets and the spicules. The former can have timescales of 200-1000 s and current sheet length scales up to 5 Mm, producing outflows of 10 km/s. On the other hand, the spicules are smaller but faster phenomena, that last 10-600 s in length scales up to 1 Mm causing outflows up to 20-150 km/s [6].

In the present work, we present a summary of the modeling of magnetic reconnection, focusing on the analytical models and explaining the possible benefits of multi-fluid modeling. The two-fluid partially ionized reactive plasma model including neutrals and charge species is presented, as well as, the Maxwell's equations describing the evolution of the electromagnetic field. Also, the radiative transfer equation is presented, leaving the coupling with the fluid model for future developments. The numerical method including a finite volume method for solving Maxwell equations using hyperbolic divergence cleaning coupled to AUSM method for the fluids is explained hereafter. Additionally, the validation of the coupling on the Hartmann flow is presented. Furthermore, a finite volume method solving the RTE and its validation is shown in the present work. Finally, the results of a 2D reconnection under chromospheric conditions are presented with preliminary 3D results using the two-fluid model.

2. Modeling of the magnetic reconnection

Magnetic reconnection is a process that happens as a result of a diffusive mechanism that produces a decay in the electrical conductivity of the plasma. The frozen-in constrain that holds in ideal plasmas (with infinite conductivity) is broken in a small region of width δ and length L. In this region, the magnetic field lines reconnect producing a rate of magnetic flux that results in the formation of a current sheet. Thus, the non-dimensional magnetic reconnection rate is defined [8] as follows:

$$M = \frac{d\Phi/dt}{v_A B_i} \tag{1}$$

where Φ is the magnetic flux per unit length in the direction perpendicular to the plane containing the

current sheet , v_A is the Alfven speed and B_i is the magnetic field evaluated upstream of the current sheet.

Therefore, it is obvious to realize that the classical ideal MHD equations that consider the conductivity to be infinite are not able to tackle the physics involved in the reconnection. Nevertheless, the resistive singlefluid theory has developed analytical models for 2D steady magnetic reconnection. The Sweet-Parker model [9] proposes a non-dimensional reconnection rate of the form:

$$M = R_m^{-1/2} \tag{2}$$

where

$$R_m = v_A L/\eta \tag{3}$$

is called the Lundquist number, and η is the resistivity.

However, the model is unable to explain the fast energy released by the solar flares or in chromospheric jets and spicules, providing reconnection rates several orders of magnitude smaller.

On the other hand, the Petschek model [10] predicts faster reconnections suggesting geometry different from the Sweet-Parker one, Eq. 4. However, the model assumes explicitly or tacitly that resistivity gives the configuration setup. Because of this controversial issue, the Petschek model has been gradually thrown back [11].

$$M = \frac{\pi}{8\ln(R_m)} \tag{4}$$

Therefore, it is necessary to consider alternative theories to model the reconnection. The multi-fluid models consider each particle species as a different fluid that interact among each other by means of collisions and chemical reactions, exchanging thus mass, momentum and energy in their interplay. Since the width of the diffusion region can be comparable to the ion scales [4], therefore, the multi-fluid description are considered to capture diffusive effects that are completely neglected by the single-fluid theory, as shown in experimental research [5].

In the literature, one can find several fluid closures accounting for the different behavior of the species of plasmas in presence of electromagnetic fields. Braginskii [12] derives a two-fluid formulation considering separate ions and electrons. In his seminal work, he proposes closures for the transport properties, accounting for the anisotropy introduced by the magnetic field. Similarly, Magin [13] proposes a multicomponent model separating heavy particles and electrons, treating the effect of the magnetic field on the transport properties. Most recently, Meier [14] has proposed a two-fluid model considering the charged particles and neutrals as separate fluids, considering both anisotropic effects in the plasma heat conduction due to the magnetic field and chemical reactions (ionization and recombination).

3. Governing Equations

3.1. Two-fluid plasma equations

The multi-fluid description used in the results shown hereafter is the model discussed in [14]. It is a two-fluid model that considers separately hydrogen neutrals and charged species, i.e. hydrogen ions and electrons. The full set of equations considered comprises mass, momentum and total energy conservation for both fluids. The chemical reactions considered are electron impact ionization and radiative recombination. The excited states are not tracked, only an effective potential is assumed ϕ_{ion} for the ionization reaction. The plasma is assumed to be optically thin, so the radiation effects are completely lost from the system. Electrons are considered to be in thermal equilibrium with ions, allowing neutrals to be in non-LTE. Charge neutrality is assumed and the electrons inertia and viscosity is neglected. This simplification yields the following system:

$$\frac{\partial \rho_i}{\partial t} + \nabla \cdot (\rho_i \vec{v}_i) = m_i(\Gamma_i^{ion} + \Gamma_i^{rec}), \tag{5}$$

$$\frac{\partial \rho_n}{\partial t} + \nabla \cdot (\rho_n \vec{v}_n) = m_n(\Gamma_n^{ion} + \Gamma_n^{rec}), \tag{6}$$

$$\frac{\partial \rho_i \vec{v}_i}{\partial t} + \nabla \cdot (\rho_i \vec{v}_i \vec{v}_i + p_i \vec{\vec{\delta}} + p_e \vec{\vec{\delta}}) = -\nabla \cdot (\pi_i) + \vec{j} \times \vec{B} + \vec{R}_i^{in} + \Gamma_i^{ion} m_i \vec{v}_n - \Gamma_n^{rec} m_i \vec{v}_i, \tag{7}$$

$$\frac{\partial \rho_n \vec{v}_n}{\partial t} + \nabla \cdot (\rho_n \vec{v}_n \vec{v}_n + p_n \vec{\vec{\delta}}) = -\nabla \cdot (\pi_n) - \vec{R}_i^{in} - \Gamma_i^{ion} m_i \vec{v}_n + \Gamma_n^{rec} m_i \vec{v}_i, \tag{8}$$

$$\frac{\partial}{\partial t}\left(\varepsilon_i + \frac{p_e}{\gamma_e - 1}\right) + \nabla \cdot \left(\varepsilon_i \vec{v}_i + \frac{\gamma_e p_e}{\gamma_e - 1}\vec{v}_i + p_i \vec{v}_i\right) = -\nabla \cdot (\vec{v}_i \cdot \pi_i + \vec{q}_i + \vec{q}_e) + \vec{j} \cdot \vec{E} + \vec{v}_i \vec{R}_i^{in} + Q_i^{in} - \Gamma_n^{rec} \frac{1}{2} m_i v_i^2 - Q_n^{rec} + \Gamma_i^{ion}\left(\frac{1}{2} m_i v_n^2 - \phi_{ion}\right) + Q_i^{ion}, \tag{9}$$

$$\frac{\partial \varepsilon_n}{\partial t} + \nabla \cdot (\varepsilon_n \vec{v}_n + \vec{v}_n p_n) = -\nabla \cdot (\vec{v}_n \cdot \pi_n + \vec{q}_n) - \vec{v}_n \vec{R}_i^{in} + Q_n^{in} + \Gamma_n^{rec} \frac{1}{2} m_i v_i^2 + Q_n^{rec} - \Gamma_i^{ion} \frac{1}{2} m_i v_n^2 - Q_i^{ion} \tag{10}$$

Where the subindices i, e, n stand for ions, electrons and neutrals. The electrical current follows Ohm's law $\vec{E} + \vec{v}_i \times \vec{B} = \eta \vec{j}$ with the resistivity η assumed to be constant. The reaction rates Γ^{ion} and Γ^{rec} and the reaction energy production Q^{ion} and Q^{rec} are taken from [26] and [27]. The momentum and energy collisional terms $\vec{R}_\alpha^{\alpha\beta}$ and $Q_\alpha^{\alpha\beta}$ considered are discussed in [6]. Ions and neutrals viscosity stress tensor are assumed to be Newtonian, with constant viscosity. Neutrals heat conduction follows Fouriers law with constant thermal conductivity, whereas ions have anisotropic heat flux accounting for the effect of the magnetic field, described in [12]. The fluid are assumed to be perfect gases with $\gamma = 5/3$.

3.2. Maxwell's equations

The electromagnetic influence is tackled with the Maxwell equations:

$$\frac{\partial \vec{B}}{\partial t} + \nabla \times \vec{E} = 0 \tag{11}$$

$$\frac{\partial \vec{E}}{\partial t} - c^2 \nabla \times \vec{B} = -\frac{\vec{j}}{\epsilon_0} \tag{12}$$

$$\nabla \cdot \vec{B} = 0 \tag{13}$$

$$\nabla \cdot \vec{E} = \frac{\rho_c}{\epsilon_0} \tag{14}$$

where ρ_c is the charge density that is assumed to be zero.

3.3. Radiative transfer equation

In the results on the chromospheric magnetic reconnection shown hereafter, the radiative effects are neglected. However, in the solar atmosphere, particularly in the lower layers, i.e., photosphere and low-chromosphere, radiation is observed to play an important role [15]. The RTE in a non-scattering medium, neglecting the time derivative which is a lower order term, can be written:

$$\vec{\Omega} \cdot \nabla I_\nu = \kappa_\nu (S_\nu - I_\nu) \tag{15}$$

Where I_ν is the radiative intensity for the frequency ν, $\vec{\Omega}$ is the direction, κ_ν is the opacity of the medium and S_ν is the radiative source.

The radiative heat flux that should be included in the species energy equations 9 - 10 is calculated, as follows:

$$\vec{q}_{rad} = \int_\nu \int_\Omega I_\nu \vec{\Omega} \, d\Omega \, d\nu, \tag{16}$$

and the divergence of the flux:

$$\nabla \cdot \vec{q}_{rad} = \int_\nu \int_\Omega \kappa_\nu (S_\nu - I_\nu) \, d\Omega \, d\nu. \tag{17}$$

4. Numerical Modeling

4.1. Finite Volume Method

The results have been obtained using the FV solver for unstructured grids provided by the COOLFluiD platform [16]. The governing equations are written in conservative form, as follows:

$$\frac{d}{dt} \int_{\Omega_i} \mathbf{U} \, dV + \oint_{\partial\Omega_i} \mathbf{F^c} \cdot \mathbf{n} \, dS = \oint_{\partial\Omega_i} \mathbf{F^d} \cdot \mathbf{n} \, dS + \int_{\Omega_i} \mathbf{S} \, dV \tag{18}$$

The conservative form of Maxwell equations is found in [17]. The cell-centered FV discretization applies the integral conservation law to each cell, assuming the solution to be constant over the cell and storing the value at the centroid of it. In order to obtain second order accuracy in space, inverse-distance weighted least square reconstruction [18] is used. The multidimensional limiter of Venkatakhrisnan [19] is used to obtain oscillation free solutions. The discretization of the inviscid fluxes is explained hereafter.

4.2. Hyperbolic divergence cleaning for Maxwell equations

One of the biggest concerns in the development of a Maxwell solver is to satisfy the two divergence constrains Eq. 13 and Eq. 14 on the discrete level. The hyperbolic divergence cleaning method [21] is discussed to be an efficient way to enforce the constrains in Finite Volume solvers. Two Lagrange multipliers ϕ and ψ are added in Maxwell equations as follows:

$$\frac{\partial \vec{B}}{\partial t} + \nabla \times \vec{E} + \gamma^2 \nabla \Psi = 0 \tag{19}$$

$$\frac{\partial \vec{E}}{\partial t} - c^2 \nabla \times \vec{B} + \chi^2 c^2 \nabla \Phi = -\frac{\vec{j}}{\epsilon_0} \tag{20}$$

$$\frac{\partial \Psi}{\partial t} + c^2 \nabla \cdot \vec{B} = 0 \tag{21}$$

$$\frac{\partial \Phi}{\partial t} + \nabla \cdot \vec{E} = \frac{\rho_c}{\epsilon_0} \tag{22}$$

Artificial waves are introduced at speeds γc and χc that remove the errors in the fulfillment of the constrains. Therefore, the two scalar parameters γ and χ should be chosen to be ≥ 1.

4.3. Steger-warming scheme for Maxwell equations

The Steger-Warming scheme [20] splits the flux at the interface into positive and negative components based on the eigenvalue structure of the system as follows:

$$\mathbf{F^c} = \mathbf{A}_+ \mathbf{U}^L + \mathbf{A}_- \mathbf{U}^R \tag{23}$$

where

$$\mathbf{A} = \frac{\partial \mathbf{F^c}}{\partial \mathbf{U}} = \mathbf{A}_- + \mathbf{A}_+ \text{ and } \mathbf{A}_\pm = \mathbf{R} \Lambda_\pm \mathbf{R}^{-1} \tag{24}$$

where $\mathbf{R}$ is the matrix of right eigenvectors, $\Lambda_\pm$ the diagonal matrix of diagonal matrices with the positive and negative eigenvalues, $\mathbf{U}$ are the conservative variables.

As mentioned in [17], when the Maxwell equations are coupled to the fluid equations, the numerical dissipation is out of balance since some terms are proportional to the speed of light while other are proportional to the speed of the fluid. In the results presented in this work, we use a novel scaling of the numerical dissipation including the two divergence cleaning equations.

4.4. AUSM scheme for fluid equations

AUSM-family schemes [24] split the inviscid flux of each fluid at the cell interface into the convective part and the pressure flux as follows:

$$\mathbf{F^c} = \mathbf{F^{conv}} + \mathbf{P} \tag{25}$$

with

$$\mathbf{F^{conv}} = \dot{m} \mathbf{\Psi}^{L/R} \tag{26}$$

$\dot{m}$ is the numerical mass flux at the interface and $\mathbf{\Psi}^{L/R}$ is a vector with the variables convected. The superindex L/R denotes that the values are taken from the left or the right neighboring cell to the cell interface as follows:

$$\mathbf{\Psi} = \begin{cases} (1,\ u,\ v,\ w,\ h)_L & \text{if } \dot{m} > 0 \\ (1,\ u,\ v,\ w,\ h)_R & \text{if } \dot{m} < 0 \end{cases} \tag{27}$$

The methods to compute the numerical mass flux $\dot{m}$ and the pressure $\mathbf{P}$ at the cell interface are discussed in [24] and [25].

4.5. Implicit time stepping

The resulting set of equations is a very stiff system since it has characteristic speeds ranging from the speed of light to the speed of sound of the different fluids. In order to deal with the strong time step requirements, implicit time stepping is used. The second-order accurate three-point Backward Euler is used:

$$\frac{3}{2}\mathbf{U}^{n+1} - 2\mathbf{U}^n + \frac{1}{2}\mathbf{U}^{n-1} = \Delta t\, \mathbf{R}^{n+1} \tag{28}$$

4.6. Validation of the coupling between Maxwell and fluid equations

The coupling of the Maxwell equations with the fluid equations is validated on the Hartmann flow [22]. In this verification, we consider only one conductive fluid. This study is used to analyze the complex coupling between the two systems, i.e., Maxwell and fluid equations, with so different characteristic speeds. The Hartmann flow considers a viscous, electrically conductive, fully developed flow between two parallel plates in the x-direction in presence of an imposed magnetic field in the y-direction ($B_{y_0} > 0$) and an imposed electric field in the direction perpendicular to the plane of the movement ($E_{z_0} < 0$). The electromagnetic field produces forces in the flow that change the velocity profile from the parabolic Poiseuille's one to a fuller profile. Also, the movement of the conductive flow produces a electric current that induces a magnetic field. The solution of the velocity and the magnetic field is compared to the analytical solution for a Hartmann number $\text{Ha} = B_{y_0} L \sqrt{\frac{\sigma}{\mu}} = 10$ is compared in Fig. 1.

The performance of the divergence cleaning method is shown in Fig. 2. One can see that around 5 orders of magnitude of $\nabla \cdot \vec{B}$ are reduced setting $\chi = 1$.

4.7. Parallel scalability of COOLFluiD Finite Volume Solver

We study the scalability of the cell-centered Finite Volume solver of COOLFluiD on an unstructured

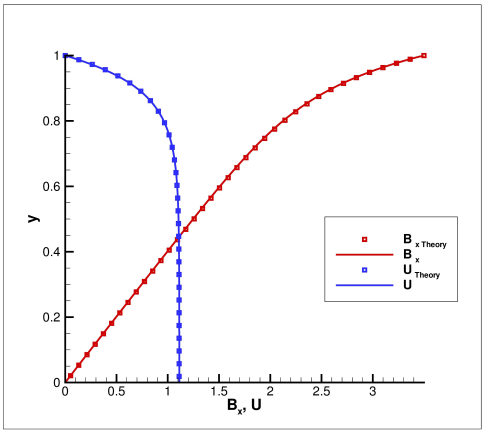

Figure 1: Comparison of non-dimensional velocity and magnetic field solution of Hartmann flow with analytical solution. Solution converged in 500 iterations on a 40×250 cells mesh.

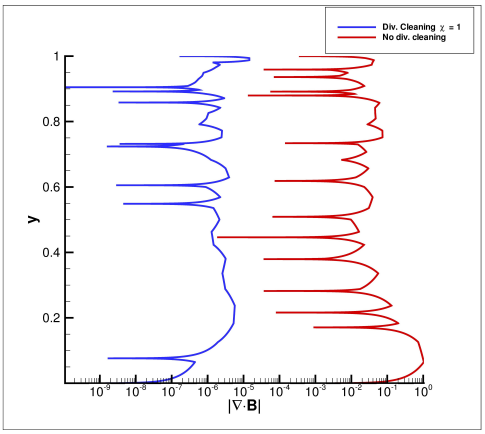

Figure 2: Non-dimensional $\nabla \cdot \vec{B}$ with and without divergence cleaning method

mesh using implicit time stepping. The parallel performance of the code is carried out using Pleiades supercomputer at NASA Ames Research Center. We test on a 14 M cell mesh up to 4096 processors. The parallel efficiency and speed-up, defined as, $S_p = 64\frac{T_{64}}{T_p}$ and $E_p = \frac{S_p}{p}$ are presented in Figure 3. The result of the test show that almost a speed-up of $S_p = 0.9$ is achieved with 4096 processors. This can be achieved thanks to the parallel architecture of COOLFluiD and it can be considered a strong advantage for the 3D simulations that are presented hereafter.

4.8. Improved finite volume method for the RTE

The RTE, i.e, Eq. 15, can be also solved using the FV method. In the present work we use the improved

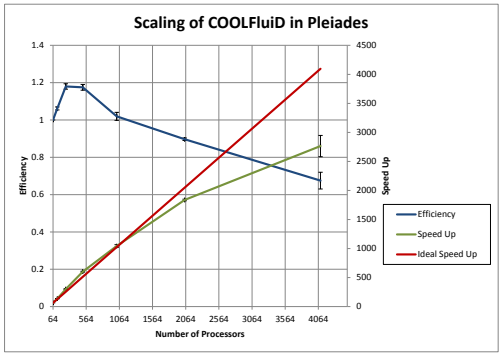

Figure 3: Parallel efficiency and speed-up of COOLFluiD cell-centered Finite Volume

method for unstructured grids explained in [23]. The method integrates Eq. 15 over the cell i, as follows:

$$\int_{\Omega_i} \vec{\Omega} \cdot \nabla I_\nu \, dV = \int_{\partial\Omega_i} I_\nu \vec{\Omega} \cdot d\vec{S} = \int_{\Omega_i} \kappa_\nu (S_\nu - I_\nu) \, dV. \tag{29}$$

The latter can be discretized as follows:

$$\sum_j I_{\nu,j}(\Omega)\vec{\Omega} \cdot \vec{n}_{ij} |\partial\Omega|_{ij} = \kappa_\nu (S_{\nu,i} - I_{\nu,i}(\Omega)) \, \Omega_i \tag{30}$$

where $S_{\nu,i}$ and $I_{\nu,i}$ are computed at the center of the cell i and $I_{\nu,j}$ at the center of the face $|\partial\Omega|_{ij}$.

The method explained in [23] approximates the value of $I_{\nu,j}$ at the interface solving the 1-d exact radiative solution for constant κ_ν and S_ν, as follows: considering a distance x along the direction $\vec{\Omega}$

$$I_\nu(x, \Omega) = I_\nu(0, \Omega) e^{-\kappa_\nu x} + (1 - e^{-\kappa_\nu x}) S_\nu \tag{31}$$

At the face where $\vec{\Omega} \cdot \vec{n}_{ij} < 0$, called in the following outgoing face, one can approximate the intensity using the previous solution. In the following expression, we use the superindex *out* for the value computed on an outgoing face and the superindex *in* for the value computed at the center of the incoming cell. Therefore,

$$I^{out}_{\nu,j}(\Omega) = \frac{\sum_{j,\vec{\Omega}\cdot\vec{n}_{ij}<0} I^{in}_{\nu,j}(\Omega)\vec{\Omega} \cdot \vec{n}_{ij} |\partial\Omega|_{ij} e^{-\kappa^{in}_{\nu,j} d}}{\sum_{j,\vec{\Omega}\cdot\vec{n}_{ij}<0} \vec{\Omega} \cdot \vec{n}_{ij} |\partial\Omega|_{ij}} + (1 - e^{-\kappa^{in}_{\nu} d}) S^{in}_{\nu,j} \tag{32}$$

One can see that the radiative intensity computed at the face center $|\partial\Omega|_{ij}$ is computed in terms of the values at the cell center of cell j and the propagation distance d that is approximated as $d = \left|\frac{\Omega_i}{\vec{\Omega}\cdot\vec{n}_{ij}|\partial\Omega|_{ij}}\right|$.

Using the approximation of the radiative transfer at the interface of the outgoing cells, assuming the source in the cell to be a piecewise-linear function, one can retrieve the radiative intensity at the center of cell i

$$I_{\nu,i}(\Omega) = \frac{\sum_{j,\vec{\Omega}\cdot\vec{n}_{ij}<0} I^{out}_{\nu,j}(\Omega)\vec{\Omega}\cdot\vec{n}_{ij}|\partial\Omega|_{ij}e^{-\frac{1}{2}\kappa^{in}_{\nu,j}d}}{\sum_{j,\vec{\Omega}\cdot\vec{n}_{ij}<0}\vec{\Omega}\cdot\vec{n}_{ij}|\partial\Omega|_{ij}} + \left(1-\frac{1-e^{-\frac{1}{2}\kappa_{\nu,i}d}}{\frac{1}{2}\kappa_{\nu,i}d}\right)S_{\nu,i} + \left(1-\frac{1-e^{-\frac{1}{2}\kappa^{in}_{\nu,j}d}}{\frac{1}{2}\kappa^{in}_{\nu,j}d}\right)S^{in}_{\nu,j} \quad (33)$$

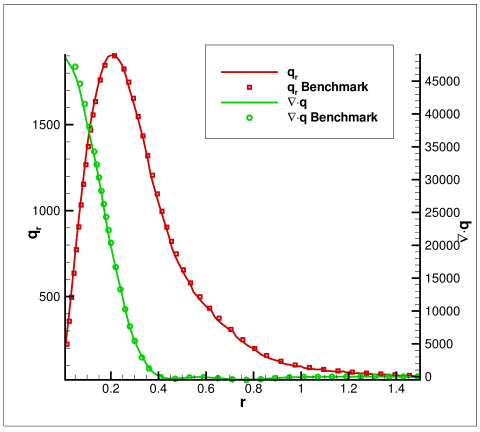

Figure 4: Verification of the RTE finite volume solver with a benchmark solution.

4.8.1. Validation of the RTE solver

We verify the method explained above studying the radiative transfer inside a sphere. We impose a Gaussian temperature profile in the radial direction. We test in a 84000 cells unstructured mesh with 60 mesh points in the radial direction and 20 in the azimuthal direction. For this study, we use the opacity table considering air composition and binning over 100 frequencies. The number of directions used for the azimuthal averaging is 24.

The solution of the heat flux over the radius and the radial heat flux vector compared to the benchmark shows great agreement as it is shown in Figure 4.

5. Results

We first study a 2D configuration of a Harris current sheet under chromospheric conditions corresponding to a height $h \sim 1500km$ over the Sun's surface. Under these conditions, collisional effects and chemical reactions play an important role in reconnection since the plasma is strongly collisional and with a very low degree of ionization. The characteristic values, taken from [6], used in our work are:

$$n = 6.6\times10^{18}m^{-3}$$
$$T = 8750K$$
$$\Psi = \frac{n_{ions}}{n_{ions}+n_{neutrals}} = 0.5\%$$
$$B = 10^{-3}T.$$

The initial magnetic field topology is chosen to be a Harris sheet, with a small perturbation in order to force the reconnection to occur in the center of the domain:

$$B_x = -1\times10^{-3}\tanh(y/5\times10^4) + 8\times10^{-10}ye^{-(x/2\times10^5)^2-(y/5\times10^4)^2}T$$

$$B_y = -5\times10^{-11}xe^{-(x/2\times10^5)^2-(y/5\times10^4)^2}T$$

The 2D domain considered extends from -36×10^5 m to 36×10^5 m in the x direction and -16×10^5 m to 16×10^5 m in the y direction. Using the symmetry of the problem, we simulate one quadrant in a 1.3 million-cell mesh.

In order to compare the 3D development with the 2D results, as a first step, we consider the simplest configuration possible. At the initial time, we consider a 2D Harris current sheet that extends homogeneously in the direction perpendicular to the plane that contains the magnetic field lines. The ultimate goal of the present research is to study the stability and evolution of perturbations in the perpendicular direction.

Due to memory limitations, the domain studied in the 3D configuration is smaller than the one used in the 2D case. It has been chosen to avoid the influence of the boundaries in the reconnection region. However, in future work, larger domains will be considered. The current domain extends from -15×10^5 m to 15×10^5 m in the x direction, -1×10^5 m to 1×10^5 m in the y direction and -1×10^4 m to 1×10^4 m in the z direction. The mesh used in the 3D case conserves

the same resolution in the xy plane with 3.8 million cells.

The results of the 2D configuration are presented below. In Figure 5, the evolution of the current sheet and the magnetic field lines are shown. As can be seen, the magnetic lines change topology, forming a current sheet in the center of the domain.

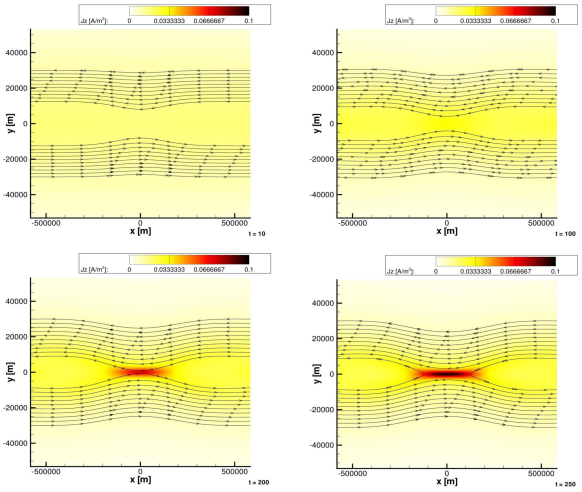

Figure 5: Evolution of the current sheet in the first seconds of simulation. Evolution of magnetic field lines and z-component of the electric current. Top: from left to right, t = 10 s and t = 100 s. Bottom: from left to right, t = 200 s and t = 250 s.

.

In the top half of Figure 6, we compare the horizontal velocity of ions and neutrals. Since the geometry is symmetric, the neutrals are shown on the right and the ions on the left without losing information. The neutrals are unaffected by the electromagnetic fields, however, the ions, which are accelerated by the Lorentz force driven by the current sheet, drag the neutrals through collisions. As can be seen, the horizontal velocity of ions and neutrals is very similar. However, in the bottom half of this figure, we show that the streamtraces of ions and neutrals are clearly different, since the vertical velocity of neutrals is seen to be smaller than that of the ions.

In Figure 7 we show the balance between the gain of ions due to the inflow (top right) and the ionization (bottom right) and the loss produced by the recombination reaction (top left) and the outflow (bottom left). We can see that under chromospheric conditions, chemical reactions play an important role in the reconnection region, especially the recombination. The loss due to recombination is comparable to the gain due to the inflow, producing an important impact

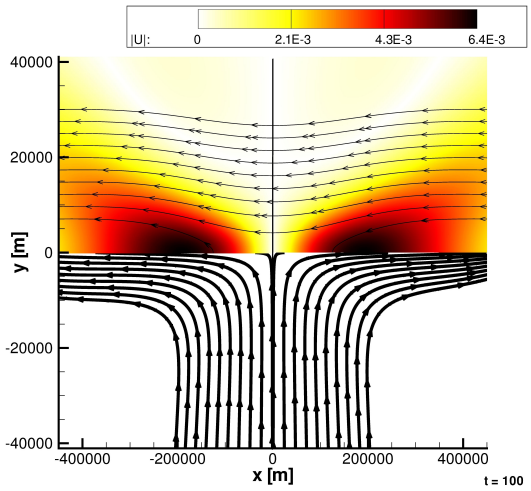

Figure 6: Top half: horizontal velocity of neutrals (right) and ions (left) at t = 100 s, non-dimensionalized with the value of the local Alfven speed outside the current sheet. Bottom half: streamtraces of neutrals and ions at (right) and ions (left) at t = 100 s

.

in the reconnection rate.

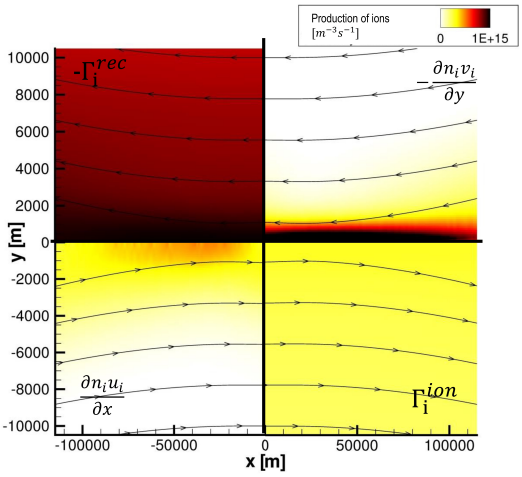

Figure 7: Gain of ions in the current sheet. The gain due to the inflow of ions (top right) and the ionization reactions (bottom right) is balanced by the outflow (bottom left) and the recombination reactions (top left).

.

Preliminary 3D results are shown hereafter. We find that the non-dimensional reconnection rate is similar to that in the 2D case, i.e., $M = \frac{\eta J_{z_{max}}}{v_{out} B} \sim 0.1$, higher than the one predicted by the Sweet-Parker scaling law $M = \sqrt{\frac{\eta}{v_A L \mu_0}} \sim 0.03$. However, the velocities in the 3D case are observed to be slower, as can be seen

in Figure 9. The reason for the disagreement between the 2D and the 3D simulations is currently being studied. Possibly, the boundaries of the 3D domain at $y = \pm 10^5 m$, unlike those of the 2D case which are set further away, have an influence on the flow field, slowing down the velocity of the fluids.

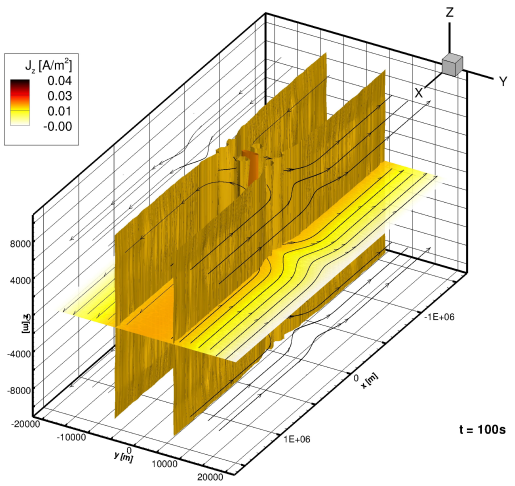

Figure 8: Electric current (Iso-surface and plot at the slice z=0) at t=100s. Contour lines represent the magnetic lines. Due to the boundary conditions and the geometry of the initial field the reconnection takes place forming a current sheet in the z direction.

.

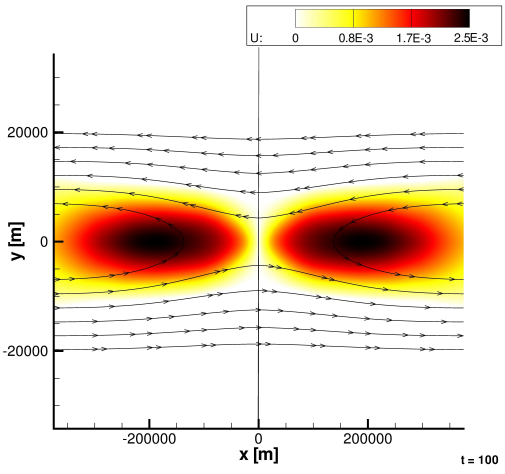

Figure 9: Absolute value of non-dimensional horizontal velocity of neutrals and ions at t=100s at the slice z=0. The horizontal velocity is almost identical in both fluids, however, the values are lower than the 2D case.

.

6. Conclusions

The present PhD project is oriented towards the development of numerical tools and models of plasma for representing the magnetic reconnection process in astrophysical and laboratory plasmas. In the present work, we have highlighted the importance of magnetic reconnection process and the necessity of improving the modeling in order to represent this phenomenon more accurately. Multi-fluid models, that consider each species as different interpenetrating fluids, are able to represent microscopic and transport phenomena that is completely neglected in the single-fluid theory. In this work we have presented a two-fluid partially ionized reactive plasma model, especially suitable for the conditions in the Sun chromosphere. As well, we have presented the finite volume method for solving the two-fluid plasma model coupled to the full Maxwell equations using hyperbolic divergence cleaning. The coupling of the equations is validated on the Hartmann flow, showing perfect agreement with the analytical solution and showing the hyperbolic divergence cleaning method to be an efficient way of enforcing the divergence constrains. The parallel scalability of the finite volume solver implemented in COOLFluiD is tested in Pleiades, NASA's supercomputer, showing high efficiency up to 4096 processors. Also, the radiative transfer equation is solved using a finite volume method that improves its accuracy by performing linear-piecewise interpolation along the radiative direction. The verification of the RTE solver was presented showing great agreement with a benchmark solution. The coupling of the radiative effects in the reconnection will be carried out in future developments.

The magnetic reconnection in the chromosphere is simulated using a multi-fluid model considering two fluids, neutrals and charged particles. The results show the different dynamics of the species as well as the importance of the chemical reactions on the magnetic reconnection. Also, preliminary 3D results studying the same configuration are presented and will be extended in future works. The first stages of a magnetic reconnection in the chromosphere have been simulated using a multi-fluid model considering two fluids, neutrals and charged particles. These results can be considered as the first steps that will be continued during the PhD targeted towards the study of the magnetic reconnection with multi-fluid models.

Acknowledgments

This research is funded through a fellowship provided by IWT (agentschap voor Innovatie door Wetenschap en Technologie). We would also like to thank Dr. Nagi N. Mansour for the supervision of this work at NASA Ames Research Center and Dr. Andrea Lani, COOLFluiD architect and advisor of this work.

References

[1] Committee on the Societal and Economic Impacts of Severe Space Weather Events, *Severe Space Weather Events Understanding Societal and Economic Impacts: A Workshop Report*, The National Academies Press, 2008.

[2] J. Birn and E. Priest, *Reconnection of Magnetic Fields*, Cambridge University Press, 2007.

[3] F. Zuccarello, *Data analysis and mathematical modeling of the initiation of coronal mass ejections*, PhD thesis, KU Leuven, 2012.

[4] M. Yamada, R. Kulsrud, and H. Ji, *Magnetic Reconnection*, Reviews of Modern Physics vol.82, 2010.

[5] Yamada, M. et al. *Conversion of magnetic energy in the magnetic reconnection layer of a laboratory plasma.* Nature Communications 5:4774 doi: 10.1038/ncomms5774 (2014).

[6] J. E. Leake, V. Lukin, M. Linton and E. Meier, *Multi-fluid simulations of chromospheric magnetic reconnection*, ApJ. 760, 2012.

[7] K. Shibata et al., *Chromospheric Anemone Jets as Evidence of Ubiquitous Reconnection*, Science, Volume 318, Issue 5856, pp. 1591, 2008.

[8] K. Shibata and T. Magara, *Solar Flares: Magnetohydrodynamic Processes*, Living Rev. Solar Phys. 8, 2011.

[9] E. N. Parker, *Sweet's mechanism for merging magnetic fields in conducting fluids*, Geophysical research 62, No. 4, 509-520, 1957

[10] H. E. Petschek. *Magnetic Annihilation*. The Physics of Solar Flares, Proceedings of the AAS-NASA Symposium, October 1963

[11] D. Biskamp, *Magnetic Reconnection in Plasmas*, Cambridge University Press, 2005

[12] S. I. Braginskii, *Transport processes in a plasma*. Reviews of Plasma Physics, Volume 1., pp. 205 311. (1965)

[13] B. Graille , T. E. Magin , M. Massot, *Kinetic theory of plasmas. Translational Energy.* Mathematical Models and Methods in Applied Sciences, Vol. 19, 04 (2009) 527-599

[14] E. T. Meier, U. Shumlak, *A general nonlinear fluid model for reacting plasma-neutral mixtures.* Physics of Plasmas, Volume 19, Issue 7, pp. 072508-072508-11 (2012).

[15] M. Carlsson and J. Leenaarts, *Approximations for radiative cooling and heating in the solar chromosphere.* Astronomy & Astrophysics, Volume 539, March 2012.

[16] A. Lani, *An object Oriented and high perforrmance platform for aerothermodynamics simulations*, PhD Thesis, von Karman Institute for Fluid Dynamics, 2009

[17] R. W. MacCormack. *Numerical Simulation of Aerodynamic Flow Including Induced Magnetic and Electric Fields.* In 39th AIAA Plasmadynamics and Lasers Conference, Seattle, June 2008.

[18] T. Barth. Aspects of unstructured grids and finite volume solvers for the euler and navier-stokes equations. 25th Computational Fluid Dynamics Lecture Series. Von Karman Institute, March 1994.

[19] V. Venkatakrishnan. *Convergence to steady state solutions of the euler equations on unstructured grids with limiters.* Journal of Computational Physics, 118:120130, 1995.

[20] J. Steger, R. F. Warming, *Flux vector splitting for the inviscid gas dynamic equations with application to finite difference methods*, J. Comp. Phys., Vol. 40, No. 2, pp. 263-293, 1981

[21] C.-D. Munz., P. Ommes, R. Schneider. *A three-dimensional finite-volume solver for the Maxwell equations with divergence cleaning on unstructured meshes*. Computer Physics Communications130, 83-117, December,1999.

[22] M. Mitchner and C. H. Kruger, *Partially ionized gases*, Wiley series in plasma physics, 1973.

[23] A. Wray, *Improved Finite-Volume Method for Radiative Hydrodynamics.*, ICCFD7-1003, July 2012.

[24] M. S. Liou, *A sequel to AUSM, part II: AUSM+ -up for all speeds.* J. Comp. Phys., 214:137170, 2006.

[25] A. Alvarez Laguna, A. Lani, N. N. Mansour, A. Kosovichev, and S. Poedts, *A two-fluid computational model to study magnetic reconnection in reactive plasmas under chromospheric conditions*, WCCM XI-ECCM V-ECFD VI, Barcelona (2014).

[26] G. S. Voronov, *A practical fit formula for ionization rate coefficients of atoms and ions by electron impact*, Atomic data nad nuclear data tables 65, 1-35, 1997

[27] B. M. Smirnov, *Physics of Atoms and Ions*, Springer-Verlag New York, Inc., 2003

[28] Vernazza, J. E., Avrett, E. H., Loeser, R., *Structure of the solar chromosphere. III. Models of the EUV brightness components of the quiet Sun*, ApJS45, 635-725, 1981

Splash Plate Nozzle Design Optimization

Nicolas De Cock

Environmental and Applied Fluid Dynamics Department, von Karman Institute for Fluid Dynamics, Belgium, nicolas.decock@vki.ac.be

Supervisor: Maria Rosaria Vetrano

Assistant Professor, Environmental and Applied Fluid Dynamics Department, von Karman Institute for Fluid Dynamics, Belgium, vetrano@vki.ac.be

University Supervisor: Frédéric Lebeau

Professor, Gembloux Agro-Bio Tech, ULg, Belgium, f.lebeau@ulg.ac.be

Abstract

Numerical simulations showed that when the liquid flows through a splash plate nozzle, the main stream velocity is increased. This increase of speed, defined here as $\frac{1}{\alpha}$, can be related to the relative gap of the nozzle $\frac{H}{R}$. By taking in account this increase of speed into the previously realized analytical development on the impact of a free jet on a horizontal surface, the height and the surface speed of a the flow generated by a splash plate nozzle can be predicted.

Keywords: Jet impact, boundary layer, nozzle design

1. Introduction

1.1. Context

Spray application is a key process in crop protection to ensure that high yields are obtained while minimizing adverse environmental and health impacts of plant protection products. During this process, the agricultural mixture is fragmented by passing through a nozzle generating a cloud of droplets.

It has been proved that the spray droplet size distribution significantly affects the global deposition process efficiency [1]. Indeed, smaller droplets have a higher drift potential [2] leading to potential product losses in air, water and soil [3]. Whilst, larger droplets, with a higher kinematic energy, are more prone to splash while impacting the target and then may reduce the target retention efficiency [4] (Fig. 1). Therefore, an ideal agricultural spray would include only medium size droplets, i.e. ranging between 200 and 300 μm for weed treatment. The droplet sizes and speeds constitutive of a spray result from the interactions between the physical properties of the liquid, the operating conditions and the nozzle geometry [5]. During the past decades, multiple researches have been performed on the effect of the liquid physical properties [6] [7] [8] as well as the nozzle type [9]. The need of a narrow drop size distribution stimulated the development of devices for spray generation using centrifugal forces such as the rotary atomizers. These atomizers produce a significantly narrower drop size distribution than the hydraulic nozzles usually used in field treatment (Fig. 2). Despite the quality of the produced sprays, the rotary atomizers are not hardly used for field spray application because of their bulkiness. However, they remain an interesting study case as a way to produce sprays with narrow drop size distribution. The contrast in the drop size distribution between the hydraulic nozzles and the rotary atomizers derives from the different breakup modes occuring with the two atomizers types. Rotary atomizers produce round liquid jets of uniform sizes at the exit of the rotating part, then these jets break in droplets by the Rayleigh-Plateau mode (Fig. 3a). Whilst, the hydraulic nozzles produce a liquid sheet that break-up in ligaments which, in turn, break-up in to droplets of various sizes (Fig. 3b).

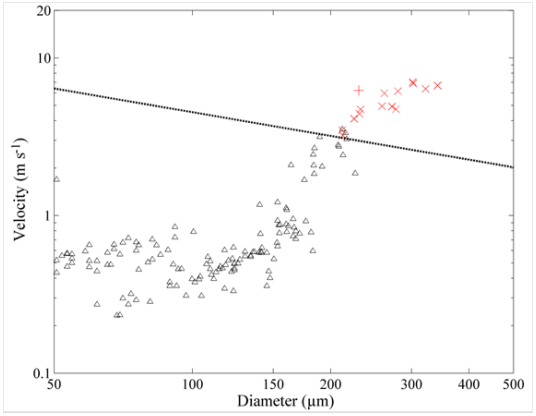

Figure 1: Behavior of the droplets while impacting a superhydrophobic surface in function of their diameter and velocity [4]. The triangles and the crosses correspond to droplet adhesion and droplet splashing respectively.

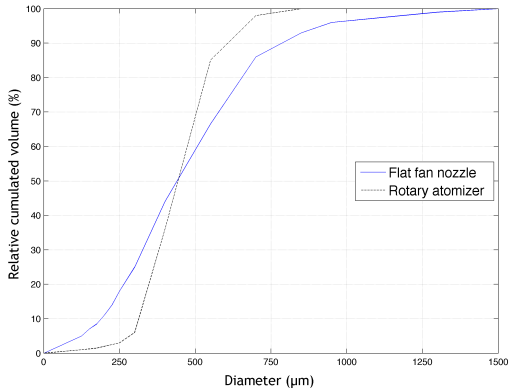

Figure 2: Comparison of spray drop size distributions with the same VMD produced by a flat fan nozzle and by a rotary atomizer. [10]

1.2. Rayleigh-Plateau Breakup

The Rayleigh-Plateau breakup regime occurs when a cylindrical jet is discharged into gas with a low inertia in respect with its capillary forces. Therefore the Weber number is used as criterion to set the limits of the Rayleigh-Plateau regime [11]. The We_L has to be higher than 8 and the gaseous Weber number We_G has to be lower than 0.4. With We_G and We_L defined as:

$$We_L = \frac{\rho_L U_L^2 d}{\sigma} \tag{1}$$

$$We_G = \frac{\rho_G U_L^2 d}{\sigma} \tag{2}$$

where ρ_L and ρ_G the liquid and the gas density respectively, U_L^2 is the liquid speed, d is the jet diameter, σ is the surface tension

Theoretical developments presented by Rayleigh [12] showed that the growth of the most unstable perturbation breaks the jet in droplets of 1.89 times the jet diameter. Jet breakup can be controlled, e.g. using acoustic waves generated by piezoelectric element with the adequate wavenumber [13].

1.3. Goals

The present project aims to design a hydraulic nozzle producing a spray with a narrow drop size distribution in order to increase the agricultural spray application efficiency. The starting design of this nozzle will be a splash plate nozzle (Fig. 4) for which the plate will be modified in order to split the liquid sheet

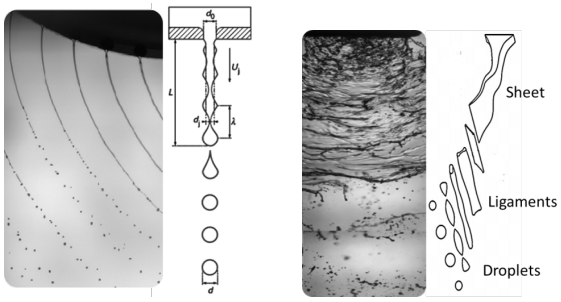

(a) Capillary breakup (b) Sheet breakup

Figure 3: Ilustration of the two breakup modes occuring at the exit of a rotary atomizer (a) and a hydraulic nozzle (b).

formed on the plate into multiple jets at its end. The jets would be in the Rayleigh-Plateau regime and then generate a narrow drop size distribution. For agricultural spraying the common flow rate is around 1 l/min and the droplet diameters would be ranging between 200-300 μm. Thus, it requires roughly 60 to 90 jets with a speed of 10 to 15 m/s in order to deliver the adequate flow rate. This paper is focusing on the formation of the liquid sheet on the plate of the splash plate nozzles. The first part of this paper is dedicated to the analytical description of a liquid jet impacting on a flat plate based on the theoretical development proposed by Watson [14]. In the second part, the theoretical development of Watson is extended to the case of a splash plate nozzle using numerical computations.

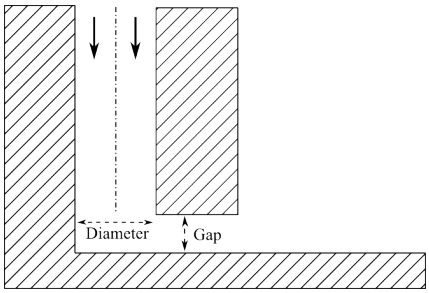

Figure 4: Illustration of the design of a splash plate nozzle

2. Study of a jet impacting a flat plate

2.1. Flow description

The impact of a round liquid jet on a flat surface generates a circular liquid layer spreading radially (Fig. 5). This two-phase flow is close to the mirror nozzle flow. The theoretical analysis provided by Watson [14] showed that this flow can be correctly described by the mean of the boundary-layer theory. Two main flow regions can be distinguished. The first region begins at stagnation point where the boundary layer starts to grow and it finishes at $r = r_0$ where the whole flow is within the boundary layer. In the second region, the height of the liquid layer is given by the boundary layer development. The liquid layer reach its minimum thickness located at $r = 1.427 r_0$. Then in a further region, a hydraulic jump may occur but it will not be discussed here.

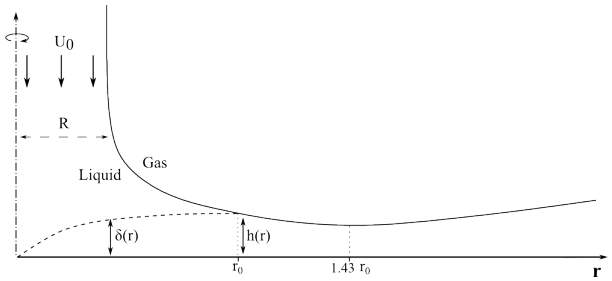

Figure 5: Half radial cut of the flow created by the impact of a round jet on a flat plate

2.2. Analytical Solution

2.2.1. Fully developed region: similarity solution

This axisymmetric flow can be described as a thin layer by the following equations:

$$\frac{\partial(ru)}{\partial r} + \frac{\partial(rw)}{\partial z} = 0 \tag{3}$$

$$u\left(\frac{\partial u}{\partial r}\right) + w\left(\frac{\partial u}{\partial z}\right) = \nu\left(\frac{\partial^2 u}{\partial z^2}\right) \tag{4}$$

Where r is the radial distance from the jet center, z is the distance upward from the plate, u and w are the corresponding velocity components, ν is the kinematic viscosity. A no slip condition is used at the plate (5), the shear stress at the free surface is considered as negligible (6) and a constant flow rate along the radial axis is assumed (7).

$$u_{z=0} = w_{z=0} = 0 \tag{5}$$

$$\frac{\partial u}{\partial z}_{z=h(r)} = 0 \tag{6}$$

$$Q = 2\pi r \int_0^{h(r)} u \, dz \tag{7}$$

The velocity profile in the axial direction u can be rewritten as function of the velocity at the free surface U and a similarity solution f:

$$u = U(r) f(\eta) \;\; with \;\; \eta = \frac{z}{h(r)} \tag{8}$$

From the equations (5), (6) and (7), the boundary conditions of the similarity solution f are:

$$f(0) = 0, \; f(1) = 1, \; f'(1) = 0 \tag{9}$$

Then, the flow rate along the radial direction (7) can be rewritten as:

$$Q = 2\pi r U h \int_0^1 f(\eta) \, d\eta \tag{10}$$

Therefore, rUh as to be constant and the equation (3) becomes:

$$w = U h' \eta f(\eta) \tag{11}$$

Then the equation of motion (4) turns into:

$$\nu f"(\eta) = U' h^2 \eta f(\eta) \tag{12}$$

From which $U'h^2$ is constant and f'' is 0 since the shearing stress is greatest at the plate. It's convenient to write:

$$h^2 U' = -\frac{3}{2} c^2 \nu \tag{13}$$

$$2f" = -3c^2 f^2 \tag{14}$$

After integration of (14) and using the boundary conditions defined in (9) it becomes:

$$f'^2 = c^2\left(1 - f^3\right) \tag{15}$$

$$c\eta = \int_0^f \frac{1}{\sqrt{1-x^3}}dx \tag{16}$$

Since $f(1) = 1$ and using the beta theorem:

$$c = \int_0^1 \frac{1}{\sqrt{1-x^3}}dx = 1.402 \tag{17}$$

Then,

$$\int_0^1 f(\eta)\, d\eta = \frac{1}{c}\int_0^1 \frac{1}{\sqrt{f(1-f^3)}} = \frac{2\pi}{3\sqrt{3}c^2} \tag{18}$$

Finally, the constant flow equation (7) can be rewritten as:

$$rUh = \frac{3\sqrt{3}c^2 Q}{4\pi^2} \tag{19}$$

Using the equations (13) and (19) U and h can be expressed:

$$U(r) = \frac{27c^2Q^2}{8\pi^4\nu(r^3 + l^3)} \tag{20}$$

$$h(r) = \frac{2\pi^2\nu(r^3 + l^3)}{3\sqrt{3}Qr} \tag{21}$$

where l is a constant length arising from the integration of U' in the equation (13). The value of l will be determined later using the boundary development region equations knowing that $h(r)$ should be equal to δ at $r = r_0$

2.2.2. Boundary development region: General approximate solution

In the present region, the boundary layer is not fully developed. Therefore, the speed outside the boundary layer is considered as equal to the free stream velocity U_0. Inside the boundary layer, the velocity profile is defined by the similarity function f:

$$u = U_0\, f\left(\frac{z}{\delta}\right) \text{ with } u = U_0 \text{ when } z \geq \delta(r) \tag{22}$$

The momentum integral equation is equal to:

$$\left(\frac{d}{dr} + \frac{1}{r}\right)\int_0^\delta (U_0\, u - u^2)dz = \nu\left(\frac{\partial u}{\partial z}\right)_{z=0} \tag{23}$$

Because of equation (22), it can be rewritten

$$\left(\frac{d}{dr} + \frac{1}{r}\right)U_0^2\,\delta\int_0^1 (f - f^2)\, d\eta = \frac{\nu U_0 c}{\delta} \tag{24}$$

$$\left(\frac{d\delta}{dr} + \frac{\delta}{r}\right)\frac{2U_0^2\left(\pi - c\sqrt{3}\right)}{3\sqrt{3}c^2} = \frac{\nu U_0 c}{\delta} \tag{25}$$

Integration of equation (25) gives:

$$r^2\delta^2 = \frac{c^3\sqrt{3}\nu r^3}{\pi - c\sqrt{3}U_0} \tag{26}$$

$$\delta(r) = \sqrt{\frac{\sqrt{3}c^3\nu r}{\left(\pi - c\sqrt{3}\right)U_0}} \tag{27}$$

The constant flow rate expression given by equation (7) can be rewritten as:

$$Q = 2\pi r\left(U_0\delta\int_0^1 f(\eta)\, d\eta + U_0(h - \delta)\right) \tag{28}$$

From which h can be extracted:

$$h(r) = \frac{R^2}{2r} + \left(1 - \frac{2\pi}{3\sqrt{3}c^2}\right)\delta \tag{29}$$

This expression is valid until the whole flow is within the boundary layer, i.e. when $r < r_0$. The r_0 expression is found at the point where the boundary layer volume flux is equal to the inlet volume flux:

$$r_0 U_0 \delta(r_0) = \frac{3\sqrt{3}c^2 Q}{4\pi^2} \tag{30}$$

Using equation (27), r_0 is equal to:

$$r_0 = 0.3155\sqrt[3]{\frac{QR^2}{\nu}} \tag{31}$$

From equation (20) and r_0 equations we can find the value of l. Indeed the value of U should be equal to U_0 when $r = r_0$.

$$l = 0.5673\sqrt[3]{\frac{QR^2}{\nu}} \tag{32}$$

Finally, the equations describing the liquid layer thickness are equation 29 when $r \leq R_0$ and equation (21) when $r > R_0$. The surface speed is equal to the initial velocity U_0 $r \leq R_0$ and then is expressed by equation 20 when $r > R_0$.

2.3. Numerical Computations

2.3.1. Free Jet

The InterFoam solver from the *OpenFoam C++* toolbox has been used to perform the numerical simulations. It is a Volume Of Fluid (VOF) solver for incompressible two-phase flow [15]. Here, all the cases are considered in a laminar mode. Therefore, no extra turbulence model has been used.

This axisymmetric flow is simulated in OpenFOAM using a wedge shaped mesh. The numerical domain and the boundary conditions are detailed in Fig. 6. The inlet is set as fixed velocity and a liquid fraction equal to 1. The oulet is set at atmospheric pressure with no liquid backflow. The walls were set as no slip, zero gradients. The wedge is the OpenFOAM boundary condition for the front and back plans of an axisymmetric domain.

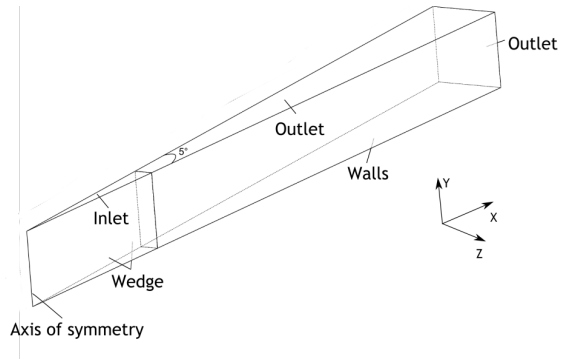

Figure 6: Boundary conditions for the free jet case

The dimensionless surface velocity and dimensionless liquid thickness are presented on the Fig. 7 with respect to the dimensionless radial distance to the jet center. The InterFoam predictions are in good agreement with the analytical solution for both the height and the surface velocity. However, there are slight discrepancies for the surface speed prediction close to the jet impact area. These differences could arise from the limitation of the Watson's solution close to the jet impact, where the boundary layer theory cannot be directly applied. However this difference doesn't affect the speed and height prediction further from the jet center.

2.3.2. Splash plate nozzle flow

A second set of simulations has been realized for a splash plate nozzle flow in order to determine the effect of the nozzle on the downstream flow. The geometries had an inlet radius of 1 and 2 mm and a relative gap ranging from 0.2 to 1.8. With the relative

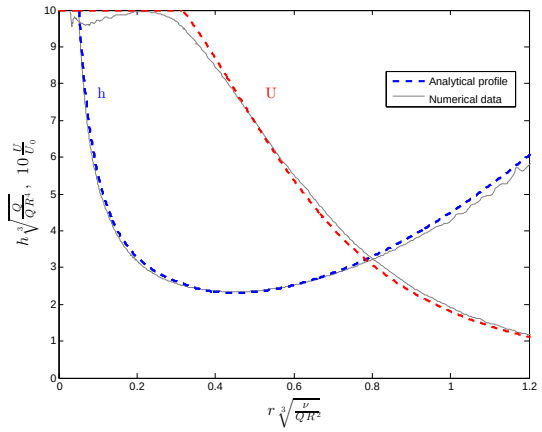

Figure 7: Surface velocity and liquid sheet height profile in respect with the dimensionless radial distance to the jet center. U is the surface speed, U_0 the initial jet speed, h the liquid thickness, R the jet radius, and r the radial distance to the jet center

gap defined as the ratio between the gap and the inlet radius $\frac{H}{R}$. The numerical domain and the associated boundary conditions are presented on the Fig. 8.

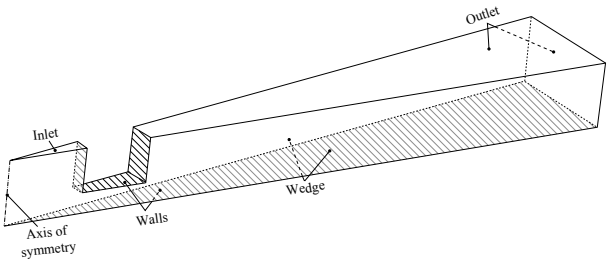

Figure 8: Boundary conditions for the splash plate nozzle cases

2.4. Effect of the splash plate nozzle

From the numerical simulations it appears that the splash plate nozzle contracts the flow and the free flow speed increases from U_0 in the inlet channel to U_1 after the nozzle restriction.

The increase of speed is defined here as $\frac{1}{\alpha}$.

$$U_1\alpha = U_0 \tag{33}$$

Considering that the main flow is equal to U_1, the main flow equations expressing the height and the surface speed of the liquid layer can be rewritten as:

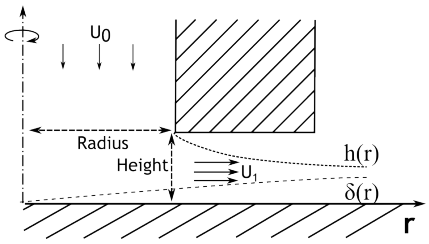

Figure 9: Illustration of the flow acceleration when it passed through the nozzle

When $r < r_0$, the equations 27 and 29 become:

$$\delta = \sqrt{\frac{\alpha\sqrt{3}c^3\nu r}{(\pi - c\sqrt{3})U_0}} \tag{34}$$

$$h = \frac{\alpha R^2}{2r} + \left(1 - \frac{2\pi}{3\sqrt{3}c^2}\right)\delta \tag{35}$$

with r_0 now equals to:

$$r_0 = 0.3155\sqrt[3]{\frac{\alpha Q R^2}{\nu}} \tag{36}$$

when $r > r_0$, the equations 20 and 21 become:

$$U = \frac{27c^2Q^2}{8\pi^4\nu(r^3 + l^3)} \tag{37}$$

$$h = \frac{2\pi^2\nu(r^3 + l^3)}{3\sqrt{(3)}Qr} \tag{38}$$

with l equal to:

$$l = 0.5673\sqrt[3]{\frac{\alpha Q R^2}{\nu}} \tag{39}$$

The liquid height equations can be rewritten as dependant of constants and the radial distance from the jet center:

$$h(r) = \frac{a^2}{2r} + b\sqrt{r} \quad when\ r \leq r_0 \tag{40}$$

$$h(r) = \frac{d(r+e)^3}{r} \quad when\ r > r_0 \tag{41}$$

where a b d and e are the functions parameters. For example, from equation 35 a is equal to $\frac{\alpha R^2}{2}$. The value of these parameters has been determined using a least squares fitting on the height profiles extracted from the CFD data. Then from equations 35 and 38, α can be retrieved from the different fitting parameters as:

$$\alpha_a = \frac{a^2}{R^2} \tag{42}$$

$$\alpha_b = \left(\frac{b\sqrt{U_0}}{0.9954\sqrt{\nu}}\right)^2 \tag{43}$$

$$\alpha_e = \frac{\nu d}{0.1826QR^2} \tag{44}$$

The values of the different α are presented in respect with the relative gap on the Fig. 10. In which, α_{PP} has been computed from the CFD data with the observed U_1 extracted after the restriction. One can see on this figure that the five differents way to compute α provided similar resultats for all the opening ratio.

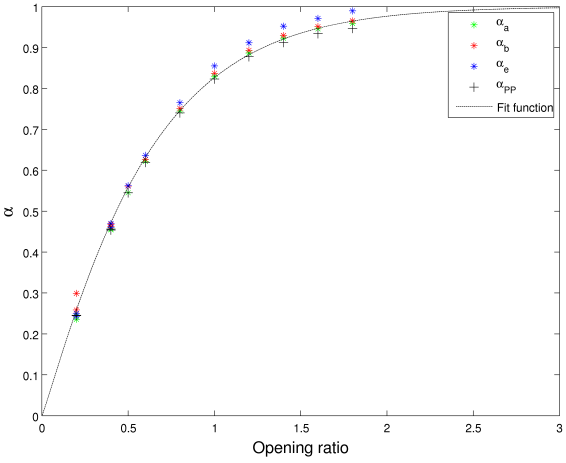

Figure 10: α parameter in respect with the relative gap

An interesting point is that α reaches 1 when $\frac{H}{R} > 3$ (Fig. 10) therefore the flow equations become equal to the one described in the section 2.2. From these data, α can be expressed as:

$$\alpha = \left(1 - e^{-1.75\left(\frac{H}{R}\right)^{1.1}}\right) \tag{45}$$

2.4.1. Comparison of the numerical and the analytical solutions

The comparisons between the analytical solution taking in account the acceleration of the flow with α and the numerical data show a good agreement for the surface speed U as well as the liquid layer thickness h. However as for the free jet the surface speeds close to the jet impact present discrepancies in the region close

to the jet impact (Fig. 11 12). Finally, the Fig. 13 presents a comparison between all the simulation and the proposed analytical solution. It appears that for all the cases the discrepancies appear mainly close to the jet impact region while in a further region a good agreement is observed.

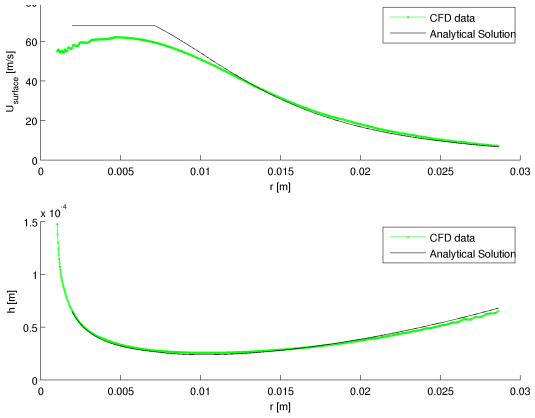

Figure 11: Surface speed and liquid thickness profile for a nozzle with an inlet radius of 1 mm and a gap of 0.2 mm

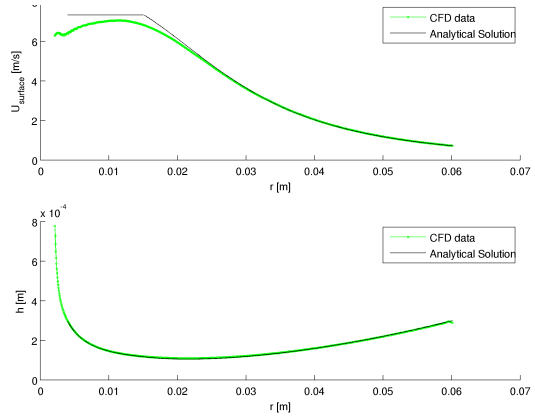

Figure 12: Surface speed and liquid thickness profile for a nozzle with an inlet radius of 2 mm and a gap of 1 mm

3. Conclusion

The present work proposes an extension of the analytical development realized by Watson on the radial spread of a liquid jet over a horizontal surface to the case of a splash plate nozzle. The numerical simulations showed that when the liquid flows through the nozzle, the main stream velocity is increased. This increase of speed, defined here as $\frac{1}{\alpha}$, can be related to the relative gap of the nozzle $\frac{H}{R}$. An expression of α in respect of $\frac{H}{R}$ is proposed. Then by adding this new parameter to the theoretical development previously realized by Watson, the height and the surface speed of a the flow generated by a splash plate nozzle can be predicted. The comparisons between the numerical data and the extended analytical law showed good agreement.

Further work will focus on the experimental validation of the proposed analytical solution and on the determination of the optimal geometrical parameters for the agricultural application.

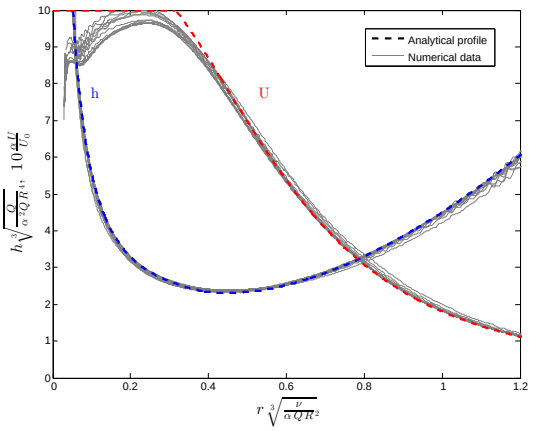

Figure 13: Non dimensionnal profile of surface velocity and liquid height in respect with the non dimensionnal radial distance for geometries with an inlet radius of 1 and 2 mm and with a relative gap ranging $\frac{H}{R}$ from 0.2 to 1.8

Acknowledgments

I would like to thanks the FNRS for the founding of my PhD through a FRIA grant.

References

[1] G. Matthews, Pesticide application methods, John Wiley & Sons, 2008.

[2] P. C. M. W. A. Taylor, A. R. Womac, B. P. Taylor, An attempt to relate drop size to drift risk, in: International Conference on Pesticide Application for Drift Management, 2004.

[3] S. Reichenberger, M. Bach, A. Skitschak, H.-G. Frede, Mitigation strategies to reduce pesticide inputs into ground- and surface water and their effectiveness; a review, Science of The Total Environment 384 (1–3) (2007) 1 – 35.

[4] M. Massinon, F. Lebeau, Experimental method for the assessment of agricultural spray retention based on high-speed imaging of drop impact on a synthetic superhydrophobic surface, Biosystems Engineering 112 (1) (2012) 56 – 64.
[5] P. Miller, M. B. Ellis, Effects of formulation on spray nozzle performance for applications from ground-based boom sprayers, Crop Protection 19 (8–10) (2000) 609 – 615, {XIVth} International Plant Protection Congress.
[6] M. Ellis, C. Tuck, P. Miller, The effect of some adjuvants on sprays produced by agricultural flat fan nozzles, Crop Protection 16 (1) (1997) 41 – 50.
[7] M. B. Ellis, C. Tuck, P. Miller, How surface tension of surfactant solutions influences the characteristics of sprays produced by hydraulic nozzles used for pesticide application, Colloids and Surfaces A: Physicochemical and Engineering Aspects 180 (3) (2001) 267 – 276.
[8] P. Holloway, M. B. Ellis, D. Webb, N. Western, C. Tuck, A. Hayes, P. Miller, Effects of some agricultural tank-mix adjuvants on the deposition efficiency of aqueous sprays on foliage, Crop Protection 19 (1) (2000) 27 – 37.
[9] D. Nuyttens, K. Baetens, M. D. Schampheleire, B. Sonck, Effect of nozzle type, size and pressure on spray droplet characteristics, Biosystems Engineering 97 (3) (2007) 333 – 345.
[10] A. Hewitt, International standards for drift reduction technology studies, Tech. rep., OECD Workshop (2005).
[11] C. Dumouchel, On the experimental investigation on primary atomization of liquid streams, Experiments in fluids 45 (3) (2008) 371–422.
[12] J. W. Strutt and Lord Rayleigh, On the instability of jets, Proc. London Math. Soc 10 (3) (1878) 4–13.
[13] G. Brenn, U. Lackermeier, Drop formation from a vibrating orifice generator driven by modulated electrical signals, Physics of Fluids (1994-present) 9 (12) (1997) 3658–3669.
[14] E. J. Watson, The radial spread of a liquid jet over a horizontal plane, Journal of Fluid Mechanics 20 (1964) 481–499.
[15] L. A. S. S. Deshpande, M. F. Trujillo, Evaluating the performance of the two-phase flow solver interfoam., Computational Science & Discovery 5 (1).

Development of a Remote Sensing Technique for Airborne Droplets and Particles using the Glory and Speckle Pattern

Sara González Ruiz

Department of Environmental and Applied Fluid Dynamics, von Karman Institute for Fluid Dynamics, Belgium, sara.gonzalez.ruiz@vki.ac.be

Supervisor: Jeroen van Beeck

Professor, Department of Environmental and Applied Fluid Dynamics, von Karman Institute for Fluid Dynamics, Belgium, vanbeeck@vki.ac.be

University Supervisor: Steve Vanlanduit

Professor, Department of Mechanical Engineering, Vrije Universiteit Brussel, Belgium, steve.vanlanduit@vub.ac.be

Abstract

The present paper describes the ongoing work for the development of an optical technique for the sizing of water droplets and irregular particles. This technique is based on the interference patterns that appear in the out-of-focus plane when laser light is scattered by a particle. Two different patterns are studied; the glory pattern, produced by water droplets, and the speckle pattern, produced by irregular particles. For both cases, theoretical models and experimental investigations are described in the paper. For the experimental study, glory and speckle pattern results are compared to shadography measurements, obtaining good agreement between both thechniques.

Keywords: light scattering, glory, speckle, size characterization, droplets, particles

1. Introduction

In the last decades, a high number of aircrafts have suffered engine power-losses and instrumentation failures while flying through convective clouds containing ice crystals [1, 2, 3]. In some cases, in order to avoid these hazardous conditions, pilots have been using a visual inspection of what is known as the glory, an optical phenomenon produced in the atmosphere due to the presence of water droplets (Fig. 1). However, a more reliable particle characterization technique is needed. Optical techniques are the most suitable, due to their non intrusive nature, but challenges arise due to the presence of irregular particles in the flow, and to the compact characteristics imposed to the experimental apparatus.

In this paper, the backscattered laser light is investigated in order to develop a reliable measurement technique for particles in the micrometric range. The main advantages of this technique are its validity for both droplets and irregular particles, and its need for only one optical window.

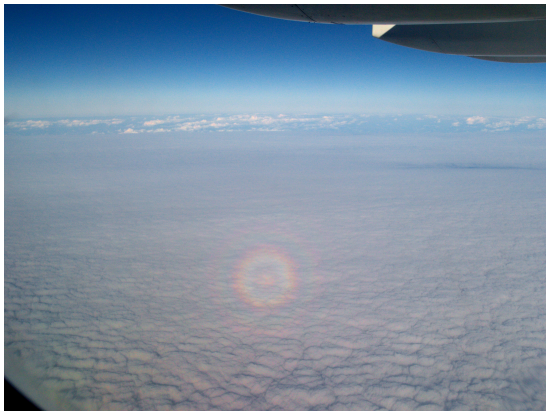

Figure 1: Atmospheric glory captured from an airplane.

2. Light backscattered by a particle

A particle illuminated by a laser beam scatters the light in all directions. When this particle is imaged in focus from a certain direction, several intensity maxima can be observed on its surface, corresponding to

the points from which the light rays are scattered towards the observer [4]. These intensity maxima in the surface of the droplet are known as glare points. The light rays scattered by the particle from the glare points interfere with each other in the out of focus plane, creating different maxima and minima of light intensity. This interference pattern can be observed when imaging the particle out of focus, and it depends on several parameters, such as the particle size, the refractive index of the particle and the surrounding medium, etc.

This paper will focus on the interference patterns produced by laser light scattered at near 180° with respect to the incident beam, in the so-called backscattering region. The light scattered in this region by a homogeneous sphere interferes in the out-of-focus plane creating concentric rings of maximum and minimum intensity. This interference pattern is known as the glory, and it is described in section 3 of this paper. On the contrary, the light scattered by an irregular particle, such as sand particles or ice crystals, produces an interference pattern with a random intensity distribution. This granular pattern is called speckle pattern, and it is described in section 4. An example of this is shown in Fig. 2, which shows the glare points observed in a water droplet (a) and an irregular particle (c) in the backscattering region, as well as their corresponding interference pattern, (b) and (d) respectively.

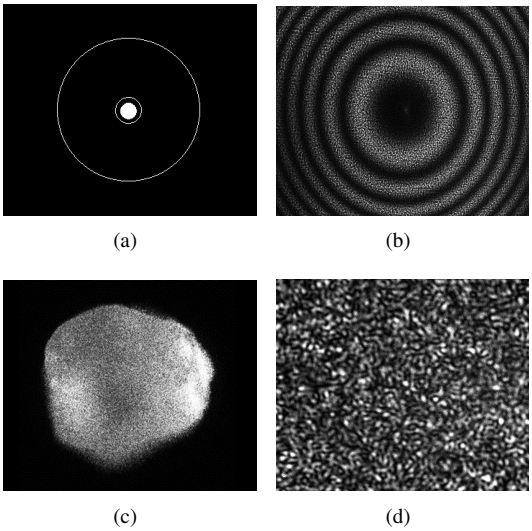

Figure 2: Sketch of the glare points seen in the in-focus image of a water droplet (a), and image of the interference pattern that a water droplet produces in the backscattering region (b). Figures (c) and (d) are images of the glare points and the interference pattern, respectively, produced by an irregular particle.

3. Glory pattern for sizing of water droplets

In nature, the atmospheric glory has been observed mainly from high altitudes, in the form of colorful rings centered around the shadow that the observer projects in a cloud [5]. In laboratory conditions, where the glory is created by the scattering of laser light instead of sunlight, a monochromatic glory pattern is observed.

In this section, an analytical solution to the monochromatic glory is given. Furthermore, a geometrical approach is presented which relates droplet size to the intensity pattern of the glory.

3.1. Analytical solution

The scattering of light as an electromagnetic wave is mathematically described by Maxwell equations, a set of partial differential equations that predict the interaction of light with an arbitrary particle. In the case of an homogeneous sphere, the Lorenz-Mie theory provides an exact solution to these equations [6, 7]. According to this solution, the glory intensity in a certain point in space is given by:

$$I = \frac{I_0}{(k_0 r)^2}\left[i_1(d,\theta)\sin^2\varphi + i_2(d,\theta)\cos^2\varphi\right] \quad (1)$$

where i_1 and i_2 are the perpendicular and parallel normalized components of the scattered light intensity, θ is the scattering angle, φ is the polarization angle, I_0 is the incident light intensity, $k_0 = 2\pi/\lambda$ is the wave number, λ is the wavelength of the incident light and r is the distance to the droplet.

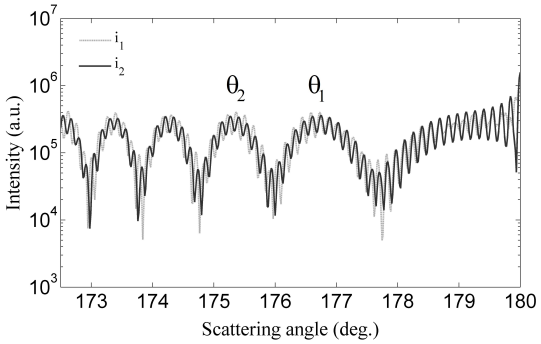

Figure 3: Normalized intensity of backscattered light by a droplet ($d = 500\mu m$, m = 1.33). θ_1 and θ_2 are two consecutive glory maxima.

Fig. 3 shows the normalized far-field intensity of the glory, i_1 and i_2, as a function of the scattering angle, for a water droplet with a diameter of $d = 500\mu m$

and a relative refractive index of m = 1.33. Several frequencies can be noted in the glory intensity profile, which will be further explained in the following subsection.

3.2. Geometrical optics approach

The geometrical optics describes the light in terms of rays that follow a rectilinear path while traveling in an homogeneous medium. This approximation can predict the angle at which the rays are scattered by a droplet, θ, by simple geometrical equations [8]. René Descartes related this angle with the incident angle of the light, τ, and the refracted angle within the droplet, τ' (defined in Fig. 4) as follows:

$$\theta = 2\tau - 2p\tau' \tag{2}$$

where p defines the number of interactions between the ray and the surface of the droplet as shown in Fig. 4. The relation between the light incident angle and the refracted angle inside the droplet is given by Snell's law as

$$\cos\tau = m\cos\tau'. \tag{3}$$

Fig. 4 shows the geometrical light rays contributing the most to the glory intensity pattern. They correspond to the near-centered rays, which suffer one internal reflection and one external reflection. In addition, the rays scattered from the edge of the droplet also play an important role in the formation of the glory pattern [9].

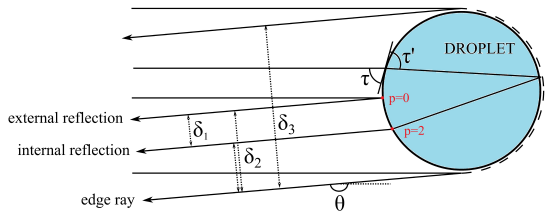

Figure 4: Schematic of geometrical optics rays giving the main contribution to the glory intensity, depicted for $\theta = 175°$.

The contribution of these rays to the glory intensity pattern can be further described by analyzing the angular frequency spectrum of the glory. Fig. 5 shows the angular frequency spectrum of the glory intensity profile produced by a water droplet with a diameter of $d = 500\mu m$ and a relative refractive index of m = 1.33.

Three dominant peaks in the angular frequency spectrum can be noted. These peaks are explained by the principle of optical interference at infinity between two parallel rays separated by a distance δ. The frequency of these peaks is then calculated similarly to those of Young's double-slit experiment [8, 10]:

$$F_i = \frac{\delta_i}{\lambda} \tag{4}$$

From eq. 4, it is possible to conclude that F_1 corresponds to the interference between two near-centered rays ($p = 0$, $p = 2$), F_2 corresponds to the interference between these two rays and the edge rays, and F_3 corresponds to the interference between edge rays.

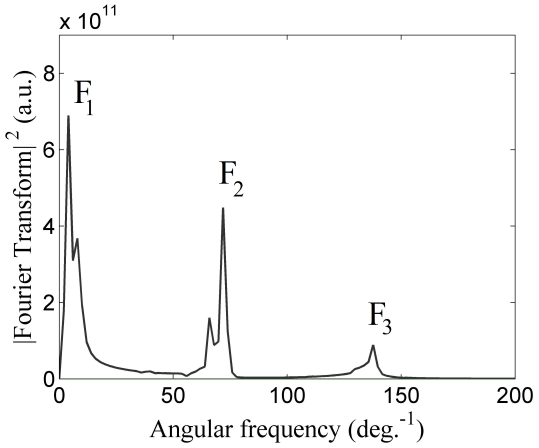

Figure 5: Fourier Transform of the light scattered by a droplet ($d = 500\mu m$, m = 1.33) in the backscattering region.

3.2.1. F_3: High-frequency oscillations

Since the distance between edge rays corresponds to the diameter of the droplet, eq. 4 can be directly used to relate F_3 to the droplet diameter [11]. This relation is specially useful when determining the diameter of small droplets, where only the highest frequencies are visible in the glory intensity pattern.

$$d = \delta_3 = F_3\lambda \tag{5}$$

Fig. 6 shows the comparison between droplet size obtained from the highest frequency in analytical intensity patterns obtained from the Lorenz-Mie theory and the imposed diameter to these computations. An excellent agreement can be noted between the Geometrical Optics model and the Lorenz-Mie theory.

3.2.2. F_1: Low-frequency oscillations

For droplet diameters bigger than $200\mu m$, the lowest frequency F_1 is dominant in the glory pattern, thus the main intensity peaks in the glory pattern are no longer due to the edge rays, but to the near-centered

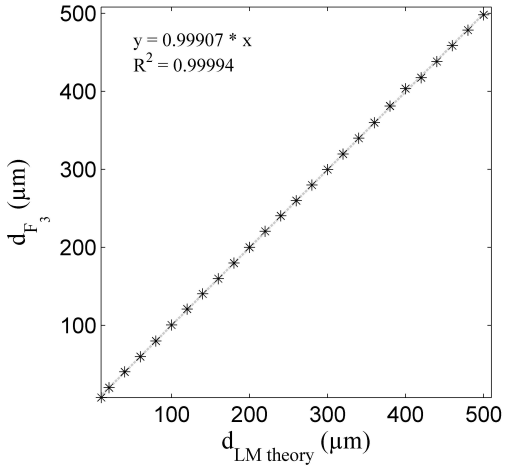

Figure 6: Comparison between droplet size obtained from the highest frequency in analytical intensity patterns obtained from LM theory and the imposed diameter, for m = 1.33.

rays. Although the geometrical optics can provide the angle at which these rays are scattered, it can not give any information about their interferece. Therefore, in order to relate the droplet diameter, d, to the low-frequency intensity maxima in the glory pattern, the phase of these rays must be added to the model.

The phase, β, of a light ray can be calculated and related to the droplet size parameter as follows:

$$\beta = \frac{2d\pi}{\lambda}\left(\sin\tau - pm\sin\tau'\right) \tag{6}$$

The interference between two light rays will be constructive when the phase difference between both rays is a multiple of 2π and destructive when the phase difference is a multiple of π[8].

The phase of the rays which have suffered one external reflection (with subindex $p0$) or one internal reflection (with subindex $p2$), is, respectively:

$$\beta_{p0} = \frac{2d\pi}{\lambda}\sin\tau_{p0} - \pi \tag{7}$$

$$\beta_{p2} = \frac{2d\pi}{\lambda}\left(\sin\tau_{p2} - 2m\sin\tau'_{p2}\right) + 2\pi \tag{8}$$

An additional term has appeared in eqs. 7 and 8 due to phase changes occurring in a light ray when it is reflected or when it crosses a focal point [6]. Since two consecutive peaks in the glory intensity profile are separated by a phase difference of 2π, the relation between these two peaks and the droplet diameter is given by:

$$d = \lambda\Big(\sin\tau_{p0\theta1} - \sin\tau_{p0\theta2} - \sin\tau_{p2\theta1} + \sin\tau_{p2\theta2} + 2m\sin\tau'_{p2\theta1} - 2m\sin\tau_{p2\theta2}\Big)^{-1} \tag{9}$$

where the subindex θ_1, θ_2 refer to the scattering angle of the two consecutive peaks. A more detailed derivation of this equation can be found in [12]. It should be noted that this equation is valid for any consecutive peak in the glory pattern.

In order to verify the validity of this model, an experimental study of the glory pattern for water droplets of different diameter was performed. The setup used for this study is shown in Fig. 7.

The He-Ne laser used to illuminate the droplet emitts linearly polarized light with a wavelength of 632.8 nm. The light scattered by the droplet in the glory region is reflected by a mirror mounted at 45° with respect to the laser beam. This mirror has a 3 × 2.5 mm elliptical hole at the center of its surface in order to allow the incident laser beam to pass through. A convergent lens (f = 205 mm) is used to converge the scattered light into a CCD camera (Camera 1), equipped with an objective lens (Nikon, f = 17 mm). This camera records a 2D image of the interference pattern at scattering angles between 174° and 180°. Another CCD camera (Camera 2) is used to record an shadowgraph image of the droplet. This camera is equipped with a Computar zoom lens, giving a final spatial resolution of 126 pixel/mm. In order to eliminate the laser component from the shadowgraph image of the droplet, a bandpass filter (532 ± 10 nm) is located in front of this camera objective.

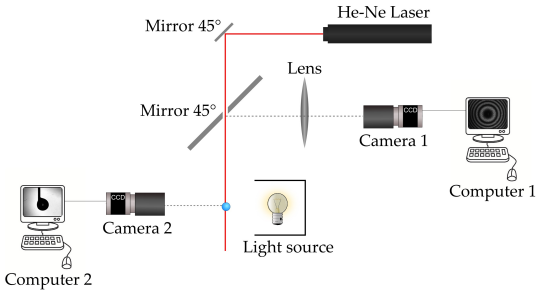

Figure 7: Sketch of the experimental setup.

In order to process the glory images, an horizontal and a vertical profile are extracted from the center of the glory pattern. These profiles are then filtered as shown in Fig. 8. For profile, the scattering angle of all the intensity peaks is extracted and the diameter of the droplet is computed for each couple of consecutive

peaks. The final droplet diameter is calculated as the mean of all the diameters calculated in one image.

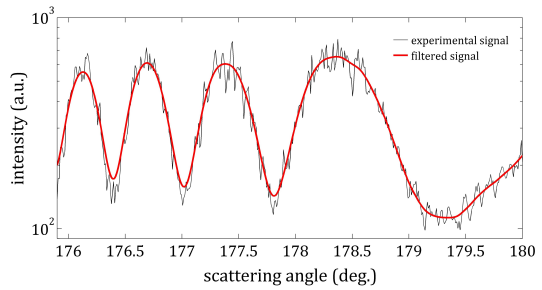

Figure 8: Example of experimental glory intensity profile and the filtered signal obtained from it.

The results obtained from the glory images were compared with the diameter of the droplet extracted by image processing from the shadography images. This comparison is shown in Fig. 9, where very good agreement can be noted between glory and shadowgraphy measurements.

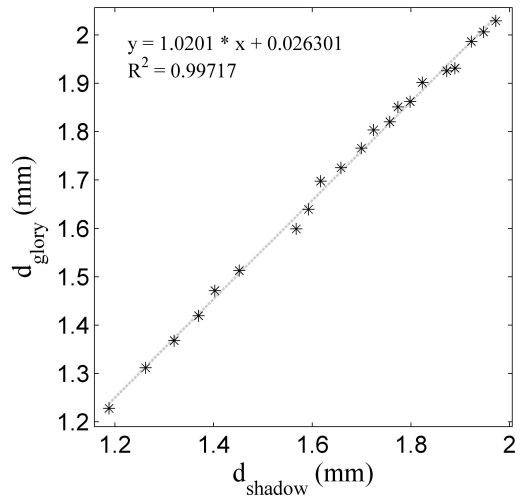

Figure 9: Comparison between the droplet diameter obtained from the image processing of the shadowgraphy images of the droplet and the droplet diameter obtained from the glory images by using the GO model.

4. Speckle pattern for sizing of irregular particles

As previously mentioned, the glare points observed in the surface of a particle are radiant points from which the light is scattered towards the observer. When the particle is a water droplet, it was seen in section 3 that the glare points are located near the center of the particle and in the edge. However, when the particle has an irregular surface, the light is scattered randomly in all directions and, therefore, the glare points are distributed over all the particle surface. According to van de Hulst, the glare points found in a certain direction within the particle surface, g(x), can be written as:

$$g(x) = \mathcal{F}\{S_1(\theta)\} \tag{10}$$

where S_1 is the amplitude function of the scattered light and $\mathcal{F}$ represents the Fourier transform. Furthermore, the light intensity can be written as:

$$i_1(\theta) = |S_1(\theta)|^2 \tag{11}$$

Applying the Wiener–Khintchine theorem [8], the relation between the glare points and the scattered light intensity can be established as:

$$|g(x) \odot g^*(x)| = |\mathcal{F}\{i_1(\theta)\}| \tag{12}$$

where $\odot$ symbolizes the autocorrelation and $*$ the complex conjugate. Therefore, the amplitude of the Fourier transform of the scattered light intensity produced by a particle equals the autocorrelation of its glare points (Fig. 10). In the case of an irregular particle, since the glare points are distributed over the whole surface, the amplitude of the Fourier transform of the scattered light intensity equals the autocorrelation of the particle itself.

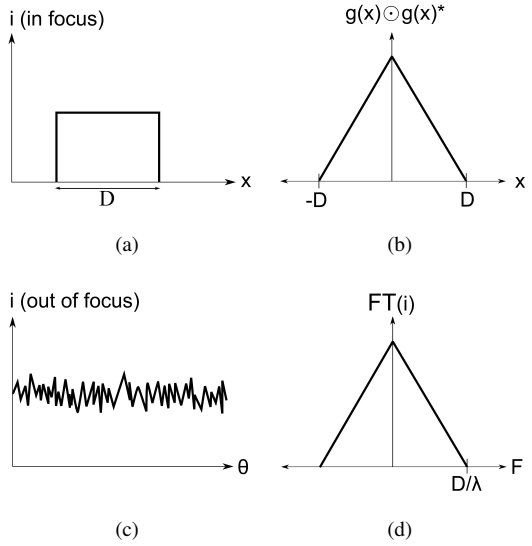

Figure 10: Schematic representation of: (a) glare points of a particle in x direction (b) autocorrelation of the particle's glare points (c) intensity profile of speckle pattern produced by the particle (d) Fourier Transform of the speckle pattern intensity profile.

If the glare points are homogeneously distributed over all the particle surface, then the Fourier transform of the glare points in a given direction will have a triangular shape. The frequency corresponding to the base of that triangle is related to the particle size by eq.12.Since this equation is independent of the scattering angle, particle size can be obtained from the speckle pattern regardless the scattering angle at which the particle is observed. However, the particle size retrieved from the speckle pattern at a specific scattering angle corresponds to the projection of the particle at that angle. A more detailed explanation about the properties of the speckle pattern can be found in [13].

In order to verify this model, several sand particles of different diameters were studied under a microscope (Fig. 11). A CMOS camera with a sensor resolution of 2048 × 2048 pixels was used to record the particles from the top of the microscope, and a 10× lens was used to magnify the image. The sand particles were placed on the microscope tray, which could be displaced vertically. When the tray was positioned at the focus plane of the camera, the particle was illuminated from below, and a shadowgraph image of the particle was recorded. The speckle pattern was recorded by vertically displacing the tray 5 mm and illuminating the particle with a He-Ne laser (632.8 nm) at 45° with respect to the vertical position.

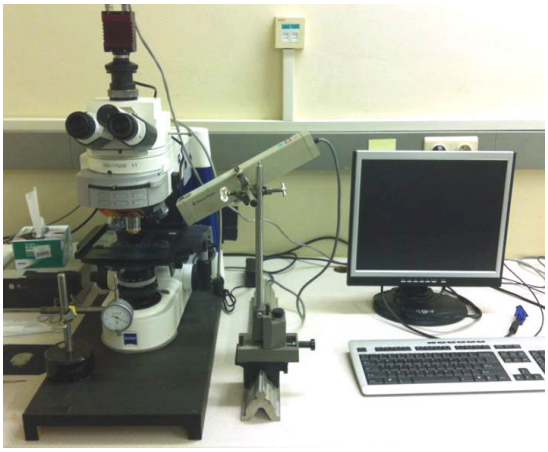

Figure 11: Photograph of the microscope used to study the speckle pattern from different sand particles.

Fig. 12 shows a shadowgraph image of a sand particle (a) and its corresponding speckle pattern (c). In the right, the 2D autocorrelation of the particle (b) and the 2D Fourier Transform of the speckle pattern (d) are shown. This figure proves experimentally that the amplitude of the particle's autocorrelation and the 2D Fourier Transform of the speckle pattern are indeed the same.

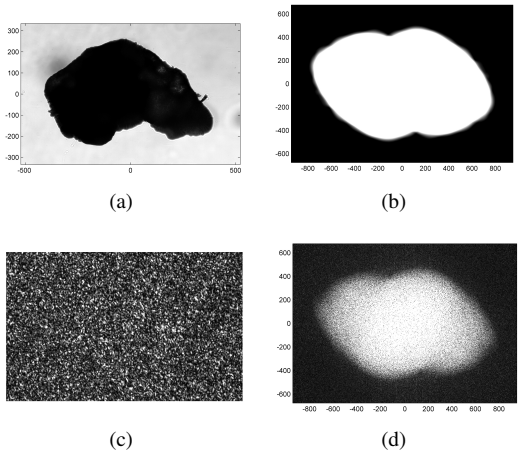

Figure 12: Image of the in-focus particle (a) and its produced speckle pattern (c). Calculated autocorrelation of the particle (b) and Fourier Transform of the speckle pattern (d).

Fig. 13 shows the average of all the horizontal profiles on the 2D Fourier Transform of the speckle pattern, for two sand particles of different sizes. The size of each particle is obtained from the maximum curvature of each profile in the Fourier transform.

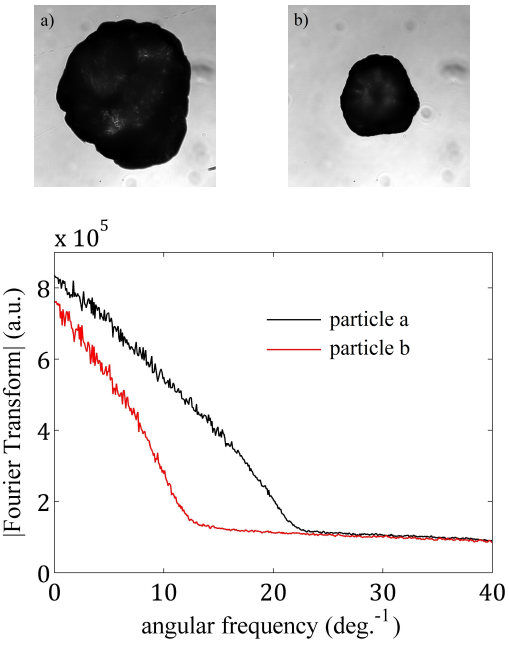

Figure 13: Fourier Transform in the horizontal direction for two different particles.

The particle size obtained from the processing the horizontal profiles of the speckle pattern images was compared to the particle size obtained from the shadowgraphy measurements, where the horizontal projection of the particle was taken as a reference. The results, shown in Fig. 14, show good agreement between both techniques.

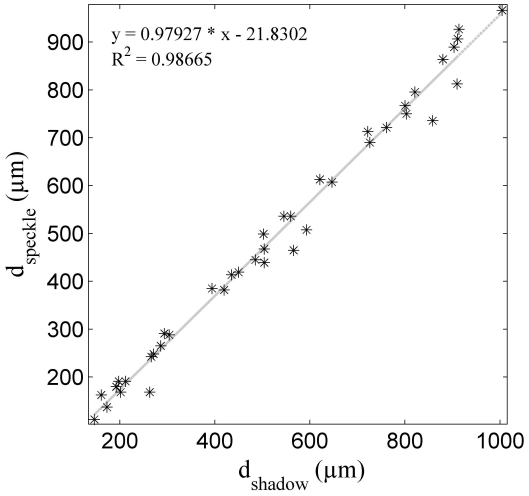

Figure 14: Comparison between the particle size obtained by image processing of the shadowgraphy image and the particle size obtained by the processing of the speckle pattern.

5. Conclusion

The interference pattern created by the backscattered light from two different type of particles was described in this paper.

First, the glory pattern, produced by water droplets was described. Two geometrical models were presented for the determination of the droplet diameter from the intensity pattern of the glory. The first model related the highest frequency in the glory intensity pattern to the droplet diameter. This model is valid for all the particles in the micrometric range, and it is specially useful for small droplets, in which the low frequencies of the glory cannot be observed. The second model related the angular position of two consecutive intensity peaks in the glory intensity pattern to the droplet diameter. This model is valid for droplet diameters bigger than 200 μm, and it is specially useful for bigger droplets, in which the low frequency is dominant and a high resolution is needed to capture the highest frequencies. The possiblity to choose between these two different models provides the advantage of measuring a high range of droplet diameters with a relatively low resolution optics, and without the need for a change in optical configuration.

Secondly, the speckle pattern, produced by irregular particles was described. In this case, the Fourier transform of the speckle pattern was related to the autocorrelation of the particle. Therefore, the projection of the particle in the direction of analysis can be retrieved from the speckle pattern. The results obtained from the experiments show good agreement between the speckle pattern measurements and the shadowgraphy measurements.

Acknowledgements

This PhD project is funded by the Agency for Innovation by Science and Technology in Flanders (IWT).

References

[1] J. Mason, Engine power loss in ice crystal conditions, Aeromagazine 04 (2007) 12–17.
[2] J. G. Mason, J. W. Strapp, P. Chow, The ice particle threat to engines in flight, 44th AIAA Aerospace Sciences Meeting and Exhibit.
[3] M. L. Grzych, Avoiding convective weather linked to ice-crystal icing engine events, Aeromagazine 01 (2010) 22–28.
[4] H. van de Hulst, R. Wang, Glare points, Applied Optics 30 (1991) 4755–4763.
[5] P. Laven, Atmospheric glories: simulations and observations, Applied Optics 44 (27) (2005) 5667–5674.
[6] H. van de Hulst, Light Scattering by Small Particles, Dover Publications, 1981.
[7] M. Kerker, The scattering of light and other electromagnetic radiation, Academic Press, 1969.
[8] E. Hecht, Optics, Addison Wesley Longman, 2002.
[9] P. Gillis, C. Deleuze, V. Henri, J. Lesceux, Backscattering of light from a water droplet: The glory effect, American Journal of Physics 50 (1982) 416–421.
[10] J. van Beeck, M. Riethmuller, Rainbow phenomena applied to the measurement of droplet size and velocity and to the detection of nonsphericity, Applied Optics 35 (1996) 2259–2266.
[11] M. Vetrano, S. G. Ruiz, J. van Beeck, Single and multiple droplet sizing by backscattering glory in the micrometric range, Optics Communications 341 (2015) 271–275.
[12] S. G. Ruiz, M. Vetrano, J. van Beeck, Feasibility of using glory and speckle patterns for sizing spherical and irregular particles, Applied Optics 53 (21) (2014) 4722–4728.
[13] P. G. Carrascal, S. G. Ruiz, J. van Beeck, Irregular particle sizing using speckle pattern for continuous wave laser applications, Exp. Fluids 55.

Particle characterization on a liquid-gas interface

Imre T. Horváth

Environmental and Applied Fluid Dynamics Department, von Karman Institute for Fluid Dynamics, Belgium, imre.horvath@vki.ac.be

Supervisor: Maria R. Vetrano

Assistant Professor, Environmental and Applied Fluid Dynamics Department, von Karman Institute for Fluid Dynamics, Belgium, vetrano@vki.ac.be.

University Supervisor: Pierre Colinet

FNRS Senior Research Associate, Transfers, Interfaces and Processes Department (TIPs), ULB, pcolinet@ulb.ac.be.

Abstract

The ultimate goal of the present doctoral research is the development of a non-intrusive optical measurement technique for characterizing small particles, which are located at a planar liquid-gas interface. The development of such technique is essential for improving our understanding of the behavior of colloidal particles at an interface. The typical application of colloidal particles trapped at an interface is flotation, which is an industrial method to extract the dispersed phase from a dispersion medium. The developed technique is based on the Light Extinction Spectroscopy (LES) method. It is sensitive to particle size and particle position relative to the interface. The technique is insensitive to the morphology of two-dimensional structures, which are formed upon destabilization.

Keywords: light extinction spectroscopy, light scattering, colloidal particles, interface

1. Introduction

The behavior of colloidal particles at a liquid-gas interface is a complex phenomenon, involving surface tension effects, particle size, particle shape and the wetting properties of the solid-liquid system. The primary experimental tool to study such systems is optical microscopy. Unfortunately, the latter limits the size of the investigated particles to be at least a few micrometers. When the quantity of interest is the particle position relative to the interface, particles in the range of tens of micrometers are used. The scientific interest in studying smaller particles is large due to their special properties. The purpose of this study is to introduce a technique, which allows the investigation of sub-micron particles at a liquid-gas interface.

The present work is divided into two parts. First, a particle monolayer is produced experimentally on the water-air interface. The monolayer is studied simultaneously using optical microscopy and the LES technique. The second part of the study is the interpretation of the acquired LES data using finite element modeling of light scattering by a particle on an interface.

2. Preparation of the particle monolayer

It is known that particles tend to accumulate on a liquid-gas interface because the latter position is energetically favorable. Namely, the free energy of detachment into the liquid phase is order of magnitudes higher than the thermal energy of the particle. [1] suggests to use spreading techniques to produce particle monolayers. The latter consists of dispersing the colloidal particles in aqueous ethanol or methanol solution. Placing a drop of the dispersion on the water surface causes immediate spreading. The subsequent evaporation of the spreading agent leaves the particles well distributed along the surface. Unfortunately, the present technique did not provide satisfactory results, probably due to the electrostatic stabilization of the particles or due to their small size: $1\mu m$. The particles remained dispersed in a $100\mu m$ thick layer. The corresponding microscopy image is shown in Figure 1.

The diffraction rings correspond to particles located behind the focal plane. The particles on the interface are in focus.

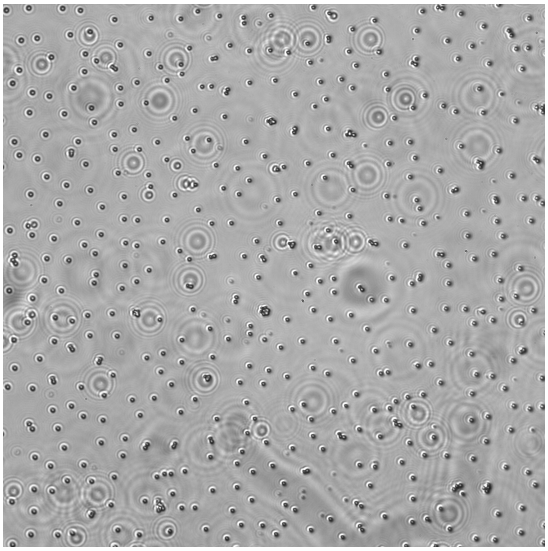

Figure 1: Microscopy image of a particle layer spanning a thickness of $100\mu m$ near a free water surface

After experimenting with various different methods and compositions, perfect monolayers were obtained. The particles are dispersed in ethanol solution as suggested by literature. The liquid layer is prepared by dissolving a small amount of NaCl in it. The particle dispersion is delivered to the liquid surface in the form of a fine spray, which is produced by a medical device. A fine wire grid is placed above the liquid surface, which captures large droplets. The method is robust and repeatable. A corresponding microscopy image is shown in Figure 2.

In addition to its high quality, the produced monolayer exhibits interesting dynamics. The almost regular spacing between particles is due to the presence of repulsive stabilization forces. These forces disappear after approx. 10 minutes and the monolayer starts to agglomerate to produce two dimensional, fractal like structures. After a time of 1.5 hours continuous particle networks can be observed (Figure 3).

The produced monolayer is a good candidate to analyze with the LES technique since the absence of submerged particles allows recording only signal coming from the interface. The slow destabilization of the monolayer allows studying the response of the technique to changes in particle morphology.

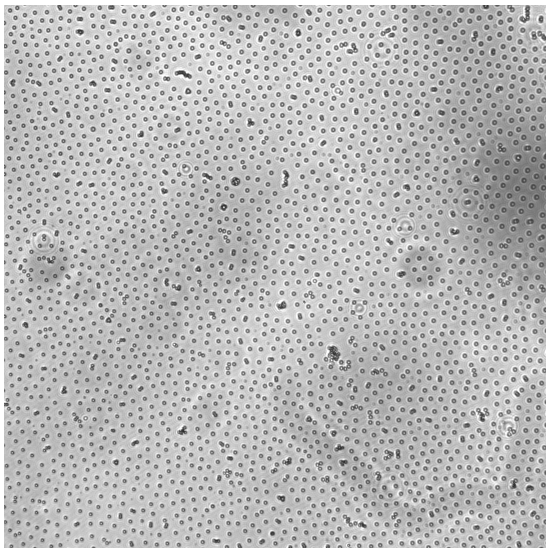

Figure 2: Microscopy image of a high quality particle monolayer.

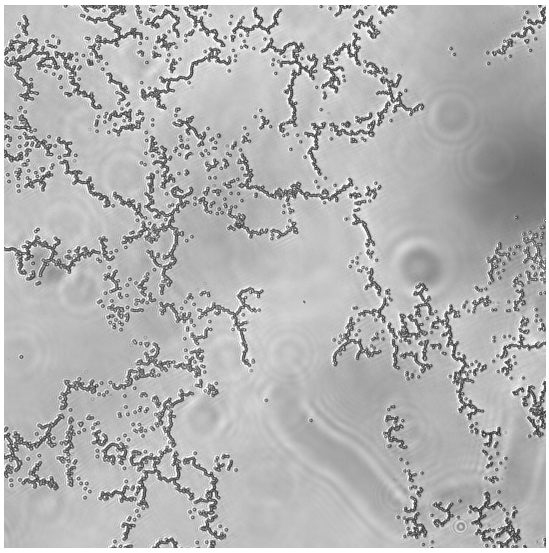

Figure 3: Microscopy image of two-dimensional particle networks formed after 1.5 hours.

3. LES measurements of the monolayer

LES measurements are performed through the liquid film at different times by recording the UV-NIR light transmission spectrum of the monolayer-liquid film system. Due to the long duration of the experiment (1.5 hours) the use of a reference beam is necessary. The recorded spectra are shown by Figure 4. It is clearly visible that the extinction spectrum is not affected by the particle morphology, since the same spectrum was recorded at any moment of the

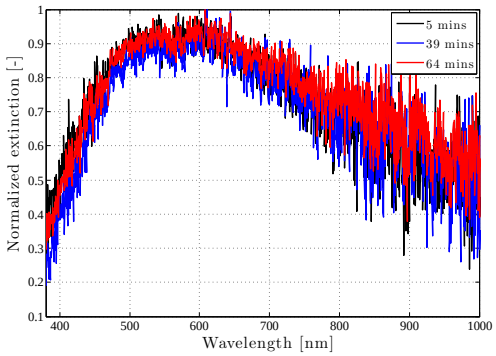

Figure 4: Normalized total extinction cross-section spectra recorded at different moments of the experiment.

experiment. This can be explained by the weak side-scattering of the used particles, which leads to weak particle-particle interactions.

It is worthwhile to compare the above experimental extinction spectra to the theoretical spectrum of the same particles fully dispersed in water and air. The comparison is presented on Figure 5. Surprisingly, the

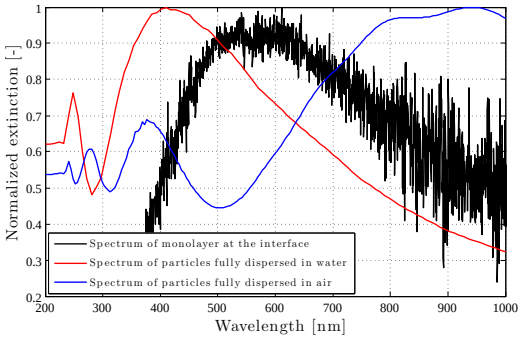

Figure 5: Normalized extinction cross-section spectra of particles dispersed in water and air and trapped at the interface

main extinction peak is located just in between those of the particles dispersed in each continuous phase. This result shows that the extinction spectrum of particles located at a liquid-gas interface is sensitive to the particle-interface relative position. This has two consequences: monolayer formation can be detected using the LES technique; it is possible to determine the particle-interface relative position from LES measurements. However, both conclusions need to be confirmed on a theoretical basis.

4. Computation of light extinction by particles on a water-air interface

The present problem did not attract many attention up to now. The analytical approaches commonly used to solve electromagnetic scattering problems are inapplicable due to the particle, which penetrates both half-spaces. The only feasible approach is to solve the time harmonic Maxwell equations in the frequency domain, using a finite element solver, namely COMSOL Multiphysics. The latter approach allows the computation of virtually any geometrical configuration.

The geometry is represented by a quarter of a sphere and symmetry boundary conditions are applied on the cutting planes. The latter is possible due to the symmetry of the electromagnetic field for a spherical scatterer. An infinite domain is modeled by applying a variant of the Sommerfeld radiation condition at the outer boundary of the domain. This simulates the undisturbed propagation of waves through the domain boundary. Unfortunately, the scattering boundary condition implemented in COMSOL is perfectly non-reflecting only for normally incident waves. Therefore a special radiation absorbing layer called Perfectly Matched Layer (PML) needs to be defined at the outer layer of the domain. The incident radiation is defined using the Fresnel coefficients of a plane wave propagating through the water-air interface at normal incidence. First, a spherical free space scatterer has

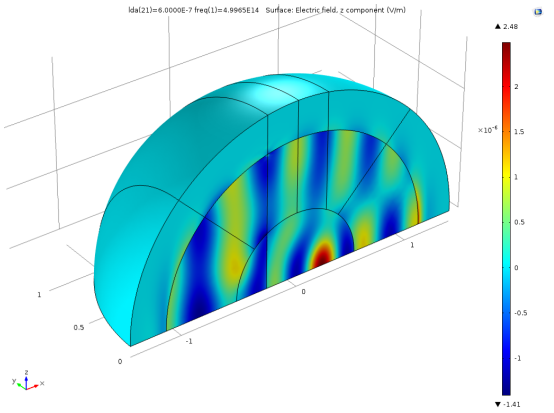

Figure 6: A typical simulation result: Z component of the total electric field at 600nm wavelength

been modeled and the computation results have been validated using traditional Mie calculations, leading to perfect agreement. Afterwards the particle on the water-air interface is modeled and particle size and

particle position are varied in order to find a reasonable fit to the experimental data. The simulation results can be qualitatively evaluated by looking at the contours of the total electric field (Figure 6). The displayed example shows a particle, which is submerged in water to $3/2$ of its radius. The domain of air is on the left-hand side. It is confirmed, that the outgoing radiation is perfectly absorbed by the PML. The distortion of the wave fronts due to the interaction of the incoming and scattered fields is also visible. The field is strongly focused inside the particle. As a preliminary result Figure 7 is presented. A reasonably good fit was obtained by setting the particle immersion to $3/2$ times its radius. The fit is not perfect and this can have several reasons. Most likely, the investigated monolayer is slightly polydisperse not only in size but also in wetting characteristics, leading to a distribution of particle-interface relative position. This is currently being evaluated by computing a large number of particle positions.

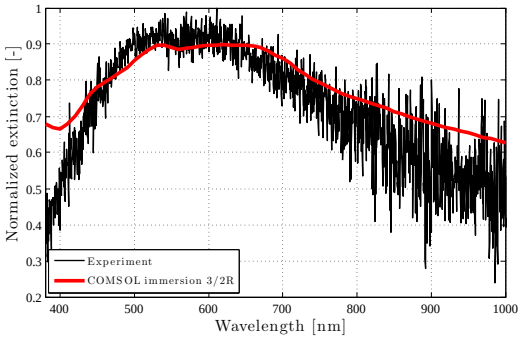

Figure 7: Fit of measured normalized extinction cross-section spectra with simulation. The particle is submerged in water by $3/2$ of its radius.

5. Conclusions

The present paper reports recent advances on the development of a non-invasive optical technique for characterizing particles trapped at a liquid-gas interface. The method is based on the Light Extinction Spectroscopy technique, which has already been successfully applied to particles dispersed in homogeneous medium from tens of nanometers up to micrometers in size. The present development is a response to the need for a method capable of characterizing colloidal particle-interface systems. First, an experimental procedure was developed for producing high quality monolayers. The monolayer was initially stable and lost its stability after approx. 10 minutes giving rise to two-dimensional particle aggregation. The monolayer was simultaneously studied by optical microscopy and the LES technique. The main findings of the research are the following. The LES technique is capable of detecting monolayer formation. It is insensitive to the morphology of the forming 2D fractal like structures. It is sensitive to the particle-interface relative position and allows the measurement of the latter quantity. Simulating electromagnetic scattering by the particle-interface system allows to estimate the latter quantity. It is estimated to be close to $3/2$ times the radius of the particles. Future work addresses the study of polydisperse wetting properties and particle size effects. The developed method makes use of a simple and inexpensive experimental setup and gives access to quantities, which are cumbersome to obtain with other methods.

References

[1] B. P. Binks, T. S. Horozov, Colloidal particles at liquid interfaces, Cambridge University Press, 2006.

Dynamics of Gas Jet Impingement on Vertical Falling Liquid Films

Mr. Miguel Alfonso Mendez

Environmental and Applied Fluid Dynamics Department, von Karman Institute for Fluid Dynamics, Belgium, mendez@vki.ac.be

Supervisor: Jean Marie Buchlin

Professor, Environmental and Applied Fluid Dynamics Department, Belgium, buchlin@vki.ac.be

University Supervisor: Prof. Herman Deconinck

Professor, Aeronautics and Aerospace Department, von Karman Institute for Fluid Dynamics, Belgium, deconinck@vki.ac.be
Département d' Aéro-Thermo-Mécanique, Faculté des Sciences Appliquées, Université Libre de Bruxelles, Belgium

Abstract

This paper analyses the stability of a turbulent slot gas jet impinging on a vertical falling liquid film. The configuration is encountered in coating applications, where the pressure gradient and the shear stress produced by the jet impingement is used to control the thickness of a liquid coat on a flat surface. A dedicated facility was designed and constructed at the von Karman Institute (VKI). This facility allows producing controlled thickness perturbation on a Dipropilene Glycol liquid film ($Ka = 4.6$, $Re = 1$–15) and studying the response of an impinging slot ($s = 1.5mm$) air jet ($Re \approx 2000$). The liquid film flow experimentally characterized using Light Absorption (LAbs) and LeDaR (Level Detection and Recording) techniques. The gas flow was experimentally characterized using flow visualization and image processing, and Particle Image Velocimetry (PIV). The results have shown that a wavy liquid film can promote gas jet oscillations if the gas-liquid interface is sufficiently deformed by the impingement, producing and asymmetric and time varying confinement of the gas flow.

Keywords: Air-Knife Coating, Pulsing Poiseuille Flows, Falling Liquid Films, Impinging Jet Oscillations, Hydrodynamic Feedback.

1. Introduction

Liquid coatings are continuously applied on thin sheets in paint, paper or galvanizing industries. Particularly in the galvanizing lines, with a world-wide production rate over 100 million tons per year of steel [1], the most common technique is the jet wiping.

In this technique the sheets are withdrawn from a coating bath and impinged by a gas jet, to control the amount of liquid forming the final coat after drying. The process is continuous, contact-less, simpler and economically more attractive than alternative electromagnetic methods [2; 3; 4].

On the other hand, the achievable coat uniformity and the production rates are limited by the formation of surface undulation on the final coat. Previous PhD thesis at VKI [5; 6] have shown the impingement configuration is unstable (Fig.1.a) and that coating undulation results from sustained oscillations of the impinging jet, at frequencies in the range $f_j \approx 10$–$100Hz$. Because of their low Strouhal number ($St \approx 10^{-3}$), these oscillations are expected to be driven by a hydrodynamic feedback [7] through the confinement. Nevertheless, a complete understanding of its origin is still lacking.

This work aimed to verify if perturbations in the liquid film, in the form of gravity waves, can trigger oscillation of the impinging jet. The simplified scenario considered for this purpose (Fig. 1.b) consists of a slot jet impinging on a liquid film falling along a fixed wall, and having a flow rate pulsing at controlled frequency and amplitude.

The facility designed to produce the pulsing liquid film is presented in § 2 and § 3. Film waves were characterized using Level Detection and Recording (LeDaR) and Light Absorption (LAbs) techniques, as summarized in § 4. The characterization of the jet response is described in § 5, and includes frequency

and amplitude of the oscillations – using flow visualization and image processing– and entrained flow topology – using Particle Image Velocimetry (PIV). The results are presented in § 6, conclusions and perspectives are discussed in § 7.

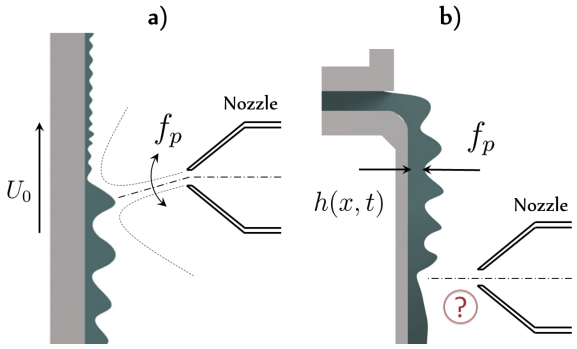

Figure 1: In jet wiping (a) the jet prints its oscillation on the final coat, producing waves at a frequency f_p. In this work (b), the jet is perturbed at a frequency f_p and its response is monitored.

2. The VKI Liquid Film Facility

The VKI liquid film facility is sketched in Fig.3. It consists of a closed loop where the liquid falls from a vertical test session (1), it is collected in a tank (2) and re-circulated, by a volumetric pump (3) and an inlet line (4), into a pneumatic chamber (5).

In this chamber, the liquid motion is minimized by splitting both the input and the by-pass flow rates into four parts, by positioning the inlet line $15cm$ below the liquid level, and by hosting a liquid volume of $18l$ during the experiment.

This allows to maintain the liquid surface flat, and to control the hydrostatic head of the liquid film flow by controlling the rotational speed of the pump and the opening of the by-pass line. The volume of the liquid gives to the system a high inertia, to simplifies the regulation of the facility and allow the user to set a constant level during the tests.

This chamber is pressurized from an inlet line (7), equipped with a pressure regulator, and discharges in atmosphere through an outlet line (8). A deflecting frame (9) avoids the impingement of the incoming air on the liquid interface within the chamber. The opening of the lines 7-8 is controlled by two butterfly valves (*), mounted with 90° phase delay on the shaft of an electric motor (Maxon EC-4pole 45).

In the steady operation mode, the motor is off, both the valves are open and a constant chamber pressure

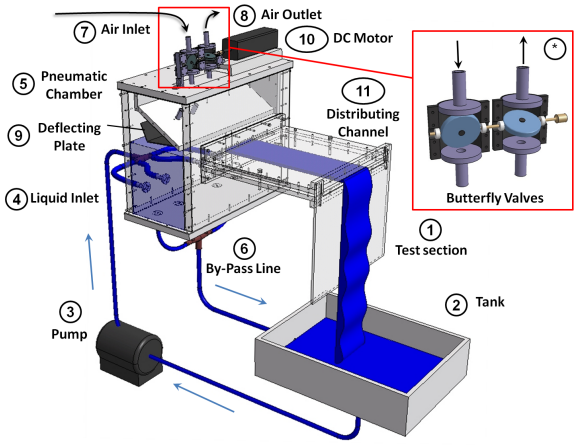

Figure 3: Sketch of the VKI liquid Film Facility All components are manufactured in ®PLEXIGLAS, with $1^{1/4} inch$ copper pipes for the connections 4-6.

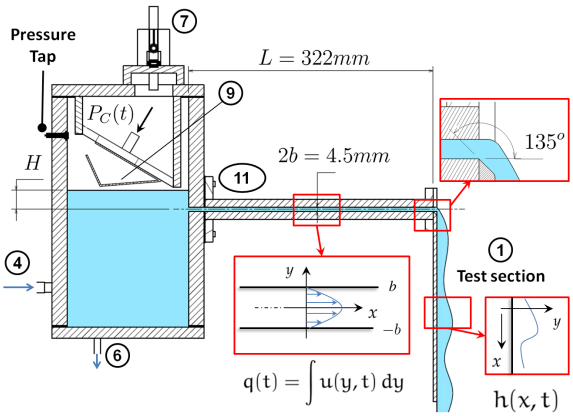

Figure 4: Facility Cross Section. The pressure pulsation $P_C(t)$ in the pneumatic chamber produces a pulsation in the channel's flow rate pulsation $q(t)$, resulting in a wavy liquid film $h(x,t)$. A smooth connection between channel and test section prevents liquid detachment.

is settled by the upstream pressure regulator. In the unsteady operation mode, the motor opens and closes lines 7 and 8 periodically, producing two charge and discharge phases at every round, thus a pressure pulsation in the chamber.

The pneumatic chamber supplies the test section through the distributing channel (11). The flow is laminar and, as recalled in Fig.4, it is sustained by a pressure head composed of two contributes: H, the hydrostatic head above the channel (steady and monitored by a floater) and $P_C(t)$, the gauge pressure in the

chamber (sinusoidal and monitored by a piezoresistive pressure transducer AMS5812).

The high aspect ratio of the distributing channel's cross section ($w/2b \approx 22$) ensures a 2D behavior of the facility, while its length ($L/2b \approx 71$) allows for the full development of the flow before it reaches the test section. The liquid used is Dipropilene Glycol, with density $\rho = 1023 \pm 0.1\%[kg/m^3]$, kinematic viscosity $\nu = 87.5 \pm 1\%[cSt]$ and surface tension $\sigma = 32 \pm 2\%[mN/m]$. The corresponding Kapitza number is $Ka = \sigma \rho\, g^{-1/3}\, \nu^{-4/3} \approx 4.6$.

3. Facility Static and Dynamic Control

The facility calibration is the transfer function between the oscillating gauge pressure $P_C(t)$ in the chamber (described in § 3.1) and the liquid flow rate $q(t)$ in the distributing channel, i.e. the test section. Due to practical difficulties in measuring $q(t)$ within the thin channel, and being the flow laminar, this transfer function was derived analytically and validated numerically as reported in § 3.2 and § 3.3.

3.1. Pressure Chamber Response

Fig.2a shows three example of pressure signals $P_C(t)$, measured in the pneumatic chamber. On each of these signals it is fitted, in red, an harmonic pulsating pressure:

$$P_C(t) = p_M + p_A \cos(2\pi f_p\, t) \qquad (1)$$

A maximal residual of 5% confirms an harmonic behavior of the pressure pulsation in the frequency range considered. The user controls the pulsation frequency f_p, through the motor speed ω_m, and the mean pressure p_M, through the pressure regulator in the inlet line. The pressure amplitude p_A, on the other hand, depends on the facility line-cavity behavior. As shown in Fig.2b, the relative pressure amplitude $\hat{p}_A = p_A/p_M$ decreases when increasing mean pressure and the pulsation frequency, though asymptotically approaching a constant value.

3.2. Channel Flow Rate Response

For an incompressible liquid ($\nabla \cdot \vec{u} = 0$), assuming that the liquid flow within the distributing channel is 2D and fully developed ($\partial_x \rightarrow 0$), the stream-wise momentum balance reduces to:

$$\frac{\partial u}{\partial t} = -\frac{1}{\rho}\frac{\partial p}{\partial x} + \nu \frac{\partial^2 u}{\partial y^2} \qquad (2)$$

Neglecting the hydrostatic pressure variation in the channel inlet yields:

$$p(t) = P_C(t) + \rho g H = P_M + p_A \cos(2\pi f_p\, t) \qquad (3)$$

The hydrostatic pressure adds to the mean channel pressure head ($P_M = p_M + \rho g H$). Moreover, it is hereinafter assumed that the pressure is instantaneously propagated in the channel and that the pressure drop remains linear at any time.

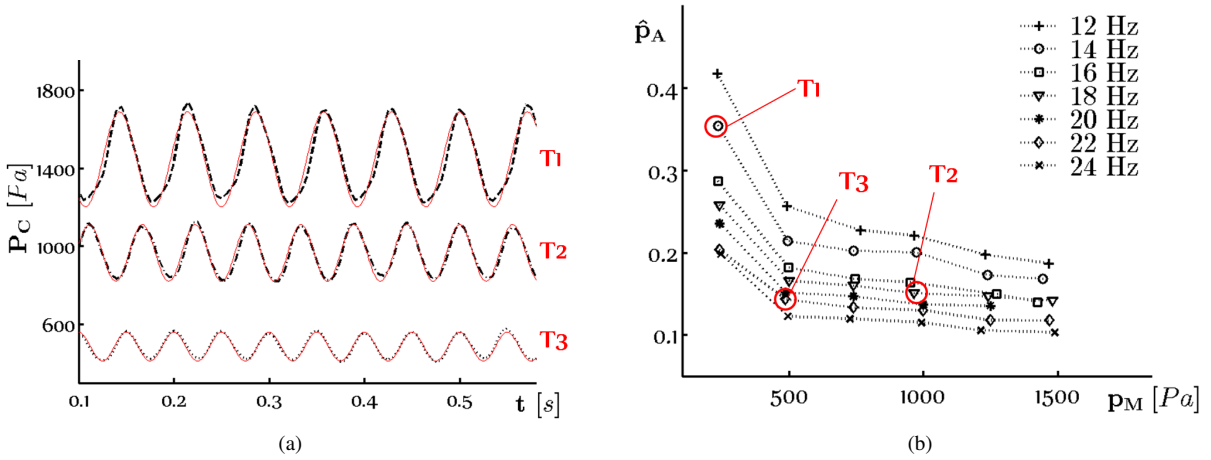

Figure 2: Pressure measurements in the pneumatic chamber. Fig.2a: examples of pressure signals $P_C(t)$ acquired from the pressure transducer at $f_s = 800Hz$. Fig.2b: relative pressure amplitude $\hat{p}_A(p_M, f)$ curves for seven different frequencies, six different mean pressures.

Therefore, pressure gradient becomes:

$$-\frac{\partial p(t)}{\partial x} = -\Big(\frac{P_M}{L} + \frac{p_A}{L}\cos(2\pi\, f_p t)\Big) \tag{4}$$

Scaling the momentum equation (2) with respect to the following reference quantities: $\hat{y} = y/b$, $\hat{x} = x/L$, $\hat{u} = u/(\mu L/P_M b^2)$, $\hat{P} = P/P_M$, $\hat{t} = t/(2\pi f_p)$, and introducing eq.(4), yields:

$$\mathcal{W}^2\,\frac{\partial \hat{u}}{\partial \hat{t}} = -\frac{\partial \hat{p}}{\partial \hat{x}} + \frac{\partial^2 \hat{u}}{\partial \hat{y}^2} = -\Big(1 + \hat{P}_A\cos(\hat{t})\Big) + \frac{\partial^2 \hat{u}}{\partial \hat{y}^2} \tag{5}$$

This scaling shows that only one dimensionless number controls the channel's flow rate response: $\mathcal{W} = b\,\sqrt{\omega/\nu}$. Known as *Womersley Number* [8], this is the ratio between the inertial forces due pressure pulsations, and the damping forces due to viscosity. It is often used in biofluid mechanics when studying pulsating flows in the cardiovascular system of animals [9; 10; 11; 12]. Since eq.(5) is linear, the flow is the superposition of a mean flow q_M, due to the mean pressure P_M, and a sinusoidal pulsating flow q_A, due to the harmonic component $p_A\cos(\omega t)$. The Reynolds number at the test section's inlet reads:

$$Re(t) = \frac{q(t)}{\nu} = Re_M + Re_A\cos(2\pi\, f_p\, t) \tag{6}$$

The strength of a perturbation is hereinafter expressed in terms of relative Reynolds number amplitude $\zeta = Re_A/Re_M$. The two components Re_M and Re_A are derived in the following subsections.

3.2.1. Mean or Steady Flow

The steady part of eq.(5) reads:

$$0 = -1 + \frac{\partial^2 \hat{u}}{\partial \hat{y}^2} \tag{7}$$

which describes the well known steady Poiseuille flow. Using the boundary conditions $u(-1) = u(1) = 0$, the velocity profile and flow rate reads:

$$\hat{u}_M(\hat{y}) = \frac{1}{2}\Big(1 - \hat{y}^2\Big) \Longrightarrow \hat{q}_M = \int_{-1}^{1} \hat{u}_M(\hat{y})d\hat{y} = \frac{2}{3} \tag{8}$$

Reversing the scaling in eq.(5) reads:

$$Re_M = \frac{q_M}{\nu} = \frac{2b^3}{3\rho\nu^2}\Big(\frac{\rho g H + p_M}{L}\Big) \tag{9}$$

The *mean* Reynolds number grows linearly with the *mean* pressure (Fig.5a). The same applies in the steady tests, where $P_C(t) = P_M$.

3.2.2. Oscillatory Flow

The harmonic part of eq.(5) reads:

$$\mathcal{W}^2\,\frac{\partial \hat{u}}{\partial \hat{t}} = -\Big(\hat{P}_A\cos(\hat{t})\Big) + \frac{\partial^2 \hat{u}}{\partial \hat{y}^2} \tag{10}$$

In unsteady condition, the inertia of the flow introduces a phase delay between pressure and flow rate pulsation and, most important in this work, a modulation. Due to the linearity of eq.(10), if a complex solution exists, both the real and imaginary parts must satisfy the equation. A periodic, variable separated, and complex solution $\tilde{u}$ is considered:

$$\tilde{u}(\hat{y}, \hat{t}) = \tilde{f}(\hat{y})e^{i\hat{t}} \tag{11}$$

Replacing eq.(11) in eq.(10) leads to a simple ordinary differential equation:

$$\tilde{f}'' - i\mathcal{W}^2\tilde{f} = -\hat{P}_A \tag{12}$$

where the *primes* indicate spatial derivatives.
With the boundary conditions $\tilde{u}(-1, \hat{t}) = \tilde{u}(1, \hat{t}) = 0$, the harmonic component of the velocity profile is the real part of the complex solution $\tilde{u}(\hat{y}, \hat{t})$:

$$\hat{u}_A(\hat{y}, \hat{t}) = \Re\{\tilde{u}\} = \Re\left\{\left(1 - \frac{\cosh(\mathcal{W}\sqrt{i}\,\hat{y})}{\cosh(\mathcal{W}\sqrt{i})}\right)\frac{i\,\hat{P}_A}{\mathcal{W}^2}\,e^{i\hat{t}}\right\} \tag{13}$$

From which the pulsing flow rate is:

$$\hat{q}_A(t) = \int_{-1}^{1} \hat{u}_A(y, t)d\hat{y} = \hat{q}_A\cos(\hat{t} - \hat{\phi})$$

The modulation function $\mathcal{T}$ between relative pressure and flow rate pulsations is finally obtained:

$$\mathcal{T}(\mathcal{W}) = \frac{\hat{q}_A}{\hat{p}_A} = \Re\left\{\int_{-1}^{1} \frac{\hat{u}_A(\hat{y}, \hat{t})}{\hat{P}_A}d\hat{y}\right\} \tag{14}$$

Using eq.(13) in eq.(14) shows that the modulation depends solely on the Womersley number. Its trend (Fig.5b) is monotonic: no modulation occurs for $\mathcal{W} \to 0$, i.e. $f \to 0$ whereas pulsations are strongly damped for $\mathcal{W} > 10$. In conclusion, the perturbation amplitude in terms of Reynolds number reads:

$$Re_A = \frac{q_A}{\nu} = \frac{3}{2}\mathcal{T}\,\hat{P}_A\,Re_M \tag{15}$$

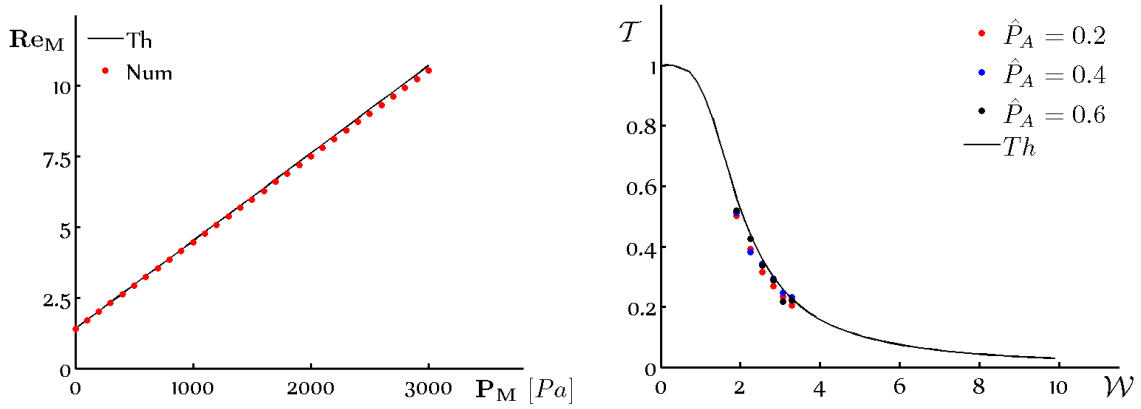

(a) (b)

Figure 5: Results of CFD laminar simulations versus theoretical derivations. a) Steady calibration of the facility. b) Modulation function in the dynamic tests.

3.3. Numerical Validations

The analytical relations in eq.(9) and eq.(15) were validated with laminar simulations of the full N-S equations using the CFD module of the commercial software COMSOL Multyphisics©. Fig.6a shows the 3D velocity contour plots at several cut planes. Steady 3D simulations at different Reynolds proved the full development of the flow and showed that the boundary layers at the channel side walls occupy less than 5% of the channel width. Therefore, steady and unsteady operations of the facility were simulated on a 2D domain whose mesh shown in Fig.6b. The pressure inlet condition was specified in the edge representing the liquid free surface within the pneumatic chamber and zero pressure outlet imposed at the channel exit. For the steady cases, the result of a set of 60 simulations are compared with ed.9 in Fig.5a. For the unsteady cases, the modulation function was computed for three sets of harmonic pressure signals with relative pressure amplitude $\hat{P}_A = 0.2, 0.4, 0.6$, in the frequency range $10-30Hz$. For each case the simulation time step was fixed at $1/10$ of the period. The results, shown in Fig. 5b, are in agreement with eq.(15), which is therefore considered the facility's transfer function.

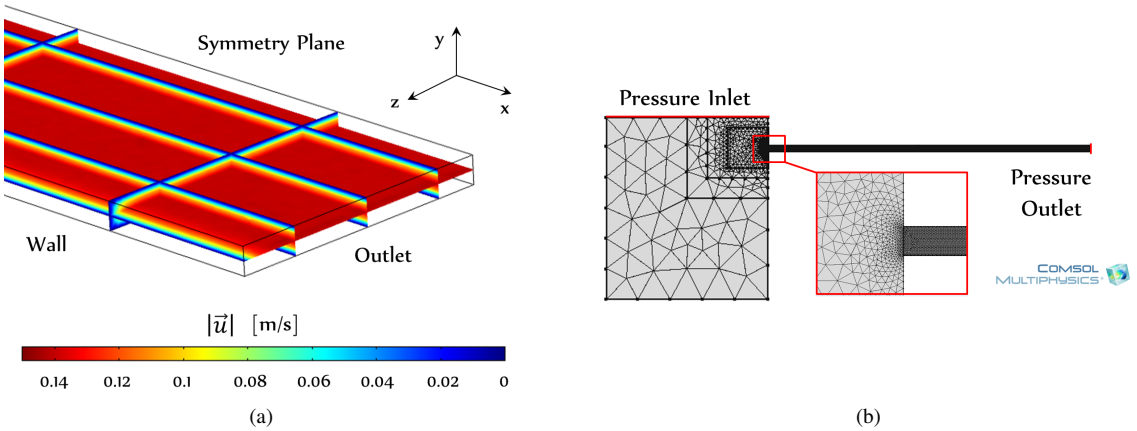

(a) (b)

Figure 6: Laminar simulations of the liquid film facility using COMSOL Multiphysics: a) 3D simulation of the channel flow, proving the assumptions of fully development and 2D flow, b) Mesh of the 2D domain used to simulate the facility dynamic behavior.

4. Film Thickness Characterization

The optical measurement techniques used to characterize the liquid film thickness were chosen for their complementary capabilities. The Light Absorption (LAbs) is a 3D technique that can easily provide a large span in the stream-wise direction ($\approx 150\,mm^2$). However, it is limited by optical distortion as the liquid interface curvature increases and its implementation on the impinged liquid film is hindered by need of positioning the Nozzle (Fig.11) in front of the liquid test section. Conversely, the Level Detection and Recording (LeDaR) is a 2D technique, with lower stream-wise span ($\approx 40\,mm$), but more robust against optical distortion, and usable for the analysis of the impinged liquid interface.

4.1. Light Absorption (LAbs)

This technique relates the thickness of a liquid film with the amount of light it absorbs from a backlighting source ([13; 14; 15]). The film thickness h is obtained from the Beer-Lambert law:

$$h(x,z,t) = \frac{1}{\gamma_g}\, ln\left(\frac{I_0(x,z)}{I(x,z,t)}\right) = \frac{A(x,z,t)}{\gamma_g} \qquad (16)$$

Where γ_g is the light absorption coefficient of the liquid, to be determined via calibration, $I_0(x,z)$ is the backlight intensity emitted, referred to as *Reference Image*, $I(x,z,t)$ is the light intensity transmitted trough the liquid film having instantaneous thickness distribution $h(x,z,t)$. The dimensionless quantity $A = ln(I_0/I)$ is referred to as *Absorbance*.

The sensitivity to high interface's curvature arises from using eq.(16): as it does not account for light refraction, the reliability of the method is limited to gently sloped interfaces. A recent implementation on a flat film is in Ref. [16].

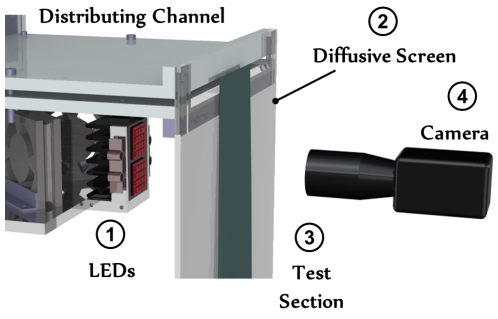

Figure 7: LAbs set up.

Fig. 7 sketches the test section used in this work. The light source (1) consists of two arrays with 4x4 LEDs of $\approx 0.7\,W$ each, with 90% emittance in the range $636 \pm 26\mu m$. They are placed $10\,cm$ behind an Opal ®PLEXIGLAS screen (2), which diffuses the light over the test section. The receiver (3) is a rolling shutter $16bits$ CMOS camera (Hamamatsu ORCA-Flash4.0), synchronized with the LEDs, to acquire at $200Hz$ with a resolution of $500x2048pixels$. The synchronization allows to determine the *Reference* image $I_0(x,z)$ with an uncertainty below 0.1%. Blue methylene colorant is diluted with a concentration[1] of $12\,mg/kg$. To maximize the sensitivity of the method, an optical band-pass filtered ($640 \pm 40\mu m$) is installed on the $50mm$ camera objective.

The measurement calibration consists in determining the absorption coefficient γ_g and ensuring that, within the thickness range of interest, eq.(16) holds for the selected concentration. As in [13], this is done using a calibration wedge which, filled with the liquid, produces a 2D thickness distribution of known slope. The absorbance coefficient γ_g is therefore obtained via linear regression from the measured absorbance map $A(x,y)$. An example of *LAbs* snapshot is shown in Fig.8.

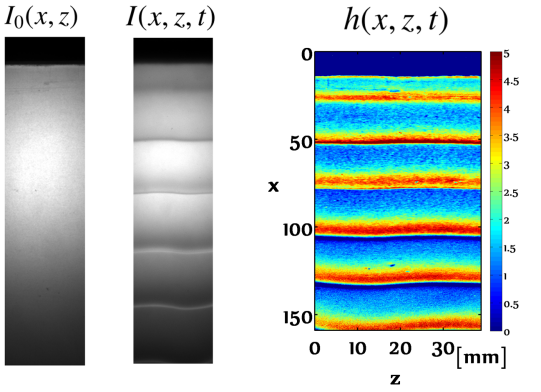

Figure 8: Reference $I_0(x,z)$, Sampled $I(x,z,t)$ images and correspondent film thickness distribution $h(x,z,t)$. Test case with $Re_M = 5.4$, $\mathcal{W} = 2.41$, corresponding to $\zeta = 11\%$.

[1] To give an order of magnitude, concentrations in the range $0.5 - 15mg/kg$ produce global light absorption coefficients linearly varyin in the range $0.3 - 0.6$. The best concentration, as shown in [17], depends on the thickness range to be investigated: higher concentrations ($\gamma_g \approx 0.5$) produce very little relative uncertainties for thin films ($h << 1\,mm$), whereas the reverse ($\gamma_g \approx 0.1$) is true for thicker layers ($h \approx 10\,mm$).

4.2. Level Detection and Recording (LeDaR)

LeDaR is an image processing method developed at VKI to detect gas-liquid interfaces from grayscale images, obtained from laser tomography [18; 19]. The experimental set up (Fig.10) consists of (1) an optical bench to produce and direct a laser sheet towards (2) the test section, and (3) a CMOS camera (Hamamatsu ORCA-Flash 4.0), equipped with 350mm zoom lens and an optical high pass filter ($> 570\mu m$).

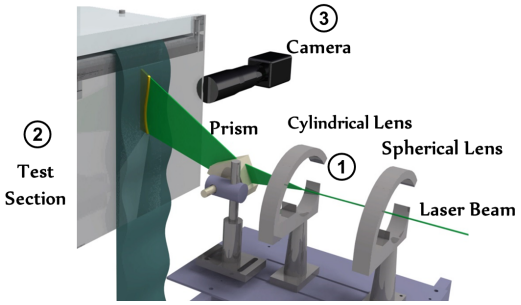

Figure 10: LeDar set up.

The laser is a continuous green laser ($\lambda_l = 532nm$), which induces fluorescence in the Rhodamine-B diluted in the liquid, to make the film interface visible in the illuminated plane. The optical filter removes laser reflections from the test section wall and the wide lens ensure a large magnification factor ($58.3 pixels/mm$) with a narrow depth of field ($DOF < 1mm$).

The liquid interface is reconstructed with an image processing algorithm developed in MATLAB®. Standard LeDaR codes relies on the convolution of each grayscale image $A(x_n, y_n)$ with a 3×3 Sobel kernel or a 21×3 version of it, known as *Maximum Forward Step Filter* [20]. Both methods require a uniform streamwise illumination, which was not available in some of the test cases studied. The high curvature interface of the largest waves (Fig. 9, a), in fact, acts as a lens which focuses the light into bright spots, hindering the interface reconstruction (Fig.9, b). To overcome this limitation, the routine developed in this work preprocesses the images to uniformy the light distribution digitally. Each grayscale frame $A(x_n, y_n)$ is scalarly multiplied with a linear operator $\Psi(x_n)$ which compares the column graylevel average $\bar{A}(x_n)$ with the whole image average $\bar{\bar{A}}$:

$$\Psi(x_n) = \frac{\bar{A}(x_n)}{\bar{\bar{A}}} = \frac{1}{Y\,\bar{\bar{A}}} \sum_{i=0}^{i=Y} A(x_n y_i) \tag{17}$$

Where Y is the number of image columns. The histogram of the resulting image $B = A \cdot \Psi$ is then recontrasted with a gamma correction of 2 (Fig.9,c) and convolved with an extended Sobel-like $[7x3]$ kernel:

$$C(x_n, y_n) = B(x_n, y_n) * \begin{pmatrix} -1 & -2 & -1 \\ -1 & -2 & -1 \\ -1 & -2 & -1 \\ 0 & -1 & 0 \\ 0 & 0 & 0 \\ 0 & 1 & 0 \\ 1 & 2 & 1 \\ 1 & 2 & 1 \\ 1 & 2 & 1 \end{pmatrix} \tag{18}$$

The resulting image (Fig.9,d) is used for detecting the interface position $h(x_n)$ as the point in which the vertical gradient $\partial_y C$ is *maximum*:

$$\partial_y C\Big(x_n,\, h(x_n)\Big) = max\Big(\partial_y C\Big(\,x_n,\, y_n\Big)\Big) \tag{19}$$

Finally, the reconstructed vector $h(x_n)$ is smoothed using the robust locally weighted polynomial regression (*rloess*) available in MATLAB®.

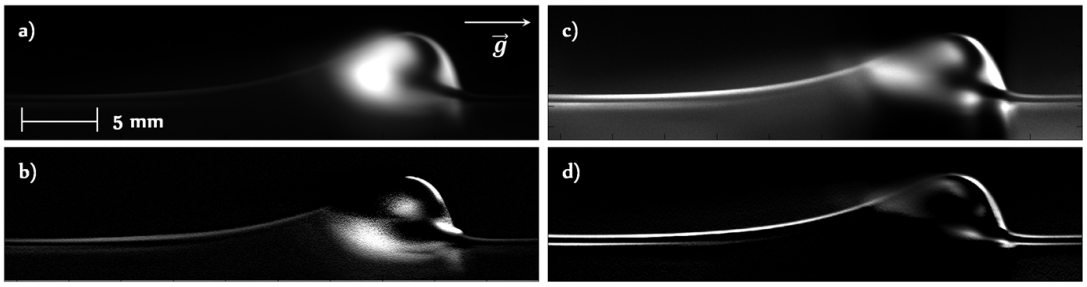

Figure 9: Improved LeDaR processing for wavy liquid film. The non uniform gray level distribution within the liquid, in (a) the raw image $A(x_n, y_n)$, produces (b) an incomplete interface detection with standard LeDaR. Recontrasting (c) with the linear operator $\Psi(x_n)$ limits this effect. The result of eq.(18) is d).

5. Impinging Gas Jet

Three aspects of the impinging configuration in Fig.1.b were investigated. Firstly, the dynamics of the impinged liquid interface, using LeDaR, as described in § 5.2. Secondly, the frequency and amplitude of the gas jet response, using flow visualization and image processing, as described in § 5.3. Thirdly, the topology of the flow entrained by the gas jet, using PIV, as described in § 5.4. The Nozzle Setup is described in § 5.1.

5.1. Nozzle Set-Up

Fig.11 shows the nozzle set-up. A slot nozzle (1) is installed on a 2-axis positioning support (2), equipped with the same optical set up as in Fig.10 for laser sheet formation (3). The nozzle is supplied with compressed air and oil particles to trace the flow for visualization purposes. Its geometry is described in [6]. In addition to the main particle injection in the nozzle, a secondary injection (4) is used to trace the air flow entrained by the gas jet.

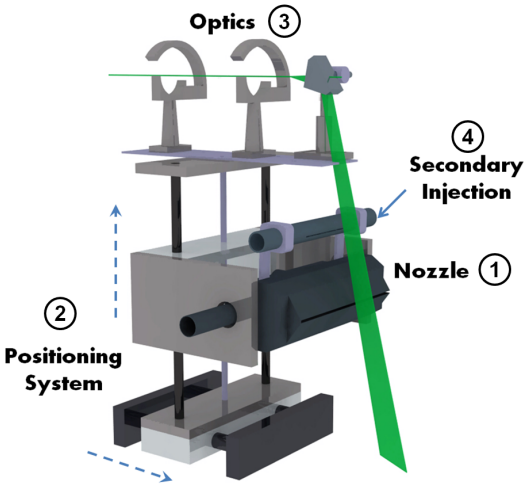

Figure 11: Nozzle set-up.

The impingement of the gas jet on the liquid film is visualized with a CMOS high speed camera (Phantom v7.1), installed on one side with a 100mm objective. The nozzle has an outlet opening $s = 1.5mm$ with a width of $w = 100mm$. It was first calibrated in free jet conditions monitoring its settling chamber pressure with a pressure transducer and its velocity profile using hot wire anemometry at 3mm distance. The calibration shows a good agreement with Bernoulli's equation and a jet turbulence intensity in the range $2\% - 5\%$. The maximum jet Reynolds number is $Re_J \approx 2000$, defined by the occurrence of liquid splashing.

5.2. Impinged Liquid Interface

During the characterization of the impinged interface both the main and the secondary injections are switched off and the liquid interface is impinged by pure air. The laser sheet induces fluorescence in the Rhodamine-B diluted in the liquid, making the liquid distinguishable from the background. Videos were taken at $f_s = 800Hz$. The LeDaR algorithm described in § 4.2 was used to detect and track the liquid interface in each frame. Fig.13 shows an example test case in which the jet is highly deforming the liquid interface, resulting in a 2D, asymmetric, confinement that oscillates as a result of the liquid film waves directed towards the impingement.

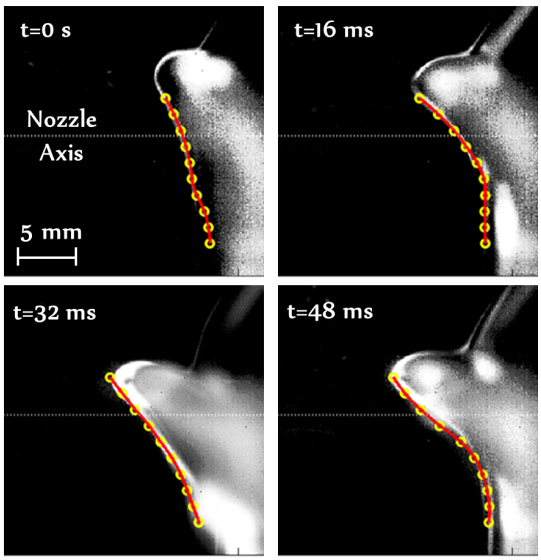

Figure 13: Snapshots of gas-liquid interface for a vertical falling liquid interface pulsing at $f_p = 14Hz$ and deformed by an impinging slot gas jet. In this example, the liquid

5.3. Gas Jet Response

During the characterization of the gas jet response, only the primary injection is active. The nozzle is traced with oil particles, which scatters the laser light and make the gas jet flow distinguishable from the background. Videos are acquired at $f_s = 1kHz$ with long exposure ($t_e \approx 400\mu s$) to filter out high frequency turbulent structures. As a result, the jet appears as a

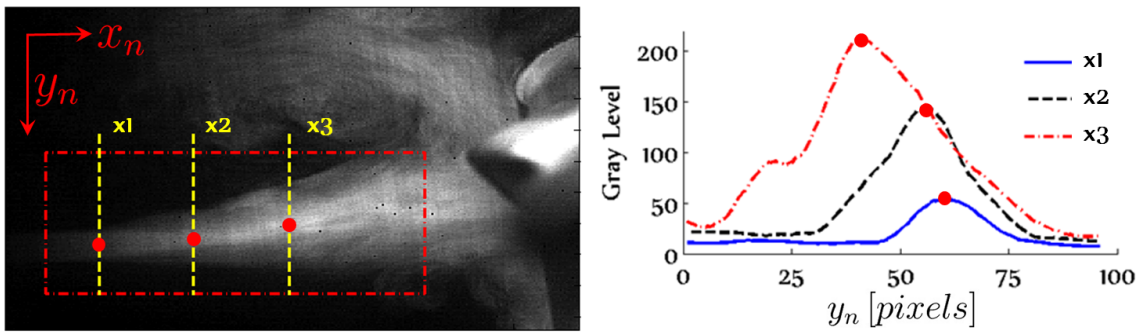

Figure 12: Image $A(x_n, y_n)$, blurred with a $4x4$ Gaussian kernel to increase the smoothness of grayscale vertical profiles. Each of these profile is low pass filtered with a Savizty-Sgolay filter and the peaks associated with the centerline position. In this snapshot, the impinging jet is considerably deflected upward during its oscillation.

connected, bright region (Fig.12). After the ROI is defined (red dashed box in Fig.12), each video frame t_n is equalized, cropped, and blurred with a 4×4 Gaussian kernel, in order to limit high frequency noise of the image. The geometrical centerline of the jet flow $C(x_n, t_n)$ is defined, in this work, as the loci of points, within the ROI, where the image is brighter.

Therefore, similarly to eq.(19), the jet centerline $C(x_n, t_n)$ is determined from the x_n columns of the gray scale image $A(x_n, y_n)$: each vertical grayscale profile is first smoothed using a Savitzky-Golay ([21]) filter, to further increase differentiability, and the centerline is detected from the position of the profile peak as shown in Fig.12. Jet oscillations are determined by tracking in time the position of the centerline $C(x_n, t_n)$ at a given position $x_n = x_p$, which was fixed as half stand-off distance between nozzle and wall.

5.4. Entrainment Flow

During the characterization of the entrained flow, both primary and secondary injection in Fig.11 are active and the entire impinging flow topology is seeded. The videos were taken at $5kHz$ with the minimum exposure time achievable[2]: $t_e \approx 20\mu s$. Below this value, even at the minimal f-number $f\# = 2.8$, the image is too dark to make particles distinguishable. Given a magnification factor of $M \approx 14\, pixels/mm$, a particle traveling at the jet velocity ($U \approx 30m/s$) displaces of $\delta x \approx 9 pixels$ during the acquisition, making the jet appear as a discontinuous set of stripes.

Conversely, the motion blurring on particles traveling at than $U < 6m/s$ proved to be tolerated by a standard multigrid PIV algorithm using a 2D Gaussian (9 point) sub-pixel estimation for cross correlation peak ([22]). PIV processing has been performed with the open-source matlab routine *PIVlab* ([23]) in a region of interest (ROI) above the jet flow (Fig.14). Each frame is first re-contrasted using *CLAHE* adjusting on $20x20$ tiles [24; 25]. Three windows refinement were selected, from $64x64$ to $8x8$ *pixels*.

As the maximum video size of $663MB$ limits the image number to 3566, i.e. an acquisition of $0.71s$, the purpose of these tests was to complement the flow visualizations with mean flow field $\overline{U}(x, y)$ and its normalized standard deviation $\hat{\sigma}_U(x, y) = \sigma_U / U$.

[2]This limit was defined by the limited illumination available, thus the laser power ($\approx 6\, W$).

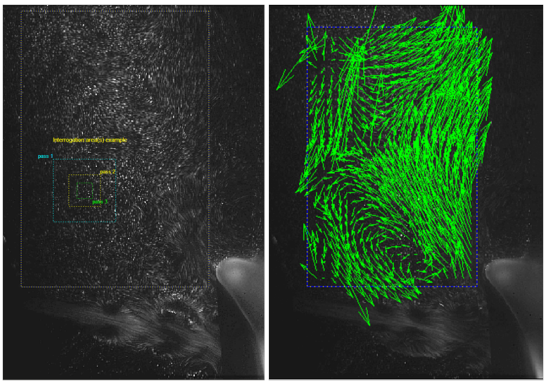

Figure 14: PIV Snapshot, ROI: $178 \times 256 pixels$, window sizes and example of instantaneous velocity field obtained with PIV.

6. Results

The study of the configuration in Fig.1 was divided into three steps. First, the characterization of the introduced film thickness perturbations, in § 6.1.Second,

the characterization of the gas jet response to the perturbation, described in § 6.2. Third, the characterization of the entrained flow bounding the jet, described in § 6.3.

6.1. Liquid Film Perturbation

Using LeDaR and LAbs, the facility was first tested in steady conditions, i.e. with $P_C(t) = P_M$. Assuming the liquid interface to be constant and uniform, the well known *Nusselt* flow links univocally flow rate q_M, thus the Reynolds number Re_M, to the film thickness h_N:

$$h_N = \left(\frac{3\nu}{g} q_M\right)^{1/3} = \left(\frac{3\nu^2}{g} Re_M\right)^{1/3} \qquad (20)$$

Using the steady calibration in eq.(9), the theoretical Nusselt film thickness is derived from the average pressure signal p_M, whereas the measured one is computed from averaging in time and in space LAbs and LeDaR measurements. Fig.15 compares the results.

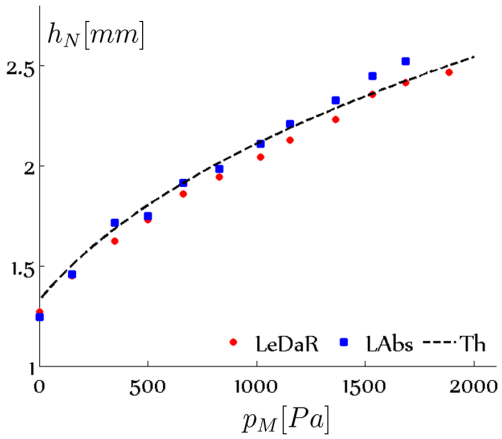

Figure 15: Nusselt film thickness validation

Fig.16 plots the evolution of the maxims $\hat{h}_M$ and the minims $\hat{h}_m$ thickness of traveling waves produced at different perturbation frequencies f_c, non-dimensionalized with respect to the Nusselt thickness h_N. While $\hat{h}_M$ grows considerably when increasing Re_M and decreasing f_c, the minims $\hat{h}_M$ approaches an asymptotic limit of $h_m \approx 0.6$.

Fig.16 was also used to set the operative range of the facility during the gas jet impingement test. It is worth observing, in fact, that increasing the perturbation frequency f_p, thus the Womersley number $\mathcal{W}$, reduces the perturbation strength ζ, as shown in Fig.5b. Moreover, Fig.16 shows that the lower the

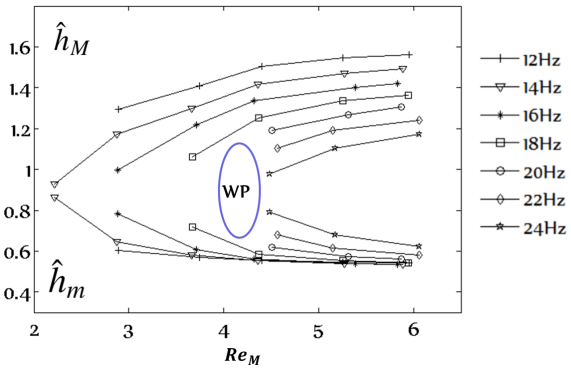

Figure 16: Wave Peaks Trends

perturbation amplitude, the higher the Reynolds number has to be to let the liquid film produce a regular train of waves. In particular, for $f_p > 18Hz$ and $Re_M < 4$, the response of the liquid film was not harmonic. In this region, referred to as *weakly perturbed* (region WP in Fig.16), the perturbation produce waves whose amplitude are comparable with those naturally developing in a falling liquid film. As a result (Fig. 17a) both natural and forced frequencies coexists and develop downstream. For higher Reynolds numbers and/or lower frequencies, the perturbation is sufficiently strong –and the liquid film sufficiently receptive– to let a set of traveling wave develop at the perturbation frequency and clearly dominate the natural film instabilities. A snapshot of this regime, referred to as *strongly perturbed* is shown in Fig. 17b.

For the purposes of this paper[3], it is was sufficient to ensure that gravity waves directed towards the impingement were 2D, had a known amplitude, and followed the perturbation frequency f_p.

6.2. Gas Jet Response

Both stable and unstable impingement were observed. In the first case the jet centerline is horizontal, in the second it is oscillating. A *stable* impingement was observed when the gas jet does not deform the liquid interface, regardless of the frequency and amplitude of the perturbation introduced. A typical flow visualization snapshot of this configuration is in Fig.18a. The jet bifurcates at the impingement in two

[3] A more detailed description of liquid wave dynamic will be collected in a paper titled *Thickness Measurement in low Kapitza liquid down a vertical wall.*

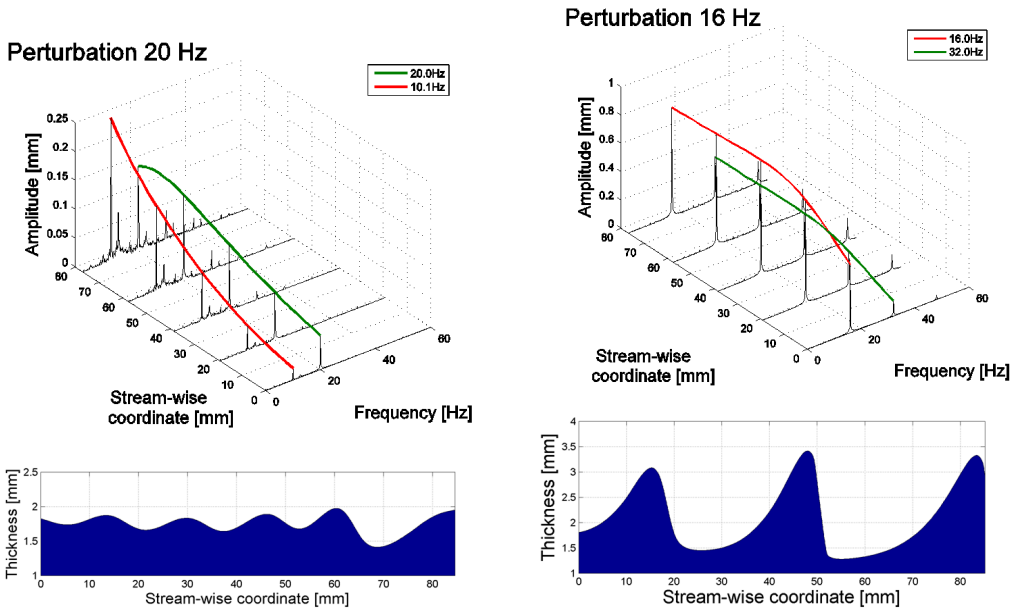

(a) (b)

Figure 17: Light Absorption measurement on vertical falling wavy liquid film. When the perturbation introduced it weak, the liquid film displays a non harmonic response (*weakly perturbed* regime, Fig.17a). If the perturbation is sufficiently strong, the liquid film displays q regular set of traveling waves (*strongly perturbed* regime, Fig.17b).

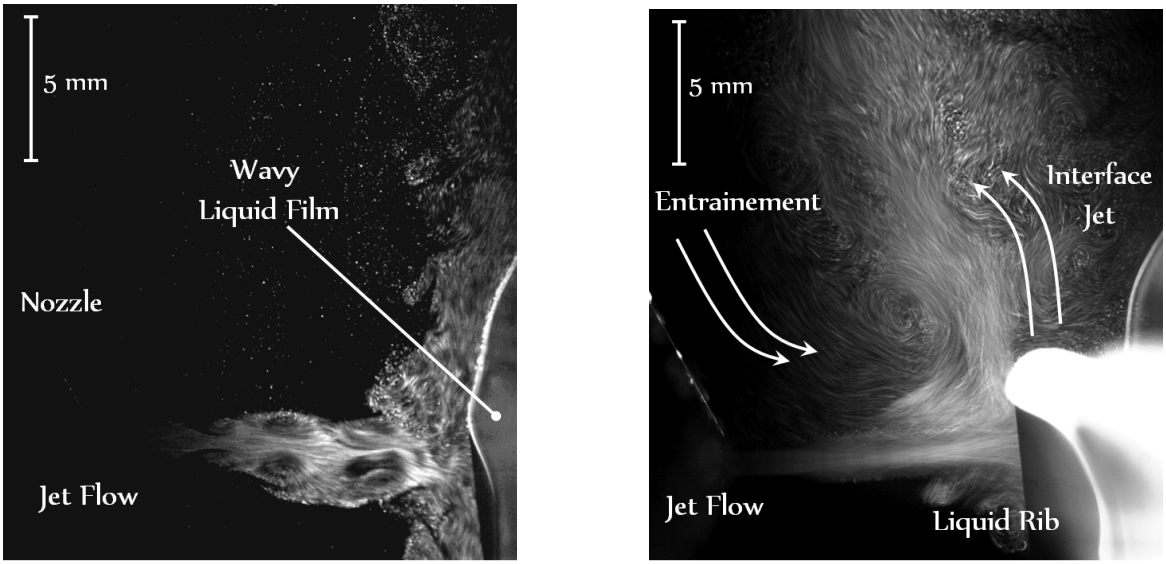

(a) (b)

Figure 18: Flow visualization of stable (Fig.18a) and unstable (Fig.18b) impingement configurations. In the first, the gentle slope of the impinged interface let the jet bifurcate symmetrically. In the second, the high curvature of the interface deflects the upper interface jet that forms recirculation structures together with the air entrainment.

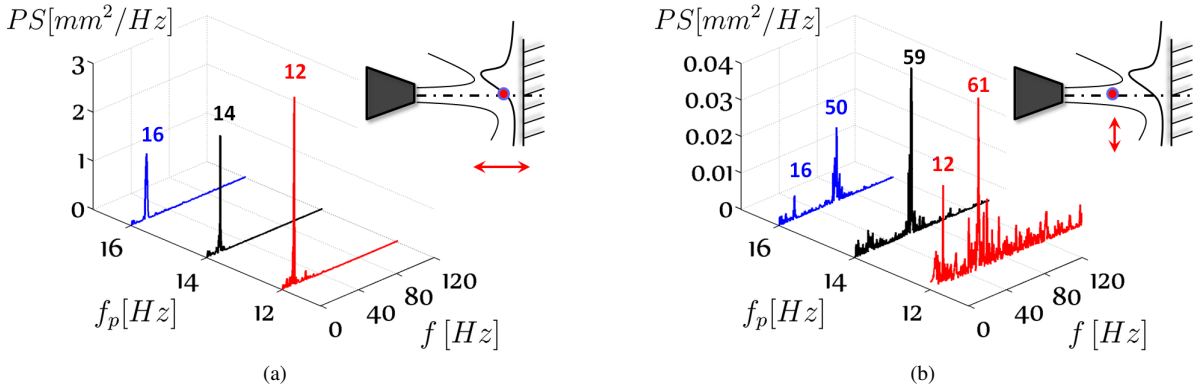

(a) (b)

Figure 19: Fig.19a: Power spectral densities of the interface horizontal oscillation, computed in the Nozzle axis position, for three perturbation frequencies: $f_p = 12, 14, 16Hz$. Fig.19b: Corresponding power spectral densities of the jet centerline vertical oscillation, computed at a distance $x_p = Z/2$ from the Nozzle.

interface jets, which remain attached to the liquid despite the opposite kinematic boundary conditions[4].

A necessary condition to trigger gas jet oscillation was found to be the deformation of the liquid interface, as shown in the example snapshot in Fig.18b. The interface forms a 2D liquid rib above the impingement and the gas flow topology is asymmetric: the bottom interface jet remains attached on the liquid, whereas the upper one is deflected back by the shape of the confinement. The impinging jet oscillates upward, where the entrained air and the deflected jet periodically forms recirculation structures. The interface forms a 2D liquid rib above the impingement and the gas flow topology is asymmetric: the bottom interface jet remains attached on the liquid, whereas the upper one is deflected back by the shape of the confinement. The impinging jet oscillates upward, where the entrained air and the deflected jet periodically forms recirculation structures.

For a given gas jet (Re_j) and liquid film (Re_M) Reynolds numbers, this configuration is produced within a narrow range of stand-off distances, of the order of $Z_s - Z_i \approx 1mm$. For $Z < Z_i$ the liquid is unaffected by the jet, for $Z > Z_s$ the liquid rib loses its bidimensionality and splashes ejecting droplets. This configuration was reached fixing Re_j and Z, then progressively reducing the liquid Reynolds number[5].

Switching off the seeding, LeDaR measurements were used to track the time evolving interface of the liquid rib in each frame and retrieve the frequency content of its oscillation. Fig.19a shows the spectra of the horizontal displacement of the interface point located at the nozzle axis, for three example test cases. The testing conditions are $Re_j = 1800$, $Z/s = 15$, $Re_M = 4.5$ with perturbations corresponding to: $f_p = 12Hz$ ($\zeta = 2.9\%$, $\hat{h}_M/\hat{h}_m = 2.8$); $f_p = 14Hz$ ($\zeta = 2.1\%$, $\hat{h}_M/\hat{h}_m = 2.6$); $f_p = 16Hz$ ($\zeta = 1.7\%$, $\hat{h}_M/\hat{h}_m = 2.4$). In all the tests, the response of the liquid rib is harmonic.

The response of the gas jet, on the other hand, is not harmonic. For a jet impinging at $5cm$ from the liquid test section inlet, Fig.19b shows the power spectra of jet response to the three test cases in Fig.19a, computed from the centerline displacement at $x_p = Z/2$. In all the three cases the spectrum is dominated by a frequency which is not related to the perturbation introduced and the harmonic response, when present, is considerably weaker.

6.3. *Entrainment Flow Response*

Fig.20 and Fig.21 compare the averaged flow field $\overline{U}(x, y)$ and normalized velocity standard deviation $\sigma_U(x, y)/\overline{U}(x, y)$ for a stable and an unstable test case. In stable configuration, the investigated ROI only displays the entrainment flow, which is unaffected by the

[4]The bottom interface jet is in *co-current* with the falling liquid, the upper one is in *counter-current*. Nevertheless, the liquid film velocities are negligible compared to those of the gas flow.

[5]Decreasing liquid film thickness makes the interface more prone to deformation, but, as already discussed, less sensitive to the perturbation introduced. A Reynolds number of $Re_M \approx 4.5$ was considered a good compromise between a liquid interface sufficiently deformable and a wavy film operating in the *stronly perturbed* regime.

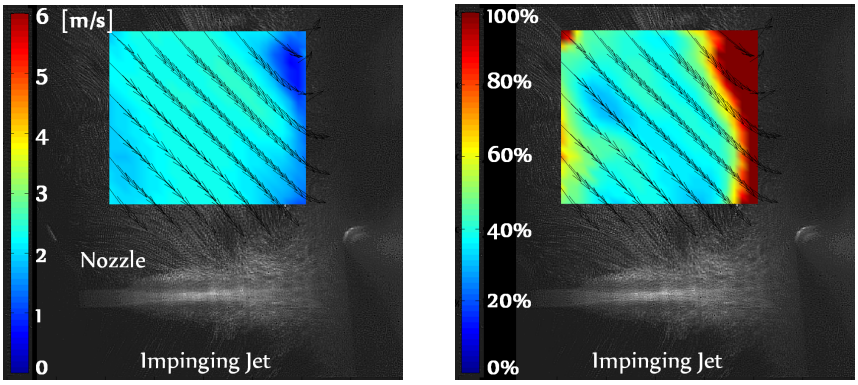

(a) (b)

Figure 20: Particle Image Velocimetry measurement on gas flow entrained by the impinging jet in *stable* configuration. Mean Flow (20a) and normalized standard deviation (20b).

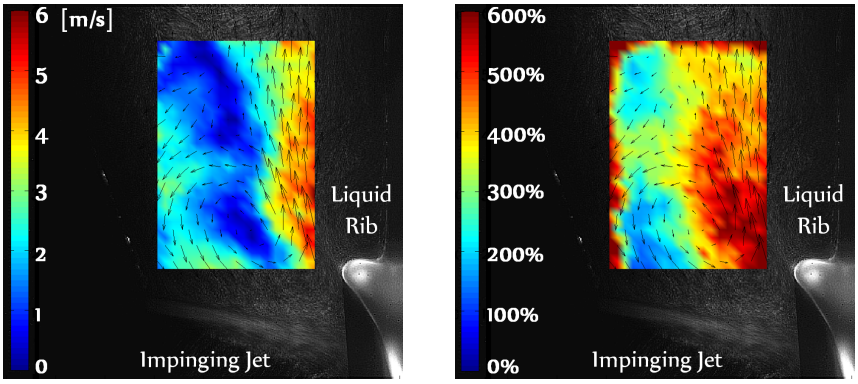

(a) (b)

Figure 21: Particle Image Velocimetry measurement on gas flow entrained by the impinging jet in *stable* configuration. Mean Flow (21a) and normalized standard deviation (21b).

liquid film perturbation introduced. In the unstable configuration, the impinging jet is bounded by a recirculation region formed by the upstream interface jet, the air entrainment and the impinging jet flow itself. This unsteady recirculation is characterized by velocity fluctuations which amplitude is considerably higher than the mean velocity, a possible footprint of an oscillatory behavior of the flow.

7. Conclusions and Perspectives

This paper analyzed the stability of a slot gas jet impinging on a liquid film which falls vertically and with a pulsing flow rate. The configuration is an academic benchmark of the jet wiping process, which is used in galvanizing, paper and paint industry to control the coating thickness on flat substrates. The design of a dedicated experimental facility was presented. A theoretical, numerical and experimental analysis of its operation allowed to determine the conditions to produce a train of 2D gravity waves, which were used to disturb the impinging gas jet at controlled frequency and amplitude. The liquid film waves were characterized with Light Absorption (LABs) and Level Detection and Recording (LeDaR); the response of the gas jet was analyzed via flow visualization and image processing, and complemented with Particle Image Velocimetry (PIV) on the gas flow entrained by the jet.

The results have shown that gas jet oscillations are produced if the interface of the liquid film is sufficiently deformed by the impingement. In this config-

uration, the liquid interface confines asymmetrically the gas flow and forms a 2D pulsing rib above it. Such geometrical confinement is similar to what occurs in jet wiping processes, being flipped upside down.

The similarity between the two configurations is supported by the fact that, in the oscillation, the impinging jet bends towards the side where the unsteady asymmetry is (upward in Fig.1.a, downward in Fig.1.b). Furthermore, it was shown that the jet flow does not oscillate at the same frequency of the confinement oscillation: a frequency of the order of $60Hz$ dominates the spectrum regardless of the perturbation introduced.

This suggests that there are two different destabilizing mechanisms, one related to the asymmetry of the confinement, the other related to its oscillation. Flow visualizations and PIV measurement show that the footprint of the instability is the formation of recirculation structures which involves the air entrainment and the interface jet issuing, from the impinging region, on the side of the asymmetry.

To investigate the different role of confinement asymmetry and confinement oscillation, it is now of interest to replace the liquid film with a solid membrane which reproduces the time evolving shape of the 2D rib, but allows a better control of the confinement.

Without the limits of liquid splashing, and with a complete de-coupling between jet parameters (Re_j, Z) and impinged geometry, the analysis will be extended to different impinging scenarios, aimed to promote, separately, harmonic and non-harmonic responses of the jet. Finally, to investigate whether the recirculation structures observed in this work are a *cause* or a *consequence* of the jet instability, it is of interest to perform time resolved PIV measurement with high time and frequency resolution.

Acknowledgments

The author is supported by a F.R.S.-FNRS FRIA grant and the research project is funded by ArcelorMittal.

References

[1] D. Willis, Developments in hot dipped metallic coated steel processing, Materials Forum.

[2] Dumont, M., Ernst, R., Fautrelle, Y., Grenier, B., Hardy, J. J., & Anderhuber, M., New dc electromagnetic wiping system for hot-dip coating, Compel 30 (2011) 1663–1671.

[3] B. H. A. . W. V. J. Lloyd-Jones, C., Investigation into magnetic wiping techniques as alternative to gas wiping on hot dip galvanising lines, Ironmaking & Steelmaking 25 (2) (1998) 117–123.

[4] Bregand, O., Crahay, J, Gerkens, P., New wiping techniques to efficiently produce suitable coating layers at high speed in the hot dip galvanising process, EU Bookshop, 2010.

[5] K.Myrillas, Experimental and numerical investigation of gas jet and liquid film interaction, Ph.D. thesis, Université Libre de Bruxelles (2011).

[6] A. Gosset, Study of the interaction between a gas flow and a liquid film entrained by a moving surface, Ph.D. thesis, Université Libre de Bruxelles (2007).

[7] D.Rockwell, Oscillations of impinging shear layers, AIAA 21 (5) (1983) 645–663.

[8] J.R.Womersley, Method for the calculation of velocity, rate of flow and viscous drag in arteries when the pressure gradient is known, J. Physiol. 127 (1955) 553–563.

[9] K.Rohlf, G.Tent, The role of the womersley number in pulsatile blood flow, Journal of biomechanics 34 (1) (2000) 141–148.

[10] G. R. D. A. Banerjee, M. K., Effect of pulsatile flow waveform and womersley number on the flow in stenosed arterial geometry, ISRN Biomathematics Article ID 853056.

[11] T. A. Loudon, C., The use of the dimensionless womersley number to characterize the unsteady nature of internal flow, Journal of Theoretical Biology 191 (1) (1998) 63–78.

[12] Y. Fung, Biomechanics: Motion, Flow, Stress, and Growth, Springer New York, 1998.

[13] A. Gosset, Measurement techniques for unstable film flows, in: Thermohydraulic Instabilities, 2006.

[14] C. M. S. G. Özgen, S, Experimental study of wave characteristics on a thin layer of de/anti-icing fluid, Phys. Fluids 14 (10) (2002) 3391–3420.

[15] P. B. Alekseenko S.V., Nakoryakov V.E., Wave Flow of Liquid Films, New York: Begell House, 1994.

[16] E. P. M. F. A.Kevin Njifenju, J.Bico, Experimental investigation of liquid films in gravity-driven flows with a simple visualization technique, Exp. Fluids 54 (1506).

[17] L. Németh, M.A. Mendez, J.-M. Buchlin, Experimental investigation of falling liquid films, Supervision: VKI SR 2015-09, von Karman Institute for Fluid Dynamics (2015).

[18] P. Planquart, Real time optical detection and characterization of water model free surface, in: proceedings of the 4th European continuous casting conference, Birmingham, UK, 2002.

[19] D. Bouchez, L. Zimmer, M.L. Reithmuller, Optical detection and characterization of interfaces, in: proceedings of the 9th Symp. of flow visualization, 2002.

[20] B. Toth, J. Anthoine, M.L. Reithmuller, Mesure dynamiques de la deformé dne surface libre, in: Congres francophone de techniques laser, 2006.

[21] R. Schafer, What is a savitzky-golay filter ?, IEEE Signal Processing Magazine (2011) 111–117.

[22] H.Nobach, M. Honkanen, Two-dimensional gaussian regression for sub-pixel displacement estimation in particle image velocimetry or particle position estimation in particle tracking velocimetry, Exp. Fluids 38 (2005) 511–515.

[23] Thielicke, W. and Stamhuis, E.J., Pivlab towards user-friendly, affordable and accurate digital particle image velocimetry in matlab, Journal of Open Research Software 2 (1) (2014) e30.

[24] U. Shavit, R. Lowe, J. Steinbuck, Intensity capping: a simple method to improve cross-correlation piv results, Experiments in Fluids 42 (2) (2007) 225–240.

[25] S. M. Pizer, E. P. Amburn, J. D. Austin, R. Cromartie, A. Geselowitz, T. Greer, B. ter Haar Romeny, J. B. Zimmerman, K. Zuiderveld, Adaptive histogram equalization and its variations, Computer Vision, Graphics, and Image Processing 39 (3) (1987) 355 – 368.

Topographic Reconstruction of Free Surface Motion Due to Harmonic Sloshing

Alessia Simonini

Environmental and Applied Fluid Dynamics Department, von Karman Institute for Fluid Dynamics, Belgium, simonini@vki.ac.be

Supervisor: Maria Rosaria Vetrano

Associate Professor, Environmental and Applied Fluid Dynamics Department, von Karman Institute for Fluid Dynamics, Belgium, vetrano@vki.ac.be

University Supervisor: Pierre Colinet

Professor, Fluid Physics - Transfer Interfaces and Processes Department, Université Libre de Bruxelles, Belgium, pcolinet@ulb.ac.be

Abstract

The motion of a free liquid surface inside its container is called sloshing and it is strongly affected by external excitations applied to the partially filled container. The understanding and the prediction of this particular motion is of special importance in many fields. It can refer to embarked containers filled of fluid, motion of cooling liquids in systems subjected to earthquake or motion of propellant inside a tank, which can dramatically influence the trajectory of vehicles. One of the important feature of sloshing is the behavior of the liquid-gas interface. The scope of this paper is to present an optical technique capable of instantaneously measure the topography of the liquid-gas interface during sloshing. This technique, so called Reference Image Topography (RIT) is based on the cross-correlation analysis of the apparent displacement between a reference pattern and its refracted image through a deformed free surface. In this paper, the sensitivity of the technique with respect to experimental parameters is studied. Finally the technique will be applied to a test case of sloshing and the results will be compared with a previous PIV experiments performed in the same facility.

Keywords: PIV, Reference Image Topography, Sloshing.

1. Introduction

Sloshing means any motion of the free liquid surface inside its container [1]. This phenomenon is strongly affected by external excitation applied to the partially filled reservoir. The understanding and the prediction of this particular motion is of great concern in many fields: it can refer to embarked containers filled of fluids, motion of cooling liquids in systems subjected to earthquake or motion of propellant inside tanks. The natural frequency of a system affected by sloshing depends on the shape and rigidity of the container, kind of fluid and its mass. In literature, analytical and mechanical analogies are widely used to model this phenomenon, whereas numerical simulations are still far from the desired reliability. Moreover the existing experimental studies give partial information about the behavior of the liquid/gas interface topography during sloshing, a key parameter for the validation of numerical codes. The aim of this work is to present an imagery technique capable of instantaneously measure the topography of a free surface. Recent works develop free surface topography techniques using the properties of light refraction [2; 3]. They are based on the detection of the deformation of a reference pattern seen through the interface. In particular the technique used in this work is a combination of Particle Image Velocimetry (PIV) and the Reference Image Topography technique [4] which has been applied for the first time by Fouras et al. [2]: the random arrangement of PIV particles in a plane illuminated by a laser sheet is used as reference pattern.

2. Sloshing theory

The theory of liquid sloshing dynamics in partially filled containers consists in developing the fluid field equations. The Navier-Stokes equations are integrated taking into accounts different hypotheses and boundary conditions relative to the particular problem. For an open surface, the boundary condition specifies either the values of the field at every point of the surface or the normal gradient to the container walls or both. Explicit solutions are possible only for few cases such as the upright partially filled cylinder. The boundary value problem is usually solved for modal analysis (free sloshing) and for the dynamic response characteristics to external excitations (forced oscillations). The fluid free-surface motion and the resulting hydrodynamic forces and moments can be estimated from the system of fluid field equations. Mechanical analogies can be found in literature beside the analytical solutions [1; 5; 6].

2.1. Analytical solution

Free oscillations. The container-fluid system investigated is shown in figure 1.

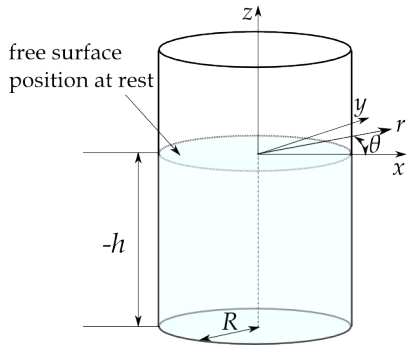

Figure 1: Circular cylindrical tank of radius R, partially filled to an arbitrary depth h.

As a first approximation, the analysis of the fluid dynamic problem is generally simplified with the following assumptions:

- rigid and impermeable container
- inviscid, incompressible and irrotational fluid
- if the system is in normal gravity environment, the effect of surface tension can be neglected

It is of interest to determine the regime of validity of these simplifications. The dimensionless parameters controlling the validity of the inviscid and negligible surface tension assumptions are the Reynolds number and the Bond number respectively. For sloshing phenomena, the Reynolds number is often express in terms of importance of gravity forces with respect to viscous forces, the so called Galilei number (eq.1) [7; 8]. The Bond number(eq.2) gives information on the relative importance of gravity forces with respect to surface tension ones (capillary forces). Physically the bond number can give a prediction on the shape of the interface: for Bo$\gg$1, gravitational forces are dominant and the free surface is flat (except at the wall where the contact angle condition must be satisfied) while for Bo$\ll$1, capillary forces are dominant and the free surface will be highly curved.

$$Re = \frac{VR}{\nu} \rightarrow Ga = \frac{gR^3}{\nu^2} \tag{1}$$

$$Bo = \frac{\rho g R^2}{\sigma} \tag{2}$$

From the hypothesis stated here-above, the field equation can be written as:

$$\nabla^2\Phi = 0 \quad \text{in} \quad \begin{cases} 0 \le r \le R \\ 0 \le \theta \le 2\pi \\ -h \le z \le 0 \end{cases} \tag{3}$$

The non permeability conditions at the rigid container are:

$$\frac{\partial \Phi}{\partial r} = 0 \qquad \text{at} \quad r = R \tag{4}$$

$$\frac{\partial \Phi}{\partial z} = 0 \qquad \text{at} \quad z = -h \tag{5}$$

Calling $\eta(r, \theta, t)$ (fig.2) the vertical displacement of the free surface above the undisturbed free surface and, for sake of simplicity, setting the value of the pressure on the free surface to zero, the dynamic condition at the free surface can be derived.

A second condition has to be expressed on the kinematic of the problem: the vertical velocity of a fluid particle located on the free surface $z = \eta(r, \theta, t)$ is equal to the vertical velocity of the free surface itself. Assuming amplitude excitations and fluid responses to be small, the problem can be linearized and the two conditions are expressed in equations 6 and 7.

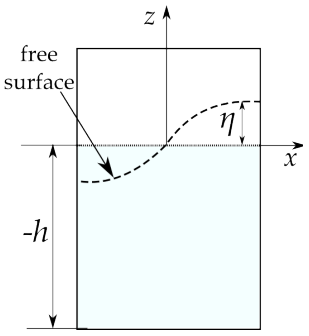

Figure 2: Surface wave in a cylindrical tank.

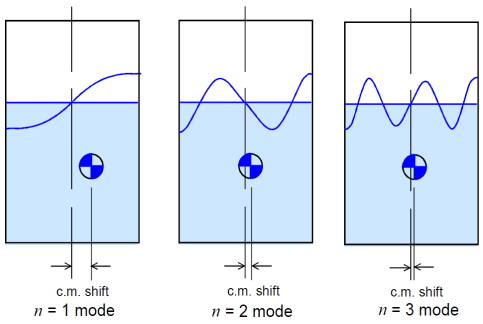

Figure 3: Scheme of first asymmetrical modes [6].

$$g\eta - \frac{\partial \Phi}{\partial t} = 0 \qquad \text{at} \quad z = \eta(r,\theta,t) \tag{6}$$

$$-\frac{\partial \Phi}{\partial z} = \frac{\partial \eta}{\partial t} \qquad \text{at} \quad z = \eta(r,\theta,t) \tag{7}$$

Combining equations 6 and 7 we obtain the linearized condition of the free surface:

$$\frac{\partial^2 \Phi}{\partial t^2} + g\frac{\partial \Phi}{\partial z} = 0 \qquad \text{at} \quad z = \eta(r,\theta,t) \tag{8}$$

With this formulation the natural frequencies of the liquid free-surface can be calculated from the following expression:

$$\omega_{mn}^2 = \frac{g\xi_{mn}}{R}\tanh\left(\frac{\xi_{mn}h}{R}\right) \tag{9}$$

where m refers to the diametral nodes and n to the circumferential nodes for the different kind of vibration[1]; ξ_{mn} are the roots $dJ_1(\xi_{mn}r/R)/dr|_{r=R} = 0$, where J_1 is the Bessel function of first order and first kind [5]. The asymmetric modes are of major concern since they are associated to a horizontal oscillation of the center of mass(fig. 3). Symmetrical modes about the vertical axis are possible but not excited so often [9]. In the case of a lateral excitation, the first asymmetric mode (m=1, n=1) is the predominant [10] and it is related to the lowest natural frequency of the system. For the first mode, m=1, we have a nodal diameter perpendicular to the direction of motion.

Small amplitude forced oscillations. It is possible to determine the linear response to a sinusoidal external excitation of the liquid contained inside the cylindrical tank of figure 1. We assume that the excitation is only acting in the x-direction and it has the form:

$$\mathbf{V}_0 = X_0 \sin(\Omega t)\mathbf{i} \tag{10}$$

[1]The number n is always referred as n-1 circumferential nodes.

The linearized fluid field equation is the same equation 3, while the linearized free surface condition (eq. 8) becomes:

$$\frac{\partial^2 \Phi}{\partial t^2} + g\frac{\partial \Phi}{\partial z} = -X_0\Omega^3 \cos(\Omega t) r\cos\theta \qquad \text{at} \quad z = \eta(r,\theta,t) \tag{11}$$

Substituting the general solution of the potential function Φ it is possible to determine the surface wave height function:

$$\eta(r,\theta,t) = \frac{X_0\Omega^2}{g}\cos\theta\cos\Omega t\,[r + B] \tag{12}$$

with

$$B = \sum_{n=1}^{\infty} \frac{2R}{(\xi_{1n}^2 - 1)} \frac{\Omega^2}{(\omega_{1n}^2 - \Omega^2)} \frac{J_1(\xi_{1n}r/R)}{J_1(\xi_{1n})}$$

and where only the first asymmetric mode is considered (m=1). It is obvious from equation 12 that as the applied external pulsation, Ω, approaches a natural frequency, ω_{mn}, the solution becomes unbounded due to the lost of validity of the linearized theory.

3. Reference Image Topography

The Reference Image Topography is based on the fact that a pattern observed through a deformed interface is also deformed. Its deformation is related to the gradient of the interface by means of the Snell's law which quantify the deviation of the light traversing an interface between two media. Referring to figure 4, the Snell's law is simply express as

$$n_1 \sin\alpha_1 = n_2 \sin\alpha_2 \tag{13}$$

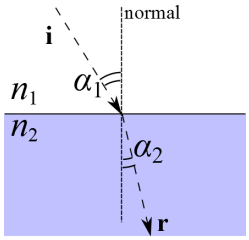

Figure 4: Scheme of Snell's law: n_1, n_2 refractive indexes, **i**, incident ray vector, **r**, refracted ray vector.

3.1. Inversion algorithm

The effect of the perturbation of the free surface on a reference pattern is shown in figure 5.

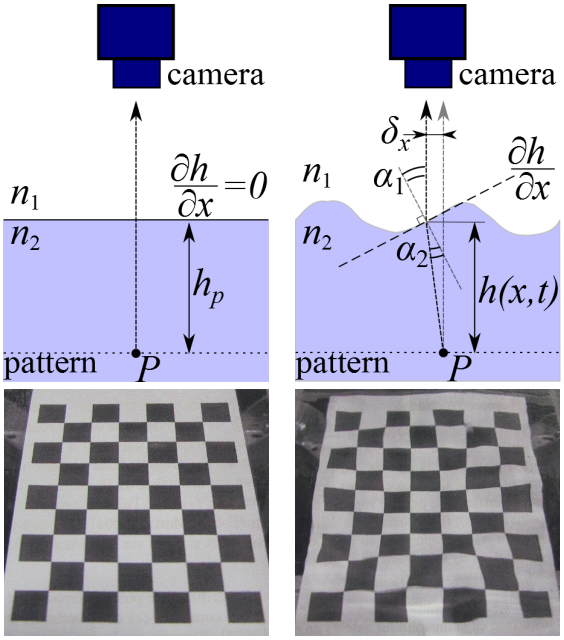

(a) (b)

Figure 5: (a) The undistorted position of a point P viewed from a distant location through an undisturbed free surface. (b) The apparent displacement δ_x of point P due to refraction through the surface at height h with a gradient $\partial h/\partial x$.

Considering a 2-D problem and with the hypothesis of perpendicularity of the camera, the apparent displacement δ_x is related to the surface gradient $\partial h/\partial x$ by means of the Snell's law and geometrical considerations as follows [2]:

$$\tan^{-1}\frac{\delta_x}{h} = \tan^{-1}\frac{\partial h}{\partial x} - \sin^{-1}[n_r \sin(\tan^{-1}\frac{\partial h}{\partial x})] \quad (14)$$

where h is the current local height of the liquid and n_r is the ratio of the refractive indexes n_2/n_1. The surface gradient can be integrated to estimate the liquid depth distribution, setting as the initial estimated height h, the reference height h_p [11] corresponding to the initial liquid level.

Moisy et al. [3] considered the 3-D problem, taking into account a small inclination of the camera respect to the normal to the pattern. The following three approximations are then applied:

- Paraxial approximation: the pattern camera distance h_c is much larger than the field size, yielding a maximum paraxial angle $\beta << 1$
- Weak slope approximation: The angle γ between the unit vector **n** and the vertical vector **z** is small.
- Weak amplitude approximation: calling $h(x, y) = h_p + \eta(x, y)$ the surface height, the amplitude $|\eta|$ of the perturbation is small compared to the mean height h_p.

These three approximations permit to linearize the relation between the deformation ∇h and the displacement $\delta\mathbf{r}$, giving forth to:

$$\nabla h = -\frac{\delta\mathbf{r}}{h^*} \quad \text{with } h^* = \frac{h_c - \alpha h_p}{\alpha h_p h_c} \quad (15)$$

Where $\alpha = 1 - n_1/n_2$ and the displacement vector $\delta\mathbf{r}$ is measured by cross-correlation between a reference image with the free surface at rest (see fig. 5a) and the image with the deformed free surface (see fig. 5b).

3.2. Invertibility condition

The invertibility condition is determined by the possibility of light ray crossings, which would results in multiple images as explained in figure 6 [3]. This can happen because waves behave like lenses for which the focal distance, EF, is smaller than the distance of the free surface from the reference pattern, h_p.

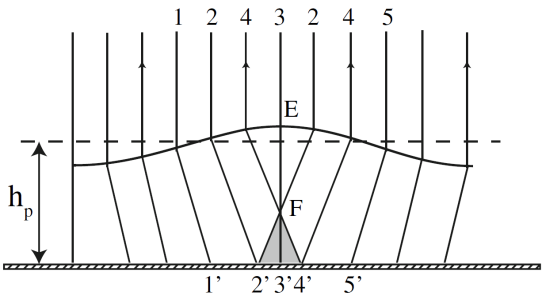

Figure 6: Invertibility condition.

3.3. Deep water experiments.

Due to the invertibility condition, it is straightforward to see how for large interface-pattern distance, this technique can not be applied when a synthetic reference pattern is used. This is the case of deep water experiments, where the distance of the pattern h_p is big and the condition $h_p > EF$ is fullfilled. Fouras et al. [2] proposed to use as pattern, the one formed by seeding particles illuminated by laser sheet light. The sketch of the setup is shown in figure 7. The two cameras acquire contemporary images: the bottom camera, looking through the flat bottom provides the reference image which is cross-correlated with the image from the top camera. This permits to obtain the displacement field. With this configuration the distance reference pattern can be decreased, going closer to the free surface, being limited only by the maximum negative wave amplitude. In the case of sloshing, an estimation of the latter can be theoretically calculated, depending on amplitude and frequency of excitation.

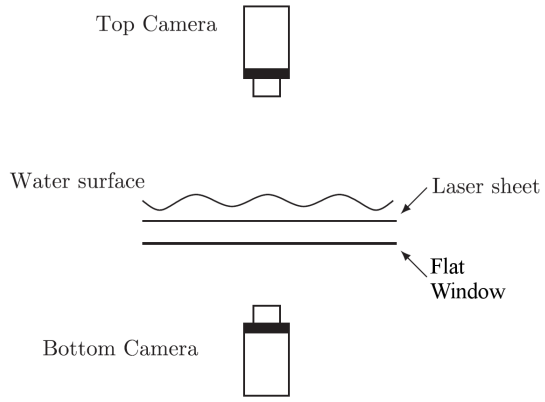

Figure 7: Reference Image Topography setup concept for deep water experiments [2].

4. Sensitivity analysis

It is possible to evaluate how the parameters, $\delta\mathbf{r}$, h_p, h_c, α affect the result on the topography of the free surface. As first step, the uncertainty $\epsilon(\nabla h)$ of the surface gradient ∇h can be evaluated from equation 15 using a standard error propagation procedure:

$$\epsilon(\nabla h) = \sqrt{(\frac{\partial \nabla h}{\partial h_c})^2(\epsilon(h_c))^2 + (\frac{\partial \nabla h}{\partial h_p})^2(\epsilon(h_p))^2 + ... \\ +(\frac{\partial \nabla h}{\partial \alpha})^2(\epsilon(\alpha))^2 + (\frac{\partial \nabla h}{\partial \delta\mathbf{r}})^2(\epsilon(\delta\mathbf{r}))^2} \quad (16)$$

where the partial derivatives, representing the sensitivity of ∇h to the different parameters, can be calculated as follows:

$$\frac{\partial \nabla h}{\partial h_c} = -\frac{\delta\mathbf{r}}{h_c^2} \quad (17)$$

$$\frac{\partial \nabla h}{\partial h_p} = -\frac{\delta\mathbf{r}}{\alpha h_p^2} \quad (18)$$

$$\frac{\partial \nabla h}{\partial \alpha} = \frac{\delta\mathbf{r}(h_c - \alpha h_p)}{\alpha^2 h_c h_p} \quad (19)$$

$$\frac{\partial \nabla h}{\partial \delta\mathbf{r}} = -\frac{h_c - \alpha h_p}{\alpha h_c h_p} \quad (20)$$

Considering the values of a typical sloshing problem analyze during this work, $h_c = 350$ mm, $h_p = 20$ mm, $\alpha = 0.24$, $\delta\mathbf{r} = (2,\ 0)$mm, it can be noticed that the gradient is more sensitive to error on the values of α and $\delta\mathbf{r}$. The latter is a crucial point since it depends on several parameters such as the spatial calibration, the overlap of reference and free surface images and on the cross-correlation algorithm.

5. Experimental Setup

A schematic of the experimental facility used to perform PIV-Reference Image Topography on a cylindrical cell partially filled of water and subjected to sinusoidal excitation is shown in figure 8. The cell has a diameter of 80 mm and it is bolted to the "sloshing table", which can generate harmonic oscillations. The position of the table is online recorded by an Optical Displacement Sensor (ODS) which has an accuracy of 18μm. The signal of the ODS can be used as input for a synchronizer in order to perform phase locked image acquisitions with the sinusoidal motion.

This setup permits to study the free surface behavior of the fluid during sloshing by means of the RIT technique combined with PIV. As explained in section 3.3, in case of deep water experiment, such as the case of sloshing, the reference pattern is created by illuminating particles using a laser sheet. Fluorescent particles (Cospheric) were used in order to avoid the presence of noise due to laser reflections inside the transparent cell and hence increase the S/N ratio. The properties of the particles are summarized in table 1. The density of the particles is very close the water one, ensuring no buoyancy effect.

5.1. Image calibration

In order to overlap the images coming from the reference and the free surface cameras (see fig. 8, a spatial calibration is needed. The idea is to put a calibration plate on the plane of the laser sheet and acquire

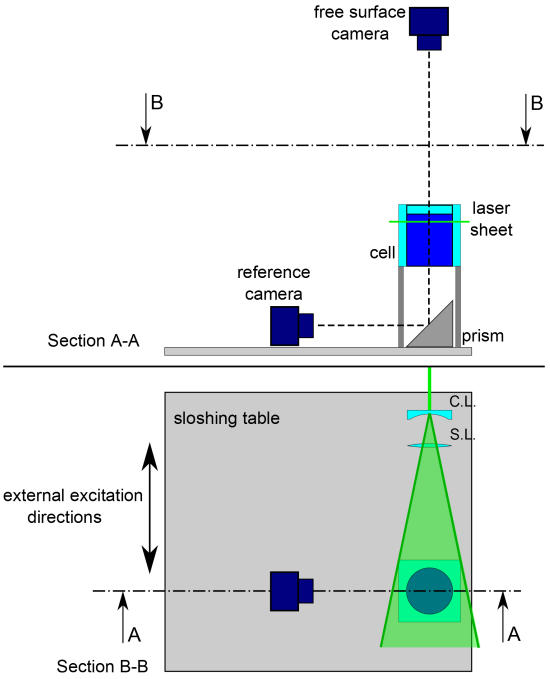

Figure 8: Setup RIT.

Table 1: Properties of fluorescent particles.

diameter μm	density kg m^{-3}	Absorption nm	Emission peak nm
10-45	998	460-650	605

an image for each camera. The calibration plate consists in a grid of dots of known diameter and pitch, printed on a transparent plastic sheet. The grid is glued between two plexiglass plate of the same thickness, hence the light distortion due to the change of refractive index will be equal in both sides. The calibration images are used into the image preprocessing algorithm of LaVision DaVis 8.2 to achieve the overlap of the images acquired instantaneously from both camera.

Since the optics conditions have to be constant when the free surface is at rest, it is important to consider that inserting the calibration plate in the cell will cause an increasing of the water level, changing h_p, which is the reference condition for the inversion algorithm. For this reason, great care has been taken in having the same optical path between the pattern plane and the mean free surface position h_p, during the image calibration and the experiment.

The calibration images and the corrected images are shown in 9.

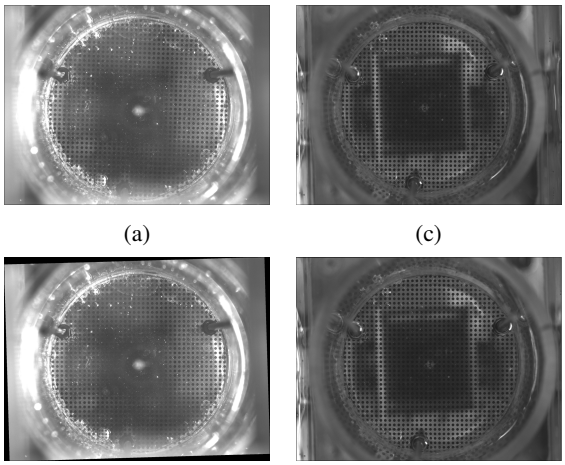

Figure 9: (a) Calibration image of the reference camera. (b) Corrected calibration image of the reference camera. (c) Calibration image of the free surface camera. (d) Corrected calibration image of the reference camera.

5.2. Test matrix and image processing

The images are acquired in phase locked mode with the sloshing table motion, and in particular the selected phases correspond to those used in a previous PIV experiments [12]. In this way the results obtained by the two techniques will be compared. The phases selected for the phase locked acquisitions are shown on the sinusoid excitation signal of figure 10. For each phase, 300 images are acquired in order to obtain a statistical information.

The sloshing test has been performed filling the cell with distilled water until 96 mm and applying a sinusoidal external excitation with an amplitude of 1.2 mm and a frequency of 3 Hz. The laser sheet has been positioned 20mm below the free surface at rest.

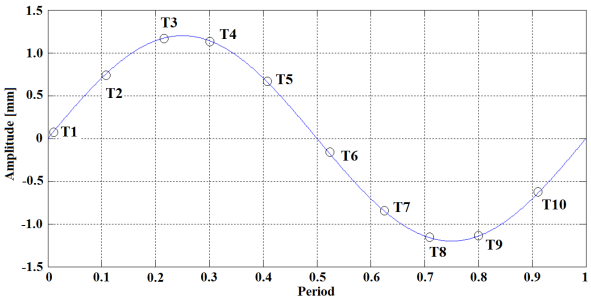

Figure 10: Phases of synchronization for phase locked acquisitions.

As for the calibration, the images are processed with the software LaVision DaVis 8.2. The two cameras are positioned at the opposite sides of the laser sheet, which create a perspective effect on the particles out of plane. This can cause an error on the cross-correlation map. For this reason, a filter on the intensity level of the images has been applied before the PIV processing: particles which are in focus are brighter, all the rest can be considered noise. The intensity threshold has been 400 counts for the reference image and 600 for the free surface image, over a maximum value of about 3000 for particles on the laser sheet. In figure 11 the effect of the intensity filter is shown.

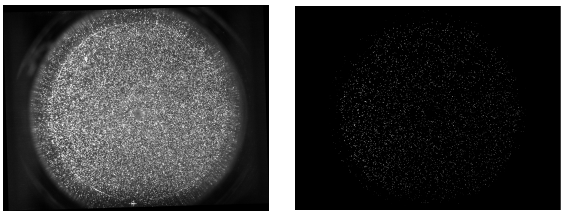

(a) (b)

Figure 11: (a) Raw intensity image. (b) Filtered intensity image.

Once the threshold on the intensity is applied, the PIV algorithm is used to detect the displacement field. The Multi pass option (decreasing size) is used, i.e. the displacement field is calculated with a decreasing interrogation window size. In our case, the initial interrogation window size is 128x128 (pixels)^2 and the final window size is 48x48 (pixels)^2 and 75% of overlap between windows. The final results have been filtered eliminating all the vector having a peak ratio Q< 1.3. For each phase, the averaged displacement field, obtained by 300 displacement phase locked images, is given as input into the Matlab function called surfheight for the reconstruction of the surface topography. It gives, as result, the average height of the surface in each window. This function is based on INTGRAD2.m by J. D'Errico which is a convenient and efficient implementation of the algorithm of least-square solution for inverting a 2D gradient using second-order centered differences [13].

6. Results and discussions

In this section the results of RIT combined with PIV applied to the sloshing phenomenon are presented. In figure 12 an example of the topography obtained by RIT for the synchronization T2 and T4 is shown.

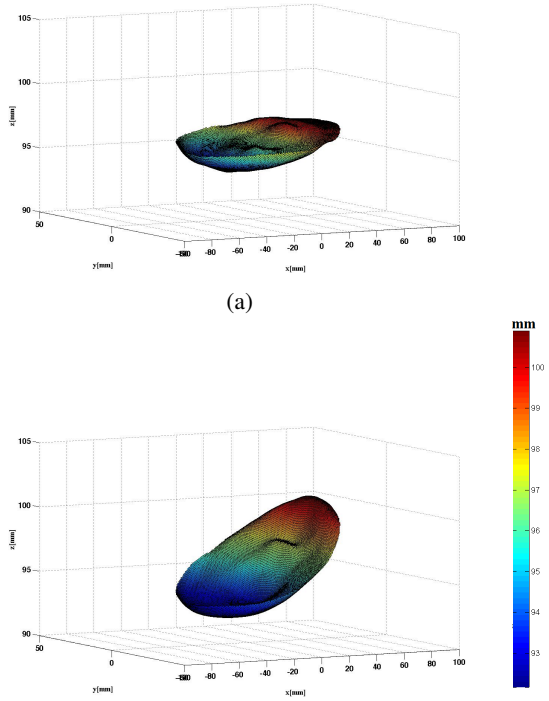

(a)

(b)

Figure 12: (a) 3D reconstruction, T2. (b) 3D reconstruction, T4.

As introduced before, previous PIV experiments were performed on the same facility with the excitation amplitude and frequency used for the RIT test and in the same phase locked positions. In figure 13 the measurement planes used for PIV and RIT are shown. PIV is done in the vertical plane while RIT is performed in the horizontal plane. For the PIV experiment, the position of the free surface has been mea-

sured for each synchronization phase, obtaining images as the one shown in figure 14.

In figure 15 the comparison between the 2D free surface line in common with both experiment (RIT and PIV) is shown for the phase synchronization T1, T2 and T4. This comparison shows a qualitatively good agreement of both techniques as far as the shape of the free surface is concerned, while it is clearly visible an offset on the absolute values.

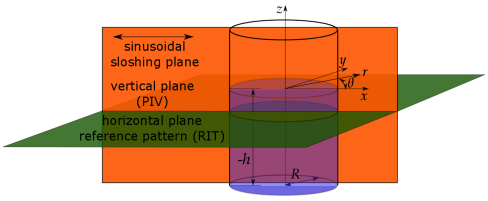

Figure 13: Measurements plane on the cylindrical cell.

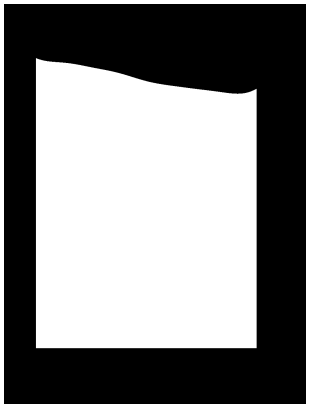

Figure 14: Example of mask extracted from vertical PIV measurements.

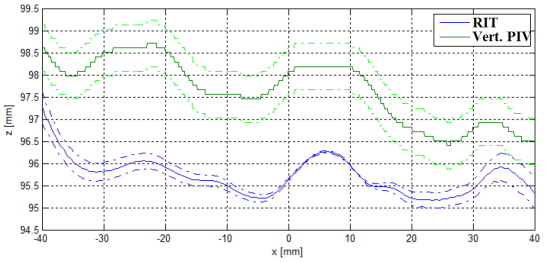

(a)

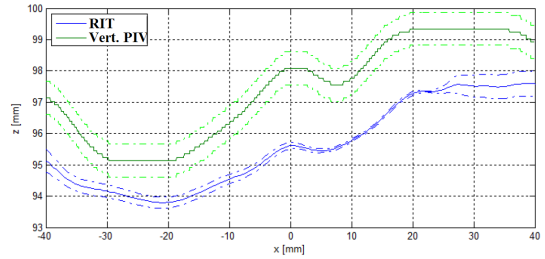

(b)

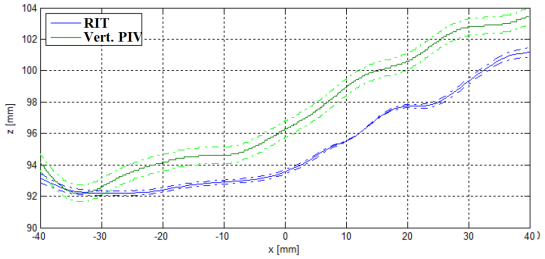

(c)

Figure 15: Comparison between RIT and Vertical PIV (a) T1 (b) T2 (c) T4

7. Conclusions

The aim of this paper is to show, for the first time, the possibility to apply a non intrusive technique, named RIT, developed for liquid film wavelet characterization, to evaluate the 3D shape of the liquid/gas interface during sloshing. The RIT technique is first introduced for a simple case of a liquid film, then its adaptation to deep liquid case is considered. The experimental set-up is shown and measurements of the 3D liquid/gas interface shape have been carried out in phase locked mode for 10 points of the sinusoidal excitation. Selected profiles of the obtained interface have been compared with the ones measured by standard PIV resulting with good qualitative agreement. It is interesting to observe that the main difference between the results obtained with the two techniques are related to the smoothness of the liquid/gas interface profile and to a bias in its absolute position of the order of 3%. As a future work a more quantitative analysis of the technique sensitivity to the experimental conditions has to be done in order to understand the reasons of this systematic bias in the absolute liquid/interface position. The results presented here, even being preliminary, show the huge potentiality of the RIT technique for the complete determination of liquid/gas interface topology. The compact configuration of the optical set-up allows the usage of this technique in environments where the space is limited. As an example, the RIT technique could be a suitable candidate for the evaluation of the sloshing interface shape in

microgravity conditions.

Acknowledgments

The financial support of the presented work was provided by Fonds de la Recherche Scientifique (FNRS), FRIA fellowship. I gratefully acknowledge also VKI-AA with which travel grant I had the possibility to train with Prof. L. David and Dr. G. Gomit on the use of refractive techniques.

References

[1] R. Ibrahim, Liquid Sloshing Dynamics: Theory and Applications, Cambridge University Press, Cambridge, 2005.

[2] A. Fouras and D. Lo Jacono and G.J. Sheard and K. Hourigan, Measurement of instantaneous velocity and surface topography in the wake of a cylinder at low Reynolds number, Journal of Fluids and Structures 24 (2008) 1271–1277.

[3] F. Moisy and M. Rabaud and K. Salsac, A synthetic Schlieren method for the measurement of the topography of a liquid interface, Experiments in Fluids 46 (2009) 1021–1036.

[4] A. Fouras and K. Hourigan and M. Kawahashi and H. Hirahara, An Improved, Free Surface, Topographic Technique, Journal of visualization 9 (1) (2006) 49–56.

[5] H. Abramson, The dynamic behavior of liquids in moving containers, SP 106, NASA (1966).

[6] F. Dodge, The new "dynamic behavior of liquids in moving containers", SP 106, SRI (2000).

[7] T. Arndt and M. Dreyer, Damping behavior of sloshing liquid in laterally excited cylindrical propellant vessels, Journal of Spacecraft and Rockets 45 (5).

[8] E.J. Hopfinger and V. Baumbach, Liquid sloshing in cylindrical fuel tanks, Progress in Propulsion Physics 1 (2009) 279–292.

[9] T. S. C. Institute, Fluid structure interaction effects on and dynamic response of pressure vessels and tanks subjected to dynamic loading, RR 527, HSE-UK (207).

[10] T. Lance, Analysis of propellant slosh dynamics and generation of an equivalent mechanical model for use in preliminary voyager autopilot design studies., TM 33-306, NASA (1966).

[11] V. Kumar and I. Ng and G.J. Sheard and E. Brocher and K. Hourigan and A. Fouras., Application of Particle Image Velocimetry and Reference Image Topography to jet shock cells using the hydraulic analogy, Experiments in Fluids 51 (2011) 543–551.

[12] A. Simonini, M. Vetrano, P. Colinet, P. Rambaud., Particle image velocimetry applied to water sloshing due to a harmonic external excitation., no. Proceedings of 17th International Symposia on Applications of Laser Techniques to Fluid Mechanics, Lisbon, 2014.

[13] J. D'Errico, inverse (integrated) gradient for matlab (2009). URL `http://www.mathworks.com/matlabcentral/.File 9734`

Multiscale Modeling of Atmospheric Dispersion

Orkun Temel

Environmental and Applied Fluid Dynamics Department, von Karman Institute for Fluid Dynamics, Belgium, orkun.temel@vki.ac.be

Supervisor: Jeroen van Beeck

Professor, Environmental and Applied Fluid Dynamics Department, von Karman Institute for Fluid Dynamics, Belgium, vanbeeck@vki.ac.be

University Supervisor: Laurent Bricteux

Professor, Fluids and Machines Department, University of Mons, Belgium, laurentbricteux@umons.ac.bel

Abstract

This PhD thesis is focused on the multiscale modeling of atmospheric boundary layer by coupling a CFD (computational fluid dynamics) code with a NWP (numerical weather prediction) code to provide realistic initial and boundary conditions for a better representation of atmospheric boundary layer. Project is mainly divided into three parts which are : development of a CFD solver at microscale with a proper modeling of turbulence, coupling developed model with NWP code, application to heavy gas dispersion and epistemic uncertainty quantification of developed turbulence models.

Keywords: atmospheric boundary layer, turbulence modeling, mesoscale modeling, non-linear eddy viscosity models

1. Introduction

In the last decades, the interest in the study of atmospheric boundary layer (ABL) over cities has been increased due to the expansion of cities. Numerical studies for the prediction of pollutant dispersion in the ABL are performed for air quality studies, pedestrian comfort and risk assessment. The main approach to deal with these problems is to employ CFD codes with inflow boundary conditions derived for neutral ABL. Even though inflow boundary conditions derived from Monin-Obukhov stability theory are available for unstable and stable cases, these inflow boundary conditions cannot be considered realistic as the Monin-Obukhov stability theory is based on the assumption of horizontally homogeneous surface layer. These inflow conditions are dependent on a scale called as meso-scale that the CFD codes are not designed for. Mesoscale studies are performed by using numerical weather prediction (NWP) codes which feature from near synoptic scales (2000 km) to individual cloud cells (1 km), based on reanalysis data. However by using the nesting technique, these codes can reach a resolution of 1 km. By this nesting technique, a more realistic representation of ABL can be provided, by sustaining micro-scale CFD models inflow conditions from meso-scale results. In addition to coupling approach, the turbulence modeling is the other main focus of the project. In most of the commercial or open source CFD codes, the already implemented RANS models and their wall functions are not derived for atmospheric boundary layer studies. Therefore these models should be modified for atmospheric boundary layer applications. Additionally, the nonlinear eddy viscosity models are found out to be performing better for the cases where the flow is affected by obstacles with recirculation zones and secondary flows exist like the urban boundary layer. Hence in this project the nonlinear eddy viscosity models will be implemented to a CFD code and their performances will be evaluated and some improvements will be proposed. The test case considered will be Oklahoma City to validate the methodology with the Joint Urban 2003 (JU2003) field measurement campaign. Different coupling and turbulence modeling approaches would be tested for Oklahoma City and finally the proposed numerical methodology will be applied to Bruxelles city. In this

project, the mesoscale code will be used is Weather Research and Forecasting (WRF) Model which is a next-generation open source mesoscale code. This code will be coupled with OpenFOAM.

2. State of the art

Due to the spreading of urban areas, the research on numerical models that can potentially predict wind flows within atmospheric boundary layer and cities has been increased in the past few years [1],[2],[3]. Even though the applicability of Bousinesq approximation is open to discussion [4], numerical studies concerning fluid flow within cities had been mostly performed by using linear-eddy viscosity models due to their low computational cost and easy implementation possibility. However flow within a city is purely anisotropic and it is well known that linear eddy viscosity models (LEVM) may fail to predict flow patterns under such circumstances [5]. Stress transport models may provide a more realistic modeling but they require much more computational cost, typically, a cpu time more than that for a k-epsilon calculation by a factor two [6]. In contrast to stress transport models, NLEVMs do not require such high computational cost but also can provide better predictions than LEVMs for flow where secondary flow may occur and flow is anisotropic [7]. In literature, different implementations of non-linear k-epsilon models can be found such as Sugas cubic non-linear k-epsilon [8], Speziales quadratic k-epsilon and k-l which is found to be performing well for separated flows [9],[10], Myong-Kasakis NLEVM, developed for wall bounded shear flows [11]. Due to their capability to deal with wall anisotropy, NLEVM are also applied to flow over cities [12]. Besides non-linear two-equation models, non-linear eddy viscosity concept had also been applied to algebraic [13] and differential [14] stress models. As NLEVM are designed to perform where turbulence is generated by wall anisotropy and secondary flows occur, it might not be useful to apply these models where the effect of urban impact on flow is negligible, therefore a novel approach had proposed by coupling Crafts NLEVM [15] with standard k-epsilon for flows around bluff bodies [16] based on the idea proposed by Parente [17]. Even if the methodology proposed by Parente is only applicable for neutral ABL and two-different linear k-epsilon models are used, a compherensive approach has been introduced for the modeling of free-atmosphere. However it must be noted that as the ABL flows are governed with variability of atmospheric stability [18], in order to provide a computational approach able to deal with non-neutral ABL, variants of the linear k-epsilon model have been proposed by Alinot and Masson [19],[20]. The inflow conditions of these models [17],[19],[20]. are based on the Monin-Obukhov Stability Theory, in other words these applicability of these inflow conditions are limited with the horizontally homogeneous surface layer assumption. Therefore, coupling CFD and NWP models is essential to provide more realistic inflow conditions [21]. It has been found that by coupling CFD and NWP models, the lower boundary layer wind and pressure gradient are better represented than deriving boundary conditions from meteorological observations [22]. Also, numerical models which are sustained by the boundary conditions derived from NWP models are capable of performing Large Eddy Simulation (LES) of pollutant dispersion in urban boundary layers [23]. Even coupled CFD-NWP models stands as a potential tool to predict wind flow in atmospheric boundary layer, evaluation and improvement of different coupling approaches have not taken specific attention by researches in the field of ABL modeling. One of the few studies on coupling [24], has shown that the use of different techniques to impose mesoscale results as boundary conditions in CFD models like translation [25], extrapolation and Cresmann interpolation [26], has great effect on the realistic representation of ABL. For initial conditions, coupled NWP/CFD models use data assimilation techniques [27],[28],[29] which are based on introducing a source term to transport equations to force numerical solution not to deviate from mesoscale results during the observation period. It must be noted that models have important sensivity to these techniques due to empirical and non-generic definition of this source term. Recently, there is an increasing interest to apply uncertainity quantification methods to CFD [30]. These methods provides the possibility of determining epistemic uncertainities related to turbulence modeling.

3. Main goals of the project

As expressed before, coupling a CFD code with a NWP model can provide a more realistic representation of ABL but numerical simulation of atmospheric flows still require proper modeling of turbulence. Even with boundary and initial conditions extracted from NWP models, results might deviate from observations if turbulence modeling is not consistent with stability of ABL and highly anisotropic

nature of turbulence due to urban environment. Performance of LEVMs are found to be satisfactory for homogeneous ABL [19],[20], however LEVMs might fail to predict flow patterns within a city due to anisotropy, secondary flows and massive boundary layers separations [7]. Therefore this project will focus on the implementation of hybrid RANS models which will use NLEVMs in building influence area and LEVMs in free atmosphere. This is similar to the novel approach proposed by Parente [17]. Within this project, free open-source CFD code OpenFOAM will be used [31]. When performing coupled NWP/CFD simulations for ABL, initial conditions are extracted from NWP model by using data assimilation techniques and mesoscale results are imposed as boundary conditions with different approaches. Proposed data assimilation techniques in literature [27],[28],[29] are based on coefficients which vary for different cases without having a physically defined relationship. In addition, due to the difference between typical grid sizes of NWP and CFD models, which are around 1 km and 1m, NWP results should be interpolated or extrapolated to define boundary conditions for CFD simulations. Consequently, within this project, an appropriate methodology has to be defined for downscaling mesoscale results of NWP to sustain boundary and initial conditions to microscale CFD model. Under the consideration of advantages of using an open-source code for development of new models, an open-source next generation mesoscale NWP code, Weather Research and Forecasting Model (WRF) will also be used in this project [32]. WRF has a large worldwide user community (over 25,000 users in 130 countries). WRF is, a Fortran code which resolves the compressible Euler equations using a finite difference method. The physical models implemented in WRF includes different turbulent parametrizations [33],[34],[35] and sub-grid scale models (Urban Canopy Models) for representation of urban impact on mesoscale flow [36],[37],[38]. In order to investigate the sensivity of microscale model to mesoscale modeling, different set of physical parameterization schemes for mesoscale code will also be tested. NELVMs found in recent literature are proposed for different applications like confined swirling flows, impinging jet or wall bounded flow. Within this project, these models will be modified and implemented for ABL applications by tuning closure coefficients and defining additional source or sink terms. Apart from NLEVMs which are developed for different applications, turbulence closure coefficients are quite different even for different LEVMs proposed for homogeneous non-neutral ABL [17],[19],[39]. Thanks to the increase in computational power and the development of UQ methodologies, it is possible to quantify this kind of epistemic uncertainities related to RANS modeling [40]. So this project is also focused on the determination of epistemic uncertainities related to turbulence modeling. Eventually, the method explained in the present proposal will be applied to the city of Bruxelles, where pollution levels are currently an important concern at present [41]. Recent measurements have shown pollution concentration is exceeding the European regulation [2008/50/CE] [42]. Due to its strong exposure to industrial pollution, the case of the Meuse Valley will also be considered. Therefore, such a multi-scale numerical model that can accurately predict pollutant concentrations thanks to its ability to represent non-neutral ABL, would be of great value.

4. Stages of the project

4.1. Development of a new solver at microscale with OpenFOAM

Before implementing NLEVMs, turbulence in the homogeneous non-neutral ABL must be modeled properly by using LEVMs. In order to achieve this, the turbulence model and wall functions proposed by Parente [17] will be extented to unstable and stable conditions. The proposed model is a modified version of k-epsilon, however it is possible to convert this model to another RANS model like k-omega [43]. Numerical results for homogeneous ABL will be validated with theoretical profiles of Monin-Obukhov Similarity Theory and using the developed model, numerical simulations will be performed for heavy gas dispersion in homogeneous ABL [44]. Then, in order to provide a basis for performance evaluation of NLEVMs and comparison with LEVMs, implemented linear models will be applied to simplified three-dimensional hill and results will be compared with wind tunnel measurements for different stabilities [45]. Several NLEVMs [11],[12],[14],[15] will be implemented and their performance will be evaluated. Finally using a similar approach to Parente [17], NLEVMs combined with linear models specifically developed for non-neutral ABL will be implemented various test cases including Askervein Hill [46].

4.2. Coupling with WRF

During Oklahoma city (JU2003), measurements were obtained for different time periods called as Intensive Observation Periods (IOP). There is four IOPs

corresponding to nights when the ABL is stable and the rest correspond to unstable ABL. The measurement data obtained during these observation periods will be used not only for validation purpose but also for analyzing stability of ABL. Using Pasquill Classes [47], time periods will be selected corresponding to different classes so that evaluation of coupling and mesoscale modeling will include the effects of atmospheric stability. For NWP, initial and boundary conditions will be acquired from National Centers for Environmental Prediction North American Regional Reanalysis data (NARR), which supply 6h resolution data [48]. Performance of mesoscale model has a crucial dependency on the turbulence parameterization [49], therefore before implementing a coupling tool different turbulence parameterization schemes will be investigated in addition to urban parameterization schemes. Another important point for mesoscale simulations is the spin-up time which is basically initialization of simulation at least one day in advance to the period of interest [50], effect of spin-up time will also be investigated. Once the mesoscale approach is validated and optimized by testing different parametrization schemes, a coupling tool will be implemented to provide boundary and initial conditions to microscale CFD model. Different techniques for coupling which are explained earlier will be evaluated in terms of accuracy and computational time.

4.3. Quantification of uncertainities related to turbulence modeling

An applicable method for the determination of epistemic uncertainity of RANS simulations is proposed by Emory [51] and applied by [40],[52] for RANS simulations. This method is based on based on introducing perturbations in the Reynolds stress tensor computed by the model and used in the momentum equations. The perturbations are defined in terms of a decomposition of the Reynolds stress tensor its magnitude and the eigenvalue decomposition of the normalized anisotropy tensor. In case of using two-equation models instead of Reynolds stress models, perturbation being introduced will be added to scalar transport equations which is being solved instead of anisotropic stress tensor. Consequently, by using this method, a set of RANS simulations will be performed to quantify epistemic uncertainity related to turbulence modeling.

4.4. Application to Bruxelles City and Meuse Valley

In this last stage of the project, final methodology will be applied to city Bruxelles. CAD software Google Sketch-Up [53] will be used to build the city geometry and OpenFOAMs SnappyHexMesh utility will be used to create computational domain by using polyhedral mesh. RANS simulations will be performed to predict pollutant concentration within the city. Thanks to its generic approach, this methodology will also be able to be applied to the Meuse valley and other cities.

5. Brief summary of current status in project

In the first half of the year, the turbulence model and wall functions proposed by Parente [17] has been succesfully extented to the unstable and stable conditions, in comparison to the standard k-epsilon model of Jones and Launder, results have been compared and validated with Monin-Obukhov Similarity Theory.

Simulations are performed for horizontally homogeneous non-neutral ABL for various atmospheric stability classes. Vertical profile of turbulent kinetic energy for an unstable case corresponding to Richardson number of -0.40 and Pasquill class B - unstable is presented.

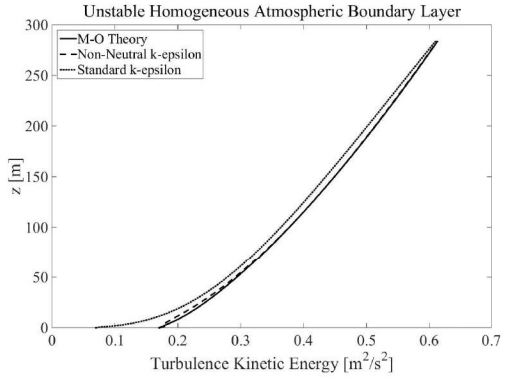

Figure 1: Vertical profiles of turbulent kinetic energy $[m^2/s^2]$

In addition to the linear eddy viscosity model developed for non-neutral ABL, Craft's cubic model has been implemented and preliminary simulations have been performed for the flow over a step case. The importance of implementation of this model is the fact that as this model contains all high order terms being employed by the other models, thanks to the generic way of implementation, recent routine can easily be converted to another NLEVM.

6. Acknowledgments

I would like to offer my sincerest gratitudes to Prof. Carlo Benocci for sharing his extensive knowledge

on the turbulence modeling of atmospheric boundary layer, to Clara Garcia Sanchez for her continous help for the implementation and debugging of new models implemented and to Prof. Laurent Bricteux for his kind and extremely important feedbacks during the proposal of the current PhD project.

References

[1] P. F. Barbante and O. Chazot, AIJ guidelines for practical applications of CFD to pedestrian wind environment around buildings, Journal of Wind Engineering and Industrial Aerodynamics 96 (2008) 1749–1761.

[2] P. Gousseau et Al., CFD simulation of near-field pollutant dispersion on a high-resolution grid: a case study by LES and RANS for a building group in downtown Montreal, Atmospheric Environment 45 428–438.

[3] Bert Blocken et Al., AIJ guidelines for practical applications of CFD to pedestrian wind environment around buildings, Atmospheric Environment 41(2) 238–252.

[4] S. Pope, A more general effective-viscosity hypothesis, Journal of Fluid Mechanics 72 (1975) 331–340.

[5] C. G. Speziale, On nonlinear k-l and k-epsilon models of turbulence, Journal of Fluid Mechanics 178 (1987) 459–475.

[6] S. B. Pope, Turbulent Flows, Cambridge University Pressl, 2000.

[7] W.P. Jones, D. Lentini, A realisable non-linear eddy viscosity/diffusivity model for confined swirling flows, International Journal of Heat and Fluid Flow 29 (2008) 1612–1627.

[8] K. Suga, Development and Application of a Non-linear Eddy Viscosity Model Sensitized to Stress and Strain Invariants, Ph.D. thesis, UMIST (1996).

[9] C. Speziale, On nonlinear K-l and K-e models of turbulence, Journal of Fluid Mechanics 178.

[10] C. Speziale, Numerical solution of turbulent flow past a backward facing step using a nonlinear j-epsilon model, International Journal of Engineering Science 26 (1988) 10991112.

[11] Myong, Hyon Kook; Kasagi, Nobuhide, A new approach to the improvement of k-epsilon turbulence model for wall-bounded shear flows, JSME International Journal, Series II (ISSN 0914-8817) 33 (1990) 63–72.

[12] Myong, Hyon Kook; Kasagi, Nobuhide, Evaluation of various non-linear k-Models for Predicting Wind Flow around an isolated high-rise Building within the Surface Boundary Layer, Journal of Building and Environment 57 (2012) 145–155.

[13] Shih, Tsan-Hsing, Zhu, Jiang, Lumley, John L, A realizable Reynolds stress algebraic equation model, Symposium on Turbulence Shear Flows August (1993) Kyoto.

[14] Robert Rubinstein and J. Michael Barton, Nonlinear Reynolds stress models and the renormalization group, Phys. Fluids 1472.

[15] T. Craft, B.E. Launder, K. Suga, Development and application of a cubic eddy-viscosity model of turbulence, Int. J. Heat Fluid flow 17 (1993) 108–115.

[16] Marc Moonens, Assesment of Two Equations Turbulence Models for Flows around Bluff Bodies, Ph.D. thesis, Universite Libre de Bruxelles and Vrije Universiteit Brussel (2014).

[17] Parente, A. et al, Improved k-epsilon model and Wall function formulation for the RANS simulation of ABL flows, J. of Wind Eng. and Ind. Aerodyn 99 (2011) 267–278.

[18] Lilly, D. K, Stratified Turbulence and the Mesoscale Variability of the Atmosphere, J. of Atmospheric Sciences 40 (1983) 749–761.

[19] C. Alinot, C. Masson, k-e Model for the Atmospheric Boundary Layer under various Thermal Stratifications, Journal of Solar Energy Engineering 127 (2005) 438–443.

[20] C. Alinot, C. Masson, Aerodynamic Simulation of Wind Turbines Operating in Atmospheric Boundary Layer with Various Thermal Stratifications, Proceedings of the 2002 ASME Wind Energy Symposiumg (2002) 206–215.

[21] Coirier, W. J., et al, Progress Towards a Coupled Mesoscale and Microscale Modeling Capability., 7th Symp. on the Urban Environment.

[22] Tewari, M., et al., Impact of coupling a microscale computational fluid dynamics model with a mesoscale model on urban scale contaminant transport and dispersion, Atmospheric Research 96(4) (2010) 656–664.

[23] Xie, Z-T. , et al., Coupled modelling of flow and dispersion in urban environments, 5th Int. Symp. on Computational Wind Engineering North Carolina (US).

[24] Jothiprakasam D V, Downscaling wind energy resource from mesoscale to local scale by nesting and data assimilation with a CFD model, Ph.D. thesis, Ecole des Ponts ParisTech-Universite Paris-Est (2014).

[25] Laporte L, Application dun code de CFD atmospherique a lestimation du productible eolien en terrain complexe, Ph.D. thesis, Ecole des Ponts ParisTech-Universite Paris-Est (2008).

[26] E. Kalnay et Al., A local ensemble transform Kalman filter data assimilation system for the NCEP global model, Tellus A 60 (2008) 113130.

[27] E. Kalnay.

[28] Stauffer, D.R., Bao, J.W., Optimal determination of nudging coefficients using the adjoint equations, Tellus 45A 45A (1993) 358–369.

[29] Haupt et Al., A preliminary study of assimilating numerical weather prediction data into computational fluid dynamics model for wind prediction, Journal of Wind Engineering and Industrial Aerodynamics 99 (2011) 320–329.

[30] Iaccarino, G, Introduction to uncertainty representation and propagation, NATO Research and Technology Organization Neuilly-sur-Seine (France).

[31] OpenFOAM User Guide, 2012.

[32] Skamarock, W., et al., A description of the advanced research WRF version 3, NCAR/TN-475+STR.

[33] P. Bougeault and P. Lacarrere, Parameterization of Orography-Induced Turbulence in a MesobetaScale Model, Monthly Weather Review 117 (1989) 18721890.

[34] T Yamada G Mellor, Development of a turbulent closure model for geophysical fluid problems, Reviews of Geophysics and Space Physics 40-41 (1982) 851–875.

[35] Nakanishi M., Improvement of the Mellor-Yamada turbulence closure model based on Large-Eddy Simulation Data, Boundary-Layer Meteorology 41-43-44 (2001) 349378.

[36] Kusaka , H. Kondo, Y. Kikegawa, and F. Kimura, A simple single-layer urban canopy model for atmospheric models: Comparison with multi-layer and slab models, Boundary-Layer Meteorology 101 (2001) 329–358.

[37] Martilli et al, An Urban Surface Exchange Parametrisation for Mesoscale Models, Boundary-Layer Meteorology 104 (2002) 261–304.

[38] Salamanca, F., and A. Martilli, A new building energy model coupled with an urban canopy parameterization for urban climate simulationsPart II. Validation with one dimension offline simulations, Theor. Appl. Climatol. 99 (2010) 345–356.

[39] Crespo, A., Manuel, F., Moreno, D., Fraga, E., Hernandez, Numerical Analysis of Wind Turbine Wakes, Workshop on Wind Energy Applications Greece.

[40] C. Gorl, M. Emory, J. Larson, G. Iaccarino, Epistemic un-

certainty quantification for RANS modeling of the flow over a wavy wall, In Center for Turbulence Research Annual Research Briefs 2012.
[41] Vanderstraeten, et al., Black Carbon Instead of Particle Mass Concentration as an Indicator for the Traffic Related Particles in the Bruxelles Capital Region, J. of Environmental Protection 2 (2011) 525–532.
[42] IBGE, La qualit de lair en rgion de Bruxelles- Capitale, 2012.
[43] T. Knoop, B. Eisfeld, J. B. Calvo, A new extension for k-omega turbulence models to account for wall roughness, International Journal of Heat and Fluid Flow 30 (2009) 54–65.
[44] S-E Gryning, H Jorgensen, S Larsen, E Batchvarova, The wind profile up to 300 meters over flat terrain, Journal of Physics: Conference Series 75.
[45] Takahashi et Al, Wind tunnel test of effects of atmospheric stability on turbulent flow over a three-dimensional hill, Journal of Wind Engineering t 93.
[46] P. A. Taylor, H. W. Teunissen, The Askervein Hill project: Overview and background data, Boundary-Layer Meteorology 39 (1987) 15–39.
[47] J. L. Woodward, Appendix A: atmospheric stability classification schemes in Estimating the Flammable Mass of a Vapor Cloud, Boundary-Layer Meteorology American I.Wiley Online Library (1998) 209–212.
[48] Colorado NOAA/OAR/ESRL PSD, Boulder. NCEP Reanalysis, http://www.esrl.noaa.gov/psdy 209–212.
[49] Xiao-Ming Hu, John W. Nielsen-Gammon, and Fuqing Zhang, Evaluation of Three Planetary Boundary Layer Schemes in the WRF Model, J. Appl. Meteor. Climatol 49 (2010) 18311844.
[50] Michal A. Kleczek, Gert-Jan Steeneveld, Albert A. M. Holtslag, Evaluation of the Weather Research and Forecasting Mesoscale Model for GABLS3: Impact of Boundary-Layer Schemes, Boundary Conditions and Spin-Up, Boundary-Layer Meteorologyl 152 (2014) 213–243.
[51] Emory, M., Pecnik, R. Iaccarino, Modeling structural uncertainties in Reynolds-averaged computations of shock/boundary layer interactions, AIAA paper.
[52] C. Gorl and G. Iaccarino, A framework for epistemic uncertainty quantification of turbulent scalar flux models for Reynolds-averaged Navier-Stokes simulations, Phys. Fluids 25 (2013) 55–105.
[53] Web reference: http://www.sketchup.com/intl.

Turbulent Heat Transfer at Different Prandtl Number Fluids in Natural Convection Boundary Layer on a Vertical Plate

Agustín Villa Ortiz

Enviromental and Applied Fluid Dynamics Department, von Karman Institute for Fluid Dynamics, Belgium, agustin.villa.ortiz@vki.ac.be

Supervisor: Jean Marie Buchlin

Head of Department, Enviromental and Applied Fluid Dynamics Department, von Karman Institute for Fluid Dynamics, Belgium, buchlin@vki.ac.be

University Supervisor: Tony Arts

Professor, Institute of Mechanics, Materials and Civil Engineering, Université Catholique de Louvain, Belgium, tony.arts@uclouvain.be

In the context of the MYRRHA project (Multipurpose Hybrid Research Reactor for High-tech Applications) [1] different substances are used to remove the produced heat during the operation or in case of accident. These fluids are characterized by different Prandtl number: Lead-Bismuth Eutectic (LBE) ($Pr = 0.02$), water ($Pr = 10$) and argon ($Pr \approx 0.7$). The first media is used as coolant agent inside the reactor [1], meanwhile water is used in the secondary coolant fluid. Argon is the cover gas above the LBE pool, which provides an inert atmosphere to the reactor.

Another interesting facilities in a nuclear plant are the spent fuel pools, which are used to remove the heat generated during the fuel decay once it has been used [2]. Air is present in case of Loss-Of-Coolant Accident (LOCA) in these pools.

Natural convection is present in all of the previous elements. In case of a maintenance operation, the pumps inside the reactor are shut down. In this case, the LBE is circulating inside the primary heat exchanger due to density changes. In any case, since argon is always circulating in the upper part of the reactor due to natural convection. In case of an accident, when the pumps inside the reactor stop, or a LOCA failure, the present heat transfer phenomena is due to natural convection. The understanding of this phenomenon is required in order to design the different facilities in this kind of scenario, and avoid safety problems and their consequences.

Nowadays, Computational Fluid Dynamics is used during the design of the facilities, to get a better insight into the flow and thermal fields. However, the actual turbulence models are not able to reproduce the turbulent heat transfer accurately in case of low Prandtl numbers [3; 4], and in natural convection flows [5]. Besides, turbulent natural convection has been studied in the past, experimentally [6; 7; 8] and numerically [9; 5; 10], but mostly in confined flows (such as cavities and Rayleigh-Benard cells) and using air as fluid (Pr=0.71).

In this PhD Direct Numerical Simulations (DNS) will be performed at different Prandtl number values, in the case of a vertical turbulent natural convection boundary layer. These Prandtl numbers range from below unity $(0.02, 0.2)$ and through unity (0.71) , but always in the turbulent regime. Kolgomorov and Batchelor turbulence scales will be resolved, and velocity and temperature fields will be studied to understand the effect of the Prandtl number in this phenomena. Experiments are planned in natural convection at $0.2, 0.71$ Prandtl numbers will provide data to validate the previous numerical models. The obtained results will be used to investigate the effect of the Prandtl number on turbulent heat transfer, and assess the accuracy of the actual turbulence models, specially the thermal ones. A reference DNS database will be established with the DNS results.

Keywords: Turbulence, Boundary Layer, Natural Convection, Low Prandtl number, Direct Numerical Simulation, OpenFOAM, Turbulence Modelling, Computational Fluid Dynamics, MYRRHA

References

[1] MYRRHA project website.
URL `http://myrrha.sckcen.be/`

[2] BelV website.
URL http://www.belv.be
[3] H. Kawamura, H. Abe, Y. Matsuo, Dns of turbulent heat transfer in channel flow with respect to reynolds and prandtl number effects, International Journal of Heat and Fluid Flow 20 (3) (1999) 196–207.
[4] M. Duponcheel, L. Bricteux, M. Manconi, G. Winckelmans, Y. Bartosiewicz, Numerical simulation of liquid metal turbulent heat transfer in a channel flow at $Re_\tau = 2000$, in: NURETH15, 2013.
[5] I. Otic, G. Grötzbach, M. Wörner, Analysis and modelling of the temperature variance equation in turbulent natural convection for low-prandtl-number fluids, Journal of Fluid Mechanics 525 (2005) 237–261.
[6] K. Kitamura, M. Koike, I. Fukuoka, T. Saito, Large eddy structure and heat transfer of turbulent natural convection along a vertical flat plate, International journal of heat and mass transfer 28 (4) (1985) 837–850.
[7] T. Tsuji, Y. Nagano, Characteristics of a turbulent natural convection boundary layer along a vertical flat plate, International journal of heat and mass transfer 31 (8) (1988) 1723–1734.
[8] P. Betts, I. Bokhari, Experiments on turbulent natural convection in an enclosed tall cavity, International Journal of Heat and Fluid Flow 21 (6) (2000) 675–683.
[9] Y. Miki, K. Fukuda, N. Taniguchi, Large eddy simulation of turbulent natural convection in concentric horizontal annuli, International journal of heat and fluid flow 14 (3) (1993) 210–216.
[10] D. G. Barhaghi, A study of turbulent natural convection boundary layers using large-eddy simulation, Chalmers University of Technology, Department of Applied Mechanics, 2007.
[11] Q. Li, P. Schlatter, L. Brandt, D. S. Henningson, Dns of a spatially developing turbulent boundary layer with passive scalar transport, International Journal of Heat and Fluid Flow 30 (5) (2009) 916–929.
[12] W. K. George Jr, S. P. Capp, A theory for natural convection turbulent boundary layers next to heated vertical surfaces, International Journal of Heat and Mass Transfer 22 (6) (1979) 813–826.
[13] K. Hishida, J. Sakakibara, Combined planar laser-induced fluorescence–particle image velocimetry technique for velocity and temperature fields, Experiments in Fluids 29 (1) (2000) S129–S140.
[14] T. Arts, Y. Kinoue, M. Abad-Lozano, S. Pierret, The unsteady temperature field in a turbine blade cooling channel, Tech. rep., DTIC Document (2003).
[15] OECD Nuclear Energy Agency. Nuclear Science Committee, Handbook on Lead-bismuth Eutectic Alloy and Lead Properties, Materials Compatibility, Thermal-hydraulics and Technologies, OECD Nuclear Energy Agency, 2007.

DEVELOPMENT OF ADVANCED CFD AND OPTIMIZATION

A GPU-accelerated Navier-Stokes Solver for Steady Turbomachinery Simulations

Mohamed Hassanine Aissa

Turbomachinery and Propulsion Department, von Karman Institute for Fluid Dynamics, Belgium, aissa@vki.ac.be

Supervisor: Tom Verstraete

Assistant Professor, Turbomachinery and Propulsion Department, von Karman Institute for Fluid Dynamics, Belgium, tom.verstraete@vki.ac.be

University Supervisor: Kees C. Vuik

Professor, Applied Mathematical Institute, TU Delft, The Netherlands, vuik@tudelft.nl

Abstract

Any tiny improvement of modern turbomachinery components require nowadays a large amount of design evaluations. Every evaluation runs time consuming simulations. Reducing the computational cost of the simulations allows to run more evaluations, thus reaching a higher design improvement.

In this work, an Nvidia Graphics Processing Unit (GPU) of Kepler generation is used to accelerate the Finite-Volume CFD flow evaluation as part of an inhouse multidisciplinary design optimization (MDO) algorithm. The validated double precision GPU solver is up to 30x times faster for inviscid applications and up to 10 times faster for turbulent viscous cases than a the serial code running on an Intel(R) Xeon(R) CPU E3-1240 v3. The gain on the CFD simulation time make it possible to run the MDO optimizer with explicit solver on a workstation under affordable time budget.

Keywords: CFD RANS , Navier-Stokes, GPU, Turbomachinery application

1. Introduction

The target for the optimization of turbomachinery components is to improve a baseline design according to a set of objectives. The results of every design evaluation has an impact on the search for better designs. The accuracy of the evaluation is therefore very important for the end results of the optimization making high-fidelity simulation essential. Direct Numerical Simulations (DNS) are the most accurate simulations solving all flow property including turbulence. They are therefore too expensive and out of reach in optimization for today computational resources. Large Eddy Simulations (LES) model partly the turbulence and are thus less expensive than DNS but still too resource-demanding for optimization tasks. Reynolds Averaged Navier Stokes simulations (RANS) model all turbulence scales and are therefore faster than LES. RANS simulation are established for solving engineering problems. Considering the large number of required design evaluation, even RANS simulations are computationally expensive for realistic optimization cases. A reduction of the computational cost of the RANS simulation is necessary to have an efficient optimizer. For this purpose the simulation has to run in parallel.

In high performance systems (HPC) two major architectures are established: *distributed-* and *shared-memory* systems. The first architecture consists of a cluster of classical CPUs. This alternative offers certainly a large number of cores but requires from the user to organize the inter-core communication. The second alternative consits of a relatively small number of cores accesses the same memory. This alternative offers an easier handle of communication but the number of cores is lower.

the Graphics Processing Units (GPU), considered as a *shared-memory* system, offer much more cores

than classical CPU shared-memory system. Every GPU core is much less powerful than a CPU core, but there very large number allows considerable performance increase in terms of computational time (speedup). GPUs can be programmed using a low-level programming languages or an automated high-level porting tool: low-level programming language ssuch as CUDA (Nvidia) or OpenCL (platform independent) offer full flexibility with the rewriting of the code . Automated high-level porting tools such as openACC [1] allow an application acceleration without rewriting the code. Beside the fact that these tools are not open-sources, they are reported in the literature to be less efficient than manual low-level porting using CUDA or openCL[2].

Nvida GPUs are programmed with CUDA. The CUDA language is a C-like language, which simplifies the rewriting burden. Many known libraries have a GPU enabled version (cuBLAS, cuRAND,cuSpare, petsc ...). This makes the rewriting easier.

In this work a steady RANS CPU code has been rewritten using CUDA language in order to run much faster on Nvidia GPU compared to serial CPU. The paper is structured as follow: sections 2 describe the governing equations, section 3 discuss the GPU implementation and the last section presents the validation of the solver and the performance gain in terms of speedup.

2. Description of the Flow Solver

2.1. Governing equations

The conservative integral form of the governing equations for internal flows in turbomachinery are [3]:

$$\frac{\partial}{\partial t}\int_\Omega \vec{W} d\Omega + \oint_{\partial\Omega} (\vec{F_c} - \vec{F_v}) dS = \int_\Omega \vec{Q} d\Omega \qquad (1)$$

where the conservative variable vector $\vec{W}$ consist of those components in three dimensions:

$$\vec{W} = \begin{bmatrix} \rho \\ \rho u \\ \rho v \\ \rho w \\ \rho E \end{bmatrix} \qquad (2)$$

and the convective flux vector is defined as follows:

$$\vec{F_c} = \begin{bmatrix} \rho V \\ \rho u V + n_x p \\ \rho v V + n_y p \\ \rho w V + n_z p \\ \rho H V \end{bmatrix} \qquad (3)$$

With following *contravariant velocity* definition:

$$V \equiv \vec{v} \cdot \vec{n} = n_x u + n_y v + n_z w \qquad (4)$$

and the viscous flux is

$$\vec{F_v} = \begin{bmatrix} 0 \\ n_x\tau_{xx} + n_y\tau_{xy} + n_z\tau_{xz} \\ n_x\tau_{yx} + n_y\tau_{yy} + n_z\tau_{yz} \\ n_x\tau_{zx} + n_y\tau_{zy} + n_z\tau_{zz} \\ n_x\Theta_x + n_y\Theta_y + n_z\Theta_z \end{bmatrix} \qquad (5)$$

where

$$\begin{aligned} \Theta_x &= u\tau_{xx} + v\tau_{xy} + w\tau_{xz} + k\frac{\partial T}{\partial x} \\ \Theta_y &= u\tau_{yx} + v\tau_{yy} + w\tau_{yz} + k\frac{\partial T}{\partial y} \\ \Theta_z &= u\tau_{zx} + v\tau_{zy} + w\tau_{zz} + k\frac{\partial T}{\partial z} \end{aligned} \qquad (6)$$

and the viscous stress tensor τ after application of stokes hypothesis ($\lambda + \frac{2}{3}\mu = 0$) reads in tensor notation:

$$\begin{aligned} \tau_{ii} &= 2\mu\left(\frac{\partial v_i}{\partial x_i} - \frac{1}{3} div\vec{v}\right) \\ \tau_{ij} = \tau_{ji} &= \mu\left(\frac{\partial v_i}{\partial x_j} + \frac{\partial v_j}{\partial x_i}\right) \end{aligned} \qquad (7)$$

with following source term Q:

$$\vec{Q} = \begin{bmatrix} 0 \\ \rho f_{e,x} \\ \rho f_{e,y} \\ \rho f_{e,z} \\ \rho \vec{f_e} \cdot \vec{v} + \dot{q}_h \end{bmatrix} \qquad (8)$$

In absence of external force and in non-rotating system the source term is equal to zero. In a rotating frame of reference the Coriolis and centrifugal forces have effects on the source term. The appropriate formulation in this case is to be found in [3].

2.2. Turbulence Modeling

In RANS equations the turbulence is fully modeled. This time-efficient method is consequently widely used in MDO algorithms.

To account for turbulence the in-house Navier-Stokes equations solver uses a modified version [4] of SpalartAllmaras (SA) one-equation turbulence model [5; 6]. The SA Model, based on a linear eddy viscosity assumption, defines the dynamic viscosity coefficient μ_T as function of the turbulent viscosity $\tilde{\nu}$ as follow:

$$\mu_T = \rho\tilde{\nu} f_{v1} \quad f_{v1} = \frac{\chi^3}{\chi^3 + c_{v1}^3} \quad \chi = \frac{\tilde{\nu}}{\nu} \tag{9}$$

the fully turbulent version of the transport equation for the variable $\tilde{\nu}$ is

$$\begin{aligned} \frac{D\tilde{\nu}}{Dt} &= \underbrace{c_{b1}\tilde{S}\tilde{\nu}}_{\text{production}} \\ &+ \underbrace{\frac{1}{\sigma}\{\nabla\cdot[(\tilde{\nu}+\nu)\nabla\tilde{\nu}] + c_{b2}(\nabla\tilde{\nu})^2\}}_{\text{diffusion}} \\ &- \underbrace{c_{w1} f_w(r)(\frac{\tilde{\nu}}{d})^2}_{\text{destruction}} \end{aligned} \tag{10}$$

Full details about the used modified Spalart-Allmaras model can be found in [4].

The SA model is linked to the Navier-Stokes equation by the extension of the dynamic viscosity μ on equation 7 [3]:

$$\mu = \underbrace{\mu_L}_{\text{laminar viscosity}} + \underbrace{\mu_T}_{\text{turbulent viscosity}} \tag{11}$$

2.3. Spatial Discretization

The time derivative of conservative variable $\vec{W}$ can be reformulated from the governing equation 1 as follow:

$$\frac{\partial\vec{W}}{\partial t} = -\frac{1}{\Omega}\left[\oint_{\partial\Omega}(\vec{F}_c - \vec{F}_v)dS - \int_\Omega \vec{Q}d\Omega\right] \tag{12}$$

The spatial discretization is the numerical approximation of the right hand side of equation 12. For this purpose the space is meshed with multi-block structured meshes. The control volumes correspond to the cells and variables describe the state of the cell-centers. The so-called cell-centered finite volume scheme requires less cell communication compared to vertex-based approach, in which variable are saved in grid points.

The numerical approximation of viscous Fluxes $\vec{F}_v$ employs a central scheme. A central scheme uses conservative variables at the left and at the right of a volume side to compute the flux through the side. The convective fluxes $\vec{F}_c$ are approximated using an upwind scheme namely the Roe scheme [7]. Upwind schemes, especially Roe scheme, allow a very accurate resolution of boundary layers. For the flux calculation left and right state are defined based on MUSCL (Monotone Upstream-centered Schemes for Conservation Law) approach[8]:

$$\begin{aligned} U_R &= U_{i+1} - \frac{1}{2}\Psi_R(U_{i+2} - U_{i+1}) \\ U_L &= U_i - \frac{1}{2}\Psi_L(U_i - U_{i-1}) \end{aligned} \tag{13}$$

For second- and higher-order flux calculation, a limiter functions Ψ prevents the solution from spurious oscillation near strong discontinuities [3]:

$$\Psi_{L/R} = \frac{1}{2}\left[(1+\hat{\kappa})r_{L/R} + (1-\hat{\kappa})\right]\Phi_{L/R} \tag{14}$$

where $r_{L/R}$ is the ratio for consecutive solution variation, Φ a slope limiter and $\hat{\kappa}$ a parameter to determine the spacial accuracy of the interpolation. In this work the second-order upwind approximation is implemented with $\hat{\kappa} = 0$ using the Venkatakrishnan slope limiter [9].

2.4. Time Integration

The time derivative equation (12) can be written as follows to highlight the time integration:

$$\frac{d(\Omega\vec{W})_i}{dt} = -\vec{R}_i \tag{15}$$

Source terms and fluxes constitute the residual R_i in every cell i with volume Ω_i. The Runge-Kutta method (see equation 16) is an established explicit method to integrate the governing equation.

$$\begin{aligned} \vec{W}_I^{(0)} &= \vec{W}_I^n \\ \vec{W}_I^{(1)} &= \vec{W}_I^{(0)} - \alpha_1\frac{\Delta t_I}{\Omega_I}\tilde{R}_I^{(0)} \\ \vec{W}_I^{(2)} &= \vec{W}_I^{(0)} - \alpha_2\frac{\Delta t_I}{\Omega_I}\tilde{R}_I^{(1)} \\ &\vdots \\ \vec{W}_I^{n+1} &= \vec{W}_I^{(m)} = \vec{W}_I^{(0)} - \alpha_m\frac{\Delta t_I}{\Omega_I}\tilde{R}_I^{(m-1)} \end{aligned} \tag{16}$$

After a series of test of different Runge-Kutta methods the 4 stages second order has been chosen with $\alpha_1 = 0.1084$,$\alpha_2 = 0.2602$, $\alpha_3 = 0.5052$, $\alpha_4 = 1.000$ and CFL number of 0.92 [3].

Source terms require in some cases a special treatment to enhance the stability and the convergence. One technique, called point implicit, change the k-th stage equation to:

$$\vec{W}_I^{(k)} = \vec{W}_I^{(0)} - \frac{\alpha_k}{\Omega_I}\left[\frac{1}{\Delta t_I} - (\frac{\partial\vec{Q}}{\partial\vec{W}})_I^{(k)}\right]^{-1}\vec{R}_I^{(k-1)} \tag{17}$$

In some testcases (compressor cascade) the use of Point implicit did not have a major impact on the solution. For other test cases (LS89) it prevents the solver from reaching non-physical states (e.g negative density).

3. Implementation

3.1. CUDA Programming Language

A GPU code consists of a set of kernels. A kernel is a function that a CPU calls to run on GPU as follow:

$$kernel_name <<< N_{Blocks}, N_{threadsPerBlock} >>> (A, B)$$

The kernel run-configuration is specified in the call. First the number of blocks of threads, then the number of threads per block has to be passed to the kernel. The GPU runs the same kernel code on a total number of threads equal to $N_{Blocks} * N_{threadsPerBlock}$. The threads execute the same code but on different data. Threads of the same block run on the same multi-Streaming Processor and thus have access to the same shared-memory. Depending on the code structure, different threads can follow different execution paths (e.g. if-else structure). This diversion is possible but not recommended. Inside a block threads are indeed grouped in warps of 32 threads (can change depending on GPU generation). Threads of the same warp execute exactly the same lines of code. A problem can occur with conditional structure: If only a part of the warp satisfies a condition, the rest of the warp has to wait until the first part execute the job related to the condition. Another implication concerns the number of started threads. The system starts enough warps to cover the number of threads per block. If the number of threads is not a multiple of the warp size, the started threads are not all active and thus the performance decreases.

The threads can access register memory which is the fastest and the most scarce. Another fast memory is shared-memory. The largest memory is local memory which is also the slowest. Latest generation of Nvidia GPUs are enhanced with L1 and L2 Caches that are progressively solving the issue of slow access of local memory.

3.2. Implemented Kernels

The GPU code is based on a CPU version. The porting procedure has been performed function by function. Every time a CPU function is replaced by its CUDA version. The GPU kernel, once added to the CFD code, should not change the flow evaluation result. Every ported kernel is checked for "side effects" comparing the pure CPU output and the CPU-GPU output. At the end of the porting only the initialization and the post-processing is performed on host CPU. The entire computation is delegated to the device GPU. For multi-block meshes the update of interfaces is performed by CPU for performance reasons (see fig. 1).

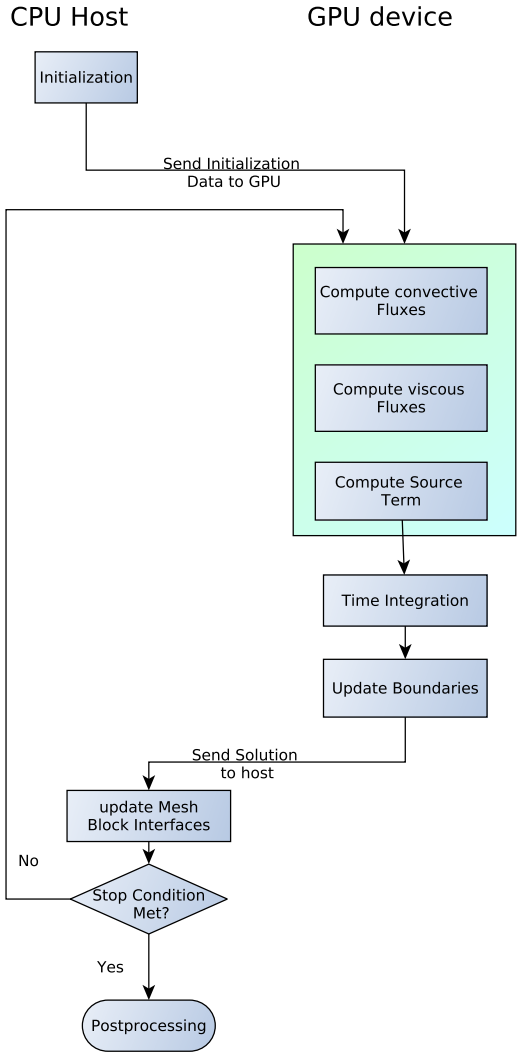

Figure 1: Structure of the GPU solver

A kernel computes the convective fluxes, a second computes the viscous fluxes and a third the source terms. The 3 kernels add, in turn, their contributions to the same residual. Another kernel performs the time integration based on the old solution and the new com-

puted right hand side (Residual). These kernels proceed on all mesh cells and have similar run configuration. Before a new iteration can start a boundary and interface update has to be done. These updates affects only a portion of the cells depending on the volume to surface ratio. For a low surface to volume ratio, few cells constitute the boundary or the block interface. The performance gain is not important or even non existing. In this case the interface update is delegated to the CPU. A solution transfer to the CPU and back is essential.

Splitting the computation into a set of kernels enables special code optimization for every kernel fitting a specific function. In addition to that kernel fusion would decrease the call to the local memory but at the same time increase the usage of register memory which is limited for every thread. This leads to a reduced number of concurrent running threads and thus a decrease in the performance.

Inside every kernel CUDA, threads are mapped to mesh cells not to flow variables. Although mapping the threads to flow variables increases the number of used threads and thus maximize the occupancy, the dependency between flow variables requires from the threads to be synchronized at some positions which harms the performance and increases the risk of memory misusage (race condition)

3.3. Code Adaptation

The CUDA language is based on C/C++ adding with few extensions to handle GPU specific functionality. Consequently porting C/C++ code is rather a code adaptation than a total rewriting. Most of the code remains untouched. Such a naive CUDA code works but with poor performance and sometimes erroneous results. The poor performance is expectable, since no adaptation are done to meet special GPU features. The possible erroneous results originates from running in parallel when write-requests for the same memory position occur at the same time (race condition). CUDA provide developer with a memory checker tool able to track memory misusage at run time. A sign for the presence of write conflicts is the change in the simulation output, if run 2 times with exactly the same configuration. Since the behavior of the program is undefined in such memory conflicts the output is not the same for 2 consecutive runs.

The first version of the convective flux calculation kernel presented a case of race condition. The computation involves, in this kernel, a stencil of neighbor cells to compute a flux at a face of a cell. The value of the flux is added to one neighbor and subtracted from the other. The original implementation loops over all faces. When running in parallel it can occur that 2 faces write their contributions at the same time to the same cell. One of the contribution will be discarded or any other undefined behavior could take place. For CPU application, developers tend to use *mesh coloring* to mark totally independent faces and so divide the faces in subsets not containing faces of the same cell. This prepossessing overhead costs in terms of computation and memory. An other alternative is to switch to a cell-wise flux calculation. The same thread loops over all 8 faces of a cell summing their fluxes. This result in all fluxes being calculated 2 times which is less harmful for structured meshed than mesh coloring.

3.4. Use of Multi-block Meshes

Simple geometries are meshed by a single structured block of cells. These single-block meshes are solved entirely in the GPU. Multi-block meshes, adapted to more complicated geometries, are however not totally solved in GPU. The CPU cooperates with the GPU through the updates of the mesh blocks interfaces. This proved to be faster than treating interfaces on GPU even though the solution needs to be copied to CPU and back in every iteration. The use of page-locked memory (pinned) for the data that has to be frequently exchanged between GPU and CPU is beneficial for the performance since pinned memory transfer has a larger bandwidth. The gain through pinned memory is proportional to the number of iterations and the amount of memory copied (see Fig. 7). Two methods have been tried to run the solver on

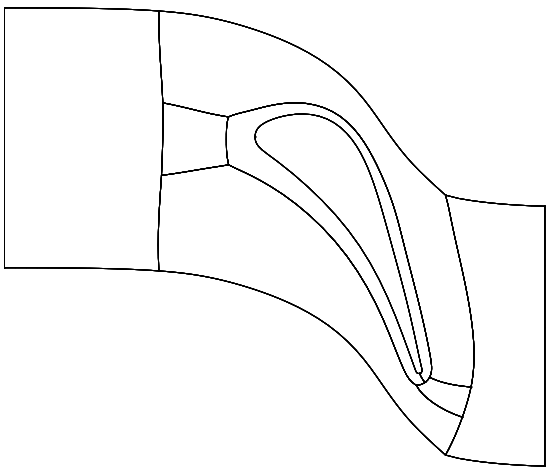

Figure 2: Example of Multi-Block Mesh (Cells not included for better visualization)

multi blocks meshes: run a kernel for every block or

run one kernel for all blocks. Inside a block the access of neighbors is straightforward. Consequently assigning 1 block to 1 kernel does not need any extra code adaptation. On the other hand, some blocks could have few cells that are not enough to keep most of the threads active (see Fig. 2). This portion of active threads, while a kernel is running, is called occupancy. Low occupancy leads in many cases to a poor performance. Assigning all blocks to 1 kernel increases the occupancy but an extra code has to be run for the identification of the position of the threads (assigned cell) in the block in order to identify the neighbor. Tests proved that 1 kernel per block is more efficient. A balancing in number of cells between blocks in the grid generation improves the occupancy.

3.5. Use of Multiple GPU

A GPU is accessed following a host-device paradigm. As an accelerator the GPU can only execute jobs started by the host CPU. One CPU can control more than 1 GPU. The system lists available N GPUs from 0 to N-1. A simple function call $cudaSetDevice(GPU_i)$ in the CUDA code sets the GPU number GPU_i to current GPU. This means that all coming kernel calls will be directed to the GPU_i, until the same CUDA function is called again with a different GPU number.

To profit from many GPUs the work has to be distributed among them following the same paradigm as with distributed memory systems. The same kernel can run in different GPU on different data. For this purpose a mesh partitioning is essential. A simple way is to group blocks of meshes to form different sets of comparable number of cells and direct every set to a different GPU. A synchronization between GPUs is required after every Runge-Kutta stage. The CPU organizes the communication and memory transfer between different GPUs. It is developer responsibility to make sure that required updated data is available for every kernel in the GPU where it will be running. A linear scaling, which means 2 GPUs are 2 times faster than 1 GPU, is not granted. The use of multi-GPU is essential only if the problem to solve is larger than the local GPU memory.

In this work the CFD solver is intended for design evaluations inside a population based optimizer. Every design within one population is totally independent from others. The only synchronization point is at the end of the evaluation of the entire population where the optimizer has to use the population fitness to form a new generation. For this application a group of GPUs is more efficient when used for different designs than for the same individual. In fact 8 GPUs for instance compute 8 designs at the same time. But 8 GPUs cannot evaluate one design 8 times faster due to communication with the host over PCI. Even direct communication is not developed for more than 2 GPUs.

3.6. Use of Multigrid

Multigrid is an established technique for solver acceleration. It is based on in the use of a set of Meshes of the same geometry but with decreasing resolution. The coarser meshes are responsible for the decrease of low frequency error. In this work the inviscid solver has been extended to support multigrid with a speedup of 2x to 3x compared to the initial one. The implementation of MG for viscous is in development. The coarse Meshes are not stored in the system. They are the result of the coarsening through cell averaging of the fine mesh. The solver will not be aware of this change since it is not in the structure but in the cell content. Extensive variables such as volume and area are summed over the involved neighbors (8 in 3D and 4 in 2D). The intensive variables are averaged according to the volume if it is a cell based variable (Temperature, density ..) or according to the face area if it is a face based variable (normal vector)

The solutions of the coarse meshes contribute to a correction of the fine mesh result. This occurs in different ways depending on the multigrid scheme.

4. Numerical Results

4.1. Verification and Validation of GPU Solver

The GPU code is a ported version of the CPU code. A first verification concerns the comparison of the GPU and CPU result of the same test-case. During the development the output exact similitude has been preserved. The GPU code reaches under these conditions the maturity level of the CPU one. Since both codes are still in development further verification and validation has been performed. The GPU code is verified first for inviscid flows against the Numeca solver. The test case is an internal transonic flow through a parallel channel having a 4.2 % thick circular bump on the lower wall with an isentropic exit Mach number of 0.85 [10]. The Mach number contours presented in figure 3 shows a supersonic pocket on trailing edge of the bump ended by a normal shock. For the sake of verification the same test case is run by Numeca FineTurbo CFD solver. Comparison of the pressure coefficient c_p of both simulations is shown in figure 4. The

two distributions are very close and predict the shock at the same position on the bump. The Numeca solver predicts however a higher pre-shock Mach number.

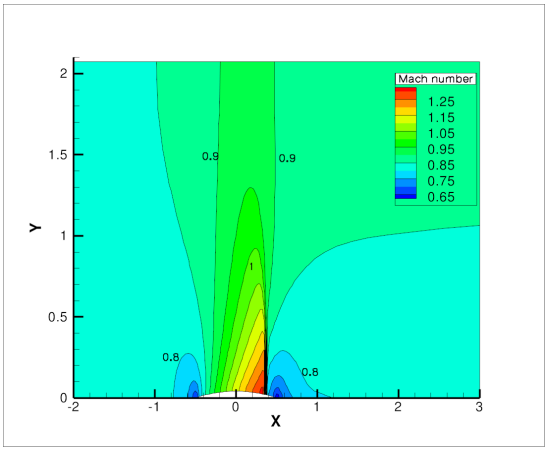

Figure 3: Mach contours for output isentropic Mach number of 0.85

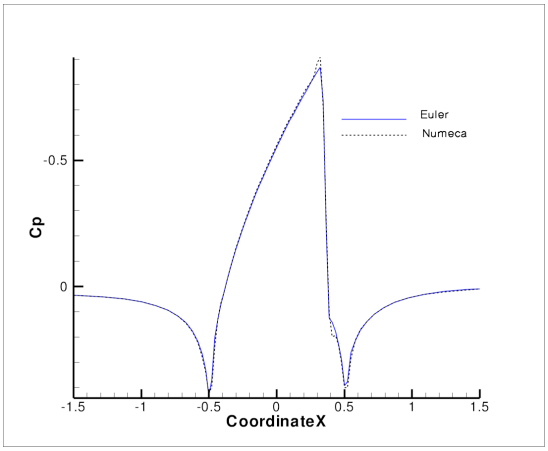

Figure 4: Cp distribution along the channel lower wall for different solvers (M2i=0.85)

For viscous turbulent cases the NGV LS89 [11] has been used for validation. Fig. 5 shows surface isentropic Mach number distribution of the turbine inlet guidance vane compared to experimental results.

4.2. *Performance Benchmark*

Once the accuracy of the solver is proved, a performance benchmark has been performed. The porting work aims at accelerating the execution time on realistic cases. A supersonic compressor cascade with a 7 blocks mesh has been chosen for performance comparison with CPU serial code. Table 1 shows the

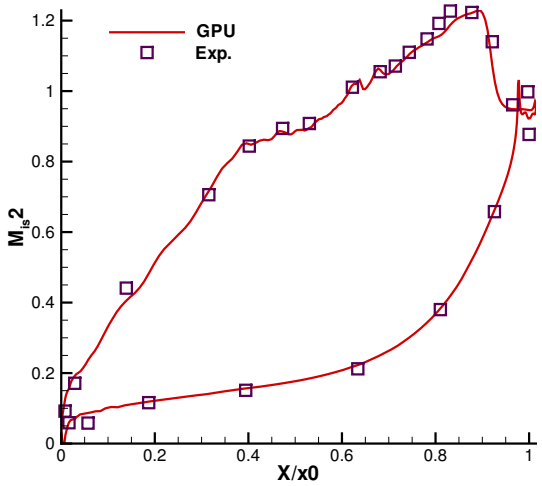

Figure 5: Computed and experimental distributions of isentropic Mach number on LS89 inlet guidance vane surface (M_{is}=1.02 P_{01}=1.605 bar)

speedup of 1 GPU over 1 CPU for different mesh resolutions. A higher mesh resolution presents more cells for every block and thus decreases the number of inactive threads advantaging the GPU over the CPU. The increase of the resolution improves the speedup until a maximal speedup is asymptotically approached. The mesh has reached a size, for which all threads are mapped to cells and the portion of inactive threads is reduced to a minimal.

Table 1: Speedup of Geforce GTX 780 over Xeon(R) CPU E3-1240v3 for different mesh resolution

N Cells	25 000	50 000	100 000	200 000
Speedup	5.96	7.44	9.49	10.9

Figure 7 shows the gain that pinned memory brings once used to store the solution array. Paged locked memory are directly copied to the GPU without being first copied into a temporary memory and then transferred to the device.

The concept of speedup summarize in a single number the performance of a GPU code compared to its CPU rival: $Speedup = \frac{T_{CPU}}{T_{GPU}}$. Fig. 8 shows the execution time of 5000 iteration on a compressor cascade on GPU and on 2 CPUs of different core frequency. The GPU is faster than both CPUs but the CPU with the highest frequency is faster than the other one. The characteristics of the reference CPU are very important for better understanding of given speedups.

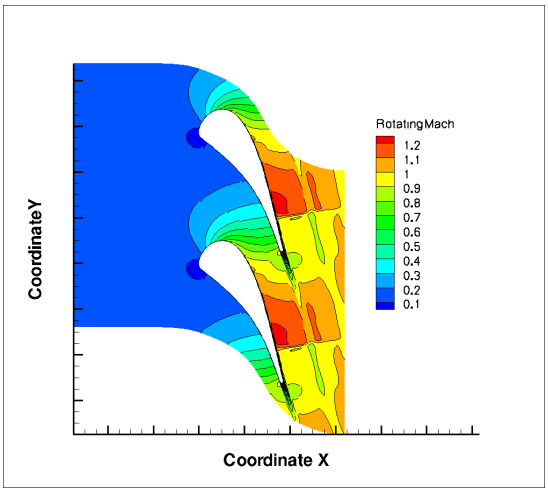

Figure 6: Mach contours of the transonic LS89 [11] turbine guide vane test case

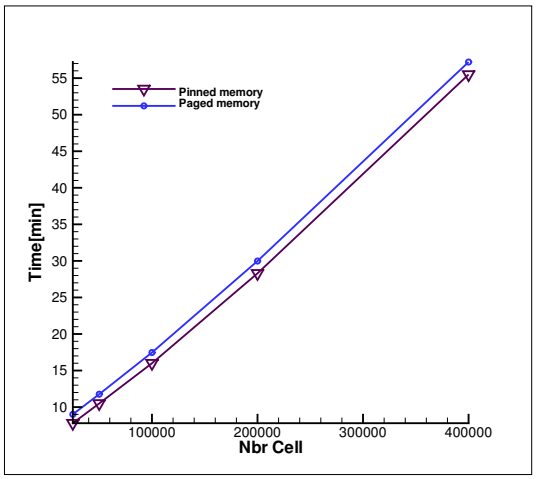

Figure 7: Effect of the use of pinned memory for the flow solution on the execution time

5. Conclusion

A GPU-accelerated RANS solved is presented. Validation and benchmark data are shown and commented. The explicit solver is by nature converging slow. Multigrid is used as additional acceleration techniques. Moreover, a porting of an implicit time integration is in progress.

Acknowledgments

This research activity is funded by a Marie Curie Action as part of the European union's Framework 7 research program (AMEDEO :Project No. 316394).

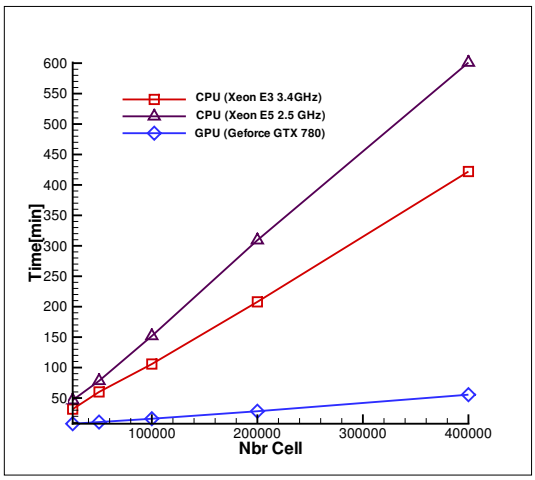

Figure 8: Comparison of the GPU execution time for 5000 iteration to the execution time of 2 CPUs of different frequency

This work is using the CPU-based Solver of Dipl.-Ing. Lasse Müller

References

[1] CAPS Enterprise, Cray Inc., NVIDIA, and the Portland Group., The OpenACC™ Application Programming Interface Version 2.0.

[2] Christgau, Steffen, et al., A comparison of CUDA and OpenACC: accelerating the tsunami simulation easywave, 27th International Conference on Architecture of Computing Systems (ARCS).

[3] J. Blazek, Computational Fluid Dynamics:Principles and Applications, Elsevier, 2001.

[4] J. R. Edwards and S. Chandra, Comparison of Eddy Viscosity-Transport Turbulence Models for Three-Dimensional, Shock-Separated Flowfields, AIAA Journal.

[5] Spalart P. R. and Allmaras S. R., A one-equation turbulence model for aerodynamic flows, AIAA-Paper 92-0439.

[6] Allmaras S. R., Johnson F. T. and Spalart P. R., Modifications and Clarifications for the Implementation of the Spalart-Allmaras Turbulence Model, ICCFD7-1902.

[7] R. P.L., Approximate riemann solvers, parameter vectors, and difference schemes., J. Computational Physics 43 (1981) pp. 357–372.

[8] B. Van Leer, Towards the ultimate conservative difference scheme v. a second order sequel to godunovs method., J. Computational Physics 32 (1979) pp. 101–136.

[9] V. Venkatakrishnan, Preconditioned conjugate gradient methods for the compressible navier-stokes equations., AIAA Journal 29 (1991) pp. 1092–1110.

[10] A. Rizzi and H. Viviand, Numerical Methods for the Computation of Inviscid Transonic Flows with Shock Waves, Notes on Numerical Fluid Mechanics (3).

[11] T. Arts, M. Lambert de Rouvroit and A.W. Rutherford, Aerothermal Investigation of a highly loaded transonic linear Turbine Guide Vane Cascade, TN 174, von Karman Institute for Fluid Dynamics (1990).

Multidisciplinary Optimization of Aero-Engine Fan Blades

Christopher Chahine

Turbomachinery and Propulsion Department, von Karman Institute for Fluid Dynamics, Belgium, christopher.chahine@vki.ac.be

Supervisor: Tom Verstraete

Associate Professor, Turbomachinery and Propulsion Department, von Karman Institute for Fluid Dynamics, Belgium, tom.verstraete@vki.ac.be

University Supervisor: Li He

Professor, Department of Engineering Science, University of Oxford, United Kingdom, li.he@eng.ox.ac.uk

Abstract

A multidisciplinary and multiobjective optimization of a transonic fan blade for a high bypass ratio turbofan engine is presented including aerodynamic as well as structural static and dynamic performance criteria. The optimization strategy applied is based on a two-level approach consisting of a Differential Evolution algorithm coupled to a Kriging metamodel in order to speed up the optimization process. High-fidelity performance evaluations are carried out by means of 3D Computational Fluid Dynamics and Computational Structural Mechanics analysis tools. Multiple key operating points are considered in the optimization process; aerodynamic performance is evaluated at top-of-climb and cruise conditions. Stresses are evaluated at take-off conditions, taking into account centrifugal and gas loads. Blade vibration is furthermore assessed over the entire operating range. Aerodynamic performance is separately evaluated for core and bypass flows in order to match the requirements specified by the engine cycle design.

Keywords: fan blade, multidisciplinary optimization, turbofan, bypass ratio

1. Introduction

In a modern high-bypass ratio turbofan engine the majority of the engine's thrust is generated by the fan, while only a small part (typically 10-20%) of the thrust is generated by the engine core. Hence, the main contribution to propulsive efficiency stems from the fan design with direct implications on specific fuel consumption (SFC) and overall engine efficiency. Besides the need to be aerodynamically efficient, fan blades are required to withstand considerable static and dynamic structural loads during operation. Their design is therefore a multidisciplinary problem which is further complicated by the fact that the involved disciplines have differing and often opposing requirements. In current industrial design practice, these disciplines are mostly handled separately from each other and the design progresses iteratively from one discipline to another until a satisfactory solution is found. The result is a time consuming and costly design process with the further disadvantage that interactions between disciplines are difficult to reveal. In contrast, this paper presents the application of a multidisciplinary and multiobjective optimization system to the design of a transonic fan blade for a typical modern high-bypass ratio turbofan engine. The optimization system enables the concurrent evaluation of aerodynamic and structural performance criteria, therefore facilitating the identification of the interaction of disciplines and allowing the design to progress towards global optimal solutions in a reduced design time.

2. Baseline design

Specified engine cycle requirements are the starting point for the fan blade design process. To enable a reasonable design space definition, a baseline design was generated using two-dimensional preliminary aerodynamic design tools based on first principles and corre-

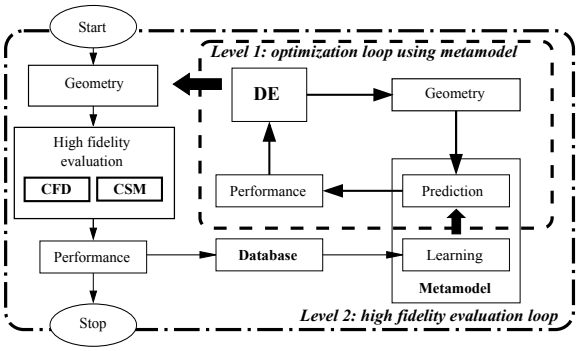

Figure 1: **FLOW CHART OF THE OPTIMIZATION SYSTEM.**

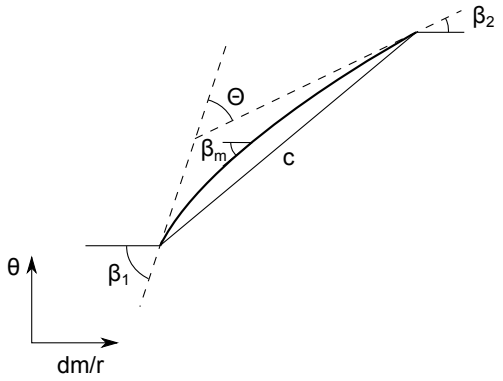

Figure 2: **CAMBER LINE DEFINITION.**

lations. The methods enable a reasonable estimation on required spanwise blade angle distributions and suitable profiles to be made. The obtained geometry was analyzed using CFD and slightly adjusted manually to meet the operating range requirements. However, not all aerodynamic specifications could be met at the end of this design stage.

3. Optimization system

A flow chart of the optimization system used in present work is shown in Fig. 1. At the core of the in-house developed system are a multi-objective Differential Evolution algorithm (DE) [1], a database, several metamodels, including Radial Basis Functions, Artificial Neural Networks and Kriging, and a high-fidelity evaluation chain including a fully automatic geometry and CAD generation, automatic meshing and high-fidelity performance evaluations by Computational Fluid Dynamics (CFD) and Computational Structural Mechanics (CSM). The optimization strategy is based on a two level approach with a Kriging metamodel being used in the present case. The first level comprises the DE optimization employed on the metamodel. On the second level, the best designs found based on the metamodel predictions are re-evaluated by the high-fidelity evaluation chain. This allows a direct feedback to be received on the metamodel accuracy in the promising regions of the design space. This additional information is stored in the database and is subsequently used to re-generate the metamodel in order to increase its accuracy. One iteration of the optimization system consists of an entire loop including DE optimization, high-fidelity evaluation and generation of the metamodel.

An initial sampling of the design space for the generation of the first metamodel is performed by a fractional factorial Design of Experiments (DOE) consisting of 128 samples, each being analyzed by the high-fidelity evaluation chain.

An in depth coverage on the optimization system and its components can be found in [2; 3; 4].

4. Fan blade parametrization

The camber surface of the fan blade is parametrized by spanwise parametric Bézier and B-Spline curves specifying the distributions of blade metal angles at the leading edge, trailing edge and an intermediate point as well as the chord length. Control points are defined on four spanwise positions which are being fixed for three of the points at 0, 50 and 100% span. The spanwise position of the fourth control point is added as an optimization parameter in order to allow additional control of the blade geometry close to the bypass splitter for all previously mentioned geometric quantities. Some of the control points are directly defined as optimization parameters, while others are defined via geometric dependencies to other control points (e.g. angles and distances). One example is the trailing edge blade angle β_2, which is indirectly defined via the leading edge blade angle β_1 and the camber angle Θ, as shown in a schematic camber line definition in Fig. 2. The chord length is modified by application of a scaling factor at each of the spanwise positions. Per default, blade sections are stacked radially along their respective center of gravity to avoid bending induced stresses in the blade, see Fig. 3. However, lean and sweep can be introduced to divert from a purely radial stacking in order to improve aerodynamic performance. There is no unique

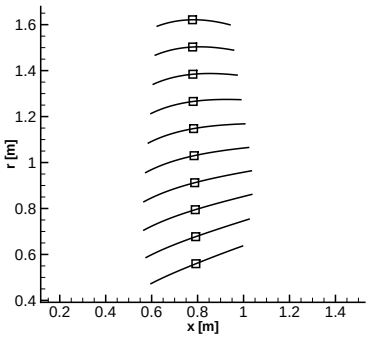

Figure 3: **RADIAL STACKING OF BLADE SECTIONS. SQUARES INDICATE THE CENTER OF GRAVITY OF EACH SECTION.**

definition of lean and sweep in the literature, but one of the most common definitions is applied here [5], shown in Fig. 4.

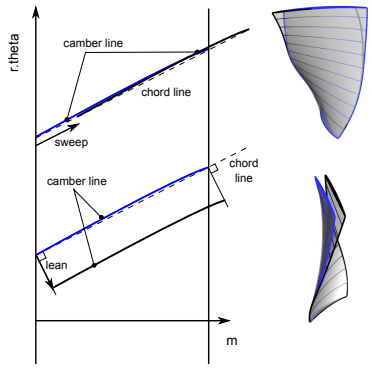

Figure 4: **LEAN AND SWEEP DEFINITION.**

Lean and sweep are both defined in length preserving $m-r\theta$ space, with m being the coordinate along the meridional streamsurface, r being the local streamsurface radius and θ the circumferential angle.

As shown in Fig. 4, sweep is defined as a translation of the camber line along the chord line, while lean defines a camber line translation normal to that direction.

A fourth-order Bézier curve is used for the definition of the spanwise distribution of sweep, as shown on the right hand side of Fig. 5. Arrows and angles indicate the optimization parameters. The tip section value of sweep is allowed to be modified directly. As for the camber surface definitions, the spanwise position of the second control point close to the hub is allowed to be changed as well. The sweep values of the intermediate control points are furthermore defined by the three angles α_1, α_2 and α_3. Lean is defined by a second-order Bézier curve with two optimization parameters as shown on the left hand side of Fig. 5. The baseline design has constant zero sweep and lean along the blade span.

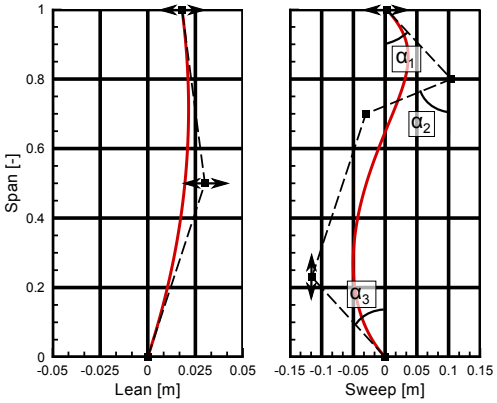

Figure 5: **LEAN AND SWEEP PARAMETRIZATION.**

The blade thicknesses at hub and tip sections are defined by B-Spline curves as shown in Fig. 6 and are designed based on [6]. Both distributions are allowed to be scaled independently by a uniform scaling factor, therefore allowing thickness changes without changing the actual distributions. The blade count is added as a last optimization parameter resulting in a total of 24 parameters in present case.

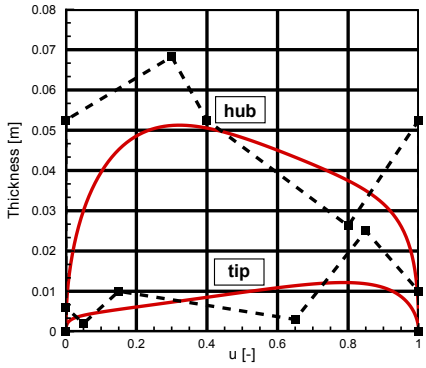

Figure 6: **THICKNESS PARAMETRIZATION.**

5. Aerodynamic performance evaluations

The aerodynamic performance of the fan blade is computed using the commercially available 3D Reynolds-Averaged Navier-Stokes solver FINE^{TM}/Turbo. The fluid domain is discretized using a multi-block structured mesh consisting of about 2 million grid points (average y+=3). Turbulence is modelled with the one-equation model of Spalart and Allmaras.

To meet the aerodynamic design and off-design targets originating from the engine cycle design, the fan blade's performance is evaluated at two key flight conditions, namely top-of-climb (ToC) and cruise. In total nine operating points are computed for each design, including four points on the ToC speedline and five points on the cruise speedline. An automatic convergence check is performed after each CFD computation to assess the mass flow error between domain inlet and outlet as well as the iteration errors of efficiency and pressure ratio. Only cases with sufficient convergence are subsequently assessed by an automatic postprocessing step, which extracts the required performance parameters needed by the optimizer, see Section 7. Non-converged cases are considered as failed and are automatically excluded from the optimization process.

The fluid domain of the fan blade including the bypass splitter is shown in Fig. 7. The fluid domain comprises one periodic section of the full annulus with periodic boundary conditions being applied at each side of the domain. Total pressure, total temperature, absolute inlet flow angle and turbulent kinematic viscosity are imposed as boundary conditions at the inlet. The low hub-to-tip radius ratio of the blade results in a transonic flow at all considered operating conditions

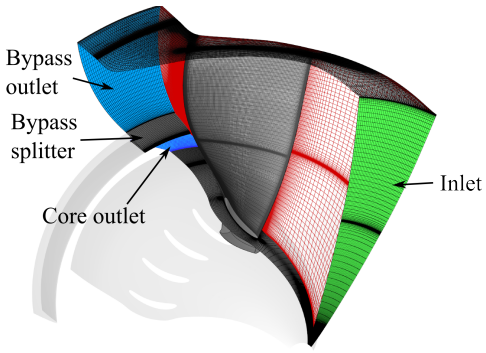

Figure 7: **FLUID DOMAIN OF THE BASELINE FAN BLADE.**

with the relative inlet flow to the blade being subsonic for the lower part of the blade extending to about 50 percent span and supersonic for the remaining part of the blade up to the blade tip. The flow at the subsonic root section (the portion of the blade feeding the engine core) is highly sensitive towards outlet pressure differences, requiring the mass flow to be imposed as the core outlet boundary condition in order to obtain a stable flow solution. In contrast, the static pressure is defined as boundary condition for the bypass outlet, with its spanwise variation being computed using the radial equilibrium law. Performance curves are computed by changing the bypass outlet static pressure.

6. Structural performance evaluations

The structural response of the fan blade including static stresses and vibrations is evaluated using the open-source finite element solver CalculiX [7]. An in-house unstructured meshing tool is applied to discretize the solid domain with quadratic tetrahedral elements, as shown in Fig. 8. The fan blade is modeled using material properties of Titanium (Ti-6Al-4V).

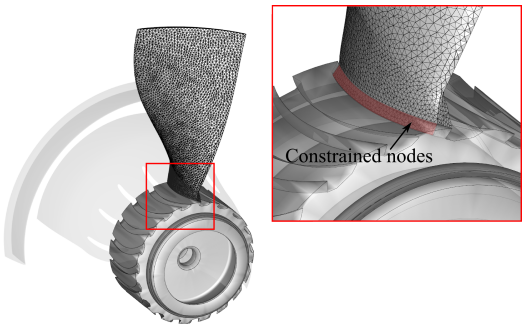

Figure 8: **SOLID MESH OF THE BASELINE FAN BLADE AND ITS RESTRAINT IN A TYPICAL DISK. THE NODES ON THE UPPER DOVETAIL ROOT SURFACE SHOWN IN RED ARE FIXED IN ALL DEGREES OF FREEDOM TO SIMULATE THE DISK ATTACHMENT (OPPOSITE CONSTRAINED SURFACE NOT VISIBLE).**

6.1. Structural static performance evaluations

A static finite element computation including geometric non-linear effects is performed to evaluate the static stresses in the fan blade. The computation is performed at take-off conditions, where both aerodynamic and centrifugal loads are at their peak values throughout the mission. The blade is subjected to centrifugal and gas loads whereas the gas loads are

extracted from the converged take-off CFD computation of the baseline geometry and interpolated onto the FEM grid.

6.2. *Structural dynamic performance evaluations*

Additionally to the structural static evaluation, fan blade vibration is assessed at all previously mentioned key operating points: take-off, top-of-climb and cruise in order to assess the risk of high cycle fatigue failure. Natural frequencies of the fan blade are determined by means of modal analysis. A geometric non-linear static pre-stressing computation is performed prior to each modal analysis to take into account the non-linear effect of centrifugal forces on the blade stiffness at different rotational speeds. The Campbell diagram is used to compute the margins between excitation frequencies and blade natural frequencies at the rotational speeds associated with the aforementioned operating points. Excitations from one-per-revolution and two-per-revolution disturbances are considered covering possible sources like unbalance and inlet flow distortion due to cross-wind.

7. Objectives and constraints

The optimization problem is composed of two objectives and a total of twelve aerodynamic and structural constraints. The first objective is the peak efficiency at cruise rotational speed, while the second objective is the stall margin of the fan blade. Both objectives are to be maximized, but are translated to an equivalent minimization problem which is formally stated as

$$Obj_1 = -\eta_{cruise,peak} \tag{1}$$

$$Obj_2 = -\left(\frac{\dot{m}_{cruise,design} - \dot{m}_{cruise,stall}}{\dot{m}_{cruise,stall}}\right) \tag{2}$$

where $\eta_{cruise,peak}$ is the isentropic total-to-total peak efficiency of the blade at cruise rotational speed, $\dot{m}_{cruise,design}$ is the cruise design point mass flow and $\dot{m}_{cruise,stall}$ is the mass flow of the last converged CFD computation towards the stall limit of the blade, see Fig. 9.

Four constraints are imposed to ensure that the operating range of the fan matches the engine cycle design requirements at cruise and top-of-climb. A top-of-climb evaluation point with a 6 % stall margin with respect to the total pressure ratio is defined as shown in Fig. 9. This is the operating point where the required total pressure ratio is the highest throughout

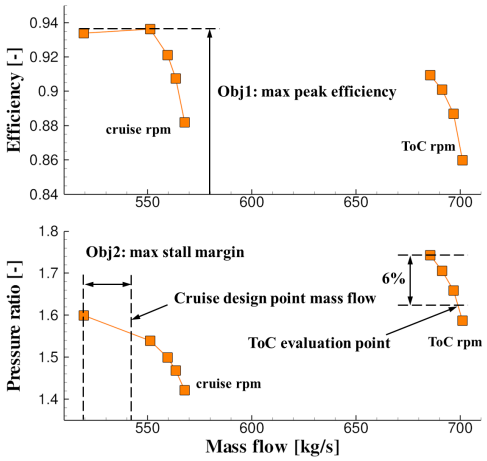

Figure 9: **DEFINITION OF OBJECTIVES AND THE TOP-OF-CLIMB EVALUATION POINT.**

the mission. Two constraints are therefore defined to ensure that the pressure ratios for core and bypass flows are not lower than the design requirements, which are defined as 1.7 for the bypass and 1.4 for the core flow. Additionally, the maximum absolute inlet Mach numbers and the maximum absolute flow angles at the bypass and core inlet are restricted to ensure that the stators located further downstream (outlet guide vane in the bypass and engine section stator in the core) receive a healthy inlet flow and performance improvements of the fan blade are not obtained at the cost of overall stage performance. The limits are set to a maximum Mach number of 0.9 and a maximum flow angle of 70 degrees measured with respect to the meridional plane. Maximum von Mises stresses in the fan blade are required to be lower than 800 MPa, leaving a 130 MPa dynamic stress margin towards the yield stress of the titanium alloy. Blade vibration is assessed at cruise, top-of-climb and take-off. A minimum required frequency margin between the first bending mode of the blade and the first harmonics of a one and two per revolution excitation are defined as constraint.

8. Results

The optimization was run for 20 iterations, which equals a total of 290 high fidelity performance evaluations. The corresponding objective space is shown in Fig. 10, where each symbol represents one design analyzed by the high fidelity evaluation chain. Improved performance is obtained towards the lower left

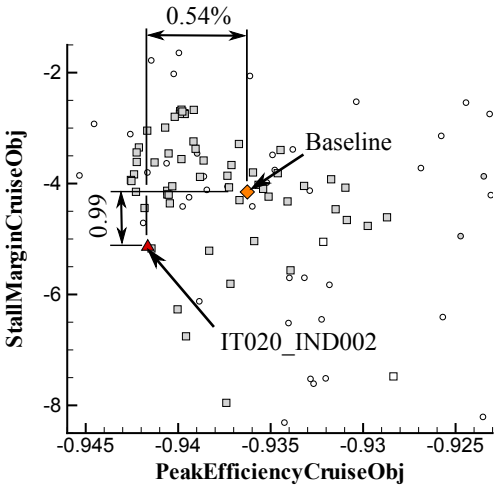

Figure 10: **OBJECTIVE SPACE AFTER 20 ITERATIONS. CIRCLES INDICATE DOE SAMPLES WHILE SQUARES INDICATE DESIGNS GENERATED DURING THE OPTIMIZATION. DESIGNS SATISFYING THE CONSTRAINTS ARE SHOWN WITH GREY FILLING.**

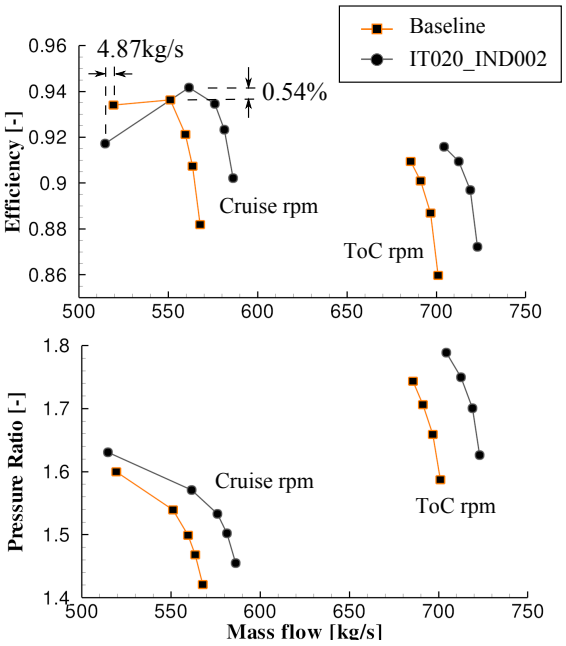

Figure 11: **PERFORMANCE MAP.**

corner of the objective space, as both objectives need to be minimized. For visualization purposes the plot in Fig. 10 was scaled to show the set of feasible designs which are shaded in gray, therefore not all DOE samples are visible. The baseline design is shown as orange diamond to provide a reference, although it has to be stressed that the baseline design violates multiple constraints and as such is not part of the feasible set of designs. However, the baseline design acted as the starting point for the definition of the design space and is therefore still a valuable sample to consider in order to assess the performance of the optimization system. Due to the high number of aerodynamic and structural constraints only three samples in the DOE database were feasible. Thus the initial challenge for the optimizer was the identification of the feasible region in the design space, which is coupled with the need for the generation of metamodels with sufficient prediction accuracy. About ten iterations were needed until all involved metamodels reached the required level of accuracy therefore allowing the Differential Evolution algorithm to find feasible designs with improved objective function values. After 20 iterations the optimizer made considerable progress with respect to both objectives. A Pareto front is clearly identifiable in Fig. 10, showing the trade-off between peak efficiency and stall margin. As such, it is the task of the designer to choose a design from the Pareto front that best fulfills the design requirements. Here, a choice was made with a higher importance on the efficiency improvement, at the cost of only a slight improvement of stall margin. The chosen design was generated in the 20th iteration and is labeled as IT020_IND002 in Fig. 10. An efficiency improvement of 0.54 % and a stall margin improvement of 0.99 were obtained with respect to the baseline design.

A more detailed view on the global aerodynamic performances of the baseline design and IT020_IND002 is obtained from Fig. 11, where the performance maps of both designs are shown. The improvement of efficiency and stall margin are readily visible and are indicated on the cruise efficiency curves, but it is important to note that the baseline design did not satisfy the pressure ratio constraints for the bypass and core flow. An overall increase of the pressure ratio was needed to reach the required pressure levels. As such, IT020_IND002 has both a higher pressure ratio and a higher peak efficiency while the stall margin did not change significantly.

Also in terms of structural performance, the baseline design showed constraint violations, which mainly originated from the fact that it was solely designed based on aerodynamic considerations. A comparison of the von Mises stress distributions on the suction side surfaces of the baseline design and

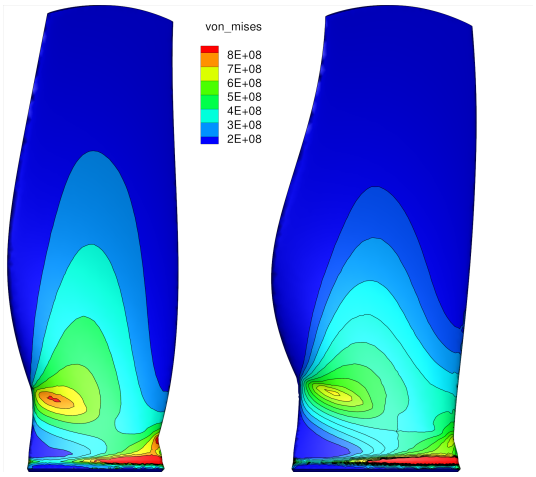

Figure 12: **VON MISES STRESS DISTRIBUTION ON THE SUCTION SURFACES OF THE BASELINE DESIGN (LEFT) AND IT020_IND002 (RIGHT).**

IT020_IND002 is shown in Fig. 12. Stresses exceeding the allowed static stresses of the titanium alloy are located at the connection of the airfoil section and the shank surfaces at the leading edge of the blade and close to the trailing edge at about 80 percent chord. As shown on the right hand side of Fig. 12, the stresses in these regions were successfully reduced towards the allowed levels in IT020_IND002. The high stress values directly on the dovetail root are originating from the fixed nodes which are set as boundary

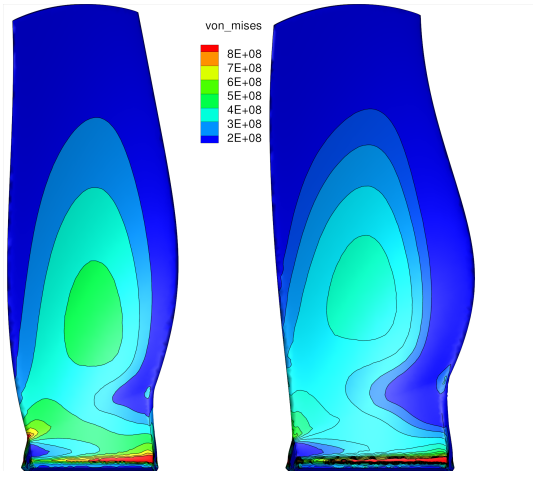

Figure 13: **VON MISES STRESS DISTRIBUTION ON THE PRESSURE SURFACES OF THE BASELINE DESIGN (LEFT) AND IT020_IND002 (RIGHT).**

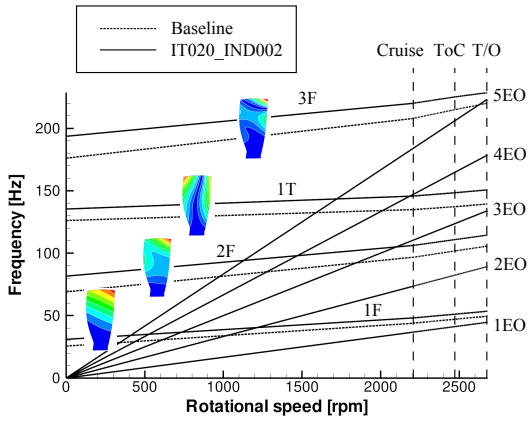

Figure 14: **CAMPBELL DIAGRAM.**

conditions in the finite element computation. In reality the dovetail root is in contact with the disk allowing small movements of the surfaces relative to each other. Fixing the nodes therefore artificially increases the stresses in these areas. For that reason, these stresses are not taken into account in the post-processing step. The corresponding stressed on the pressure side surfaces are shown in Fig. 13.

The vibration characteristics of baseline design and IT020_IND002 are shown in the Campbell diagram plotted in Fig. 14. The eigenfrequencies of the first four eigenmodes are plotted for both designs and the operating speeds at cruise, top-of-climb and take-off are separately indicated. Excitation from the first five engine orders is shown. A dangerously low frequency margin exists between the eigenfrequency of the first bending mode (1F) of the baseline design and the first engine order at take-off rotational speed. To raise this margin above the constraint value the optimizer increased the stiffness of the blade resulting in globally higher eigenfrequencies for IT020_IND002. The second engine order, which represent the first harmonic of a two per revolution excitation, is not critical.

9. Conclusions

The application of a multidisciplinary and multiobjective optimization system to the design of an aero-engine fan blade for a modern high-bypass ratio turbofan engine was presented. A particular novelty in this work was the consideration of the bypass splitter in the fluid domain, therefore allowing the core and bypass flow requirements from the engine cycle design to be directly included in the optimization process. Aerodynamic and structural performance was

considered at multiple key operating points, including cruise, top-of-climb and take-off.

The baseline design in this work was generated solely based on aerodynamic considerations. However, it was not attempted to satisfy all aerodynamic requirements in the manual aerodynamic design step. This task was purposefully left to the optimization system, which was fulfilled flawlessly. The optimizer successfully identified the feasible region in the design space after 10 iterations (210 high fidelity evaluations) and subsequently improved both objectives until the optimization was stopped after 20 iterations. The final design chosen from the Pareto front has a peak efficiency improvement of 0.54 % and a slight stall margin improvement of 0.99 with respect to the baseline design while satisfying all imposed structural and aerodynamic constraints.

For further considerations, the mass flow requirements for both cruise and top-of-climb might be taken into account as a third objective. In addition, the substitution of the titanium alloy with a composite material is currently underway.

Acknowledgments

The research leading to these results has received funding from the European Union Seventh Framework Programme (FP7/2007-2013) under grant agreement no [316394].

References

[1] R. Storn, K. Price, Differential Evolution - A simple and efficient adaptive scheme for global optimization over continuous spaces, Journal of Global Optimization 11 (4) (1997) 341–359.

[2] T. Verstraete, CADO : a Computer Aided Design and Optimization Tool for Turbomachinery Applications, in: 2nd International Conference on Engineering Optimization, Lisbon, Portugal, 2010.

[3] T. Verstraete, Introduction to Optimization and Multidiciplinary Design, in: Introduction to Optimization and Multidisciplinary Design in Aeronautics and Turbomachinery, no. VKI LS 2010-07, Von Karman Institute for Fluid Dynamics, Rhode-Saint-Genese, 2010.

[4] T. Verstraete, Multidisciplinary Optimization of Turbomachinery Components using Differential Evolution, in: Introduction to Optimization and Multidisciplinary Design in Aeronautics and Turbomachinery, no. VKI LS 2010-07, Von Karman Institute for Fluid Dynamics, Rhode-Saint-Genese, 2010.

[5] J. D. Denton, The effects of lean and sweep on transonic fan performance: a computational study, in: ASME Turbo Expo 2002: Power for Land, Sea and Air, American Society of Mechanical Engineers, Amsterdam, 2002. doi:10.1115/GT2002-30327.

[6] A. Wennerstrom, Design of Highly Loaded Axial Flow Fans and Compressors, Concepts ETI, 2001.

[7] G. Dhondt, CalculiX CrunchiX USER S MANUAL version 2.5 (2012).

Turbine Tip Flow Optimization for Modern Aero-Engines

Cis De Maesschalck

Turbomachinery and Propulsion, von Karman Institute for Fluid Dynamics, Belgium, cis.demaesschalck@vki.ac.be

Guillermo Paniagua

Adjunct Professor, Aeronautics and Aerospace Department, von Karman Institute for Fluid Dynamics, Belgium, gpaniagua@me.com

Associate Professor, Department of Mechanical Engineering, Purdue University, United States

University Supervisor: Chris Lacor

Professor, Faculty of Applied Sciences, Department of Mechanical Engineering, Vrije Universiteit Brussel, chris.lacor@vub.ac.be

Abstract

Superior rotor tip geometries possess the potential to simultaneously mitigate aerodynamic losses and severe thermal loads onto the rotor overtip region. However, classical design strategies are usually constrained to a specific type of geometry, narrowing the spread of shape topologies considered during the design phase. The current paper presents two novel multi-objective optimization methodologies that enable the exploration of a broad range of distinct tip configurations for unshrouded rotor blades.
The first methodology is a shape optimization process that investigates fully carved blade tip geometries, applied at two tip gap sizes: 0.85% (tight) and 1.38% (design) of the blade span. The second methodology is based on a topology optimization process that targets the creation of arbitrary tip shapes comprising one or multiple rims with a fixed height. The current numerical study was carried out on a modern high-pressure turbine operating at engine-like Reynolds and high subsonic outlet Mach numbers. Adopting RANS simulations on fully hexahedral unstructured meshes, 4 multi-objective optimizations were run targeting higher aerodynamic rotor efficiencies and simultaneous minimization of the heat load.
Additionally, the design of an experimental campaign in the transient turbine facility of the von Karman Institute is presented, capable of testing simultaneously 7 distinct turbine blade tip profiles and validating the performance improvements predicted through the numerical optimization.
This paper illustrates the potential of the novel optimization methodologies to reach a wide variety of new, unexplored types of blade tip designs with enhanced aerothermal performances and presents how these performances will be accurately assessed through an extensive experimental campaign.

Keywords: high pressure turbine, tip leakage flow, design optimization

1. Introduction

Despite the developments during the last decades in the turbine hot-gas path, the overtip leakage flow still remains the primary factor defining the machine durability for the periodic removal of the turbine components during overhaul [1]. Hence, the design of the rotor tip region is a crucial challenge to any turbine designer. Subjected to temperatures far above the metal creep temperature, severe thermal stresses are generated inside the blade material and an adequate design of both the aerodynamic shape as well as the complex cooling configurations is essential to avoid an early blade failure. Additionally, the tip leakage vortex causes a significant loss in rotor efficiency and generates considerable flow non-uniformities travelling towards the downstream turbine stage.
In unshrouded rotors, many different tip concepts have been proposed to reduce the detrimental effects of the overtip leakage flow: tight running flat tip designs, contoured shapes, squealer and even winglet designs. An extensive review of the performance of flat tips in

a high pressure turbine environment was reported by Bunker [2]. A multitude of numerical and experimental investigations [3, 4] confirm the existence of a separation bubble near the pressure side (PS), establishing an effective vena contracta that limits the massflow travelling from the PS to suction side (SS). In order to limit further the overtip fluid spillage, squealer tip designs are commonly used nowadays in high-pressure turbines, featuring a single cavity surrounded by a thin rim that contracts the flow twice across the overtip passage. Additionally, the rim forces the entrained fluid inside the cavity to turn into the direction of the main flow resulting in a delayed jet exit compared to a flat tip design [5, 6]. Another method employs PS and SS overhangs to reduce the pressure differential that drives the overtip flow [7, 8]. The winglet design induces aerodynamic losses similar to shrouded configurations with two fins, but induces much larger heat transfer than in a flat tip.

With increasing turbine blade loading, the gap flow gets choked and reaches supersonic velocities. Hence, the overtip pressure loading may be decoupled from the leakage massflow and the subsequent loss generation [9], which offers the possibility to further increase the work extraction at the tip section while preserving similar aerodynamic performance. Anticipating this observation, researchers investigated smoothly contoured or 'carved' designs, attempting to reduce further the heat transfer through a continuous acceleration all over the tip channel. Shyam and Ameri assessed the performance of such designs using a simplified quasi-2D approach [10] and Zhang and He proposed a fully 3D contoured tip shape to promote choking in the front section of the blade [11]. Investigations by the authors, both in 2D [12] and applied in 3D [13] showed the potential for a significant heat flux reduction in highly loaded blade tip configurations.

Although the optimization of the main blade shape by means of evolutionary algorithms is becoming the prevalent practice [14], a holistic approach has not been yet extended to the tip geometry to cover a wide range of geometry configurations. While typical shape optimization methods are mostly confined to one specific type of geometry only (e.g. a fixed amount of cavities, etc), topology optimization strategies offer the potential to obtain a broad range of completely different geometry configurations during one single optimization. Moreover, a proper choice of the shape parametrization, vital for the success of conventional optimization methodologies, often requires prior knowledge of the actual physical phenomena to be modeled which is rarely available. The topology optimization technique, well established for treating structural design problems [15], divides the design space into discrete 'blocks' that can be either part of the fluid or solid domain. Topology optimization methods overcome the limitations entailed with conventional optimization approaches and enabling the generation of novel unconventional and non-intuitive designs. Although seldom applied to fluid machinery design, the topology optimization technique has already shown promising results in a number of alternative applications (e.g. cars [16], microfluidic mixers [17] or complex duct flows [18]).

The current paper presents the performance of two distinct novel strategies. A first shape parametrization encompassed a wide variety of fully contoured shapes while the second one can cover every possible rim-cavity layout using a topology optimization approach. This research simulated in total over 1500 diverse blade tip profiles comprising several designs that could never be found otherwise. This paper presents the combined Pareto fronts and outlines the aerothermal trends associated with the different types of turbine tip profiles. Additionally, a description of the experiments design is presented that will validate the predicted performances.

2. Numerical Optimization

2.1. Computational methodology

The investigated rotor is part of a modern high pressure turbine stage, operating at a Reynolds number of 2.4 x 10^5 and a exit relative Mach number ($M_{r,exit}$) of 0.73. Relevant specifications of the rotor blade are given in Table 1.

Table 1: Turbine specifications

Parameter	
Reynolds number (rotor outlet and C_{ax})	$2.4x10^5$
Exit Relative Mach number ($M_{r,exit}$)	0.73
Blade count	48
Non Dimensional Speed ($RPM/\sqrt{T_{tot,a,in}}$)	281
Tip gap - Design (% span)	1.38%
Tip gap - Tight (% span)	0.85%
Rotor pressure ratio ($P_{tot,a,in}/P_{s,out}$)	2.2
$T_{tot,a,gas}/T_w$	1.47
$T_{tot,r,gas}/T_w$	1.33

A periodic section of the blade row is modeled while only the top 6% of the rotor span is allowed

to change shape (Fig. 1). The simulated geometry is divided into 2 subdomains: one 'downblock' that does not change during the optimization and an 'upperblock' that is meshed according to the requirements of the particular tip design under consideration. For the current optimization, an uncooled geometry was considered. However, the dimensions of the tip parameterized features were constrained based on real-engine manufacturing capabilities, minimum requirements for mechanical strength and demands for the installation of coolant holes in a later design stage.

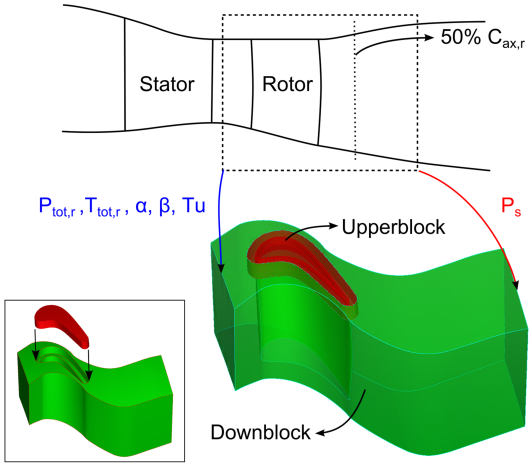

Figure 1: Computational domain

A full hexahedral mesh is subsequently generated by means of Numeca Hexpress, separately for down- and upper-blocks. A thorough grid sensitivity analysis has been conducted in order to assess the optimal mesh properties that were then applied to all the geometries generated during the optimization. The simulations for the sensitivity study were performed by increasing the mesh density isotropically for one of the blocks while keeping the same grid resolution in the other one. Fig. 2a presents the influence of the grid density on the efficiency for a single squealer configuration. The lower and left axis of Fig. 2a and Fig. 2b refer to the down-block refinement (blue curves with square labels), while the right and upper axis define the upperblock mesh resolution (red curves with circular labels). One can observe that refining the upperblock beyond 2 million cells does not improve the estimation. However, grid refinement of the downblock reveals a clear asymptotic trend. It is important to note that all the profiles are evaluated with the same downblock mesh in the optimization loop. Hence, the same efficiency offset associated with the downblock grid will equally affect each tip configuration, ensuring a valid comparison among different profiles. Fig. 2b illustrates the influence of the discretization levels for both blocks on the tip heat transfer (compared to the finest grid solution) in the case of three tip arrangements: a flat tip, a single squealer and a complex squealer configuration. Refinement of the downblock (with simple squealer) does not provide significant variations in the tip heat transfer ($\Delta Q_{tip} < 1\%$). On the contrary, the tip heat transfer is more sensitive to the upperblock mesh resolution as can be expected. However, the error between the finest and the 2nd finest grids remains relatively small, below 1.5% for every investigated tip shape.

Based on the outcome of the grid-dependency study, the computational domain was meshed using the grid settings of the 2nd finest grid: the downblock mesh counts about 6 million cells while the upperblock can contain between 1.5 up to 3 million cells, depending on the specific tip design. The main passage includes over 140 spanwise divisions and a minimum of 40 grid points inside the tip gap. These mesh settings are comparable to values used in previous numerical investigations where a satisfactory resolution of the tip flow region was obtained [19, 20]. The first cell size was set such that the y^+ values remain below 0.2 along all solid surfaces to accurately resolve the complete aerothermal boundary layer.

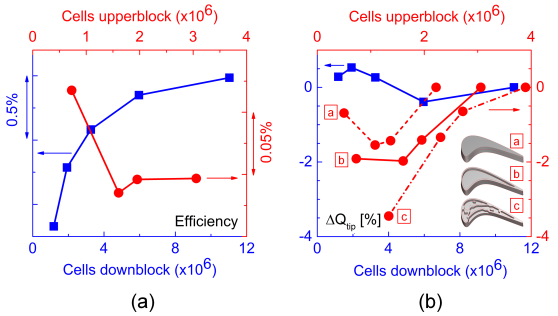

Figure 2: Grid sensitivity analysis: a) effect on rotor efficiency, b) effect on tip hat transfer.

The steady-state RANS simulations were performed by means of Numeca Fine/OPEN using the k-ω SST model for the turbulence closure [21]. This turbulence model has been demonstrated to be suitable for obtaining accurate aerothermal simulations in the case of transonic overtip flows [20]. An experimental validation of the solver capability to predict the aerothermal field in a high-pressure turbine environment can be found in [13]. In the latter study,

a good agreement was found for the rotor isentropic Mach number and Nusselt number distributions comparing the experimental data with the numerical predictions performed on a similar turbine stage using the same solver (Numeca Fine/OPEN), turbulence model and grid resolution.
In order to simulate correctly the tip flow problem [22], pitchwise-averaged radial profiles of relative total pressure, total temperature, flow angles and turbulent quantities were extracted from the NGV exit plane of a full stage calculation (see Fig. 1) and imposed at the rotor inlet. At the domain exit, the static pressure was set to satisfy the radial equilibrium for a total to static pressure ratio of 2.20. The solid walls were isothermal in order to retrieve the heat flux at an engine representative gas to wall temperature ratio of about 1.5.

2.2. *Parametrization and geometry generation*

Two distinct parametrizations were developed during this investigation, each targeting a different type of profiles. The first parametrization creates smoothly carved blade tip surfaces using a shape optimization methodology, while the second parametrization encompasses squealer-like tip designs by means of a topology-like strategy.

Carved tip designs.. The parametrization for the carved tip optimization aims to cover a wide range of smoothly contoured tip profiles. The full procedure is illustrated in Fig. 3 and consists of a general rectangular Bezier control surface, which is mapped onto the tip profiles. The tip surface is discretized in 8 predefined sections along the rotor camberline where the tip contouring can be adjusted separately by means of 6 control points, equally spaced from PS to SS (Fig. 3). In this way, a rectangular Bezier surface is constructed through 48 control points (6 x 8) that set the radius evolution over the complete tip surface. Each control point is a design variable for the optimization and can take a value ranging from 0, when located at the maximum deformation depth, up to 1, when the point reaches the minimum tip clearance. To reduce the amount of design variables and to ensure the tip manufacturability, the profiles of the leading edge (LE) and trailing edge (TE) sections are forced to lie on a straight line and their definition only requires 4 (2 x 2) design variables. In this way, the shape parametrization counts a total of 40 design parameters. By means of Matlab, the rectangular Bezier surface is subsequently mapped onto an auxiliary surface that extends slightly beyond the tip contour (see Fig. 3, bottom left). Eventually, the blade is cut with the generated surface resulting in the final contoured tip shape (through Numeca IGG and Gambit). The maximum deformation depth was set to 5.6% of the blade span (about four times the design tip clearance). This range was judged sufficient to allow for a significant influence on the overtip flow field with a minimum deformation of the overall blade profile. Moreover, the use of such a Bezier surface guarantees that the final surface will not exceed the minimum clearance nor deform the profile outside the prescribed deformation region.

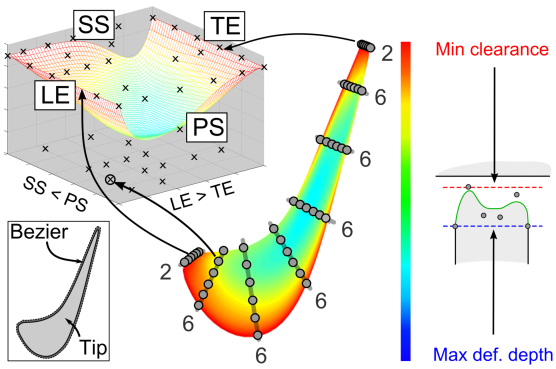

Figure 3: Illustration of the carved tip parametrization.

Squealer-like tip designs.. [23] This type of tip parametrization is inspired by a topology-based optimization rather than a pure shape optimization. The goal of the parametrization is to enable the creation of a very wide range of squealer-like designs, which shall consist of an arbitrary amount of rims which separate one or multiple cavities. Hence, the tip surface has been divided in about 200 different blocks (see Fig. 4a). Each block can be either up (and so it becomes part of a rim) or down (which makes it part of a cavity floor), Fig. 4b. The minimum dimensions of the blocks are set based on real-engine manufacturing capabilities and requirements dictated by the mechanical strength and coolability. The cavity depth was set to 4.5% of the blade span, about three times the design tip clearance. The reference squealer design adopts one single rim along the tip outer profile with a thickness of about 2% of the blade span. The real blade tip corner radius was not modeled and all the rim blocks were defined with sharp edges in the CFD geometry.

In order to define whether a certain block is set up or down, two different approaches were used: The **binary approach** uses a binary string that defines the position of every block separately (Fig. 5). Since the

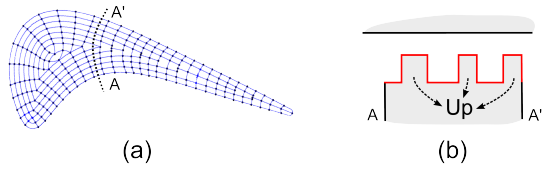

Figure 4: Illustration of the carved tip parametrization.

binary string contains about 200 elements there will be an equal amount of design variables.
In an attempt to reduce the number of optimization parameters and exclude non-relevant configurations, a **level-set approach** [24] was implemented. This methodology is illustrated in the top side of Fig. 5.

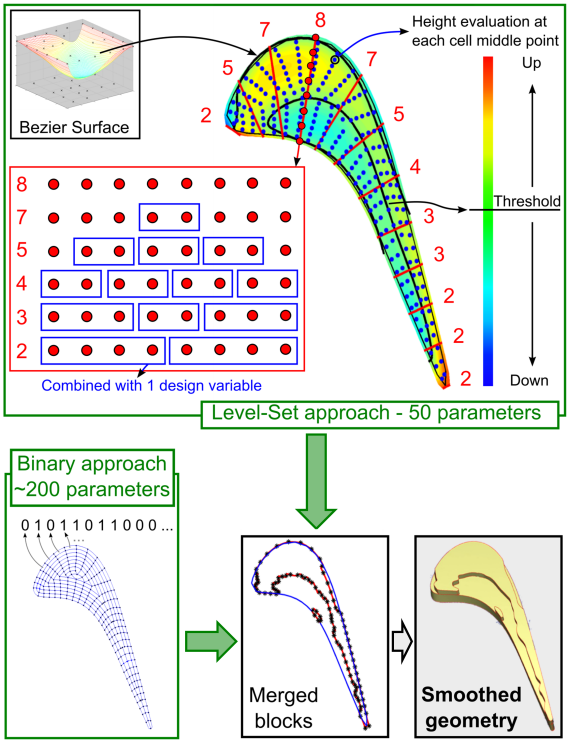

Figure 5: Binary and level-set approach for the squealer-like optimization.

Similarly to what is done in the carved shape parametrization, the procedure starts from a general Bezier surface which is mapped onto the tip. The surface is built based on 12 sections disposed along the rotor camberline where the shape evolution from PS to SS is defined through a maximum of 8 equally spaced design parameters (8 x 12 = 96 parameters varying from 0 to 1). To discriminate whether a block is up or down, the mapped Bezier surface is evaluated at the center of every cell (Fig. 5, blue dots). If this value is higher than a chosen threshold (in this case the threshold is set at 0.5), the block is set to be 'up'. In the case the value is below the threshold, the considered block becomes part of the cavity floor. In general, 8 design parameters are not always necessary to define the contour from PS to SS in all the tip sections along the chord. For very thin sections of the rotor blade (e.g. the aft part of the blade), some of the Bezier control points are combined together with one design variable. The amount of design variables is reported in Fig. 5 next to each section. The strategy used to combine the control points is demonstrated in the top-left side of Fig. 5. For example, in the case the section is defined by only 5 design parameters (instead of all 8 required for a 8 x 12 Bezier surface), one variable is attributed to each of the two outer control points. The other control points are combined two-by-two, and the height of each duo is set equally through one design parameter. In case for example only 2 design variables describe the section (e.g. the last three sections near the TE), the first four control points take the value of the first design variable while the last 4 control points adopt the height set by a second design parameter. This approach brings the total amount of required design variables for the level-set approach down from 96 to 50.
Once the position of each of the blocks is established, the upstanding blocks are merged through a Matlab script and the edges of each of the rims are identified (Fig. 5). For each cell at the border of a rim, the middle point on its edge is exported and a B-Spline interpolation generates the smoothed rim sides (performed through Numeca IGG). Eventually, the rim volumes are created and merged with the rest of the blade geometry to compose the solid domain which is consequently cut away from the upperblock to define the fluid domain (using the commercial softwares Gambit and Numeca Hexpress).

2.3. Optimization methodology

The current study comprises a multi-objective optimization that aims at the reduction of the rotor tip thermal loads and the concurrent improvement of the rotor efficiency.
The heat transfer objective parameter is defined as the heat transfer integrated over the entire rotor surface exposed to the tip deformation (red area in Fig.5b). Although the tip design also affects the heat transfer distribution on other relevant regions of the rotor blade (pressure and suction side, shroud), only the tip heat

load was considered as the optimization objective being the tip the most critical area to refrigerate in a turbine blade. In order to provide an accurate assessment of the rotor heat transfer performances, the heat flux magnitude and distribution were also determined on all the other rotor surfaces and results are discussed in the paper.
The second objective parameter which lumps up the aero-dynamic performances is the rotor efficiency evaluated according to:

$$\eta = \frac{T\omega}{\dot{m}C_p T_{tot,in}\left[1 - \left(\frac{P_{tot,exit}}{P_{tot,in}}\right)^{\frac{\gamma-1}{\gamma}}\right]} \quad (1)$$

Fig. 6 presents a general overview of the methodology for the three types of optimizations that have been conducted: the carved tip optimization, the squealer-like optimization with the Binary approach and finally with the Level-Set approach. An optimizer (Fig. 6, top) is coupled to the evaluation routine (Fig. 6, bottom) which handles the sequence from the CAD generation through the meshing, the flow solving and the data post-treatment.
The optimization routines are part of an in-house developed code of the von Karman Institute, specifically designed for the enhancement of turbomachinery components [25, 26]. The optimization strategies all use the concept of Evolutionary Algorithms (EA), created in the sixties by J. Holland [27] and I. Rechenberg [28]. These algorithms are based on the theory of Darwinian evolution where populations of individuals evolve inside a design space and adapt to the imposed environment through the use of several mechanisms such as crossover, mutation and selection. Individuals with an enhanced 'fitness' will have a larger probability to survive, get reproduced and to be part of the final Pareto front of optimal solutions (e.g. Fig. 9).

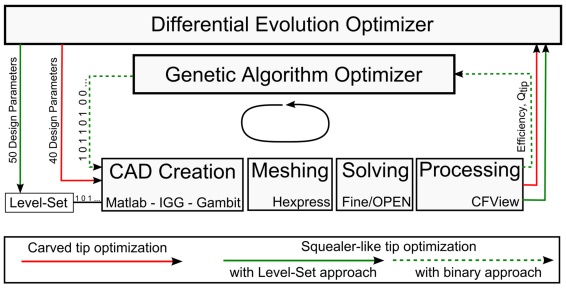

Figure 6: Flow-chart of the optimization methodology.

In this case, a multi-objective optimization is considered, targeting simultaneously a maximization of the efficiency and a minimization of the tip heat transfer. The way both optimizers (Differential Evolution (DE) and Genetic Algorithm (GA) Optimizer) treat the multiple objectives is common and has been implemented based on the NSGA-II routine originally presented by Deb et al. [29]. The difference however originates from the type of design variables: Genetic Algorithms use a binary string while Differential Evolution uses real numbers bounded by a lower and an upper limit [30].
The optimization starts typically with an evaluation of the performance of the profiles from an initial database, the DoE ('Design of Experiments'). For the current investigation, a fractional factorial approach [31] was used to select the subset of the design space to be evaluated during the DoE. Subsequently the tip profiles are ranked and the prime geometries constitute the first population. Based on the process of crossover and mutation (controlled through user-defined constants), the 'children' are generated and their design parameters are passed on to the evaluation routine (in the form of optimization parameters between 0 and 1 for the DE code and a binary string for the GA routine). Once the performances are assessed, this information is fed back to the optimizer that adds the newly evaluated 'children' to the previous population including the 'parents'. Eventually this enlarged database is ranked and the prime individuals compose the next population. From the latter population, new children are created through the aforementioned recombination procedure and the iterative loop continues until no significant improvements in the Pareto front can be noticed anymore. The latter Pareto front contains the individuals for which one of the performance parameters cannot be enhanced without deteriorating the other.
For the GA optimization, the crossover likelihood was set to 0.8 and the mutation probability to 0.005 (1 out of 200, resulting in about one 'mutated' block per new tip design). The population size was set to 20 individuals, fixing the amount of new tip designs per iteration. This number was deemed to be sufficiently large in order to capture the inherent variety contained in the final Pareto front. For the optimization of the carved tip geometry and the squealer-like optimization with the level-set approach, the DE algorithm provides the design parameters of the geometries to be evaluated. For this optimization, the crossover and mutation constants were set respectively to 0.8 and 0.6. The population size for the carved design

optimization was fixed to 20. For the optimization of the squealer-like tip with a level-set approach, a population size of 40 was imposed to allow for a larger spread in the Pareto front.

Carved tip optimization sequence. . The optimization of the contoured tip profiles was conducted for the two rotor tip clearances under investigation: 1.38% of the blade span (design gap case) and 0.85% of the blade span (tight gap case). The design sequence is presented in Fig. 7. Firstly, the DoE (129 designs) was constructed for the tight clearance case from which the DE optimization was initiated (highest ranked 20 designs). After 14 iterations (about 270 extra evaluated designs), the Pareto front was deemed to be converged and 9 optimal designs were selected and recalculated at the design tip clearance. Combined with the DoE of the design clearance, this pool of 138 tip shapes formed the basis for the 2nd DE optimization. Eventually, the optimization of the rotor tip section at the design tip clearance converged after 7 iterations and about 300 designs were generated.

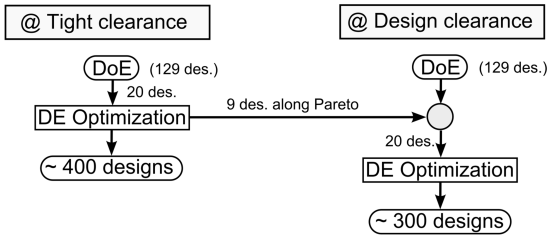

Figure 7: Strategy sequence for the carved tip optimization.

Squealer-like tip optimization strategy.. The sequence for the squealer like optimization is illustrated in Fig. 8. The DoE was created first with the Level-Set approach from which the 40 best profiles were selected to initiate the population for the DE optimization. After 11 populations of 40 individuals (~540 designs), no significant improvement could be discerned. The prime designs along the Pareto front were then combined with some additional conventional profiles. The optimization was restarted with the Binary Approach up to a total of 17 iterations employing the GA routine.

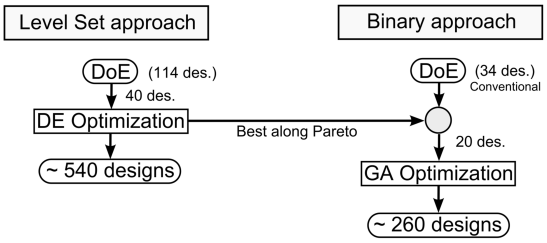

Figure 8: Strategy sequence for the squealer-like optimization.

3. Results

3.1. Carved tip optimization.

Fig. 9 presents the Pareto front for the carved tip optimization where each evaluated tip profile is identified by the two objective functions: aerodynamic efficiency and tip heat transfer. For both the design and tight clearance optimizations, the tip heat load is normalized by the heat flux over the flat tip blade at the nominal gap. For consistency, the aerothermal performance of this flat tip profile will be used as the reference case throughout the results section. Furthermore, the color code used in Fig. 9 to distinguish the different optimization strategies is also kept in the following figures.

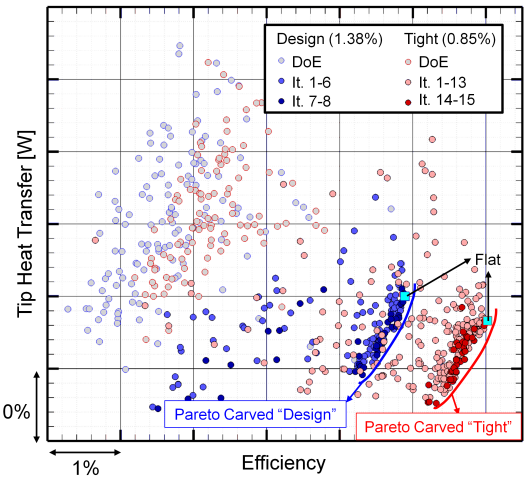

Figure 9: The Pareto front for the carved tip optimization at design and tight clearance.

In Fig. 9, the individuals generated during the DoE expose a large scatter of the performance with differences in heat transfer higher than 40% and about 4% in efficiency. As the optimization evolves, the new individuals move towards enhanced efficiencies and reduced heat fluxes. Eventually, for both tip clearance

levels, the optimization was deemed converged when no significant improvements were obtained in the last 2 populations. Additionally, the location of the flat tip performances at the tight and design clearance is reported for each of the optimizations. A reduction of the gap size by 0.5% of the blade span enhances the rotor efficiency by about 1% and help reducing the total heat transfer by 4% despite the larger wetted surface. For both of the investigated clearances little to no improvement in efficiency could be obtained considering 3D carved tip profiles. However, the Pareto front indicates that the exchange rate between rotor efficiency and the tip heat load is approximately 1:20. In other words, the use of the contoured tip design strategy allows to trade a small reduction in efficiency ($\Delta\eta \sim 0.5\%$) with a reduction in tip heat load of about 10%.

Fig. 10a presents a zoom of the Pareto front for the fully carved tip shape optimizations. Additionally, Fig. 10b shows the contoured surface of four optimized tip geometries selected along the Pareto lines of the two investigated tip clearance cases: profiles 'A' and 'C' represents the best compromise between aerodynamics and thermal performances, while profiles 'B' and 'C' are tip designs tailored for heat transfer minimization. Eventually, a sketch of the tip cross section for two overtip streamlines ('1' and '2') for geometry B and D are presented.

The color bar in Fig. 10b ranges between 1, when the profile is at the minimum clearance, and 0.75, when the tip surface is contoured for about 25% of the deformation depth (Fig. 3). The results show that over most of the tip surface such deformation depth span is sufficient to obtain significant reductions in heat transfer (Fig. 10b). The 25% deformation length corresponds approximately to the size of the design clearance.

The designs located in the central part of the Pareto front for both clearances (profile B and D) indicate that a divergent passage in the aft section of the blade produces an immediate reduction of the overall heat transfer by 5%. In the front section, the tight clearance profile (C) exposes a slightly larger absolute deformation with respect to the optimal profile at the design clearance (A). From the tip geometries in the lower region of the Pareto front (B and D) the low radius of the profile at the suction side extends up to the rotor leading edge. These optimal design solutions attempt to create a continuous converging-diverging flow path in the front section of the rotor blade that is beneficial to alleviate the thermal loads. Remarkably, tighter tip gaps demand more aggressive contouring (i.e., deeper blade radius variations) in the front blade region to achieve reduction in heat transfer as high as 12%.

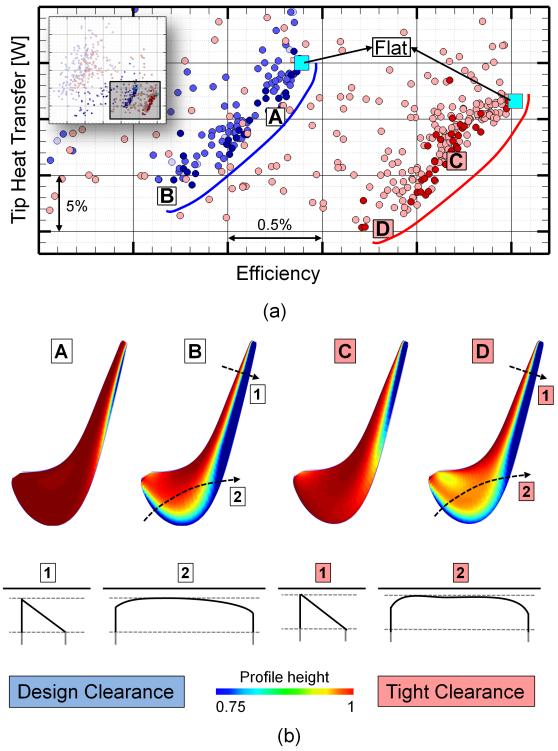

Figure 10: Zoom on the carved optimization Pareto front (a), and a detailed view of four optimal shapes (b).

3.2. *Squealer-like tip optimization.*

The Pareto front for the squealer-like optimization is depicted in Fig. 11 for both the level-set optimization and the optimization based on the binary approach. Additionally, the performances of two types of conventional designs, the flat and single squealer tip geometry, are explicitly indicated in the graph. As it was done for Fig. 9, the performance of the flat tip design at the nominal clearance is used to normalize the heat transfer of all the individuals. Similar to the carved tip optimization, a fast advancement towards the lower right region in the objective space is obtained. However, at the end of the optimization with the level-set method, the distribution of the tip profiles along the Pareto line is characterized by discontinuities. The optimization using the binary approach succeeded in making the Pareto front denser and to generate additional tip profiles with enhanced efficiency. This improvement was achieved by including every possible binary combination into the parametrization to enable the exploration of a much larger design space.

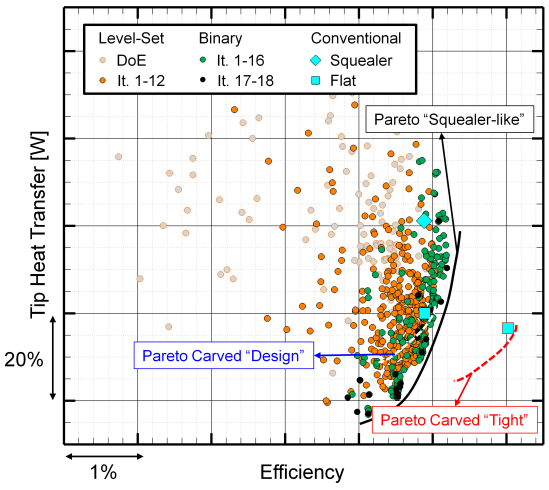

Figure 11: The Pareto front for the squealer-like optimizations.

The outcome of these optimizations clearly points out that the proposed design methodologies can generate a large number of tip geometries that outperform the conventional squealer and flat tip design. For this particular state-of-the-art turbine blade, there exist tip configurations that would allow a reduction in the tip heat load by 10% compared to a flat tip and nearly by 30% in comparison with a squealer design, while preserving the aerodynamic performance. Other superior tip geometries provide an increase of the rotor efficiency by 0.3% in combination with a 10% drop in the total heat transfer when compared to the squealer tip configuration. Fig. 11 additionally displays the Pareto fronts for the two carved tip optimizations represented by dashed lines. Overall, the squealer-like Pareto spans an efficiency range of 1%, similarly to what was observed for the carved tip designs. On the contrary, the corresponding tip thermal loads exhibit a much large scatter (~40%) with respect to the Pareto line predicted for the contoured tip optimization. The exchange rate between the efficiency and the tip heat flux for the squealer-like optimal profiles ($\Delta\eta$ = 1% yields ΔQ = 40%) is twice the exchange rate associated with the carved tip design strategy ($\Delta\eta$ = 1% yields ΔQ = 20%). In other words, the squealer-like configuration is likely to offer a stronger reduction in heat load at the price of smaller aerodynamic loss.

4. Experimental Campaign Design

In order to validate the performance increase predicted from the numerical optimization, an experimental campaign was designed in the transient turbine facility at the von Karman Institute for Fluid Dynamics (CT-3) [32], Fig. 12. In particular, the test section was completely refurbished to hold the new high pressure turbine stage. Additionally, the rotor disk was divided into 7 distinct sectors (Fig. 12) where each sector has a turbine blade with a different tip section, i.e. 6 sectors of 7 blades and one sector with 6 blades. This approach allows to test multiple different turbine designs simultaneously. However, in order to distinguish the downstream aerothermal signatures for each of the profiles, advanced fast response (and data-processing routines) are required.

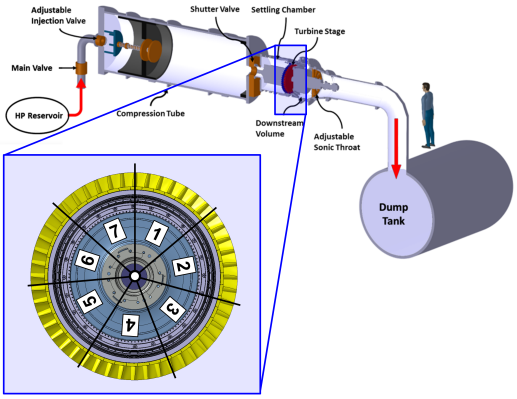

Figure 12: Illustration of the facility with the implementation of 7 distinct rotor sectors.

Fig. 13 gives an overview of the envisioned instrumentation of the wind tunnel. At the inlet of the turbine stage, the incoming flow will be characterised through total pressure and temperature probes while the turbulent characteristics will be measured through hot-wire anemometry. The stator vane is instrumented with a multitude of static pressure taps (and later on with thin films) at both 50% and 90% of the blade span. This data will not only give an accurate description of the vane aerodynamics and heat transfer, but will additionally serve for the validation of CFD codes in a high subsonic regime. On the rotor casing, right above the rotor tip, the full unsteady pressure and heat transfer field will be retrieved through the use of fast-response piezoresistive pressure sensors and thin film gauges. Eventually, about 50% C_{ax} downstream the rotor trailing edge, the aerothermal flow field will be measured through five-hole and miniaturized pressure probes, cold-wires, etc....
This will allow us to distinguish the performance of each of the blade profiles separately, compare it with the numerical simulations and eventually validate the predicted performance increase of the 7 optimized tur-

bine blade profiles.

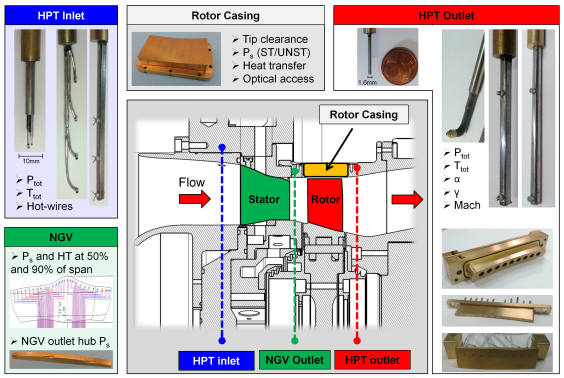

Figure 13: Illustration of the envisioned turbine instrumentation.

5. Conclusion

The current paper introduces two novel optimization strategies for the design of the blade tip section of unshrouded turbine rotors with enhanced aerothermal performances.
A first strategy evaluates fully three-dimensional contoured blade designs based on a general Bezier surface (40 parameters) mapped onto the tip geometry. The optimization was performed at two different tip clearances using a Differential Evolution algorithm. The second methodology uses an approach similar to a topology optimization strategy to overcome the major drawback associated with more conventional shape optimization strategies: the restriction to one particular type of blade tip profile. For this optimization method, the tip area was divided in about 200 distinct blocks which can be either part of an upstanding rim or be set down to constitute the cavity floor.
In total, around 700 carved tip profiles and 800 squealer-like geometries were evaluated during 4 consecutive multi-objective optimizations which targeted the simultaneous increase of the aerodynamic efficiency and the reduction of the overtip heat load.
The results have shown that a flat tip represents a prime design choice in terms of efficiency for the investigated turbine hardware when the optimization space is limited to the carved tip shape approach. However, the Pareto front for these optimizations revealed the possibility of an immediate heat transfer reduction of 5% through the creation of a diverging passage in the aft part of the blade. Further heat transfer reduction is accessible by reducing the suction side tip radius up to the blade leading edge region. Interestingly, tip profiles running at a tight clearance require a more aggressive tip contouring than what is demanded by geometries at the design clearance to achieve the same heat transfer enhancement.
The final Pareto front for the squealer-like tip optimization showed to be less sensitive to the efficiency compared to the contoured blade design approach. Moreover, optimal geometries were identified, revealing a 0.3% increase of efficiency compared to the prevalent turbine tip designs. The exchange rate between the aerodynamic performance and the tip heat flux for the squealer-like optimal profiles was proven to be twice as high as for the carved tip design strategy.
Eventually, the design of an experimental campaign in the transient turbine facility of the von Karman Institute is presented, capable of testing simultaneously multiple distinct turbine blade tip profiles. Advanced measurement an processing techniques will allow us to distinguish the performance of each of the blade profiles separately, compare it with the numerical simulations and eventually validate the predicted performance increase of 7 optimized turbine blade profiles.
One of the most important conclusions of this investigation was the demonstration that a significant number of new heterogeneous tip geometries exist that can offer increased aerothermal performances, beyond the standards of prevalent conventional tip designs adopted in modern gas turbine engines. Finally, the application of the presented optimization strategies might also be extended to the design of a wider class of fluid machinery components.

6. Acknowledgements

The authors would like to thank Prof. Lavagnoli for his work on the design of the experimental campaign and Prof. Verstraete for his help during the numerical optimization. Additionally, this investigation was made possible through the PhD fellowship of Mr. De Maesschalck (Nb. 121270) from the Agency for Innovation by Science and Technology (IWT) in Belgium.

7. References

[1] Bunker, R. S., 2006, "Axial Turbine Blade Tips: Function, Design, and Durability," *J. Propul. Power*, **22**(2), pp. 271-285.
[2] Bunker, R. S., 2001, "A Review of Turbine Blade Tip Heat Transfer in Gas Turbine Systems," *Ann. N.Y.*

Acad. Sci., 934, pp. 64-79.
[3] Shyam, V., Ameri, A., and Chen, J., 2012, "Analysis of Unsteady Tip and Endwall Heat Transfer in a Highly Loaded Transonic Turbine Stage," *ASME J. Turbomach.*, **134**(4), p. 041022.
[4] Newton, P. J., Lock, G. D., Krishnababu, S. K., Hodson, H. P., Dawes, W. N., Hannis, J., and Whitney, C., 2006, "Heat Transfer and Aerodynamics of Turbine Blade Tips in a Linear Cascade," *ASME J. Turbomach.*, **128**(2), pp. 300-309.
[5] Key, N. L., and Arts, T., 2006, "Comparison of Turbine Tip Leakage Flow for Flat Tip and Squealer Tip Geometries at High-Speed Conditions," *ASME J. Turbomach.*, **128**(2), pp. 213-220.
[6] Mischo, B., Behr, T., and Abhari, R. S., 2008, "Flow Physics and Profiling of Recessed Blade Tips: Impact on Performance and Heat Load," *ASME J. Turbomach.*, **130**(2), p. 021008.
[7] Harvey, N. W., Newman, D. A., Haselbach, F., and Willer, L., 2006, "An Investigation Into a Novel Turbine Rotor Winlet: Part I-Design and Model Rig Test Results," ASME Paper No. GT2006-585.
[8] O'Dowd, D. O., Zhang, Q., He, L., Oldfield, M. L. G., Ligrani, P. M., Cheong, B. C. Y., and Tibbott, I., 2011, "Aerothermal Performance of a Winglet at Engine Representative Mach and Reynolds Numbers," *ASME J. Turbomach.*, **133**(4), p. 041026.
[9] Zhang, Q., and He, L., 2011, "Overtip Choking and Its Implications on Turbine Blade-Tip Aerodynamics Performance," *J. Propul. Power*, **27**(5), pp. 1008-1014.
[10] Shyam, V., and Ameri, A., 2011, "Comparison of Various Supersonic Turbine Tip Designs to Minimize Aerodynamic Loss and Tip Heating," ASME Paper No. GT2011-46390.
[11] Zhang, Q., and He, L., 2013, "Tip-Shaping for HP Turbine Blade Aerothermal Performance Management," *ASME J. Turbomach.* **135**(5), 051025
[12] De Maesschalck, C., Lavagnoli, S., and Paniagua, G., 2014, "Blade Tip Shape Optimization for Enhanced Turbine Aerothermal Performance," *ASME J. Turbomach.*, **136**(4), p. 041016.
[13] De Maesschalck, C., Lavagnoli, S., and Paniagua, G., 2015, Blade Tip Carving Effects on the Aerothermal Performance of a Transonic Turbine, *J. Turbomach.* **137**(2), 021005
[14] Shahpar, S., Caloni, S., 2013, "Aerodynamic Optimization of High-Pressure Turbines for Lean-Burn Combustion System," *J. Eng. Gas Turbines Power*, **135**(5), 055001
[15] Rozvany, G., 2009, "A critical review of established methods of structural topology optimization," *Structural and Multidisciplinary Optimization*, **37**(3), pp. 217-237
[16] Othmer, C., 2006, "CFD Topology and Shape Optimiza-tion with Adjoint Methods," VDI Fahrzeug- und Verkehrstechnik, 13 Internationaler Kongress Berechnung und Simulation im Fahrzeugbau (Wurzburg), 1967, p. 61
[17] Andreasen, C. S., Gersborg, A. R., Sigmund, O., 2009, "Topology optimization of microfluidic mixers," *International Journal for Numerical Methods in Fluids*, **61**(5), p.498-513.
[18] Kontoleontos, E. A., Papoutsis-Kiachagias, E. M., Zymaris, A.S., Papadimitriou, D. I., Giannakoglou, K. C., 2013, "Adjoint-based constrained topology optimization for viscous flows, including heat transfer," *Engineering Optimization*, **45**(8), pp. 941-961.
[19] Krishnababu, S. K., Newton, P. J., Dawes, W. N., Lock, G. D., Hodson, H. P., Hannis, J., and Whitney, C., 2009, "Aerothermal Investigations of Tip Leakage Flow in Axial Flow TurbinesPart I: Effect of Tip Geometry and Tip Clearance Gap," *ASME J. Turbomach.*, **131**(1), p. 011006.
[20] Wheeler, A. P. S., Atkins, N. R., and He, L., 2011, "Turbine Blade Tip Heat Transfer In Low Speed And High Speed Flows," *ASME J. Turbomach.*, **133**(4), p. 041025.
[21] Menter, F. R, 1994, "Two-equation eddy-viscosity turbulence models for engineering applications," *AIAA Journal*, Vol. 32, No. 8, pp. 1598-1605.
[22] Coull, J. D., Atkins, N. R., 2013, "The Influence of Boundary Conditions on Tip Leakage Flow", ASME paper TBTS2013-2057.
[23] Olive, R., Lavagnoli, S., De Maesschalck, C., Paniagua, G., "Procd de modlisation d'une baignoire d'une aube", FR Brevet d'Invention, FR1456680, July 10th, 2014.
[24] Dijk, N. P., Maute, K., Langelaar, M., Keulen, F., 2013, "Level-set methods for structural topology optimization: a review," *Struct. Multidiscip. Optim.* **48**(3), 437-472.
[25] Verstraete, T., Amaral, S., Van den Braembussche, R. A., and Arts, T., 2010, "Design and Optimization of the Internal Cooling Channels of a High Pressure Turbine Blade-Part II: Optimization," *ASME J. Turbomach.*, **132**, p. 021014.
[26] Verstraete, T., Alsalihi, Z., and Van den Braembussche, R. A., 2010, "Multidisciplinary Optimization of a Radial Compressor for Microgas Turbine Applications," *ASME J. Turbomach.*, **132**, p. 031004.
[27] Holland, J.H., 1975, "Adaption in Natural and Artificial Systems", University of Michigan Press.

[28] Rechenberg, I., 1973, ”Evolutionsstrategie - Optimierung technischer Systeme nach Prinzipien der biologischen Evolution”, Fommann-Holzboog, Stuttgart.
[29] Deb, K., Pratap, A., Agarwal, S., Meyarivan, T., 2002, ”A fast and elitist multiobjective genetic algorithm: NSGA-II”, *IEEE Transactions on Evolutionary Computation*, **6**(2):182197
[30] Storn, R., and Price, K., 1997. ”Differential evolution a simple and efficient heuristic for global optimization over continuous spaces”. *Journal of Global Optimization*, **11**, pp. 341359.
[31] Montgomery, D. C., 1997, ”Design and Analysis of Experiments”, John Wiley and Sons, New York, ISBN978-1118146927
[32] Paniagua, G., Sieverding, C. H., Arts, T., 2013, ”Review of the von Karman Institute Compression Tube Facility for Turbine Research,” ASME Paper No. GT2013-95984

Experimentally and Numerically Driven Optimization of High Performance Instrumentation for Real Engine Testing

Aude Lahalle

Turbomachinery and Propulsion Department, von Karman Institute for Fluid Dynamics, Belgium, aude.lahalle@vki.ac.be

Supervisor: Tony Arts

Head of department, Turbomachinery and Propulsion Department, von Karman Institute for Fluid Dynamics, Belgium, arts@vki.ac.be

Co-Supervisor: Fabrizio Fontaneto

Assistant Professor, Turbomachinery and Propulsion Department, von Karman Institute for Fluid Dynamics, Belgium, fontaneto@vki.ac.be

Throughout the complete development phase of a new gas turbine, testing is extensively performed. This provides benchmarks for the design, as well as certification of the final product for ground and flight conditions. For each step, the quality of the instrumentation employed is crucial as artifacts can lead either to an incorrect interpretation of the experimental data, either to the uncertification of the final product. Therefore it is common practice to submit the instrumentation to a careful calibration process. The latter can be static or dynamic, and realized for different flow speeds and directions.

The design and manufacturing time for one single probe lasts typically two months, while the full calibration requires up to two or three weeks. As engines are heavily instrumented, calibrations represent a substantial entry in the costs and time budgets.

The output of a calibration is the evaluation of the performance of the instrumentation to retrieve the real quantities of the flow field such as total pressure and total temperature or flow angles.

This performance is expressed in terms of Recovery Factor (RF) and is defined as follows:

$$RF = \frac{X_{meas}}{X_{real}} \tag{1}$$

Probes at the state of the art (a typical example is illustrated in Figure 1) provide a temperature or pressure RF which is as high as 99,8%. In other words, when considering only the measured data, i.e. not recovered, the margins tolerated by the certification requirements are exceeded as nowadays, engines need to be certified on a basis of one hundredth of the efficiency.

This project focuses on the development of highly reliable design procedures in the optic of providing a methodology which delivers probes of high RF. By doing so, the correction introduced by the RF would be negligible in comparison with the standards requested by industrials, i.e. the certification limitations, allowing therefore to suppress the calibration phase, and drastically reducing the costs and save time.

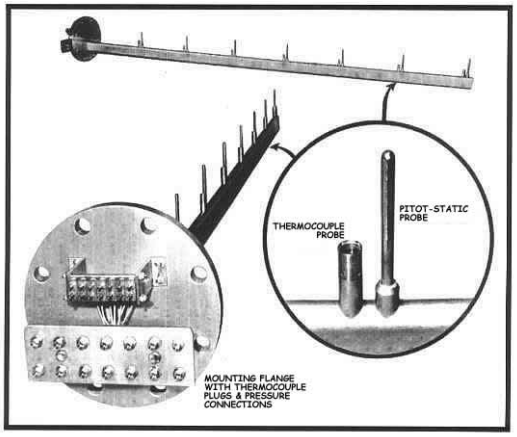

Figure 1: Illustration of a temperature and pressure probe - *Source:* United Sensor Corp.

Over the past months VKI developed a calibration method, which proved to be robust and reliable enough to meet industrial requirements. Through

these different experiences, an experimental database has been built, pointing out the numerous differences according to the shape and nature of the sensors. Additionally, importance has been given to the uncertainty computation in such a way that it fits with industrial standards as described by [1].

The data recorded in the so built database would be used in a second step of the project as a benchmark for numerical simulations whose target would be to provide a full understanding of the flow physics in and around the probe. These simulations will be run using OpenFoam, starting from a steady 3D configuration, which will be extended in a second phase to an unsteady case, in order to better describe the transient heat transfer phenomena taking place.

The enhanced understanding of the flow field which would result from the numerical investigation will provide a detailed understanding of the parameters affecting the RF as reported by [2].

Finally, in the last phase of the project, the results obtained with the numerical computations will be used as inputs for an optimization process whose outcome will be the enhancement of the RF.

Keywords: Instrumentation, engine testing, high performance probes, optimization.

References

[1] Collège Francais de Métrologie, 27 exemples d'évaluation d'incertitudes d'étalonnage, Les guides techniques du Collège Francais de Métrologie, Lexitis éditions, (2013).

[2] Bonham et al., Stagnation temperature measurement using thin-film platinum resistance sensors, Measurement Science and Technology, 25 (2014).

Development of a Gradient-Based Optimization Framework for Turbomachinery using a CAD-Based Discrete Adjoint Method

Lasse Mueller

Turbomachinery and Propulsion Department, von Karman Institute for Fluid Dynamics, Belgium, lasse.mueller@vki.ac.be

Supervisor: Tom Verstraete

Associate Professor, Turbomachinery and Propulsion Department, von Karman Institute for Fluid Dynamics, Belgium, tom.verstraete@vki.ac.be

University Supervisor: Herman Deconinck

Professor, Univ. Libre de Bruxelles (ULB), Aero-Thermo-Mechanics Department, Belgium, hdeconink@ulb.ac.be

Abstract

A gradient-based aerodynamic shape optimization methodology using a CAD-based discrete adjoint approach is described. The core of the optimization system is 3D multi-block structured Navier-Stokes solver, the corresponding discrete adjoint solver, and a sequential quadratic programming optimization algorithm. A CAD-based shape parametrization is used inside the design loop to evaluate cost function sensitivities efficiently and robustly. The development of the discrete adjoint solver follows a hybrid approach in which both selectively applying automatic differentiation (AD) and hand-coded differentiation are used. This is regarded as a good compromise between solver performance and code development time. The accuracy of the discrete adjoint solver is verified by comparison with finite differences. Finally, the capability of the optimization algorithm is demonstrated by redesigning the LS89 turbine blade for transonic conditions aiming at minimizing entropy generation while constraining the exit flow angle.

Keywords: Gradient-Based Optimization, CFD, Adjoint, Turbomachinery

1. Introduction

Efficient numerical optimization methods have made a significant contribution to the recent advances in the design of turbomachinery [1; 2; 3; 4]. The different optimization techniques may be classified into two categories [5]: gradient-free and gradient-based methods.

Gradient-free optimization methods have proven to be well suited for industrial design applications and have been successfully applied to three-dimensional design optimization. However, they require a large number of function evaluations. Hence, for large design problems with many design parameters or for detailed analysis with tight convergence tolerances the computational cost is considered too high for the use in the regular design process. Gradient-based methods are more efficient and require less iterations to converge [6], as they use the functional gradient during the search for the optimum. However, the performance and accuracy of the gradient-based algorithm is significantly determined by the gradient calculation. Finite-differences, complex-step method [7], or the adjoint approach [8; 9] may be used. Both finite differences and complex-step method have the major drawback that the computational cost of evaluating the objective function derivative scales with the number of design variables. The adjoint method instead offers a means to calculate the cost function gradients practically independent of the number of design variables at a computational cost of solving one flow solution and one adjoint solution.

The application of the adjoint method to aerodynamic design optimization based on computational fluid dynamics (CFD) was pioneered by [10], using the continuous adjoint of the Euler equations. This

involves adjointing the continuous flow equations before discretizing them. As opposed to this, in the discrete adjoint approach [11] the discretized Navier-Stokes equations are linearized to form the adjoint system.

In present project the discrete adjoint formulation is preferred primarily due its straightforward code implementation. However, the development of the discrete adjoint solver by hand is by no means trivial, since it involves the linearization of the entire Navier-Stokes solver and may take several months. One way to reduce the code development time is to use algorithmic differentiation (AD), either by differentiating the entire code [12; 13], or by selectively differentiating only parts of code to compute the partial derivatives required by the adjoint method [14; 15]. In this work the discrete adjoint solver has been developed following a hybrid approach in which both selectively applying AD and hand-coded differentiation are used. This is regarded as a good compromise between solver performance and code development time.

In the following the developed gradient-based optimization system will be outlined: first the adjoint principle will be introduced in Sec. 2, followed by a general overview of the optimization algorithm (Sec. 3). Implementation details of the developed flow and discrete adjoint solver are provided in Sec. 4 and Sec. 5, respectively. In Sec. 6 the calculation of functional gradients is discussed. Finally the potential of the developed system is demonstrated in Sec. 7 by redesigning the LS89 turbine blade for transonic conditions.

2. Adjoint Principle

The principle of the adjoint formulation may be derived in different ways [9]. The result is a linear system of equations (the adjoint equations), which allows to efficiently compute the functional gradients independent of the number of design variables. The function of interest can be either the objective function or any of the constraints specified in the optimization problem. In general, such scalar functions J depend not only on the design variables $\boldsymbol{\alpha} = \{\alpha_1, \alpha_2, ..., \alpha_n\}^T$, but also on the flow variables $\boldsymbol{W}_c = [\rho, \rho\mathbf{V}, \rho E]^T$

$$J = J(\boldsymbol{W}_c(\boldsymbol{\alpha}), \boldsymbol{\alpha}). \tag{1}$$

The gradient of the objective function (or constraint function) with respect to the design variables is obtained by applying the chain rule to the above expression:

$$\frac{dJ}{d\boldsymbol{\alpha}} = \frac{\partial J}{\partial \boldsymbol{\alpha}} + \frac{\partial J}{\partial \boldsymbol{W}_c}\frac{d\boldsymbol{W}_c}{d\boldsymbol{\alpha}}. \tag{2}$$

$(\partial J/\partial \boldsymbol{\alpha})$ and $(\partial J/\partial \boldsymbol{W}_c)$ are partial derivatives and may be computed analytically. However, the flow variable sensitivity $(d\boldsymbol{W}_c/d\boldsymbol{\alpha})$ requires a converged flow solution for every design variable, thus, the computational cost scales linearly with the number of design variables. The adjoint approach eliminates the dependence of the gradient on the flow variable sensitivity and is considerably more efficient for real life problems where the number of design variables exceeds the number of objective functions.

In computational fluid dynamics (CFD), the objective function J is the result of a converged flow simulation of a non-linear flow solver

$$\boldsymbol{R}(\boldsymbol{W}_c(\boldsymbol{\alpha}), \boldsymbol{\alpha}) = 0, \tag{3}$$

which establishes the dependence of the flow variables on the design variables. Differentiating Eqn. 3 and rearranging yields an expression for the flow variable sensitivity $(d\boldsymbol{W}_c/d\boldsymbol{\alpha})$:

$$\frac{\partial \boldsymbol{R}}{\partial \boldsymbol{\alpha}} + \frac{\partial \boldsymbol{R}}{\partial \boldsymbol{W}_c}\frac{d\boldsymbol{W}_c}{d\boldsymbol{\alpha}} = 0, \tag{4}$$

$$\Rightarrow \frac{d\boldsymbol{W}_c}{d\boldsymbol{\alpha}} = -\Big(\frac{\partial \boldsymbol{R}}{\partial \boldsymbol{W}_c}\Big)^{-1}\frac{\partial \boldsymbol{R}}{\partial \boldsymbol{\alpha}}. \tag{5}$$

Inserting Eqn. 5 into Eqn. 2 eliminates the dependence on the flow variable sensitivity

$$\frac{dJ}{d\boldsymbol{\alpha}} = \frac{\partial J}{\partial \boldsymbol{\alpha}} + \frac{\partial J}{\partial \boldsymbol{W}_c}\Big[-\Big(\frac{\partial \boldsymbol{R}}{\partial \boldsymbol{W}_c}\Big)^{-1}\frac{\partial \boldsymbol{R}}{\partial \boldsymbol{\alpha}}\Big], \tag{6}$$

which may be rewritten for convenience as

$$\frac{dJ}{d\boldsymbol{\alpha}} = \frac{\partial J}{\partial \boldsymbol{\alpha}} - \underbrace{\Big[\frac{\partial J}{\partial \boldsymbol{W}_c}\Big(\frac{\partial \boldsymbol{R}}{\partial \boldsymbol{W}_c}\Big)^{-1}\Big]}_{\boldsymbol{\psi}^T}\frac{\partial \boldsymbol{R}}{\partial \boldsymbol{\alpha}}, \tag{7}$$

where $\boldsymbol{\psi}$ is the adjoint or co-state vector defining the adjoint equations

$$\left[\frac{\partial \boldsymbol{R}}{\partial \boldsymbol{W}_c}\right]^T \boldsymbol{\psi} = \left[\frac{\partial J}{\partial \mathbf{W}_c}\right]^T. \tag{8}$$

The adjoint equations do not depend on any design variable $\boldsymbol{\alpha}$, and thus, the gradient of the objective function to all the design variables can be obtained by solving two sets of equations: the flow equations (Eqn. 3) and the adjoint equations (Eqn. 8). The resulting adjoint solution $(\boldsymbol{\psi})$ is used to compute the functional gradients by Eqn. 7. Since a flow solver, in general, does not handle the design variables $\boldsymbol{\alpha}$ directly, but rather a computational mesh defined by the coordinates of each node $\boldsymbol{X}(\boldsymbol{\alpha})$, it is convenient to use

the chain rule of differentiation to express the sensitivity of the function of interest with respect to the design variables as (see also Sec. 6)

$$\frac{dJ}{dX} = \frac{\partial J}{\partial X} - \boldsymbol{\psi}^T \frac{\partial \boldsymbol{R}}{\partial X}, \tag{9}$$

$$\frac{dJ}{d\boldsymbol{\alpha}} = \frac{dJ}{dX}\frac{dX}{d\boldsymbol{\alpha}}. \tag{10}$$

3. Optimization Algorithm

The optimization system is illustrated in Fig. 1. It makes use of a gradient-based optimization algorithm, a 3D multi-block structured Navier-Stokes solver, and the corresponding discrete adjoint solver to evaluate cost function sensitivities efficiently.

The optimization package SNOPT [16] is integrated into the framework. It is a general-purpose optimization software for large-scale constrained optimization and employs a sequential quadratic programming (SQP) algorithm (cf. [17] for more details).

In each iteration the gradient-based optimizer requires both the function value J and gradient $dJ/d\boldsymbol{\alpha}$ for the search for the optimum. Hence, a sequence of operations are performed to accomplish this, which are illustrated in Fig. 1. In turbomachinery design a high-level geometrical definition is preferred (e.g. chord, stagger angle, etc.) rather than using the nodes of the computational grid. For this reason a CAD-kernel using Bézier and B-spline curves and surfaces is employed to generate the different geometries. The Navier-Stokes solver evaluates the aerodynamic performance and provides both the converged flow solution ($\overline{W}$) to the adjoint-based gradient evaluation (cf. Sec. 2) and the objective value J to the gradient-based optimizer. The adjoint-based gradient evaluation chain computes efficiently the entire gradient vector $dJ/d\boldsymbol{\alpha}$ at a computational cost roughly twice as much as the non-linear flow solver. This process is repeated until no further improvement could be found by the gradient-based optimization algorithm.

4. Primal Flow Solver

A parallelized 3D multi-block structured finite volume solver has been developed to solve the compressible Reynolds-Averaged Navier-Stokes (RANS) equations. Block-to-block communication on distributed memory computers is realized using the MPI standard. In the following section the flow governing equations, the numerical implementation and solution

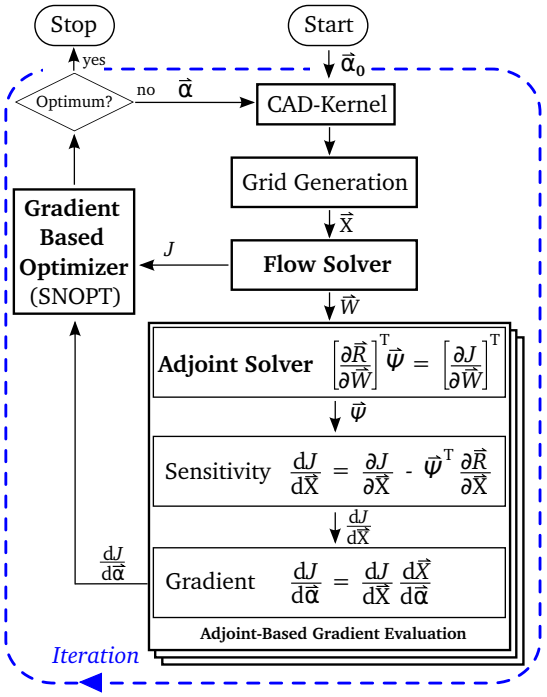

Figure 1: **Schematic Gradient-Based Optimization Algorithm.**

strategy will be addressed. The validity of the solver will be demonstrated with the LS89 turbine blade [18].

4.1. Governing Equations

The flow governing equations are formulated in relative frame of reference using absolute velocity components $\mathbf{V} = [V_x, V_y, V_z]^T$. Written in time-dependent integral form the three-dimensional compressible RANS equations read

$$\frac{\partial}{\partial t}\int_\Omega \mathbf{W}_c d\Omega + \oint_{\partial\Omega} (\mathbf{F}_c - \mathbf{F}_v) dS = \int_\Omega \mathbf{Q} d\Omega \tag{11}$$

where Ω denotes a control volume with a surface element dS. $\mathbf{W}_c = [\rho, \rho\mathbf{V}, \rho E]^T$ defines the vector of conservative variables comprising the density ρ and the specific total energy of the fluid per unit mass $E = e + (\mathbf{V}\cdot\mathbf{V})/2$ with the internal energy e. The inviscid flux vector $\mathbf{F}_c$ and the viscous flux vector $\mathbf{F}_v$ through a surface element dS with unit normal vector $\mathbf{n} = [n_x, n_y, n_z]^T$ are given by

$$\mathbf{F}_c = \begin{pmatrix} \rho \\ \rho\mathbf{V}W_n + \mathbf{n}P \\ \rho E W_n + V_n P \end{pmatrix} \tag{12}$$

and

$$\mathbf{F}_v = \begin{pmatrix} 0 \\ n_x\tau_{x_i x} + n_y\tau_{x_i y} + n_z\tau_{x_i z} \\ n_x\Theta_x + n_y\Theta_y + n_z\Theta_z \end{pmatrix} \tag{13}$$

with $x_i = x, y, z$ and

$$\Theta_{x_i} = V_x\tau_{x_i x} + V_y\tau_{x_i y} + V_z\tau_{x_i z} + k\frac{\partial T}{\partial x_i}. \tag{14}$$

The source term vector $\mathbf{Q}$ in Eqn. 11 accounts for forces due to centrifugal and Coriolis effects which are present in rotating turbomachinery flows and reads as $\mathbf{Q} = [0, -\rho\boldsymbol{\omega} \times \mathbf{V}, 0]^T$. In Eqn. 12, $V_n = \mathbf{V} \cdot \mathbf{n}$ and $W_n = \mathbf{W} \cdot \mathbf{n}$ represent the absolute and relative contravariant velocity, where the absolute velocity is the sum of the relative velocity and the peripheral speed $\mathbf{V} = \mathbf{W} + \boldsymbol{\omega} \times \mathbf{r}$. For a calorically perfect gas, the static pressure in Eqn. 12 is defined by the equation of state $P = (\gamma - 1)\rho[E - (\mathbf{V} \cdot \mathbf{V})/2)]$ with the gas dependent ratio of specific heats γ. Assuming a Newtonian fluid and applying Stokes's hypothesis the shear stress tensor my be defined by

$$\overline{\tau} = \mu_l \left[\nabla\mathbf{V} + (\nabla\mathbf{V})^T - \frac{2}{3}\overline{\boldsymbol{I}}\nabla\mathbf{V} \right] \tag{15}$$

with the laminar dynamic viscosity μ_l computed by Sutherland's law. In Eqn. 14, the heat flux is computed with the thermal conductivity coefficient and the static temperature $k = c_p\mu_l/Pr$ and $T = P/(\rho R)$, respectively. The constant fluid properties are defined by the specific heat at constant pressure c_p, the Prandtl number Pr, and the gas constant R. In order to account for the influence of turbulence without resolving every turbulent eddy, the flow equations are Favre averaged and the Boussinesq's assumption is applied, which lead to scalar expression for the effective viscosity

$$\mu = \mu_l + \mu_t \tag{16}$$

and the effective thermal conductivity

$$k = c_p\left(\frac{\mu_l}{Pr} + \frac{\mu_t}{Pr_t}\right), \text{with } Pr_t = \text{const.} \tag{17}$$

The turbulent viscosity μ_t is modeled by a turbulence model defined in Sec. 4.2.

4.2. Numerical Implementation

The flow governing equations are discretized using a finite volume method with a cell-centered structure. The semi-discrete formulation may be written as

$$\sum_i^{\#Cell} \Omega_i \frac{\partial \boldsymbol{W}_{c,i}}{\partial t} = -\sum_i^{\#Cell} \boldsymbol{R}_i. \tag{18}$$

with the residual vector of cell i

$$\boldsymbol{R}_i = \sum_j^{\#Face} (\boldsymbol{F}_c - \boldsymbol{F}_v)\Delta S_j - \boldsymbol{Q}_i\Omega_i \tag{19}$$

containing the spatial discretization of convective and viscous fluxes, the source term and all boundary conditions. Two types of upwind schemes have been implemented to evaluate convective fluxes. The flux-difference-splitting scheme by Roe [19] and the flux-vector-splitting AUSM$^+$-scheme [20]. Both schemes employ a MUSCL reconstruction of primitive variables $\boldsymbol{W}_p = [\rho, V_x, V_y, V_z, P]^T$ supplemented by a van-Albada type limiter [21] to attain 2nd-order accuracy. Viscous fluxes are centrally discretized applying Green's theorem [22] to compute the spatial gradients of primitive variables at cell faces. Boundary conditions are imposed weakly, by utilizing dummy cells [22], which virtually extend the physical domain. Several turbomachinery related boundary conditions are implemented:

- Sub-/Supersonic inlet and outlet,
- adiabatic no-slip wall,
- slip wall, and
- symmetry plane.

For the turbulence closure the standard Spalart-Allmaras turbulence model [23] is used, optionally with the extension proposed by [24] to take rotation and curvature correction into account.

An implicit Euler time integration strategy is used to converge to steady-state for both the mean-flow and the turbulent equations. In both cases the linear system of equations take at each time step n following general form:

$$\left[\frac{\Omega}{\Delta t}\overline{\boldsymbol{I}} + \widetilde{\frac{\partial \boldsymbol{R}}{\partial \boldsymbol{W}_c}}\right]^n \Delta\boldsymbol{W}_c = -\boldsymbol{R}(\boldsymbol{W}_c) \tag{20}$$

with

$$\boldsymbol{W}_c^{n+1} = \boldsymbol{W}_c^n + {}^n\Delta\boldsymbol{W}_c. \tag{21}$$

The jacobian matrix $\widetilde{\frac{\partial \boldsymbol{R}}{\partial \boldsymbol{W}_c}}$ on the left-hand side of Eqn. 20 is a low order approximation of the exact linearized residual, to which a fictitious time term is added in order to improve the diagonal dominance of the system matrix. Finally, the linear system of equations is solved using the publicly available PETSc [25] library, which includes a variety of sparse linear solvers and preconditioners in a parallel environment using MPI standard.

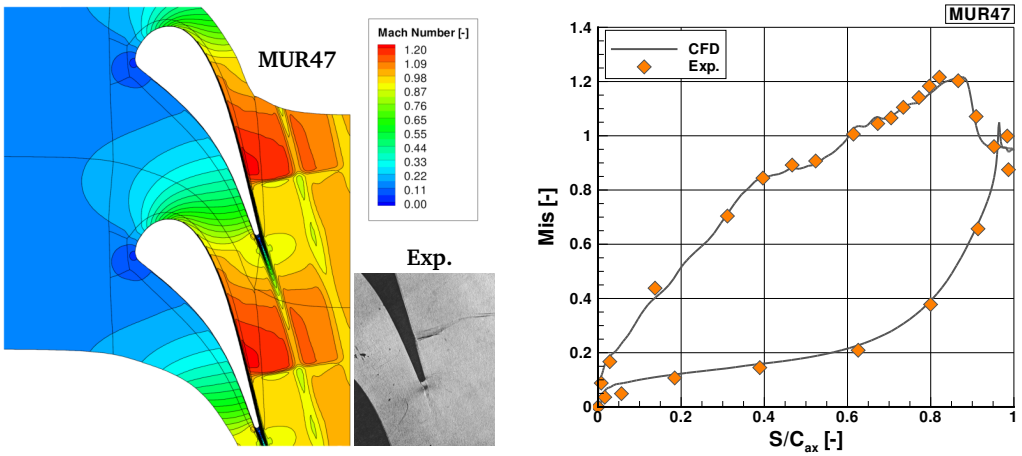

Figure 2: **Mach Number Plot (left) and Isentropic Mach Number Distribution (right) of the LS89 Turbine Blade [18] at Test Condition MUR47**

4.3. Validation

The solver has been validated against several test cases in both stationary and rotating frame. In Fig. 2 numerical predictions of the LS89 turbine blade [18] for transonic conditions are presented. At outlet, the isentropic Mach Number and Reynolds Number are $Ma_{is,2} = 1.02$ and $Re_2 = 10^6$, respectively. Characteristic feature is the normal shock on the rear part of the suction side, which can be seen in Fig. 2 (left) in both the predicted Mach Number distribution and in the Schlieren visualization. The predicted shock location is consistent as compared to the experiments, which is visible in Fig. 2 (right) showing the blade isentropic Mach number. The steep acceleration on the suction side of the blade until $S/C_{ax} \approx 0.4$ is well captured followed by a small plateau ($S/C_{ax} \approx 0.4 - 0.55$) and a re-acceleration until the shock occurs at $S/C_{ax} \approx 0.85$.

5. Discrete Adjoint Solver

For large 3D cases, a direct inversion of the system matrix of the adjoint equation (Eqn. 8) is often prohibitive due to memory limitations. Instead of solving the linear system of equations directly a time-like derivative is added and the solution is obtained by marching in time like in the primal flow solver [26]:

$$\left[\frac{\Omega}{\Delta t}\bar{\boldsymbol{I}} + \frac{\widetilde{\partial \boldsymbol{R}(\boldsymbol{W}_c^*)}}{\partial \boldsymbol{W}_c}\right]^T {}^n\Delta\boldsymbol{\psi} = \boldsymbol{RHS} \tag{22}$$

$$\boldsymbol{RHS} = \left[\frac{\partial J}{\partial \mathbf{W}_c}\right]^T + \left[\frac{\partial \mathbf{R}(\mathbf{W}_c^*)}{\partial \mathbf{W}_c}\right]^T \boldsymbol{\psi}^n \tag{23}$$

$$\boldsymbol{\psi}^{n+1} = \boldsymbol{\psi}^n + {}^n\Delta\boldsymbol{\psi} \tag{24}$$

The system matrix on the left-hand side of Eqn. 22 is equal to the transposed system matrix of the primal flow solver (Eqn. 20). It is computed once using the converged flow solution $\boldsymbol{W}_c^*$ and stored in memory during the solution process. The right-hand side (RHS) in Eqn. 23 contains both the linearized discrete cost function $[\partial J/\partial \mathbf{W}_c]$ and the transposed exact[1] differentiated residual $[\partial \mathbf{R}(\mathbf{W}_c^*)/\partial \mathbf{W}_c]^T$ multiplied by the co-state vector $\boldsymbol{\psi}$. Again, the linearized discrete cost function is computed once and stored in memory, while the matrix-vector product is assembled on-the-fly during convergence to steady-state in order to alleviate the memory consumption. In the following the implementation of linearized discrete cost function and the differentiation of the residual will be detailed.

5.1. Linearized Discrete Cost Function

In turbomachinery design, global quantities (efficiency, pressure ratio, etc.) based on averaged inlet and outlet quantities are commonly used to assess the performance of a machine. Given that boundary conditions are imposed utilizing dummy cells the linearized function of interest reads as

$$\frac{\partial J}{\partial \mathbf{W}_D} = \frac{\partial J}{\partial \mathbf{W}_B}\frac{\partial \mathbf{W}_B}{\partial \mathbf{W}_D} \tag{25}$$

where $(\partial \mathbf{W}_B/\partial \mathbf{W}_D)$ is a linear operator which includes the differentiation of the boundary condition at

[1] Approximations are allowed but may affect the accuracy of the function gradient [27; 28].

inlet and outlet (see Fig. 3). In practice, primitive variables are used as working variables such that Eqn. 25 may be expanded to

$$\frac{\partial J}{\partial \mathbf{W}_{c,D}} = \frac{\partial J}{\partial \mathbf{W}_{p,B}} \frac{\partial \mathbf{W}_{p,B}}{\partial \mathbf{W}_{p,D}} \frac{\partial \mathbf{W}_{p,D}}{\partial \mathbf{W}_{c,D}} \tag{26}$$

with the primitive-to-conservative transformation matrix ($\partial \mathbf{W}_{p,D}/\partial \mathbf{W}_{c,D}$) defined in Appendix A. This simplifies both the linearization of the cost function ($\partial J/\partial \mathbf{W}_{p,B}$) and the boundary transformation matrix ($\partial \mathbf{W}_{p,B}/\partial \mathbf{W}_{p,D}$). E.g. for a subsonic outlet boundary condition defined in [22] with prescribed static pressure P_{outlet}

$$\boldsymbol{W}_{p,B} = \begin{pmatrix} \rho_D + \frac{\Delta P}{c_D^2} \\ V_{x,D} - \frac{n_x \Delta P}{\rho_D c_D} \\ V_{y,D} - \frac{n_y \Delta P}{\rho_D c_D} \\ V_{z,D} - \frac{n_z \Delta P}{\rho_D c_D} \\ P_{outlet} \end{pmatrix}$$

it reads as:

$$\frac{\partial \mathbf{W}_{p,B}}{\partial \mathbf{W}_{p,D}} = \begin{pmatrix} 1 + \frac{\Delta P}{\rho_D c_D^2} & 0 & 0 & 0 & -\frac{P_B}{P_D c_D^2} \\ n_x \frac{\Delta P}{2\rho_D^2 c_D} & 1 & 0 & 0 & \frac{n_x\left[1+\frac{P_B}{P_D}\right]}{2\rho_D c_D} \\ n_y \frac{\Delta P}{2\rho_D^2 c_D} & 0 & 1 & 0 & \frac{n_y\left[1+\frac{P_B}{P_D}\right]}{2\rho_D c_D} \\ n_z \frac{\Delta P}{2\rho_D^2 c_D} & 0 & 0 & 1 & \frac{n_z\left[1+\frac{P_B}{P_D}\right]}{2\rho_D c_D} \\ 0 & 0 & 0 & 0 & 0 \end{pmatrix} \tag{27}$$

$\Delta P = P_B - P_D$ is the static pressure difference across the boundary, whereas c_D and ρ_D are the speed of sound and density in the domain cell next to the outlet boundary.

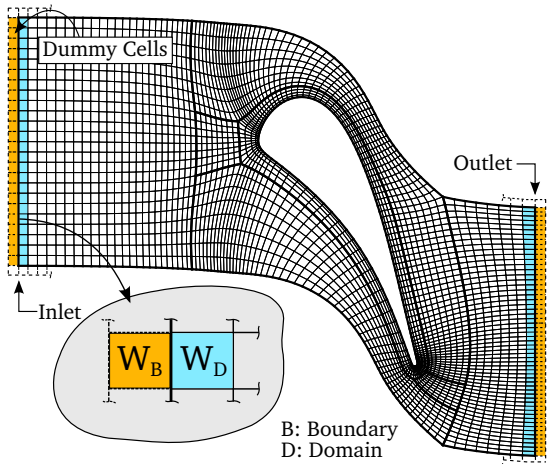

Figure 3: **Illustration for Linearization of the Cost Function at Domain Inlet and Outlet Boundaries. Dashed Lines at Inlet and Outlet Represent Dummy Cells**

Different averaging techniques may be used, which eventually lead to similar results, but as pointed out by [4], the linearized function might differ noticeably and, hence, might affect the adjoint solution. Using mass-flow averaging of quantities at inlet and outlet, a derivation of a linearized cost function may be found in [4].

5.2. *Differentiation of the Residual*

The differentiation of the residual is the most time consuming part within the development of discrete adjoint solvers due to the complexity of the numerical scheme, the neighboring cell dependency, and the accurate treatment of boundary conditions. While the former may be simplified using algorithmic differentiation (AD) tools, the latter two still remain a demanding task with increased complexity depending on the order of the spatial accuracy.

Differentiating the residual vector of cell i yields

$$\left[\frac{\partial \mathbf{R}}{\partial \mathbf{W}_{c,i}}\right]^T \boldsymbol{\psi} = \left[\frac{\partial \hat{\mathbf{F}}_c}{\partial \mathbf{W}_{c,i}} - \frac{\partial \hat{\mathbf{F}}_v}{\partial \mathbf{W}_{c,i}} - \frac{\partial \hat{\mathbf{Q}}}{\partial \mathbf{W}_{c,i}}\right]^T \boldsymbol{\psi} \tag{28}$$

where the fluxes $\hat{\mathbf{F}}_c$, $\hat{\mathbf{F}}_v$, and source term $\hat{\mathbf{Q}}$ are multiplied by the respective face area and cell volume. The source term jacobian ($\partial \hat{\mathbf{Q}}/\partial \mathbf{W}_{c,i}$) is straightforward to compute, whereas the convective and viscous flux jacobians are more complex, either due to the underlying numerical scheme of the convective flux or due to the next-neighbor cell dependence by the Green's theorem used to compute the spatial gradients for the viscous flux.

For the sake of convenience a one dimensional problem is considered in Fig. 4 for the inviscid flux, although the same methodology applies for the other two directions of the computational domain. Thus, the 2nd-order inviscid flux jacobian for cell i reads in

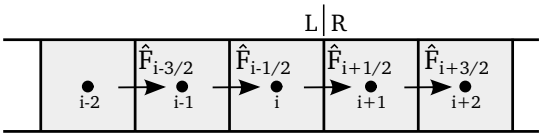

Figure 4: **One Dimensional Stencil for 2nd-Order Inviscid Flux Residual Computation of Cell$_i$.**

expanded formulation as

$$\begin{aligned}\left[\frac{\partial\hat{\mathbf{F}}_c}{\partial\mathbf{W}_{c,i}}\right]^T\boldsymbol{\psi} &= \left[\frac{\partial\hat{\mathbf{F}}_{c,i+1/2}}{\partial\mathbf{W}_{c,i}} - \frac{\partial\hat{\mathbf{F}}_{c,i-1/2}}{\partial\mathbf{W}_{c,i}}\right]^T\boldsymbol{\psi}_i \\ &+ \left[\frac{\partial\hat{\mathbf{F}}_{c,i-1/2}}{\partial\mathbf{W}_{c,i}} - \frac{\partial\hat{\mathbf{F}}_{c,i-3/2}}{\partial\mathbf{W}_{c,i}}\right]^T\boldsymbol{\psi}_{i-1} \\ &+ \left[\frac{\partial\hat{\mathbf{F}}_{c,i-3/2}}{\partial\mathbf{W}_{c,i}}\right]^T\boldsymbol{\psi}_{i-2} \\ &+ \left[\frac{\partial\hat{\mathbf{F}}_{c,i+3/2}}{\partial\mathbf{W}_{c,i}} - \frac{\partial\hat{\mathbf{F}}_{c,i+1/2}}{\partial\mathbf{W}_{c,i}}\right]^T\boldsymbol{\psi}_{i+1} \\ &+ \left[-\frac{\partial\hat{\mathbf{F}}_{c,i+3/2}}{\partial\mathbf{W}_{c,i}}\right]^T\boldsymbol{\psi}_{i+2} \end{aligned} \tag{29}$$

where e.g. the index i+1/2 indicates the face index between cell i and i+1. Regardless whether the Roe- or the AUSM$^+$-scheme with MUSCL reconstruction of primitive variables is employed, the inviscid flux jacobian may be expressed as, e.g. at face i+1/2

$$\begin{aligned}\frac{\partial\hat{\boldsymbol{F}}_{c,i+1/2}}{\partial\boldsymbol{W}_{c,i}} = [&\frac{\partial\hat{\boldsymbol{F}}_{c,i+1/2}}{\partial\boldsymbol{W}_{p,L}}\frac{\partial\boldsymbol{W}_{p,L}}{\partial\mathbf{W}_{p,i}} + \\ &\frac{\partial\hat{\boldsymbol{F}}_{c,i+1/2}}{\partial\boldsymbol{W}_{p,R}}\frac{\partial\boldsymbol{W}_{p,R}}{\partial\mathbf{W}_{p,i}}]\frac{\partial\boldsymbol{W}_{p,i}}{\partial\mathbf{W}_{c,i}}.\end{aligned} \tag{30}$$

$(\partial\hat{\boldsymbol{F}}_{c,i+1/2}/\partial\boldsymbol{W}_{p,L})$ and $(\partial\hat{\boldsymbol{F}}_{c,i+1/2}/\partial\boldsymbol{W}_{p,R})$ denote the exact differentiated flux function with respect to the left and right extrapolated state at the interface i+1/2 (see Fig. 4), while $(\partial\boldsymbol{W}_{p,L}/\partial\boldsymbol{W}_{p,i})$ and $(\partial\boldsymbol{W}_{p,R}/\partial\boldsymbol{W}_{p,i})$ are the differentiated van-Albada type MUSCL reconstruction scheme. Since primitive variables are used in the 2nd-order reconstruction, Eqn. 30 is multiplied by the primitive-to-conservative transformation matrix $(\partial\mathbf{W}_{p,i}/\partial\mathbf{W}_{c,i})$ defined in Appendix A. In order to shorten the development time of the discrete adjoint solver, the algorithmic differentiation tool TAPENADE [29] was used in forward mode for the exact differentiated inviscid flux functions in Eqn. 30.

Viscous flux jacobians (Eqn. 31) are differentiated by hand utilizing the constant eddy-viscosity (CEV) assumption, that is the turbulent viscosity does not depend on the flow variables $(\partial\mu_t/\partial\boldsymbol{W}_p = 0)$

$$\frac{\partial\hat{\boldsymbol{F}}_v}{\partial\mathbf{W}_c} = [\frac{\partial\hat{\boldsymbol{F}}_v}{\partial\mathbf{W}_p}\Big|_{\mu_t=const} + \frac{\partial\hat{\boldsymbol{F}}_v}{\partial\mu_t}\underbrace{\frac{\partial\mu_t}{\partial\boldsymbol{W}_p}}_{=0}]\frac{\partial\boldsymbol{W}_p}{\partial\boldsymbol{W}_c}. \tag{31}$$

This greatly simplifies the development of the discrete adjoint solver as the turbulence model is not differentiated. On the downside, it is a rather crude approximation and may cause inaccurate gradients in the design of transonic blades with strong shocks [30]. However, studies [30; 31] have shown that although gradients may differ the CEV assumption is a valid approach in engineering applications as the optimization convergences to nearly identical solutions.

The accuracy of the functional gradients depends heavily on the correct implementation of boundary conditions in the discrete adjoint solver. However, the differentiation of the boundary condition itself is straightforward and was already presented, e.g. for a subsonic outlet boundary in Eqn. 27. Instead, it is rather a systematic procedure, which has to be addressed and may be summarized as follows:

1. Apply boundary conditions, i.e. set dummy cell values,
2. set boundary-type specific transformation matrix $\partial\mathbf{W}_{p,B}/\partial\mathbf{W}_{p,D}$ (see Fig. 3),
3. compute boundary flux jacobian.

For a general case the flux jacobian comprising the linearized boundary condition reads as

$$\frac{\partial\hat{\boldsymbol{F}}}{\partial\mathbf{W}_{c,D}} = \frac{\partial\hat{\boldsymbol{F}}}{\partial\mathbf{W}_{c,D}} + \frac{\partial\hat{\boldsymbol{F}}}{\partial\mathbf{W}_{p,B}}\frac{\partial\mathbf{W}_{p,B}}{\partial\mathbf{W}_{p,D}}\frac{\partial\mathbf{W}_{p,D}}{\partial\mathbf{W}_{c,D}} \tag{32}$$

where the subscript (B) and (D) denote the boundary cell and domain cell, respectively. Again, $(\partial\mathbf{W}_{p,D}/\partial\mathbf{W}_{c,D})$ is the primitive-to-conservative transformation matrix defined in Appendix A. For the convective flux at a boundary two different scenarios are considered:

1) Inlet and outlet boundary condition

At inlet and outlet boundaries the computational stencil of the 2nd-order inviscid boundary flux includes two dummy cells (B1) and (B2) (see Fig. 5). Hence, the convective flux jacobian may be expressed as

$$\begin{aligned}\frac{\partial\hat{\boldsymbol{F}}_c}{\partial\mathbf{W}_{c,D}} = &\frac{\partial\hat{\boldsymbol{F}}_c}{\partial\mathbf{W}_{c,D}} + \\ &[\frac{\partial\hat{\boldsymbol{F}}_c}{\partial\mathbf{W}_{p,B1}}\frac{\partial\boldsymbol{W}_{p,B1}}{\partial\boldsymbol{W}_{p,D}} + \frac{\partial\hat{\boldsymbol{F}}_c}{\partial\mathbf{W}_{p,B2}}\frac{\partial\boldsymbol{W}_{p,B2}}{\partial\boldsymbol{W}_{p,D}}]\frac{\partial\boldsymbol{W}_{p,D}}{\partial\mathbf{W}_{c,D}}.\end{aligned} \tag{33}$$

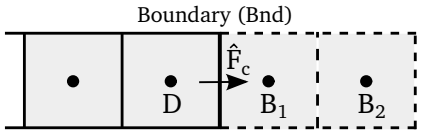

Figure 5: **One Dimensional Stencil for Inviscid Boundary Flux. Dashed Lines Indicate Dummy Cells.**

The convective flux next to the boundary, i.e. one face inside the domain is treated similarly, since the 2nd-order stencil includes one dummy cell.

2) Solid wall

At solid walls the relative contravariant velocity vanishes ($W_n = 0$) and the convective flux (Eqn. 12) can be specified explicitly with the extrapolated static pressure at the wall P_{wall}:

$$\boldsymbol{F}_{c,wall} = \begin{pmatrix} 0 \\ \mathbf{n}P_{wall} \\ V_n P_{wall} \end{pmatrix} \tag{34}$$

Hence, the differentiated wall flux reads as

$$\frac{\partial \hat{\boldsymbol{F}}_{c,wall}}{\partial \mathbf{W}_{c,D}} = 0.5\Big[\frac{\partial \hat{\boldsymbol{F}}_{c,wall}}{\partial \mathbf{W}_{p,D}} + \frac{\partial \hat{\boldsymbol{F}}_{c,wall}}{\partial \mathbf{W}_{p,B1}} \frac{\partial \boldsymbol{W}_{p,B1}}{\partial \mathbf{W}_{p,D}}\Big] \frac{\partial \boldsymbol{W}_{p,D}}{\partial \mathbf{W}_{c,D}}. \tag{35}$$

The boundary-type transformation matrix ($\partial \boldsymbol{W}_{p,B1}/\partial \mathbf{W}_{p,D}$) depends on the extrapolation of the static pressure at the wall P_{wall} (0-th or 1st-order) and is given in Appendix B.

6. Gradient Calculation

Once Eqn. 8 is solved, the adjoint solution ($\boldsymbol{\psi}$) is used to obtain the cost function sensitivities with respect to the grid coordinates ($dJ/d\boldsymbol{X}$) in a post-processing routine. If inlet and outlet boundaries are fixed, i.e. do not change during the optimization process, Eqn. 9 simplifies to

$$\frac{dJ}{d\boldsymbol{X}} = \underbrace{\frac{\partial J}{\partial \boldsymbol{X}}}_{=0.0} - \boldsymbol{\psi}^T \frac{\partial \boldsymbol{R}}{\partial \boldsymbol{X}}, \tag{36}$$

where ($\partial \boldsymbol{R}/\partial \boldsymbol{X}$) is computed using algorithmic differentiation (AD) in forward mode. Since the grid coordinates ($\boldsymbol{X}$) do not appear explicitly in the residual formulation (Eqn. 19), but in the geometrical properties (face normal vectors $\boldsymbol{S}$, cell volumes Ω, cell centers C), which are used to compute the fluxes and source term, it is convenient to split the expression in chunks:

$$\frac{\partial \boldsymbol{R}(\boldsymbol{S},\Omega,C)}{\partial \boldsymbol{X}} = \frac{\partial \hat{\boldsymbol{F}}_c(\boldsymbol{S})}{\partial \boldsymbol{X}} - \frac{\partial \hat{\boldsymbol{F}}_v(\boldsymbol{S},\Omega)}{\partial \boldsymbol{X}} - \frac{\partial \hat{\boldsymbol{Q}}(\Omega,C)}{\partial \boldsymbol{X}} \tag{37}$$

and further

$$\begin{aligned} \frac{\partial \boldsymbol{R}(\boldsymbol{S},\Omega,C)}{\partial \boldsymbol{X}} = {} & \frac{\partial \hat{\boldsymbol{F}}_c}{\partial \boldsymbol{S}} \frac{\partial \boldsymbol{S}}{\partial \boldsymbol{X}} \\ & - \Big[\frac{\partial \hat{\boldsymbol{F}}_v}{\partial \boldsymbol{S}} \frac{\partial \boldsymbol{S}}{\partial \boldsymbol{X}} + \frac{\partial \hat{\boldsymbol{F}}_v}{\partial \Omega} \frac{\partial \Omega}{\partial \boldsymbol{X}}\Big] \\ & - \Big[\frac{\partial \hat{\boldsymbol{Q}}}{\partial \Omega} \frac{\partial \Omega}{\partial \boldsymbol{X}} + \frac{\partial \hat{\boldsymbol{Q}}}{\partial C} \frac{\partial C}{\partial \boldsymbol{X}}\Big]. \end{aligned} \tag{38}$$

($\partial \boldsymbol{S}/\partial \boldsymbol{X}$), ($\partial \Omega/\partial \boldsymbol{X}$), and ($\partial C/\partial \boldsymbol{X}$) involve the linearization of algorithms, which generate the geometrical properties and may be found in [22].

Finally, the cost function gradients ($dJ/d\boldsymbol{\alpha}$), i.e. with respect to design variables are computed as follows

$$\frac{dJ}{d\boldsymbol{\alpha}} = \frac{dJ}{d\boldsymbol{X}} \frac{d\boldsymbol{X}}{d\boldsymbol{\alpha}}, \tag{39}$$

which is like a scalar product of two vector fields over the entire computational grid. ($d\boldsymbol{X}/d\boldsymbol{\alpha}$) involves the linearization of the CAD-kernel and the grid generation and is currently computed in parallel by finite differences.

7. LS89 Test Case

The LS89 turbine blade was designed and optimized for a downstream isentropic Mach number of $Ma_{is,2} = 0.9$ by means of an inverse design method [32]. In order demonstrate the capabilities of the developed gradient-based optimization system it has been redesigned for transonic conditions with an outlet isentropic Mach number of $Ma_{is,2} = 1.02$ ($Re_2 = 10^6$) aiming at minimizing losses, while retaining the flow turning.

7.1. CAD-Based Parametrization

A CAD-based parametrization is used to define the geometry of the turbine blade profile and has certain advantages related to use of engineering design parameters, the control of geometrical constraints, and eventually the manufacturing. Furthermore, it allows for smooth shape variations, while implicitly suppressing high frequency sensitivity oscillations [33; 34].

In present work the parametrization method proposed in [35] is used to define the turbine blade and is

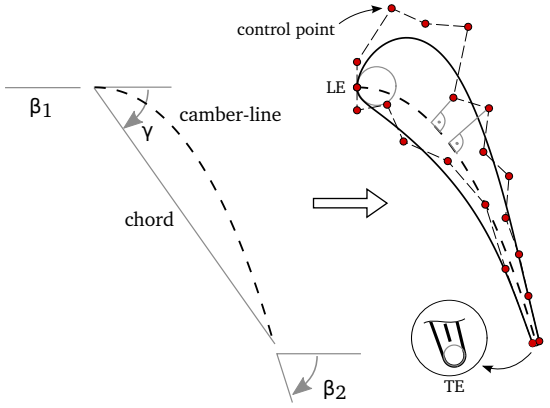

Figure 6: **Parametrization of the LS89 Turbine Blade, with Camber-line Construction (left) and Suction- and Pressure Side Construction (right).**

7.2. Objective and Constraint Definition

The aim of the redesign of the LS89 blade for transonic conditions is to minimize total pressure loss, while retaining the exit flow angle. Instead of using the loss coefficient from TN174 [18]

$$\zeta_2 = 1 - \frac{1 - \frac{P_2}{P_{02}}^{\frac{\gamma-1}{\gamma}}}{1 - \frac{P_2}{P_{01}}^{\frac{\gamma-1}{\gamma}}} \tag{40}$$

the objective is to minimize the mass-flow averaged normalized entropy difference between inlet and outlet of the domain

$$Obj. = \Delta s = \frac{s_{out} - s_{in}}{s_{ref}}, \quad s = \frac{P}{\rho^\gamma}. \tag{41}$$

This eventually lead to similar results as compared to a loss coefficient but simplifies the linearization of the objective function in the discrete adjoint solver [4].

The objective is constrained by the mass-flow averaged outlet flow angle

$$Constr. = \alpha_{out} \geq 74°, \tag{42}$$

which should not be smaller than 74° from axial direction in order to maintain the flow turning and hence the work of the original blade.

7.3. Design Variables and Gradient Verification

Design variables are the set of control points defining the pressure- and suction-side curves (see Fig. 6), i.e. the normal distance of each point with respect to the blade camber-line. In total 13 design parameters are used (pressure side: 4, suction side: 9), whereas the remaining parameters (blade chord, inlet and outlet metal angle, stagger angle, leading and trailing edge radius) remain unaltered during the optimization.

The adjoint-based gradients ($dJ/d\boldsymbol{\alpha}$) have been verified with 2nd-order finite differences, which is illustrated in Fig. 7 for both the objective function gradients (top) and constraint function gradients (bottom). Each function required 26 CFD simulations to fill the complete gradient vector using finite-differences, while only two simulations (1 CFD + 1 Adjoint simulation) were required per function to get the entire adjoint-based gradient vector.

In Fig. 7 the design variables α_1-α_4 and α_5-α_{13} represent the pressure side and suction side control points, respectively. Two conclusions may be drawn from this plot: first, finite-difference and adjoint-based gradients are in fair agreement for all design parameters, but more importantly the direction of the functional gradients is consistent. Second, the gradient deviation of design parameters α_9 and α_{10} may be related to the CEV assumption, as both parameters influence the shock strength and its position on the suction side and hence the region of adverse pressure gradient, where this assumption might be invalid. However, this has also been observed by [30] and is still considered moot for this test case.

7.4. Results

In Fig. 8 the convergence history of the gradient-based optimization is presented showing both the evolution of the objective function (entropy generation Δs) to the left and constraint function (exit flow angle α_{out}) to the right. Both values have been normalized with their respective initial value. Additionally, the loss coefficient (Eqn. 40) is included in this plot to illustrate that it closely resembles the entropy generation objective. Only three iterations were necessary for the optimization algorithm to converge. In the first iteration the entropy generation could be reduced by about $\Delta(\Delta s) = -11$ %, followed by minor

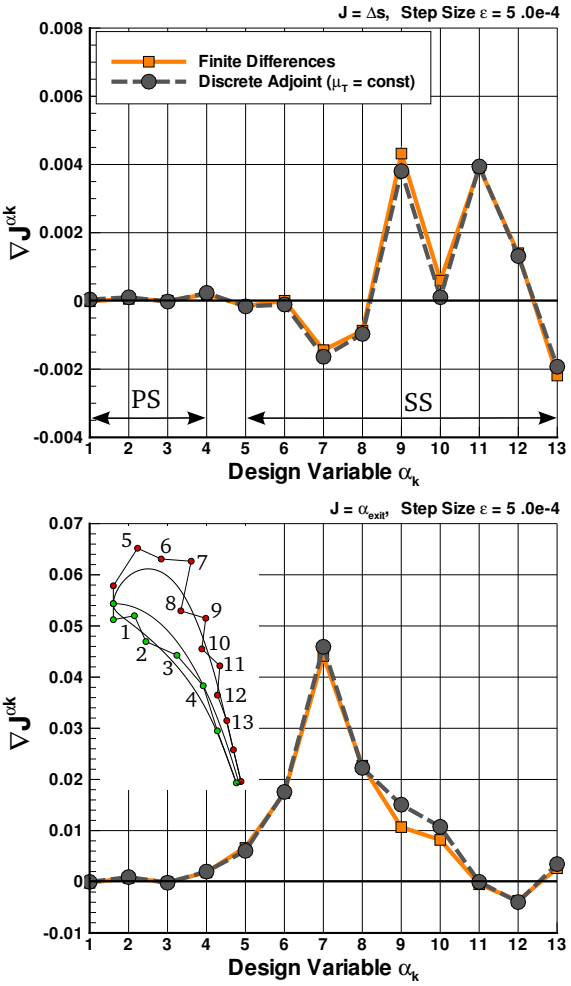

Figure 7: **Comparison of Functional Gradients of Discrete Adjoint Method with Finite differences (Step Size $\epsilon = 5e$-4). Top: Entropy Generation, Bottom: Exit Flow Angle. PS and SS Denote Control Points on Pressure and Suction Side.**

improvements in the next two iterations until the process stopped in the third iteration as no further improvement could be archived. As can be seen in Fig. 8, the optimization algorithm was able to retain the exit flow angle to $\alpha_{out} \geq 74°$, and thus, satisfy the constraint.

The improvement of the objective function value (Δs) of the redesigned blade profile is mainly attributed to a weaker and delayed shock on the suction side (see Fig. 9). Since the shock has been shifted further downstream closer to the trailing edge, the region of adverse pressure gradient is reduced where large portion of losses are accumulated.

This is further illustrated in Fig. 10 showing the entropy difference contour close to the rear part of the suction-side between the redesigned and the original geometry. Since a negative difference indicates reduced losses, the weaker and delayed shock of the redesigned blade profile may be identified as the main cause for the improved objective.

In general, the redesigned blade was only slightly modified as compared to the original profile (Fig. 11) although no geometrical limitations were imposed on the design parameters. However, it is difficult to draw conclusions from Fig. 11. Instead, Fig. 12 provides more insight into the design modifications. It shows the blade isentropic Mach number M_{is} next to the suction side curvature κ. Two regions may be identified: first ①, between $S/C_{ax} \approx 0.3 - 0.57$ the curvature of the redesigned blade is increased and hence the acceleration is steeper as compared to the original blade due to higher convex curvature. Second ②, when the flow reaches sonic conditions at $S/C_{ax} \approx 0.57$ the curvature is sightly reduced for the redesigned blade until $S/C_{ax} \approx 0.87$. Thanks to the gradient-based optimization method, the necessary (small) modifications were found to improve the objective by 11 % and redesign the blade for a downstream isentropic Mach number $Ma_{is,2} = 1.02$, while retaining the flow turning of the original blade.

7.5. *Sensitivity Map*

The sensitivity of the cost function ($dJ/d\boldsymbol{X} = \partial J/\partial \boldsymbol{X} - \boldsymbol{\psi}^T \partial \boldsymbol{R}/\partial \boldsymbol{X}$) is an intermediate solution in the adjoint-based gradient evaluation chain (see. Fig. 1). However, it provides valuable insight into the design

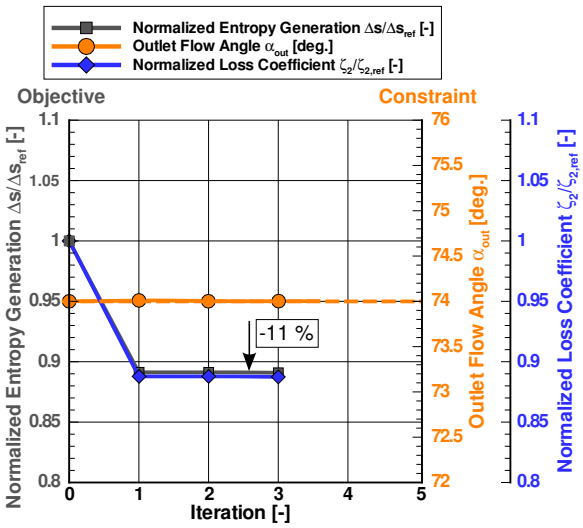

Figure 8: **Convergence History of the Gradient-Based Optimization.**

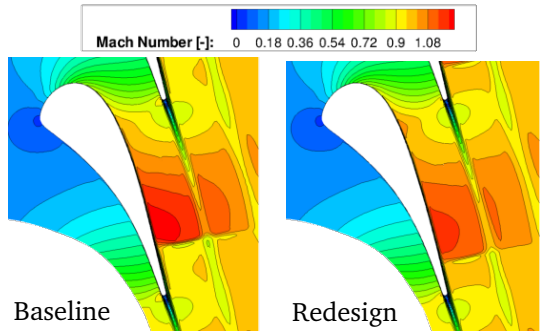

Figure 9: **Mach Number contour of the baseline (left) and the redesigned blade profile (right).**

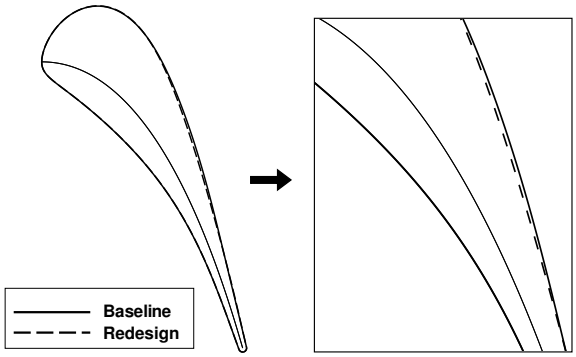

Figure 11: **Blade Profile of Baseline and Redesigned Geometry**

problem as illustrated in Fig. 13 showing the surface sensitivities of the objective function (right) and the constraint function (left). Each surface grid vector indicates the direction and magnitude of decreased function value of the entropy generation Δs in Fig. 13 (left) and of the exit flow angle α_{exit} in Fig. 13 (right). On the one hand it directly shows how to modify the blade profile for the respective target, on the other hand, this demonstrates the conflicting design requirements of reducing losses and retaining the blade turning as some vectors are pointing in opposite direction on the suction side of the blade.

8. Conclusions

A gradient-based aerodynamic shape optimization methodology using a CAD-based discrete adjoint approach is described. The core of the optimization system is 3D multi-block structured Navier-Stokes solver, the corresponding discrete adjoint solver, and a sequential quadratic programming optimization algorithm. A CAD-based shape parametrization is used inside the design loop to evaluate cost function sensitivities robustly.

The potential of the developed system is demonstrated by redesigning the LS89 turbine blade for transonic conditions aiming at minimizing entropy generation, while retaining the exit flow angle. Only three iterations were necessary for the optimization system to converge. Thanks to the gradient-based optimization method, the necessary (small) modifications were found to improve the objective by 11 % and redesign the blade for a downstream isentropic Mach number $Ma_{is,2} = 1.02$, while retaining the flow turning of the original blade.

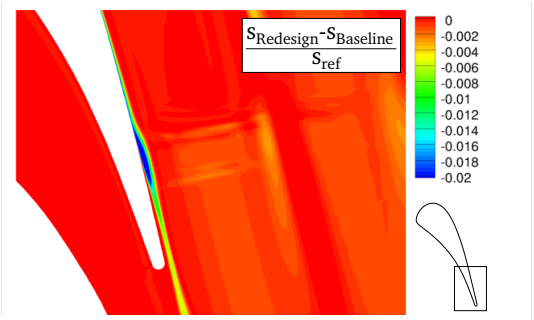

Figure 10: **Entropy Difference Plot Between Redesigned Blade and Baseline Geometry.**

References

[1] Wang D.X.; He L., Adjoint Aerodynamic Design Optimization for Blades in Multi-Stage Turbomachines: Part I -

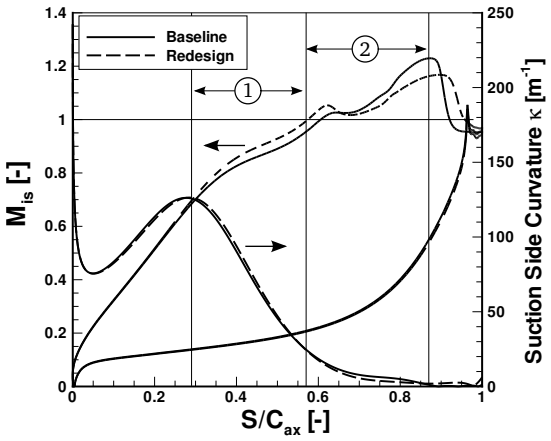

Figure 12: **Blade Isentropic Mach Number Distribution of the Baseline and the Redesigned Blade and Suction Side Curvature Distribution.**

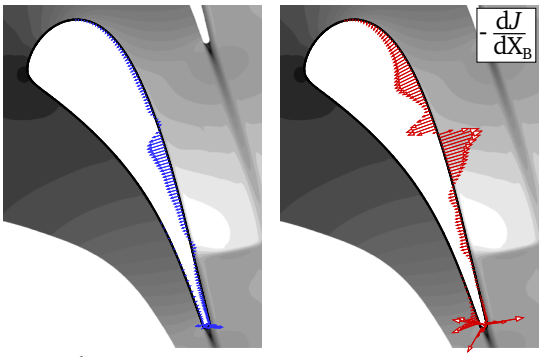

Figure 13: **Normalized Blade Surface Sensitivities (-** dJ/dX_B**) of the 1st-Iteration of the Objective Function (left) and Constraint Function (right) with Mach Number Contour in Background.**

Methodology and Verification, Journal of Turbomachinery 132 (2) (2010) 14 pages.

[2] Mueller L.; Alsalihi Z.; Verstraete T., Multidisciplinary Optimization of a Turbocharger Radial Turbine, J. Turbomach. 135 (2) (2013) 9 pages.

[3] Joly M.; Verstaete T.; Paniagua G., Multidisciplinary Design Optimization of a Compact Highly Loaded Fan, Structural and Multidisciplinary Optimization 49 (3) (2014) 471–483.

[4] Walther B.; Nadarajah S., Optimum Shape Design for Multirow Turbomachinery Configurations Using a Discrete Adjoint Approach and an Efficient Radial Basis Function Deformation Scheme for Complex Multiblock Grids, Journal of Turbomachinery 137 (8) (2015) 20 pages.

[5] Vanderplaats G.N., Numerical Optimization Techniques for Engineering Design, Vanderplaats Research and Development, Inc, 2001.

[6] Zingg D.W.; Nemec M.; Pulliam T.H., A Comparative Evaluation of Genetic and Gradient-Based Algorithms Applied to Aerodynamic Optimization, European Journal of Computational Mechanics 17 (1-2) (2008) 103–126.

[7] Newman J.C.; Anderson W.K. Whitfield D.L., Multidisciplinary Sensitivity Derivatives Using Complex Variables, Tech. Rep. MSSU-COE-ERC-98-08, Mississippi State University (1998).

[8] Jameson A., VKI Lecture Series on Aerodynamic Drag Prediction and Reduction, von Karman Institute for Fluid Dynamics, 2003, Ch. Aerodynamic Shape Optimization Using the Adjoint Method.

[9] Giles M.B.; Pierce N.A., AnIntroduction to the Adjoint Approach to Design, Flow,Turbulence and Combustion 65 (2000) 393–415.

[10] Jameson A., Aerodynamic Design Via Control Theory, Journal of Scientific Computing 3 (3) (1988) 233–260.

[11] Giles M.B.; Duta M.C; Mueller J.D.; Pierce N.A., Algorithm Developments for Discrete Adjoint Methods, AIAA Journal 41 (2) (2003) 198–205.

[12] Bischof C.; Corliss G.; Green L.; Griewank A.; Haigler K.; Newman P., Automatic Differentiation of Advanced CFD Codes for Multidisciplinary Design, Computing Systems in Engineering 3 (6) (1992) 625–637.

[13] V. M. Sherman L. L.; Taylor III A. C.; Green L. L.; Newman P. A.; Hou G. W.; Korivi, First-and Second-order Aerodynamic Sensitivity Derivatives via Automatic Differentiation with Incremental Iterative Methods, Journal of Computational Physics 129 (2) (1996) 307–331.

[14] Mader C.A.; Martins R.R.A.; Alonso J.J.; van der Weide E., ADjoint: An Approach for the Rapid Development of Discrete Adjoint Solvers, AIAA Journal 46 (4) (2008) 863–873.

[15] Z. Lyu, G. K. W. Kenway, C. Paige, J. R. R. A. Martins, Automatic Differentiation Adjoint of the Reynolds-Averaged Navier-Stokes Equations with a Turbulence Model, in: 43rd AIAA Fluid Dynamics Conference and Exhibit, 2013, aIAA 2013-2581.

[16] Gill P.E., Murray W., Saunders M.A., User's Guide for SNOPT Version 7: Software for Large-Scale Nonlinear Programming (2008).

[17] Gill P.E., Murray W., Saunders M.A., An SQP algorithm for Large-Scale Constrained Optimization, SIAM J. Optim. 12 (2002) 979–1006.

[18] Arts T.; de Rouvroit L.; Rutherford A.W., Aero-Thermal Investigation of a Highly Loaded Transonic Linear Turbine Guide Vane Cascade, Techncal Note 174, von Karman Institute for Fluid Dynamics (1990).

[19] Roe P.L., Approximate Riemann Solvers, Parameter Vectors, and Difference Schemes, Journal of Computational Physics 43 (1981) 357–372.

[20] Liou M.-S., A Sequel to AUSM, Part 2: AUSM+-Up for All Speeds, Journal of Computational Physics 214 (2006) 137–170.

[21] van Albada G.D.; van Leer B.; Roberts Jr. W.W, A Comperative Study of Computational Methods in Cosmic Gas Dynamics, Journal of Astronomy and Astrophysics 108 (1982) 76–84.

[22] Blazek J., Computational Fluid Dynamics: Principles and Applications, Elsevier Science Ltd, Amsterdam, 2001.

[23] Spalart P. R.; Allmaras S. R., A One-Equation Turbulence Model for Aerodynamic Flows, Recherche Aerospatiale 1 (1994) 5–21.

[24] Zhang Q.; Yang Y., A new simpler rotation-curvature correction method for Spalart-Allmaras turbulence model, Chinese Journal of Aeronautics 26 (2) (2013) 326–333.

[25] S. Balay, S. Abhyankar, M. F. Adams, J. Brown, P. Brune, K. Buschelman, V. Eijkhout, W. D. Gropp, D. Kaushik, M. G. Knepley, L. C. McInnes, K. Rupp, B. F. Smith, H. Zhang, PETSc Web page, `http://www.mcs.anl.gov/petsc` (2014).
URL `http://www.mcs.anl.gov/petsc`

[26] Nielsen E.J.; Anderson W.K., Aerodynamic Design Optimization on Unstructured Meshes Using the Navier-Stokes Equations, AIAA Journal 37 (11) (1999) 1411–1419.

[27] Dwight R.P.; Brezillion J., Effect of Approximation of the Discrete Adjoint on the Gradient-Based Optimization, AIAA Journal 4412 (2006) 3022–3031.

[28] Carpentieri G.; von Tooren M.J.L; Koren B.:, Computational Fluid Dynamics 2006, Springer, 2009, Ch. Comparison of Exact and Approximate Discrete Adjoint for Aerodynamic Shape Optimization, pp. 1–6.

[29] L. Hascoët, V. Pascual, The Tapenade Automatic Differentiation tool: Principles, Model, and Specification, ACM Transactions On Mathematical Software 39 (3).
URL `http://dx.doi.org/10.1145/2450153.2450158`

[30] Kim C.S.; Kim C.; Rho O.H., Feasibility Study of Constant Eddy-Viscosity Assumption in Gradient-Based Design Optimization, Journal of Aircraft 40 (6) (2003) 1168–1176.

[31] Marta A.C.; Shankaran S., On the Handling of Turbulence Equations in RANS Adjoint Solvers, Computer & Fluids 74 (2013) 102–113.

[32] van den Braembussche R.A.; Leonard O.; Nekmouche L.,

Subsonic and Transonic Blade Design by Means of Analysis Codes, in: Computational Methods for Aerodynamic Design (Inverse) and Optimization, 1989.
[33] Yu G.; Müller J.-D.; Jones D.; Christakopoulos F., CAD-Based Shape Optimization Using Adjoint Sensitivities, Computer & Fluids 46 (2011) 512–516.
[34] Xu S.; Jahn W.; Müller J.-D., CAD-Based Shape Optimization with CFD Using a Discrete Adjoint, Int. J. Numer. Meth. Fluids 74 (3) (2014) 153–168.
[35] Pierret S., Designing Turbomachinery Blades by Means of the Function Approximation Concept Based on Artificial Neural Network, Genetic Algorithm, and the Navier-Stokes Equations, Ph.D. thesis, Faculté Polytechnique de Mons (1999).

9. Nomenclature

Latin

c	Speed of sound
C	Cell center
C_{ax}	Axial chord length
e	Specific internal energy
E	Specific total energy
$\boldsymbol{F}_c$	Convective flux vector
$\hat{\boldsymbol{F}}_c$	Convective flux vector multiplied by face area ($\boldsymbol{F}_c \Delta S$)
$\boldsymbol{F}_v$	Viscous flux vector
$\hat{\boldsymbol{F}}_v$	Viscous flux vector multiplied by face area ($\boldsymbol{F}_v \Delta S$)
$\overline{\boldsymbol{I}}$	Identity matrix
J	Function of interest, Cost-Function
k	Thermal conductivity coefficient
M_{is}	Isentropic Mach number
$\boldsymbol{n}$	Unit normal vector
$\boldsymbol{Q}$	Source term vector
$\hat{\boldsymbol{Q}}$	Source term vector multiplied by cell volume ($\boldsymbol{Q}\Omega$)
P	Static pressure
P_0	Absolute total pressure
$\boldsymbol{R}$	Residual vector
s	Specific entropy
S	Meridional length
$\boldsymbol{S}$	Normal vector
U	Peripheral speed
$\boldsymbol{V}$	Absolute velocity vector
V_n	Absolute contravariant velocity
$\boldsymbol{W}$	Relative velocity vector
W_n	Relative contravariant velocity
$\boldsymbol{W}_c$	Vector of conservative variables
$\boldsymbol{W}_c^*$	Converged flow solution
$\boldsymbol{W}_p$	Vector of primitive variables
$\boldsymbol{X}$	Vector of grid coordinates

Greek

α	Absolute flow angle
$\boldsymbol{\alpha}$	Vector of design variables
γ	Ratio of specific heats
Δ	Delta/difference
ΔS	Face area
Δt	Time step
ϵ	Step size
ζ	Loss coefficient
κ	Curvature
μ	Viscosity
ρ	Density
$\boldsymbol{\psi}$	Adjoint vector/co-state vector
$\boldsymbol{\omega}$	Angular rotational speed
Ω	Cell volume

Subscripts and Superscripts

$1, 2$	Inlet,outlet
B	Boundary
D	Domain
i	Cell index
j	Face index
k	Design variable index
l	Laminar
L	Left
R	Right
ref	Reference
t	Turbulent
x, y, z	Coordinate directions

AD	Algorithmic Differentiation
CAD	Computer Aided Design
CFD	Computational Fluid Dynamics
CEV	Constant Eddy Viscosity
Constr	Constraint
LE	Leading edge
Obj	Objective
PS, SS	Pressure Side, Suction Side
MPI	Message Passing Interface
MUSCL	Monotonic Upstream-Centered Scheme for Conservation Laws
PETSc	Portable, Extensible Toolkit for Scientific Computation
RANS	Reynolds-Averaged Navier-Stokes
RHS	Right-hand side
SNOPT	Sparse Nonlinear OPTimizer
SQP	Sequential Quadratic Programming
TE	Trailing edge

Appendix A. Primitive to Conservative Jacobian

$$\frac{\partial \mathbf{W}_p}{\partial \mathbf{W}_c} = \begin{pmatrix} 1 & 0 & 0 & 0 & 0 \\ -\frac{V_x}{\rho} & -\frac{1}{\rho} & 0 & 0 & 0 \\ -\frac{V_y}{\rho} & 0 & -\frac{1}{\rho} & 0 & 0 \\ -\frac{V_z}{\rho} & 0 & 0 & -\frac{1}{\rho} & 0 \\ \frac{\gamma-1}{2}(V_x^2+V_y^2+V_z^2) & (1-\gamma)V_x & (1-\gamma)V_y & (1-\gamma)V_z & \gamma-1 \end{pmatrix}$$

Appendix B. Boundary Transformation Matrix at Solid Wall with Slip Boundary Condition

1) 0-th order pressure extrapolation ($P_{wall} = P_{D1}$)

$$\frac{\partial \mathbf{W}_{p,B1}}{\partial \mathbf{W}_{p,D1}} = \begin{pmatrix} 1 & 0 & 0 & 0 & 0 \\ 0 & 1-2n_xn_x & -2n_xn_y & -2n_xn_z & 0 \\ 0 & -2n_yn_x & 1-2n_yn_y & -2n_yn_z & 0 \\ 0 & -2n_zn_x & -2n_zn_y & 1-2n_zn_z & 0 \\ 0 & 0 & 0 & 0 & 1 \end{pmatrix}$$

2) 1-th order pressure extrapolation ($P_{wall} = 0.5(3P_{D1} - P_{D2})$)

$$\frac{\partial \mathbf{W}_{p,B1}}{\partial \mathbf{W}_{p,D1}} = \begin{pmatrix} 1 & 0 & 0 & 0 & 0 \\ 0 & 1-2n_xn_x & -2n_xn_y & -2n_xn_z & 0 \\ 0 & -2n_yn_x & 1-2n_yn_y & -2n_yn_z & 0 \\ 0 & -2n_zn_x & -2n_zn_y & 1-2n_zn_z & 0 \\ 0 & 0 & 0 & 0 & 2 \end{pmatrix}$$

$$\frac{\partial \mathbf{W}_{p,B1}}{\partial \mathbf{W}_{p,D2}} = \begin{pmatrix} 0 & 0 & 0 & 0 & 0 \\ 0 & 0 & 0 & 0 & 0 \\ 0 & 0 & 0 & 0 & 0 \\ 0 & 0 & 0 & 0 & 0 \\ 0 & 0 & 0 & 0 & -1 \end{pmatrix}$$

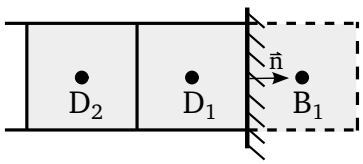

Figure B.14: **One Dimensional Stencil at Solid Wall. Dashed Lines Indicate Dummy Cell.**

One-Dimensional Assessment of Supersonic Inlet Turbines

Jorge Sousa

Aeronautics and Aerospace Department, von Karman Institute for Fluid Dynamics, Belgium, jorge.sousa@vki.ac.be

Supervisor: Guillermo Paniagua

Adjunct Professor, Aeronautics and Aerospace Department, von Karman Institute for Fluid Dynamics, Belgium, gpaniagua@vki.ac.be

University Supervisor: Iskender Gokalp

Director of the ICARE laboratory, Université d Orleans, France, iskender.gokalp@cnrs-orleans.fr

Abstract

Turbines operating with supersonic flows offer a potential reduction of the power plant size as a result of the increase in specific mass flow rate and higher specific power. This paper presents a one-dimensional methodology to evaluate the performance of turbines operating with axial supersonic flow, which represents a necessary step towards the optimized design. The predicted evolution of the losses with inlet Mach number ($M_{inlet} = 1.5 - 3.0$) and the influence of the chord to pitch ratio were confirmed through comparisons with three dimensional RANS evaluations. The paper presents an analysis of the most relevant sources of entropy, which in the investigated operating range, are caused by the leading edge shock waves. Finally, the proposed methodology narrowed the design space to all operable configurations and searched for an optimal design that maximizes the work output.

Keywords: Supersonic turbine, loss prediction, shock losses, viscous losses

1. Introduction

Novel massively compact fluid machinery can be developed through the implementation of fully supersonic turbines. However, internal flow operating in the supersonic regime is a challenge due to the associated large shock wave losses and narrow operational range [1; 2]. The public available literature on supersonic turbines is restricted to subsonic axial inlet conditions. Those turbines were developed in the 1950s for rocket propulsion due to the inherently higher specific power per blade row, allowing a substantial reduction in the length of the overall engine [3; 4]. A further reduction in the cross sectional area can be achieved through a specific mass flow rate increase, regulated by the axial Mach number. Fig. 1 depicts the normalized specific mass flow rate ($kg/s.m^2$) as a function of the axial Mach number, which is maximized at sonic conditions. At Mach one, a reduction of the turbine number of stages, and diameter is attainable, indeed the specific mass flow rate is 3 times larger than conventional sub-sonic turbines (operating in a low subsonic axial inlet velocity, $M_{inlet} = 0.2$).

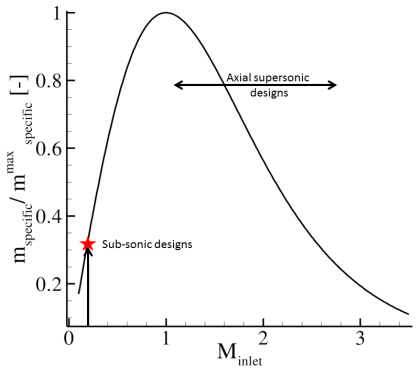

Figure 1: Specific flow rate normalized its maximum value ($M_{inlet} = 1$) for the same total inlet conditions.

However, the operation at sonic conditions requires a very limited turning to ensure that the initial starting shock wave is expelled (supersonic starting). Previous attempts to operate conventional turbine designs with supersonic inlet flows have led to inadequate efficiencies, which endangered the viability of any minia-

turized engine [5]. Convergent passages, such as the ones found in turbine nozzles, when subjected to supersonic inlets may not be able to swallow all the imposed mass flow which results in undesired operation know as unstarted. Fig. 2 plots the inlet Mach number and the area contraction ratio between the throat and the inlet (A_{throat}/A_{inlet}). From an isentropic analysis one can compute, the area ratio for which sonic conditions are obtained at the throat (choked condition). This isentropic limit is represented by the dashed red line in Fig. 2 and its value can be obtain with Eq. 1 for a certain inlet Mach number (M_{inlet}).

$$\frac{A_{throat}}{A_{inlet}} = \frac{1}{M_{inlet}} \left(\frac{2(1+(\gamma-1)/2)M_{inlet}^2}{\gamma+2} \right)^{-(\gamma+1)/(2(\gamma-1))} \quad (1)$$

When considering an area contraction below the isentropic limit the total amount of the mass flow rate cannot pass through the throat. Consequently, a normal shock wave moves upstream towards the combustor and the power plant operation is physically not possible. Additionally, as observed by Kantrowitz [6] in most of the applications the establishment of supersonic flow is preceded by a normal shock (when passing from sub-sonic to supersonic flow) traveling across the engine. If one considers that this normal shock stands momentarily in front of the blades subsonic flow move into the passage (with the conditions after a normal shock). Hence, the previously defined isentropic limit does not ensure anymore an operable design. In this case the throat needs to have sufficient area to pass all the mass flow of a gas with the post-shock properties. Only then, the normal shock wave is convected through the passage and supersonic flow can be established. When this occurs the passage is considered to be started. An inviscid approximation of the contraction ratio that, ensures this condition, can be found from conventional one-dimensional flow theory. Considering an incoming Mach number M_1 the conditions after the normal shock can be computed based on Eq. 2.

$$M_2^2 = \frac{(\gamma-1)M_1^2+2}{2\gamma M_1^2-(\gamma-1)} \quad (2)$$

Hence, one can compute the correct isentropic limit based on the updated Mach number (M_2) with Eq 1. This restriction is named the Kantrowitz limit and is represented in Fig. 2 by the solid blue line. The region between the isentropic and the Kantrowitz limit is known as dual solution zone, where both started and unstated solutions can occur, depending on the establishment history of the supersonic flow. Hence, the area ratio of a supersonic passage should always stand above the Kantrowitz limit, in order to invariably ensure a fully self-started machine.

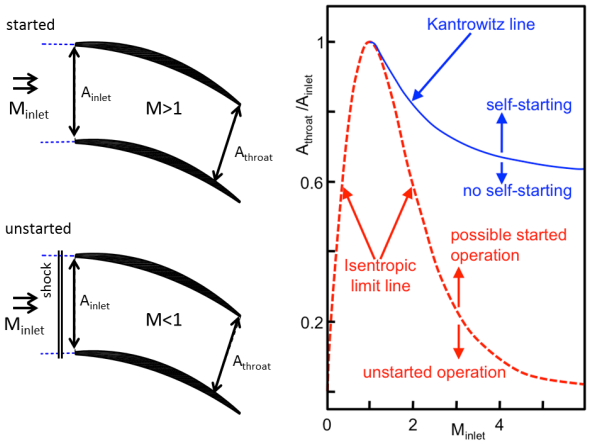

Figure 2: Possible turbine operation: The red dashed line represents the isentropic limit (in terms of area contraction) in function of the inlet Mach number. The blue solid line marks the Kantrowitz limit. The area above the solid line represents the self-starting zone and below the dashed lines the unstarted zone.

Due to mechanical and coolability constraints, sharp leading edges are not feasible; therefore, detached shock waves appear at the leading edges. In the case $M_{axial} > 1$, as illustrated in Fig. 3, the two shock waves and the correspondent expansion fans move inside the passage. As a consequence, both shock waves interact with the boundary layer of the neighbor airfoil, and two reflected shocks are generated and propagated further downstream. The shock waves themselves and its interactions with the boundary layer are responsible for important entropy generation that deteriorates the turbine performance.



Figure 3: Numerical Schlieren visualization of the shock waves in supersonic passages

The objective of this paper is to evaluate the im-

plementation of supersonic turbine designs, addressing the potential size, weight and stage reduction in virtue of the supersonic flow velocities, while delivering a higher work output than conventional designs. The paper first presents two detrimental aspects: the aerodynamic design constraints and the prediction of the most relevant loss generation mechanisms. Afterward, the 1D design and assessment methodology is described and the optimum designs are evaluated.

2. Inlet supersonic aerodynamic constraints

Currently there are no turbine losses correlations available in the open literature for supersonic inlet conditions. This paper proposes a methodology to compute the main loss mechanisms, which is pivotal towards the geometrical definition of the most suitable turbine in each specific application.

2.1. Flow turning limitation

As shown in Fig. 4, the cross-sectional area (A) of a turbine passage is specified by the pitch (g), throat angle (which is nearly the outlet flow angle, α_{throat}), and the height of the channel (H): $A = g.cos(\alpha).H$

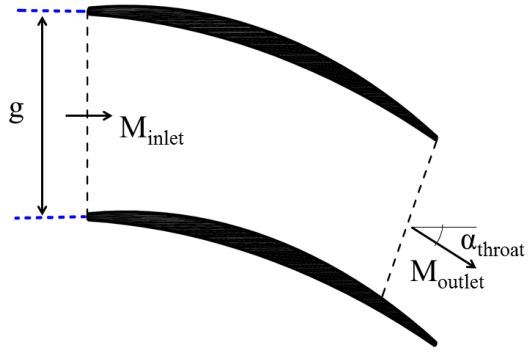

Figure 4: Definition of the geometrical characteristics of an axial passage.

To ensure that the turbine passage is started, namely that the initial shock wave is able to travel through the turbine, the inlet to throat area contraction is bounded by the Kantrowitz limit. Therefore, the throat angle (α_{throat}) to inlet angle (α_{inlet}) ratio is related to the variation of of the channel height across the passage and the inlet Mach number as expressed in Eq. 3:

$$\frac{A_{throat}}{A_{inlet}} = \frac{gH_{throat}cos(\alpha_{throat})}{gH_{inlet}cos(\alpha_{inlet})} > \frac{1}{M_2}\left(\frac{2(1+(\gamma-1)/2)M_2^2}{\gamma+2}\right)^{(-(\gamma+1)/(2(\gamma-1)))} \quad (3)$$

Fig. 5 depicts the maximum throat angle as a function of the inlet angle (α_{inlet}) and Mach number (M_{inlet}). Let us consider the case of a nozzle blade where the incoming flow is fully axial (α_{inlet} =0), when the M_{inlet}= 2.0 the maximum turning through the particular turbine passage (a vane or rotor) would be limited to 31 [deg.]. Increasing the inlet Mach number (M_{inlet}=3), allows higher turnings (α_{throat} could be 60 deg.). Conversely, at the same inlet Mach number, an increase of inlet flow angle allows an increase of the turning. Hence, without considering aerodynamic losses, it is desirable to enter a turbine passage with highest inlet angle and Mach number. However, considering conservation of mass, the higher is the turning in a passage the lower is the outlet Mach number. Therefore in a stator-rotor configuration one would propose maximum outlet swirl in the stator, with the highest possible Mach number, which would require increasing the channel height.

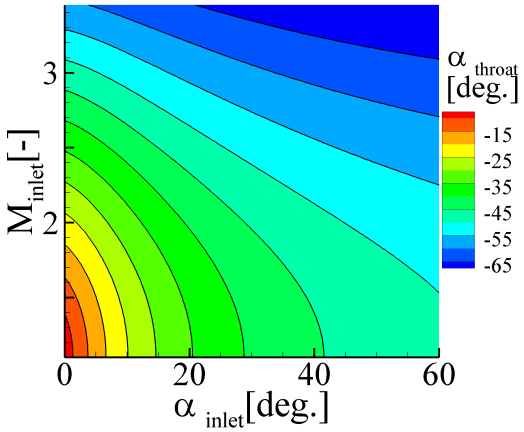

Figure 5: Maximum blade turning in function of the inlet angle (α_{inlet}) and Mach number (M_{inlet}) according to the Kantrowitz limit (Hthroat=Hinlet).

2.2. Aerodynamic loss generation

The flow pattern in turbine airfoils, immersed in high supersonic flows, is illustrated in Fig. 6. One can identify the appearance of strong shock waves at the leading edges (sudden blockage), which propagate through reflections all along the passage, which represent the major contribution to the aerodynamic losses. A second loss mechanism arises from the boundary layer development along the airfoil surface and the end walls, interacting with the shock waves. This type of loss is magnified by the diffusion process taking place along the converging passage (a diffuser at

supersonic conditions). Further loss mechanisms are originated from the trailing edge shock system, wake mixing losses and secondary flow development. The present analysis only considers the leading edge shock losses (in Fig. 6, a flow particle moving from point a to b and from b to c), profile and mixing losses.

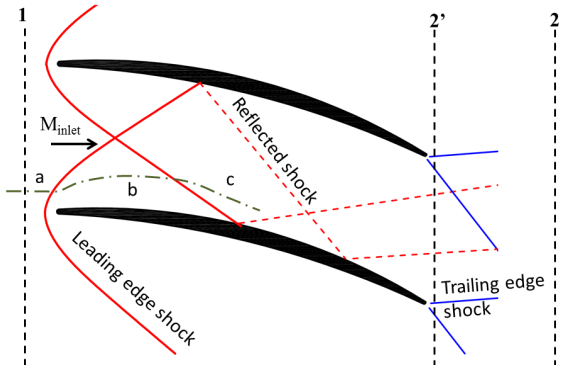

Figure 6: Typical flow pattern in a supersonic passage .

The shock waves generated in rounded leading edges can be predicted using the empirical method developed by Moeckel [7] based on the incident Mach number and leading edge radius. Fig. 7 outlines the formation of the leading edge shock wave. The detachment angle (θ) is the maximum possible turning angle a shock wave with given inlet Mach number can impose on the flow [8]. The inclination defined by θ, and tangent to the leading edge determines two points:

- x_0, the intersection to the symmetry plan, where the detached shock wave begins;
- y_{sb}, x_{sb} the location of the sonic line, $L = x_{sb} - x_0$, $L/y_{sb} = cot(\theta)$, the inclination of the sonic line is assumed to be perpendicular to the surface at point Sb.

The detached shock approximates to an asymptotic line for large distances from the leading edge, Moeckel proposed the use of a simple curve with the characteristics of a hyperbola represented by Eq. 4.

$$y_{shock} = \frac{(x^2_{shock} - x^2_0)^{1/2}}{\beta} \tag{4}$$

where β is the Mach angle. x_0 is computed in an iterative manner to ensure that the Mach number, after the shock wave, at the intersection with the sonic line is unity.

Senoo and Ono [9] and Dvork et al [10] proposed the use of wedge type leading edges for transonic

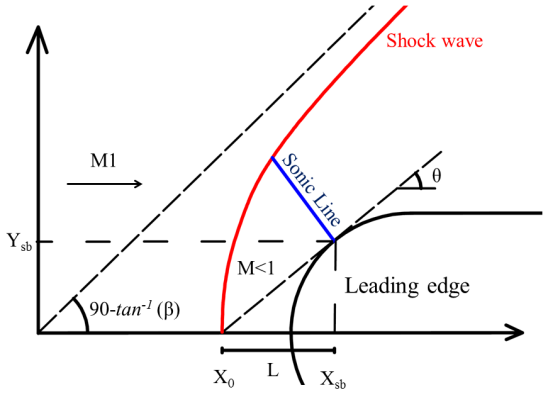

Figure 7: Turbine leading edge shock wave modelling.

steam turbine airfoils. Wedge type leading edges reduce the intensity of the shock waves resulting in significant aerodynamic improvements. Therefore, in the present research the Moeckel approach was altered to consider both the wedge type geometries and the intersection between the shock waves, which required multitude of numerical simulations to assess the methodology. Based on 3D Navier-Stokes solutions obtained with the commercial solver CFD++ developed by MetacompTechnologies [11] the Mach angle value (β) was corrected to $\beta_{corrected} = +13$ [deg.], in the range of inlet Mach numbers 1.5 to 3.0. Fig. 8 (a) depicts the modeled shock wave (red line) and the numerical Schlieren results, for different inlet Mach numbers. Based on the inlet Mach number, and flow direction the overall area-averaged entropy generation across the shock wave was computed [8], considering only the shock waves prior to the intersection (from location a to b in Fig. 6). Fig. 8 b) represents the total pressure loss along the tangential direction, across one passage (g, pitch) at three inlet Mach numbers. Most of the losses are produced close to the leading edge, where the shock wave inclination is highest. Increasing the inlet Mach number results in higher losses, and higher gradient along the tangential direction.

In order to estimate the shock losses downstream of the intersection of the leading edge shock waves (from location b to point c in Fig. 4 the local upstream Mach number needs to be evaluated. Based on the location of the sonic line, the Mach number passed the leading edge expansion fan is computed using the Prandlt-Meyer function, Eq 5. The turning angle downstream of the sonic line was approximated to the detachment angle (θ). The enthropy evaluation allowed the com-

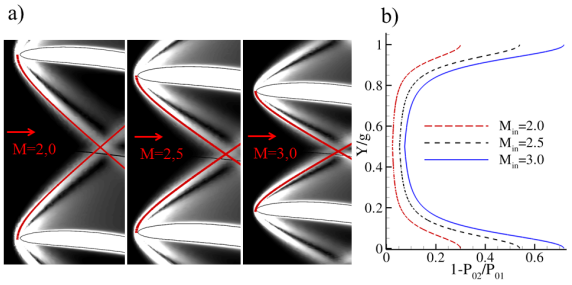

Figure 8: (a) Numerical Schlieren at different inlet Mach numbers, red line represents the predicted/modeled leading edge shock wave, (b) Leading edge shock losses prediction along the tangential direction at three inlet Mach numbers.

putation of the pressure losses due to the intersection of the leading edge shock waves.

$$\theta = \sqrt{\frac{\gamma+1}{\gamma-1}} tan^{-1} \sqrt{\frac{\gamma+1}{\gamma-1}(M^2-1)} - tan^{-1}\sqrt{M^2-1} \quad (5)$$

The second loss mechanism arises from the development of the boundary layer on the airfoils and on the end walls and the subsequent mixing process downstream of the cascade. In supersonic configurations large chord to pitch ratio are being considered [5] which magnifies the boundary layer importance. In order to estimate this loss a fully turbulent boundary layer was presumed, and in particular the empirical correlation for compressible flow proposed by Stratford and Beavers [12] for arbitrary pressure gradients. The average evolution of the Mach number across the passage is estimated based on the inlet and the outlet metal angles. Following Stewart [13] the two-dimensional overall airfoil boundary layer momentum is defined as:

$$\theta^*_{2D} = (\theta_{ss} + \theta_{ps})/(gcos(\alpha_2)) \quad (6)$$

According to Stewart et al. [14] the three dimensional momentum displacement thicknesses is scaled up from the two-dimensional overall airfoil boundary layer momentum, namely the boundary layer develops similarly along the airfoil surface and end walls. Hence, the overall three-dimensional momentum thickness is evaluated with a ratio of areas:

$$\theta^*_{3D} = \frac{A_{blade} + A_{endwalls}}{A_{blade}} \theta^*_{2D} = \left(1 + \frac{cos(\alpha_2)}{\sigma A_r}\right)\theta^*_{2D} \quad (7)$$

Where, $\sigma = c/g$ is the blade solidity and A_r (H/c) is the blade aspect ratio. In order to compute the profile and mixing losses, the compressible conservation of mass, momentum and energy equations are applied to a control volume downstream of the turbine cascade (between the stations 2′ and 2 shown in Fig. 6). Conservation of mass flow between station 2 and 2 leads to Eq. 8:

$$cos(\alpha'_2)(1-\delta^*-\delta_{te})\left(\frac{\rho'_2}{\rho_{02'}} M_{2'}\right) = \left(\frac{\rho_2}{\rho_{02}} M_{2x}\right)\frac{P_{02}}{P_0} \quad (8)$$

The compressible momentum in the tangential direction leads to Eq. 9.

$$sin(\alpha'_2)cos(\alpha'_2)(1-\delta^*-\delta_{te}-\theta^*)\left(\frac{\rho_2}{\rho_0 2} M^2_{2x} M^2_{2y}\right)\frac{P_{02}}{P_{01}} \quad (9)$$

Finally the momentum in the axial direction can be defined by Eq. 10.

$$\frac{P'_2}{P_{01}}\left(\frac{\gamma+1}{2\gamma}\right) + cos(\alpha'_2)^2(1-\delta*-\delta_{te}-\theta^*) \quad (10)$$
$$\left(\frac{\rho'_2}{\rho_{02'} M'^2_2}\right) = \frac{P_2}{P_{02}}\frac{P_{02}}{P_{01}}\left(\frac{\gamma+1}{2\gamma}\right) + \left(\frac{\rho_2}{\rho_{02}} M^2_{x2}\right)\frac{P_{02}}{P_{01}}$$

Where, δ_{te} is the ratio trailing edge thickness to blade pitch. Once the conditions in station 2′ are defined one can solve Eq. (8-10) in function of P_{02}/P_{01} and consequently the outlet of the control volume or mixing process are evaluated (M_2 and α_2). This approach includes both the compressibility effects and mixing losses, allowing the evaluation and dissection of the total pressure losses for different geometries at any inlet Mach number.

Full three-dimensional Navier-Stokes simulations were performed on a supersonic turbine airfoil with an inlet angle of 0 deg. and an outlet flow angle of 20 deg. The chord to pitch ratio was increased with the inlet Mach number to ensure the same outlet flow angle. Fig. 9 displays the overall prediction in total losses $(1 - P_{02}/P_{01})$ with the solid line, and the detailed budgeting into profile and mixing losses (dashed dotted line) and leading edge shock waves (dashed line). Both type of losses increase with the Mach number. The agreement with the Navier-Stokes simulations (represented by the squared symbols) is better than 2% at M=1.5. The prime contribution to the loss is the shock losses nearly 85% of the overall value. Additionally, Fig. 9 depicts the results of non-viscous (Euler) simulations (circular symbols), which match the predicted trend in shock losses with Mach number and an absolute uncertainty lower than 2%,.

Further loss mechanisms, such as shock-wave boundary layer interactions with the trailing edge shock system and the reflected shocks appear to play a minor role in the enthropy generation.

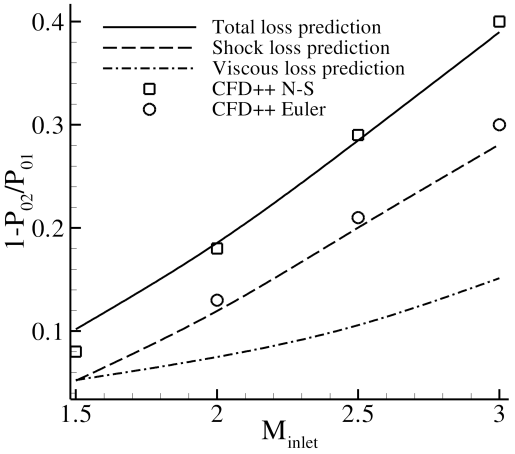

Figure 9: Prediction of the total pressure loss due to the boundary layer development (dashed doted line), the leading edge shock waves (dashed line) and the combination of both sources (solid line). Comparison with Euler solutions (circular symbols) and Navier-Stokes (squared symbols).

The present approach allows to evaluate quickly a wide range of geometrical characteristics operating at different inlet Mach numbers. Fig. 10 depicts the predicted total pressure loss in function of the chord to pitch ratio (c/g) at different inlet Mach number. For validation purposes several three-dimensional Navier-Stokes results were also added to the figure. Which again demonstrate the ability of the present methodology to predict both the trend and actual value of the losses.

3. One dimensional (1D) design approach

Contrary to subsonic designs, in axial supersonic flow passages the downstream static pressure is not a boundary condition. Instead, this is a consequence of the inlet conditions, geometry of the passage, and aerodynamic losses. The non-dimensional mass flow rate equation expressed by Eq. 11 defines the flow properties along the passage [15].

$$\frac{m\sqrt{CpT_0}}{AnP_0} = \frac{\gamma}{\sqrt{\gamma-1}} M\left(1+\frac{\gamma-1}{2}M^2\right)^{-0.5\frac{\gamma+1}{\gamma-1}} \quad (11)$$

where m is the mass flow rate, P_0 and T_0 represent the total conditions and M is the Mach number at a

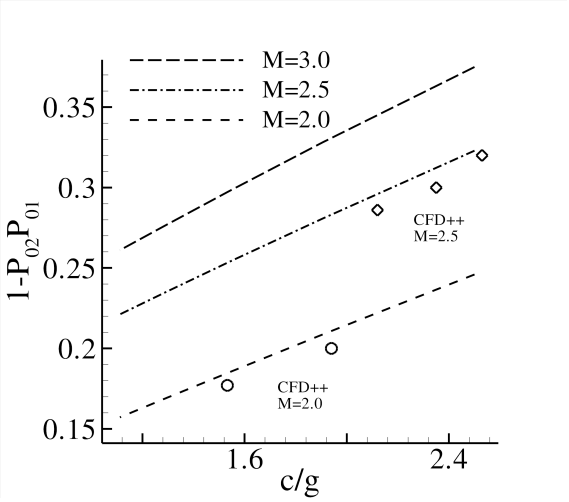

Figure 10: Total pressure loss (1-P02/P01) prediction arising from the leading edge shocks and boundary layer development at 3 different inlet Mach numbers.

certain point in the machine. Particularly, one can estimate the outlet conditions of a blade row, once the inlet conditions and the pressure losses are known. If we consider now a stationary blade row $T_{01} = T_{02}$ hence, the inlet and outlet flow properties can be related in the following manner:

$$M_{out}\left(1+\frac{\gamma-1}{2}M_{out}\right)^{-0.5(\frac{\gamma+1}{\gamma-1})} = \frac{H_{in}}{H_{out}}\frac{cos(\alpha_{in})}{cos(\alpha_{throat})} \frac{P_{0in}}{P_{0out}} M_{in}\left(1+\frac{\gamma-1}{2}M_{in}\right)^{-0.5(\frac{\gamma+1}{\gamma-1})} \quad (12)$$

In the previous equation Hin/Hout represents the blade height ratio between the inlet and the outlet of the blade row. Different outlet angles (α_{throat}) can be investigated up to the value bounded by the Kantrowitz limited as shown in Fig. 2. From Fig. 10 it is possible to compute the total pressure loss (P_{0in}/P_{0out}) across the passage. Finally, an iterative procedure is used to compute the outlet Mach number (M_{out}). The previously defined methodology can be applied to a rotating blade row when the relative quantities are used:

$$\frac{P_{0in,rel}}{P_{0out,rel}}, \frac{cos\beta_{out}}{cos(\beta_{out})}, M_{in,rel}, M_{out,rel} \quad (13)$$

The present approach explores all the possible preliminary design space. It starts by defining all the operable designs (with started configurations) and finally chooses the 1D design that maximizes the work output.

4. Evaluation of the 1D designs

It is now possible to analyze all the configurations and select the geometry with the highest specific work output for a certain inlet Mach number. In the present analysis, α_2 (outlet metal angle of the stator), β_3 (outlet metal angle of the rotor), the height of blades (H) across the stator and the rotor and the peripheral speed are used as design variables. Fig. 11 a) depicts the specific work output normalized by the inlet total temperature (T_0) in function of the outlet stator (α_2) and rotor (β_3) angles for M_{inlet}=2,0. In Fig. 11 a), the design space is limited (on the right) by the maximum α_2 ($\alpha_{2max} = 35deg.$) defined by Eq. 3 for M_{inlet}=2.0. This is a direct consequence from the Kantrowitz limit. If higher angles would be considered the passage would become unstarted and therefore inoperable. The same type of limitation can be observed for β_3 where the maximum turning in the rotor is now a function of relative Mach number to the rotor (M_{w2}) and the relative inlet rotor angle (β_2). When α_2 augments more turning is initially provided to the flow however, the higher area contraction in the stator leads also to a decrease of inlet Mach number in the rotor. Under these conditions the unstarting risk on the rotor augments and its total turning has to be reduced.

Fig 11 b) plots the evolution of the maximum specific power and the isentropic efficiency, defined in Eq. 14 in function of inlet Mach numbers (for the same total inlet conditions). Since static downstream conditions are not known when the axial Mach number is supersonic, the isentropic outlet condition cannot be determined. Hence, in the present analysis the isentropic work (ΔW_{max}) extraction is computed by repeating the procedure explained in section III where no pressure losses are considered ($P_{0in} = P_{0out}$, $P_{0in,rel} = P_{0out,rel}$).

$$\eta_t = \frac{\Delta W}{\Delta W_{max}} \tag{14}$$

A clear increase of the specific power can be observed in the low Mach number range. As previously discussed the higher turning and flow velocities lead to an increase of the specific power with the Mach number. Although, the overall losses increase with the Mach number, its relative important when compared to the increase of specific power is decreased, hence the efficiency augments. Nonetheless, in the high Mach number range, the increases of the overall losses, due to the stronger shocks and higher turnings, becomes more relevant than the increase in specific power which leads to a decrease in efficiency and an optimum value can be identified around $M_{inlet} = 2.7$.

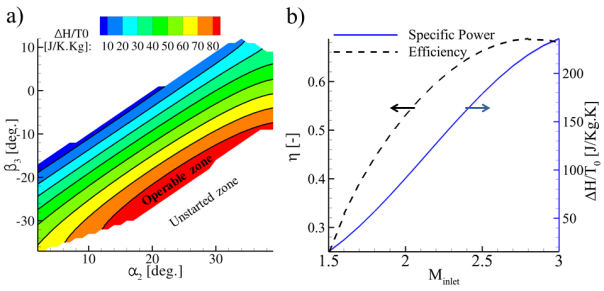

Figure 11: a) Specific power output normalized by T_0 in function of stator outlet angle (2) and rotor outlet angle (β_3) for M_{inlet}=2.0. Specific power output normalized by T_0 and isentropic efficiency (η) in function of the inlet Mach number.

5. Conclusion

This paper investigates the potential size reduction of turbines operating in the fully supersonic range. The high flow velocities allow an increase of the specific work output per stage. However, conventional turbine design are not suitable in the supersonic domain. Therefore, a novel methodology had to be developed to perform the 1D design of axial supersonic turbines considering the actual shock and mixing losses. First of all, the proposed methodology defines the operational design space that ensures shock waves are swallowed through the turbine (started configurations). Afterwards, the main entropy sources were identified and a procedure was developed to compute both the inviscid and viscous losses. The prime source of losses in the present designs are: leading edge shocks; boundary layer development along the passage; compressible mixing process downstream of the turbine passage. The predicted results were assessed with 3D Navier-Stokes simulations at several inlet Mach numbers. Finally, all the design space was evaluated in the quest for the optimal stage layout, which revealed an optimal design at Mach 2.7.

Acknowledgments

This work was conducted at the von Karman Institute for Fluid Dynamics, Belgium in cooperation with Turbomeca, and the University of Orleans, France. This research was funded by a Ph.D. CIFRE grant from the French Agency ANRT.

References

[1] A. Kantrowitz, The supersonic axial-flow compressor, Tech. rep., NACA ACR LF02 (1946).

[2] A. Ferri, Perliminary analysis of axial-flow compressor having supersonic velocity at the entrance of the stator, Tech. rep., NACA RM L6G06 (1949).

[3] A. Verneau, Supersonic turbines for organic fluid rankine cycles from 3 to 1300 kw, in: von Karman Institute Lecture Series on "Small High Pressure Ratio Turbines", 1987.

[4] U. Whalen, The aerodynamic design and testing of a supersonic turbine for rocket engine application, in: 3rd European Conference on Turbomachinery: Fluid dynamics and Thermodynamics, 1999.

[5] G. Paniagua, M. C. Iorio, N. Vinha, J. Sousa, Turbine airfoil design for high supersonic pulsating flows, in: ISABE, 2013.

[6] A. Kantrowitz, C. Donaldson, Preliminary investigation of supersonic diffusers, Tech. rep., NACA (1945).

[7] W. E. Moeckel, Approximate method for prediction form and location of detached shock waves ahead of plane or axially symmetric bodies, Tech. rep., NACA (1921).

[8] J. D. Anderson, Modern compressible flow, McGrawHill, 2004.

[9] S. Senoo, H. Ono, Development of design method for supersonic turbine aerofoils near the tip of long blades in steam turbines, in: Proceedings of ASME Turbo Expo 2013: Turbine Technical Conference and Exposition, 2013.

[10] R. Dvorak, P. Safarik, M. Luxa, D. Simurda, Optimizing the tip section profiles of a steam turbine blade, in: Proceedings of the ASME 2013 Turbine Blade Tip Symposium, 2013.

[11] M. Technologies, Supersonic hypersonic shock shear layer interaction.

[12] B. S. Startford, G. S. Beavers, The calculation of the compressible turbulent boundary layer in an arbitary pressure gradient - a correlation of certain previous methods, Tech. rep., Aeronautical Research Council (1955).

[13] W. Stewart, Analysis of two-dimensional compressible-flow loss characteristics downstream of turbomachine blade row in terms of boundary layer characteristics, Tech. rep., NACA (1955).

[14] W. Stewart, W. Whitney, R. Wong, Use of mean-section boundary layer parameters in predicting three-dimensional turbine stator losses, Tech. rep., NACA (1956).

[15] S. L. Dixon, C. A. Hall, Fluid Mechanics and Thermodynamics of Turbomachinery, Butterworth-Heinemann, 2010.

Full Rotor CFD Simulations of the MEXICO Wind Turbine Including the Nacelle in OpenFOAM

Nikolaos Stergiannis

Environmental and Applied Fluid Dynamics Department, von Karman Institute for Fluid Dynamics, Belgium, nstergiannis@gmail.com

Supervisor: Jeroen van Beeck

Environmental and Applied Fluid Dynamics Department, von Karman Institute for Fluid Dynamics, Belgium, vanbeeck@vki.ac.be

University Supervisor: Chris Lacor

Fluid Mechanics and Thermodynamics Research Group, Department of Mechanical Engineering, Vrije Universiteit Brussel, Belgium, chris.lacor@vub.ac.be

Industrial Supervisor: Rory Donnelly

3E S.A., Belgium, rory.donnelly@3e.eu

Abstract

Wind energy is one of the fastest growing renewable energy industries. Within the last decades this development has created a demand for increasingly accurate and efficient models for wind applications. Deeper knowledge of the wind behavior, around the blades and downstream of wind turbines, will aid the optimization of the design process from aerodynamics to the final wind farm layout. Computational Fluid Dynamics is a promising tool that can be employed nowadays even to complex industrial applications. These methods can efficiently capture the multiphysics of flow, with a continuous perspective of reduction on their final cost. Still, there are several challenges that need to be overcome. For the case of wake prediction it is more efficient, in terms of computational costs, to use simplified models to represent the presence of the rotor (such as Actuator Disc Models). However, the effects due to neglect of the physics, particularly in the near region of the wake, remains an open question. In an attempt to describe better these effects, a comprehensive study on the rotor aerodynamics and the near wake region of the MEXICO wind turbine is described.

The open-source software OpenFOAM was used in order to solve the 3-D Reynolds Average Navier-Stokes (RANS) equations. The computational domains were designed with the OpenFOAM meshing tools blockMesh and snappyHexMesh. Simulations were divided in two rounds of calculations, including the MEXICO full rotor, the hub and the nacelle. Three different cases with a pitch angle of -2.3°, yaw angle 0° and flow velocities of 10, 15 and 24 m/s respectively, were simulated. The first round consists of preliminary tests of the rotor in parked conditions. Here a study of the computational mesh independence, the performance of the solver with different boundary conditions and schemes and a mapping of the initial conditions has been performed. Turbulence was modelled by three different closure schemes, namely standard $k-\epsilon$, standard $k-\omega$ and $k-\omega$ SST. Results of $k-\omega$ showed better performance and the model was used also at the second round of calculations. At the second round of calculations a momentum source was added to the flow field to describe the rotation of the blades. The cell-zone condition namely MRF (Multiple Rotating Frame) of OpenFOAM was used with a constant rotating speed of 424.5 rpm. Obtained results will be compared and validated with PIV measurements of the new-MEXICO experiment. A further investigation with Large Eddy Simulation will be realized in the future by the authors.

Keywords: CFD, OpenFOAM, snappyHexMesh, RANS, MRF, full rotor simulations, near wake effects.

CFD Analysis of the Mutual Effect Between Different Components of a Turboengine: Application to the Combustor - High Pressure Turbine and to the Inlet Duct - Compressor Interaction

Stefano Vagnoli

Turbomachinery Department, von Karman Institute for Fluid Dynamics, Belgium, vagnoli@vki.ac.be

Supervisor: Tom Verstraete

Associate Professor, Turbomachinery Department, von Karman Institute for Fluid Dynamics, Belgium, tom.verstraete@vki.ac.be

University Supervisor: Francesco Martelli

Professor, Energy Engineering Department, University of Florence, Italy, francesco.martelli@unifi.it

Abstract

The aim of this PhD is to go in depth with the analysis of the mutual effect between different components of a turboengine. The interaction between combustor and turbine as well as between compressor and inlet duct will be examined, since these are identified in the last years as the main areas of interest in terms of mutual influence between different components.
This paper, in particular, focuses on the analysis of the combustor - turbine aerothermal interaction. The main requirements for an effective analysis of the hot streak migration in turbine will be discussed in detail. In particular, the importance of a correct imposition of the inlet boundary conditions for the turbine clearly appears, as well as an accurate reproduction of the turbulent mixing within the NGV.
Due to the difficulty to correctly model the turbulent mixing by means of RANS, LES should be considered for a more accurate analysis of the phenomenon. Because of that, the application of a density based LES code implemented in the $OpenFOAM^{®}$ platform on high pressure turbines will be validated.

Keywords: Combustor - Turbine interaction, Turbulence, hot streak migration

1. Introduction

The improvement of turbine efficiency is strongly linked to the increase of the flow temperature at the combustor outlet, to increase the maximum temperature of the thermodynamic cycle. In modern gas turbine engines, the gas temperature at the high pressure turbine (HPT) inlet exceeds the melting temperature of the metal, and the gas turbine failure is avoided only by advanced cooling tecniques.
As the design of the engines goes towards more complex combustor structures, characterized by highly nonuniform swirl flows to stabilize the flame and more compact combustor-HPT modules, a separated analysis of the two components is not anymore sufficient to guarantee a correct operability of the high pressure turbine.
At the state of the art, designers are forced to optimize the turbine taking into account higher mass-averaged temperature than the real working temperature, to take into account the presence of hot spots at the combustor outlet. This leads to oversizing of cooling systems and of the structural resistance of the rotor blades. In this sense, a clear understanding of the migration mechanisms of the nonuniform hot streak in the high pressure turbine would be crucial to improve the general performance of the engine.
The flow field at the combustor outlet is characterized by (i) a very high turbulent content (ii) a distorted total temperature profile (iii) a swirling and highly unsteady velocity field. The interaction of this flow with

the HPT has been experimentally studied by several authors by engine representative facilities, in which the combustor is replaced by a cold mixer, whose aim is to generate nonuniform conditions at the NGV inlet [1; 2; 3]. Usually, simplified inlet conditions are generated for the HPT, which represent only in part the flow at the outlet of a real combustor.
The scientific community generally agrees that the reproduction of realistic inlet conditions have an important influence on the turbine performance. Based on the results obtained on the QinetiQ test rig installed in England [1], Beard et als. [4] reported a drop of -0.88% of the turbine stage efficiency when realistic inlet conditions are employed with respect to standard uniform conditions. Dyson et al. [5] point out how the clocking (i.e. the relative position between temperature peak and NGV LE) has to be carefully taken into account when the hot streak propagation is studied, since a clear worst case cannot be individuated among all the possible combinations of NGV - hot spot relative position.
Among all the articles, Povey et al. [1] and Qureshi et al. [6] experimentally study the migration of the hot spot in turbine generating a nonuniform temperature profile at the HPT inlet. The authors observe a migration towards the pressure side when the hot spot is aligned with the NGV, and towards the SS when at the center of the passage. Nevertheless, the results are obtained for simplified operating conditions, without modeling the residual swirl at the combustor outlet.
In recent times, a clear interest in reproducing more realistic HPT inlet conditions can be pointed out. From the experimental point of view, Koupper et al [3] designed a cold test case to exactly reproduce the behavior of a DLN combustor. From the numerical point of view, Insinna et al. [7] , Schluter et al. [8] and Klapdor et al. [9] reproduce the mutual combustor - turbine interaction by meas of a resolution of the full combustor - HPT module.
In particular, in recent times an approach is proposed based on the numerical resolution of the problem using two different codes for the combustor and HPT, communicating between each other (usually referred as coupled approach). This idea is rather new and very promising, due to the possibility of using two different softwares, optimized to solve combustor and turbine separately. At the actual state, Insinna et al.[7] and Schluter et al.[8] give example of two approaches which could give appreciable results, for computations based on RANS-RANS and LES-URANS of combustor and turbine respectively. Nevertheless, both the technical requirements to get a correct coupling and the identification of the best computational approach are still to be clarified in the scientific community.
The objective of this work is to point out the main requirements to perform accurate aerothermal simulations in turbine with realistic inlet conditions. In the first part of the paper, RANS is applied in turbine to study the effect of the main parameters on the reproduction of the hot streak migration. Among the results obtained, the importance of a correct reproduction of the turbulent mixing clearly comes out. Based on that consideration, in the second part a LES density based code is validated for applications in high pressure turbine. The ongoing work, not discussed in this paper, is based on the coupling of the density based code with a reactive pressure blade code, to simulate the whole combustor-turbine configuration using a coupled approach.

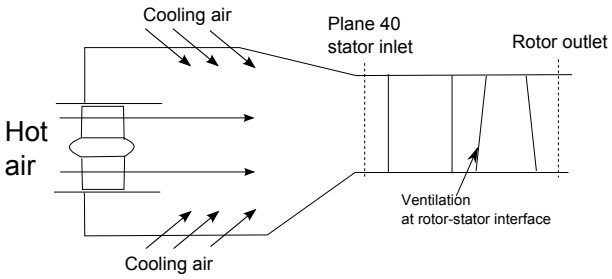

Figure 1: Scheme of the FACTOR configuration.

2. The Aerothermal Combustor - Turbine Interaction

In this section, the mutual interaction of combustor and turbine will be studied by RANS simulations of the whole turbine stage, imposing realistic inlet conditions. The aim of the study is to individuate which are the main flow features to be taken into account to numerically reproduce the aerothermal propagation of the hot spot in turbine.
The current analysis was assessed on the Factor experimental configuration, described in detail by Koupper et al. [3]. The set-up of the experimental test rig is schematically shown in Fig.1. Pre-heated air is injected in a chamber by a swirler, and mixed with cooling air injected by perforated liners, to mimic the effusion cooling holes which can be found in real DLN combustors. No combustion is enforced, and the non-uniform field created at the outlet is simply

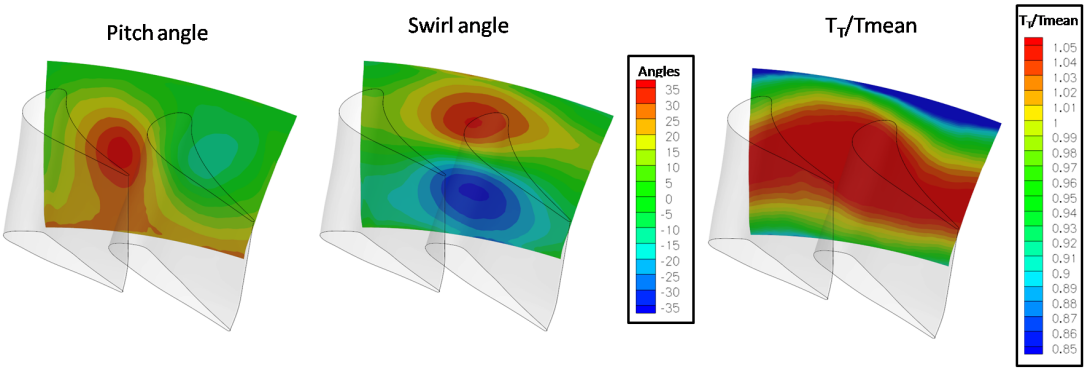

Figure 2: Swirl, pitch and total temperature field obtained at the mixing chamber outlet by Koupper et al. [10].

due to mixing between hot and cold air. The design is done in such a way that the hot spot and swirling flow are well marked with respect to other similar projects [10].

Downstream from the mixing chamber, a high pressure turbine is installed. On the whole annulus, the swirlers are 20, while the HPT counts 40 blades for the NGV and 60 blades for the rotor. The ratio is particularly favorable for CFD, since the whole periodic test case can be represented including one swirler, two NGV and three rotor blades only. The aim of the experimental set-up is to represent modern aeronautical engines, therefore the blades are 3D, and the possibility of film cooling is included for the NGV.

The complete mixing chamber - HPT full annulus test rig will be built at DLR in 2016. Despite this, simpler configurations are already operational at the University of Florence, a first test case reproduces the mixing chamber in smaller scale, including only 3 swirlers (whose results are already available in literature [3; 10]), while a second one includes one swirler and two stator blades (the experimental results are expected for this year).

The mixing chamber is also studied in detail numerically by means of LES [10], therefore a detailed overview of the flow behavior at its outlet can be obtained. The 2D fields at the outlet, obtained by LES, are shown in Fig. 2 as reference in terms of pitch, swirl and total temperature. The temperature disuniformity at the inlet can be measured in terms of $T_c(r)/T_{ave}$, i.e. the circumferentially averaged temperature in function of the radius, over the surface averaged temperature. The value goes from a minimum of 0.85 to the hub and shroud to a peak of 1.1 at the channel center, being representative of a realistic combustor. The residual swirl at the turbine inlet is 45°, indicating that the hot spot is still clearly present. The turbulence intensity, measured by the experiments [3] and calculated by LES [10], is very high (around 22%) and therefore its effect has to be carefully taken into account during a simulation of the HPT. This observation is in agreement with the experiments performed by Cha et al. [11] on an industrial configuration.

2.1. The Numerical Method

The software used for this investigation is the cell centered finite-volume code ElsA, developed by Onera [12]. A second order central scheme in space is used to discretize the 3d Navier Stokes equations. The discrete equations are integrated a 4th order by multistage Runge-Kutta scheme with implicit residual smoothing.

The mesh used for the computations is shown in Fig. 3. It counts 3.5MLN cells, keeping a $Y+$ lower than one at the solid surface, to solve directly the boundary layer. Two stator blades are reproduced to impose the exact periodicity between NGV and swirlers, while a mixing plane is imposed between stator and rotor, based on a circumferential average of the characteristic waves entering the rotating domain. The ventilation between NGV and rotor is modeled by imposing a uniform velocity field at the hub, upstream of the rotor.

The turbulence model used is $k-\omega$ wilcox.

2.2. The Effect of Turbulence in the Hot Streak Propagation

The correct reproduction of the entering turbulence level in turbine by means of RANS requires not only

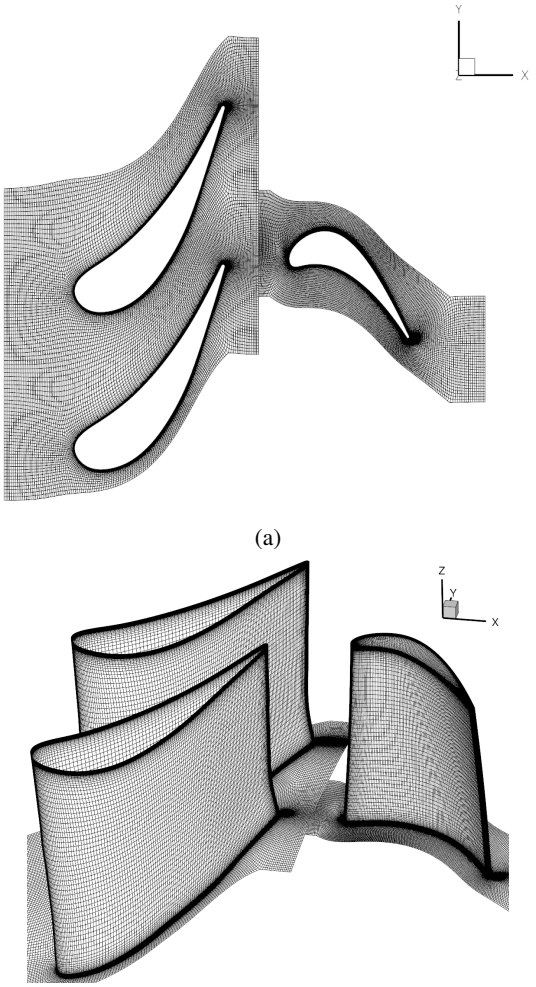

(a)

(b)

Figure 3: Details of the mesh used for the analysis of the hot spot migration in HPT. (a)2D view of the plane at midspan (b) View of he blades and the hub.

a realistic imposition of the inlet turbulent kinetic energy, but also a realistic reproduction of the turbulent decay (defined by the second turbulent variable).
When the inlet conditions for the turbine can be obtained from a LES of the combustor, Schluter et al. [8] suggests to obtain the inlet value of k by directly using the rms velocity components calculated at the LES outlet:

$$k = \sqrt{u_{x,rms}^2 + u_{y,rms}^2 + u_{z,rms}^2} \quad (1)$$

and to impose an arbitrary value for the second turbulent variable ω.
To find out a more physical criterion to impose the second variable, the results obtained by the LES of

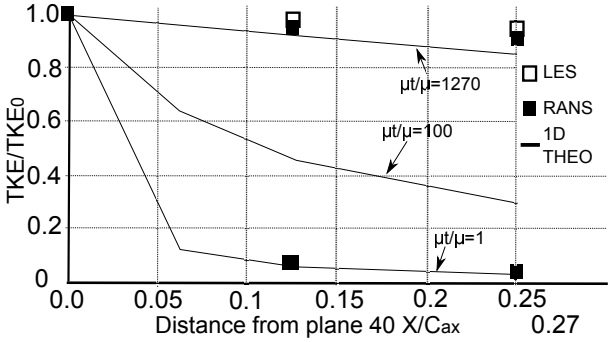

Figure 4: Turbulent Kinetic Energy decay upstream from the blade trailing edge: RANS is evaluated for $\mu_t/\mu = 1$ and for a more physical value of μ_t/μ, based on the decay computed by LES.

Koupper et al. on the Factor mixing chamber are interpolated at the turbine inlet, in terms of ρU, T_t and TKE. The configuration with the hot spot at the passage center is chosen. In this case, the area averaged turbulent kinetic energy has been computed on three different planes, enclosed between the HPT inlet and a plane located at a distance $X/c_{ax} = 0.5$ from the position where the NGV leading edge should be located. Two different RANS simulation of the turbine are then performed, imposing a value of ω to match an arbitrary condition of $\mu_t/\mu = 1$ at inlet and one more physical value, in which ω is imposed to get the same turbulent decay of LES upstream of the channel.

The results in terms of turbulent kinetic energy calculated for the three planes are shown in Fig. 4, also compared to the theoretical turbulent decay obtained for simplified uniform conditions.The graph clearly shows that the $\mu_t/\mu = 1$ case completely fails in reproducing the turbulent decay obtained by LES, getting a completely laminar flow at the turbine leading edge. On the other hand, a value of ω based on physics leads to a much closer prediction to LES decay, as expected.

Figure 5 shows impressively the effect of a correct imposition of the inlet turbulence on the hot streak propagation within the NGV passage. For $\mu_t/\mu = 1$, the hot spot is attracted towards the suction side of NGV 1. The high swirl content of the entering flow clearly appears in the distortion of the hot spot, which impacts the hub of NGV 1 and the tip of NGV 2. At the outlet the hot spot is still clearly evident, and will influence the skin temperature distribution of the rotor blade.
For the second case, a higher turbulent content for the

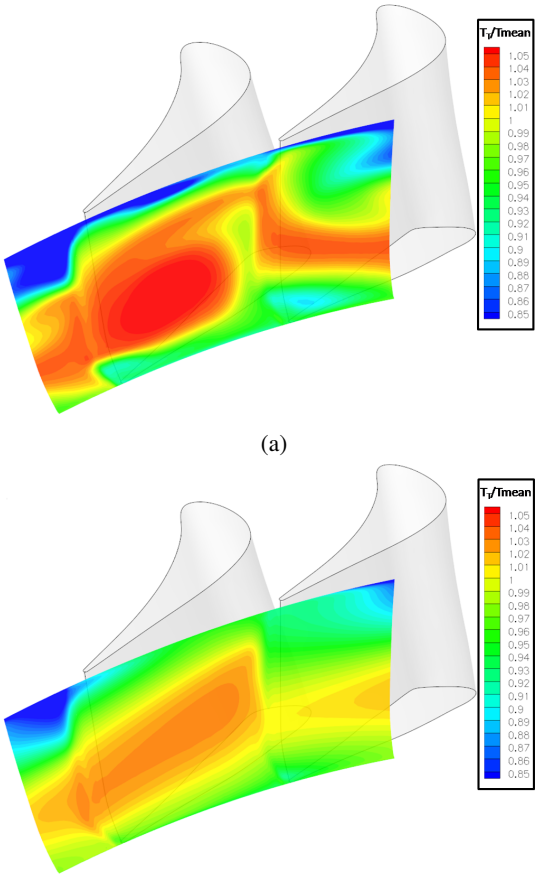

(a)

(b)

Figure 5: Outlet NGV total temperature obtained imposing the inlet boundary conditions obtained by LES. (a) ω imposed to get $\mu_t/\mu = 1$ (b) ω imposed to match the LES turbulence decay upstream from the leading edge.

flow entering in the passage is kept by the more physical imposition of ω. The mixing induced by turbulence leads to the attenuation of the temperature peak at the NGV outlet, where the hot spot results much weaker and diffused with respect to the previous case. As a consequence, its effect on the rotor blade will be less intense.

As already mentioned, experimental results on the configuration are not still ready, therefore a direct comparison cannot be discussed at this stage. Anyway, the conclusions obtained about the effect of turbulence on the hot streak propagation are in line to the experiments of Jenkins et al. [2; 13]. The authors, in this case, apply two different turbulence levels (3.5% and 20%) to an experimental setup in which

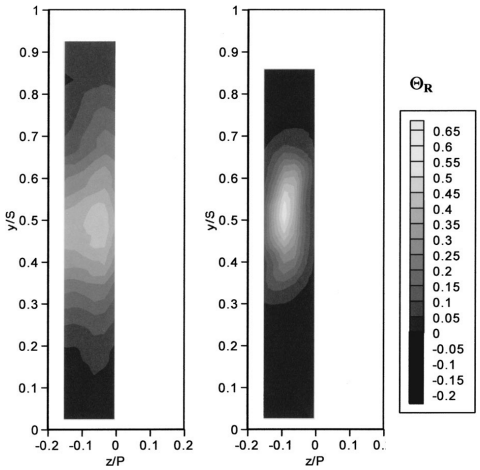

(a) (b)

Figure 6: Effect of the Turbulent Kinetic Energy on the hot spot diffusion at the turbine outlet. Turbulence level at the inlet: (a) 20% (b) 3.5% (from Jenkins et al. [13].

a hot streak is generated and convected through a NGV. The temperature distortion, evaluated as $\theta_R = (T - T_{ave})/(T_{peak} - T_{ave})$, is then measured downstream of the blade, on a plane perpendicular to the flow, including the 15% of the pitch (z direction) and the 95% of the span (y direction). The results of the flow visualization, shown in Fig.6, impressively show the important effect of the turbulent mixing on the hot streak.

2.3. The Metal Effect on the Rotor Temperature Distribution

The intense mixing imposed by the turbulent field determines a more uniform temperature field at the NGV outlet. Therefore, it is interesting to study wether the effect of the hot streak is still evident on the rotor blade.

The conductivity of the turbine blade can have an important influence on the temperature distribution. To take it into account, a CHT computation is performed for the rotor blade, using the same boundary conditions presented in the previous section. A Flux Forward Temperature Back (FFTB) method is employed, for which the heat is given from the CFD to the FEA calculation and the temperature is received back in an iterative loop until convergence [14]. The heat conduction equation is solved for the 3D model of the rotor blade by using $ANSYS^{®}$. The blade material is a titanium alloy characterized by a

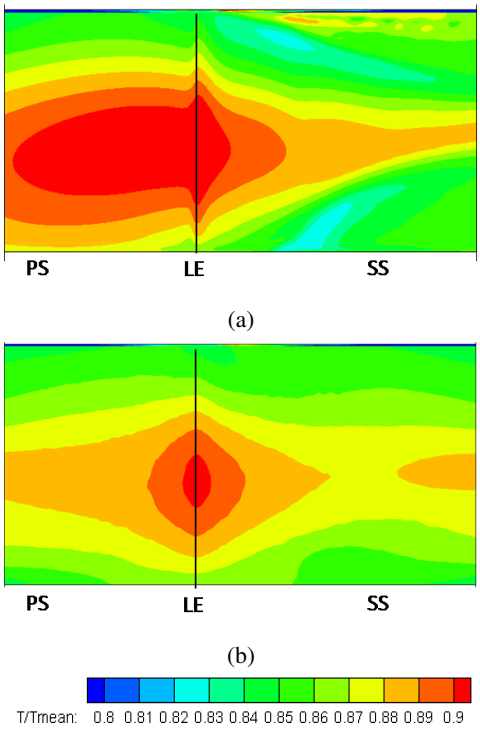

Figure 7: Skin temperature of the rotor blade. (a) adiabatic computation (b) CHT coupled computation.

conductivity $k = 11\ wm^{-1}K^{-1}$. A fixed temperature is imposed for the part of blade in contact with the disc, obtained from a previous 2D thermal calculation of the whole test section. The CHT calculation was considered converged when the maximum local temperature variation between two subsequent iterations was lower than 0.2% of the local value, and convergence was obtained after about 11 coupling cycles.

The rotor blade temperature distribution is shown in Fig. 7 for the adiabatic and the CHT case. The plot is obtained by developing the blade skin in local coordinates. In both cases, the blade temperature is adimensionalized by the average T_T evaluated downstream of the ventilation. The hot spot spreads close to the pressure side and become thinner along the suction side due to the effect of the contra rotating passage vortices formed within the passage. A higher skin temperature is observed along the pressure side. Comparing the case with conduction to the adiabatic one, an important reduction of pressure side temperature is observed, accompanied by an increase along the suction side. The temperature field results therefore more uniform, and a relevant peak can be observed for the blade nose only. In general the temperature disuniformity for the rotor blade remains limited, between 86% and 90% of the total temperature at the inlet.

2.4. *The Effect of the 2D Inlet Distortion in the Hot Streak Propagation*

At the state of the art, the hot spot propagation within the turbine is usually analyzed by the imposition of a 1D circumferentially averaged profile, mainly to limit the dimension of the computational domain to one single stator blade. This limitation doesn't allow to take into account neither the clocking effects between NGV and hot spot nor the swirl of the flow at the inlet.

To understand the effect of a 1D approximation of the inlet condition on the hot streak migration, 1D and a 2D profiles of ρU, T_T and TKE are imposed at the NGV inlet. The 2D profile, obtained by the LES calculations, is considered for two different clocking position: imposing the hot spot at the center of the passage (clocking PA) and with the hot spot impacting the blade LE (clocking LE). The 1D profile is obtained by a circumferential average of the non uniform condition, to keep the same mass averaged values. Adiabatic boundary conditions are considered for all blades.

Table 1: Pressure losses for different clocking conditions.

Parameter	Clocking PA	Clocking LE
$(P_{T,in} - P_{T,out})/P_{T,in}$	7.31%	7.23%

The hot spot migration within the stator passage is represented in Fig.8 for the two clocking position considered. For clocking PA, the hot spot is attracted towards the suction side of NGV 2, but remains within the passage without impacting the blade surface. For clocking LE, on the other hand, the high temperature flow impacts the blade and is attracted along the pressure side. In terms of aerodynamic performance, shown in Tab. 1, the impact of the hot spot on the NGV LE seems more favorable for the effectiveness, leading to a reduction of total pressure losses of 0.3%.

The blade temperature distribution is shown in Fig.9 for clocking PA and for clocking LA. As expected,

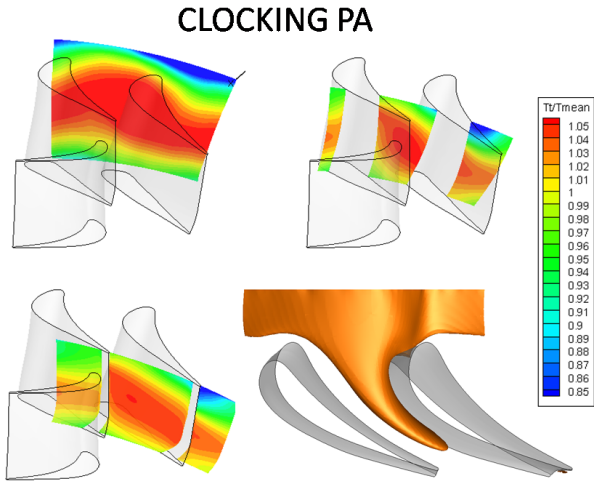

(a) Clocking PA: hot spot position at the passage center.

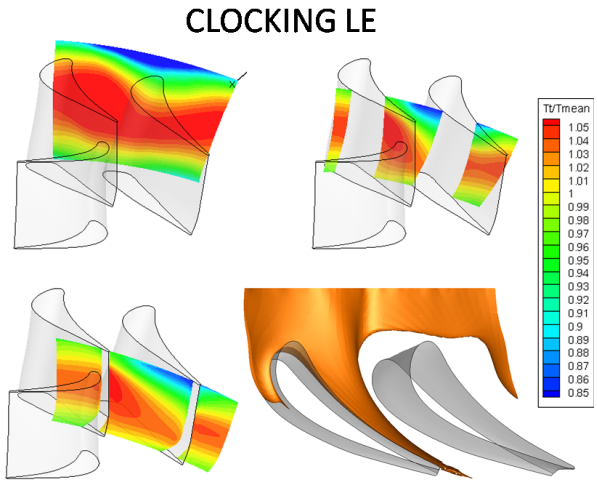

(b) Clocking LE: hot spot impacting the leading edge.

Figure 8: Hot spot diffusion within the NGV passage.

the NGV 1 results hotter when directly impacted by the hot spot, while a lower temperature peak is reached on NGV 2. For both cases, the hot streak development is highly affected by the swirl, being distorted towards the tip of the pressure side of NGV 1 and towards the hub of the suction side of NGV 2.
A remarkable impact of the coolant on the temperature distribution for all NGVs can also be identified. In general, the coolant impacts the leading edge close to the tip, and is spread by the swirl and the secondary flows along the suction side. When the clocking PA is imposed the coolant flow migrates instead all around NGV 2. No evident impact of the clocking is

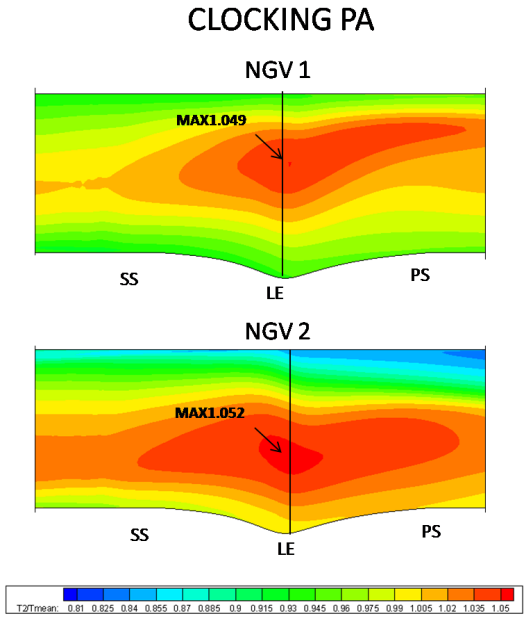

(a) Clocking PA: hot spot position at the passage center.

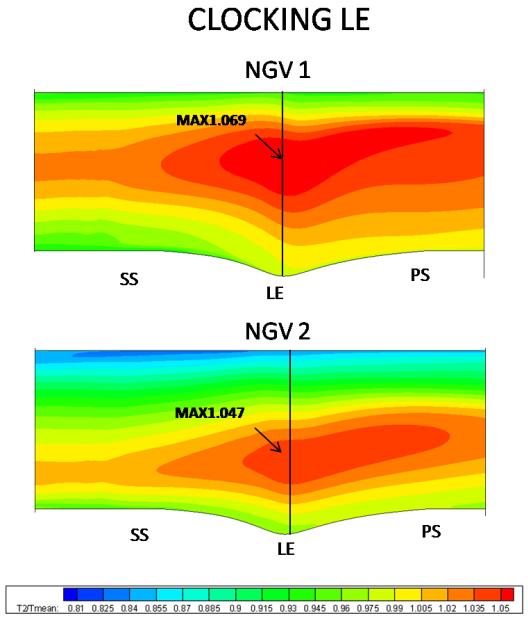

(b) Clocking LE: hot spot impacting the leading edge.

Figure 9: Temperature profile for the stator blades.

observed on the rotor temperature, which remain very close to Fig. 7 (a) also for clocking LE.
The development of the hot spot in turbine is shown in Fig. 10 when a 1D profile is imposed at the inlet.

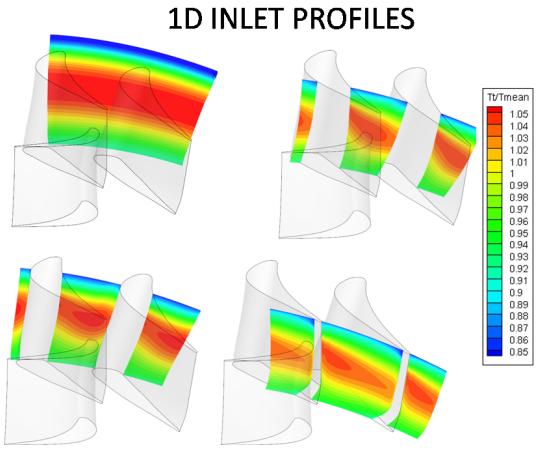

Figure 10: Hot spot diffusion within the NGV passage for 1D inlet profiles.

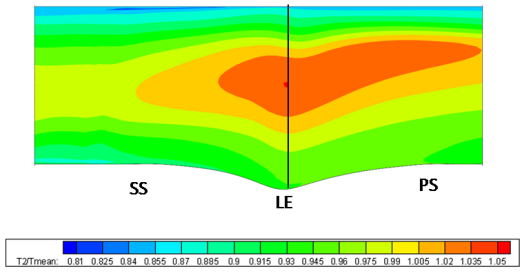

(a) NGV blade

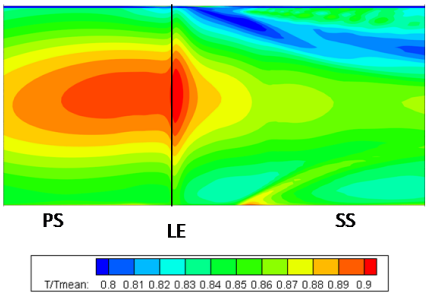

(b) Rotor blade

Figure 11: Temperature profile for the NGV and rotor blades: 1D inlet profiles.

In this case, the mixing and the stretching of the hot streak are limited, and the high temperature flow remains cofined at the center of the passage. At the NGV outlet, the total temperature profile can be still described as a 1D radial profile, since the effect of the secondary flow in the radial distortion is very limited. The imposition of a 1D inlet profile leads also to relevant differences on the rotor blade temperature. In this case, in fact, the cold flow generated by the cooling is still clearly distinguishable at the hub and tip of the NGV outlet. This generates low temperature pockets which are convected and spread along the blade suction side. Figure 11 shows the rotor skin temperature for the 1D case. A comparison with Fig. 9 lead to a discrepancy of about 25K (6% of $T_{T,ave}$ at the NGV outlet) on the skin adiabatic temperature. From this analysis, it clearly appears how the 1D approximation of the nonuniform inlet flow is not adequate for a correct study of the hot streak propagation both within the NGV and the rotor passage.

2.5. Main Remarks on the Numerical Analysis of Hot Streak Migration in Turbine

A complete series of numerical analyses was performed to understand which are the parameters that mainly influence the hot streak transport prediction from the numerical point of view. The following conclusions are obtained:

1. A 1D modeling of the flow field at the inlet, useful to contain the dimension of the domain to one single stator blade, doesn't give any useful information on the hot spot development in the NGV passage.
2. The high turbulence generated in the combustor has the effect to increase the mixing within the NGV passage, diffusing the hot streak. Therefore, the correct imposition of turbulent variables at the turbine inlet has to be carefully taken into account.
3. The hot spot effect on the rotor blade is rather limited (4% of temperature disuniformity for the FACTOR configuration).

3. Application of LES to High Pressure Turbines

According to the conclusions obtained from the previous analysis, a method that accurately reproduces the turbulent mixing within the passage would be an important added value for high fidelity simulations of the hot streak migration. In this sense, the application of LES to the problem is proposed and discussed.

The advantage in using LES rather than RANS lies in the fact that the biggest turbulent structures, responsible of the mixing of the hot streak, are directly resolved. The feasibility of LES on high pressure turbines is discussed in detail by several authors [15; 16],

but it is still far to be applied in the current state of the art.
In this work, a validation of a code based on the *OpenFOAM*® platform for LES in turbine will be presented, being the first time that LES is applied to a HPT blade at VKI. In the following chapter, the tecnical problem chosen to validate the code will be described in detail. The numerical method used will be described in section 3.2, while its validation will be presented in sections 3.3 and 3.4.

3.1. The Technical Problem: Turbine Trailing Edge Flow

The von Karman Institute has a long tradition in the research of turbine blade trailing edge flows. The first important contribution was the publication of a base pressure correlation based on experimental data on a wide variety of blade profiles [17].
One major assumption in establishing the base pressure correlation was that there exists an isobaric pressure dead air region at the trailing edge allowing measuring the base pressure with a single pressure tube in the center of the trailing edge. The small size of the blades used for the correlation did thus not allow verifying the assumption of an isobaric region. There was nevertheless an absolute need to verify this assumption, because the separation of the boundary layers at the trailing edge was known to be a highly unsteady phenomenon leading to the formation of large coherent structures, known as the von Karman vortex street.
The solution came from performing very large scale cascade tests with one of the blades fitted with a rotatable trailing edge cylinder and equipped side by side with a fast response pressure sensor and a pneumatic pressure tap. These series of tests, discussed in detail in Cicatelli and Sieverding [18], Sieverding et al. [19], Vagnoli et al. [20], allowed to obtain a complete map of the trailing edge pressure distribution in function of the outlet isentropic Mach number $M_{2,is}$.

Figure 12 summarizes the experimental resuls obtained, demonstrating impressively the impact of the trailing edge vortex shedding on the pressure distribution. Up to $M_{2,is} = 0.65$ the trailing edge is characterized by an extended nearly isobaric region since enrollment of the separating shear layers from pressure and suction side into alternating vortices occurs sufficiently far downstream to not affect the base region. Increasing the downstream Mach number, the vortices are generated closer to the trailing edge, leading progressively to an increasingly non-uniform

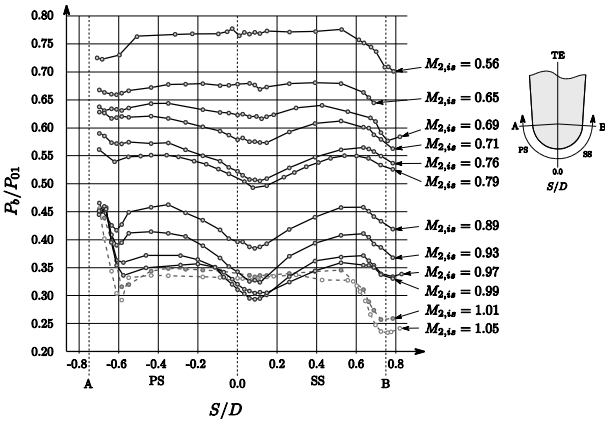

Figure 12: Effect of downstream Mach number on trailing edge pressure distribution (from Vagnoli et al. [20]).

pressure distribution with a strong pressure minimum near the trailing edge center. At $M_{2is} = 0.79$, the pressure drops to a minimum of $P_{b,min}/P_t = 0.495$ [19].
At $M_{2,is} = 1.0$, the non-uniformity drops to zero and the base region is again characterized by an isobaric pressure zone, the vortex shedding does not anymore affect the trailing edge base pressure.
The experimental set-up described represents a very challenging and interesting test to validate LES codes for several reasons.
- The turbine analyzed is a 2D profile, leading to a much lower computational cost with respect to a 3D profile.
- The application of URANS to the problem leads to a clear overestimate of the pressure minimum at the trailing edge for $M_{2is} = 0.79$ [21; 22].
- A preliminary LES study performed by Leonard et al. [22] gave encouraging results about the ability of LES to reproduce the trailing edge pressure distribution.

In this paper, the LES approach is validated studying three different configurations of the flow and the trailing edge shock system, namely the conditions at $M_{2,is} = 0.79$, 0.97 and 1.05.

3.2. The Numerical Method

The solver used to perform the LES analysis is a density based solver implemented in the OpenFOAM platform [23]. All simulations are performed with an implicit first order Euler scheme in time and a second order central scheme in space, with upwind treatment

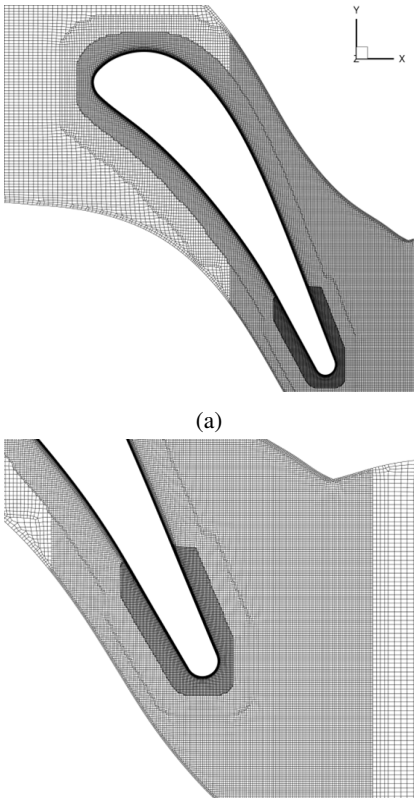

Figure 13: (a) 2D view of the final mesh around the blade. (b) detail of the mesh at trailing edge.

of the advection terms. The time step is chosen to keep the maximum Courant number lower than 1.3. The Smagorinsky model is used to represent the small turbulent scales, including the van Driest formulation at wall.

The computational span to chord ratio was set to 7.5% for all cases analyzed, based on the LES analysis of Leonard et al. [22]. The domain is reproduced by unstructured meshes, using hexahedral elements as much as possible to increase the quality of the solution. Prismatic layers are added at wall to accurately reproduce the boundary layer. To this end, the software Hexpress from Numeca was used.

The grid independence was obtained studying the case at $M_{2,is} = 0.79$ with three different meshes, mainly focusing the analysis on the prismatic layers at wall and in the wake region. The final mesh used for the investigation, shown in Fig. 13, is characterized by 2.53M nodes and an averaged $Y+ = 0.4$ is kept at wall. X+ and Z+ are included between 48 and 105.

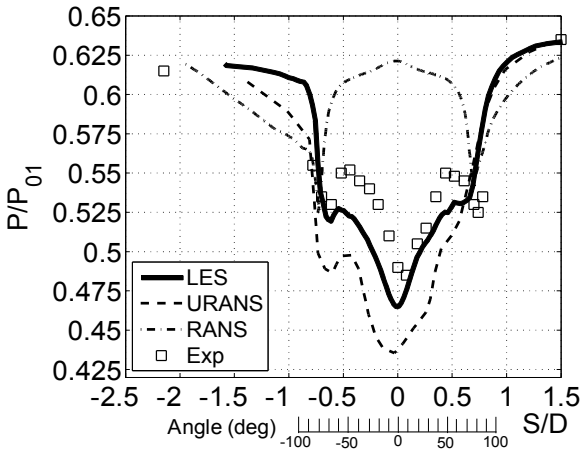

Figure 14: Time averaged pressure distribution along the trailing edge. RANS and URANS results are from Leonard et al. [22].

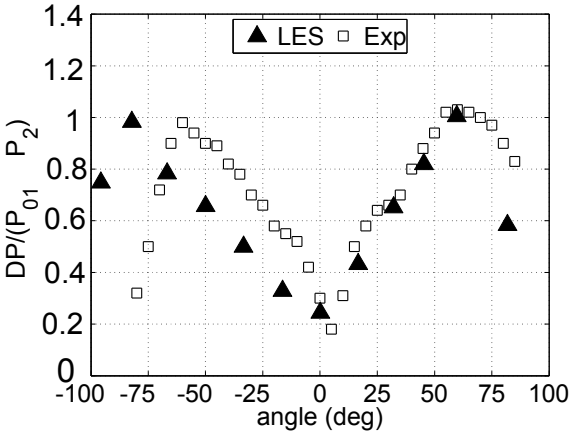

Figure 15: Angular distribution along the trailing edge of the phase-lock averaged amplitude of pressure fluctuations

3.3. The Case at $M_{2,is} = 0.79$

Fig. 14 represents the time averaged static pressure distribution at the trailing edge. The overall agreement between LES and experiments is good. The maximum error in the pressure prediction is lower than 3% of $P_{T,in}$ and is located along the compression taking place after the separation.

The LES results are also compared to RANS and URANS computations obtained by Leonard et al.

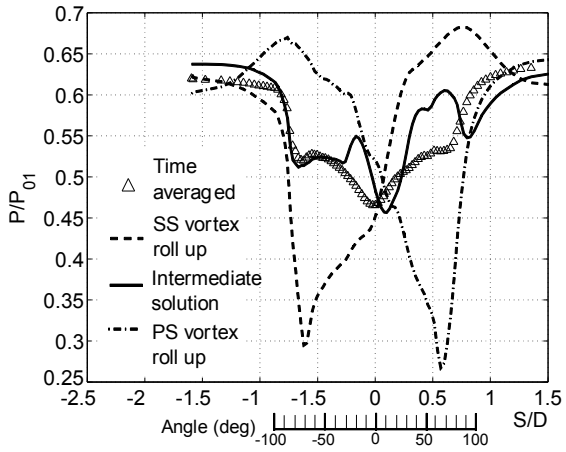

Figure 16: Snapshots of the instantaneous static pressure distribution along the trailing edge.

[22]. The first thing that clearly comes out is that a steady simulation reproduces an unphysical isobaric region at the trailing edge, completely missing the central pressure minimum. Passing from RANS to URANS, the general match with experimental pressure distribution improves, but a remarkable underestimation of the trailing edge pressure is still observed. Compared to URANS, LES is in general more accurate. This is due to the ability to directly solve the turbulent structures generated in the near wake region after separation, which are not resolved by URANS. We can therefore conclude that a LES approach, even though more computationally expensive, leads to a remarkable increase of accuracy when a highly separated flow has to be analyzed in detail.

In terms phase-lock amplitude of pressure fluctuations, Fig. 15, the numerical results (evaluated for 12 discrete points along the trailing edge) point out correctly the presence of two peaks near the boundary layer separation points. The position of the peak of fluctuations on the pressure side is predicted with a difference of 20 with respect to experiments, but the global trend and the absolute values of amplitude are correctly reproduced.

To clearly point out the intensity of the pressure unsteadiness at trailing edge, the average pressure profile compared to three instantaneous snapshots of the field, taken during one vortex shedding period is shown in Fig. 16. During the roll-up of the vortices, the shear layer of the pressure and suction side is alternatively entrained into the wake by a large pressure minimum formed on the opposite side of the trailing edge circumference. The trailing edge center doesn't appear to be particularly affected by the fluctuations, and the pressure locally remains close to the averaged value.

Fig. 17 shows experimental schlieren photographs

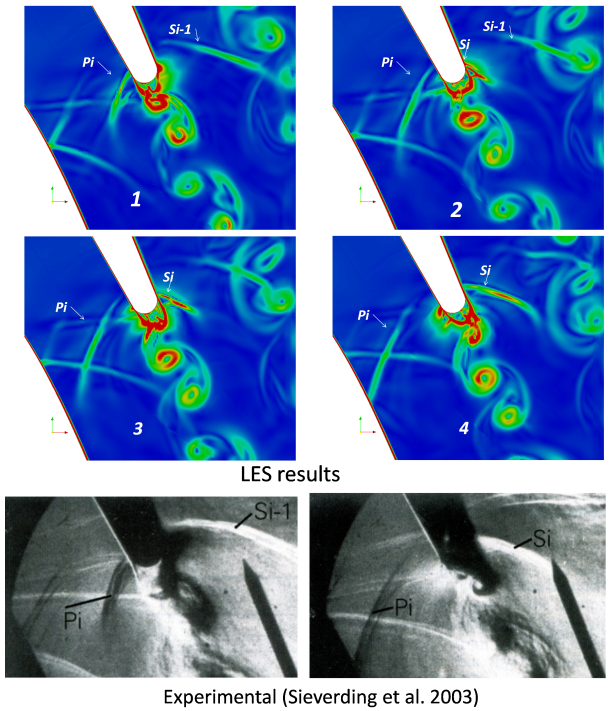

Figure 17: Schlieren visualization of the flow field at $M_{2,is} = 0.79$.

(below) and numerical results (above) for direct comparison. During the vortex shedding cycle, pressure waves are alternatively generated at the pressure and suction side (indicated as P_i and S_i respectively) by the inward and outward motion of the shear layers separating from the trailing edge. The wave indicated with R_p in images 1 and 2 represents the reflected wave by the closest blade. To catch this effect, the grid has to be fine enough in the entire rear suction side area of the domain, as it was also noticed by Leonard et al. (2010).

3.4. The Case at $M_{2,is} = 0.97$ and 1.05

Similar to the flow conditions at $M_{2,is} = 0.79$ LES at M2,is = 0.97 in Fig. 18 agrees very well with experimental data on the right side of the trailing edge center towards the suction side while the agreement is a bit less satisfactory to the pressure side between $S/D = 0$ and 0.5 (although the maximum difference

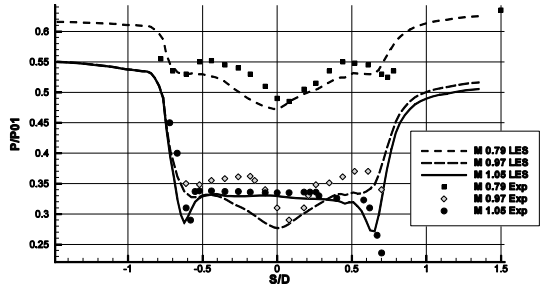

Figure 18: Comparison of trailing edge base pressure variation at transonic outlet conditions.

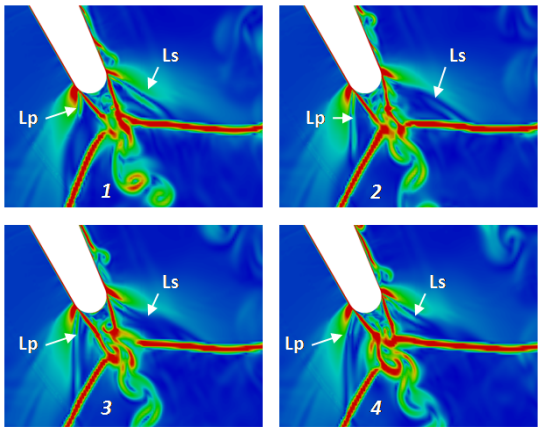

Figure 19: Schlieren visualization of the flow field at $M_{2,is}$ = 1.05.

is limited to 5% of the total pressure). The return to an isobaric base pressure distribution at $M_{2,is}$ = 1.05 is well predicted, and the agreement between experimental and numerical data is perfect. This applies also to the prediction of the over expansion of the flow before separation causing a separation shock referred to in the literature also as lip shock.
A visualization of the flow field is given in Fig. 19 for $M_{2,is}$=1.05. An oblique shock system is originated from the zone of confluence of the pressure and suction side shear layers. The roll-up of the shear layers into vortices is delayed to the region of their confluence, leaving an isobaric near wake region close to the trailing edge circumference.

Conclusions

An accurate CFD resolution of the hot streak migration from combustor to turbine requires a detailed modeling of all quantities at the interface. Nevertheless, at the state of the art, clear indications to faithfully reproduce the effect of the highly turbulent and nonuniform field generated by the combustor at the turbine inlet are not ready.
In this work, RANS simulations are performed on a set-up designed to reproduce a realistic combustor-turbine configuration. Two NGVs are included in the computational domain to represent the correct periodicity with the swirlers. The hot streak is distorted within the NGV passage by the residual swirl at the combustor outlet, leading to a very different adiabatic temperature distribution for the two NGVs. The impact of the hot streak on the rotor blade is instead rather limited (4% of temperature distortion with respect to the inlet total temperature). The analisys clearly points out that a 1D approximation of the flow field at the inlet, usually employed to limit the dimension of the computational domain, doesn't give any useful information on the hot spot development within the NGV passage. Moreover, a remarkable effect of the turbulent field is observed, and an accurate imposition of the turbulent quantities is required at the turbine inlet.
Based on this conclusion, the application of LES to the problem would give more accurate results to correctly quantify the mixing of the hot streak within the NGV stage. In this sense, a LES solver is validated for application to high pressure turbines on a classical test case, analyzing the unsteady wake flow characteristics of a cylindrical geometry. The code is able to predict accurately the peak of the minimum average pressure at the trailing edge formed for high subsonic outlet conditions as well as the formation of the isobaric region observed for sonic conditions. We can therefore conclude that the tool is mature enough to be used on more complex 3D cases.

Acknowledgments

The numerical research presented in this paper has received funding from the European Community's Seventh Framework Programme (FP7, 2007-2013), PEOPLE programme, under the grant agreement No FP7-290042 (COPAGT project). The work on the FACTOR geometry was performed during a three months secondment in Turbomeca. The author is grateful to Guillaume Bonneau, Charlie Koupper, Lorenzo Pons and to all the other colleagues for the fruitful collaboration. The FACTOR project has received fundings from the European Community's

Seventh Framework Programme (FP7, 2007-2013), grant agreement No FP7-265985.

References

[1] T. Povey, K. S. Chana, T. V. Jones, J. Hurrion, The Effect of Hot Streaks on HP Vane Surface and Endwall Heat Transfer: an Experimental and Numerical Study, Journal of Turbomachinery 129 (1) (2007) 32–43.

[2] S. Jenkins, K. Varadarajan, D. G. Bogard, The effects of high mainstream turbulence and turbine vane film cooling on the dispersion of a simulated hot streak, Journal of Turbomachinery 126 (1) (2004) 203–211.

[3] C. Koupper, G. Bonneau, G. Caciolli, B. Facchini, L. Tarchi, L. Gicquel, F. Duchaine, Development Of An Engine Representative Combustor Simulator Dedicated To Hot Streak Generation, Journal of Turbomachinery 136 (11) (2014) 111007.

[4] P. F. Beard, A. Smith, T. Povey, Impact of Severe Temperature Distortion on Turbine Efficiency, Journal of Turbomachinery 135 (1) (2013) 011018.

[5] T. Dyson, D. Helmer, J. Tallman, Large-Scale Simulation of the Clocking Impact of 2D Combustor Profile on a Two Stage High Pressure Turbine, no. Proceedings of the ASME Turbo Expo 2014, Dusseldorf, Germany, 2014.

[6] I. Qureshi, A. Beretta, T. Povey, Effect of Simulated Combustor Temperature Nonuniformity on HP vane and End Wall Heat ransfer: an Experimental and Numerical Investigation, Journal of Engineering for Gas Turbines and Power 133 (3) (2010) 031901.

[7] M. Insinna, S. Salvadori, F. Martelli, Simulation of Combustor-NGV Interaction using RANS Solvers: Validation and Application to a Realistic Test Case, no. Proceedings of the ASME Turbo Expo 2014, Dusseldorf, Germany, 2014.

[8] J. U. Schluter, H. Pitsch, P. Moin, Outflow Conditions for Integrated Large Eddy Simulation/Reynolds-Averaged Navier Stokes Simulations, AIAA Journal 43 (1) (2005) 156–164.

[9] E. V. Klapdor, R. Eggels, S. Pyliouras, J. Janicka, Towards Investigation of Combustor Turbine Interaction in an Integrated Simulation, no. Proceedings of the ASME Turbo Expo 2010, Glasgow, UK, 2010.

[10] C. Koupper, Towards the Unsteady Multi-Physic Simulations of Aeronautical Gas Turbine Combustion Chamber and Turbine Components, Ph.D. thesis, Institut Suprieur de l'Aronautique et de l'Espace (2015).

[11] C. M. Cha, P. Ireland, P. Denman, V. Savarianandam, Turbulence Levels Are High at the Combustor-Turbine Interface , no. Proceedings of the ASME Turbo Expo 2012, Copenhagen, Denmark, 2012.

[12] L. Cambier, J. P. Veuillot, Status of the elsA CFD Software for Flow Simulation and Multidisciplinary Applications, no. 46th AIAA Aerospace Sciences Meeting and Exhibit, Reno, USA, 2008.

[13] S. Jenkins, D. G. Bogard, The effects of the vane and high mainstream turbulence level on hot streak attenuation, Journal of Turbomachinery 127 (1) (2005) 215–221.

[14] T. Verstraete, Heat transfer and multi disciplinary optimization applied on micro gasturbines, Ph.D. thesis, Universiteit Gent (2008).

[15] J. Kopriva, G. M. Laskowsky, H. Reza, H. Sheikhi, Large Eddy Simulation of a High Pressure Turbine Stage: Effects on Sub-Grid Scale Modeling and Mesh Resolution, no. Proceedings of the ASME Turbo Expo 2014, Dusseldorf, Germany, 2014.

[16] J. Tyacke, P. Tucker, R. Loveday, N. Vadlamani, R. Watson, I. Naqavi, Y. Xiaoyu, Large Eddy Simulation for Turbines: Methodologies, Cost and Future Outlook, Journal of Turbomachinery 136 (6) (2014) 061009.

[17] C. H. Sieverding, C. Stanislas, M. Snoeck, The Base Pressure Problem in Transonic Turbine Blades, Journal of Engineering for Power 102 (3) (1980) 711718.

[18] G. Cicatelli, C. H. Sieverding, The Effect of Vortex Shedding on the Unsteady Pressure Distribution Around the Trailing Edge of a Turbine Blade, Journal of Turbomachinery 119 (4) (1999) 810819.

[19] C. H. Sieverding, H. Richard, J. M. Desse, Turbine Blade Trailing Edge Flow Characteristics at High Subsonic Outlet Mach Number, Journal of Turbomachinery 125 (2) (2003) 298309.

[20] S. Vagnoli, T. Verstraete, B. Mateos, C.H. Sieverding, Prediction of the Unsteady Turbine Trailing Edge Wake Flow Characteristics and Comparison with Experimental Data, no. Proceedings of the ETC conference 2015, Madrid, Spain, 2015.

[21] J. Kopriva, G. M. Laskowsky, H. Reza, H. Sheikhi, Assessment of High Pressure Cooled and Uncooled Turbine Blade Wakes via RANS and URANS at Engine Scale Conditions, no. Proceedings of the ASME Turbo Expo 2013, San Antonio, USA, 2013.

[22] T. Leonard, F. Duchaine, N. Gourdain, L. Gicquel, Large Eddy Simulation of a High Pressure Turbine Stage: Effects on Sub-Grid Scale Modeling and Mesh Resolution, no. Proceedings of the ASME Turbo Expo 2014, Glasgow, UK, 2010.

[23] O. Borm, H.P. Kau, Unsteady Aerodynamics of a Centrifugal Compressor Stage - Validation of Two Different CFD Solvers, no. Proceedings of the ASME Turbo Expo 2012, Copenhagen, Denmark, 2012.

NUMERICAL APPROACH FOR HYPERSONIC AND PLASMA FLOWS

Development of Advanced Gas Surface Interaction Models for Reusable Materials

Georgios Bellas-Chatzigeorgis

Aeronautics and Aerospace Department, von Karman Institute for Fluid Dynamics, Belgium, georgios.bellas.chatzigeorgis@vki.ac.be

Supervisor: Thierry E. Magin

Associate Professor, Aeronautics and Aerospace Department, von Karman Institute for Fluid Dynamics, Belgium, magin@vki.ac.be

University Supervisor: Paolo Barbante

Assistant Professor, Department of Mathematics, Politecnico di Milano, Italy, paolo.barbante@polimi.it

Abstract

During the (re-)entry phase of a space vehicle, the gas flow in the shock layer can be in a state of strong thermal non-equilibrium. Under these circumstances, the population of the internal energy levels of the atoms and molecules of the gas deviates from the Boltzmann distribution. A substantial increase of the heat flux transferred from the gas to the vehicle is possible, as the thermal protection system of the vehicle acts as a catalyst. The objective of the paper is to show how thermal non-equilibrium and catalysis can jointly influence wall heat flux predictions. In order to study thermal non-equilibrium effects a coarse-grained State-to-State model for nitrogen is used coupled with a phenomenological model for catalysis. From the numerical simulations performed, an important effect on the heat flux has been observed due to the interaction of catalysis and thermal non-equilibrium at the wall.

Keywords: catalysis, gamma model, state-to-state models, accommodation coefficient, stagnation line, DRNSE

1. Introduction

The design of the thermal protection system for a spaceship during an atmospheric entry is a very challenging task due to the multi-physics phenomena occurring in the shock layer of the space vehicle [1]. These phenomena include strong deviation from thermochemical equilibrium [23], radiative heating [18] and gas-surface interaction (catalysis and ablation) between the vehicle's surface and the surrounding gas [6]. These phenomena are strongly coupled between each other and this makes the prediction of the flow-field properties very difficult. Currently, most researchers try to deal with each of these phenomena separately or with simplified coupling strategies.
For a relevant fraction of the re-entry trajectory the flow-field behind the shock wave and in the boundary layer is in a state of thermal non-equilibrium; the populations of the internal energy levels of atoms and molecules deviates from the Boltzmann distribution. A substantial increase in the heat flux can be observed as the catalytic properties of the wall of a re-entry vehicle increases with wall temperature [5; 27]. Currently, most of the simulations performed by the community assume thermal equilibrium in the flow field. The objective of this contribution is to study the joint effect of thermal non-equilibrium and catalysis on the predicted heat flux.

2. Physical Model

Thermal non-equilibrium is studied with a state-to-state rovibrational specific nitrogen model developed by the NASA Ames Research Center [12]. The model can simulate flows that depart from Boltzmann equilibrium, like strongly compressing, expanding and boundary layer flows [22]. Each internal energy level is assumed to be a distinct pseudo species. Chemical reactions are the mechanisms responsible for transforming one of these pseudo species to another one.

Even though state-to-state models are more accurate than multi-temperature ones, they lead to a drastic increase of the computational cost. A possible strategy to reduce the computational cost is presented in this paper.

2.1. Energy Levels

The nitrogen model has 9390 different rovibrational levels, which can be split into two categories, bound ($\mathcal{B}$) and predissociated ($\mathcal{P}$). The bound levels are the levels whose total energy is less than the dissociation energy ($9.75eV$) of nitrogen molecule in its electronic ground state. The predissociated levels are the levels whose energy is higher than the dissociation energy relative to the first rovibrational energy, but lower than the rotational dependent centrifugal barrier [12].
A simulation with all the 9390 different levels would have a huge computational cost. In order to reduce the computational cost coarse-grained models are developed. The reduction strategy chosen is the Uniform Rovibrational Collisional bin model (URVC) [17]. The rovibrational energy levels are sorted in an increasing energy levels ladder. Then, this ladder is divided into two parts, the first one containing only the bound levels and the second one only the predissociated levels. Lastly, each of these two regions is divided with equal energy spacing:

$$\Delta E_{\mathcal{B}} = \frac{2E_{fN}}{\mathcal{N}_{\mathcal{B}}}, \quad \Delta E_{\mathcal{P}} = \frac{E_{max} - 2E_{fN}}{\mathcal{N}_{\mathcal{P}}} \tag{1}$$

where E_{fN} is the formation energy of N and E_{max} the energy of the last energy level of N_2. $\mathcal{N}_{\mathcal{B}}$ and $\mathcal{N}_{\mathcal{P}}$ are the number of bound and predissociated bins, which can be chosen freely. The higher their number the better is the fidelity of the model. Here we have chosen $\mathcal{N}_{\mathcal{B}} = 7$ and $\mathcal{N}_{\mathcal{P}} = 3$. A sensitivity analysis has been performed in [19] and it was shown that no big effect on the heat flux was observed going from 10 bins to 100 bins. The population distribution, n_l, of the energy levels contained in each bin is chosen to be uniform:

$$n_l = \frac{g_l \sum_i n_i}{\sum_i g_i} \tag{2}$$

where g_i is the degeneracy of level i and n_i its population. The number density n_k of each bin is $\sum_l n_l$; its degeneracy g_k is $\sum_l g_l$. The average energy of bin k is equal to:

$$\bar{E}_k = \frac{1}{\sum_l g_l} \sum_i g_i E_i \tag{3}$$

where E_i is the internal energy of the ith level. Alternative strategies of model reduction can be found in [16; 19]. The advantages of the URVC model are the simple implementation, the fact that the average energy of the bins is not a function of the thermodynamic state and good quality of the results, especially at high temperatures. A non equal energy spacing for the bins might also improve the quality at lower temperatures. The main disadvantage of this model is that it cannot reach Boltzmann equilibrium at a fine-grain level.
As a post processing result an internal temperature (T_{int}) has been defined by solving the following equation:

$$\frac{\sum_k n_k \bar{E}_k}{n_{N_2}} = \frac{\sum_k \bar{E}_k g_k \exp(\bar{E}_k / k_B T_{int})}{\sum_k g_k \exp(\bar{E}_k / k_B T_{int})} \tag{4}$$

Physically, it represents the temperature that would exist in the flow field if the internal energy levels of N_2 were populated following the Boltzmann distribution, with the mixture having the same amount of total internal energy.

2.2. Reaction Mechanism

In a $(N(^1S_u) - N_2(^1\Sigma_g^+))$ mixture two kind of interactions can exist. The first one is the collision between nitrogen atoms and molecules, the second one the collision between nitrogen molecules. In the present model only the first category of collisions has been considered. The second one has not been taken into account because only a portion of all the possible transitions rates are currently available [21].
Spontaneous dissociation was also assumed to be negligible [19]. The total number of reactions that are needed to describe the possible transitions from one rovibrational level to any other or to dissociated nitrogen, with the third body being a nitrogen atom, is of the order of 10^7. The reactions belong to two different categories, the third body dissociation reaction and the inelastic transitions reaction between rovibrational levels:

$$N_2(l) + N \underset{k_l^{rec}}{\overset{k_l^{dis}}{\rightleftharpoons}} N + N + N \tag{5}$$

$$N_2(l) + N \underset{k^{in}_{l' \to l}}{\overset{k^{in}_{l \to l'}}{\rightleftharpoons}} N_2(l') + N \tag{6}$$

The forward reaction rates are computed with the quasi-classical trajectory (QCT) method, using potentials calculated from ab-initio quantum mechanics computations [12]. The backward reaction rates are computed with the microreversibility principle.
For the URVC bin model the same reaction categories

apply, but on each single bin. The forward reaction rates of bin k are obtained from the formulas:

$$k_k^{dis} = \frac{1}{g_k} \sum_l g_l k_l^{dis} \quad k_{k\to k'}^{in} = \frac{1}{g_k} \sum_{k,l} g_l k_{l\to l'}^{in} \tag{7}$$

The backward reaction rates are not connected through the micro-reversibility principle to the forward ones; they are computed using the equilibrium constant which is obtained by minimizing the Gibbs free energy of the bins. In this way equilibrium is obtained at a bin level. In order to correctly compute the minimum Gibbs free energy, even without electronic energy, the degeneracy of the first electronic level of N is required, that for the state-to-state model is equal to 12.

3. Governing Equations

The dynamical evolution of the bins is governed by the Navier-Stokes equations:

$$\frac{\partial \rho_i}{\partial t} + \nabla \cdot (\rho_i \mathbf{u} + \mathbf{j}_i) = \dot{\omega}_i, \tag{8}$$

$$\frac{\partial \rho \mathbf{u}}{\partial t} + \nabla \cdot (\rho \mathbf{u} \otimes \mathbf{u} + p\underline{\underline{I}} + \underline{\underline{\tau}}) = \mathbf{0}, \tag{9}$$

$$\frac{\partial \rho E}{\partial t} + \nabla \cdot (\rho \mathbf{u} H + \underline{\underline{\tau}}\mathbf{u} + \mathbf{q}) = 0. \tag{10}$$

ρ_i is the partial density of bin i, $\rho\mathbf{u}$ and ρE are momentum and total energy of the whole mixture. $\mathbf{j}_i$ is the diffusion flux and $\dot{\omega}_i$ is the chemical production/destruction term of bin i. The identity matrix is symbolized with $\underline{\underline{I}}$, p is the mixture pressure, $\underline{\underline{\tau}}$ is the stress tensor and $\mathbf{q}$ is the heat flux. If Eqs. 8 are summed up over all the species in the mixture, the total continuity equation will be obtained, since $\sum_i \rho_i = \rho$. For the state-to-state approach, one distinct continuity equation for each bin is solved. Each bin is supposed to behave as a perfect gas.

3.1. Transport Properties

In order to close the Navier-Stokes equations that govern the bins dynamic, expressions for diffusion flux, stress tensor and heat flux should be obtained. The transport properties are computed using the *Mutation++* library, developed by Scoggins and Magin [25] at the von Karman Institute for Fluid Dynamics. In the computation of the transport properties it is assumed that the elastic collisions cross sections are the same for all internal quantum states and inelastic collisions have no influence.

The diffusion flux is computed with the Stefan-Maxwell equations (there is one of these equations for each bin):

$$\frac{M}{\rho} \sum_k \left(\frac{x_i \mathbf{j_k}}{M_k \mathcal{D}_{ik}} - \frac{x_k \mathbf{j_i}}{M_i \mathcal{D}_{ik}} \right) = \nabla x_i \tag{11}$$

where ∇x_i is mole fraction gradient of bin i. $\mathcal{D}_{ik}$ is the binary diffusion coefficient.
Stress tensor reads classically:

$$\underline{\underline{\tau}} = -\mu[\nabla \mathbf{u} + (\nabla \mathbf{u})^T - \frac{2}{3}\nabla \cdot \mathbf{u}\underline{\underline{I}}], \tag{12}$$

where μ is the shear viscosity.
Heat flux reads:

$$\mathbf{q} = -\lambda \nabla T + \sum_i h_i \mathbf{j}_i \tag{13}$$

where λ is the thermal conductivity associated with the translational temperature T of the gas species and the second term is the diffusive heat flux, which will be referred as q_{diff}.

3.2. Numerical solution

The above formulation has still a high computational cost because of the subdivision into bins. For this reason a special formulation of the Navier-Stokes equations, called Dimensionally Reduced Navier-Stokes equations (DRNSE) [14], that simulates the flow field only on the stagnation line of the re-entry vehicle is solved. The Navier-Stokes equations are written in spherical (r, θ, ϕ) coordinates. The flow is assumed to be axisymmetric and therefore $u_\phi = 0$ and $\partial/\partial\phi = 0$. The symmetry of the flow implies that u_r, p, T and ρ_i are symmetric (cosine) with respect to the stagnation line axis (located at $\theta = 0$) and u_θ is anti-symmetric (sine) with respect to it. Furthermore, the Newtonian theory for pressure distribution of hypersonic flows is assumed. Finally, by taking the limit of $\theta \to 0$ the DRNSE equations [14] are obtained. The DRNSE system of equations is solved using the finite volume method in space, with an implicit Backward Euler method in time [11]. Detailed information about the numerical method can be found in [19].

4. Catalytic Wall

The surface of the thermal protection system can act as a catalyst with respect to the gas mixture chemical species that impinge on it. If this is the case, the recombination of dissociated species is promoted and

the chemical energy released increases the heat load of the vehicle. In order to model this phenomenon, a correct boundary condition should be imposed at the wall surface for the mixture's chemical species. For a catalytic wall at a steady state, the mass of each species produced or destroyed by surface reactions should be equal to the diffusion flux of the species at the wall. Hence:

$$\mathbf{j}_i \cdot \mathbf{n}_w = \dot{w}_{i,cat} \tag{14}$$

where $\mathbf{n}_w$ is the unit vector normal to the surface and $\dot{w}_{i,cat}$ is the mass of species i produced or destroyed per unit of area and unit time. The right hand side is modeled using a phenomenological approach, the γ model, widely used in the aero-thermodynamics community [4; 7]. The recombination probability γ_i is defined as:

$$\gamma_i = \frac{M_{i,rec}}{M_i^{\downarrow}}, \tag{15}$$

where $M_i^{\downarrow}$ is the flux of species i impinging the surface and $M_{i,rec}$ is the flux of species recombining at the surface. A fully catalytic wall has γ_i equal to 1, which means that all the particles of species i impinging the surface recombine at the wall. γ_i equal to 0 means that no reaction takes place and corresponds to a non-catalytic wall. Anything between these two extreme cases is a partially catalytic wall. Knowing the probability γ_i, the right hand side of Eq. 14 is equal to [4]:

$$\dot{w}_{i,cat} = \gamma_i m_i M_i^{\downarrow} \tag{16}$$

When the translational energy modes of gas species close to the wall have a Maxwellian distribution function and there is no temperature slip, the impinging flux, $M_i^{\downarrow}$, is equal to [4]:

$$M_i^{\downarrow} = n_i \sqrt{\frac{kT_w}{2\pi m_i}} \tag{17}$$

where T_w is the wall temperature. For the state-to-state model specific wall recombination reactions are considered for every different rovibrational bin, each one with their own recombination probabilities γ_i:

$$N + N \xrightarrow{\gamma_i} N_2(i). \tag{18}$$

Since in literature there are no available values for γ_i, three cases are considered. In the first case γ_i is assumed to be equal for every bin. γ_i is obtained by dividing a global recombination probability γ by the number of bins considered in the model. For this contribution, $\gamma = 0.01$ and because we consider 10 bins $\gamma_i = 0.001$. This case will be referred as the equiprobable catalytic case. In the second case, it is assumed that recombination occurs only in the lower energy bin, which means that $\gamma_{i=1} = 0.01$ and the others are equal to 0. This case is called the lower catalytic case. In the third case recombination occurs only to the highest energy bin. This will be the upper catalytic case.

As a concluding remark, it should be mentioned that the purpose of the paper was not to find a rigorous value for recombination probabilities. The aim was to check how the heat flux is affected in each case. In the future, there are plans to extract from a finite rate chemistry and a dynamical Monte Carlo approach more accurate recombination probabilities γ_i and couple them with the bin model [8; 26; 9].

4.1. Accommodation Coefficient

The recombination of atoms at the surface releases their chemical energy. Nonetheless, not all of this energy should be transferred to the surface. Some of it may be saved within the created molecule as internal energy (rotational, vibrational or electronic). One of the aims of using state-to-state models for catalysis is to determine how much of this energy is released to the wall and how much is saved as energy of the molecules. A suitable parameter, the chemical energy accommodation coefficient β, is introduced [10]:

$$\beta = \frac{q_{diff}}{\sum_i \dot{\omega}_{i,cat} \Delta H_{i,R}(T_{wall})}, \tag{19}$$

where q_{diff} is the diffusive heat flux and $\Delta H_{i,R}(T_{wall})$ is energy released by the recombination reaction that involves bin i at thermal equilibrium. The β coefficient is non-dimensional and can take values between 0 and 1. $\beta = 0$ means that none of the energy released during the catalytic recombination is transferred to the wall and $\beta = 1$ means the opposite.

Researchers often use the product of β and γ coefficients defining an overall effective catalytic probability, γ_{eff}, in order to characterize the catalytic efficiency derived from experiments [5]. In this paper the chemical energy accommodation coefficient is explicitly determined. Similar approaches for the determination of the accommodation coefficient can be found in [3].

5. Results

The flow on the stagnation line around a spherical blunt body of radius $r = 0.4\,m$ is studied. The free

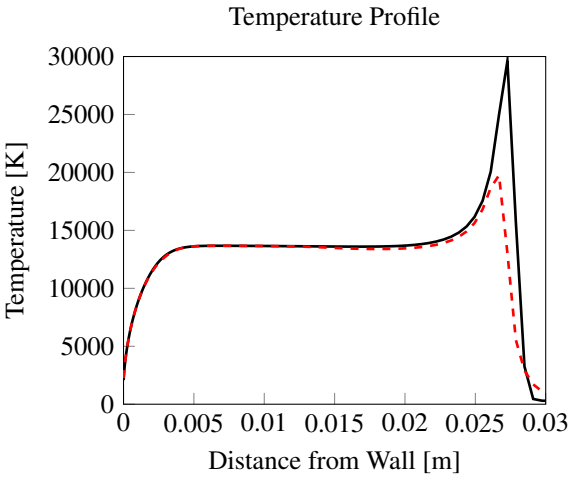

Figure 1: State-to-state N simulations for the non-catalytic case. Temperature profile along the stagnation line. (***unbroken line***): Translational temperature; (***dashed line***): Internal temperature.

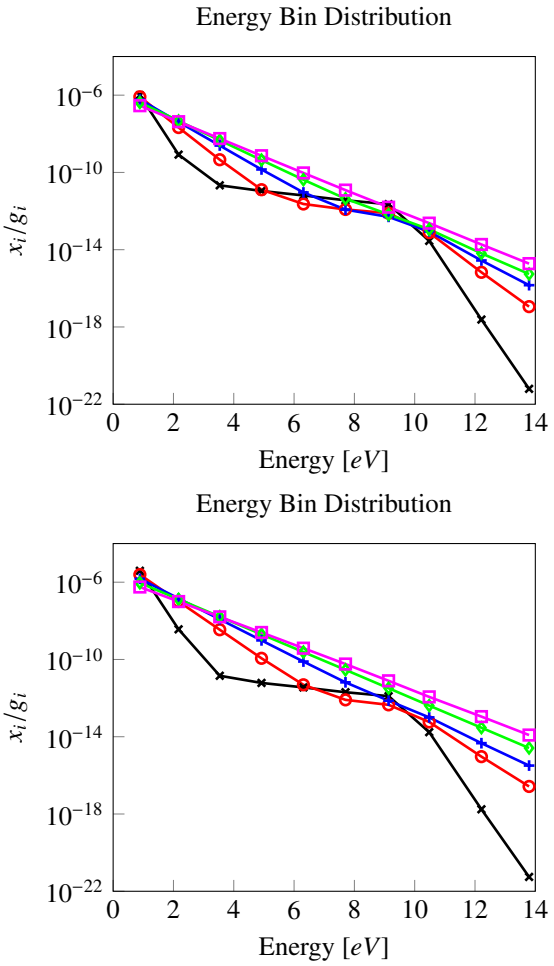

Figure 2: Distribution of the internal energy bins close to the surface for the non-catalytic (*top*) and lower (*bottom*) case. (**x**: $x = 0\,m$; **o**: $x = 2 \cdot 10^{-4}\,m$; **+**: $x = 4 \cdot 10^{-4}\,m$; **diamond**: $x = 6 \cdot 10^{-4}\,m$; **square**: $x = 8 \cdot 10^{-4}\,m$).

stream pressure is equal to $p_\infty = 44\,Pa$, the temperature is $T = 300\,K$ and the free stream velocity is equal to $10000\,m/s$ ($M = 28.33$). Since only $N_2 - N$ collisions are considered, the free stream is seeded with 2.8% per mole of atomic nitrogen. The wall is considered in equilibrium with temperature equal to $2000K$. This temperature is relatively high for catalytic studies, nonetheless it has been chosen for validation purposes in order to have a test case consistent to the previous ones [19; 20].

In Fig. 1 the temperature profiles for the non-catalytic case along the stagnation line are presented; translational and the internal (see Eq. 4) temperatures are shown. The free stream is not in thermal equilibrium, because at low temperatures the URVC model stores an excess of energy in the first bin; this effect fades away once the temperature increases. An area of strong thermal non-equilibrium is observed across the shock wave. At a distance of $x = 0.02\,m$ from the wall the two temperatures become practically equal. The two temperatures are very close to each other inside the boundary layer, except at the wall $x = 0\,m$.

The internal energy bins population inside the boundary layer, close to the wall, is plotted in Figs. 2 and 3 in terms of their molar fractions divided by the bin degeneracy. In Fig. 2-top the non-catalytic case is shown. Inside the boundary layer, up to a distance from the wall equal to $x = 4 \cdot 10^{-4}\,m$, the energy levels have a Boltzmann distribution, as it is seen by the straight line in the logarithmic plot, which changes its slope because of the decrease in temperature due to the influence of the wall. At $x = 2 \cdot 10^{-4}\,m$ the Boltzmann character starts to be lost; the non predissociated higher energy states get more and more populated, while the predissociated states are depleted. This effect is maximized at the wall.

Figure 2-bottom shows the distribution of internal energy bins for the lower catalytic case. The behaviour is similar to the non-catalytic case, except that the first bin is overpopulated, because the wall promotes recombination of nitrogen atoms into molecules belonging to the first bin.

Figure 3 shows the distribution of the internal energy bin for the, equiprobable (top) and upper catalytic (bottom) cases. The two cases show a similar trend. Up to a distance of the order of $x = 2 \cdot 10^{-4}\,m$ from

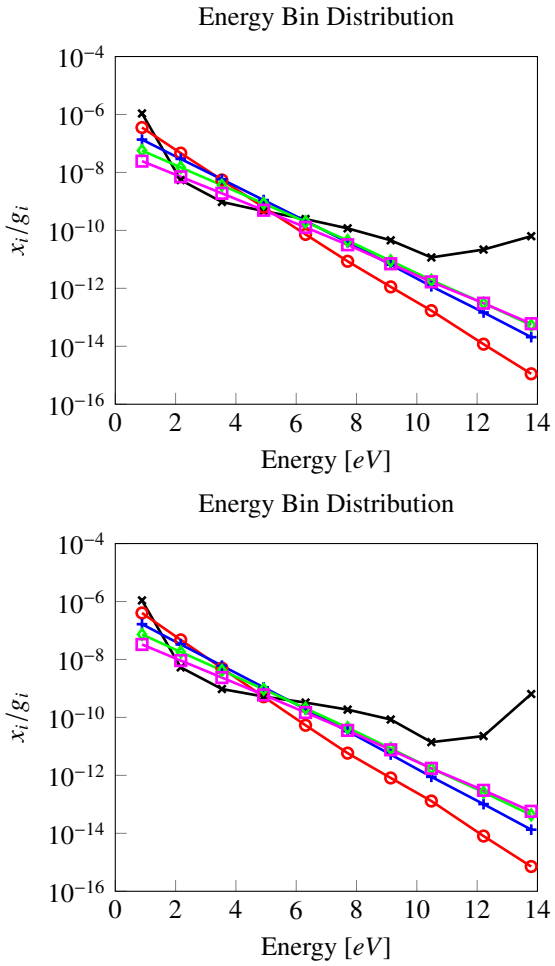

Figure 3: Distribution of the internal energy bins close to the surface for the equiprobable (*top*) and upper (*bottom*) catalytic case. (**x**: $x = 0\,m$; **o**: $x = 2 \cdot 10^{-4}\,m$; **+**: $x = 4 \cdot 10^{-4}\,m$; **diamond**: $x = 6 \cdot 10^{-4}\,m$; **square**: $x = 8 \cdot 10^{-4}\,m$).

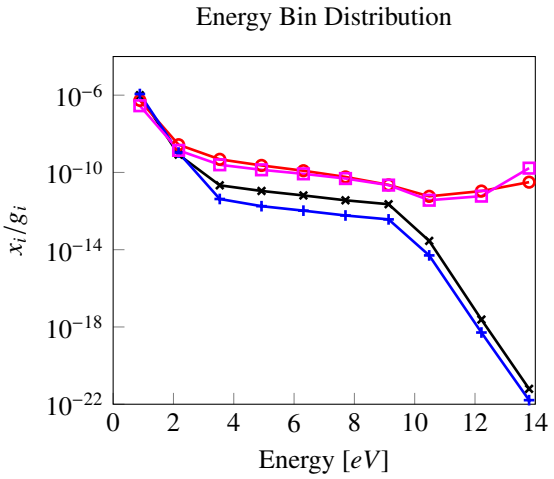

Figure 4: Comparison of distributions of internal energy bins for the four catalytic cases. **x**: Non-catalytic case; **+**: Lower catalytic case; **o**: Equiprobable catalytic case; **square**: Upper catalytic case.

the wall the levels are populated with a Boltzmann distribution. Very close to the wall the Boltzmann distribution does not hold any more and the higher energy bins are overpopulated in both cases; catalysis promotes thermal non-equilibrium at the wall. For the sake of comparison the distributions of energy bins at the wall, for all the four cases, are plotted together in Fig. 4.

Fig. 5 depicts the molar fraction of N along the stagnation line for the four cases. In the non-catalytic case (*unbroken line*) the recombination is due only to the recombination reactions in the gas phase. The recombination predicted by the present model is lower compared to the one predicted by the Park model [19; 24]. In the lower catalytic case (*dotted-dashed line*) the nitrogen molar fraction is further reduced because of wall recombination. This does not happen for the equiprobable and upper catalytic cases, where the populations of the N atoms are higher. This is mainly due to two combined effects. First of all, it can be seen in Fig. 5 that the boundary layer is less thick in the equal and upper catalytic cases. This leads to a reduced recombination, because of the less time available for the reactions. Secondly, since in these two cases nitrogen molecules are preferentially formed in high vibrational states, they are much more likely to dissociate after desorption and to transform their internal energy into translational one, a phenomenon known as quenching. This effect can be inferred from the temperature profiles inside the boundary layer. Fig. 6 shows the translational and internal temperature profiles in the boundary layer for the four cases. The profiles of the non-catalytic and lower catalytic cases are very similar and the same happens for the equally and fully catalytic cases. The translational temperature gradient increases going from non-catalytic to the upper catalytic case, because highly excited desorbed molecules transfer their internal energy to translational one. In Fig. 6-bottom the internal temperatures of the flow field are presented. In the non-catalytic case the internal temperature at the wall is equal to $2252\,K$ which is higher than the imposed translational temperature. Therefore, the assumption of thermal equilibrium at the wall is not valid and this effect should be taken into consideration in multi-temperature simulations. The internal temperature in-

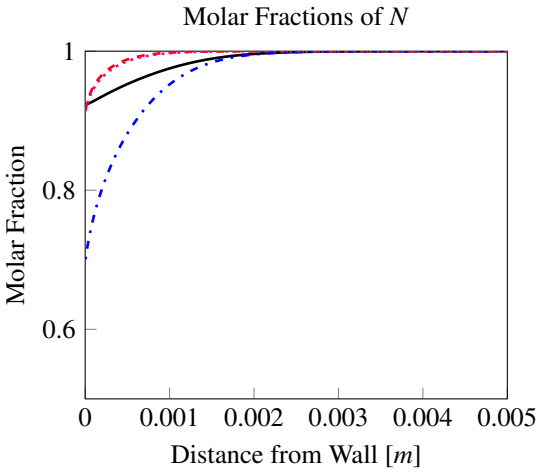

Figure 5: Comparison of N molar fraction for the four cases. ***unbroken line***: Non-catalytic case; ***dotted-dashed line***: Lower catalytic case; ***dashed line***: Equiprobable catalytic case; ***dotted line***: Upper catalytic case.

creases with the wall catalysis and it reaches the highest value of 4384 K for the upper catalytic case. These results are consistent with similar ones available in literature [19].

Heat fluxes are shown in Tab. 1. The wall heat flux for the non-catalytic case is 3.02 MW/m^2; the diffusive heat flux contribution is zero since it is a non-catalytic wall. In the catalytic cases heat flux is the sum of the conductive contribution $\mathbf{q_{con}} = -\lambda\nabla T$ and the diffusive one $\mathbf{q_{diff}} = \sum_i h_i \mathbf{j}_i$. For the lower catalytic case the conductive heat flux increases due to the increase in the slope of the temperature. The diffusive heat flux is also high and of the order of magnitude of the conductive heat flux. As we impose equiprobable recombination or recombination to the upper energy bin the heat flux greatly increases mainly due to the contribution of the conductive heat flux. The diffusive heat flux though decreases, because, as already mentioned in the comments of Fig. 5, there is little net recombination of nitrogen atoms. The results shown in this paragraph for our nitrogen state-to-state model agree qualitatively with the ones obtained for a vibrational specific oxygen model in [2; 15].

The values of the β coefficient computed accordingly to Eq. 19 are shown in Tab. 2. In the non-catalytic case the β coefficient cannot be defined. In the catalytic cases, as already explained, β can take values between 0 and 1. In the lower catalytic case only a small part of the recombination energy is transferred to the internal energy of the desorbed N_2 molecule.

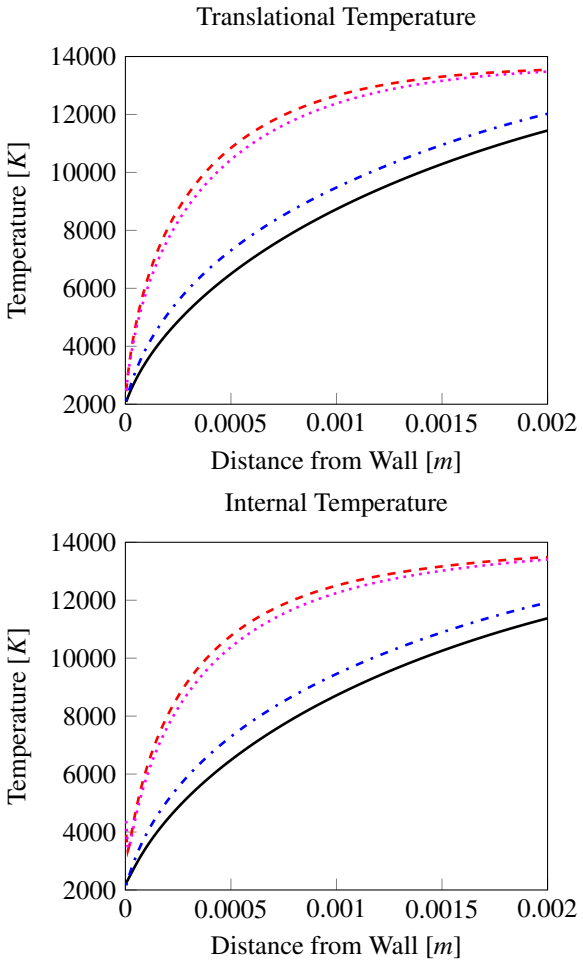

Figure 6: Comparison of the translational and internal temperature profiles for the four cases. (***unbroken line***): Non-catalytic case; (***dotted-dashed line***): Lower catalytic case; (***dashed line***): Equiprobable catalytic case; (***dotted line***): Upper catalytic case.

Most of the energy is therefore transferred to the surface and for this reason we have $\beta = 0.9325$, very close to one. This is the maximum value attained by the β coefficient. In the upper catalytic case, where all of the N atoms recombine into the highest energy bin of N_2, the β coefficient is equal to 0.1005 meaning that very small part of the recombination energy is directly transferred to the wall. The equiprobable catalytic case stays in between with $\beta = 0.5757$. In the last two cases, even though only a small part of the recombination energy is directly transferred to the surface, the heat flux increases substantially, because the quenching phenomenon enhances the conductive part of the heat flux. Therefore, even though the β coefficient has an important physical meaning, it cannot

Table 1: Heat flux $[MW/m^2]$ for the URVC bin model.

	$\mathbf{q_{total}}$	$\mathbf{q_{con}}$	$\mathbf{q_{diff}}$
Non-catalytic	3.02	3.02	–
Lower catalytic	7.48	3.85	3.63
Equal catalytic	17.58	15.07	2.51
Upper catalytic	15.3	14.87	0.43

Table 2: β coefficient and T_{int} $[K]$ for the URVC bin model

	β	T_{int}
Non-catalytic	–	2252
Lower catalytic	0.9325	2159
Equal catalytic	0.5757	3917
Upper catalytic	0.1005	4834

be used as an accurate indicator for the total heat flux transferred to the wall, but only as an indicator of the diffusive (reactive) portion of heat flux directly transferred to the wall.

6. Conclusions

In this paper the joint effects of thermal non-equilibrium and catalysis have been studied on the stagnation line flow field of a cylinder in hypersonic conditions. The Uniform Rovibrational Collisional coarse-grained model of nitrogen has been used. The coarse-grained model is based on an ab-initio rovibrational nitrogen model developed at NASA Ames research center. The gamma model has been used in order to simulate the catalytic properties of the re-entry body thermal protection system and it has been extended in order to account for the rovibrational model. The flow field has been modeled by solving the Navier-Stokes equations using an implicit Finite Volume method.

Heat flux is strongly affected by the mutual interaction of catalysis and thermal non-equilibrium. The diffusive heat flux decrease when catalysis acts only on the higher energy levels, with a specular decrease of the β coefficient. Nonetheless the conductive heat flux is strongly enhanced by the quenching phenomenon, leading, in the end, to a net increase of the overall heat flux. These results are in agreement with previous literature data.

As a future work, the Boltzmann rovibrational collisional model can be used in order to remove some of the weak points of the Uniform Rovibrational Collisional model. $N_2 - N_2$ collisions should also be included, as well as electronic energy levels beyond the ground one. Extension to a full air mixture including the O_2 and NO molecules would be also of interest, making the comparison to experimental results easier. As far as the treatment of the wall is concerned, treating catalysis with a microkinetic model is in view. The latter model can be coupled directly with a flow solver or used as a test bench for obtaining more accurate values for the catalytic recombination probability γ. Validation of the results is also necessary by comparing the simulations with experimental results on catalysis, performed at von Karman Institute or by other experimental teams.

Acknowledgements

The authors are grateful to James B. Scoggins for his time and support concerning the usage and further development of the *Mutation++* library, to Erik Torres for his tools for the reduction of the full NASA model into the Uniform Rovibrational Collisional one and to Alessandro Munafò for the stagnation line code. Research of G. B. C. and T. E. M. is sponsored by the European Research Council Starting Grant #2549354.

References

[1] J.D. Anderson. *Hypersonic and High-Temperature Gas Dynamics*. AIAA Education Series. American Institute of Aeronautics and Astronautics, 2006.

[2] I. Armenise, M. Capitelli, Cl. Gorse and M. Rutigliano. Nonequilibrium vibrational kinetics of an O_2/O mixture hitting a catalytic surface. *Journal of Spacecraft and Rockets*, 37:3:318–323, 2000.

[3] M. Balat-Pichelin, V.L. Kovalev, A.F. Kolesnikov and A.A. Krupnov. Effect of the incomplete accommodation of the heterogeneous recombination energy on heat fluxes to a quartz surface. *Fluid Dynamics*, 43(5):830–838, 2008.

[4] P. F. Barbante. *Accurate and Efficient Modeling of High Temperature Nonequilibrium Air Flows*. PhD thesis, Université Libre de Bruxelles, 2001.

[5] O. Chazot. Experimental studies on hypersonic stagnation point chemical environment. *RTO-EN-AVT-142 von Karman Institute Lecture Series: Experiment, Model and Simulation of Gas-Surface Interactions for Reactive Flows in Hypersonic Flights*, 2007.

[6] I. Chorkendorff and J.W. Niemantsverdriet. *Concepts of Modern Catalysis and Kinetics*. Wiley, 2006.

[7] R. Goulard. On catalytic recombination rates in hypersonic stagnation heat transfer. *Jet Propulsion*, 28:737–745, 1958.

[8] V. Guerra. Analytical model of heterogeneous atomic recombination of silica-like surfaces. *IEEE Transaction on plasma science*, 5:35, 2007.

[9] V. Guerra and J. Loureiro. Dynamical Monte Carlo simulation of surface atomic recombination. *Plasma Sources Sci. Technol.*, 13:85, 2004.

[10] B. Halpern and D. E. Rosner. Chemical energy accommodation at catalyst surfaces. Flow reactor studies of the association of nitrogen atoms on metals at high temperatures. *Transactions of the Faraday Society*, 74:1883–1912, 1978.

[11] C. Hirsch. *Numerical Computation of Internal and External Flows: The Fundamentals of Computational Fluid Dynamics*. Elsevier Science, 2007.

[12] R. Jaffe, W. Schwenke and. G. Chaban and W. Huo. Vibrational and rotational excitation and relaxation of nitrogen from accurate theoretical calculations. *AIAA paper 2008-1208. 46th AIAA Aerospace Sciences Meeting and Exhibit, Reno, NV*, pages 9,49,50,54, 2008.

[13] R. Jaffe, W. Schwenke, and G. Chaban. Theoretical analysis of N2 collisional dissociation and rotation-vibration energy transfer. *AIAA paper 2009-1569. 47th AIAA Aerospace Sciences Meeting and Exhibit, Orlando, FL*, pages 9,49,50, 2009.

[14] A. Klomfass and S. Müller. A quasi-one dimensional approach for hypersonic stagnation-point flows. Technical report, RWTH Aachen, 1996.

[15] E. Kustova, E. Nagnibeda, I. Armenise and M. Capitelli. Nonequilibrium kinetics and heat transfer in O_2/O mixtures near catalytic surfaces. *Journal of Thermophysics and Heat Transfer*, 16:2:238–244, 2002.

[16] T. E. Magin, M. Panesi, A. Bourdon, R. Jaffe and D. Schwenke. Internal energy excitation and dissociation of molecular nitrogen in a compressing flow. *AIAA 2009-3837. 41st AIAA Thermophysics Conference, San Antonio, Texas*, 2009.

[17] T.E. Magin, M. Panesi, A. Bourdon, R. L. Jaffe and D. W. Schwenke. Coarse-grain model for internal energy excitation and dissociation of molecular nitrogen. *Chemical Physics*, 398(0):90 – 95, 2012. Chemical Physics of Low-Temperature Plasmas (in honour of Prof Mario Capitelli).

[18] M.F. Modest. *Radiative Heat Transfer*. Chemical, Petrochemical & Process. Academic Press, 2003.

[19] A. Munafò. *Multi-Scale models and Computational methods for Aerothermodynamics*. PhD thesis, Ecole Central Paris, 2014.

[20] A. Munafò and T. E. Magin. Modeling of stagnation-line nonequilibrium flows by means of quantum based collisional models. *Physics of Fluids*, 26(9):–, 2014.

[21] M. Panesi, R. Jaffe and D. Schwenke. Energy transfer study of N2-N2 interactions by using rovibrational state-to-state model. *AIAA 2013-3147. 44st AIAA Thermophysics Conference*, 2013.

[22] M. Panesi. *Physical models for nonequilibrium plasma flow simulations at high speed re-entry conditions*. PhD thesis, Università degli Studi di Pisa, 2009.

[23] C. Park. *Nonequilibrium Hypersonic Aerothermodynamics*. Wiley, 1990.

[24] C. Park. Review of chemical-kinetic problems of future NASA missions. I: - earth entries. *Journal of Thermophysics and Heat Transfer*, 7-3:385–398, 1993.

[25] J. B. Scoggins and T. E. Magin Development of Mutation^{++}: MUlticomponent Thermodynamics And Transport properties for Ionized Plasmas written in C++. *AIAA 2014-2966. 11th AIAA/ASME Joint Thermophysics and Heat Transfer Conference*, 2014.

[26] C. Sorensen, P. Valentini and T. E.Schwartzentruber Uncertainty Analysis of Reaction Rates in a Finite-Rate Surface-Catalysis Model. *Journal of Thermophysics and Heat Transfer*, 26-3:407-416

[27] J. Thoemel. *Surface catalysis in high enthalpy flows*. PhD thesis, RWTH Aachen, von Karman Institute for Fluid Dynamics, January 2013.

[28] W.G. Vincenti and C.H. Kruger. *Introduction to physical gas dynamics*. Krieger, 1967.

SPARK: Simplified PlasmA models based on Reduced Kinetics

Aurélie Bellemans

Aeronautics and Aerospace Department, von Karman Institute for Fluid Dynamics, Belgium, aurelie.bellemans@vki.ac.be

Supervisor: Thierry Magin

Associate Professor, Aeronautics and Aerospace Department, von Karman Institute for Fluid Dynamics, Belgium, magin@vki.ac.be

University Supervisor: Alessandro Parente

Associate Professor, Service d'Aéro-Thermo-Mécanique, Université Libre de Bruxelles, Belgium, alessandro.parente@ulb.ac.be

Abstract

The present work considers the development of reduced chemistry models for plasma flows using Principal Component Analysis (PCA) based methods. Starting from an electronic specific Collisional-Radiative model, a reduction of the variable set (i.e., mass fractions and temperatures) is proposed by projecting the full set on a reduced basis made up of its principal components. Thus, the flow governing equations are only solved for the principal components. The proposed approach originates from the combustion community, where Manifold Generated Principal Component Analysis (MG-PCA) has been developed as a successful reduction technique. Applications consider ionizing shock waves in Argon. The results obtained show that the use of the MG-PCA technique enables for a substantial reduction of the computational time.

Keywords: plasma, argon, ablation, chemistry reduction, principal component analysis

1. Introduction

During the last decade considerable research efforts have been spent on developing techniques with the aim of reducing the computational cost of plasma flow simulations. The complexity of modeling a plasma flow lies in the multi-scale nature of the problem. The gas mixture is usually made of hundreds of species which are, in turn, involved in a large number of reactions (e.g.,dissociation and ionization) each one having its own time-scale. A further complication comes from non-equilibrium effects, occurring when the reacting time-scales become comparable with the macroscopic time-scales of interest. In this situation, one has to express mass conservation for each of the gas species. For Collisional-Radiative (or State-to-State) models [1], this may lead to prohibitively expensive calculations in the case of 3D simulations.

Different strategies can be considered to reduce the complexity of a kinetic mechanism. One possible approach (which is more mathematical) consists in projecting the system on a reduced base of variables according to different reduction techniques. Examples of this are the works of Kim [2] , Pope [3], Ren [4], Keck [5; 6] and Massot [7], where singular perturbation analysis and rate-controlled constrained equilibrium are combined to propose a time-scale based reduction of a reacting system. It is stated by Massot that the dynamics of reactive mixtures can be divided in a fast and a slow reacting part. The goal is to project the fast reacting kinetics on the slow varying base of the system to provide a reduced system.

A possible alternative to the aforementioned methods is provided by physics-based methods. Examples of this approach are the coarse-grained models proposed by Magin et al. [8], Munafò et al. [9; 10], Liu et al. [11; 12] and Panesi and Lani [13]. In the aforementioned papers the mechanism reduction is realized by lumping the internal energy levels in bins (where a distribution for the levels is prescribed). The work by Panesi and Lani [13] focuses on electronic excitation and ionization in air (ABBA model [14; 15; 16; 17]), while those by Magin et al. [8], Munafò et al. [9; 10], Liu et al. [11; 12] focus on the rovibrational kinetics of the $N_2(^1\Sigma_g^+)$-$N(^4S_u)$ system. The

database for the $N_2(^1\Sigma_g^+)$-$N(^4S_u)$ has been developed by the Computational Quantum Chemistry Group at NASA Ames Research Center [18; 19; 20; 21]. This database, beside the development of reduced models, has been also used to gain insight on molecular dissociation and internal energy excitation in hypersonic flows [22; 23]. The results obtained for flows across normal shock waves, within nozzles and along the stagnation-line of blunt bodies have shown that the proposed coarse-grained models can correctly reproduce the dynamics of $N_2(^1\Sigma_g^+)$ dissociation by using only 10-20 energy bins [8; 9; 10]. Other examples of coarse-grained models for plasma flows are the works by Le et al. [24] and Guy et al. [25]. The work of Le at al. [24] focuses on electron induced ionization and excitation in atomic systems. In the aforementioned reference the authors were able to capture the main features of macroscopic ionization with only 2 energy bins. The work of Guy et al. [25] is based on a vibrational State-to-State model obtained from Force-Harmonic-Oscillator (FHO) rate coefficients [26; 27]. In this case, the vibrational levels of $N_2(^1\Sigma_g^+)$ are grouped into two or three groups to reduce the computational cost of the model. An interesting coarse-grained model is the 2-Level Distribution Kinetics method developed by Colonna et al. [28]. Its original formulation was based on a vibrational State-to-State model for N_2. More recently this reduced-order model has been extended to include radiation [29]

Another category of reduction techniques, the one investigated in this work, is based on Principal Component Analysis (PCA). PCA is a statistical approach for projecting a system of equations on a reduced reference system identified by the so-called principal components (PC's) [30]. The reduced base is obtained after solving an eigenvalue problem on the full thermo-chemical state identified, in the present work, by mass fractions and temperatures. This method has recently been developed and mainly been verified for combustion applications. In the work of Parente et al. [31] and Isaac et al. [32], Manifold-Generated Principal Component Analysis (MG-PCA) has been developed starting from the conventional PCA method. Two formulations can be adopted for the MG-PCA method: (i) local and (ii) global. In the local approach the dataset is divided in several clusters or bins, and MG-PCA is applied on each of them to obtain an optimal reduction as described in the work of Coussement et al. [33], where MG-local-PCA has been applied on a DNS code for simulating flame-vortex interactions. In case of global MG-PCA, the full dataset is kept as one principal cluster. Principal component analysis can also be combined with non-linear regression methods to obtain a further reduction and a better accuracy as suggested by Yang et al. [34], Biglari and Sutherland [35] and Mirgolbabaei and Echekki [36], [37] for combustion simulations, as well as by Peerenboom et al. [38] for plasma flows. Although coupling PCA with non-linear regression has the potential of ensuring very strong compression, the approach strongly relies on the ability of the chosen non-linear model to reproduce the system physics. On the other hand, keeping the full original mechanism results in lower reduction but allows, at the same time, to increase the range of applicability and the generality of the reduced models.

The purpose of the present paper is to apply the MG-PCA method on plasma flows in thermo-chemical non-equilibrium. An electronic specific Collisional-Radiative model for weakly ionized Argon plasmas mixture is reduced. This represents, to the authors knowledge, the first application of the MG-PCA technique on a relatively large kinetic scheme accounting for hundreds of reactions. As a matter of fact, previous MG-PCA investigations focused on simple combustion chemistry (syngas). Both the global and local formulation of the MG-PCA reduction technique are verified and validated with Argon shock tube experiments from UTIAS (University of Toronto, Institute for Aerospace Studies) shock tube facility [39; 40].

The paper is structured as follows. The Collisional-Radiative model for Argon plasmas is described in Sect. 2. Section 3 introduces the Principal Components Analysis (PCA) reduction technique, together with its related pre-processing. Results of the application of MG-PCA to ionizing shock waves in Argon are discussed in Sect. 4. Conclusions are outlined in Sect. 5.

2. Physical modeling

2.1. Collisional-Radiative Model

The Collisional-Radiative (CR) model used in the present work has been originally developed by Vlcek [41] and Bultel [42], and later validated by Kapper and Cambier [43; 44] against experimental data acquired in the UTIAS shock tube. CR models naturally allow for taking into account the effects of non-Boltzmann distributions, as the internal energy levels are treated as separate *pseudo-species* [1].

This leads to more accurate predictions compared to Multi-Temperature (MT) models, which are based on Maxwell-Boltzmann distributions [45; 46]. Examples of applications of CR models to plasma flows can be found in works of Laux and co-workers [47; 48; 49], Bultel and co-workers [42; 14; 50], Panesi et al. [15; 16], Yanguas-Gil [51], Bogaerts [52], Colonna et al. [53; 54] and Munafò et al. [17].

The gas mixture is made of Argon and its ionization products: e^-, Ar and Ar^+. The influence of additional components, such as Ar^{++} and Ar_2^+, has been neglected [42]. The number of electronic levels of Ar and Ar^+ are 31 and 2, respectively. Thus, the total number of species is 34. Table 1 provides the excitation energy (E_i), degeneracy (g_i) and core angular momentum (j_c) for the 31 electronic levels of Ar. To account for thermal non-equilibrium between heavy-particles and free-electrons, separate translational temperatures (denoted in what follows with T_h and T_e, respectively).

i	$E_i[eV]$	g_i	j_c	i	$E_i[eV]$	g_i	j_c
1	0	1	1.5	17	13.864	3	1.5
2	11.548	5	1.5	18	13.903	5	1.5
3	11.624	3	1.5	19	13.979	9	1.5
4	11.723	1	0.5	20	14.013	7	1.5
5	11.828	3	0.5	21	14.063	5	1.5
6	12.907	3	1.5	22	14.068	5	1.5
7	13.076	7	1.5	23	14.090	3	1.5
8	13.095	5	1.5	24	14.099	7	1.5
9	13.153	3	1.5	25	14.153	3	1.5
10	13.172	5	1.5	26	14.214	5	0.5
11	13.273	1	1.5	27	14.234	5	0.5
12	13.283	3	0.5	28	14.236	7	0.5
13	13.302	5	0.5	29	14.241	1	0.5
14	13.328	3	0.5	30	14.255	3	0.5
15	13.480	1	0.5	31	14.304	3	0.5
16	13.845	1	1.5				

Table 1: Energy data of the electronic states of Ar.

The kinetic mechanism accounts for the following collisional and radiative processes [41; 42; 43; 44]:

(i) excitation and ionization by electron impact:

$$\mathrm{Ar}(i) + \mathrm{e}^- \rightleftarrows \mathrm{Ar}(j) + \mathrm{e}^-, \quad i < j, \quad (1)$$

$$\mathrm{Ar}(i) + \mathrm{e}^- \rightleftarrows \mathrm{Ar}^+(j) + \mathrm{e}^- + \mathrm{e}^-, \quad (2)$$

(ii) excitation and ionization by heavy-particle impact:

$$\mathrm{Ar}(i) + \mathrm{Ar}(1) \rightleftarrows \mathrm{Ar}(j) + \mathrm{Ar}(1), \quad i < j, (3)$$

$$\mathrm{Ar}(i) + \mathrm{Ar}(1) \rightleftarrows \mathrm{Ar}^+(j) + \mathrm{e}^- + \mathrm{Ar}(1), \quad (4)$$

(iii) spontaneous emission/absorption (*bound-bound*):

$$\mathrm{Ar}(j) \rightleftarrows \mathrm{Ar}(i) + \mathrm{h_P}\nu_{ij}, \quad i < j, \quad (5)$$

(iv) photo-ionization/radiative recombination (*free-bound* and *bound-free*):

$$\mathrm{Ar}(i) + \mathrm{h_P}\nu \rightleftarrows \mathrm{Ar}^+(j) + \mathrm{e}^-, \quad (6)$$

(v) Bremsstrahlung radiation (*free-free*).

In Eqs. (1)-(6), the indices i and j denote the electronic levels of Ar and Ar^+ involved in the transitions. Quantities h_P and ν in Eqs. (5)-(6) stand for Planck's constant and the radiation frequency, respectively. In the present work, radiation re-absorption is taken into account via the use of escape factors [43]. The former can take values between 0 and 1, which correspond, respectively, to an optically thick and thin plasma. An optically thin plasma is considered in the present work. The total number of processes (both collisional and radiative) taken into account in the adopted CR model is 962.

The mass production terms for the free-electrons and the electronic levels of Ar and Ar^+ (indicated, respectively, with ω_e and ω_i) are evaluated based on the zeroth-order reaction rate theory. The related rate coefficients are computed as explained by Kapper and Cambier [43]. The same holds true for the radiative source terms due *bound-bound* (Ω^R_{bb}), *bound-free* (Ω^R_{bf}) and *free-free* (Ω^R_{ff}) transitions, and the collisional energy transfer terms for free-electrons due to elastic (Ω^C_{el}), inelastic (Ω^C_{in}) and ionizing (Ω^C_{ion}) collisions.

2.2. Governing equations

The equations describing the motion of an inviscid gas undergoing ionization behind a shock wave are the one-dimensional Euler equations. These comprise the continuity equations for each species, the global momentum and energy equation, and the free-electron

energy equation [15]. When expressed in the shock reference frame, these equations read:

$$\frac{\partial(\rho y_e u)}{\partial x} = \omega_e, \quad (7)$$

$$\frac{\partial(\rho y_i u)}{\partial x} = \omega_i, \quad (8)$$

$$\frac{\partial(p+\rho u^2)}{\partial x} = 0, \quad (9)$$

$$\frac{\partial(\rho u H)}{\partial x} = \Omega^R_{bb} + \Omega^R_{bf}, \quad (10)$$

$$\frac{\partial(\rho y_e u\, e_e)}{\partial x} = \Omega^C_{el} + \Omega^C_{ex} + \Omega^C_{ion} \quad (11)$$

$$+\Omega^R_{bf} + \Omega^R_{ff} - p_e \frac{\partial u}{\partial x}. \quad (12)$$

In Eqs. (7)-(12), quantities ρ, p, u and H denote the gas density, pressure, speed and total enthalpy per unit mass. The symbols y_e and y_i stand for the mass fractions of free-electrons and the electronic levels of Ar and Ar^+, respectively. Quantity p_e, on the right-hand-side of Eq. (12), denotes the pressure of free-electrons. Details regarding the evaluation of the aforementioned thermodynamic properties can be found in the work of Kapper and Cambier [43].

In the present work, the shock is treated as discontinuity and placed, for the sake of convenience, at the location $x = 0$. Post-shock conditions are obtained based on the Rankine-Hugoniot jump relations under the assumption of frozen kinetics within the shock [55]. Precursor ionization is disregarded in this work.

To obtain numerical solutions, Eqs. (7)-(12) are re-written as a system of Ordinary Differential Equations in canonical form for the mass fractions, and the heavy-particle and free-electron temperatures [15; 16; 9; 56; 57]. Numerical integration is performed by using the SHOCKING_F90 [9; 57] code which uses the LSODE library for stiff initial value problems [58].

3. Principal component analysis

Manifold-Generated Principal Component Analysis (MG-PCA) has been introduced by Parente et al. [31] as a mathematical method for reducing a dynamical system by projecting it on a base made up of its principal components. This reduction technique has been derived from the conventional PCA formulation and improved with the objective of reducing error propagation with respect to chemical source terms. In the works of Isaac et al. [59] and Coussement et al. [33], MG-PCA has been applied and verified on combustion applications and relatively small kinetic mechanisms. The present paper extends the model to sensibly larger kinetic schemes for Argon plasmas in thermo-chemical non-equilibrium.

The application of the MG-PCA method requires a full simulation to be performed to retrieve a training dataset composed of species mass fractions and temperatures: $\mathbf{X} = [y_1, ..., y_N, T_h, T_e]$. Our dataset is composed of 36 variables for our specific Argon plasma case: 34 mass fractions and 2 temperatures. The flow speed, u, must not be taken into account in PCA.

3.1. Pre-processing

Before PCA is carried out, a pre-processing step has to be performed to remove outlier observations, and to center and scale the data. Centering allows foreseeing on fluctuations, while scaling is necessary to compare variables in different units and covering a very broad range of scales. Different scaling methods exist as it has been shown in previous works by Isaac [32] and Parente [31]. Table 2 shows the different scaling methods together with the corresponding scaling variable.

Scaling technique	Scaling variable
Auto (*STD*)	s_j (standard deviation)
Level	$\bar{x}_j$ (mean value)
Range	$max(x_j) - min(x_j)$
MAX	$max(x_j)$
PARETO	$\sqrt{s_j}$
VAST	$s_j^2/\bar{x}_j$

Table 2: Scaling techniques for MG-PCA data pre-processing.

A comparative study has been carried out to determine the best scaling method for our considered 34-species ionized argon mixture. The results of this a priori model evaluation are described in Sect. 4.

3.2. System reduction

MG-PCA solves an eigenvalue problem on the covariance matrix of this dataset to obtain the eigenvalues, $\mathbf{L}$, and the eigenvectors, $\mathbf{A}$:

$$\mathbf{S} = \mathbf{A}\mathbf{L}\mathbf{A}^T. \quad (13)$$

This matrix of eigenvectors can be truncated to a matrix $\mathbf{A}_q$ containing only the eigenvectors with the highest variance. When projecting the original dataset on

this truncated matrix, one obtains the principal variables or principal components which correspond to the most important variables of the system as they change the most (Eq. (14)). The original sample can be found back via:

$$\mathbf{Z}_q = \mathbf{X}\mathbf{A}_q, \quad (14)$$

$$\tilde{\mathbf{X}}_q = \mathbf{Z}_q\mathbf{A}_q^{\mathrm{T}}. \quad (15)$$

Previous investigators have shown that Eq. (15) can lead to uncontrolled error propagation leading to a non favorable reconstruction of the source terms, since the error is evenly distributed among the state variables. To control the error propagation during the reconstruction of the original sample, Manifold Generated PCA has been originally developed. The main idea is to reconstruct the non-transported variables (the non principal components), by using an optimal square and inverted subset of the eigenvector matrix $\mathbf{A}_q$, matrix $\mathbf{B}$:

$$\mathbf{B} = (\mathbf{A}_q^T)^{-1} = \mathbf{X}_q^+\mathbf{Z}_q, \quad (16)$$

where $\mathbf{X}_q^+$ is the generalized inverse of $\mathbf{X}$, with $\mathbf{X}_q^+ = (\mathbf{X}_q^T\mathbf{X}_q)^{-1}$. The non-principal reconstructed variables, given by the vector $\tilde{\mathbf{X}}(Q-q)$, are reconstructed by multiplying the vector containing the principal components, $\mathbf{X}(q)$, with this matrix $\mathbf{B}$ and the square subset of matrix $\mathbf{A}(Q-q)_q$:

$$\tilde{\mathbf{X}}(Q-q) = \mathbf{X}(q)\mathbf{B}\mathbf{A}(Q-q)_q^{\mathrm{T}}. \quad (17)$$

There exist different criteria to retrieve these principal variables as explained by Parente et al. [31]. The different PV extraction methods studied in this work are: the B4 Forward method, the B2 Backward method, the M2 Backward method and the Mc Cabe criterion. The B4 and B2 method are forward and backward elimination procedures respectively where variables are discarded until only the ones with the average eigenvalue size remain. The M2 method is also a backward elimination method which uses the second optimal minimizing Mc Cabe criterion as a variable selection procedure. Mc Cabe defined also 3 other selection criteria for retaining an optimal set of principal variables, which are described in his published work [60]. A complete description of every method is given in the paper by Cumming and Wooff [61]. The results of the comparison between the different principal variable extraction methods can be found in Sect. IV.

3.3. MG-local-PCA

Besides global MG-PCA, a local formulation of the method exists. This approach consists in dividing the dataset in several bins or clusters, and to apply the reduction technique locally on each of them. To define the clusters a conditioning variable, such as the gas temperature, for instance, is used. This technique is called MG-local-PCA. Consequently a better reduction will be obtained as each bin has its optimized base. This local formulation has successfully been applied on combustion cases as investigated by Isaac et al. [32] and Coussement et al. [33].

4. Results

The present section describes the results obtained using the global and local formulations of MG-PCA for a weakly ionized Argon plasma. Section 4.1 describes the main thermo-physical features of the numerically reproduced UTIAS shock tube experiments. The *a priori* model evaluation, where the different scaling and principal variable extraction techniques are compared, is discussed in Sect. 4.2. Finally, in Sect. 4.3, the predictions obtained by using the reduced and CR models are compared.

4.1. Simulations of ionizing shocks in Argon

The one-dimensional shock fitting code described in Sect. 2 has been used to simulate the UTIAS Argon shock tube experiments [43]. Table 3 provides the experimental free-stream conditions. In the present work, only cases 1, 4 and 5 (corresponding to intermediate, low and high shock speed, respectively), have been considered.

	Free-stream		
Case	**Ma**	**P [Pa]**	**T [K]**
1	15.9	685.32	293.6
2	16.1	686.65	295.9
3	16.5	682.65	296.6
4	13.0	667.98	296.6
5	17.2	274.66	297.8
6	13.6	682.65	297.0
7	14.7	543.99	297.8

Table 3: UTIAS shock tube free-stream conditions.

The main flow characteristics can be visualized on Figs. 1b and 1a. Figure 1b shows the ionization fraction and the gas density behind the shock. Once thermal equilibrium conditions are reached (i.e. $T_\mathrm{h} = T_\mathrm{e}$), the ionization fraction keeps decreasing as a result of radiative transitions. This can also be observed from Fig. 1a showing the spatial evolution

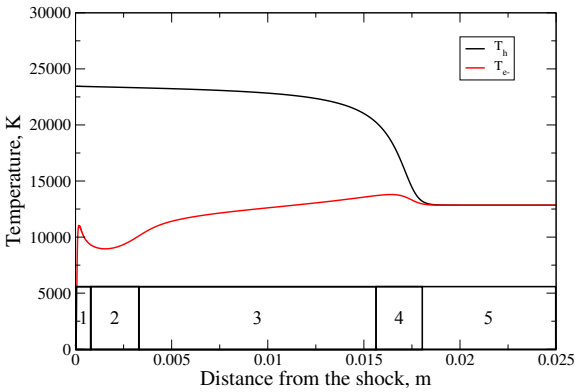

Figure 2: 5-zone structure of an ionizing shock wave in Argon. Shock-tube case 1. Free-stream conditions: Ma= 15.9, T=293.6 K, p=685.3 Pa.

of the radiative source terms. The *bound-bound* transitions (green curve) represent the most important contribution.

The relaxation region behind the shock can be divided in 5 distinct parts (see Fig. 2), each one having its own dynamics.

- **Zone 1:** Production of priming cold electrons through ionization by heavy-particle impact, $\mathrm{Ar}(i) + \mathrm{Ar}(1) \rightleftharpoons \mathrm{Ar}^+ + \mathrm{e}^- + \mathrm{Ar}(1)$.
- **Zone 2:** Once enough priming electrons are produced, Ar atoms start undergo ionization through electron impact reactions, $\mathrm{Ar}(i)+\mathrm{e}^- \rightleftharpoons \mathrm{Ar}^+ + \mathrm{e}^- + \mathrm{e}^-$. Starting from this zone, electron impact processes become dominant over those induced by heavy-particle collisions.
- **Zone 3:** The free-electron temperature slowly rises to due to the combined effects of elastic collisions with heavy-particles (which tend to heat up the electron gas), and inelastic and ionizing collisions (which tend to deplete the energy content of free-electrons).
- **Zone 4:** Electron avalanche. The ionization of Ar by electron impact continues and stimulates the further productions of free-electrons. This leads to an avalanche behavior which is finally balanced by three-body recombination of Ar^+ ions.
- **Zone 5:** Thermal equilibrium between heavy-particles and free-electrons. In this zone, the plasma can be described by one single temperature. This temperature keeps decreasing because of the radiative transitions within the plasma.

4.2. *A priori model evaluation*

	10 PV's			5 PV's	
var	B2	B4	M2	B2	B4
T_h	PV	PV	1	0.9918	1
T_e	PV	PV	PV	PV	PV
y_e	1	1	1	0.9916	1
$y_{Ar(1)}$	1	1	1	0.9916	1
$y_{Ar(2)}$	1	1	1	PV	1
$y_{Ar(3)}$	PV	PV	0.9998	1	PV
$y_{Ar(4)}$	PV	PV	1	1	1
$y_{Ar(5)}$	PV	PV	0.9969	PV	PV
$y_{Ar(6)}$	1	1	1	1	1
$y_{Ar(7)}$	PV	1	PV	PV	1
$y_{Ar(8)}$	1	1	PV	1	1
$y_{Ar(9)}$	1	1	1	1	1
$y_{Ar(10)}$	1	1	1	1	1
$y_{Ar(11)}$	1	1	1	1	1
$y_{Ar(12)}$	1	1	1	1	1
$y_{Ar(13)}$	1	1	1	1	1
$y_{Ar(14)}$	PV	1	1	1	1
$y_{Ar(15)}$	1	PV	1	1	0.9999
$y_{Ar(16)}$	1	PV	1	1	1
$y_{Ar(17)}$	PV	PV	1	PV	PV
$y_{Ar(18)}$	1	1	1	1	1
$y_{Ar(19)}$	1	1	PV	1	1
$y_{Ar(20)}$	1	1	PV	1	1
$y_{Ar(21)}$	1	1	PV	1	1
$y_{Ar(22)}$	1	1	PV	1	1
$y_{Ar(23)}$	1	1	PV	1	1
$y_{Ar(24)}$	1	1	1	1	1
$y_{Ar(25)}$	1	1	1	1	1
$y_{Ar(26)}$	1	1	1	1	1
$y_{Ar(27)}$	1	1	1	1	1
$y_{Ar(28)}$	1	1	1	1	1
$y_{Ar(29)}$	1	1	1	1	1
$y_{Ar(30)}$	1	1	1	1	1
$y_{Ar(31)}$	PV	1	1	PV	1
$y_{Ar+(1)}$	PV	PV	1	0.9916	PV
$y_{Ar+(2)}$	1	PV	PV	0.9914	PV

Table 4: Comparison of different principal variable extraction methods. (PV = Principal Variable, B2 = B2 Backward Method, B4 = B4 Forward Method, M2 = M2 Backward Method)

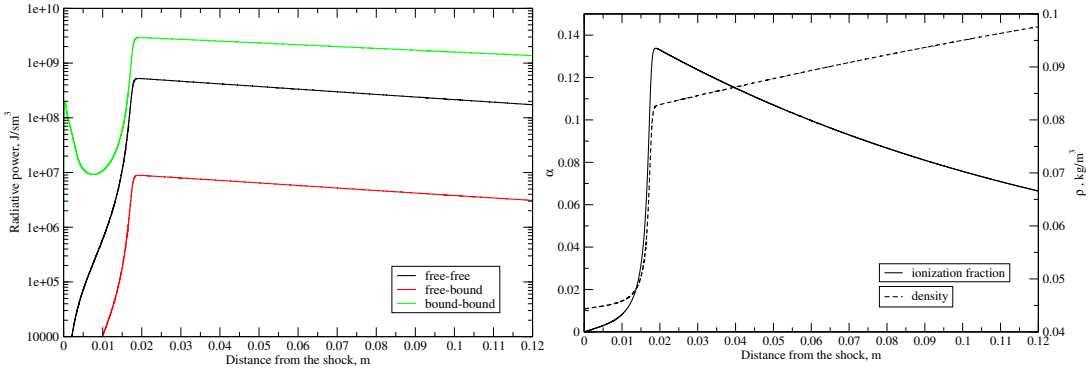

(a) Radiative power.

(b) Density and ionization fraction.

Figure 1: Density, ionization fraction, and radiative source terms for shock case 1.

Before applying the MG-PCA reduction, the optimal parameters for centering and scaling must be found. Also the principal variable extraction methods must be compared for an optimal reduction. Figure 4 plots the reconstruction error for the Ar^+ and Ar electronic ground-state mass fraction, as a function of the number of retained principal components for six scaling techniques: STD, PARETO, RANGE, VAST, LEVEL and MAX. The smallest reconstruction error is obtained with PARETO scaling.

The different principal variable extraction methods have been compared by investigating the reconstruction error of every variable after principal component analysis. To better see the effect of the reconstruction we only retained 10 principal variables in the first PCA analysis, and 5 principal variables in the second analysis. Table 4 compares three principal variable extraction methods: the B2 Backward Method, the B4 Forward Method and the M2 Backward Method. From Table 4 we can see the B4 Forward Method performs best. It is interesting to notice similar preprocessing parameters are found back for the application of MG-PCA on combustion cases as investigated by Isaac [59].

4.3. A posteriori model evaluation

The Argon plasma under investigation is characterized by 36 flow variables: 34 mass fractions and 2 temperatures. The flow speed has also been retained as a flow variable to ensure total energy conservation. When performing MG-PCA we want to decrease this number of variables to a minimum, for obtaining the smallest set of governing equations. The work starts with the simulation of shock tube experiment 1 from Table 3. After retrieving mass fractions and temperatures form this full 1D simulation, one performs MG-PCA with the selected extraction method and scaling technique derived from the *a priori* model evaluation. During the *a priori* model evaluation, the B4 Forward Method was selected as the best principal variable extraction method. However, the B2 Backward extraction method performs better during the actual simulations.

4.3.1. Model verification

In a first instance, the correct implementation of the MG-PCA method will be verified. The verification consists in retaining all 36 variables as flow variables. Consequently, no reduction will be obtained. To compare the reduced model to the full (i.e., CR) model one visualizes the temperature evolution behind the ionizing shock. There is a perfect correlation between the reduced and the full model. The correct implementation of the MG-PCA method has been verified. It can now be use for reduction.

4.3.2. Global Manifold Generated Principal Components Analysis (MG-PCA)

After the successful verification, the number of retained variables has been decreased to obtain a reduced model. The formulation based on the 37 flow variables has been reduced to a model considering 26 principal variables. The results of this simulation are shown in Figure 4a. To obtain a further reduction another test case has been considered. Shock tube experiment 4 has been retained because of its low pre-shock speed (Ma 13). When applying MG-PCA on this test case the number of retained variables

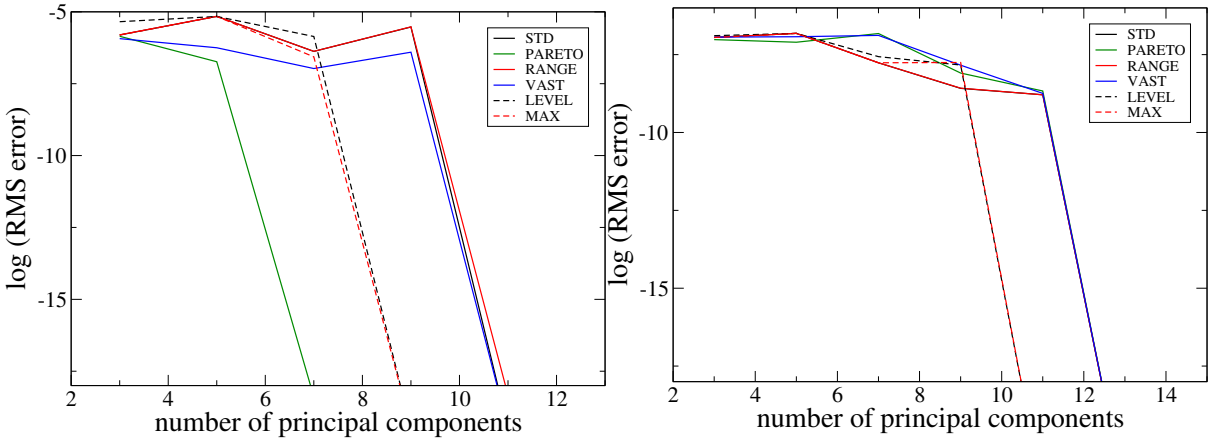

(a) Reconstruction of the Ar^+ mass fraction.

(b) Reconstruction of the Ar(1) mass fraction.

Figure 3: The effect of scaling: RMS error in function of the amount of principal components. Scaling methods: Standard, PARETO, RANGE, VAST, Level, Max.

could be reduced to 22 which corresponds to reduction of 40%. The result is shown in Figure 4b. Table 5 represents the retained principal components for both the global and local MG-PCA method.

Method	var	Retained PC's
global	23	1 2 3 5 6 7 8 9 10 11 12 14 15 16 19 20 22 23 33 34 36 37
local	16	1 2 3 5 6 7 8 9 10 11 16 22 23 33 36 37

Table 5: Retained principal components after MG-PCA. Principal components: 1= T_h, 2= T_e, 3= u, 4= y_{e-}, 5= $y_{Ar(0)}$, 35= $y_{Ar(31)}$, 36=$y_{Ar^+(1)}$, 37=$y_{Ar^+(2)}$

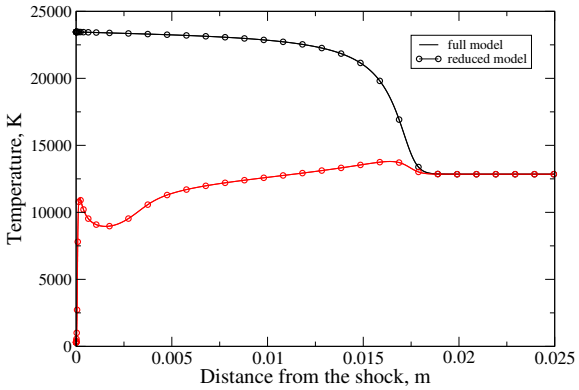

Figure 5: Global MG-PCA on a CR model. Model verification. Principal variable extraction method: B2 Backward Method. Scaling: PARETO. Reduction: 0%

The numerical solution of the reduced set of flow governing equations leads to instability problems when lowering the number of retained variables below 23 for Case 4, and 26 for Case 1. It couldn't reach equilibrium (region 5 in Figure 2). The region of the discontinuity corresponds to the electron avalanche process after the shock, as explained previously (region 4 in Figure 2). This region is characterized by a steep decrease of the heavy-particle temperature. The kinetic processes involved are electron induced ionization and three-body recombination. It can be concluded the reduced model needs more principal components to reproduce the more complex chemistry occurring in this region after the shock.

In the next experiment, the pressure has been decreased to 300 Pa to obtain stronger non-equilibrium conditions with a depopulation of the higher energy levels. Indeed, when considering the free-stream conditions in the shock tube, one obtains a quasi-Boltzmann population of the energy levels. Figure 8a represents the heavy particle and electron temperature for both the full and reduced model. From this figure can be seen the PCA-based reduce model has more trouble reproducing the full CR mechanism. Figure 6 shows the population distribution of the electronic levels of Ar for both the full and reduced model. Due to radiative transitions, the population of some of the excited electronic states of Ar experiences under-

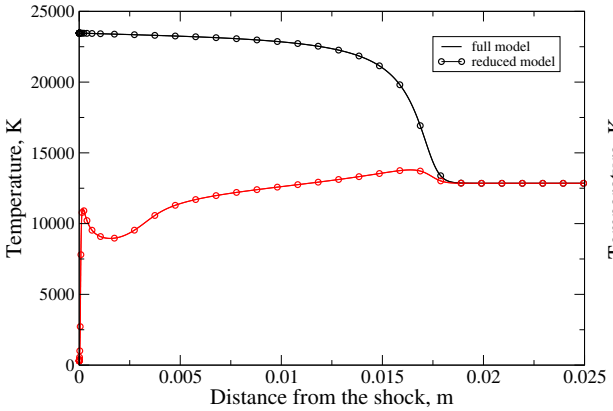

(a) Case 1. Retained variables: 26/36. Reduction: 28 %

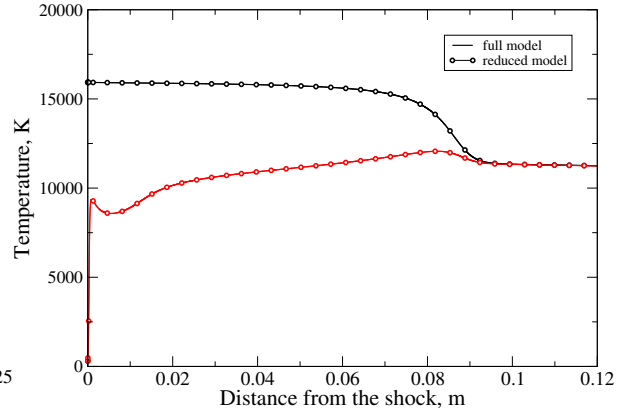

(b) Case 4. Retained variables: 23/36. Reduction: 36 %

Figure 4: Global MG-PCA. Principal variable extraction method: B2 Backward Method. Scaling: PARETO

population. In Figure 6 one can clearly see that the population distribution deviates from a straight line (corresponding to Maxwell-Boltzmann distribution). Moreover, MG-PCA is able to correctly reproduce the population of all electronic states. This shows the PCA techniques are promising for applications such as atmospheric re-entry where strong depopulation of the excited species occur because of non-equilibrium effects.

4.3.3. *Local Manifold Generated Principal Component Analysis (MG-l-PCA)*

MG-local-PCA divides the plasma data-set, which includes the mass fractions of all species and both temperatures, in several clusters or bins, and applies the MG-PCA reduction technique on each of them. Consequently, a better reduction will be obtained as an optimal reduced representation is used in every cluster. An appropriate conditioning algorithm is needed, as well as the definition of a conditioning variable ensuring a bijective correspondence with any variable defining the state-space. The conditioning variable chosen for this plasma case, is the ionization fraction, α, as represented in Figure 1b, which indicates that such a choice allows a unique partitioning of the data-set. As each cluster is optimized, the reconstruction error of each species should decrease with an increasing number of clusters. This has been verified *a priori*. In Figure 7 can be seen how the normalized RMS error for both the electron mass fraction reconstruction decreases when increasing the number of clusters.

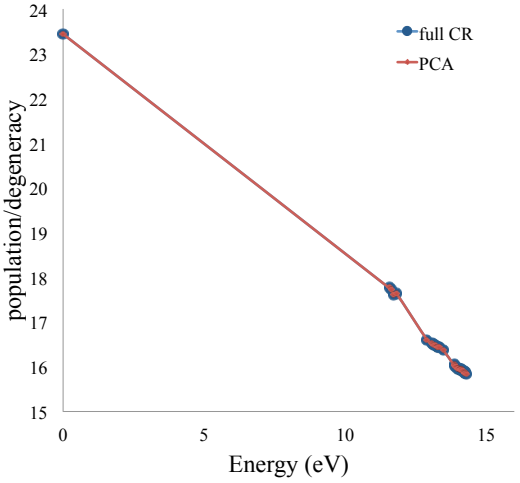

Figure 6: Population/degeneracy in function of the energy levels for the 31 excited states of argon. Non-Boltzmann distribution due to radiation. Shock tube experiment 4. Local MG-PCA. Dotted line: reduced model. Full line full CR model.

Shock tube experiment 4 has been subjected to MG-local-PCA. The flowfield data obtained from the full simulation has been divided in two clusters. The conditioning variable, which is the ionization fraction, has defined the cluster border to be at 8,35 cm from the shock front. MG-PCA has been applied on both clusters with q, the number of retained principal components, equal to 16 out of 36. Unfortunately, this is the best reduction that could be obtained with MG-local-PCA. For less retained variables, the code blows up in the region of the electron avalanche as

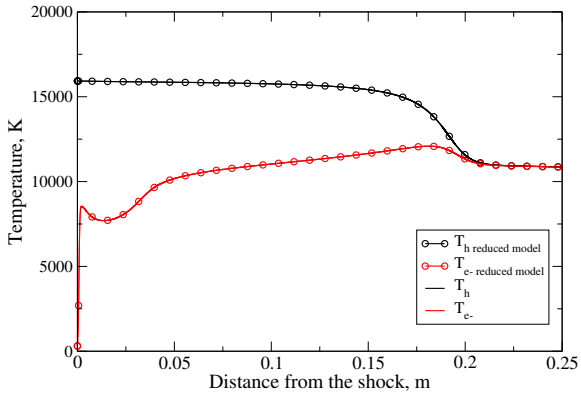

(a) Global MG-PCA. Reduction: 36%

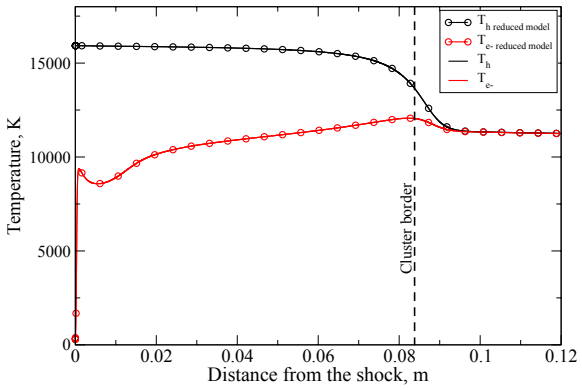

(b) Local MG-PCA. Cluster border at x= 8,35 cm from the shock. Reduction: 56%

Figure 8: Global and local MG-PCA on 300 Pa case. Principal variable extraction method: B2 Backward Method. Scaling: PARETO

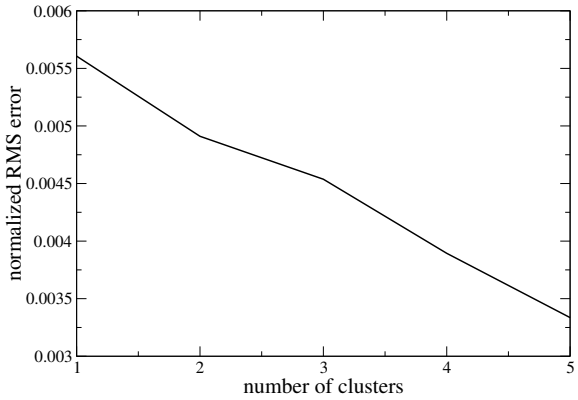

Figure 7: Normalized error in function of the number of clusters for the reconstruction of the electron mass fraction.

described previously. The final reduction is thus of 57%. Isaac [59], working in the combustion field, obtained a reduction of 38% for the application of MG-local-PCA on a 1D laminar pre-mixed flame calculation. There can be concluded local PCA performs well for plasma cases.

5. Conclusion

This paper demonstrates the use of Principal Component Analysis (PCA) based methods for detailed chemistry reduction of relatively large plasma kinetic mechanisms. Manifold Generated Principal Component Analysis (MG-PCA) has been applied to reduce a Collisional-Radiative model for weakly ionized argon plasmas. Both the global and local MG-PCA formulation have been considered. The plasma mixture contains 34 species (electrons, excited and ionized argon) and 962 reactions (ionization, recombination, excitation, de-excitation reactions). An *a priori* model evaluation investigates the parameters for the optimal MG-PCA pre-processing parameters such as the selection of a good scaling method and an appropriate principal variable extraction method. A reduction of 40 % has been obtained with global MG-PCA. With the local formulation, a model reduction of 57 % is performed with two clusters. PCA based techniques are also capable of capturing detailed chemistry features such as the depopulation of excited energy levels in case of non-equilibrium. There is still room for improvement with respect to these low pressure cases for simulating atmospheric re-entry conditions. Future work will focus on the improvement of PCA for capturing non-equilibrium by studying non-linear and log scale PCA together with non-linear regression.

Acknowledgments

The research of A. Bellemans, is sponsored by the Belgian FRIA-FNRS grant. The authors wish to acknowledge the European Research Council, Starting Grant No. 259354 , for the research of Prof. T.E. Magin.

References

[1] M. Capitelli, C. M. Ferreira, B. F. Gordiets, A. I. Osipov, Plasma Kinetics in Atmospheric Gases, Springer, 2000.

[2] J. Kim, S. B. Pope, Effects of combined dimension reduction and tabulation on the simulations of a turbulent premixed flame using a large-eddy simulation/probability density funcion method, Combustion Theory and Modelling 18 (3) (2014) 388–413.

[3] S. B. Pope, The computation of constrained and unconstrained equilibrium compositions of ideal gas mixtures using gibbs function continuation, FDA 03-02.

[4] Z. Ren, S. B. Pope, A. Vladimirsky, J. M. Guckenheimer, The invariant constrained equilibrium edge preimage curve method for the dimension reduction of chemical kinetics, The Journal of Chemical Physics 124 (2006) 114111.

[5] J. C. Keck, Rate-controlled constrained equilibrium theory of chemical reactions, AIP Conf. Proc. 1033 (329).

[6] J. C. Keck, Rate-controlled constrained equilibrium theory of chemical reactions in complex systems, Prog. Energy Combust. Sci. 16 (1990) 125–154.

[7] M. Massot, Singular perturbation analysis for the reduction of complex chemistry in gaseous mixtures using the entropic structure, Discrete and Continuous Dynamical Systems - Series B 3 (3).

[8] T. Magin, M. Panesi, A. Bourdon, R. Jaffe, D. W. Schwenke, Coarse-graining model for internal energy excitation and dissociation of molecular nitrogen, Chem. Phys. 398 (90).

[9] A. Munafò, M. Panesi, T. E. Magin, Boltzmann rovibrational collisional coarse-grained model for internal energy excitation and dissociation in hypersonic flows, Phys. Rev. E 89 (2) (2014) 023001.

[10] A. Munafò, T. E. Magin, Modeling of stagnation-line nonequilibrium flows by means of quantum based collisional models, Phys. Fluids 26 (9) (2014) 097102.

[11] Y. Liu, M. Vinokur, M. Panesi, T. E. Magin, A multi-group maximum entropy model for thermo-chemical nonequilibrium, AIAA Paper 2010–4332, 10th AIAA/ASME Joint Thermophysics and Heat Transfer Conference, Chicago, IL (2010).

[12] Y. Liu, M. Panesi, M. Vinokur, P. Clarke, Microscopic simulation and macroscopic modeling of thermal and chemical non-equilibrium gases, AIAA Paper 2013–3146, 44th AIAA Thermophysics Conference, San Diego, CA (2013).

[13] M. Panesi, A. Lani, Collisional radiative coarse-grain model for ionization in air, Phys. Fluids 25 (5) (2013) 057101.

[14] A. Bultel, B. G. Chéron, A. Bourdon, O. Motapon, I. F. Schneider, Collisional-radiative model in air for earth re-entry problems, Phys. Plasmas 13 (4) (2006) 043502.

[15] M. Panesi, T. E. Magin, A. Bourdon, A. Bultel, O. Chazot, Fire II flight experiment analysis by means of a collisional-radiative model, J. Thermophys. Heat Transfer 23 (2) (2009) 236–248.

[16] M. Panesi, T. E. Magin, A. Bourdon, A. Bultel, O. Chazot, Electronic excitation of atoms and molecules for the FIRE II flight experiment, J. Thermophys. Heat Transfer 25 (3) (2011) 361–374.

[17] A. Munafò, A. Lani, A. Bultel, M. Panesi, Modeling of non-equilibrium phenomena in expanding flows by means of a collisional-radiative model, Phys. Plasmas 20 (7) (2013) 073501.

[18] R. L. Jaffe, D. W. Schwenke, G. Chaban, W. Huo, Vibrational and rotational excitation and relaxation of nitrogen from accurate theoretical calculations, AIAA Paper 2008–1208, 46th AIAA Aerospace Sciences Meeting and Exhibit, Reno, NV (2008).

[19] G. Chaban, R. L. Jaffe, D. W. Schwenke, W. Huo, Dissociation cross-sections and rate coefficients for nitrogen from accurate theoretical calculations, AIAA Paper 2008–1209, 46th AIAA Aerospace Sciences Meeting and Exhibit, Reno, NV (2008).

[20] D. W. Schwenke, Dissociation cross-sections and rates for nitrogen, in: Non-Equilibrium Gas Dynamics - From Physical Models to Hypersonic Flights, Lecture Series, von Karman Institute for Fluid Dynamics, 2008.

[21] R. L. Jaffe, D. W. Schwenke, G. Chaban, Theoretical analysis of N_2 collisional dissociation and rotation-vibration energy transfer, AIAA Paper 2009–1569, 47th AIAA Aerospace Sciences Meeting and Exhibit, Orlando, FL (2009).

[22] M. Panesi, R. L. Jaffe, D. W. Schwenke, T. E. Magin, Rovibrational internal energy transfer and dissociation of $N(^4S_u) + N_2(^1\Sigma_g^+)$ sytem in hypersonic flows, J. Chem. Phys 138 (4) (2013) 044312.

[23] M. Panesi, A. Munafò, T. E. Magin, R. L. Jaffe, Study of the non-equilibrium shock heated nitrogen flows using a rovibrational state-to-state method, Phys. Rev. E 90 (2014) 013009.

[24] J. L. Cambier, H. P. Le, A. R. Karagozian, Complexity reduction of collisional-radiative kinetics for atomic plasma, Phys. Plasmas.

[25] A. Guy, A. Bourdon, M.-Y. Perrin, Consistent multi-internal-temperatures models for nonequilibrium nozzle flows, Chem. Phys. 420 (2013) 15–24.

[26] I. V. Adamovich, S. O. Macheret, J. W. Rich, C. E. Treanor, Vibrational relaxation and dissociation behind shock waves. Part 1: kinetic rate models, AIAA J. 33 (6) (1995) 1064–1069.

[27] I. V. Adamovich, S. O. Macheret, J. W. Rich, C. E. Treanor, Vibrational relaxation and dissociation behind shock waves. Part 2: master equation modeling, AIAA J. 33 (6) (1995) 1070–1075.

[28] G. Colonna, I. Armenise, D. Bruno, M. Capitelli, Reduction of state-to-state kinetic to macroscopic models in hypersonic flows, J. Thermophys. Heat Transfer 20 (3) (2006) 477–486.

[29] G. Colonnaa, G. DAmmandob, L. D. Pietanza, M. Capitelli, Radiation transfer, level and freeelectron kinetics in nonequilibrium atomic hydrogen plasma, in: Proc. of the 27th Int. Symposium on Rarefied Gas Dynamics, AIP, 2010.

[30] J. Shlens, A tutorial on principal component analysis, ArXiv e-prints.

[31] A. Parente, J. Sutherland, Prinicpal component analysis of turbulent combustion data: Data pre-processing and manifold sensitivity, Combustion and Flame 160 (2) (2013) 340–350.

[32] B. Isaac, A. Parente, Reduced-order pca models for chemical reacting flows, Combustion and Flame.

[33] A. Coussement, A. Parente, O. Gicquel, Mg-local-pca method fo reduced order combustion modeling, Proceedings of the Combustion Institute 34 (1) (2013) 1117–1123.

[34] Y. Yang, S. B. Pope, J. H. Chen, Empirical low-dimensional manifolds in composition space, Combustion and Flame 160 (10) (2013) 1967 – 1980.

[35] A. Biglari, J. C. Sutherland, A filter-independent model identification technique for turbulent combustion modeling, Combustion and Flame.

[36] H. Mirgolbabaei, T. Echekki, Nonlinear reduction of combustion composition space with kernel principal component analysis, Combustion and Flame 161 (1) (2014) 118 – 126. doi:http://dx.doi.org/10.1016/j.combustflame.2013.08.016.

[37] H. Mirgolbabaei, T. Echekki, N. Smaoui, A nonlinear principal component analysis approach for turbulent combustion composition space, International Jour-

nal of Hydrogen Energy 39 (9) (2014) 4622 – 4633. doi:http://dx.doi.org/10.1016/j.ijhydene.2013.12.195.
[38] K. Peerenboom, A. Parente, T. Kozak, A. Bogaerts, G. Degrez, Dimension reduction of non-equilibrium plasma kinetic models using principal component analysis, Plasma Sources Science and Technology.
[39] I. I. Glass, Over forty years of continuous research at UTIAS on nonstationary flows and shock waves, Springer, 1991.
[40] K. Miki, M. Panesi, E. E. Prudencio, A. Maurente, S. H. Cheung, J. J. Jagodzinski, D. Goldstein, S. Prudhomme, K. Schulz, C. Simmons, J. Strand, P. Varghese, On the (in)validation of a thermochemical model with east shock tube radiation measurements, in: Aerospace Sciences Meeting Including the New Horizons Forum and Aerospace Exposition, AIAA, Orlando, Florida, 2010.
[41] J. Vlcek, A collisional-radiative model applicable to argon discharges over a wide range of conditions. i: Formulation and basic data, J. Phys. D 22 (1989) 623–631.
[42] A. Bultel, B. van Ootegem, A. Bourdon, P. Vervisch, Influence of Ar_2^+ in an argon collisional-radiative model, Phys. Rev. E 65 (4) (2002) 046406.
[43] M. G. Kapper, J.-L. Cambier, Ionizing shocks in argon. part 1: collisional-radiative model and steady-state structure, J. Appl. Phys. 109.
[44] M. G. Kapper, Ionizing shocks in argon. part 2: Transient and multi-dimensional effects, J. Appl. Phys. 109.
[45] C. Park, Review of chemical-kinetic problems of future NASA missions, I: Earth entries, J. Thermophys. Heat Transfer 7 (3) (1993) 385–398.
[46] C. Park, J. T. Howe, R. L. Jaffe, G. V. Candler, Review of chemical-kinetic problems of future NASA missions, II: Mars entries, J. Thermophys. Heat Transfer 8 (1) (1994) 9–23.
[47] R. J. Gessman, C. O. Laux, C. Kruger, Experimental study of kinetic mechanisms of recombining atmospheric pressure air plasmas, AIAA Paper 1997–2364, 28th AIAA Plasmadynamics and Lasers Conference, Atlanta, GA (1997).
[48] L. Pierrot, L. Yu, R. J. Gessman, C. O. Laux, C. Kruger, Collisional-radiative modeling of nonequilibrium nitrogen plasmas, AIAA Paper 1999–3478, 30th Plasmadynamics and Lasers Conference, Norfolk, VA (1999).
[49] C. O. Laux, Radiation and nonequilibrium collisional radiative models, in: Physico-Chemical Models for High Enthalpy and Plasma Flows, Lecture Series, von Karman Institute for Fluid Dynamics, 2006.
[50] J. Annaloro, A. Bultel, Elaboration of collisional-radiative models for flows related to planetary entries into the Earth and Mars atmospheres, Plasma Sources Sci. Technol. 22 (2) (2013) 025008.
[51] A. Yanguas-Gil, J. Cotrino, A. R. Gonzalez-Elipe, Collisional radiative model of an argon atmospheric capillary surface-wave discharge, Physics of Plasmas 11 (12) (2004) 5497–5505.
[52] A. Bogaerts, R. Gijbels, J. Vlcek, Collisional-radiative model for an argon glow discharge, Journal of Applied Physics 84 (1998) 121.
[53] G. Colonna, M. Tuttafesta, M. Capitelli, D. Giordano, Non-Arrhenius NO formation rate in one-dimensional nozzle airflow, J. Thermophys. Heat Transfer 13 (3) (1999) 372–375.
[54] G. Colonna, M. Capitelli, Self-consistent model of chemical, vibrational, electron kinetics in nozzle expansion, J. Thermophys. Heat Transfer 15 (3) (2001) 308–316.
[55] W. J. Vincenti, C. H. Kruger, Introduction to Physical Gasdynamics, Wiley, New York, NY, 1965.
[56] F. Thivet, Modeling of Hypersonic Flows in Thermal and Chemical Nonequilibrium, Ph.D. thesis, Ecole Centrale Paris, Châtenay-Malabry, France, in French (1992).
[57] A. Munafò, Multi-Scale Models and Computational Methods for Aerothermodynamics, Ph.D. thesis, Ecole Centrale Paris, Châtenay-Malabry, France (2014).
[58] K. Radhakrishnan, A. C. Hindmarsh, Description and use of LSODE, the Livermore solver for ordinary differential equations, NASA Report 1327 (1993).
[59] B. Isaac, Reduced-order modelling for reacting flows based on principal component analysis, Ph.D. thesis, University of Utah (2014s).
[60] G. P. M. Cabe, Principal variables., Technometrics 26 (2) (2004) 137–144.
[61] J. A. Cumming, D. A. Wooff, Dimension reduction via principal variables, Computational Statistics and Data Analysis 52 (2007) 550–565.

Simulation of the Atmospheric Entry of Meteors with Application to Radio Detection

Bruno Dias

Aeronautics and Aerospace Department, von Karman Institute for Fluid Dynamics, Belgium, bruno.ricardo.barros.dias@vki.ac.be

Supervisor: Thierry Magin

Associate Professor, Aeronautics and Aerospace Department, von Karman Institute for Fluid Dynamics, Belgium, magin@vki.ac.be

University Supervisor: Philippe Chatelain

Assistant professor, Thermodynamics and fluid mechanics - TFL, Université catholique de Louvain, Belgium, philippe.chatelain@uclouvain.be

Abstract

The present project aims at understanding meteoroids and the meteor phenomena. We propose to develop a model with the objective of studying the ablation of meteors and to predict the electron concentration in the wake of the object, during their trajectory. The novelty of this project it is to develop more accurate simulation tools based on the expertise of aerospace engineers to better understand the meteor phenomena. State of the art of Computational Fluid Dynamics (CFD) and Direct Simulation Monte Carlo (DSMC) codes for meteor entries will be developed and applied to the BRAMS database.

Keywords: meteors, ablation, radiation, radars, DSMC, CFD, debris

1. Introduction

Meteoroids are small planetary bodies (from 1 m across down to micron-size grains). Our planet is continuously bombarded by meteoroids that burn up in the atmosphere, creating the meteor phenomena, i.e., entry in the atmosphere causing their degradation. Meteors are small and fast, which makes them hard to detect in situ with space-borne instruments or with remote sensing techniques. The present project aims at understanding meteoroids and the meteor phenomena.

Recent efforts have been made by the **Belgian Institute for Space Aeronomy** in order to predict velocity, trajectory and composition of the meteors, by means of an innovative technique based on radar waves [1]. The **Belgian Radio Meteor Stations (BRAMS)** [2] experiment (Fig.2), consists in a series of receivers spread all over Belgium to collect and standardize the meteor observations by a scattering of the radio signal.

Similarly to hypersonic entries of spacecraft, when meteors interact with the atmosphere, their surface temperature can reach more than 2000 degree kelvin causing ablation (melting and evaporation of the meteor) leading to its degradation. These ablation products are driven to the wake and are assumed to influence the free electron concentration detected by radars. For planetology atmospheric models, it is also

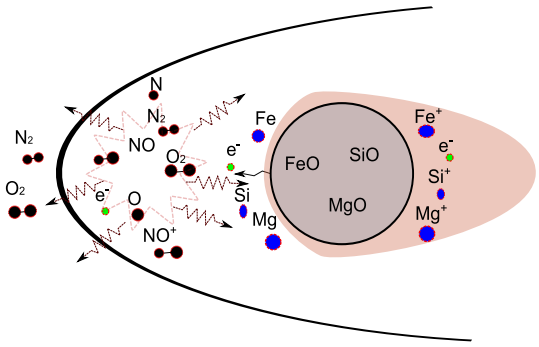

Figure 1: Critical phenomena during meteor atmospheric entry: material ablation, shock layer radiation

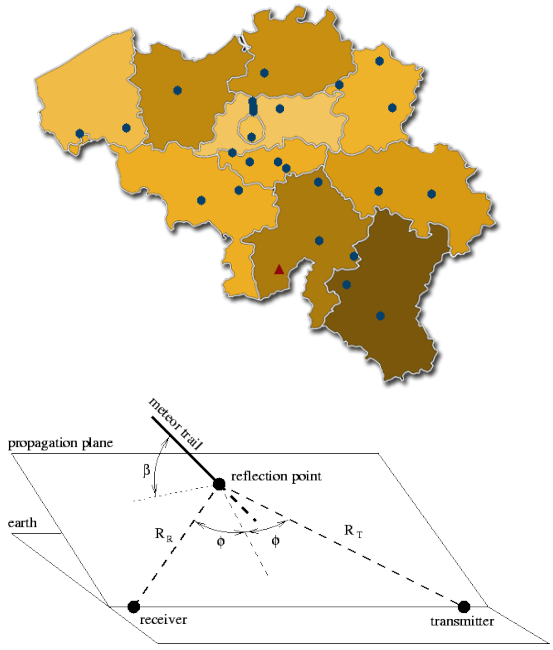

Figure 2: top) BRAMS radio station network in Belgium; bottom) Forward scattering of a radio signal by meteor trail

important to estimate at which altitude and in which quantity the ablation products are released.

2. Objectives

Most of the simulations used for meteor atmospheric entry rely on a simplistic zero dimensional approach, based mostly on ad hoc correlations for physico-chemical models, describing for instance ablation and radiation. The ambition of this project is thus the development of more accurate simulation tools based on the expertise of aerospace engineers to better understand the meteor phenomena. We will **develop state of the art CFD and DSMC codes, apply them to meteor entries**, and enable the deduction of meteor characteristics from its signature in the BRAMS database.
More specifically, the envisioned numerical models will be able to predict the meteor degradation during the entry into Earths atmosphere. These models will give the possibility to estimate the free electron concentration in the wake of meteors as well as the deposition of the ablation products into the atmosphere. These tools will be crucial to study the meteor characteristics (speed, composition and population), using the radar signals captured by BRAMS by means of reverse engineering.

3. Methodology

The current project is mainly divided in **three phases**:

- Modelling and study of the meteor ablation in the **continuum regime**
- Elaboration and implementation of the ablative boundary conditions in the **rarefied regime**
- Analysis of the meteor trajectory and comparison of the electron concentration with **radar observations**

a). Continuum Flow Modelling

The thermodynamic properties of each species will be evaluated using thermodynamic databases, NASA-9 and NASA-7 developed by [3] and [4]. At high temperatures the evaluation of the transport properties [5] requires the collision integrals [6]. A vast database based on the Lennard-Jones potential for other chemical species rather than air constituents, found in the meteor ablation products, can be found in [7], [8], [9], [10], [11] and [12] among others.

b). Surface Reactions

The heterogeneous surface reactions, due to ablation, will be considered to be in thermochemical equilibrium. The approach is similar to the one proposed by [13]. Unlike TPS material ablation, melting of the meteor must be taken into consideration. It will be assumed that the molten layer is completely removed if the viscous stresses of the fluid overcome the shear stress of this layer. Finally, the diffusion of the ablated species into the shear layer can create additional ionized species. Therefore, the fluid part (ablation products + air species) will be treated with finite rate chemistry.

c). Shock Layer Radiation

For high velocities, the shock layer radiation will become an important cooling mechanism. Along with convective heating, radiative heat transfer must also be considered to make an accurate meteor degradation prediction. We propose to couple both radiation and flow field in the same domain and to model the radiation as a cooling source term in the energy equation.

d). 2D and 3D CFD

The work will be implemented within a pre-existing computational code, Argo, developed by Cenaero [14]. A fully implicit method is currently developed in this computational code to simulate multi-phase reacting flows. This approach is currently being developed to simulate both the flow and wall phenomena in a unified manner [15]. This methodology will be extended to account for hypersonic flows and a shock capturing method will be included. A melted phase present during meteorite ablation will also be included. The CFD code will be coupled with a thermochemical library, Mutation++ developed at the von Karman Institute for Fluid Dynamics [16], which provides thermodynamic, transport, and chemical properties. Briefly, the flow field, radiation field and material will be unified in an accurate and stable manner. Another extension of the code will enable the tracking of the electron concentration in the wake of the meteor.

e). Direct Simulation Monte Carlo (DSMC)

One method to treat the ablation of meteor at high altitudes is to use Direct Simulation Monte Carlo (DSMC). The implementation of the ablative boundary conditions will follow the same approach as the one used for the CFD method. The melted phase will not be included due to the extreme complexity and also the fact that the melting of meteors is only observable at low altitudes [17]. As mentioned above, the motion of free electron will be a challenge. A first possible solution is offered by the RGDAS code, a 3D DSMC solver, which computes the neutral-neutral collision of the heavy species. The electron concentration can then be obtained, through post-processing of the resulting pressure and temperature fields under assumptions of chemical equilibrium. Another method to circumvent this problem is to use a Particle in Cell method.

f). Radar waves detection

As a final step, we propose to conduct a parametric study of velocity, meteor size/composition and entry angle. DSMC will be used for altitudes from 120 to 70 km. The remaining trajectory will be computed by continuum CFD methods. From this study, we will estimate the electron concentration in wake. The numerical results will be compared to radar observations and by reverse engineering we will be able to characterize the meteor. With this knowledge, it will be possible to study the change of the atmospheric properties by the deposition of ablation products in the atmosphere, and to predict if the meteor is completely destroyed over its trajectory

4. Preliminary Results

The preliminary results were obtained by CFD calculations of the stagnation streamline for spherical bodies. The object has a 10 cm initial radius, a mass of 32.965 kg of solid iron and a wall temperature of 2500 K. Figure 3 shows the temperature, the mole fractions of the iron species, the velocity and density along the stagnation line. The iron species diffuse up

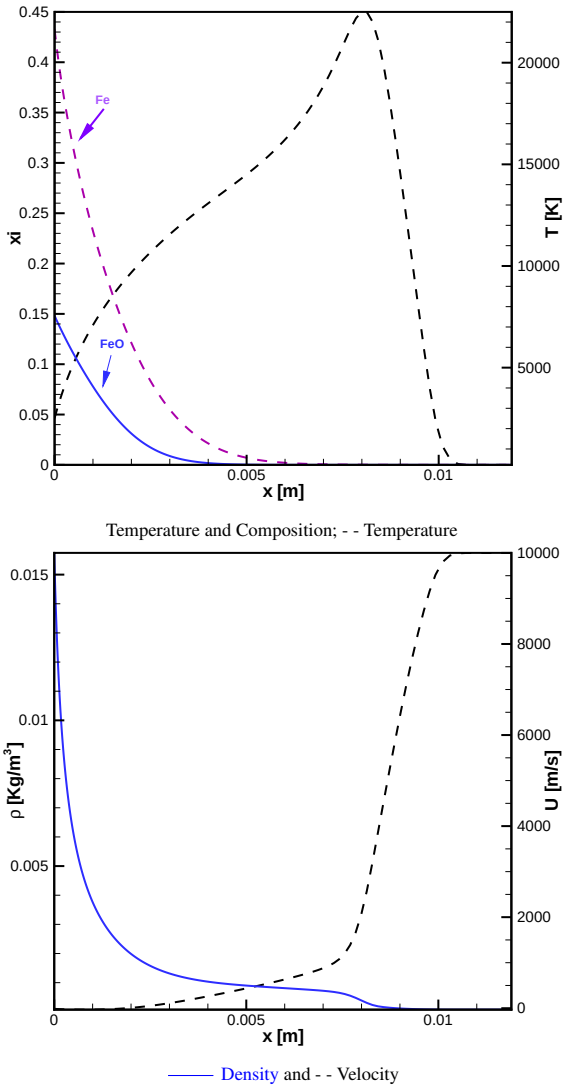

Figure 3: T_w=2500 K, r=10 cm, H=70 km

to 0.06 m from the wall and the concentration of Fe is bigger than FeO at the wall.

From the bottom figure is it shown the velocity decreasing and the density increasing through the shock wave. The velocity at the wall is not exactly zero due to the blowing velocity, which has an opposite direction than the velocity of the flow. Therefore, the stagnation point moves towards the shock wave.

Figure 4 shows the iron species concentration along the altitude. For the highest altitude Fe concentration is bigger than FeO and the opposite is shown for the remaining altitudes. These are important results which can relate the deposition of the ablation products in function of the altitude. From Fig. 5 is possible to see the mass blowing rate and variation of mass along the trajectory. The mass blowing rate is very small, reason why the variation of mass is insignificant, losing 50 grams during its travel.

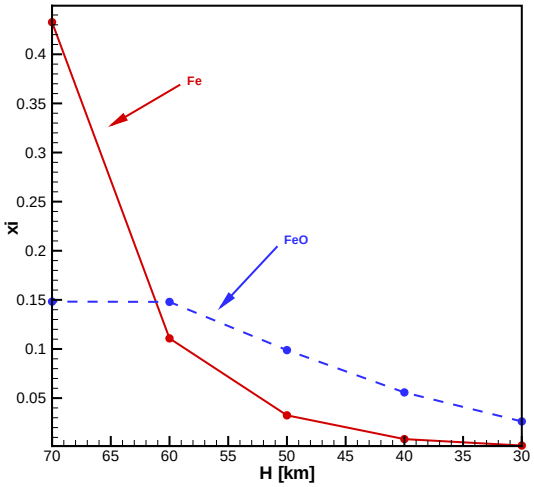

Figure 4: Iron species Concentration (wall) vs Altitude T_w=2500 K, r=10 cm

5. Conclusion and Related Applications

There are several motivations for the growing interest on studies dedicated to the physical understanding of meteor entries. Nowadays, characterizing the atmosphere becomes a very important topic.

The approach presented here is focused to develop a computational tool to study atmospheric entries of meteors. This methodology can be extended to other applications:

- Study of the atmospheric entry of space debris orbing Earths atmosphere. Space debris from launcher stages and satellites and end of life are more and more a threat when undestroyed debris impact the Earth. More than 5000 tonnes of debris is cluttering space around the Earth as a result of 50 years abandoning spacecraft. The ablation of space debris can also change significantly the properties of the upper atmosphere.

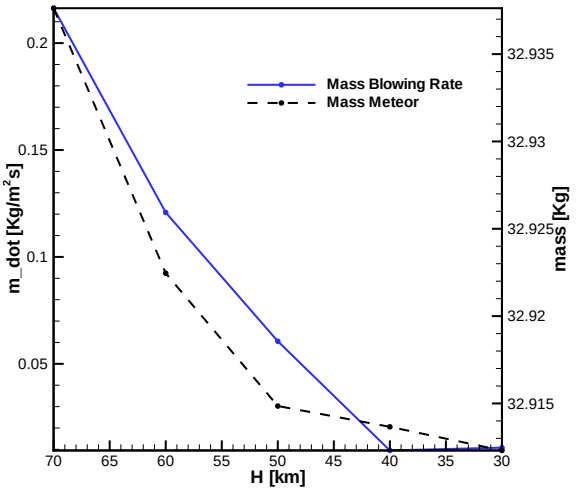

Figure 5: Mass Blowing rate and Meteor Mass T_w=2500 K, r=10 cm; ——*Mass Blowing Rate*, - - Mass Meteor

- Recently, the planetary community has a huge interested of studying the atmosphere of other planets. This method can also be extend to study the ablation of meteors on different planets, in order to understand better the composition of their atmosphere.

References

[1] Z. Ceplecha, J. Borovicka, W. Elford, D. ReVelle, R. Hawkes, V. Porubcan, M. Simek, Meteor phenomena and bodies, Space Science Reviews 84 (3-4) (1998) 327–471.

[2] B. I. for Space Aeronomy, Brams (belgian radio meteor stations), `http://brams.aeronomie.be/pages/home`.

[3] B. J. McBride, S. Gordon, Computer Program for Calculation of Complex Chemical Equilibrium Compositions and Applications II. User's Manual and Program Description, NASA RP-1311-P2, Lewis Research Center, Cleveland, Ohio (Jun. 1996).

[4] B. C. McGee, M. L. Hobbs, M. R. Baer, Exponential 6 Parameterization for the JCZ3-EOS, SAND98-1191, Sandia National Laboratories (1998).

[5] T. E. Magin, A Model for Inductive Plasma Wind Tunnels, Ph.D. thesis, Universitè Libre de Bruxelles (2004).

[6] A. Murphy, Transport coefficients of plasmas in mixtures of nitrogen and hydrogen, Chemical Physics 398 (0) (2012) 64 – 72.

[7] R. A. Svehla, Estimated Viscosities and Thermal Conductivities of Gases at High Temperatures, NASA TR R-132, Lewis Research Center, Cleveland, Ohio (1962).
[8] R. A. Svehla, Transport Coefficients for the NASA Lewis Chemical Equilibrium Program, NASA TM-4647, Lewis Research Center, Cleveland, Ohio (1995).
[9] F. M. Mourits, F. Rummens, A Critical Evaluation of Lennard-Jones and Stockmayer Potential parameters and of some correlation methods, Canadian Journal of Chemistry 55 (16) (1977) 3007–3020.
[10] L. Monchick, E. Mason, Transport Properties of Polar Gases., The Journal OF Chemical Physics 35 (5) (1962) 1676–1697.
[11] M. Linteris, D. Rumminger, D. Reinelt, V. Babushok, Numerical Study of the Inhibition of Premixed and Diffusion Flames by Iron Pentacarbonyl, Combustion and Flame 116 (1-2) (1999) 207–219.
[12] A. Jasper, J. Miller, Lennard-jones parameters for combustion and chemical kinetics modeling from full-dimensional intermolecular potentials, Combustion and Flame 161 (1) (2014) 101–110.
[13] D. Bianchi, Modeling of ablation phenomena in space applications, Ph.D. thesis, Università degli Studi di Roma "La Sapienza" (2007).
[14] K. Hillewaert, Development of the discontinuous galerkin method for large scale/high-resolution cfd and acoustics in industrial geometries, Ph.D. thesis, Universite Catholique de Louvain (2013).
[15] P. Schrooyen, Development of a numerical simulation tool for the aerothermal flow through an ablative thermal protection system for atmospheric entry, VKI PhD Symposium (2013).
[16] J. Scoggins, Development of Mutation++: MUlticomponent Thermodynamics And Transport properties for IONized gases library in C++, VKI PhD Symposium (2013).
[17] V. A. Bronshten, Physics of Meteoric Phenomena, D. Reidel Pub. Co., 1983.

Non-Linear Extensions of Global Flow Stability Theory

Koen J. Groot

Aerodynamics Section (AWEP), Delft University of Technolgoy, The Netherlands, k.j.groot@tudelft.nl

Supervisor: Olivier Chazot

Professor, Aeronautics and Aerospace Department, von Karman Institute for Fluid Dynamics, Belgium, chazot@vki.ac.be

Co-Supervisor: Fabio Pinna

Research Engineer, Aeronautics and Aerospace Department, von Karman Institute for Fluid Dynamics, Belgium, fabio.pinna@vki.ac.be

University Supervisor: Bas W. van Oudheusden

Associate Professor, Aerodynamics Section (AWEP), Delft University of Technology, The Netherlands, b.w.vanoudheusden@tudelft.nl

University Promotor: Fulvio Scarano

Professor, Aerodynamics Section (AWEP), Delft University of Technology, The Netherlands, f.scarano@tudelft.nl.

Abstract

The project's goal is to incorporate non-linear mechanisms in global stability approaches, which requires eigensolutions *a priori*. Boundary and compatibility conditions are derived to approach the in-/outflow issue in the streamwise eigenvalue problems. Spatial stability characteristics vary significantly per condition; optimized Robin conditions yield most unstable behaviour. Further investigations should indicate whether the retrieved eigenfunctions are physical.

Keywords: laminar-to-turbulent transition, e^N-method, BiGlobal stability

1. Introduction

Laminar to turbulent transition of flows causes an increase in the local skin friction and heat transfer. Therefore taking into account this phenomenon is important for the design of airliners, regarding their fuel consumption, and re-entry vehicles, with respect to their thermal protection systems. The classical numerical approach to this phenomenon, originally proposed in 1956 by Van Ingen [1], is the combination of Linear Stability Theory (LST), which determines the growth rate of the eigenmodes (Tollmien-Schlichting (TS) waves) that live on a laminar flow, and the semi-empirical e^N-method, which establishes a correlation between the transition "location" and the total growth (or: gain) that the eigenmodes undergo.

The different mechanisms involved in the transition phenomenon are shown in Fig. 1. Disturbances are entrained into the boundary layer via *receptivity mechanisms*. Thereafter the perturbations experience an amplification phase before they breakdown and lead to a turbulent state. What kind of amplification will take place is strongly dependent on the disturbance environment. For a low disturbance environment, the most unstable exponentially growing eigenmode will become dominant and lead to parametric instability (path A). However, for larger initial disturbance levels, multiple eigenmodes can have relatively large amplitudes yielding that their linear superposition displays algebraic *transient growth* (paths B and C). For even larger environmental disturbances, strong non-linearities can set in very early, thereby "by-passing" the aforementioned linear growth mechanisms (paths D and E). Another interpretation of the *by-pass mechanisms* is that they by-pass the current knowledge of what is going on.

Clearly, the final evolution of the perturbations is highly non-linear. The success of the classical ap-

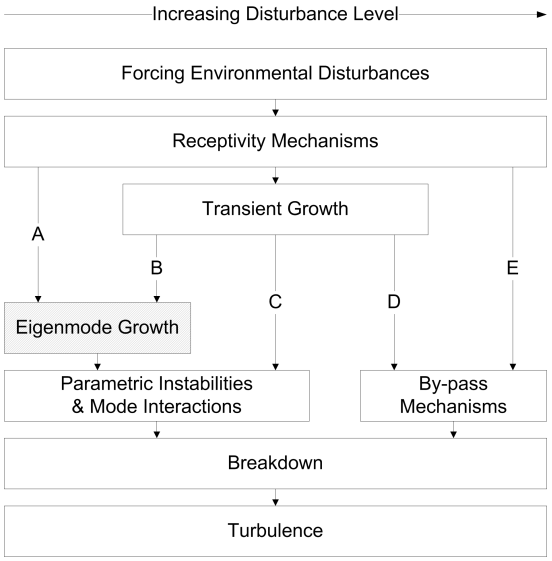

Figure 1: Mechanisms leading to turbulence for different disturbance levels. Original by Reshotko [2].

proach that only accounts for linear growth therefore seems surprising. The omission of non-linear effects is argued to be reasonable with respect to the small spatial extent where they are dominant. The goal of the current PhD project is to extent the approach to include more physics, most prominently: the non-linear mechanisms. The first effect that can be taken into account is eigenmode interaction. Methods that can take these interactions into account fully ought to be able to incorporate the transient growth, by-pass and breakdown mechanisms as well. An important problem is that, as an apparent snowball effect, the receptivity mechanisms have to be accounted for in that case as well, which is equivalent to effectively handling the butterfly effect inherently associated with chaos. This is what makes improving transition analysis very difficult.

In addition to the distinction between the different mechanisms involved, it is important to distinguish different kinds of perturbations. As indicated in Fig. 2, *absolute instabilities* (a) remain finite at the location of their generating source, while *convective instabilities* (b) move away. Due to their definite direction of movement, the convective instabilities can be analysed using parabolized approaches (posing an initial-value problem in space), while it is more convenient to apply an elliptic approach (posing a boundary-value problem in space) to the absolute instabilities.

In what follows first the two-dimensional generalization of the classical linear stability method is elaborated on followed by the non-linear extension in Section 2. This *BiGlobal stability* framework is to be associated with the aforementioned elliptic approach. Thereafter, because the linear problem provides the initial condition for the non-linear problem, the application of the linear BiGlobal approach to the Blasius boundary layer, regarding the initial BiGlobal tool verification, is elaborated on in Section 3.

This study motivated the investigation of boundary/compatibility condition derivations for the in-/outflow problem, which is treated in Section 4. The application of these conditions to a supersonic boundary layer is handled in Section 5. The treatment is concluded in Section 6.

2. Stability theory

As indicated, perturbations are the main interest. Therefore the instantaneous flow q is decomposed into a *steady* base flow $\overline{Q}$ and perturbation q':

$$q = \overline{Q} + q', \tag{1}$$

Substituting Eq. 1 into the Navier-Stokes equations yields the *non-linear perturbation equations* for q' from which the combination of terms involving $\overline{Q}$ only (forming steady Navier-Stokes) can be dropped. In the linear theory, the perturbations are assumed to be negligibly small with respect to the base flow, allowing the linearisation of the latter equations, resulting in *linearized Navier-Stokes*.

The latter equations are still rather expensive to solve. They are therefore simplified regarding the dimensionality of the base flow. Partial Differential Equation (PDE) theory dictates that the solution must

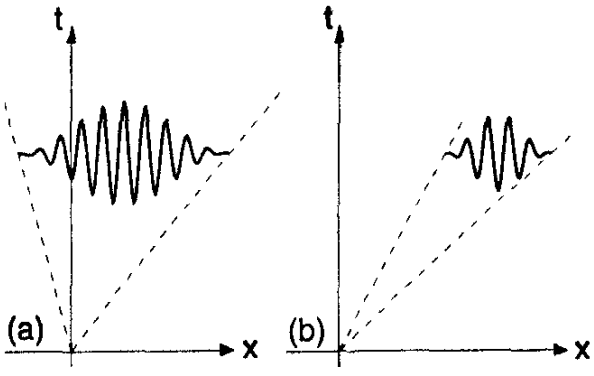

Figure 2: Evolution in space and time of an absolute (a) and convective (b) instability. Original image by Schmid & Henningson [3].

vary "generally" in the directions in which the coefficients, here $\overline{Q}$, vary. The solutions behave exponentially in the remaining directions and time. Regarding boundary layer flow, the streamwise development is classically neglected as opposed to the more prominent wall-normal gradients. This yields the classical (LST) ansatz:

$$q' = \tilde{q}(y)e^{i(\alpha x+\beta z-\omega t)} + c.c., \tag{2}$$

where $\tilde{q}$ denotes the perturbation amplitude, α and β are the stream- and spanwise wavenumbers, ω is the frequency and $c.c.$ abbreviates complex conjugate.

The assumption that the base flow is homogeneous in the x- and z-directions implies, through mass conservation, that the wall-normal velocity component is zero and is therefore also referred to as the *parallel flow assumption*. See the monograph of Mack [4] for an extensive elaboration on LST.

In flows like separation bubbles or those over backward facing steps this assumption breaks down. Another direction has to be considered inhomogeneous leading to the BiGlobal ansatz (see the review of Theofilis [5]):

$$q' = \tilde{q}(x, y)e^{i(\beta z-\omega t)} + c.c. \tag{3}$$

Inserting either Eq. 2 or 3 leads to the LST or BiGlobal *stability equations* which form eigenboundary-value problems. Deriving the BiGlobal stability equations for a compressible flow is difficult because of their length. The automatic derivation tools in the VKI Extensible Stability and Transition Analysis (VESTA) toolkit were created with the purpose of tackling the problem of deriving large stability equations. The first error free compressible BiGlobal system was reported by Pinna & Groot [6].

The extension to non-linear perturbation dynamics lies in considering the non-linear perturbation equations. In the non-linear case, one can no longer separate the eigenmodes in the ansatz; they ought to be superposed, thereby allowing them to interact. This leads to the following Wentzel-Kramers-Brillouin-Jeffreys (WKBJ) ansatz (see Holmes [7]):

$$q' = \sum_{m=0}^{N_m} A_m \tilde{q}_m(x, y, t)e^{i\left(m\beta z-\int_{t_0}^{t}\omega_m(\tau)d\tau\right)} + c.c., \tag{4}$$

where τ is the dummy time variable, $\{\omega_m, \tilde{q}_m\}$ are the BiGlobal eigensolutions and $\{A_m\}$ are their associated amplitudes. Inserting Eq. 4 into the governing equations and balancing the harmonics yields a system of systems of equations for the harmonics that forms an initial-value problem that can be solved by a time marching procedure.

The BiGlobal eigensolutions are used to set the initial condition of the initial-value problem. Therefore the linear problem has to be considered before the non-linear one can be dealt with. Up to now, the main focus has been on the linear streamwise analysis of the boundary layer, which logically followed from a tool verification case.

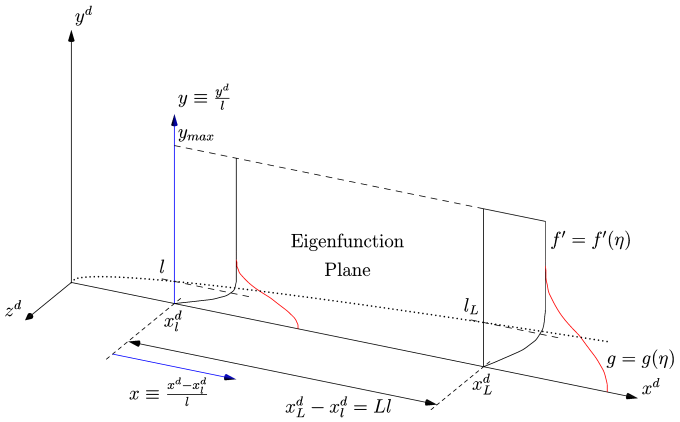

Figure 3: Setup of the streamwise BiGlobal analysis of the Blasius boundary layer.

3. Streamwise Blasius verification test case

Among other more complicated and more decisive cases, the streamwise BiGlobal analysis of the incompressible Blasius boundary layer was used as a verification case for the BiGlobal tools in VESTA. The (general compressible) set-up is illustrated in Fig. 3, where the symbol l is used as the reference length scale. The verification was performed using the treatments of Ehrenstein & Gallaire [8] and Alizard & Robinet [9], in which $(Re_l, L, y_{max}, \beta) = (O(700), O(400), O(20), 0)$, as references. The two dimensional boundary layer field is generated in VESTA using self-similar profiles, while Navier-Stokes solvers were used in the references. The verification was performed by trying to replicate the computation performed in the literature as closely as possible, thereby including potential theoretical inconsistencies.

It was found to be difficult to reproduce the reported spectra, even when using the tools in VESTA on the base flows kindly provided by both pairs of authors. The transfer of the data helped to clear up what discrepancies were involved per reference to a qualitative extent.

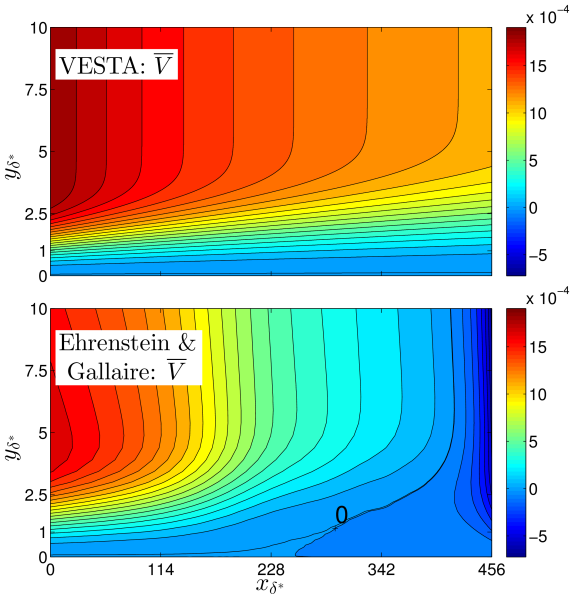

Figure 4: Vertical base velocities calculated with (top) self-similar profiles (VESTA) and (bottom) Navier-Stokes solver (Ref. [8]).

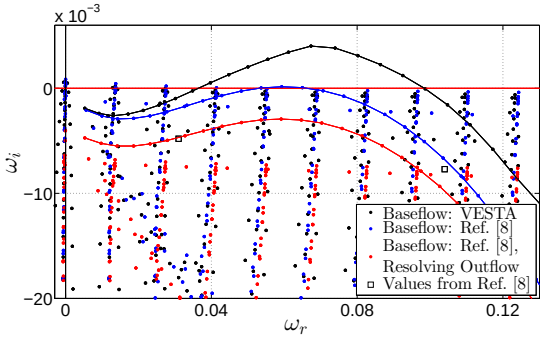

Figure 5: Spectrum verification with Ref. [8].

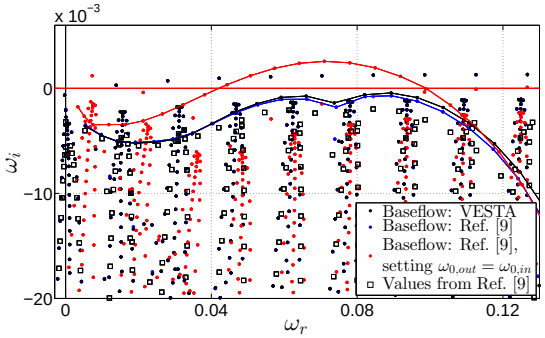

Figure 6: Spectrum verification with Ref. [9].

The dataset provided by Ehrenstein & Gallaire, generated using a Navier-Stokes code, was conjectured to be incompletely converged in time. A comparison of the vertical base flow velocity fields is shown in Fig. 4, where the subscript δ^* is used to indicate the use of the displacement thickness as reference length (to be consistent with Fig. 3, $l = \delta^*$ here). A definite negative wall-normal velocity region is clearly visible in a large portion of the domain, which, via classical theory, implies a stabilizing effect. The branches of TS waves in the spectra, shown in Fig. 5 as the connected modes, clearly reflect this. When resolving the outflow region, the overall stabilizing shift becomes even more pronounced for the spectrum in its entirety. Furthermore, a persistent mismatch exists between the eigenvalues reported in the reference and the results returned by the stability tools in VESTA. It is unclear how to explain this discrepancy. Nevertheless, the downwards shift of the spectrum in the literature is deemed to be understood qualitatively.

Another observation can be made regarding the nearly vertical branches in Fig. 5: in the spectrum corresponding to the base flow generated with VESTA, seemingly parabolic branches exist next to a nearly vertical line. They are not present when considering the erroneous base flow.

The base flow received from Alizard & Robinet [9] agreed very closely to the one generated using VESTA. In turn, this resulted in nearly identical spectra when applying the stability tools in VESTA to either base flow. However, again, a persistent mismatch with the published values is observable in Fig. 6. Moreover, a large discrepancy is encountered with respect to the black spectrum reported in Fig. 5. In this case the (conceptual) difference in the approach is in the boundary conditions (BCs). The in-/outflow BCs pose a closing problem for the streamwise problem in general, which is in both references approached using what here is referred to as *Robin-Gaster* BCs, which will be elaborated on in Subsection 4.2. In the current reference a different "target frequency" is used for the in- and outflow BCs, while they ought to be identical. When these frequencies are equated, a large unstable shift results as shown in Fig. 6. The explanation for this is that when the target frequencies are distinct, the in- and outflow BCs have a detuning effect. When they are equal, as ought to be the case theoretically, they yield an additive, resonant, effect causing the spectrum to experience an unstable shift. This explains the qualitative discrepancy between the black spectra in Figs. 5 and 6. Again, the cause for the discrepancy with the published values is unknown, although the principal reason for the qualitative downwards shift is deemed to be understood in both cases.

Note that the parabolic structures around the nearly vertical branches are present in all spectra regarding

Fig. 6, showing the relevance of the wall-normal base velocity. These branches correspond to modes that are dominant in the freestream; they are a discrete representation of the *continuous spectrum*. Rodríguez [10] reports that the branch splitting in the non-parallel base flow is 'the most remarkable effect' with respect to the parallel flow case, but argues that no physical interpretation is possible because the discretization method resolves these modes inadequately. A near future publication will elaborate on the fact that the branch splitting is analogous to the Doppler effect.

It is important to note that both references report that the BiGlobal eigenmodes all ought to be stable, because the 'boundary layer is convectively unstable but absolutely stable and consequently globally stable' (Ref. [9]). The upwards shifts into the unstable regime are therefore rather controversial.

4. In-/outflow boundary and compatibility conditions

The aforementioned findings motivate a study of the in- and outflow BCs' effect on the eigensolutions. Another argument lies in the use of the streamwise BiGlobal approach in design applications. A single BiGlobal simulation replaces two loops of LST simulations; one over the streamwise direction and one over frequencies. If these loops can be effectively captured in one BiGlobal simulation, there is a break even point beyond which the BiGlobal approach is more desirable due to the fact that it takes into account additional physics. The in-/outflow BCs play a crucial role regarding the latter fact. The following treatment is analogous to the publication of Groot, Pinna & Van Oudheusden [11].

Regarding the perturbation BCs in general, as elaborated on by Theofilis [5]: 'The only situation in which they are clear is at solid walls'. There, through Eq. (1), the no-penetration, no-slip and zero temperature conditions are to be applied. Lastly, the BiGlobal wall-normal momentum equation is used as a Compatibility Condition (CC) for the pressure. The boundary for $y \to \infty$ is also equipped with the aforementioned *wall conditions*. The streamwise in-/outflow boundaries pose the largest problem.

Oscillator type disturbances, characteristically present in absolutely unstable flows, remain contained in the domain entirely. In that case, following Theofilis [5; 12], the truncation boundaries can be adequately equipped with Dirichlet BCs so to "focus" exclusively on disturbances generated internally. Problems arise in the case of convectively unstable flows; strong artificial layer behaviour results in those cases.

A variety of BCs/CCs is derived here, intended to yield *partial* solutions to this problem by somehow including external information in the BiGlobal problem or linking it to the subset stability frameworks, i.e. LST or Parabolized Stability Equations (PSE); for the latter see the review of Herbert [13]. In doing so, more physics is included in the BCs allowing the assessment of the inherent assumptions' importance.

Two condition classes are distinguished: the *non-autonomous* class, requiring pre-processing to calculate specific input parameters, and the *autonomous* (compatibility) class, for which no calculations have to be done *a priori*. In the ideal case, the latter CCs should be valid for all eigenvalues ω. From the physical viewpoint, the only way to do this without extra assumptions is to apply the BiGlobal stability equations themselves. This implies leaving the PDEs unconstrained, which cannot yield useful results. For this reason some restricting assumptions have to be incorporated, which is closely linked to the historical non-parallel flow problem.

4.1. Non-autonomous condition #1: Robin conditions

The Robin condition is a standard condition, which, in this context, is written most conveniently as follows:

$$\frac{\partial \tilde{Q}}{\partial x} = i\alpha\tilde{Q}, \qquad \alpha = \alpha_r + i\alpha_i. \tag{5}$$

This condition prescribes an inflowing disturbance with the local spatial wavenumber α_r and growth rate $-\alpha_i$.

Assuming that α is constant in y and equal for all amplitudes, one can use a truncated version of an expansion of the *local spatial dispersion relation* $\alpha = \alpha(\omega_r) \in \mathbb{C}$ about a specific real frequency, $\omega_{s,0}$, at leading order to yield:

$$\alpha_s = \alpha_s|_{\omega_{s,0}} + O(\varepsilon_T),$$
$$\text{where:} \quad \varepsilon_T \equiv \omega_s - \omega_{s,0} \ll 1.$$

Here, the subscript s emphasizes the spatial nature of the parameters and the subscript T refers to Taylor. Note that $\omega_s \in \mathbb{R}$ and $\alpha_s|_{\omega_{s,0}}$ can be determined ideally by a spatial LST calculation, in line with the aforementioned assumptions.

In what follows, the reference length scale is based on the Blasius length scale $l = \sqrt{\overline{\nu}_e^d x^d / \overline{U}_e^d}$ where the d (explicitly) denotes dimensional quantities and the

e refers to a reference quantity. In the BiGlobal set-up, the Blasius length scale evaluated at the inlet position is used as a global reference length scale, defining Re. In contrast, the reference length in the LST set-up is the local length scale, introducing a scaling problem with respect to the parameters for the outlet condition. Furthermore, the parameters for the in- and outflow conditions are related to each other, because the corresponding BiGlobal eigenvalue, ω, is a global variable. This reasoning yields the discrepancy with the approach of Alizard & Robinet [9].

In the local scaling, a perturbation that travels with constant (dimensional) frequency:

$$\omega_r^d = \omega_r \frac{\overline{U}_e^d}{l} \quad \text{or, equivalently:} \quad F = \omega_r^d \frac{\overline{\nu}_e^d}{(\overline{U}_e^d)^2} = \frac{\omega_r}{Re_l},$$

describes a linear path in the (Re_l, ω_r)-plane as is shown by the red line in Fig. 7. The in- and outlet of the BiGlobal domain correspond to $Re_{in} \equiv Re$ and Re_{out}, respectively. When the local characteristics of the *target perturbation* with the frequency ω_0^d, or ω_0 in the BiGlobal scaling, have to be calculated, the input parameters $(\omega_{l,in}, Re_{in}) = (\omega_0, Re)$ and $(\omega_{l,out}, Re_{out}) = (\omega_0 \frac{Re_{out}}{Re}, Re_{out})$ should be used for the respective LST simulations. It is important to note that the outflow wavenumber obtained from LST is to be multiplied by $\frac{Re}{Re_{out}}$ to comply with the BiGlobal scaling (because $\alpha^d = \alpha/l$).

The downside of using this set-up is the specific optimization of the BCs for the target perturbation only. When ω_r deviates from ω_0, a first order deviation from the local dispersion relation (with respect to $\omega_r - \omega_0$) is to be expected in the BCs. Despite of this, the current set-up is qualitatively consistent as no qualitative error is introduced. For this reason, this configuration is considered as a baseline.

4.2. *Non-autonomous condition #2: Robin-Gaster conditions*

As the Robin conditions can only be set to represent a single radial frequency F, they can be interpreted as being rather inefficient. By involving the *temporal* frequency $\omega_t \in \mathbb{C}$ in the BC, the domain of validity is extended. This is done via the *Gaster transformation* [14], which, in combination with the first order truncation of the dispersion relation, yields:

$$\alpha_s = \alpha_{s,r}\big|_{\omega_{s,0}} + \left.\frac{d\alpha_{s,r}}{d\omega_s}\right|_{\omega_{s,0}} (\omega_t^* - \omega_{s,0}) + O(\varepsilon_T^2) + O(\omega_{im}^2), \tag{6}$$

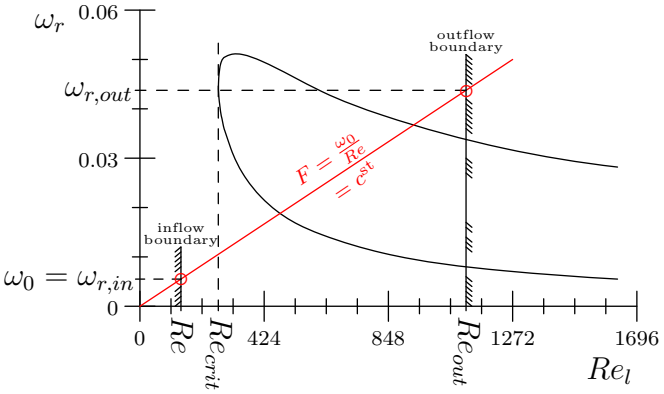

Figure 7: Indication of the target perturbation's frequency in the local and global scaling systems and the associated parameters for the Robin conditions.

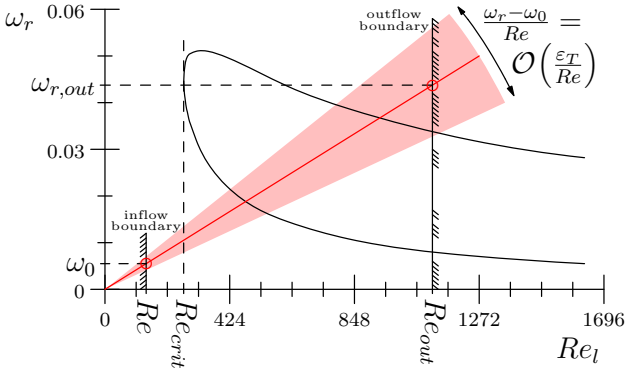

Figure 8: Indication of the domain of validity when Robin-Gaster conditions are employed (displayed size is not intended to be on scale).

where the subscript t denotes temporal variables, the star denotes complex conjugation and $|\omega_{im}| < \varepsilon_T \ll 1$ is the absolute value of the maximum the imaginary part of ω_t attains. When substituted into Eq. (5), the resulting condition is referred to as the *Robin-Gaster condition*. By taking into account the variation of ω_t, the domain of validity is extended to a region around the target perturbation as in Fig. 8, where the BCs comply with the local dispersion relation up to second order in ε_T. The parameter $d\alpha_{s,r}/d\omega_s\big|_{\omega_{s,0}}$ is calculated using finite differences.

The appearance of ω_t^* is a consequence of the Gaster transformation. It yields a problem, because the problem now has the form $A\Xi = \omega B\Xi + \omega^* C\Xi$, which cannot be cast into the standard generalized eigenvalue problem form. A "quick-fix" simply foresees the omission of the complex conjugation in Eq. (6) at the cost of introducing a first order *qualitative* error in (2)ω_{im}; rendering the growth rate $-\alpha_{s,i} = -\alpha_{s,i}(\omega_r)$ to have the wrong sign [8; 9; 15].

4.3. Other non-autonomous conditions

Some other non-autonomous CCs based on other stability equations could be used. Examples are the LST or PSE equations. The incompressible PSE y-momentum equation (the incompressible case is considered because of conciseness):

$$i\beta\tilde{v}\overline{W} + \tilde{v}\overline{V}_y + \tilde{v}_y\overline{V} + \tilde{v}_x\overline{U} + i\alpha\tilde{v}\overline{U} - i\omega\tilde{v} = -\tilde{p}_y + \frac{\tilde{v}_{yy}}{Re} + \frac{2i\alpha\tilde{v}_x}{Re} - \frac{\beta^2\tilde{v}}{Re} + \frac{i\alpha_x\tilde{v}}{Re} - \frac{\alpha^2\tilde{v}}{Re} \quad (7)$$

shows that x-derivatives are present in which it resembles the Robin conditions. The corresponding dispersion relation is: $D(\omega; Re, \alpha, \frac{d\alpha}{dx}) = 0$, requiring $\frac{d\alpha}{dx}$ in addition to Re and α in the case of LST, which is determined by finite differences. These CCs are interpreted as a generalization of the Robin conditions, incorporating the change of $\alpha_{s,r}$ in x and representing slowly varying large wavelength structures, while preserving fast oscillatory behaviour.

It must be noted that, when applying one of the aforementioned CCs, the to be solved problem still has the form $A\Xi = \omega B\Xi$; coefficients containing ω are collected in the B- and the others in the A-matrix.

4.4. Autonomous condition #1: Parabolized CCs (assuming $\frac{\partial}{\partial x} = O(\epsilon), \overline{V} = O(\epsilon)$)

The *autonomous* conditions are derived by applying certain restricting assumptions to the BiGlobal stability equations. The first assumptions set is related to the artificial layer behaviour. A way to avoid such behaviour is to apply the PSE ansatz, yielding the behaviour mentioned at the end of Subsection 4.3. Unfortunately, incorporating the fast oscillatory behaviour requires dispersion relation information, resulting in the *non-autonomous* CC of Subsection 4.3.

To avoid involving the dispersion relation, one can parabolize the BiGlobal equations *directly*; i.e. assuming $\frac{\partial}{\partial x} = O(\epsilon)$ and $\overline{V} = O(\epsilon)$ and neglecting $O(\epsilon^2)$ terms. Taking the incompressible BiGlobal y-momentum equation:

$$i\beta\tilde{v}\overline{W} + \underbrace{\tilde{v}\overline{V}_y}_{O(\epsilon)} + \underbrace{\tilde{u}\overline{V}_x}_{O(\epsilon^2)} + \underbrace{\tilde{v}_y\overline{V} + \tilde{v}_x\overline{U}}_{O(\epsilon)} - i\omega\tilde{v} = \underbrace{\frac{\tilde{v}_{xx}}{Re}}_{O(\epsilon^2)} - \tilde{p}_y + \frac{\tilde{v}_{yy}}{Re} - \frac{\beta^2\tilde{v}}{Re}.$$

Removing all second order terms yields a PDE without second order x-derivatives; it is a Robin type CC for $\tilde{v}$. This CC is also retrieved from Eq. (7) by setting $\alpha = \frac{d\alpha}{dx} = 0$; implying omission of all fast oscillatory behaviour.

4.5. Autonomous condition #2: Parallel CCs (assuming $\frac{\partial}{\partial x} = O(1), \overline{V} = 0$)

The second set of CCs corresponds to another objective: to solve the LST equations at the boundaries, so to represent the local dispersion relation, but without involving it explicitly. I.e. α has to be linked to the data in the domain's interior; performed exactly by formally replacing every α by $-i\partial/\partial x$; inversely Fourier transforming the LST equations.

From the perspective of the BiGlobal equations, all mean variables related to non-parallel features are set to zero (in the incompressible case: $\overline{U}_x$, $\overline{V}$, $\overline{V}_x$, $\overline{V}_y$ and $\overline{W}_x$), while keeping all x-derivatives of the amplitudes:

$$i\beta\tilde{v}\overline{W} + \underbrace{\tilde{v}\overline{V}_y + \tilde{u}\overline{V}_x + \tilde{v}_y\overline{V}}_{=0} + \tilde{v}_x\overline{U} - i\omega\tilde{v} = -\tilde{p}_y + \frac{\tilde{v}_{yy}}{Re} + \frac{\tilde{v}_{xx}}{Re} - \frac{\beta^2\tilde{v}}{Re}.$$

Note that this equation still has second order x-derivatives; it does not close the problem. Therefore, using this CC cannot be expected to yield useful solutions in general. Nevertheless, one can discretize and apply it. Surprisingly, for non-parallel boundary layer flows (in which case the CCs are distinct from the BiGlobal equations) they are observed to yield spectra that match very closely with those obtained applying the Robin conditions. They do not yield a rigorous set-up, but they can be demonstrated to work successfully in particular cases.

5. Application to supersonic boundary layer

This section relates to the preliminary work of the analysis of a supersonic boundary layer experimentally investigated in the TST-27 supersonic windtunnel of Delft University of Technology. The base flow solution is calculated using finite differences as presented by White [16], on a $N_\xi \times N_\eta = 1201 \times 500$ uniform grid using explicit forward differencing in x and central differencing in y, assuming constant pressure throughout the domain and an adiabatic wall. Sutherland's law and Stokes' hypothesis were used to calculate the viscosity. The BiGlobal parameters are: $(Re, M, \gamma, Pr) = (414; 1.7; 1.4; 0.71)$, on the domain: $(x, y) \in [0; 6215.3] \times [0; 49.723]$, or in physical space: $(x^d, y^d) \in [5mm, 80mm] \times [0mm; 0.60139mm]$. Under these conditions, the most dominant mode is oblique, i.e. $\beta \neq 0$.

6 different kinds of streamwise BCs were applied to the in-/outlets: the Robin, Robin-Gaster (see Subsections 4.1 and 4.2), wall and Neumann BCs and

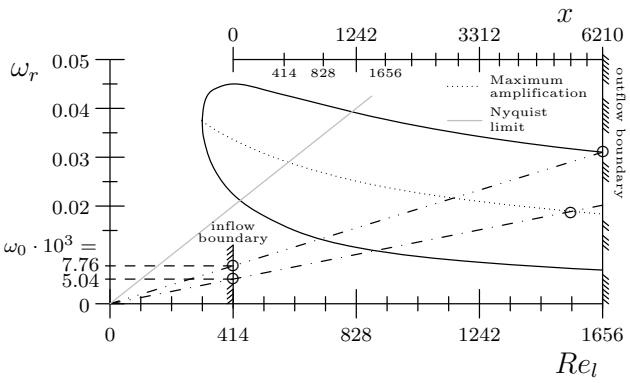

Figure 9: Local neutral curve, evolution paths and associated (BiGlobal) frequencies of the two target perturbations indicated by two dashdotted lines. Nyquist limit based on maximal resolution considered in x ($N_\xi = 240$).

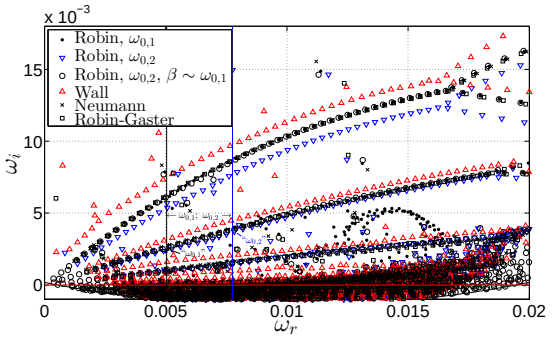

Figure 10: Spectrum comparison between the Robin condition based on $\omega_{0,1}$, the Robin condition based on $\omega_{0,2}$ and the similar condition but with an adjusted value of β, the wall, Robin-Gaster and Neumann conditions (vertical lines indicate target frequencies).

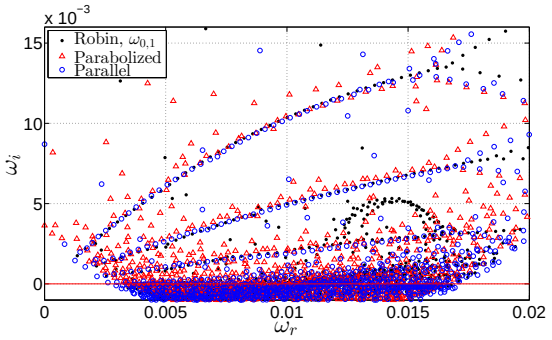

Figure 11: Spectrum comparison between the Robin condition based on $\omega_{0,1}$, the parabolized and parallel CCs.

the parabolized and parallel CCs (see Subsections 4.4 and 4.5). Two different target frequencies were selected based on the local neutral curve, shown in Fig. 9, where β is always based on a wave angle of $60deg$. The first target perturbation (singly dotted), with $\omega_0 = \omega_{0,1}$, has the maximal amplification rate near the experimentally observed transition point ($x_{tr}^d \approx 70mm$), while the second (doubly dotted), with $\omega_0 = \omega_{0,2}$, behaves neutrally at the outlet; all according to spatial LST. Please consider the work of Groot, Pinna & Van Oudheusden [11] for all parameters values. It is important to note that, globally speaking, α_r varies according to the dispersion relation $\alpha_r(\omega_r)$, which, in turn, implies that the wave angle $\arctan\left(\frac{\beta}{\alpha_r}\right)$ varies with ω_r. Therefore only the modes with ω_r close to ω_0 have a $60deg$ wave angle; for larger ω_r the wave angle decreases and vice versa. All simulations with other BCs were equipped with the value of β corresponding to $\omega_{0,1}$. So, in summary, 7 BCs were distinguished: 2 Robin cases with different target frequencies and the 5 other BC types focusing on $\omega_{0,1}$ through the value of β.

5.1. Comparing the spectra

In Figs. 10 and 11, the spectra corresponding to the different BCs are displayed. The most evident features are the (at least) three unstable branches. The absolute eigenfunctions corresponding to the uppermost branch have their maximum in the domain's center, conflicting with LST. Regarding different BCs, at fixed resolution, the third most unstable branch is sometimes "polluted" with clouds of modes and therefore hard to distinguish properly. The second most unstable branch displays features reminiscent of the local theory. For these reasons, only the latter is analysed here; specific peculiarities are discarded as well. A more thorough analysis of the physics will follow. Here solely the BCs' effect is focused on.

The three branches retrieved in the Robin cases are fully converged using a $N_\eta \times N_\xi = 180 \times 45$ grid. A mapping is used to map one third of the nodes between $y = 6$ and 12 and $x = \frac{1}{3}x_{max}$ and $\frac{2}{3}x_{max}$ in the y- and x-direction, respectively, resolving the most requiring features, while preserving a dense boundary spacing. Convergence characteristics for other BCs are sometimes worse than the Robin case, requiring more than 180×45 nodes for convergence. Nevertheless, using this resolution is argued to yield a fair comparison of the "performance" of the different conditions.

By comparing the first two Robin cases in Fig. 10, it follows that a higher target frequency yields a stabilizing shift. As can be seen from the third Robin condition, this is mainly caused by the change in β. Comparing the other BCs, the spectra corresponding to the $\omega_{0,1}$-Robin, Robin-Gaster and Neumann BCs are observed to nearly overlap. In the Robin case, the branch

departs slightly from the others near $\omega_{0,1}$, most probably caused by the different applied spatial growth rates. In the wall BCs case, the branches are more unstable, which is argued to be induced by strongly adverse convergence characteristics caused by fixing the amplitudes. Generally, artificial layers are introduced in the quantities that are applied by the BCs. So, applying a quantity that is not directly resolved usually yields a "regular" result for relatively low resolution.

Inspecting Fig. 11, surprisingly, the parallel CCs' spectrum lies nearly on top of the Robin case, although at some frequencies it departs slightly when N_ξ is increased. The parabolized CCs reproduce modes scattered around the three branches (also for higher resolutions), caused by the omission of fast oscillatory behaviour.

5.2. *Comparing the eigenfunctions*

For each target frequency, an eigenfunction comparison was made using specific characteristics of the modes closest to these frequencies. The common eigenfunction shape is shown in figure 12, corresponding to large ω_r, which clearly displays the two maxima in y near the inlet. Generally, the uppermost maximum is most dominant for small x and decays while entering the boundary layer. The second maximum ultimately becomes more dominant than the other maximum at a certain x-position. The *exchange of dominance* can be shown by plotting the y-location of the global maximum of $|\tilde{u}|$ over y, see Fig. 13, which also displays the N-factor curves based on the latter maximum, i.e. the natural logarithm of $\max_y |\tilde{u}|$ with respect to the neutral position. These curves' neutral points are always set as close as possible to the point where the maxima exchange dominance.

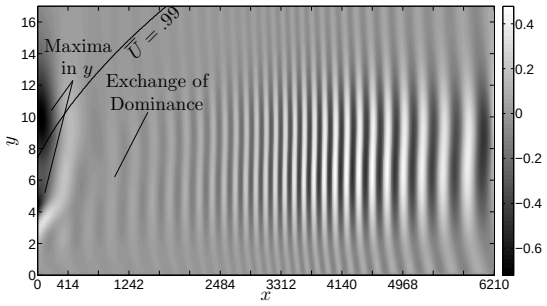

Figure 12: Scaled eigenfunction $\tilde{u}_r / \max_{x,y} |\tilde{u}|$ representative of the common shape corresponding to the first target frequency Robin BCs case, having the eigenvalue: $\omega = (10.020 + i\,5.0029) \cdot 10^{-3}$.

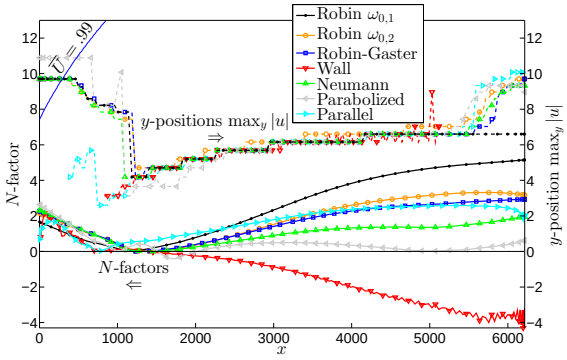

Figure 13: Comparison of eigenfunctions for different BCs by the N-factors (solid lines) based on the maximal value of $|\tilde{u}|$ w.r.t. the y-direction and these maxima's y-locations (dashed lines) for the modes closest to the target frequency $\omega_{0,1}$. The slender blue line shows the boundary layer thickness, δ_{99}.

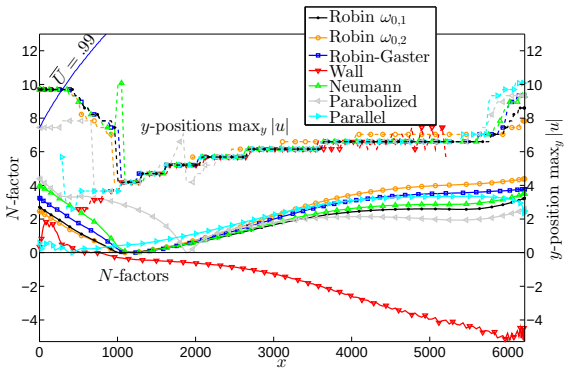

Figure 14: Comparison of eigenfunctions for different BCs by the N-factors (solid lines) based on the maximal value of $|\tilde{u}|$ w.r.t. the y-direction and these maxima's y-locations (dashed lines) for the modes closest to the target frequencies $\omega_{0,2}$. The slender blue line shows the boundary layer thickness, δ_{99}.

In Fig. 13, nearly all y-distributions start outside the boundary layer, enter it and undergo a steep jump, which indicates the exchange of dominance and, as expected, usually coincides with the minimum of most N-curves. In the wall BCs case, the eigenfunctions are spurious near the in-/outlet reflected by very large jumps in the y-distributions, which are therefore cut in those regions. The odd behaviour of the N-curves of this case is to be attributed to the fact that it is strongly under resolved. For the parallel CCs case, the y-distributions are cut because they jump "into" the N-curves at both in- and outlets. Although they are quite jumpy as well, they stay within the boundary layer for all x.

Regarding the N-curves in Fig. 13, the different BCs yield very different results. Moreover, the BCs' effect is not confined to in-/outlet boundary layers.

The largest amplification is found using the $\omega_{0,1}$-Robin BCs, which also corresponds to the straightest y-distribution near the outlet. In Fig. 14 again the Robin BCs optimized for the considered frequency, now $\omega_{0,2}$, yields the largest growth and straightest y-distribution near the outlet. Although in this figure the wave angle is quite smaller than $60deg$ for all but the $\omega_{0,2}$-Robin BCs, the N-curves lie much closer; some of them have increased quite significantly. Although the Robin-Gaster BCs only apply a different spatial growth rate at $\omega_{0,1}$, they are demonstrated to heavily underestimate the amplification with respect to the $\omega_{0,1}$-Robin case.

The wall BCs clearly yield a problem that requires far more resolution relative to less restrictive BCs and are therefore deemed very inefficient. The Neumann BCs yield regular eigenfunctions, but Fig. 13 demonstrates they can underestimate the maximal growth significantly. The very small N values resulting from the parabolized CCs show that neglecting fast oscillatory behaviour has a very pronounced impact on the overall amplification. Moreover, the y-distributions deviate markedly from the main trend at several positions. On the other hand, the parallel CCs are the only conditions that yield the most dominant maximum to be completely immersed in the boundary layer near the inlet. Although these CCs yield spurious functions at the inlet and all other BCs show the same distinct inflow trend, they hint that the occurrence of the uppermost maximum in the amplitudes might not be physical. This inflow pattern might be induced solely by the presence of the truncation boundary.

5.3. Discussion

Regarding the fact that the boundary layer is convectively unstable, the unavoidable truncation of the domain implies that the sole existence of perturbations in the domain is dictated by the unknown BCs. Although particular characteristics pass over from condition to condition, the aforementioned results show that the in-/outflow BC closure problem can be very crucial with respect to obtaining quantitative spatial growth information; it is not restricted to layer regions near the in-/outflow boundaries.

The Robin-Gaster BCs, primarily used in the literature, cannot be argued to be the solution for the problem. At the current stage of the investigation it is not clear which condition is most effective or whether the eigensolutions are physical. A next step in this investigation will be the detailed comparison of the current results with LST simulations to completely avoid the boundary closure problem.

An interesting recurring feature is the fact that the tuned Robin BCs seem to consistently yield the spatially most amplified mode. Further investigations are to point out whether this characteristic carries over to other cases, i.e. Falkner-Skan wedge flows and flows at other Mach numbers. If the fact is demonstrated that the Robin BCs are the only reliable solution, this implies that a target frequency loop has to be executed to retrieve the complete spectrum. This means that the LST frequency loop cannot be effectively captured by a single BiGlobal simulation. Applying the streamwise BiGlobal approach to convectively unstable flows is therefore shown to be very inefficient. It will be unsuitable for design applications.

6. Conclusion

The goal of the overarching PhD project is to extend the stability approaches used for transition prediction to include more physics, e.g. base flow dimensionality and non-linear mechanisms. The base flow dimensionality is included by considering the BiGlobal stability framework, which in turn can be extended to incorporate non-linear behaviour. The non-linear approach requires the solution of the linear problem as an initial condition and therefore the linear BiGlobal eigenvalue problem was focussed on mainly up to this stage in the project.

The main test case considered is the streamwise BiGlobal analysis of the Blasius boundary layer, which proved to be a hard test case with respect to tool verification because particular discrepancies were encountered in the approaches applied in the literature. These differences yielded a stabilizing shift in both used reference spectra, which motivated an investigation into the in-/outflow boundary closure problem alongside the potential of two ODE based classical Linear Stability Theory (LST) loops being captured by a single BiGlobal simulation, yielding a set-up interesting for design applications.

Particular boundary and compatibility conditions were derived for this purpose with the intention to approach the problem in a structured and physically arguable way. It was shown that the Robin-Gaster conditions used in the literature incorporate a qualitative error in the applied spatial growth rate. Moreover, a competition between neglected physics and a restricted domain of validity was encountered.

When applied to a supersonic boundary layer, the different conditions were found to reproduce very similar spectra, with several exceptions. When regarding the eigenfunctions, it was found that, for the

considered cases, the Robin conditions yield the most spatially amplified mode when considering the mode belonging to the target frequency for which the conditions are optimised. The other conditions that where considered can yield a significant underestimation, showing that their effect is not limited to layers around the in- and outflow boundaries. It is very important to note that it is unknown whether the obtained eigenfunctions represent physical perturbation structures. Further investigations ought to shed light on the performance of the Robin conditions for other cases.

The fact that the Robin conditions yield the most reliable behaviour implies that the LST frequency loop cannot be captured by a single BiGlobal simulation. Therefore, the latter set-up is deemed structurally inefficient, at least for design applications.

Acknowledgments

KJG wishes to thank Alizard & Robinet and Ehrenstein & Gallaire for sharing their base flow datasets, to express his gratitude to the supervisors and professors for their advice and guidance and acknowledge the AWEP department of TUD for the financial support.

References

[1] J. L. Van Ingen, The e^n-method for transition prediction. historical review of work at tu delft, in: 38th Fluid Dynamics Conference & Exhibit, no. 2008-3830, AIAA, ISBN: 978-1-60086-989-1, Seattle, Washington, 2008.

[2] E. Reshotko, Paths to transition in wall layers, in: Advances in laminar-turbulent transition modeling, Von Kármán Institute for Fluid Dyanmics, ISBN: 978-92-837-0900-6, 2008.

[3] P. J. Schmid, D. S. Henningson, Stability and Transition in Shear Flows, Springer Verlag, New York, ISBN: 0-387-98985-4, 2001.

[4] L. Mack, Special course on stability and transition of laminar flow, in: AGARD, Special Course of Stability and Transition of Laminar Flows, North Atlantic Treaty Organization, ISBN: 92-835-0355-4, 1984.

[5] V. Theofilis, Global linear instability, Annual Review of Fluid Mechanics 43 (1) (2011) 319–352.

[6] F. Pinna, K. J. Groot, Automatic derivation of stability equations in arbitrary coordinates and different flow regimes, in: 44th AIAA Fluid Dynamics Conference, AIAA, ISBN: 978-1-62410-289-9, 2014.

[7] M. H. Holmes, Introduction to Perturbation Methods, Texts in Applied Mathematics, Springer, ISBN: 978-0-387-94203-2, 1995.

[8] U. Ehrenstein, F. Gallaire, On two-dimensional temporal modes in spatially evolving open flows: the flat-plate boundary layer, Journal of Fluid Mechanics 536 (2005) 209–218.

[9] F. Alizard, J. Robinet, Spatially convective global modes in a boundary layer, Physics of Fluids 19 (11) (2007) 114–105.

[10] D. Rodríguez, Global instability of laminar separation bubbles, Ph.D. thesis, Universidad Politécnica de Madrid (2010).

[11] K. J. Groot, F. Pinna, B. W. van Oudheusden, On closing the streamwise biglobal stability problem: the effect of boundary conditions, in: 8th IUTAM-ABCM Symposium on Laminar-Turbulent Transition, Elsevier, Rio de Janeiro, 2014.

[12] V. Theofilis, Advances in global linear instability analysis of nonparallel and three-dimensional flows, Progress in Aerospace Sciences 39 (4) (2003) 249–315.

[13] T. Herbert, Parabolized stability equations, Annual Review of Fluid Mechanics 29 (1997) 245–283.

[14] M. Gaster, A note on the relation between temporally-increasing and spatially-increasing disturbances in hydrodynamic stability, Journal of Fluid Mechanics 14 (1962) 222–224.

[15] E. Åkervik, U. Ehrenstein, F. Gallaire, D. Henningson, Global two-dimensional stability measures of the flat plate boundary-layer flow, European Journal of Mechanics B/Fluids 27 (5) (2008) 501–513.

[16] F. White, Viscous Fluid Flow, McGraw Hill Series in Mechanical Engineering, McGraw-Hill Professional Publishing, ISBN: 007-124493-X, 1991.

Assessment of Gas-Surface Interaction Modelling for Lifting Body Re-Entry Flight Design

Alan Viladegut

Aeronautics and Aerospace Department, von Karman Institute for Fluid Dynamics, Belgium, alan.viladegut@vki.ac.be

Supervisor: Olivier Chazot

Professor, Aeronautics and Aerospace Department, von Karman Institute for Fluid Dynamics, Belgium, olivier.chazot@vki.ac.be

University Supervisor: Roberto M. Flores

Professor, Aerospace Department, Universitat Politècnica de Catalunya (UPC), Spain, rflores@cimne.upc.edu

Abstract

Spacecrafts intended to re-enter the atmosphere at hypersonic regimes should consider the wall catalytic activity on their design phase. Accurate catalytic models are required to maximize mission efficiency. This paper reviews different approaches to describe catalysis and proposes a simple catalytic model based on the *Recombination Probability* γ. The model is first applied on copper for freestream definition at the Plasmatron. A reference catalysis of $\gamma_{ref} = 0.0265 \pm 26.42\%$ at 50 mbar and $\gamma_{ref} = 0.0156 \pm 40.81\%$ at 100 mbar is obtained. Then, the results of a testing campaign suggesting that probe geometry and freestream conditions could influence the *Recombination Probability* in such a simplified modelling are discussed.

Keywords: Catalysis, Modelling, Plasmatron, Mini-Max methodology, Probe geometry.

1. Introduction

Space vehicles re-entering an atmosphere at hypersonic velocities face extreme heat flux conditions. A bow shock wave appears in front of the vehicle after which molecules dissociate into atoms and the gas becomes a mixture of species. Diffusive effects are confined inside a thin boundary layer close to the body. The processes involved within this layer are responsible for the energy balance at the wall of the Thermal Protection System (TPS). If conduction inside the TPS is neglected, both convective and diffusive heatings should be compensated by radiative heat flux. An accurate characterization of the flow diffusive properties and an appropriate gas-surface interaction model is necessary for both payload integrity and overall mission efficiency.

One important term in the energy balance at the wall is the diffusive heat flux, which is induced by the gas-surface interaction phenomena. Its expression can be found in Eq. 1, where ρ is the gas density, c_i the mass fraction of i-species, D the mass diffusion coefficient and h_i is the enthalpy of the reaction. Wall catalysis rules the diffusive heat flux if ablation does not take place.

$$\dot{q}_d = \sum \rho D \frac{\partial c_i}{\partial \eta} h_i \tag{1}$$

Many efforts have been made since the late 50's to account for chemical reactions in hypersonic boundary layers. Lees [1] introduced in 1956 the relevance of the Lewis number ($Le = \rho D c_p / \lambda$) in both frozen and equilibrium boundary layers. Then, in 1958 Fay and Riddell [2] gave a mathematical expression that is still in use for flight extrapolation methodologies such as the Local Heat Transfer Simulation developed at IPM by Kolesnikov [3] and adapted at VKI [4]. Also in 1958 Goulard [5] extended the conservative assumption of full recombination at the wall used by Lees and Fay and Riddell to finite rate catalytic activity, being the first to introduce the concept of *Recombination Probability* (γ) for re-entry applications. This coefficient is still in use in many non-equilibrium CFD computations.

It is the purpose of this work to review different approaches for modelling catalysis. In Section 2 two strategies are presented: finite rate chemistry models (microscopic description) and γ-model (macroscopic approach) . The second one is applied at the VKI-Plasmatron for both plasma freestream and material characterization. The VKI post-processing tools are reviewed in Section 3 and the consolidation of the Mini-Max method for a reference catalysis definition on copper is presented in Section 4. After that, another testing campaign is carried out in Section 5 to identify other variables involved in the modelling that were not fully understood in previous VKI studies.

2. Catalytic modelling

During a recombination process between two atoms into a molecule, the presence of a third body is generally required. It could be either another atom/molecule if the process is a volume reaction or the wall itself for surface reactions. The third body remaining unchanged, it is named a catalyst of the process. Catalysis is nothing else than a quantification of the wall microscopic properties that enhance recombination while acting as a third body. There are different but equivalent ways to express these properties depending on the level of approach. The direct modelling of the reaction rate constant (k_w) belongs to what we call here the *microscopic* description of catalysis, while the so-called γ-models (being γ the *Recombination Probability*) is a *macroscopic* approach due to the implied simplifications. Either k_w or γ require modelling for wall boundary conditions implementation in CFD.

2.1. The microscopic description

The mass production (or consumption) of species i at the wall is described by the reaction rate ($\dot{\omega}$) given in Eq. 2 and depends on three variables: partial density of reactants ($\rho_i = \rho c_i$), reaction order (n) and reaction rate constant (k_w). The backward reaction rate constant is normally neglected in the production rate for surface reactions [6; 7]. Eq. 3 is implemented as wall boundary condition for the species equations to consider mass conservation at the surface. This expression becomes more complex in multispecies mixtures as explained by Ramshaw [8], Scott [9] and Barbante [10]. The units of k_w vary depending on the reaction order. For instance, it has velocity units assuming first order reaction ($n = 1$).

$$\dot{\omega} = k_w \left(\rho c_i\right)^n \tag{2}$$

$$\rho D \left.\frac{\partial c_i}{\partial \eta}\right|_w = k_w \rho c_i \tag{3}$$

Many microscopic catalytic models can be found in literature. They are known as Finite Rate Chemistry models. Most of them are based in different steps to describe wall processes. The relevance of each process normally depends on wall temperature T_w and pressure P establishing different levels of catalysis. Some of the steps are shown in Fig. 1.

- Diffusion of atoms towards the wall.
- Chemical Adsorption: Atoms attach to the surface through a chemical bond. They are known as adatoms.
- Eley-Rideal Mechanism: A gas-phase atom reacts with an adatom. It takes place at low T_w when there are large numbers of adatoms spread over the surface. It is related to low catalytic conditions.
- Langmuir-Hinshelwood Mechanism: At higher T_w, adatoms diffuse throughout the surface until they react with another adatom. Catalysis increases with T_w.
- Thermal Desorption: Adatoms leave the surface in the form of an atom at even higher T_w.
- Diffusion of molecules away from the wall.

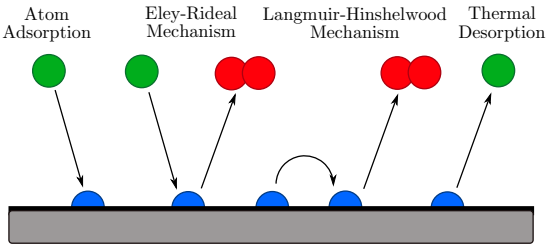

Figure 1: Catalytic processes in wall reaction.

Considering literature, it is worth to remark the work of Seward [11] who proposed a description for adsorption, E-R recombination and thermal desorption processes and balanced them at steady state. New parameters such as surface coverage θ and sticking coefficient S were introduced among others to model catalysis. They turned out to be extensively used in nowadays models. For instance, Nasuti [12] in 1996 and Barbato [13] in 2000 followed the same strategy

but considering all four wall processes for each reaction. Moreover, they proposed to express $\dot{\omega}$ as an Arrhenius function where activation energies (E_a) had also to be defined. In addition, Armenise [14] extended the modeling by considering non-Boltzmann behavior on the vibrational distribution functions near the surface in 2006. It was not until 2010 that Di Benedetto and Bruno [15] proposed that a model simplification might be convenient for further experimental validation.

The effect of P can be seen in Thoemel's thesis [16]. He showed kinetic Monte Carlo computation results for a mixture of O and CO where the increase of P (and partial pressures) turned into a catalysis reduction. It is worth mentioning also his study of material roughness effects on catalysis determination [17]. Following the idea of Y. C. Kim [18], he considered atoms diffusion to account for the wet surface seen by the gas due to material roughness. Other models taking P into account are presented by Fertig [19] and MacLean et al. [20; 21], with the last one being very interesting for the Equilibrium concentrations reached at the wall under the highest catalytic conditions.

2.2. The macroscopic description

It is important to mention that k_w and γ are directly related by the expression in Eq. 4 given by Goulard [5] for binary mixtures and first order reactions. He defines γ as the ratio of the number of atoms recombining on a surface per unit area and time to the total number of atoms striking the surface per unit area and time. Using the *microscopic* models described in the previous section under non-binary mixtures one could obtain the *Recombination Probability* for each recombining element through a steady-state mass balance at the wall. This balance could not only consider the atom recombination in the form of $2X \rightarrow X_2$ but also the coupling between species to form two element based molecules such as NO in air mixtures: $O + N \rightarrow NO$.

$$\gamma = k_w \sqrt{\frac{2\pi m}{k_B T_w}} \tag{4}$$

The γ-model used at VKI is a macroscopic approach that simplifies the problem by considering the gas mixture as a binary mixture, where there is no coupling between different elements and characterizes all surface catalytic reactions in one single parameter. The detailed description offered by the microscopic models is lost but the wall boundary conditions for species equations is simplified in such a way that experimental validation in plasma facility is feasible. The change of perspective due to the assumptions made in this model might be weak but, if valid enough, it would be applicable for a faster thermal protection system design. This work assesses the validity of such an engineering approach applied at the VKI-Plasmatron facility and gives the first steps towards the validation for catalytic modelling.

3. The VKI-Plasmatron facility

Plasma facilities are used to reproduce the high temperature environment encountered during re-entry. Inductively Coupled Plasma (ICP) wind tunnels are specially suitable for catalytic studies due to the gas purity they provide. The VKI-Plasmatron is a 1.2MW ICP facility able to use 2kV at 400kHZ to create the plasma and expand it into a 2.5m long and 1.4m diameter test chamber through a 160mm diameter torch.

A copper calorimeter is normally used to measure the heat flux $\dot{q}_w$ for boundary layer outer edge enthalpy H_e rebuilding. It is installed at the center of a water cooled flat-faced 50mm diameter holder with 11.75mm radii on the edge (ESA *Standard Probe*). Heat flux is measured considering that all the energy is transferred to the water circulating inside the calorimeter by Eq. 5. The uncertainty of this method is ±10%. Static pressure P_s is measured with an absolute pressure transducer (Memberanovac DM 12, Leybold Vacuum, OC Oerlikon Corporation AG, Switzerland) with ±0.7 hPa accuracy. Dynamic pressure P_{dyn} data is taken with a variable reluctance pressure transducer (DP-15, Valydine Engineering Corp, Northridge, CA USA) of ±0.2% uncertainty. Due to torch instabilities, uncertainties increase to ±2% for both static P_s and P_{dyn}.

$$\dot{q}_w = \frac{\dot{m}_w c_p \left(T_{out} - T_{in}\right)}{A} \tag{5}$$

3.1. Outer edge enthalpy rebuilding

An in-house developed stagnation line boundary layer code (*CERBOULA*) interacts with Plasmatron measurements in order to quantify other relevant variables. This code assumes thermal equilibrium and chemical non-equilibrium to establish a relation between H_e and wall catalysis γ for given $\dot{q}_w$, P_s and T_w measurements. This relation is shown in Fig. 2.

The shape of this relation makes the use of high catalytic materials (such as copper or silver) suitable for H_e determination. As a matter of fact, Kolesnikov [22]

used to consider silver as fully catalytic for his measurements. However, testing these materials under Air plasmas make an oxide layer appear at the wall. This is shown by Kolesnikov [22] for Ag_2O and by Driver [23] for both CuO and Cu_2O. Material oxidation tends to reduce the surface catalytic activity. Thus, the H_e can only be estimated if an accurate γ is previously given. A method to estimate a γ_{ref} on copper for enthalpy rebuilding is presented in the following section.

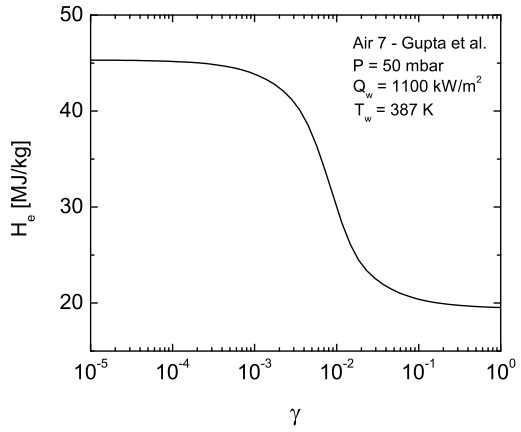

Figure 2: Example of the relation between H_e and γ given by *CERBOULA*.

4. Mini-Max methodology application at VKI

The Mini-Max method to estimate a reference *Recombination Probability* for copper (γ_{ref}) is first applied by Krassilchikoff [24] and a model dependent on P_s at $T_w = 350K$ is proposed by Panerai [25]. Experiments presented in this section provide consolidation of γ_{ref} model considering other chemical models and direct T_w measurements.

The Mini-Max procedure is rather simple. Three heat flux measurements are taken under the same plasma conditions but on three different materials. Differences in $\dot{q}_w$ are the consequence of different catalytic activities. Materials used during the Mini-Max application are silver (high γ), copper (γ_{ref}) and SiO_2-Quartz (low γ). The three $\dot{q}_w$ measurements provide three H_e-γ relations, whose intersection over Copper provides a range for both H_e and γ as shown in Fig. 3. H_e can only be found within the range defined by two limiting cases: Non-Catalytic Quartz as a maximum and Full-Catalytic Silver as a minimum. Thus, this method defines a range for both γ_{ref} and H_e.

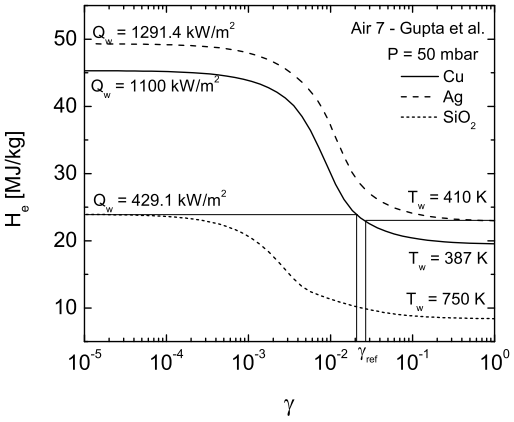

Figure 3: Mini-Max Method Application.

4.1. Mini-Max testing campaign

A testing campaign has been carried out for Mini-Max methodology application. Two P_s conditions have been considered: 50 and 100 mbar. All measurements are taken under Air plasma at $\dot{m} = 16g/s$. Plasmatron Power has been adapted in order to target certain $\dot{q}_w$ measurement conditions on the reference material calorimeter (copper). Nine heat flux conditions are fixed for each P_s considered. This allows to obtain a distribution of γ throughout different plasma conditions. All probes are located at 445mm from the torch exit. P_{dyn} has been measured under the same configuration prior to Mini-Max application because only three samples can be introduced in the test chamber. Measurements are listed in Tab. 1. In addition, a type-E Thermocouple has been attached on the rear part of both silver and copper calorimeters for T_w measurements (see Figure 4). On SiO_2-Quartz a surface temperature of $750K$ has been assumed following the experiments of Kolesnikov [22].

4.2. Reference Recombination Probability determination

Different chemical models for 7-species Air mixture have been considered during the postprocessing. While Dunn & Kang [26] and Park [27] models give similar results, Gupta et al. [28] leads to a higher H_e at low catalytic activities providing a broader range of data. Nevertheless, catalycity could not be retrieved from all plasma conditions since intersection of both silver and SiO_2-Quartz over copper's H_e-γ relations did not take place. This is expected to be a problem of uncertainties on the chemical model chosen

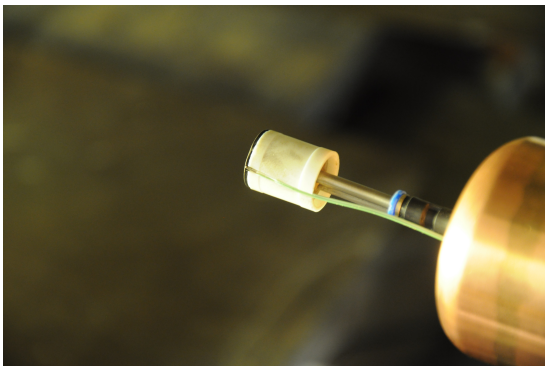

Figure 4: Thermocouple attached to the rear metallic part of the calorimeter for surface temperature measurement.

for numerics. This issue is already mentioned by Kovalev [29] using a similar H_e rebuilding procedure.

Results of γ_{ref} and H_e are summarized in Tab. 2 and shown in Fig. 5-6. Heat flux measurements are interpolated with a linear fit to match the target conditions of the testing campaign on copper before the numerical post-processing. Given a range of γ for each intersecting plasma condition, an average value is chosen as γ_{ref}. The corresponding interval is computed as a percentage over γ_{ref} and named γ^{err}_{ref}. The reference catalysis allows the determination of H_e, which is also associated to a range due to the intersection of the curves. This range is given also as a percentage over the rebuilt H_e and it is named H^{err}_e.

Testing results show that at 50 mbar an average γ_{ref} of 0.0265 with an associated range of 26.42% leads to maximum H_e variations of 13.05%, making γ_{ref} model much more accurate at this pressure. To mention that Fletcher [30] measured the O *Recombination Probability* as 0.027 in an ICP facility using LIF methods and Cauquot [31] 0.025 on Cu_2O in a microwave plasma reactor. At 100 mbar and above 900 kW/m^2 heat fluxes, an average γ_{ref} of 0.0156 within a range of 40.81% is obtained with a maximum enthalpy tolerance of 12.81%.

As final remark, if one intends to rebuild H_e using the γ_{ref}-model, it is highly recommended either to check the database provided above before testing or apply the Mini-Max methodology at the desired Plasmatron conditions prior the testing campaign. With this study the Mini-Max is consolidated for catalysis determination. However, it is only useful at certain pressure and power conditions.

Table 1: Heat flux measurements during Mini-Max application: b)50 mbar; c)100 mbar.

Test	Power	$\dot{Q}^{Cu}_w$	$\dot{Q}^{Ag}_w$	$\dot{Q}^{Qz}_w$
	kW	kW m^{-2}	kW m^{-2}	kW m^{-2}
1b	128	306.1	349.5	144.1
2b	153	511.3	575.2	190.4
3b	190	716.5	749.1	223.1
4b	228	902.8	1074.6	278.3
5b	256	1088.7	1315.4	380.1
6b	282	1295.8	1553.7	486.1
7b	291	1544.8	1840.2	684.7
8b	349	1700.7	2000.9	754.1
9b	426	2003.6	2369.7	795.1
1c	128	301.8	420.7	289.4
2c	157	504.8	573.9	404.5
3c	175	706.4	789.0	498.5
4c	195	905.4	997.8	537.6
5c	229	1102.6	1223.5	560.9
6c	259	1322.5	1430.7	660.2
7c	268	1521.2	1652.6	739.6
8c	294	1701.3	1905.7	815.9
9c	343	2024.7	2271.0	892.7

5. Catalysis on the Damköhler probes

An additional testing campaign is carried out at the VKI Plasmatron in order to address the possible relation between the chemical reactions inside the boundary layer and the wall catalysis extracted from *CERBOULA*. For this, the three Damköhler probes shown in Fig. 7 are injected inside the same plasma conditions with a copper calorimeter at the center of each probe. Increasing the size of the sample promotes recombination within the bulk of the boundary layer. Similar tests were performed by Panerai [25] over C/SiC samples. He showed how different probe geometries lead to different values of γ on the same material. The main difference with the current campaign is the control of T_w on the calorimeters. While TPS surface temparatures can change by several hundreds from one probe to another, calorimeter surface temperature is assumed to remain at 350K for all of them.

The same testing conditions shown in Section 4 are applied here. Measurements are resumed in Tab. 3. Dynamic pressure is computed with the relations given by Marotta [32]. A linear extrapolation is done over the *Standard* probe to define heat flux measurements that could not be taken during the campaign. The relation between H_e-γ is again computed with *CERBOULA* for each measurement. Gupta et al. [28]

Table 2: *Recombination Probability* and boundary layer outer edge enthalpy results with Gupta et al. [28] chemical model after Mini-Max methodology application: b)50 mbar; c)100 mbar.

Test	γ_{ref}	γ^{err}_{ref}	H_e	H^{err}_e
	-	%	MJ/kg	%
5b	0.02367	11.59	23.33	4.10
6b	0.02423	18.87	26.98	8.58
7b	0.02596	22.66	30.45	11.44
8b	0.02783	24.98	33.57	13.05
9b	0.03081	26.42	37.46	12.47
2c	0.00456	80.32	15.66	36.31
3c	0.00762	56.03	18.27	22.01
4c	0.01100	40.81	20.86	12.81
5c	0.01505	24.88	23.33	6.35
6c	0.02079	6.81	25.65	1.44

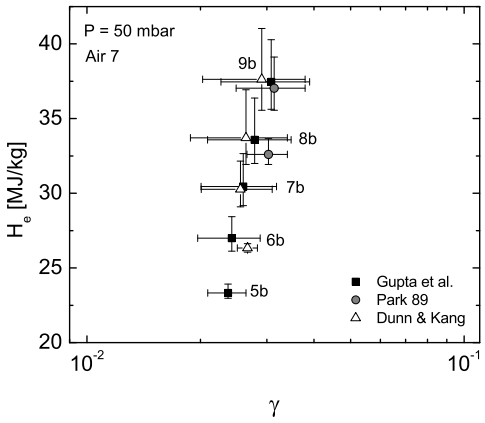

Figure 5: Copper *Recombination Probability* at 50 mbar.

chemical model is used (Penarai [25] used Dunn & Kang [26] for the post-processing). The γ_{ref} model consolidated with the Mini-Max method defines H_e and *Recombination Probabilities* for both *Frozen* and *Equilibrium* probes. Results are summarized in Tab. 4 and shown in Fig. 8-9.

While differences between catalytic activities on both *Standard* and *Frozen* probes can not be appreciated, the *Equilibrium* probe shows not only a significantly different value of γ on most of the testing conditions but also a growing catalytic activity with H_e. At this moment there is no physical explanation to support that conclusion. However, one should remember that the γ-model is just a simplification of the typical Finite Rate Chemistry models. Thus, it is possible that other variables different than T_w and P_s

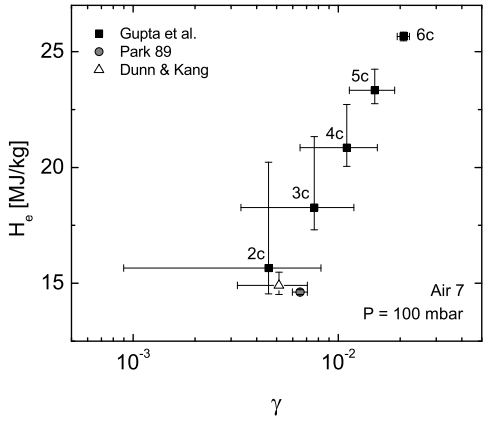

Figure 6: Copper *Recombination Probability* at 100 mbar.

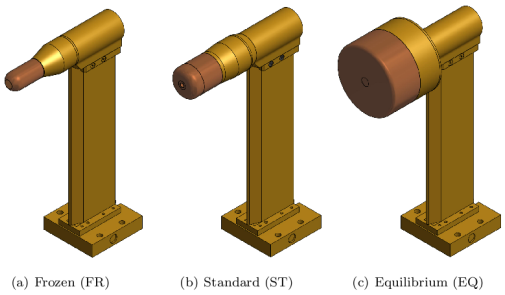

(a) Frozen (FR) (b) Standard (ST) (c) Equilibrium (EQ)

Figure 7: The VKI Damköhler probes.

could be used to model catalysis in order to keep the hypotesis of first order reactions, air as a binary mixture and that there is no coupling between O and N. More testing with different geometries is encouraged in order to verify this behavior.

6. Conclusions

Theory behind Finite Rate Chemistry models has been reviewed and a new simpler catalytic model based on the *Recombination Probability* of atoms has been proposed. The new modelling strategy is focused on its feasible validation in Plasma facility. The simplistic approach that is proposed could be used for fast and accurate enough TPS designs in the future. The first steps toward its validation at the Plastmatron facility have been shown. A method to estimate copper catalytic activity under different plasma conditions and different probe configurations have been presented.

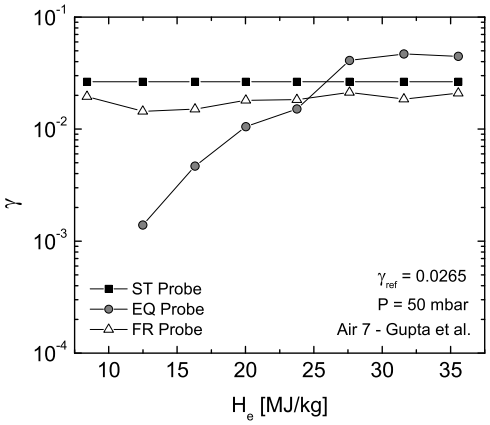

Figure 8: *Recombination Probability* of the Damköhler probes at 50 mbar.

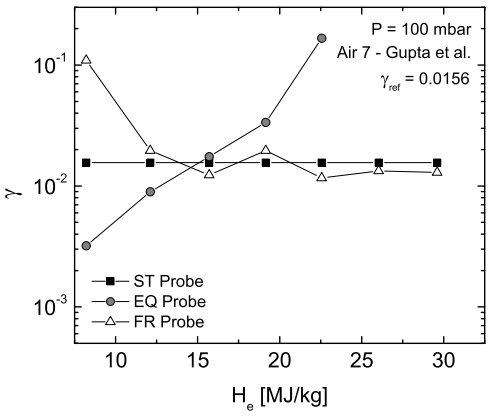

Figure 9: *Recombination Probability* of the Damköhler probes at 100 mbar.

Table 3: Heat flux measurements during Damköhler probes testing campaign: b)50 mbar; c)100 mbar.

Test	$\dot{Q}_w^{ref}$ kW m^{-2}	$\dot{Q}_w^{ST}$ kW m^{-2}	$\dot{Q}_w^{EQ}$ kW m^{-2}	$\dot{Q}_w^{FR}$ kW m^{-2}
1b	300	-	-	-
2b	500	-	-	-
3b	700	-	-	-
4b	900	-	-	-
5b	1100	-	-	-
6b	1300	1338.5	821.1	1492.2
7b	1500	1518.7	987.4	1726.4
8b	1700	1740.0	1136.9	1900.6
9b	2000	2018.9	1389.7	2315.1
1c	300	276.6	122.4	367.8
2c	500	524.2	262.3	642.6
3c	700	703.4	415.0	1184.0
4c	900	926.5	577.2	124.2
5c	1100	-	-	-
6c	1300	1309.4	743.5	1797.2
7c	1500	1536.5	822.4	1849.9
8c	1700	1713.1	977.2	2083.0
9c	2000	2001.4	1187.7	2412.6

The Mini-Max methdology provides copper catalysis for further boundary layer outer edge enthalpy determination. It has been shown that *Recombination Probability* is independent of enthalpy levels at 50 and 100 mbar. Unfortunately, the number of results provided by this methodology depends on the chemical model used to solve the stagnation line non-equilibrium boundary layer.

In addition, tests on different geometries provide different catalytic activities. This conclusion only stands for one probe. Experimental consolidation of this behavior is on going using hemispherical probes. The key question to answer is if this result is a consequence of the model simplication or it is something implicit in the real microscopic processes at the wall.

References

[1] L. Lees, Laminar Heat Transfer Over Blunt-Nosed Bodies at Hypersonic Flight Speeds, Jet Propulsion 26, Num. 4 (1956) 259–269.

[2] J. A. Fay, F. R. Riddell, Theory of Stagnation Point Heat Transfer in Dissociated Air, Journal of the Aeronautical Sciences 25, Num. 2 (1958) 73–85.

[3] A. Kolesnikov, The Concept of Local Simulation for Stagnation Point Heat Transfer in Hypersonic Flows: Application and Validation, AIAA Paper 2000-2515.

Table 4: Damköhler probes catalycities: b)50 mbar (γ_{ref} = 0.0265 ± 26.42%); c)100 mbar (γ_{ref} = 0.0156 ± 40.81%).

Test	H_e MJ/kg	γ^{EQ} -	γ^{EQ}_{Err} %	γ^{FR} -	γ^{FR}_{Err} %
1b	8.41	-	-	0.01954	26.26
2b	12.48	0.00139	94.75	0.01441	45.63
3b	16.31	0.00467	82.38	0.01506	43.15
4b	20.03	0.01052	60.30	0.01812	31.61
5b	23.76	0.01515	42.83	0.01831	30.9
6b	27.61	0.04105	54.91	0.02129	19.66
7b	31.60	0.04687	76.87	0.01855	29.99
8b	35.57	0.04474	68.83	0.02092	21.05
1c	8.20	0.00320	79.49	0.10938	601.17
2c	12.12	0.00894	42.69	0.01964	25.88
3c	15.70	0.01744	11.79	0.01231	21.11
4c	19.15	0.03359	115.3	0.01958	25.51
5c	22.56	0.16663	968.1	0.01164	25.40
6c	26.04	-	-	0.01335	14.44
7c	29.61	-	-	0.01295	16.97

[4] P. F. Barbante, O. Chazot, Flight Extrapolation of Plasma Wind Tunnel Stagnation Region Flowfield, Journal of Thermophysics and Heat Transfer 20, Num. 3 (2006) 493–499.

[5] R. Goulard, On Catalytic Recombination Rates in Hypersonic Stagnation Heat Transfer, Jet Propulsion 28, Num. 11 (1958) 737–745.

[6] P. W. Atkins, Physical Chemistry, Oxford University Press, 1994.

[7] P. M. Chung, Chemically Reacting Non-Equilibrium Boundary Layers, Advances in Heat Transfer, 1965.

[8] J. D. Ramshaw, Self-Consistent Binary Diffusion in Multicomponent Gas Mixture, J. Non-Equilib. Thermodyn. 15 (1990) 295–300.

[9] C. D. Scott, Wall Catalytic Recombination and Boundary Conditions in Non-Equilibrium Hypersonic Flows, Second Joint Europe/US Short Course in Hypersonics.

[10] P. F. Barbante, Accurate and Efficient Modelling of High Temperature Nonequilibrium Air Flows, Ph.D. thesis, von Karman Institute for Fluid Dynamics / Université Libre de Bruxelles (2001).

[11] W. A. Seward and E. J. Jumper, Model for Oxygen Recombination on Silicon-Dioxide Surfaces, Journal of Thermophysics 5, Num. 3 (July-September 1991) 284–291.

[12] F. Nasuti, M. Barbato, C. Bruno, Material-Dependent Catalytic Recombination Modeling for Hypersonic Flows, Journal of Thermophysics and Heat Transfer 10, Num. 1 (January-March 1996) 131–136.

[13] M. Barbato, S. Reggiani, C. Bruno, J. Muylaert, Model for Heterogeneous Catalysis on Metal Surfaces with Applications to Hypersonic Flows, Journal of Thermophysics and Heat Transfer 14, Num. 3 (July-September 2000) 412–420.

[14] I. Armenise, M. Barbato, M. Capitelli, E. Kustova, State-to-State Catalytic Models, Kinetics, and Transport in Hypersonic Boundary Layers, Journal of Thermophysics and Heat Transfer 20, Num. 3 (2006) 465–476.

[15] S. D. Benedetto, C. Bruno, Novel Semi-Empirical Model for Finite Rate Catalysis with Application to PM1000 Material, Journal of Thermophysics and Heat Transfer 24, Num. 1 (January-March 2010) 50–59.

[16] J. Thoemel, Surface Catalysis in High Enthalpy Flows, Ph.D. thesis, von Karman Institute for Fluid Dynamics / Rheinisch-Westfälische Technische Hochschule Aachen (2012).

[17] J. Thoemel, O. Chazot, P. Barbante, Aspects of Advanced Catalysis Modeling for Hypersonic Flows, Center for Turbulence Research Proceedings of the Summer Program 2008.

[18] Y. C. Kim, M. Boudart, Recombination of O, N, and H Atoms on Silica: Kinetics and Mechanisms, Langmuir - American Chemical Society 7 (1991) 2999–3005.

[19] M. Fertig, G. Herdrich, M. Auweter-Kurtz, SiO_2 Catalysis Modeling for CFD Calculations, 39th AIAA Thermophysics Conference.

[20] J. Marschall, M. MacLean, Finite-Rate Surface Chemistry Model, I: Formulation and Reaction System Examples, 42nd AIAA Thermophysics Conference AIAA 2011-3783.

[21] M. MacLean, J. Marschall, D. M. Driver, Finite-rate surface chemistry model, ii: Coupling to viscous navier-stokes code, 42nd AIAA Thermophysics Conference AIAA 2011-3784.

[22] A. Kolesnikov, A. Gordeev, S. Vasilevskii, Study of Catalytic Heating Effects on Metals and Quartz for ExoMars Entry Conditions, 5th European Conference for Aeronautics and Space Sciences (EUCASS 2013), Munich, Germany,.

[23] A. Nawaz, D. Driver, I. Terrazas-Salinas, S. Sepka, Surface Catalysis and Oxidation on Stagnation Point Heat Flux Measurements in High Enthalpy Arc Jets, 44th AIAA Thermophysics Conference, San Diego CA, United States 2013-3138.

[24] H. W. Krassilchikoff, Procedure for the Determination of the Cold Copper Catalycity, VKI Project Report VKI Project Report 2006-18.

[25] F. Panerai, Aerothermochemistry Characterization of Thermal Protection Systems, Ph.D. thesis, von Karman Institute for Fluid Dynamics / Università Degli Studi Di Perugia (2012).

[26] M. G. Dunn, S.-W. Kang, Theoretical and Experimental Studies of Reentry Plasmas, Contractor Report 2232, NASA Langley Research Center, Hampton, VA, USA. Prepared by Cornell Aeronautical Laboratory, Inc. Buffalo, NY, 14221.

[27] C. Park, Nonequilibrium Hypersonic Aerothermodynamics, Wiley-Interscience, John Wiley & Sons, 1990.

[28] R. N. Gupta, J. M. Yos, R. A. Thompson, K.-P. Lee, A Review of Reaction Rates and Thermodynamic and Transport Properties for an 11-Species Air Model for Chemical and Thermal Nonequilibrium Calculations to 30000K, NASA Reference Publication 1232.

[29] R. V. Kovalev, V. I. Vlasov, G. N. Zalogin, Experimental and Numerical Modelling of Heterogeneous Recombination for Martian Entry Conditions, 5th European Conference for Aeronautics and Space Sciences (EUCASS 2013), Munich, Germany,.

[30] J. M. Meyers, W. P. Owens, D. G. Fletcher, Surface Catalyzed Reaction Efficiencies in Nitrogen and Oxygen Plasmas from Laser Induced Fluorescence Measurements, 44th AIAA Thermophysics Conference, San Diego CA, United States 2013-3139.

[31] P. Cauquot, S. Cavadias, J. Amouroux, Thermal Energy Accomodation from Oxygen Atoms Recombination on Metallic Surfaces, Journal of Thermophysics and Heat Transfer 12, Num. 2 (April-June 1998) 206–213.

[32] Marotta, Investigation on the Driving Phenomena Characterization GSI in Plasmatron Facility, VKI Project Report VKI PR 2011-17.

UNCERTAINTY QUANTIFICATION

Quantifying Inflow Uncertainties for CFD Simulations of Dispersion in the Atmospheric Boundary Layer

Clara García Sánchez

Environmental and Applied Fluid Dynamics Department, von Karman Institute for Fluid Dynamics, Belgium, clara.garciasanchez@vki.ac.be

Supervisors: Catherine Gorlé and Jeroen van Beeck

Assistant Professor, Department of Civil Engineering and Engineering Mechanics, Columbia University, New York, USA, catherine.gorle@columbia.edu

Associate Professor, Environmental and Applied Fluid Dynamics Department, von Karman Institute for Fluid Dynamics, Belgium, vanbeeck@vki.ac.be

University Supervisor: Gustaaf van Tendeloo

Professor, EMAT, Department of Physics, University of Antwerp, Belgium, staf.vantendeloo@uantwerpen.be

Abstract

The prediction of air quality within the built environment is a main concern in our present society due to the rapid increase of pollution. The prediction of wind and pollution footprints is a challenging task for the computational wind engineering community, due to the high intrinsic variability of the wind conditions combined with the complexity of the building structures. One main approach to forecast Atmospheric Boundary Layer (ABL) flows in complex geometries is the use of Reynolds-averaged Navier-Stokes (RANS) simulations. The traditional boundary conditions used to perform RANS simulations of the ABL are based on a neutral stratified boundary layer, where the velocity, the turbulent kinetic energy and the dissipation rate profiles are exact solutions to the Reynolds-averaged equations. Nevertheless, the natural variability of wind direction and magnitude implies that time-independent neutral ABL might not provide a realistic representation of the boundary conditions. Therefore, the present research explores the application of an innovative boundary condition based on different fields extracted from the mesoscale model Weather Research and Forecasting (WRF), which is capable of forecasting atmospheric flow patterns and their evolution based on global models. These boundary conditions based on mesoscale motions will allow the definition of a methodology for including inflow condition variability through an uncertainty quantification (UQ) approach based on larger scale fields, granting the approach applicability in any location.

Keywords: boundary conditions, dispersion, ABL, RANS, WRF

1. Introduction

Nowadays, the high expansion rate of urban areas due to the population growth is increasing the interest in accurately assessing wind and dispersion patterns inside complex and diverse configurations, such as high rise buildings and residential neighbourhoods. Correctly forecasting wind flows is essential for a wide range of applications such as pedestrian wind comfort, air quality level assessments or potential urban wind energy resources. However, considering that the urban environment is characterized by complex and heterogenous structures, the application of Computational Fluid Dynamics (CFD) to predict wind fields represents the most appropriate approach in order to efficiently forecast three-dimensional wind flows and concentration fields within the urban canopy.

The traditional boundary conditions used in CFD simulations of the ABL correspond to a steady state neutral ABL. The profiles specified for the velocity

and the turbulence quantities are an exact solution to the governing RANS equations [1; 2; 3]. These boundary conditions are widely used in the field of wind engineering, and they are recognised as best practice guidelines for CFD simulations of the atmospheric boundary layer [4].

However, in the past few years, there is a growing interest in improving the realism within the boundary conditions applied for simulations of the atmospheric boundary layer. The atmosphere is constantly evolving due to large scale motions, which lead to a wide variability in wind direction and velocity. Consequently, a time-averaged solution corresponding to an steady-state neutral ABL does not represent a realistic boundary condition. In order to improve this, the boundary conditions applied to predict flows in the ABL should include the effect of larger scale motions, such as mesoscale phenomena. Within this article, the first step towards addressing this challenge is presented through the coupling between the mesocale model WRF and the CFD software OpenFOAM.

The work presented here focuses on transferring information from the mesoscale to the microscale, by interpolating the velocity fields extracted from the WRF outcome of a deterministic simulation, and using them as boundary conditions for the microscale domain in OpenFOAM. Once the boundary conditions are interpolated onto the CFD domain, RANS simulations are performed, and the results from the coupled simulations are compared to the measurement available from the Joint Urban 2003 (JU2003) field experiment. The remainder of the paper is organised as follows. In the first section a short introduction to the set of field measurements, Joint Urban 2003 (JU2003) is presented. Section 3 and 4 present the corresponding mesoscale and microscale simulation set ups. Lastly, section 5 adds the results and conclusions.

2. Joint Urban 2003 field campaign

The main goal of the joint urban 2003 field campaign was to provide quality-assured meteorological and tracer data sets, to establish confidence in CFD simulations of indoor and outdoor dispersion [5]. The experiments were carried out within and around Oklahoma City during one full month in 2003. They include 10 Intensive Observation Periods (IOPs) during which different tracer releases took place, and concentration fields were measured. Wind speed and direction were monitored through different systems, including sonic anemometers and profilers.
The work presented here focuses on the night of the 26th of July 2003, from 23:05 to 23:30. This period is close to IOP9, which is of interest in an on-going dispersion study. In order to compare the CFD results, data from two different types of measurement stations is used: SuperWIDS and PWIDS.
SuperWIDS stations are sonic anemometers capable of measuring three velocity components at a sampling frequency of 10Hz. PWIDS stations are wind monitors which provide velocity magnitude and direction information, sampling each second and averaging each 10 seconds [6]. A map including the location from all the stations is included in figure 1.

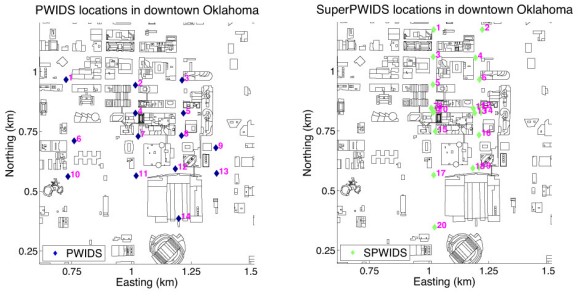

Figure 1: PWIDS and SuperWIDS measurement stations location

3. Numerical Weather Prediction simulations

The mesoscale model used for the coupling is the open-source Weather Research and Forecasting (WRF) developed by Skamarock et al. in 2008 [7]. This numerical weather prediction code reproduces mesoscale dynamics based on reanalysis data. The model covers the atmospheric phenomena that range from synoptic scales ($\sim 2000km$) to individual cloud cells ($\sim 100km$), for example, forecasting convective systems, thunderstorms or hurricanes. In addition, the code includes nesting capability, which allows to reach a resolution of about 1km through embedded nests.

The model integrates the fully compressible non-hydrostatic Euler equations, which are cast in flux form. The equations are written in a terrain-following hydrostatic-pressure coordinate, η, which is defined as:

$$\eta = \frac{(p_h - p_{ht})}{(p_{hs} - p_{ht})} \tag{1}$$

In equation 1, p_h is the pressure at a particular level, p_{hs} is the surface pressure below that p_h and p_{ht} is the top pressure above p_h. The number of η levels chosen

in WRF is specially important considering the resolution of the CFD mesh. Therefore, a higher density of η levels is assigned in the first 100m, where our microscale domain is placed.

3.1. WRF simulation set-up

Several mesoscale simulations were run with different configurations regarding the number of vertical levels, the planetary boundary layer parameterisation and the size of the parent domain. The results were compared to balloon soundings [8] and to the measurements provided by PWIDS15 (inflow station) in order to select the most appropriate configuration, based on the minimisation of the differences between the measurements and the mesoscale outcome [9].. The mesoscale domain configuration finally chosen is presented in figure 2, where four domains are embedded over Oklahoma state, covering an approximate area of 1400 x 1400 km^2. The domains resolutions are progressively: 27 km (parent domain), 9km (d02), 3km (d03), and 1km for the last embedded domain (d04). The total number of grid points in horizontal direction is correspondingly 52, 64, 76, and 76, while in the vertical direction the number of grid points is conserved to 45 in all the domains.

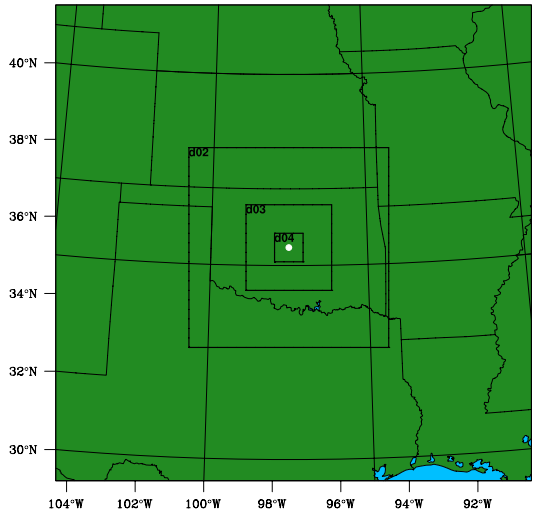

Figure 2: Mesoscale domain configuration.

The simulation is set up for the period of 23:05 to 23:30 of the 26th of July 2003. This period was selected due to the fact that the release of interest was carried out in the same Park location, where high density of monitoring systems was set up, and to the near-neutral stratification during that night time.

The boundary and initial conditions used for the mesoscale simulations are based on 3 hours resolution data extracted from the National Center for Environmental Prediction North American Regional Reanalysis data (NARR, NCEP Reanalysis). The simulation is started one day in advance before the period of interest, in order to spin-up the mesoscale content as indicated previously by different authors [10; 11]. The Mellor-Yamada-Nakanishi-Niino (MYNN) planetary boundary layer scheme is used to run the simulations [12].

3.2. WRF simulation results

The results obtained from the final selected mesoscale simulation are presented in figure 3. The figure presents a contour plot of the horizontal velocity fields extracted at a height of $\sim 30m$, where the central black point represents the location of Oklahoma City. The arrows indicate the flow direction within the mesoscale domain, while the contours present the wind magnitude.

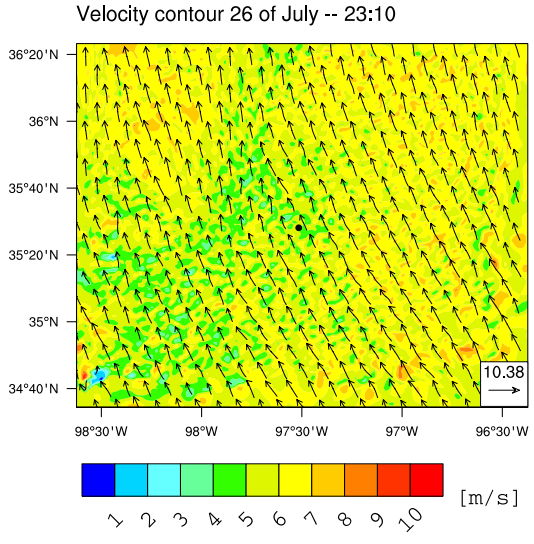

Figure 3: Mesoscale horizontal velocity fields.

As it can be observed through figure 3 the flow inflow direction would correspond to the bottom and right boundaries, corresponding to south-east directions, while the wind outflow would be set for the upper and left boundaries, which correspond to north-west domain boundaries.

4. OpenFOAM CFD simulations

The tool wrf2FOAM developed by CFD+engineering [13] is used to extract the boundary and initial conditions from one time slice of results obtained from the mesoscale simulation presented in the previous section. Wind fields and boundary layer height are interpolated onto the OpenFOAM mesh, which consists of 5.27 million cells, reaching a resolution at the ground of about 2 m. The total domain extends 2 km x 2.4 km horizontally and 1 km in the vertical direction, in order to be consistent with the highest resolution from the WRF simulation (last nested domain $\sim 1km$ resolution). Figure 4 presents a schematic view of the domain, while figure 5 presents the profile of vertical levels included in the first km from the WRF domain.

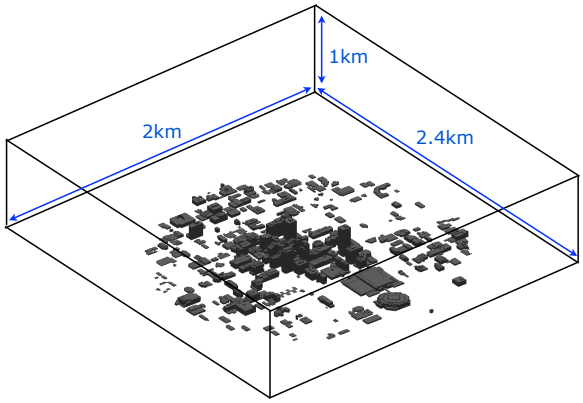

Figure 4: Microscale domain configuration.

The turbulence model selected to close the RANS equations for the simulations is the standard k-ε, widely used for CFD simulations of the atmospheric boundary layer [14; 15; 16]. The wall function applied is the modified rough wall function from Parente et al. [3], for turbulent kinetic energy and epsilon. The discretisation schemes used were second order for pressure and velocity, and first order for the turbulent variables. The simulations are run for 2000 iterations, resulting in a converged solution with residuals under 10^{-7} for all variables.

The boundary conditions provided by the mesoscale code used in the CFD simulations are velocity, friction velocity, and boundary layer height. These fields are extracted from the WRF domain and interpolated onto the OpenFOAM domain at every cell. Furthermore, the friction velocity and the boundary layer height are used to construct the turbulence field [17].

$$u_* = \frac{u(z)\kappa}{ln\left(\frac{z}{z_0}\right)} \quad k = \frac{u_*^2}{\sqrt{C_\mu}}\left(1-\frac{z}{h_g}\right)^2 \quad \varepsilon = \frac{u_*^3}{\kappa z}$$
$$h_g = \frac{u_*}{6f} \quad \mu_t = \rho\kappa u_* z\left(1-\frac{z}{h_g}\right)^4 \quad f = 2\Omega sin(\lambda) \tag{2}$$

In the equations, h_g represents the height of the atmospheric boundary layer; f is the Coriolis term, and Ω is the angular velocity of the earth's rotation, while λ is the latitude of the location of interest. As the total height of the ABL is being simulated, it is necessary to use profiles that vary with increasing height. The previous equations asure that the turbulent kinetic energy and shear stress profiles decrease with height until they vanish at the free atmosphere. These profiles are somehow more realistic than the constant profiles which are only valid for the lower part of the ABL.

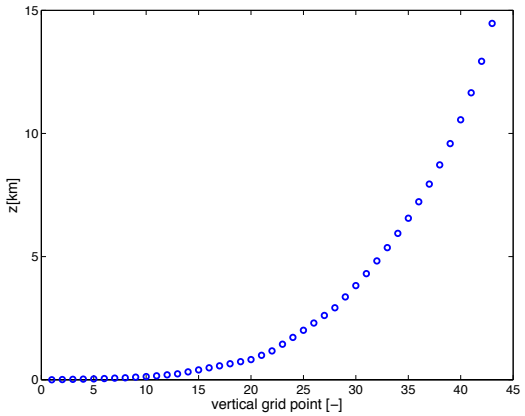

Figure 5: Vertical grid levels WRF simulation.

In order to define the roughness length for the Oklahoma terrain, a 3D minimisation methodology is applied in order to assure consistency between the roughness length provided by WRF, and the logarithmic inflow profile applied for velocity in the CFD simulations. Equation 3 presents the approach applied, while figure 6 shows the evolution of the error with the increase in roughness length, providing an optimum value for the simulation roughness length of $\sim 0.21m$.

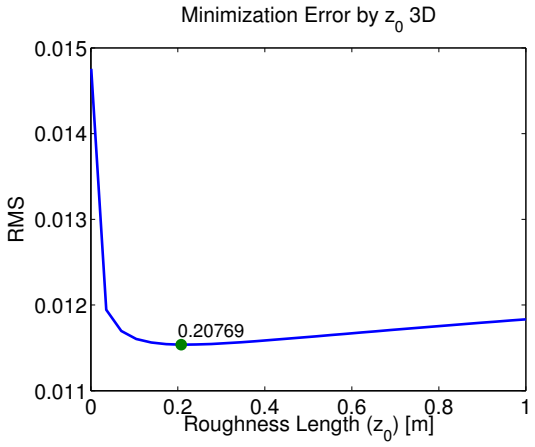

Figure 6: Roughness length error minimisation.

$$error_{rms} = \frac{1}{N} \sum \left(U_{log} - U_{WRF} \right) \tag{3}$$

After running the coupled RANS simulation, a comparison with the available wind measurements was performed. The results are presented in figure 7 where the velocity contour at 8 m height is extracted from the coupled mesoscale-CFD results. From the figure, it can be observed how the flow presents the same wind flow direction as the mesoscale simulation showed in the previous figure 3, therefore the south and south east boundaries are inlets, whereas the north and north west are both outlets. These boundaries are automatically set up based on the wind direction from mesoscale. Due to this flow direction, recirculation areas are created by the buildings mainly in the north-west part of the city, were the outlets are set up.

In order to compare with the experiments, also located at 8 m height, the measurements provided are averaged over 25 minutes corresponding to the period of interest. The relative differences between the coupled simulation outcome and the experiments are presented by circles, whose radius are determined following equation 4,

$$error = \frac{|U_{CFD} - U_{exp}|}{|U_{exp}|} \tag{4}$$

The average error over all the measurement stations is 0.43. The color inside each circle corresponds to the type of station, white for PWIDS and grey for SuperWIDS. The edge colour is based on the Hit Rate criterium, N_i, computed through equation 5 [18]:

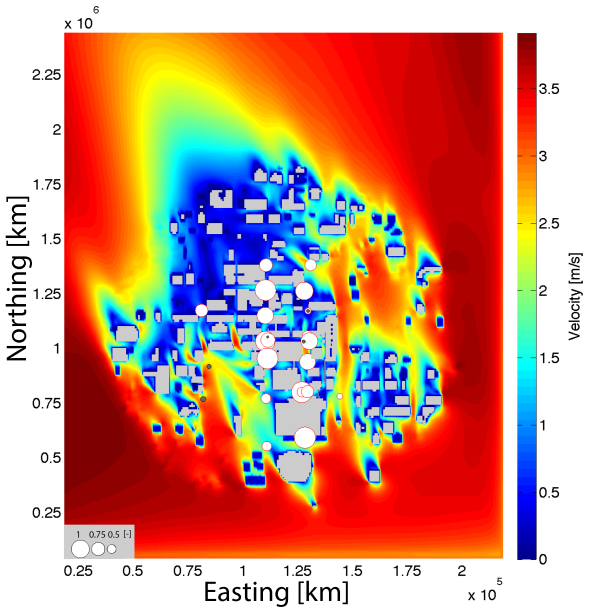

Figure 7: Velocity relative error contour plot [9].

$$q = \frac{1}{n} \sum_{i=1}^{N} N_i \quad \text{with} \quad N_i = \begin{cases} 1 & \text{for } |\frac{P_i - O_i}{O_i}| \leq 0.25 \\ & \text{or } |P_i - O_i| \leq 0.05 \\ 0 & \text{else} \end{cases} \tag{5}$$

In the previous equation, P_i represents the simulation results, while O_i represents the experimental results. The hit rate specifies the fraction of model results that differ within an allowed range D or W from the comparison data. D accounts for the relative uncertainty of the comparison data, having a value of 0.25. While W describes the repeatability of the comparison data, set in this case to 0.05 based on the experimental uncertainty. Consequently, in figure 7 the edge colour indicates if the Hit Rate criterium is satisfied or not: red for $N_i = 0$ and blue for $N_i = 1$.

In order to clarify the contour plot, scatter plots are included in figure 8 and 9, comparing the non dimensional velocity magnitude and direction from the coupled simulation and the experiments. The blue lines represent the band of acceptance which is defined based on relative uncertainty of the comparison, D. The read lines represent the fractional deviation, based on the repeatability value, W. Results are accepted as hits if they are either within a band of acceptance defined by blue lines, or within one

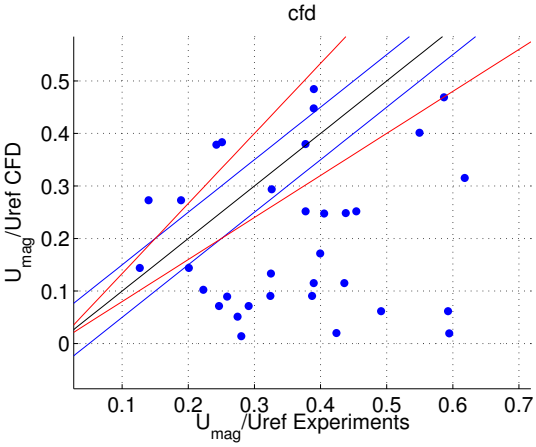

Figure 8: Velocity magnitude hit rate.

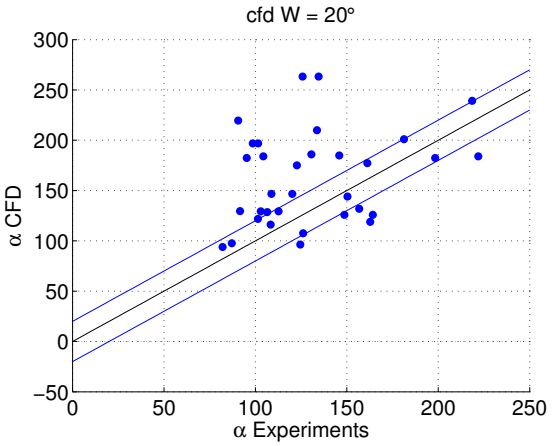

Figure 9: Velocity direction hit rate.

of the two sectors defined by the red lines [18]. Observing the figures, in 6 out of 33 stations compared, $N_i = 1$ for the velocity magnitude, while in 11 out of 33 stations $N_i = 1$ for the velocity direction. This implies that the Hit Rate, q is 0.18 for the velocity magnitude and 0.33 for the velocity direction.

Regarding the velocity magnitude, the results present several differences in the error depending on the location with respect to the city, for example in the south part of the domain, closer to the inlet and where the density of the buildings is lower, the errors in the velocity magnitude are smaller. The northern part of Oklahoma presents larger errors in velocity magnitude. In general an under prediction of the wind magnitude can be observed [19].

Considering the wind direction, only the absolute deviation criterion is used, setting the value to 20°. In this case, the hits are higher than for the velocity magnitude, but not satisfactory. Figure 9 shows an over prediction of the angles derived from the CFD coupled results. Following the experiments, the wind direction should be in the order of 70° to 200°, while the CFD presents a shift in these values of approximately 40°.

5. Conclusions and future work

In order to perform coupled mesoscale-microscale simulations there are several best practice guidelines that should be taken into account. Firstly, the mesoscale simulations should be compared with soundings or high height sodar/lidar measurements in order to verify the set up of the simulation. Within this work, several mesoscale simulations were carried out, with different configurations for mesh refinements close to the surface and for parent domain size. Afterwards, all the runs were compared with soundings. Unfortunately, a comparison with higher quality experiments was not possible, due to a lack of data. The existence of good quality measurements at high altitude, necessary to carry out validation when coupled simulations are run, remains a challenge for wind and dispersion engineering problems.

Once the mesoscale results were obtained, the code provided by CFD+engineering is used to couple velocity and boundary layer height fields extracted from the NWP simulation. These fields are directly interpolated onto the OpenFOAM mesh, as boundary and initial conditions for the CFD simulation over Oklahoma city. A new methodology is proposed to correctly specify a consistent roughness length, which is used in the modified wall function applied for turbulent kinetic energy and dissipation rate [3]. The results provided by the coupled simulations demonstrate a clear under prediction of the velocity fields. Regarding the wind direction, there is an overestimation of the angles compared to the experiments, which can be related the overall domain size combined with the set up of the boundary conditions (two inlets and two outlets).

5.1. Future work

The work presented here presented an approach for a coupled framework between OpenFOAM and the mesoscale code WRF, which is possible using the code provided by CFD+engineering. However, the results indicate that a direct interpolation from WRF

to OpenFOAM might not be the optimal approach. In future work, a different coupling strategy is targeted, which will include fields other than velocity speed and direction [20].
Additionally, non-neutral stratification of the ABL is another possible source of uncertainty. Therefore, efforts are being made to enable modelling stratified boundary layer, which can lead to changes in wind direction, when stable stratification of the ABL occurs in particular.

Lastly, the application of the previous methods still does not include the inflow variability of the atmospheric boundary layer condition. In previous work, this effect was included by using an uncertainty quantification framework. This approach is based on defining the inflow boundary conditions through three uncertain parameters which are characterized by probabilistic beta functions based on the experiments: wind speed, wind direction, and ABL roughness height. The propagation of these uncertainties is done using a tensor grid Clenshaw-Curtis Stochastic Collocation approach, and a polynomial chaos representation of the velocity at different field measurement locations is constructed to extract the mean and standard deviations. Within this previous work, in order to characterize the uncertain variables a determined period of the experiments was used [9]. Therefore, in order to improve the predictive capabilities of CFD simulations of the ABL and to make the approach applicable anywhere, the main goal is to define the uncertain parameters based on the mesoscale outcome.

Acknowledgments

The author was supported by the Agency for innovation by Science and Technology (IWT) in Belgium. The author acknowledges the support and resources provided by the company CFD+engineering. The author acknowledges the resources provided by the Centre for Turbulence Research, Stanford University. The reanalysis data were extracted from NCEP Reanalysis by the NOAA/OAR/ESRL PSD, Boulder, Colorado, USA (NCEP Reanalysis).

References

[1] P.J. Richards, et al., Appropriate boundary conditions for computational wind engineering models using the k-ε turbulence model., Journal of Wind Engineering and Industrial Aerodynamics 46 (1993) 145–153.

[2] Y. Yang, et al., New inflow boundary conditions for modelling the neutral equilibrium atmospheric boundary layer in computational wind engineering., Journal of Wind Engineering and Industrial Aerodynamics 97 (2009) 88–95.

[3] A. Parente, et al., A comprehensive modelling approach for the neutral atmospheric boundary layer: consistent inflow conditions, wall function and turbulence model closure., Boundary Layer Meteorology 140 (3) (2011) 411–428.

[4] e. a. J. Franke, Best practice guideline for CFD simulation of flows in the urban environment., COST Action 732, 2007.

[5] e. a. K. J. Allwine, Joint Urban 2003: Study Overview and Instrument Locations, PR 15967, PNNL (2006).

[6] D. Storwold, Meteorology Division CSTE-DTC-DP-WD-ME-M, UT 84022-5000, Building 4034/Room 111 Dugway (2003).

[7] W. S. et al., A description of the advanced research WRF version 3., NCAR TN-475+STR, Boulder, Colorado, USA (2008).

[8] D. of Atmospheric Science, Weather Wyoming., Tech. Rep. http://weather.uwyo.edu/upperair/sounding.html, University of Wyoming.

[9] C. García-Sánchez, et al., Extracting RANS CFD inflow boundary conditions from mesoscale model for simulations of the Joint Urban 2003 experiment., no. 6th International Symposium on Computational Wind Engineering, Hamburg, Germany, 2014.

[10] J. K. Lundquist, et al., Interaction of nocturnal low-level jets with urban geometries as seen in Joint Urban 2003 data., Journal of Applied Meteorology and Climatology 47 (2008) 44–58.

[11] D. Muñoz-Esparza, et al., Turbulent fluxes, stability and shear in the offshore environment: Mesoscale modelling and field observations at FINO1., Journal of Renewable and Sustainable Energy 4 (2012) 063136.

[12] M. Nakanishi, et al., An improved Mellor-Yamada level 3 model: its numerical stability and application to a regional prediction of advecting fog., Boundary Layer Meteorology 119 (2006) 397–407.

[13] A. Fisher, et al., Coupling of an OpenFOAM based site assessment CFD tool to WRF mesoscale simulations., no. 1st Symposium on OpenFOAM for wind energy, Oldenburg, Germany, 2013.

[14] B. Blocken, et al., CFD simulations of the atmospheric boundary layer: wall function problems., Atmospheric Environment 41 (2) (2007) 238–252.

[15] C. Gorlé, et al., CFD modelling of small particle dispersion: the influence of the turbulence kinetic energy in the atmospheric boundary layer., Atmospheric Environment 43 (2009) 673–681.

[16] M. Balogh, et al., RANS simulation of ABL flow over complex terrains applying an Enhanced k-ε model and wall function formulation: Implementation and comparison for fluent and OpenFOAM., Journal of Wind Engineering and Industrial Aerodynamics 104 (106) (2012) 360–368.

[17] X. Zhang, CFD simulation of neutral ABL flows., Tech. Rep. R-1688, RISO (2009).

[18] e. a. M. Schatzmann, Quality assurance and improvement of microscale meteorological model., COST Action 732, 2010.

[19] A. A. Wyszogrodzki et al., Evaluation of the coupling between mesoscale-WRF and LES?EULAG models for simulating fine-scale urban dispersion, Atmospheric Research 118 (2012) 324–345.

[20] Y. Wang et al., Coupled Mesoscale-Large-Eddy Modeling of Realistic Stable Boundary Layer, to be submitted (http://arxiv.org/pdf/1307.2484v1.pdf).

NOISE AND AEROACOUSTICS

Design of a Facility for Shock-Cell Noise Investigation on a Subsonic/Supersonic Coaxial Jet

Daniel Guariglia

Aeronautics and Aerospace Department, von Karman Institute for Fluid Dynamics, Belgium, daniel.guariglia@vki.ac.be

Supervisor: Christophe Schram

Associate Professor, Aeronautics and Aerospace Department & Environmental and Applied Fluid Dynamics Department, von Karman Institute for Fluid Dynamics, Belgium, christophe.schram@vki.ac.be

University Supervisor: Fulvio Stella

Associate Professor, Mechanical and Aerospace Engineering Depertment, Università di Roma "La Sapienza", Italy, fulvio.stella@dima.uniroma1.it

Abstract

The shock-cell noise is a phenomenon that occurs in aeronautic engines when the nozzle is not adapted to the atmospheric pressure. In civil aircraft at cruise it happens that the secondary flow is supersonic, thus the onset of a shock-cells system and broadband noise. This paper aims to describe the design of the new facility FAST (Free jet AeroacouSTic laboratory), started in 2013, with the aim to investigate experimentally the shock-cell noise phenomenon on a dual stream jet. The rig consists of a coaxial open jet with supersonic capability for both primary and secondary flow. A coaxial silencer is used to remove the spurious noise coming from the feeding lines. The design has been validated by the use of CFD simulations.

Keywords: Aeroacoustics, shock-cell noise, coaxial jet, supersonic, under-expanded, shock leakage, design.

1. Introduction

This project is part of the Marie Curie Initial Training Network AeroTraNet2, focused on the investigation of shock-cell noise. This aeroacoustic mechanism is encountered in aeronautical engines working in off-design conditions, usually when the secondary flow of a turbofan is exhausted in under-expanded conditions. This leads to the formation of annular shock-cells as sketched in Fig. 1. The interaction between the coaxial jet shear layers and the annular shock-cell pattern leads to the production of tonal and broadband noise, which represents an environmental issue and a threat to passenger comfort. The aim of the study is to characterize the flow in different conditions, in order to provide a phenomenological noise source model to be used by the aviation industry.

The discovery by Powell in 1953 [2] of the self-sustained feedback loop involving the shock-cells, generally known as 'screech', opened the route for more detailed investigation. Compared

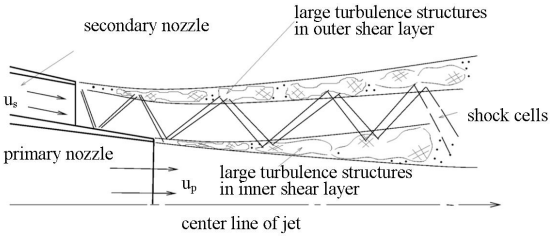

Figure 1: Sketch of the flow topology of shock-cells. Tam *et al* [1].

to the subsonic jet noise, the sound from a supersonic jet is more intense, and it can present tonal and broad peaks in the spectrum at high frequency (Fig. 2).

The seminal work of Harper-Bourne & Fisher [3] showed first the directivity of the shock-cell noise. With their model of localized sources, they obtained a frequency peak prediction formula for singular under-expanded jets:

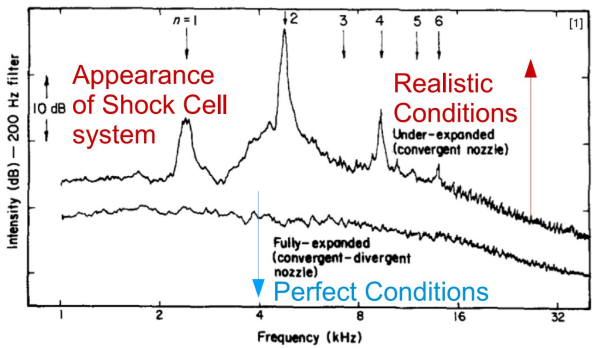

Figure 2: Comparison of spectra from fully-expanded and underx-epanded supersonic jets: $P_R/P_0 = 3.06$, $T_R/T0 = 1.00$, $M_j = 1.37$, $\theta = 90$. Tanna [4].

$$f_p = \frac{U_c}{L(1 - M_c \cos\theta)}, \tag{1}$$

where U_c is the vortical structures convection speed, $M_c = U_c/c_0$ is the Mach number, L is the average shock-cell length and θ is the directivity ($\theta = 0$ corresponds to the backwards direction).

Tam and Tanna [5] reviewed this argument opposing a more physics-based model where the sound is generated from the interaction of the convected vortical structures and a fixed shock-cell system. During the ensuing years, other authors presented their research activities on both broadband shock-associated noise (BBSAN) and on the screech [6 - 10]. These studies, numerical and experimental, investigated the noise generation mechanism, the near and far-field noise, the effect of temperature, and flight effects.

However, in the literature, there is still not as much on dual flow coaxial jets. An extensive parameter study has been made by Viswanathan on a dual stream jet [11]. Based on these experiments, Tam *et al* developed an algorithm to simulate the shock-cell system based on spatial Fourier modes decomposition, and simulated the interaction of wavepackets with it. With this technique he was able to retrieve correctly the peaks in the spectrum of the BBSAN, except for small angles in the forwards direction [12]. In another work, he proposed two different mechanisms of sound generation [1]. The first one is due to the interaction of the external shear layer with the shock-cells, which radiates mainly backwards, while the second one is due to the interaction of the inner shear layer with the shock-cells. This second noise component cannot travel upstream in the supersonic region of the jet, it is thus convected downstream until it reaches the external shear layer. There it radiates mainly in the forwards arc (Fig. 3). This corrected model was able to predict the peaks location in the spectrum, at smaller angles, in accordance with the results of [11]. From the experimental point of view, also Baht performed a parameter study [13]. In his work, starting from microphone measurements on a coaxial jet, he computed a Band Limited Overall Power Level (BLOPWL). This method aims to extract only the shock-cell noise energy content from a spectrum. He showed that in certain combinations of Primary and Secondary Nozzle Pressure Ratio, the BLOWPL is not monotonically increasing, meaning the shock-cell noise lower.

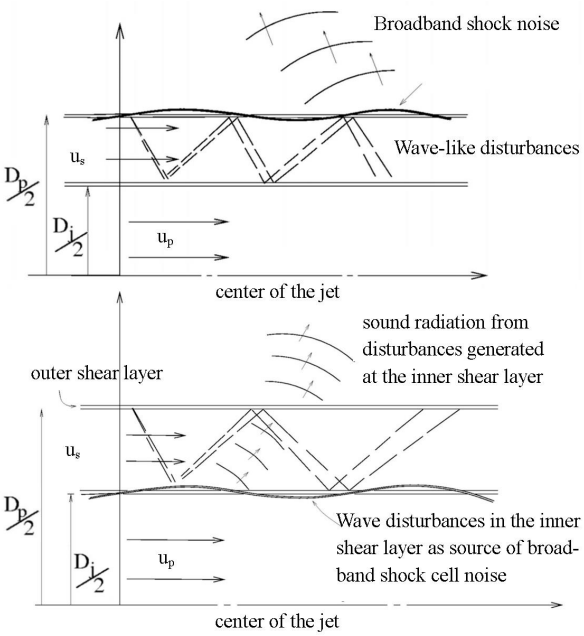

Figure 3: Wave-like disturbances in the outer and inner shear layer as source of broadband noise. Tam *et al* [1]

However, none of these works were able to identify or detect, at small scales, the physical mechanism of the noise generation. Manning first showed how the Mach waves in a supersonic stream are normally reflected on the shear layer when they approach a subsonic region; but in the presence of traveling turbulence structures, the waves can pass through and propagate outside [14]. This behavior has been then named by Suzuki and Lele as 'Shock Leakage' in [15] and it has been confirmed numerically by Daviller [16]. Reference [17] presents an up-to-date review on the past research activities, where the author observes that there is still no univocal experimental evidence of the shock-leakage phenomenon, because of the difficulties to detect it with the actual techniques.

Always in [17] is presented an analytical model, based on acoustic analogies, that aims to predict the far field of a single stream jet, taking into account the evolution in space and time of the wavepackets. The results are in partial agreement with experimental measurements, suggesting the possibility of further improvements.

2. Aims of the project

In the framework of the AeroTraNet2 project, our main goal is to characterize a coaxial subsonic/supersonic jet with flowfield and acoustic measurements, in different test conditions. The database acquired will be used by partners for data post-processing and for the validation of aeroacoustic models based on CFD. The experimental techniques intended to be used are: synchronized measurements of microphones, Schlieren, PIV and LDV. Intrusive measurements using hot wires and static probes are also considered.

Secondary but still scientifically challenging goals are:

- understanding of the sound generation and propagation of sound in the different regions of the jet;
- recreation of acoustic far-field using acoustic analogies;
- research of the shock leakage experimental evidence;
- research of conditions for an attenuation of the overall power level as experienced by Bath [13];
- acoustic beamforming on the jet.

The design of the entire facility and of the coaxial silencer constituted also a challenging engineering goal, which will be verified soon in the commissioning phase.

3. Methodology

In this section we introduce the concept design of the new facility and the case studies that have been agreed with our partners.

3.1. Facility Conceptual Design

A feasibility study has been first performed based on the initial flow requirements for the coaxial jet: $M_p = 0.71, M_s = 1.36$ for the primary and secondary flow respectively. The initial chosen geometry was taken from [18]. As constraint, we selected an indicative total mass flow of $\dot{m} = 1.0$ kg/s, compatible with the VKI pipeline system, and the possibility to seed the flow with oil particles for PIV measurements. The solutions proposed in [19] correspond to the limiting options of a continuous and a blow-down facility. The continuous facility would have the advantage of ensure long test duration, but susceptible to the fluctuation in the feeding line, and difficulty to seed uniformly the flows. The blow-down facility, instead, could ensure more stable conditions, with the usage of tanks, but for a short time. The necessity to have a dual flow would require the duplication of all the technical instrumentation, with a sensible increase of costs.

The solution proposed here, instead, allows to put together many of the positive aspects of both limit configurations (Fig.4). The facility will be supplied by

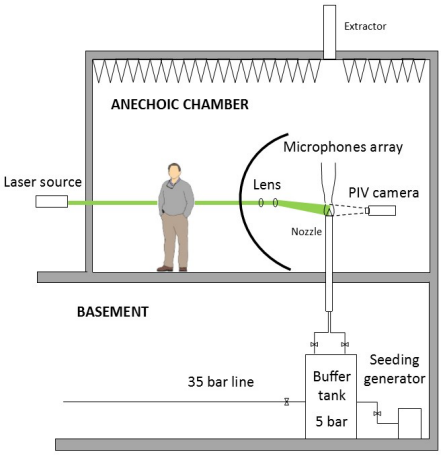

Figure 4: Selected concept for the facility. Directly feed by the VKI pressure line, one buffer tank, two lines in output.

the VKI pressure distribution system at 35 bar for long test duration estimated in 25-30 minutes, and it constitutes the base for future upgrades. A unique buffer tank will damp the eventual pressure oscillation from the pipeline and will ensure a common uniform seeding for the two flows. The reduction of complexities and components will led to a substantial decrease of the costs and times. On the other hand, it will not be possible to have flows with different total temperature, and different seeding concentration.

3.2. Test Cases Definition

The final geometry of the nozzle and the test cases have been chosen in agreement with Airbus, partner of

the project. To simplify the design, the primary nozzle will have a conical shape, while the secondary one a 3rd order polynomial shape. The primary jet will be at the same total temperature of the secondary jet. The control parameter will be the *Fan Nozzle Pressure Ratio (FNPR)* and the *Core Nozzle Pressure Ratio (CNPR)*, defined as $p_0/p_{ambient}$ for the fan and the core respectively. For the test cases, we selected the operative points of major industrial interest for a future very high by-pass aeronautic engine (Table 1).

Test	$FNPR$	$CNPR$	M_{fan}	M_{core}	$\dot{m}_{tot}$ kg/s
1	2.450	1.675	1.21	0.89	1.09
2	2.500	1.720	1.22	0.91	1.11
3	2.400	1.626	1.19	0.86	1.06
4	2.350	1.589	1.18	0.84	1.04
5	2.250	1.518	1.14	0.80	0.99
6	2.150	1.450	1.11	0.75	0.94
7	2.050	1.385	1.07	0.70	0.90
8	2.000	1.353	1.05	0.67	0.87
9	1.800	1.235	0.96	0.56	0.77

Table 1: Test conditions matrix

4. Facility Detailed Design

Fig.5 shows the final configuration of FAST. The maximum operative pressure is p_{max}=11 bar (except for the seeding generator, which can work up to 5 bar). The facility is operated remotely from the ground floor. An electric valve opens the pressurized circuit, and closes it automatically in case of emergency or power cut thanks to a safety battery.
The pressure is first lowered from 35 to 10 bar with the use of two pressure regulators, installed in parallel to ensure the sufficient mass flow. The pressure is further reduced from 10 to 5 bar by a pilot controlled pressure regulator, before it enters the buffer tank.
To further decrease the complexities during the operative phase, the seeding generator is located on the ground floor, near the computer station. This will help the operator in selecting the better seeding condition for PIV without changing floor all the time. So, part of the flow at 10 bar is diverted to the seeding generator (described in section 4.2). The particles are then injected in the buffer tank, at a pressure of 5 bar, before it enters the two main flow lines.

The primary and secondary lines have been designed with the same valves, and they are thus perfectly interchangeable. However, for the conditions where the secondary flow is supersonic, and the primary flow is subsonic, a flow meter is required to measure the mass flow (see section 6.6). For this reason, the primary line, is equipped also with a conditioned orifice mass flow meter (described in section 4.3). The pressure is tuned in a feedback loop by a remotely controlled precise pressure regulator, which is connected with the stagnation chamber just before the nozzle. This valve controls a volume booster, which variates the flows passing through it until the desired pressure is reached in the stagnation chamber (Fig.6). After the regulators, and before to enter in the coaxial silencer, each flow is split in ten flexible tubes of

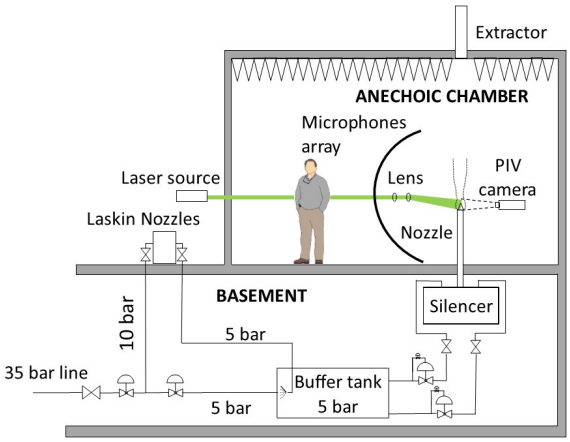

Figure 5: Sketch of the FAST final configuration.

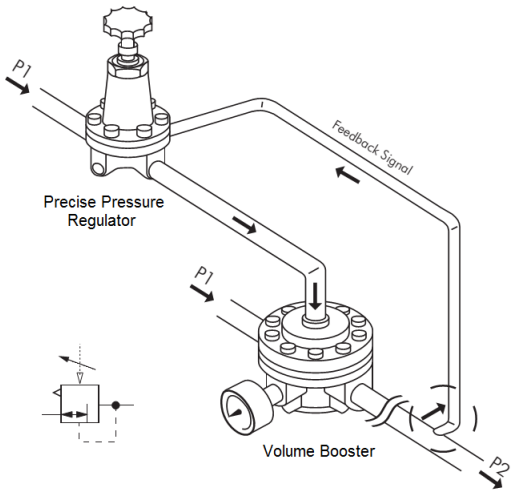

Figure 6: The combination of the precise pressure regulator and the volume booster in feedback loop should ensure precise pressure settings even for big mass flows.

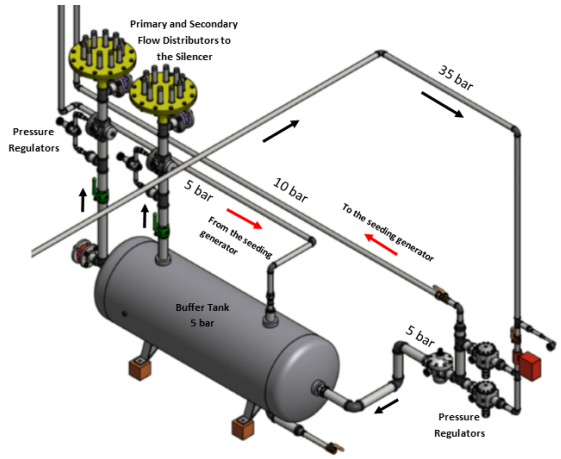

Figure 7: CAD drawing of the air supply system following the sketch in Fig.5.

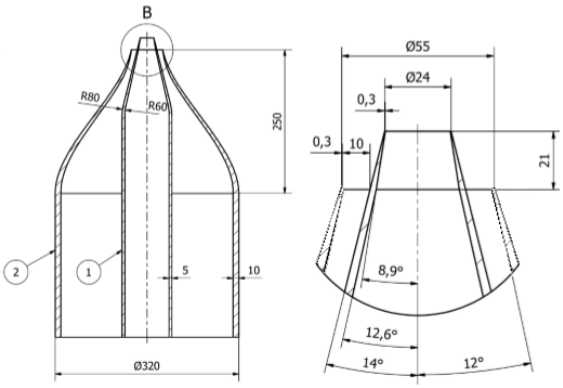

Figure 8: Drawing of the coaxial nozzles: overall (left) and detail (right) view.

equal length, to enter the silencer equispaced. This coaxial silencer has been designed with the aim to eliminate all the noise produced by the valves, which otherwise will strongly pollute the acoustic measurements, as will be explained in detail in section 5. After the coaxial silencer, the last trait is a vertical straight coaxial conduct equipped with honeycomb and three screens to dump the turbulence developed in the silencer. The conducts internal diameters are $\varnothing_p$ = 8.0 cm and $\varnothing_s$ = 30.0 cm for the primary and secondary flows respectively. In Figs. 7 and 9 it is possible to see the 3D layout of the air supply system and of the section of the silencer and conduits.

4.1. Nozzle design

The nozzle has been designed taking into consideration the desired geometry by our partners with the facility limitations in terms of mass flow rate and test duration. The final shape, validated through CFD, is shown in Fig. 8. The primary nozzle has a simple conical shape, with the semi-aperture angle α=14°. The secondary nozzle profile follows a 3rd order polynomial function, modified '*ad hoc*' in the last part to ensure sonic speed only at the exit.

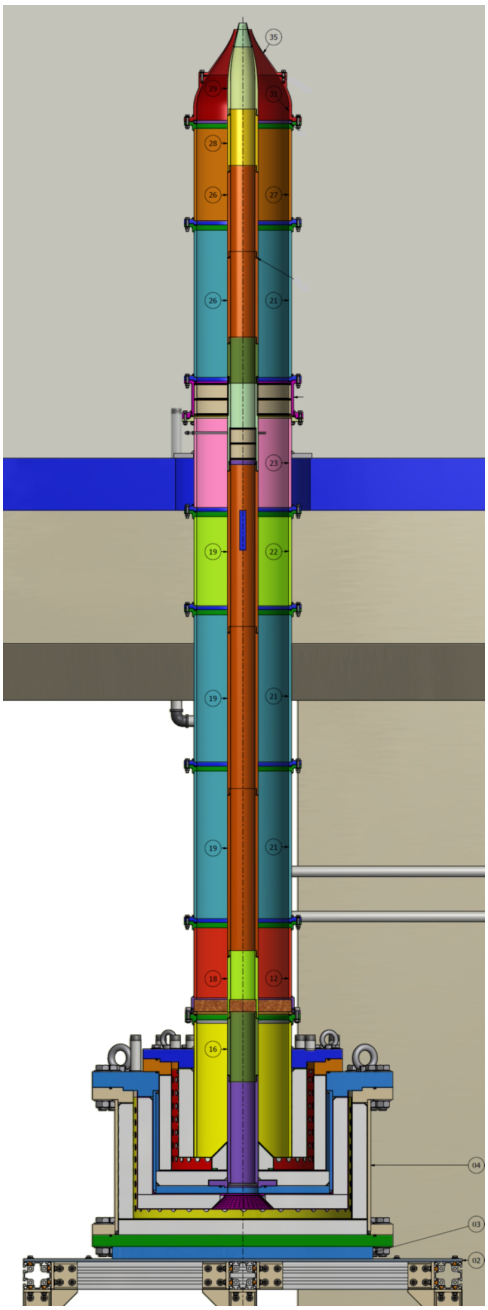

Figure 9: Section of the silencer and main conduits.

4.2. Seeding Generator

The seeding generator has been selected taking into account the quality requirements in terms of number of particles and size. Because of the presence of shock-waves, the inertia of the particles must be very small in order to follow the velocity jumps in the flow field. The motion of the particle in a fluid has been studied by Oseen [20] and Tchen [21] which derived the fundamental equations. In [22] the author measured the time response for different sizes of vegetable oil particles in an open jet at Mach $M = 4$. She concluded that particles of the size $\varnothing = 1\ \mu$m, or smaller, are required in order to study flows with shock-waves. The PivPart-45M by PIVTEC Gmbh can provide particles of 1 μm size and in large quantities, furthermore, it is designed to work also at high operative pressures.

4.3. Conditioning Orifice Flow Meter

To measure the mass flow rate of the primary flow, it was necessary to install an orifice plate. Because of the small available space, we decided to use a four holes conditioning orifice plate (Fig. 10)

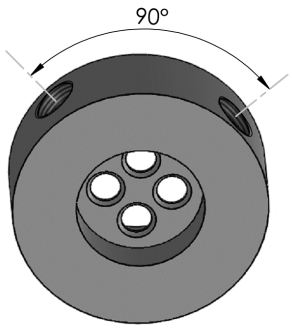

Figure 10: Conditioning orifice plate with four holes.

It is a differential pressure device based on measuring the pressure in two locations of the *vena contracta*. This particular configuration multi-holes is not prescribed in the norms [23], but it has been tested extensively with good results and it necessitate of only two diameters of clean section before and after the plate [24].

5. Silencer

The idea at the base is to have a strong noise absorption putting a phono-absorbing material perpendicular to the direction of the flow; this is achieved by making the flow turning 90° twice (Fig.11).

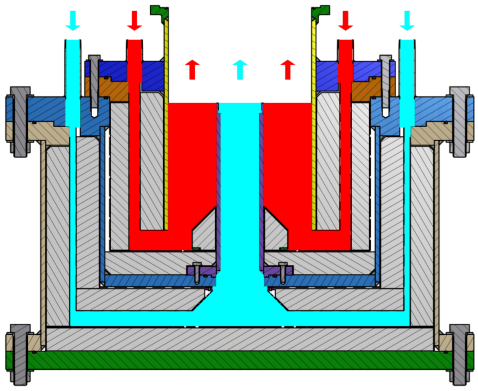

Figure 11: Section of the coaxial silencer. The clean passage areas for the primary and secondary flow are colored in cyan and red respectively. The gray zones represents the phono-adsorbent material.

This shape with two 'chicanes' is very effective for sound reduction and it fits very well with the requirements of coaxiality. The air enters the circuit from the top plate, where ten inlets equally spaced are present. The colored zones represent the clean passage areas, while the gray dashed zones are the phono-absorbing material. Based on previous experiences, it has been decided to use a fixed thickness for all the absorbing layers, equal to $d_{abs} = 5$ cm. The clean passage areas have been sized in order to decrease the flow velocity in order to reduce both pressure losses and undesired noise production. The chosen absorbing material is composed by very fine stainless steel wool (type #000). The relevant dimensions are summarized in Tab.2.

$\varnothing_{max}$	0.98 m	A_p	$2.39{\cdot}10^{-2}$ m^2
h_{max}	0.76 m	A_s	$2.90{\cdot}10^{-2}$ m^2
m_{dry}	~1200 kg	$\varnothing_{p,eq}$	0.192 m
p_{max}	11 bar	$\varnothing_{s,eq}$	0.174 m

Table 2: Silencer maximum dimensions and clean passage area for primary and secondary flow. $\varnothing_{max}$ and h_{max} are the main diameter and height respectively, m_{dry} is the weight without the foam, p_{max} is the max operative pressure, A_p and $\varnothing_{p,eq}$ are the clean passage area and the equivalent diameter for the primary circuit, A_s and $\varnothing_{s,eq}$ are the clean passage area and the equivalent diameter for the secondary circuit.

5.1. Acoustic Performances

The acoustic performances of the silencer have been numerically verified with COMSOL Multiphysics® 5.0, a commercial FEM solver. We

used the acoustic module of the software to compute the transmission loss between the ten inlets and the silencer outlet, including the effects of the phono-absorbing material and the grids that hold it in position.
It is assumed that the flow is not moving inside the silencer, so no sound production and no convection effect. This hypothesis justified by the small Mach number inside the silencer (M≃0.01), thus we expect small noise production compared with the valve noise intensity, where the flow is choked. COMSOL solves the problem in the frequency domain using the Pressure Acoustics, Frequency Domain interface. The model equation is a slightly modified version of the Helmholtz equation for the acoustic pressure p:

$$\nabla \cdot \left(-\frac{\nabla p}{\rho}\right) - \frac{\omega^2 p}{c^2 \rho} = 0, \tag{2}$$

where ρ is the density, c equals the speed of sound, and ω gives the angular frequency.

In the absorbing steel wool, modeled as a Poroacoustic domain, the damping enters the equation as a complex speed of sound, $c_c = \omega/k_c$, and a complex density, $\rho_c = k_c Z_c/\omega$, where k_c is the complex wave number and Z_c equals the complex impedance. With this equivalent fluid model for the porous domain, the losses are modeled in a homogenized way. For a highly porous material with a rigid skeleton, the well-known model of Delany and Bazley estimates these parameters as functions of frequency and flow resistivity. Using the original coefficients of Delany and Bazley [25], the expressions are:

$$k_c = k_a \cdot \left(1 + 0.098 \cdot \left(\frac{\rho_a f}{R_f}\right)^{-0.7} - i \cdot 0.189 \cdot \left(\frac{\rho_a f}{R_f}\right)^{-0.595}\right) \tag{3}$$

and

$$Z_c = Z_a \cdot \left(1 + 0.098 \cdot \left(\frac{\rho_a f}{R_f}\right)^{-0.734} - i \cdot 0.189 \cdot \left(\frac{\rho_a f}{R_f}\right)^{-0.732}\right), \tag{4}$$

where R_f is the flow resistivity, $k_a = \omega/c_a$ and $Z_a = \rho_a/c_a$ are the free-space wave number and impedance of air, respectively. This model is the default selected for the Delany-Bazley-Miki model in the Poroacoustics domain feature. It is possible to find flow resistivities in tables [26] or by measuring it. For glass-wool-like materials, Bies and Hansen [27] give an empirical correlation:

$$R_f = \frac{3.18 \cdot 10^{-9} \cdot {\rho_{ap}}^{1.53}}{{d_{av}}^2}, \tag{5}$$

where ρ_{ap} is the material apparent density and d_{av} is the mean fiber diameter. For grade #000 fine steel wool d_{av}=35 μm, ρ_{ap}=166 kg/m^3 and R_f=6472 kg/(m^3·s).

For the perforated plate containing the steel wool COMSOL Multiphysics calculates the transfer impedance using the following model expression by Bauer [28]:

$$\frac{Z}{\rho_c c_c} = \left(\frac{1}{\sigma}\sqrt{\frac{8\mu k_{eq}}{\rho_c c_c}}\left(1 + \frac{t_p}{d_h}\right) + \theta_f\right) + i\frac{k_{eq}}{\sigma}\left(t_p + \delta_h\right), \tag{6}$$

where μ is the dynamic viscosity, σ=0.4 is the area porosity (the hole's fraction of the boundary surface area, a dimensionless number between 0 and 1), t_p=1.5 mm is the plate thickness, d_h=4 mm is the holes diameter, d_h is the end correction to the reactance (the default is 0.25dh), θ_f=0 is the flow resistance (a contribution to the resistive part of the impedance that can be used, for example, to include the effects of a mean flow or nonlinear effects at large sound pressure levels).

The boundary conditions are of three types: solid boundaries, inlet and outlet. At the solid boundaries, which are the outer walls of the resonator chamber and the pipes, the model uses sound hard (wall) boundary conditions. The condition imposes that the normal velocity at the boundary is zero. The boundary condition at the inlet involves a combination of incoming and outgoing plane waves [29]. This boundary condition is valid as long as the frequency is kept below the cutoff frequency for the second propagating mode in the tube, as it happens in the case studied. At the outlet boundary, the model specifies a radiation condition for an outgoing plane wave, a valid assumption in the case studied.
The domain has been meshed with tetrahedral linear elements, with the maximum element length equal to $1/10^{th}$ of the smallest computed wavelength. It includes the whole silencer, plus a portion of the conduits and the nozzle. This allows take into account also the area restriction of the nozzles, which guaran-

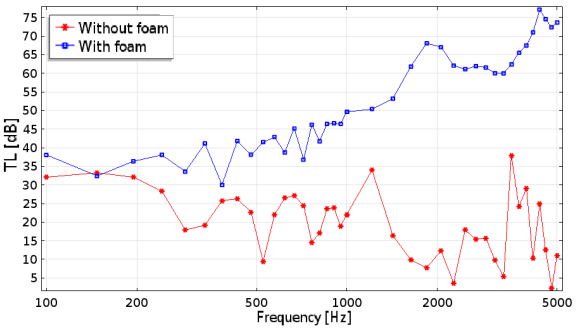

Figure 12: Transmission Loss of the silencer for the primary flow.

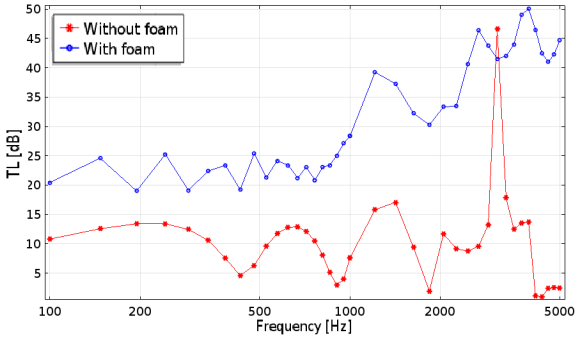

Figure 13: Transmission Loss of the silencer for the secondary flow.

tee the respect of the plane wave boundary condition at the outlet, for the simulated frequencies. Instead, the length of the conduits should not take a relevant role, because they are sufficiently long to guarantee the modes fully development. The other simplification is to neglect the presence of the honeycomb and the screens which are in the conduits. Nevertheless, in reality these will dump or reflect further more the noise in the flow, thus this assumption is conservative. We carried out the simulations for fifty frequencies in the range $100 \leq f_s \leq 5000$; this to limit the computational cost, as we expect the higher frequencies to be efficiently damped by the phono-absorbing material. The transmission loss is defined as the ratio between the incoming and outgoing acoustic energy. The attenuation TL (in dB) of the acoustic energy is defined by the following equation:

$$TL = 10 \log \left(\frac{w_{in}}{w_{out}} \right). \tag{7}$$

Here w_{in} and w_{out} denote the incoming power at the inlet and the outgoing power at the outlet, respectively. It is possible to calculate each of these quantities as an integral over the corresponding surface:

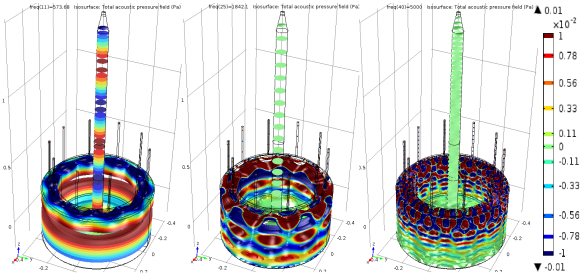

Figure 14: Acoustic pressure field isosurfaces in the primary flow circuit at 570 Hz (left), 1840 Hz (center) and 5000 Hz (right). The scale enhances the modes visualization that otherwise would be very faint at full scale.

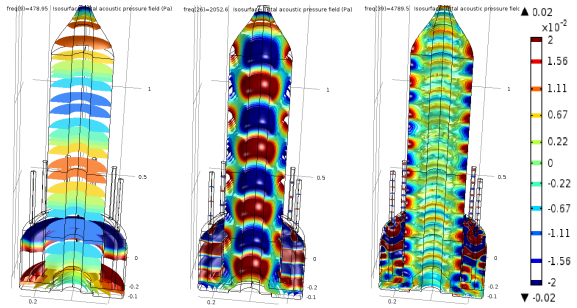

Figure 15: Acoustic pressure field isosurfaces in the secondary flow circuit at 480 Hz (left), 2050 Hz (center) and 4790 Hz (right). The scale enhances the modes visualization that otherwise would be very faint at full scale.

$$\omega_{out} = \int_{\delta\Omega} \frac{|p|^2}{2\rho c} dA \quad \text{and} \quad \omega_{in} = \int_{\delta\Omega} \frac{{p_0}^2}{2\rho c} dA \tag{8}$$

The results of the simulations are shown in Figs. 12 and 13. From the two graphs we can see how the silencer without foam is already very effective at low frequencies, with some negative peaks that represents the cavity resonant modes, at higher frequencies. With the foam, instead, the damping is extremely effective especially at higher frequencies, thus confirming the design choices.

In Figs.14-15 we can see the pressure waves propagating with different modes. We can see as increasing the frequency, more modes are developing in the silencer and in the conduits, especially for the secondary flow circuit; however, when the waves approach the convergent nozzle, they become planar again, avoiding spurious reflection at the boundary. To verify that it is not the boundary that impose the wave planarity to the flow, we run a simulation also without the nozzle, and in Fig. 16 we can see how higher modes are

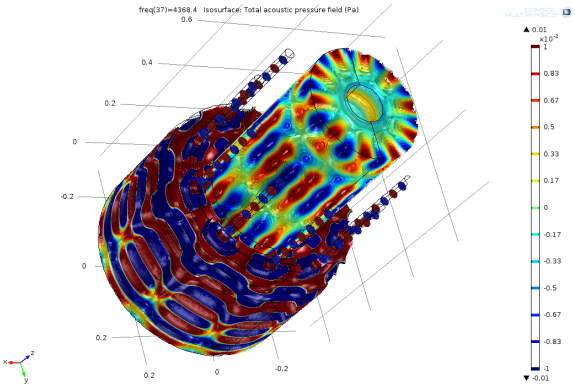

Figure 16: Acoustic pressure field isosurfaces in the secondary flow circuit at 4370 Hz, with a short conduit trait and no nozzle. We can observe at this enhanced scale how the mode propagation at the exit is not forced to plane wave mode by the boundary condition.

leaving the domain without modification.

6. RANS simulations of the coaxial jet

We performed RANS simulations of the dual flow jet to validate the nozzle geometry and to have a first insight of the flow field. The computations have been carried out using COMSOL Multiphysics® 4.4 using linear triangular Finite Elements. We coupled the fluid dynamic problem with the heat transfer in solids with the aim to verify possible influences of the heat transfer, through the nozzle walls itself, on the shock-cells systemn. Because the nozzle lip is only 0.3 mm thick, we used the Solid Mechanics interface to verify that we will not have excessive deformations due to the combined stresses of the shear stress, pressure and thermal stress.

6.1. Geometry

The geometry is 2D axial-symmetric. This gave us a substantial advantage in terms of computational time, which has been used to compute more refined meshes. The final geometry has been obtained after that preliminary computations showed an incorrect position of the sonic throat in the external nozzle. Some small adjustments had been manually added to the inner profile of the secondary nozzle to fix the problem (Fig. 8).

6.2. Fluid Dynamics Model

The simulation of the coaxial flow is carried out by means of the interface High Mach Number Flow using a k-ϵ model. The computational domain is rectangular, extending for 18 $\varnothing_s$ after and 6 $\varnothing_s$ before the nozzle in the axial direction, 5.5 $\varnothing_s$ in the radial direction. The ambient pressure was p_a = 101325 Pa and the initial temperature was set to 293.15 K. We selected three boundaries inlet at the bottom of the domain, two boundaries inside the nozzles (p_{01}, p_{02}, T_{01}=T_{02}=293.15 K, M_1=M_2=0.01) and the third outside (p_3=101325 Pa, T_3=293.15 K, M_3=0.01). The outlet boundaries are the side and top edge of the domain with $p_{a,outlet}$=101325 Pa. The default model Wall, no slip, was applied to all surfaces of the nozzle. We carried out the simulations varying only the total pressure at the two nozzle inlets. The test conditions are the same of Tab. 1.

6.3. Heat Transfer Model

The Heat Transfer in Solids Interface is a component of the CFD module, which consented us to run a coupled simulation simply adding this interface to the 'Physics' interface. The reason to to apply the model is because we expect a heat transfer through the thin walls of the nozzle; in particular from the internal flow (warmer) to the external one (colder). Because a positive heat flux has destabilizing effects on the boundary layer, we wanted to verify if this could affect the developing of the supersonic region (in particular the position of the first shock-wave). We selected from the COMSOL material library two materials currently in use at VKI for manufacturing, brass and steel. These have significantly different thermal conductivity as well as Youngs module and yielding stress. As boundary conditions we imposed a fixed temperature, T_m = 293.15 K, at the bottom edge of the nozzles, then we set the same as initial temperature inside the material.

6.4. Structural Model

The simplest way to couple CFD problems with structural problems would have been to use the Fluid-Structure Interface. This option was unfortunately not available for our license, so we interpolated a load function with the pressure extracted from the CFD results. The other boundary conditions, we simply imposed the Fixed Constraints to the bottom edge of the nozzle.

6.5. Mesh Sensitivity

for the mesh sensitivity, we started from the built-in 'Physics Controlled Mesh' with the 'Extremely fine' option, meaning free triangles and boundary layer elements on the walls. However, we realized that it was not sufficiently fine in the supersonic region, so we

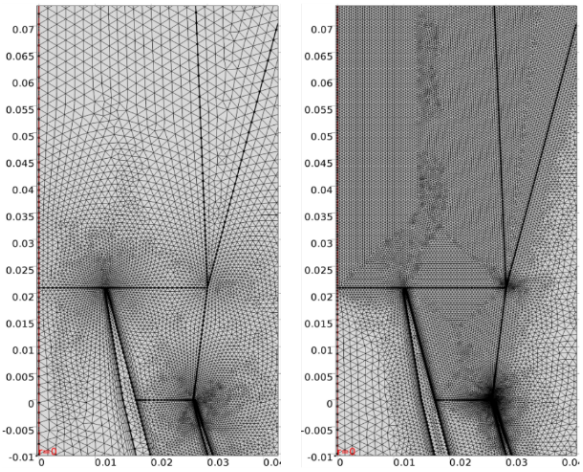

Figure 17: Comparison of 'Physics Controlled' Mesh 1 and 'User-defined' Mesh 2.

created two other meshes with higher resolution and we tested on the same conditions. An example of the Mesh 1 and Mesh 2 in the nozzles exit region is shown in Fig. 17; being the minimum size of Mesh 3 the half of Mesh 2, it has been omitted for clarity. Details on the three meshes are shown in Tab. 3.

	Maximum element size in the shock region	Total number of elements
Mesh 1	0.002	$3.4{\cdot}10^5$
Mesh 2	0.0005	$2.7{\cdot}10^5$
Mesh 3	0.00025	$6.0{\cdot}10^5$

Table 3: Meshes main characteristics

The comparison between the three meshes has been done plotting the Mach number along a line starting at the beginning of the supersonic region. The graph in Fig. 18 shows how the results for Mesh 1 has poor resolution in comparison of Mesh 2 and Mesh 3. The Mesh 2 is capable to calculate the first peak in accord with Mesh 3, but the amplitude for the other peaks is slightly different. In conclusion, because of the relatively high computational cost of Mesh 3, we decided to make all the simulations using the Mesh 2.

6.6. Results

The flow field presents a system of shock-cells starting from the exit of the secondary nozzle that changes significantly varying the pressure conditions.

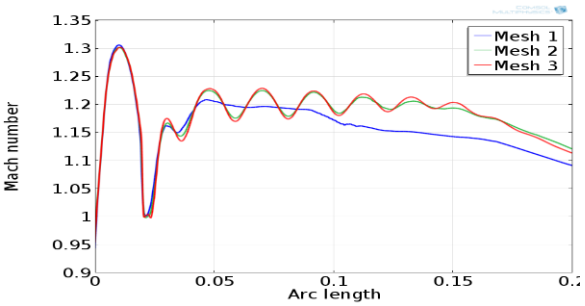

Figure 18: Comparison of 'Physics Controlled' Mesh 1 and 'User-defined' Mesh 2 and Mesh 3. Data has been extracted from the dashed line in Fig. 19.

At higher pressure, a strong, oblique, shock-wave develops from the lip of the primary nozzle and reflects back into the flow when it impinges the external shear layer (Fig. 19). After that, the external flow becomes again supersonic and we have the formation of shock-cells in the wake, between the internal shear layer and the external shear layer. Reducing the total pressure we can observe a progressive reduction on the length of the shock-cells. It is worthy to note that pressure in the wake is oscillating according to the shock-cells and it is transmitted from the supersonic to the subsonic region (Fig. 20). From an aeroacoustic point of view, the length of the shock-cells is related to the broadband noise frequency peak. According to Tam *et al* [1] we have a pressure wave emission each time a turbulent structure passes a shock-cell. This means that lowering the pressure we should expect in the experiments higher broadband noise frequencies, because the wavelength is reducing. By lowering the pressure, we arrive to another flow regime. In Fig. 21 we can recognize the formation of shock-cells both in the wake and in the region between the external shear layer and the wall of the internal nozzle. This could have a negative effect on the aeroacoustic point of view. Because the length of the two kind of shock-cells are different, we should expect the appearance of other broadband or tonal noise. Lowering further the total pressure, we assist at the disappearance of the shock-cells in the wake, while they are still present in the region immediately after the secondary nozzle (Fig. 22).

Finally, we can compare all the test conditions in a unique plot where we can appreciate the differences. In particular, in Fig. 23 we can observe the fluid transition into the three flow regimes described above.

The presence of the oblique shock waves alters significantly the expected results using the isoentropic

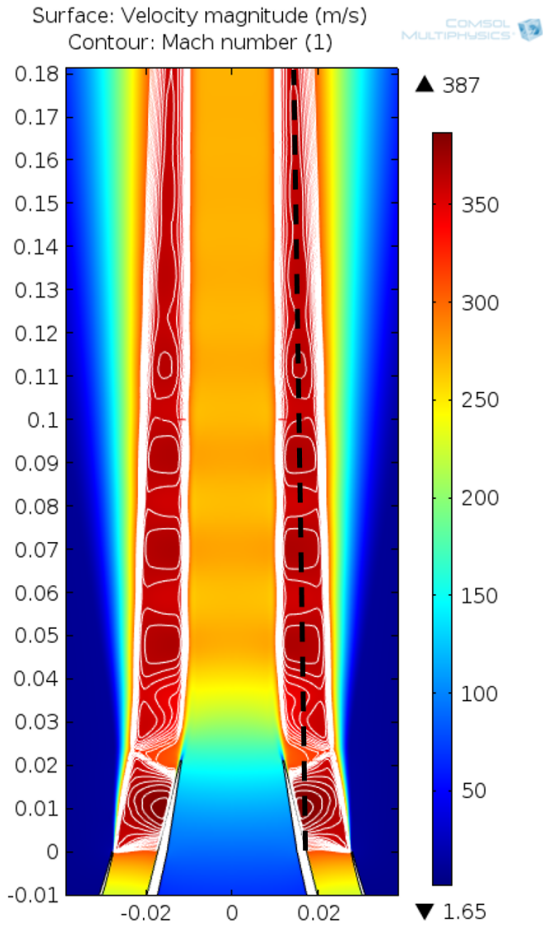

Figure 19: Velocity flow field of test ID #1. The contour plot shows the regions with Mach> 1. It is possible to recognize the shock-cells in the wake. The black dashed line corresponds to the chosen location where data is extracted for comparison.

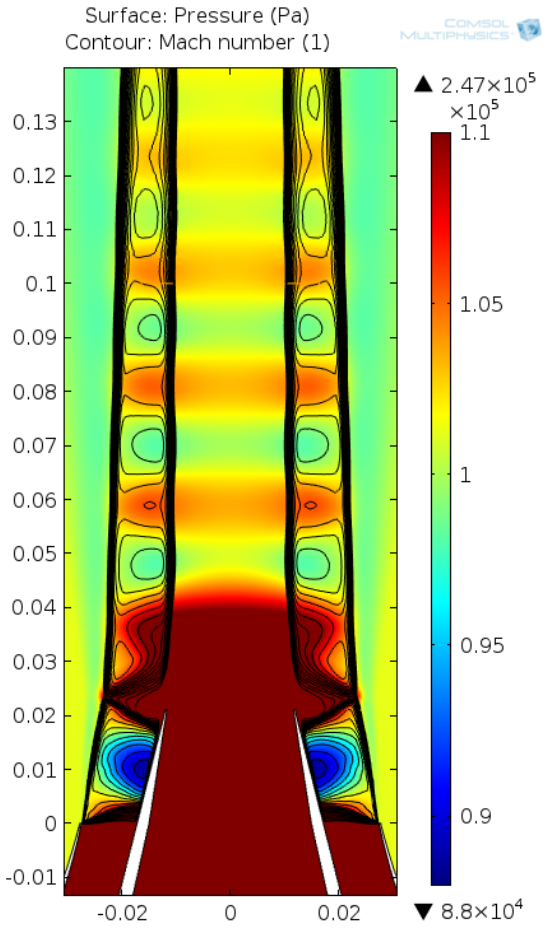

Figure 20: Pressure flow field of test ID #1.

relations. We found important differences especially in the mass flow rate for the primary nozzle, shown in Tab. 4 . We can find two explanation for this behavior: when the external flow is supersonic, we have a strong shock at the end of the primary nozzle. The strong re-compression affect the primary flow too, and this cause the minor mass flow rate, because the nozzle is not adapted to ambient pressure.

Concerning the influence of the heat transfer, we carried out simulations with and without the heat flux through the walls. Results showed how with both steel and brass, despite being good conductors, the difference of temperature is not sufficient to influence the shock-cells pattern. To further verify this, we tried increasing the total temperature in the primary flow up to T_{0p}= 1000 K. The results shown as the oblique shock-wave anticipated a bit due to a larger separation at the end of the nozzle lip.

For the structural part, in Fig. 24 we can see the results of the simulation for test ID #2 (the most loaded condition), in case of brass. The maximum von Mises stress is well below the yielding point of the material, despite the small thickness of the lip edge. The displacements as well (magnified 14000 times in the figure), are negligible.

7. Measurement techniques

Below we summarize the expected measurement techniques that we want to use to study the flow. Basically we can group them into three categories: flow visualization, acoustic investigation and point-wise measurements:

- **Schlieren and PIV.** The aim using Schlieren is to have an insight of the flow field. Averaged and

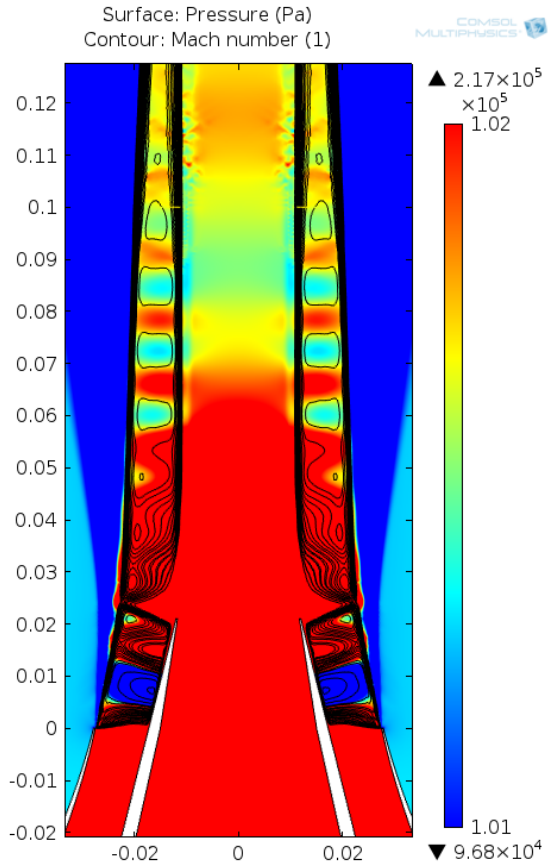

Figure 21: Pressure flow field of test ID #7.

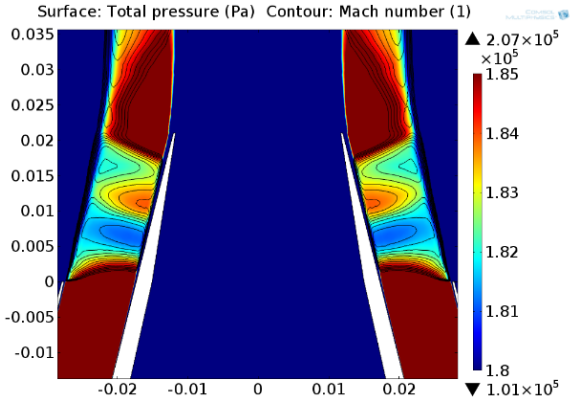

Figure 22: Pressure flow field of test ID #8.

instantaneous images will be used to validate the setup and to assess the axial-symmetry of the jet. Also the shock-wave patterns in different conditions will be easy to detect. Successively, we will collect PIV images at several conditions to characterize quantitatively the flow field. The generated database will be used for validation of numerical studies by the partners of the project.

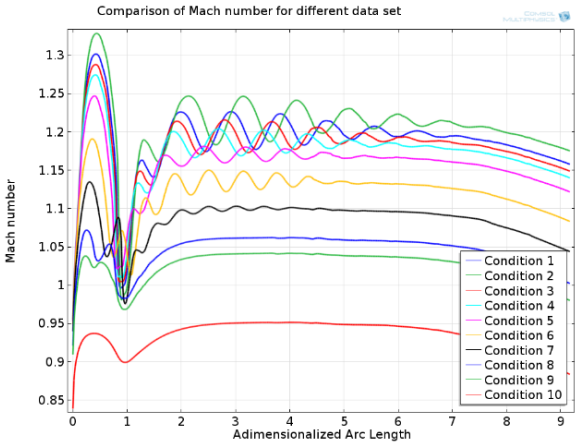

Figure 23: Comparison of Mach number of all test IDs along a line described in Fig. 19. The x axis has been non-dimensionalized by the primary nozzle diameter.

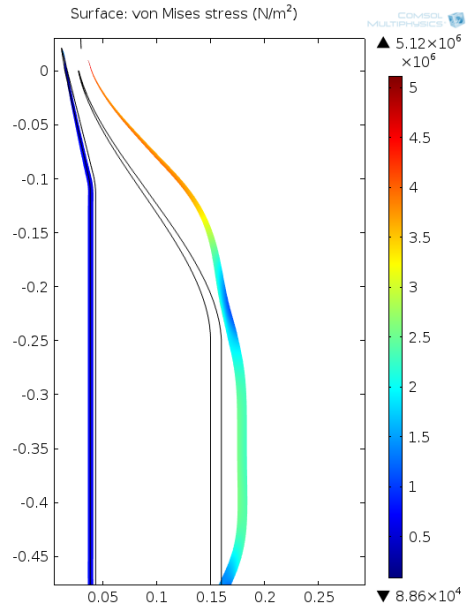

Figure 24: von Mises stresses and displacements magnified 14000 times for test ID #2.

- **Pressure probes, hot wires and LDV.** We will use these point-wise techniques to have quantitative measurements of the turbulent regions (boundary layer, shear layer) and inside the jet. Special care is necessary to avoid to disturb the flow field, especially in the shock-cells region.

	mass flow COMSOL		Variation respect to isoentropic relations in percentage	
Test ID #	$\dot{m}_1$ [Kg/s]	$\dot{m}_2$ [Kg/s]	$\Delta\dot{m}_1$ %	$\Delta\dot{m}_2$ %
1	0.118	0.817	-31.9	-4.9
2	0.121	0.834	-32.1	-4.9
3	0.115	0.809	-32.1	-4.9
4	0.114	0.801	-31.9	-4.9
5	0.111	0.784	-31.6	-5.0
6	0.104	0.750	-31.9	-5.0
7	0.091	0.716	-36.5	-5.1
8	0.082	0.681	-38.4	-5.3
9	0.077	0.664	-39.3	-5.4
10	0.058	0.591	-44.7	-6.4

Table 4: Mass flow rate comparison between the theoretical values of Tab. 1 and those calculates with COMSOL

Contemporary use of Schlieren could be useful to verify the importance of the caused disturb. We will perform also synchronous measurements with microphones to characterize the source of the noise. The data collected will be used by our partners for post processing techniques such POD, Proper Orthogonal Decomposition, and LSE, Linear Stochastic Estimation.

- **Acoustic investigation.** Near and far field acoustic measurements will be used to capture the signature of the shock-cell noise, with expected frequencies up to 70 Khz. Synchronized use of the Schlieren technique with a high speed camera might be useful to recognize periodic variation in the shock-wave patterns that are referable to collected acoustic spectra .

8. Future plans

The next steps of this project will be the installation and commissioning of the facility. The transverse for the microphones and for the LDV system will also be designed to achieve a good level of accuracy and efficiency.

Acknowledgments

I wish to acknowledge the European Commission for funding this project through the Marie Curie Grant Agreement ITN AeroTraNet2 as part of FP7 program, the VKI Technical Drawing Office and the Workshop for the high level of accuracy and cooperation.

References

[1] C. Tam, N. Pastouchenko, K. Viswanathan, Broadband Shock-Cell Noise from Dual Stream Jets, in: Aeroacoustics Conferences, American Institute of Aeronautics and Astronautics, 2008.

[2] A. Powell, On the mechanism of choked jet noise, Proceedings of the Physical Society. Section B 66 (12) 1953 1039.

[3] M. Harper-Bourne, M. Fisher, The noise from shock waves in supersonic jets, in: AGARD Conference on Noise Mechanisms, 1973.

[4] H. Tanna, An experimental study of jet noise part ii: Shock associated noise, Journal of Sound and Vibration 50 (3) 1977 429 – 444.

[5] C. Tam, H. Tanna, Shock associated noise of supersonic jets from convergent-divergent nozzles, Journal of Sound and Vibration 81 (3) 1982 337 – 358.

[6] T. D. Norum, J. M. Seiner, Broadband shock noise from supersonic jets, AIAA Journal 20 (1) 1982 68–73.

[7] T. D. Norum, J. M. Seiner, Measurements of Mean Static Pressure and Far Field Acoustics of Shock-Containing Supersonic Jets, NASA TM84521d (1982).

[8] C. Tam, J. Seiner, J. Yu, Proposed relationship between broadband shock associated noise and screech tones, Journal of Sound and Vibration 110 (2) 1986 309 – 321.

[9] C. Tam, Stochastic model theory of broadband shock associated noise from supersonic jets, Journal of Sound and Vibration 116 (2) 1987 265 – 302.

[10] C. Tam, Broadband shock-associated noise of moderately imperfectly expanded supersonic jets, Journal of Sound and Vibration 140 (1) 1990 55 – 71.

[11] K. Viswanathan, Parametric study of noise from dual-stream nozzles, in: Aerospace Sciences Meetings, American Institute of Aeronautics and Astronautics, 2003, pp. –.

[12] C. Tam, N. Pastouchenko, K. Viswanathan, Computation of shock cell structure of dual-stream jets for noise prediction, AIAA Journal 46 (11) 2008 2857–2867.

[13] T. Bhat, U. Ganz, A. Guthrie, Acoustic and flow-field characteristics of shock-cell noise from dual flow nozzles, in: Aeroacoustics Conferences, American Institute of Aeronautics and Astronautics, 2005, pp. –.

[14] T. Manning, S. Lele, S. U. D. of Aeronautics, Astronautics, A Numerical Investigation of Sound Generation in Supersonic Jet Screech, Stanford University, 1999.

[15] T. SUZUKI, S. K. LELE, Shock leakage through an unsteady vortex-laden mixing layer: application to jet screech, Journal of Fluid Mechanics 490 2003 139–167.

[16] G. Daviller, G. Lehnasch, P. Jordan, Numerical investigation of the influence of upstream conditions on properties of shock noise in shock/mixing layer interaction, in: International Symposium of Turbulence and Shear Flow Phenomena, Vol. 1, Poitiers, 2013.

[17] A. Savarese, Experimental study and modelling of shock-cell noise, Ph.D. thesis, Ecole Nationale Suprieure D Ingenieurs De Poitiers (2014).

[18] S. Miller, P. Morris, The Prediction of Broadband Shock-Associated Noise from Dualstream and Rectangular Jets Using RANS CFD, in: Aeroacoustics Conferences, American Institute of Aeronautics and Astronautics, 2010.

[19] Z. E. Yildirim, Design of a Transonic/Supersonic Coaxial Jet Facility for the Investigation of Shock-Cell Noise by Means

of Simultaneous PIV and Microphones Measurements, Industrial Design Exercise, Von Karman Institute.
[20] C. W. Oseen, Neuere Methoden und Ergebnisse in der Hydrodynamik, Akademische Verlagsgesellschaft m. b. h., Leipzig, 1927.
[21] C.-M. Tchen, Mean value and correlation problems connected with the motion of small particles suspended in a turbulent fluid, Nijhoff, The Hague, 1947.
[22] A. Jeronimo, Application of PIV to a Supersonic Jet, Project Report 2001-28, von Karman Institute (June 2001).
[23] ISO/TR 15377:2007, Measurement of fluid flow by means of pressure-differential devices guidelines for the specification of orifice plates, nozzles and venturi tubes beyond the scope of iso 5167, Tech. rep.
[24] EMERSON, Conditioning orifice plate technology; taking the standard to a new level of capability, Tech. rep., 1595_2_01_*AA* (2004).
[25] M. Delany, E. Bazley, Acoustical properties of fibrous absorbent materials, Applied Acoustics 3 (2) 1970 105–116.
[26] T. J. Cox, P. D'antonio, Acoustic absorbers and diffusers: theory, design and application, CRC Press, 2009.
[27] D. Bies, C. Hansen, Flow resistance information for acoustical design, Applied Acoustics 13 (5) 1980 357–391.
[28] A. B. Bauer, Impedance theory and measurements on porous acoustic liners, Journal of Aircraft 14 (8) 1977 720–728.
[29] D. Givoli, B. Neta, High-order non-reflecting boundary scheme for time-dependent waves, Journal of Computational Physics 186 (1) 2003 24–46.
[30] G. M. Carlomagno, T. Astarita, Slides from course of Gasdynamics, Università degli Studi di Napoli "Federico II" (2009).
[31] A. Savarese, P. Jordan, S. Girard, E. Collin, M. Porta, Y. Gervais, Experimental study of shock-cell noise in underexpanded supersonic jets, in: Aeroacoustics Conferences, American Institute of Aeronautics and Astronautics, 2013, pp. –.
[32] A. Kiran, Jet Noise: Aeroacoustic Distribution of a Subsonic Co-Axial Jet, Ph.D. thesis, University of Warwick (2008).
[33] K. Viswanathan, Instrumentation Considerations for Accurate Jet Noise Measurements, AIAA Journal 44 (6) 2006 1137–1149.

Numerical Investigation of the Noise Produced by a Tandem Diaphragm in a Cylindrical Duct Using LES Data

Ugur Karban

Environmental and Applied Fluid Dynamics Department, ugur.karban@vki.ac.be

Supervisor: Christophe Schram

Associate Professor, Environmental and Applied Fluid Dynamics Department, christophe.schram@vki.ac.be

University Supervisor: Wolfgang Polifke

Professor, Lehrstuhl fr Thermodynamik, Boltzmannstrasse 15, polifke@tum.de

Abstract

The aeroacoustic installation effects on a ducted tandem diaphragm are investigated using various numerical methods based on compressible Large Eddy Simulation (LES) analysis. Three different approaches which use the characteristic waves inside the duct, the dipolar sources on the diaphragm surfaces and the quadrupolar sources near the diaphragm are aimed to be compared to each other. The first two methods are already implemented and yielded satisfactory results in the plane wave region. Implementation of the third method and extension of the analysis for higher frequencies are yet to be completed. Comparison data for LES analysis and noise estimation is provided via hotwire and acoustic measurements, respectively.

Keywords: aeroacoustics, characteristic based filtering, tandem diaphragm, LES

1. Introduction

The motivation of this study is to investigate the aeroacoustic installation effects that take place in typical Environmental Control Systems (ECS) found in aircrafts. The focus here is placed on local singularities: isolated and tandem diaphragms. Flow restrictions are indeed implemented in complex ECS configurations in order to balance the mass flow rate between different branches of the ventilation network. To model this problem, we designed a simple case: a tandem diaphragm placed in a cylindrical duct (see Fig. 1).

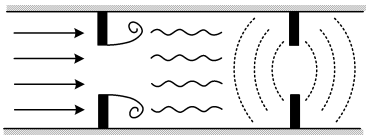

Figure 1: Schematic representation of the model problem. The first diaphragm is used as a turbulence generator, the second one as the main source for the noise generation

The upstream diaphragm induces a complex detached turbulent flow, which perturbations are then convected through the downstream diaphragm. This mechanism is known to generate significant extraneous noise, compared to the noise that would be emitted by the diaphragms if they were not interacting [1]. To have a clear understanding of the tandem diaphragm configuration, a single diaphragm case obtained by removing the downstream diaphragm is also investigated. Diaphragm-to-duct ratio in diameter is set as 0.57 for all cases. For the tandem diaphragm case, the two diaphragms are separated from each other with a distance such that the flow interactions between the diaphragms dominated the noise field without facing any whistling. The frequency of interest of this study is restricted to the plane wave region not to consider complex scattering mechanisms inside the duct. The noise generated on these configurations are aimed to be compared using three numerical methods based

on characteristic based filtering, dipolar sources replacing the diaphragm(s), and quadrupolar sources near the diaphragm(s). All three methods rely on the flow data obtained from compressible LES analysis. The first method is introduced by [2] to be used for providing non-reflecting boundary conditions in LES analyses. Using the pressure fluctuations on the diaphragm surfaces as an input of a Helmholtz solver using Boundary Element and Finite Element Methods is investigated by [3]. The method using the quadrupolar sources is implemented by the author of this paper in [4].

Comparison data for LES and the numerical estimations is provided through the hotwire and in-duct acoustic measurements, respectively. The details of the rig and the measurements are explained in the following chapter.

2. Aeroacoustic Installation Effect: Experimental Analyses

The experimental rig for the duct flow test case is installed in the anechoic room of the von Karman Institute for Fluid Dynamics.The anechoic chamber, specifically designed for studying and certifying free and ducted fan noise, is split in two rooms, connected through acoustic dampers to an external blower that permits controlling the mass flow rate through the ducted diaphragms in this work. The duct is composed of modules corresponding to various flow obstructions and instrumented sections (static pressure probes, radial and azimuthal hot wire traversing system, microphone multi-ports, loudspeaker arrays). The modules are made of plexiglass to have optical access for the PIV measurements. An inlet bellmouth provides a clean inlet flow. The duct system installed for this analysis can be seen in Fig. 2.

Experimental analyses are conducted in two phases: flow velocity measurements and acoustic measurements. To measure the flow velocity, a hotwire traverse mechanism is used at different axial positions on the duct. At each axial position, a radial scan is performed between the center line and the duct surface. For the acoustic field measurements inside the duct, the rig is equiped with axial and azimuthal microphone arrays comprising eight microphones on each side of the diaphragm(s) modules, which are used to isolate the planar and first azimuthal modes radiated through the duct. For both the upstream

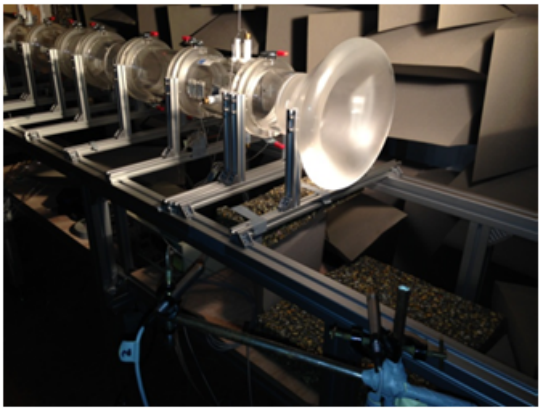

Figure 2: Duct system made of plexiglass

and downstream parts of the diaphragm(s), two consecutive sections of microphone arrays are formed by putting four microphones on each section which are evenly distributed in azimuthal direction.

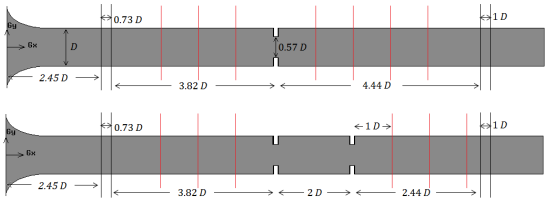

Figure 3: Sections for hotwire and in-duct acoustic measurements. Red vertical lines (separated from each other by 1D) are the sections where hot wire scan from center to duct surface is performed. Black vertical lines indicate the cross-sections where the microphones installed. Four microphones evenly distributed in azimuthal direction are located at each cross-section.

Measurement sections are kept far from the diaphragm(s) to minimize the flow related noise contained in the microphone measurements and the distance between the consecutive microphone array sections are selected large enough for this noise to be uncorrelated. The details are depicted in Fig. 3.

The noise spectra for the single and the tandem diaphragm configurations on the section closest to the inlet are presented in Fig. 4. As a future work, the procedure developed by Sack and Åbom [**?**] for the projection of the acoustic field in the duct modes, using microphone arrays, will be followed to eliminate the uncorrelated turbulent noise and to identify the planar modes from the in-duct measurements.

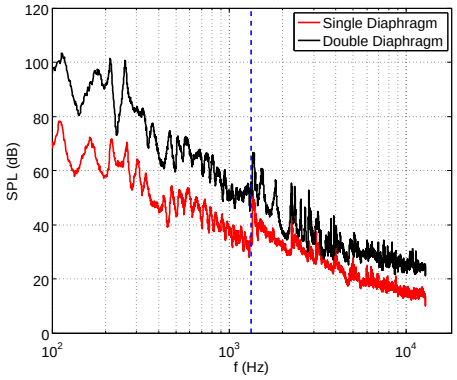

Figure 4: Noise spectrum obtained from inside-duct acoustic measurements for single and double diaphragm configurations. The vertical dashed line indicates the first cut-off frequency.

3. Flow Realizations: Large Eddy Simulation

The LES solver adopted in this work is AVBP [1], developed by CERFACS. This code solves the fully compressible Navier-Stokes equations on unstructured meshes. A second order Lax-Wendroff scheme and an explicit Euler scheme is selected to discretize the spatial and the temporal derivatives respectively. The time steps of the simulations is fixed after reaching the stationary flow condition, to afford a CFL number of 0.7. The latter let to achieve stable simulations while granting low acoustic dissipation and dispersion errors in the domain under analysis. The large turbulent eddies (compared to the mesh elements size) are resolved whereas the subgrid scales are resolved by means of the so called Wall-Attached-Layer-Eddy (WALE) model.

The computational mesh consists of 1.2×10^7 elements for the single diaphragm case whereas for the tandem diaphragms case 1.55×10^7 elements is utilized. Both meshes consists of hexahedral elements structured according to an O-grid topology around the diaphragm. The grid is refined in radial direction with elements of the order of the Taylor microscales. This choice let to resolve correctly the inertial turbulent scales whereas the viscous scales are handled as sub-grid scales. In order to capture correctly the turbulent-generated noise, the boundary layer developed at the diaphragms is resolved. This is done by further refining the computational grid to have the first cell near the wall in the viscous sublayer, i.e. for a radial unit wall $r^+ = 5$.

The simulations are carried out assuring as less acoustic reflections as possible at the boundaries. Therefore boundary conditions adopted consists of a modified version of the Navier-Stokes Characteristic Boundary Conditions (NSCBCs) [5] based on the so called Plane Wave Masking method [2]. The wall boundary is described by an adiabatic no-slip condition. At the inlet a constant velocity profile of $U = 6m/s$ is assumed whereas at the outlet a constant standard pressure $P = 101325Pa$ is imposed.

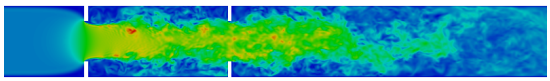

Figure 5: Instantaneous velocity field obtained from LES computation.

The mean velocity profiles obtained at various sections of the duct from $r = 0$ to $r = D/2$ is computed using both hot-wire and LES data. The results are compared in Fig. 6. It can be seen that the velocity profiles between LES and hot-wire data are in good agreement at the sections not close to the diaphragm(s). However LES has a clear tendency to overestimate the jet velocity for the sections near the diaphragm. This may be due to the non-matching diaphragm edge conditions between the simulation and the experimental rig. Radius of curvature at the edges of the diaphragm(s) is 0 in the simulation while this cannot be the case for the experimental setup.

4. Noise Prediction Approaches

4.1. Prediction Using Characteristic Based Filtering

As mentioned before, the acoustic velocity and pressure fluctuations are contained in the unsteady data obtained from the compressible LES, however they are contaminated by the turbulent fluctuations. To extract the pure acoustic data, those turbulent fluctuations are to be eliminated. In this section, an averaging method based on the characteristic waves is introduced to eliminate this turbulence contamination. It is named as *characteristic based filtering* and introduced by Polifke et al [2] to provide non-reflecting boundary conditions in plane wave region for LES analyses.

The acoustical information inside a flow domain is carried along the characteristic waves. These characteristic waves, named as left-going and right-going waves, f and g, respectively in a duct flow case, are

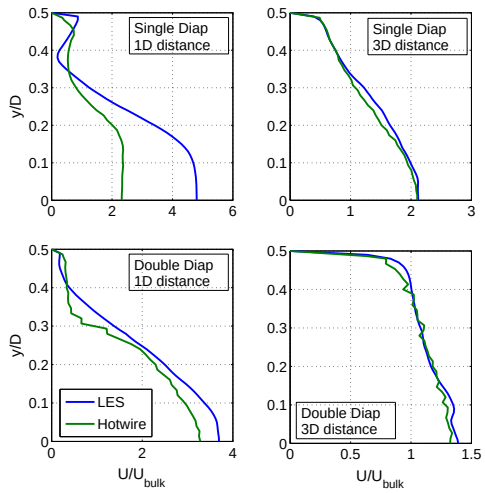

Figure 6: Comparison of the mean velocity profiles for single (top) and double (bottom) diaphragm cases. Figures on the left are measured at a distance of $1D$, figures on the right are measured at a distance of $3D$ downstream the diaphragm(s).

related to acoustical velocity - u' and pressure - p' through the following set of equations;

$$f = \frac{1}{2}(p' + \rho c_0 u') \tag{1}$$

$$g = \frac{1}{2}(p' - \rho c_0 u') \tag{2}$$

where ρ and c_0 are density and speed of sound, respectively. Considering a flow passing through a duct from left to right with a speed U, the convection speed for the left-going and right-going waves becomes $u - c_0$ and $u + c_0$, respectively. Based on the fact that averaging of statistically uncorrelated data yields zero, taking two axial positions x and $x + d$ where d - the separation between the two positions - is large enough to have uncorrelated turbulent fluctuations, an averaging between these positions as follows,

$$f = \frac{f(x|t) + f(x + d|t + \tau)}{2}, \qquad d > I \tag{3}$$

$$f = \frac{f(x + d|t) + f(x|t + \tau)}{2}, \qquad d > I \tag{4}$$

where I denotes the integral length scale of the flow, and τ is equal to $d/(u + c_0)$ for the right-going-wave and $d/(u - c_0)$ for the left-going-wave, can be used to eliminate the turbulent contamination in the characteristic waves and a pure acoustic field can be obtained.

4.2. *Prediction Using Dipolar Source(s) Replacing the Diaphragm(s)*

The main noise generating mechanism in the current configuration is the unsteady pressure fluctuations on the surfaces having an axial component, i.e. direction of propagation in plane wave region. In the current duct-diaphragm configuration, only the frontal and rear surfaces of the diaphragm(s) have such components. The pressure fluctuations on these surfaces can be modeled as dipolar sources and replace the diaphragm itself, since the scattering effects of the diaphragm can be ignored within the plane wave region. Listener points being located far from the diaphragm(s), a further simplification can be made by summing the distributed sources up to a single equivalent dipole (see Fig. 7), whose strength is equal to the magnitude of the resultant unsteady drag force on the diaphragm(s). The single-dipole-inside-cylindrical-

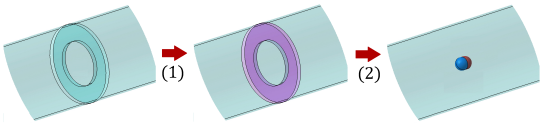

Figure 7: Procedure for calculating the noise sources in LES based method. First the dipoles on the faces of the diaphragm(s) perpendicular to the longitudinal axis are computed (1), and these distributed dipoles are summed up to a resultant point dipole which represents the effect of the diaphragm (2).

duct problem is solved by using the analytical Green's function for cylindrical ducts [6] in Helmholtz equation.

4.3. *Prediction Using Quadrupolar Sources Near the Diaphragm(s)*

Given a wave propagation for any variable φ

$$\frac{\partial^2 \varphi}{\partial t^2} - c_0^2 \frac{\partial^2 \varphi}{\partial x_i^2} \tag{5}$$

and normalization parameters L for length scale, and τ for time scale so that $\tilde{t} \equiv t/\tau$ and $\tilde{x} \equiv x/L$, wave equation becomes;

$$\frac{\partial^2 \varphi}{\partial \tilde{t}^2} = \left(\frac{L}{c_0 \tau}\right)^2 \frac{\partial^2 \varphi}{\partial \tilde{t}^2} \tag{6}$$

where $L/(c_0\tau$ is defined as Helmholtz number He. It can be easily seen that as $He \to 0$, Eq. 6 reduces to;

$$\nabla^2 \varphi = 0 \tag{7}$$

which is the Laplace equation describing an incompressible irrotational flow. This brief analysis shows that, for small Helmholtz numbers; namely, acoustically compact regions, wave propagation equation reduces to incompressible potential flow equation. Therefore, given the source terms and using a wave equation solver, for instance a Helmholtz solver, it is possible to obtain an incompressible flow solution for an acoustically compact region. Based on this approach, a method which computes the unsteady aerodynamic pressure on the diaphragm surfaces due to the quadrupolar sources computed using the compressible LES data in an acoustically compact region near the diaphragm(s) is intended to be implemented. For single diaphragm case, the quadrupoles downstream the diaphragm will be used while for double diaphragm case, the quadrupoles between the diaphragms and downstream the downstream diaphragm will be used (see Fig. 8 and 9).

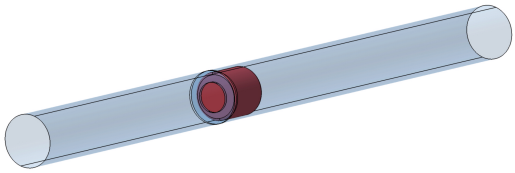

Figure 8: Quadrupole set selected downstream the diaphragm in an acoustically compact region with respect to the first cut-off frequency for single diaphragm case.

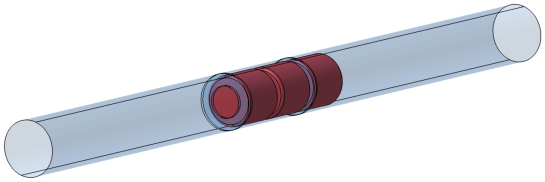

Figure 9: Quadrupole set selected upstream the diaphragm in an acoustically compact region with respect to the first cut-off frequency for tandem diaphragm case.

To compute the acoustic field at the listener points due to these sources, a commercial Helmholtz solver (LMS Virtual Lab Rev.13) is aimed to be used. However, considering the memory restrictions and computational time costs, it is not possible to directly implement to the solver the quadrupoles computed using the LES mesh since the number of sources reaches upto $5x10^5$ and $1.5x10^6$ for single and tandem diaphragm configurations, respectively. This brings the necessity of reducing the number of quadrupoles. Taking the quadrupoles computed using the LES mesh as a set, the reduction in the number of quadrupoles is performed by dividing the entire set into smaller subsets and summing up the quadrupoles contained in each subset to an equivalent source. To understand and minimize the effect of this collocation on the acoustic pressure induced by the quadrupoles on the diaphragm surfaces, a convergence analysis is performed. In the following subsection, this convergence analysis is investigated in detail.

4.3.1. Convergence analysis for the collocation of the quadrupoles

The collocation of the quadrupoles is performed using an oct-tree structure which offers systematically grouping the quadrupoles at different quantities to perform a convergence analysis on this collocation procedure. The convergence analysis is performed removing the diaphragm(s) from the duct with the assumption that a converged incident field inside the duct will imply a converged scattered field with the existence of the diaphragm(s). Having the sources placed in an empty duct, the analytical Green's function which is available for cylindrical ducts is used to compute acoustic field. The entire set of quadrupoles is divided into 9 blocks of one-duct-diameter length. And each block is re-collocated at levels from 1 to 3 as shown in Fig. 10

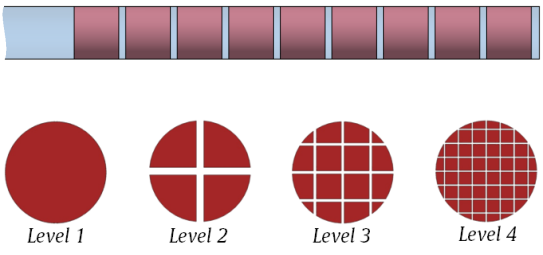

Figure 10: Collocation of the quadrupoles using oct-tree structure.

The listener point is located at the beginning of the first block (at $x/D = 0$) which also coincides with the diaphragm position in the actual case. Regarding the convergence of the acoustic pressure at the listener point induced by each block of quadrupoles grouped at different levels, it can be deduced that for the blocks positioned downstream the $x/D = 2$ point, a collocation at *level 1* yields sufficiently converged acoustic, i.e. an equivalent quadrupole positioned at the volumetric center of the block can sufficiently represent

the entire block (only the first six blocks are shown in Fig. 12).

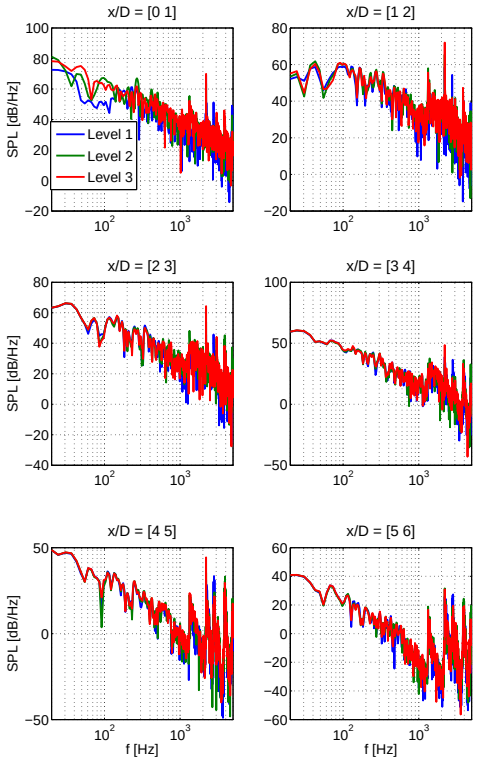

Figure 11: Acoustic pressure spectra at $x/D = 0$ induced by the quadrupoles collocated at levels from 1 to 3.

For the quadrupoles positioned upstream the $x/D = 3$ point, the same process is repeated at *level 2*. They are divided into 6 half-duct-diameter length blocks and each block is re-collocated at levels from 2 to 4. The results of these collocations are shown in Fig. where it can be seen that for the half-blocks between $x/D = 2$ and $x/D = 3$, the collocation at *level 2* gives sufficiently converged acoustic field at the listener point.

This process is applied repetitively with increasing level of collocation for the quadrupoles closer to the listener point until a converged collocation scheme is reached. The positional thresholds for each level determined based on this convergence analysis is given in Table 1.

The resulting collocation scheme is shown in Fig. 13 where the quadrupoles obtained from the LES mesh are summed upto 3815 equivalent quadrupoles.

The acoustic pressure field obtained from this

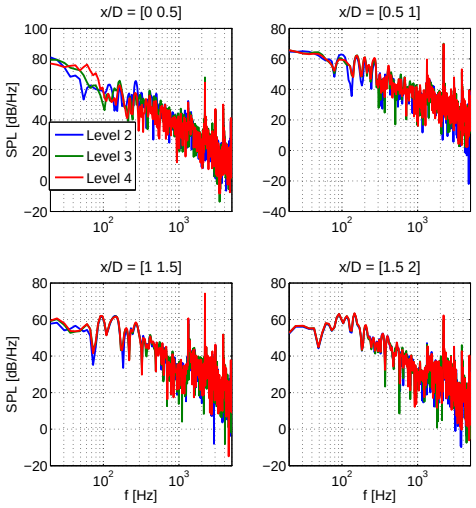

Figure 12: Acoustic pressure spectra at $x/D = 0$ induced by the quadrupoles collocated at levels from 2 to 4.

Table 1: Limits for converged collocation at levels from 1 to 6

Levels	1	2	3	4	5	6
$x/D >$	2	1	0.5	0.375	0.125	0

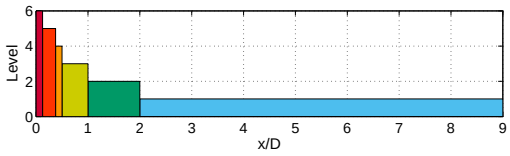

Figure 13: Level of collocation with respect to the non-dimensional axial positions for a converged solution.

converged collocation scheme is used as reference for a further reduction in the number of equivalent quadrupoles used. Selecting a collocation scheme as shown in Fig. 14 where the levels are reduced, the number of equivalent quadrupoles are reduced to 509 and the resultant acoustic field is compared to the one

obtained from the reference scheme. It can be seen in Fig. 15 that the scheme with lower level of collocation does not create a significant change in the acoustic field while it provides a substantial decrease in the number of equivalent quadrupoles used. Based on this reduced scheme, the collocation scheme for the tandem diaphragm case is selected as seen in Fig. 16 yielding 1497 equivalent quadrupoles in total.

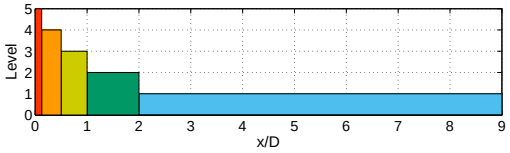

Figure 14: Reduced level of collocation with respect to the non-dimensional axial positions.

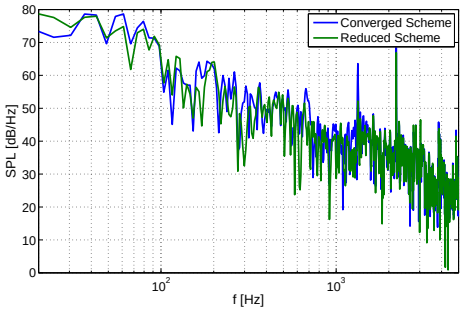

Figure 15: Comparison of pressure spectrum induced by the converged collocation scheme with the reduced scheme.

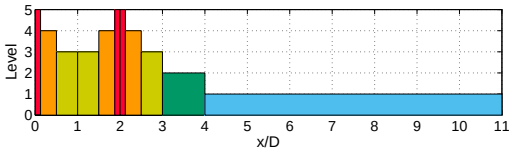

Figure 16: Reduced level of collocation for the tandem diaphragm case (second diaphragm is located at $x/D = 2$).

The implementation of these quadrupoles to the Helmholtz solver is still ongoing. Hence the noise estimation obtained from this method will not be presented in this paper.

The results of first two methods in comparison with the acoustical measurements are given in Fig. 17 and 18 for the single and tandem diaphragm configurations, respectively.

It can be seen that the both methods are capable of extracting the acoustical information contained in the

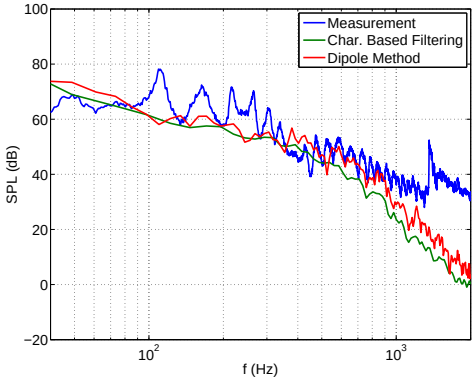

Figure 17: Noise spectra comparison for single diapragm case.

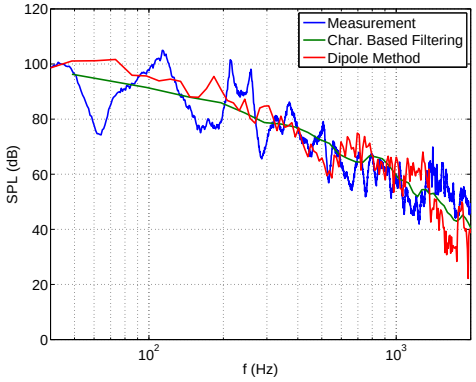

Figure 18: Noise spectra comparison for tandem diapragm case.

compressible LES data. The discrepancies between the measurements exclusively in single diaphragm case are considered to be due to the improper realization of the flow with LES.

5. Conclusions and Future Work

Flow passing through a tandem diaphragm configuration placed in a duct is investigated by implementing different numerical methods using characteristic based filtering and diaphragm-dipole replacement. A third method using the quadrupolar sources near the diaphragm(s) is also mentioned but since implementation is ongoing, no results obtained with this method are shown. Regarding the velocity field comparison between LES analysis and hotwire measurements, it is clearly seen that LES overestimates the recirculation zone behind the diaphragm in both configurations. However, regarding the acoustic field comparison with the in-duct acoustic measurements, this

discrepancy in the velocity field is not seemed to have drastic effects on noise estimation. The deviation in noise estimation is seemed to be more clear for the single diaphragm configuration. This is most likely due to the excessive sensitivity of the acoustic field to the inflow conditions in single diaphragm case. As a future work, LES analysis for single diaphragm case will be repeated with more realistic inflow conditions. The entire investigation will be extended the higher frequencies beyond the plane wave region. And finally, the implementation of the quadrupole method which will form a basis for the stochastic approach introduced in [4] will be completed.

References

[1] A. Sengissen, B. Caruelle, P. Souchotte, E. Jondeau and T. Poinsot, LES of Noise Induced by Flow Through Double Diaphragm System, no. 15th AIAA/CEAS Aeroacoustics Conference, Miami, 2009.

[2] W. Polifke, C. Wall and P. Moin, Partially reflecting and non-reflecting boundary conditions for simulation of compressible viscous flows, Journal of Computational Physics 213 (2006) 437–449.

[3] P. Martinez-Lera, R. Hallez and H. Beriot, Computation of Sound in a Simplified HVAC Duct based on Aerodynamic Pressure, no. 18th AIAA/CEAS Aeroacoustics Conference, Colorado Spring, 2012.

[4] U. Karban, K. Kucukcoskun, G. Ogus, C. Schram, C. Sovardi, W. Polifke, Generation and Scattering of Acoustic Modes in Ducts with Flow, no. 20th AIAA/CEAS Aeroacoustics Conference, Atlanta, 2014.

[5] T. J. Poinsot and S. K . Lele, Boundary conditions for direct simulation of compressible viscous flows, Journal of Computational Physics 101 (1992) 104–129.

[6] S. W. Rienstra and A. Hirschberg, An Introduction to Acoustics, Eindhoven University of Technology, 2012.

ABLATION

Absolute Radiation Measurements of Ablation Products in the Boundary Layer of Carbon Based Ablators

Bernd Helber

Aeronautics and Aerospace Department, von Karman Institute for Fluid Dynamics, helber@vki.ac.be
Department of Electrochemical and Surface Engineering, Vrije Universiteit Brussel

Supervisor: Thierry Magin

Associate Professor, Aeronautics and Aerospace Department, von Karman Institute for Fluid Dynamics, magin@vki.ac.be

University Supervisor: Annick Hubin

Professor, Department of Electrochemical and Surface Engineering, Vrije Universiteit Brussel, anhubin@vub.ac.be

Abstract

A multidisciplinary effort in theoretical, numerical, and experimental investigation is required to understand the complex material response of a new class of ablators under severe re-entry conditions. In the last few years, ablation research including assessment of the ablation products by emission spectroscopy became a new expertise at the von Karman Institute. This study is an attempt to address the issue of locally resolved emission intensities in the ablation boundary layer, with focus on the data treatment to obtain mole fractions of reaction products. An intensified camera with a 2D CCD array connected to an Acton Series spectrograph recorded the full radial and spectrally resolved boundary layer emission profile. Under the assumption of axisymmetry and an optically thin medium, the inverse Abel transformation yielded locally resolved emission intensities of ablation products such as CN and C_2. Both assumptions were examined and found to be valid.

Estimated CN mole fractions were in the order of 0.0005 to 0.005, C_2 mole fractions ranged close to 10^{-5}. All of those values wait for comparison with numerical data coming from new ablation models currently at development at the VKI.

Keywords: ablation, plasma flows, gas-surface interaction, emission spectroscopy, radiation

Nomenclature

Roman symbols

c_i	molar concentration, mole/m^{-3}
I	spectral radiance, W/m^2/sr/nm
k	number of spectral points, -
M	molar mass, g/mol
N	number of particles, m^{-3}
r	radius, m
$S_{\lambda 1-\lambda 2}$	integrated local emission, W/m^3/sr
T	temperature, K
x	mole fractions, -

Greek symbols

ϵ	spectral power density, W/m^3/sr/nm
λ	wavelength, nm
ρ	density, kg/m^3
τ	time, s

Sub- and Superscripts

$_{abs}$	self-absorption
$_g$	gas
$_i$	species i
$_{oI}$	of interest
$_{rot}$	rotational
$_s$	solid
$_{th}$	theoretical
$_{vib}$	vibrational

Acronyms

HSC	High-speed camera
LTE	Local Thermodynamic Equilibrium
MSL	Mars Science Laboratory
NRMSE	Normalized Root Mean Squared Error
TPS	Thermal Protection System

1. Introduction

On August 6, 2012, NASA's Mars Science Laboratory (MSL) mission successfully dropped a rover on the Martian surface that includes an automated sample collection system for chemistry and mineralogy analysis. Next steps will be to identify, develop, and qualify required technologies for returning Martian and other asteroid samples safely to Earth.

Such sample returns at very high re-entry speeds will use ablative materials for the thermal protection system (TPS), shielding the spacecraft from the severe heating. Chemical and physical decomposition of ablators transform the thermal energy into mass loss and recession, whilst the remaining solid material insulates the vehicle substructure [1; 2]. To achieve high performance characteristics of the ablative Thermal Protection Material (TPM) engineers of planetary probes and space vehicles make use of a wide range of composites [3; 4]. TPMs are generally composed of a rigid precursor and a filling matrix, to serve as a pyrolyzing, ablating, and insulating material at low weight with reasonable mechanical properties. A current example of a new family of porous Lightweight Ceramic Ablators (LCA) for high-speed entry missions is made of a carbon fiber preform impregnated with phenolic resin such as PICA (phenolic-impregnated carbon ablator) developed by NASA [5; 6], and European ablator Asterm, developed by Airbus DS [7]. Most recent examples for the successful performance of PICA are the Stardust (2006 [8]), and MSL [9] missions. With the work presented in this paper, we want to contribute with new experimental data to the ongoing efforts of improving the heat shield reliability, reducing design uncertainties and developing new thermo-chemical ablation models.

Selection and sizing of the thermal protection material (TPM) are the two key performance parameters in TPS design and prediction inaccuracies can be fatal for the crew or the success of robotic missions. The prediction tools for ablative TPS design are still inherited from the Apollo program [10; 11] and new high fidelity material response models are proposed [12] in order to take into account the porous micro-structure of the new class of materials as well as a non-constant elemental composition for the pyrolysis gas mixture [13].

Comprehensive experimental data are required for the development and validation of the new numerical prediction tools. For instance, there is still insufficient research on the pyrolysis products in the high temperature boundary layer to draw any firm conclusions about their evolution when released by the material. Our study is oriented towards the reacting boundary layer of pyrolyzing and ablating materials with the aim to quantify mole fractions of species ejected by the material.

In a foregoing analysis, we studied the non-pyrolyzing carbon preform material as well as the carbon-phenolic ablators Asterm and AQ61 [14; 15]. Three spectrometers recorded the line-of-sight integrated emission signature within the chemically active boundary layer. A stagnation line numerical model made it possible to compare the recorded emission of CN violet with predicted mole fractions of the CN radical along the stagnation line [16]. A new spectroscopic setup is proposed in this work, utilizing an intensified camera with a 2D CCD array to record the full radial boundary layer emission profile. Under the assumption of axisymmetry and an optically thin medium, the inverse Abel transformation yielded locally resolved emission intensities (spectral power density) of carbonic molecules such as CN and C_2. The comparison with spectroscopic models allowed direct estimation of local mole fractions in the boundary layer.

We used graphite as basic carbon ablator for assessment of the experimental and numerical methods, followed by experiments of P50 cork to simulate a pyrolyzing composite ablative material. The P50 ablation tests were carried out in the frame of the Qarman project at VKI and are closer discussed elsewhere [17].

The paper is organized according to the following objectives:

- Review of the ablation process of charring materials (section 2);
- Description of the VKI Plasmatron facility, experimental methods and treatment of spectroscopic data to obtain local emission intensities (section 3);
- Numerical methods for simulated emission intensities (section 4);
- Preliminary results on graphite ablation in nitrogen (CN) and preliminary results on P50 cork ablation in air (CN & C_2) (section 5);
- Conclusions and perspectives (section 6).

2. Ablation of charring materials

The processes through which ablators are able to accommodate high heat fluxes are balanced between surface radiation, phase transitions (melting, sublimation) as well as chemical reactions (charring, oxidation) on the surface and inside the material. To achieve high performance characteristics of ablative materials, mostly composite materials are used for the ablative heat shield. When subjected to increasing temperature, the virgin material successively transforms following two mechanisms (Fig. 1):

a) During ***pyrolysis*** the phenolic resin is progressively carbonized into a low density, porous char and loses around 50% of its mass producing pyrolysis gases by vaporization. The pyrolysis gases are transported out of the material by diffusion and convection, and exhaust into the boundary layer, providing a further barrier for the heat exchange (blowing), and undergo additional chemical reactions, consuming more heat. Making use of polymers such as phenolic resins for the matrix of the composite takes advantage of their endothermic degradation nature, thereby absorbing energy, and serving as a binder for the other components [4].

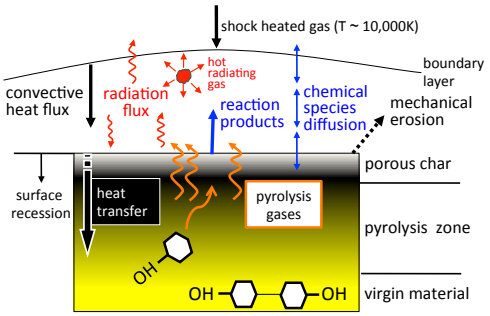

Figure 1: Ablation and pyrolysis processes of a charring material

b) ***Ablation*** of the char layer (composed of the carbonized resin and the remaining carbon fibers) is then promoted by heterogeneous chemical reactions, phase change and mechanical erosion (e.g. spallation), altogether leading to recession of the material. The rate at which an ablator recesses is a consequence of its prevention of heat conduction and strongly coupled to the aerothermal conditions it encounters. In other words, the material will primarily respond with a higher ablation rate to increased heating whilst the heat conducted to the bondline will stay constant. This illustrates the great importance of material response models to accurately predict recession of the material. However, due to limited experimental data, this quantity remains as one of the largest uncertainties in material response analysis [18].

3. Experimental facility, measurement techniques and methods

To enable a proper design of heat shields based on porous, low-density composite ablators, a complete experimental analysis with parallel modeling is necessary. The following phenomena have to be analyzed and described accurately: **finite-rate chemistry** for pyrolysis gas, **transport phenomena in porous medium** as well as in the **boundary layer**, and **volume ablation** with a possible ablation zone (microscopic description of the porous medium).

3.1. Plasmatron facility description

The Plasmatron facility is extensively utilized at the von Karman Institute for Fluid Dynamics for the reproduction of the aero-thermodynamic environment of re-entry plasma flows, creating a high-enthalpy, highly dissociated subsonic gas flow[19]. It is equipped with a 160 mm diameter ICP (Inductively Coupled Plasma) torch powered by a high frequency, high power, high voltage (400 kHz, 1.2 MW, 2 kV) generator. In order to achieve heat fluxes higher than ~5 MW/m^2, As the gas is heated by induction through a coil, the advantages of ICP torches are the high purity of the plasma flows produced, due to the absence of electrodes and their associated erosion. The experimental techniques for characterization of the plasma freestream are reviewed below.

A 50 mm diameter copper water-cooled probe, mounting a copper calorimeter in the center of the front face, is used for the calibration of plasma flow conditions. The cold wall (~350 K) stagnation point heat flux is determined by the cooling water mass flow, controlled by a calibrated rotameter, and the inlet/outlet temperature difference, measured by two type-E thermocouples. A Teflon insulator is inserted between the calorimeter and the probe's wall in order to have side-wall adiabatic conditions. Both the probe and calorimeter have copper surfaces which are high catalytic to nitrogen and oxygen atoms recombination. The heat flux can be measured with ±10% accuracy. A water-cooled Pitot probe is used to perform stagnation pressure measurements. The pressure line is connected to a Validyne variable reluctance pressure transducer and a voltage demodulator amplifies the output. Beside the calorimeter and dynamic pressure

probe for free-stream characterization, the measurement techniques included temperature measurements (two-color pyrometer, broadband radiometer and thermocouples), emission spectroscopy and high speed camera imaging. Validyne and amplifier are calibrated prior to the test by means of a Betz water manometer, leading to an uncertainty of ±0.2 %. The Plasmatron chamber is also equipped with an absolute pressure transducer that measures the static pressure with ±2 Pa accuracy. The probes are mounted inside the Plasmatron test chamber at 0.445 m distance from the ICP torch exit. The placement ensures that the axis of the probe and the axis of the torch itself coincide.

The mass flow was kept at $\dot{m} = 16$ g/s. For the results presented throughout this paper, the time indication $t = 0$ s corresponds to the injection of the test sample into the plasma flow. The sample was attached to a sample holder located 445 mm downstream of the plasma jet exit in an actively cooled sample conditioning system to prevent preheating and early pyrolysis. After reaching the favored test condition (static pressure & heat flux), the sample was injected using a pneumatic mechanism.

3.2. *Experimental methods for ablation characterization*

A comprehensive experimental setup is installed at the facility to offer a most complete database for ablation testing, including intrusive and non-intrusive techniques [20]. The instrumentation equipment involves a video camera, a high-speed camera, a 2-color pyrometer, a broad-band radiometer, and low as well as high resolution spectrometers. This series of instruments provide data on the surface state which are used to detect the surface evolution during the ablation test and outgassing products from the material's interior if a pyrolzing sample is used. Emission Spectroscopy has been implemented with temporal and spatial resolution to characterize the reacting boundary layer around the sample. Figure 2 presents the instrumentation set-up at the VKI Plasmatron facility for ablation testing as used for this work.

For a non-intrusive determination of the surface recession, a Vision Research Phantom 7.1 CMOS high-speed camera (HSC) is used, synchronized with an optical emission spectrometer. The accuracy of this method is constrained by the resolution of the HSC and the successive conversion of pixels to millimeters, therefore, the uncertainty is assumed to be one pixel as a higher sensitivity of detecting a surface change is not possible, resulting in a recession uncertainty of $\delta HSC = \pm 0.25\, mm$.

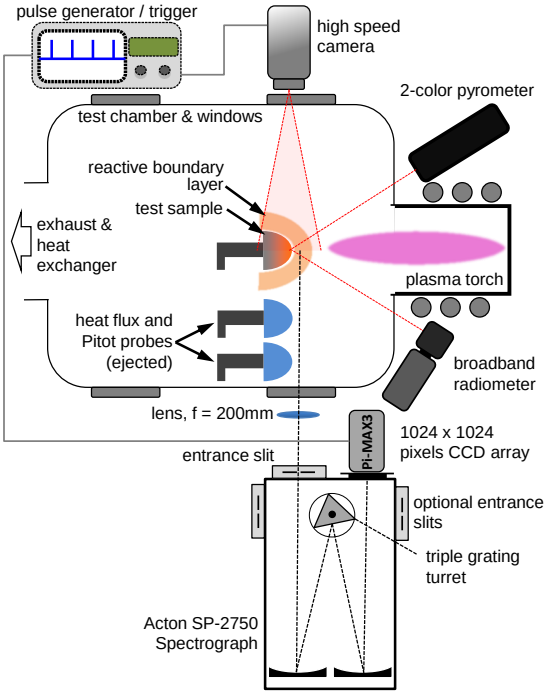

Figure 2: Schematic of experimental setup for ablation characterization including spectrometer setup with intensified CCD detector.

The boundary layer in front of the ablating sample was observed with an Acton Series spectrograph of 75 cm focal lengths combined with an ICCD PI-MAX camera with a frame of 1024×1024 pixels. The two-dimensional ICCD array enabled spectral measurements across the complete jet diameter of 20 cm. The spectrometer is equipped with three gratings of 150, 1200, and 3600 grooves/mm, which can be interchanged interactively. The three gratings allow both low resolution spectra of wide-range (120 nm) molecular features in the range 200-1000nm (variable center wavelength), as well as high resolution spectra in the range of a few nm.

3.3. *Experimental spectra elaboration*

The light emitted by the plasma and boundary layer was detected by the ICCD camera placed at the spectrograph exit. For each single recording, a data matrix was obtained with wavelength distributed along the horizontal axis and the different lateral positions along the observed plasma radius distributed along the vertical axis, as highlighted in Fig. 3.

The integration time of the spectrometer was set to 40-150 ms for all tests (comparable to the shutter of a camera), averaging the acquired spectrum during this acquisition period. For experiments on graphite samples in nitrogen, 10 frames were averaged to increase

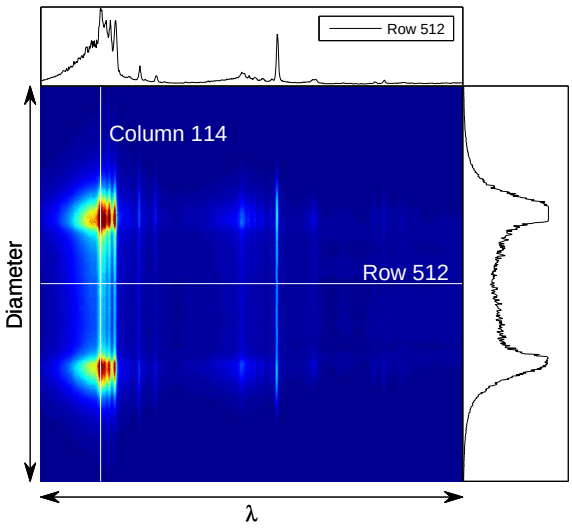

Figure 3: Example of single data frame captured by PI-Max ICCD during ablation test: wavelength is distributed along the horizontal axis and the the radius is distributed along the vertical axis.

the signal to noise ratio. This was not done for cork ablation test in air to resolve time-dependent features such as pyrolysis and surface recession. The optical diagnostic bench was mounted on a movable holding system, which enabled horizontal movements to be able to place the line of sight to the desired position. The positioning of the probing location was checked and adjusted before each experiment. The raw data obtained from the spectrometer are in the form of counts. To convert the data into spectral radiance of $W/(m^2.sr.nm)$, calibration of the whole system consisting of the light collection mechanism and the spectrometer efficiency, was performed between 350-900 nm by placing a tungsten ribbon lamp (OSRAM WI 17G) in the focus of the collection optics inside the test chamber. The spectral signature of the calibration lamb below 350 nm is too low, and calibrated spectra are only reported within the range 350-900 nm.

As the plasma jet is being observed in the side-on direction, the recorded signal is a result of the local emission integrated along the line-of-sight over the depth of the plasma source. If we assume axisymmetry and an optically thin medium, the laterally observed signal can be transformed into a radial distribution profile by using the inverse Abel transformation. The averaged line-of-sight spectra are deconvolved, and radially resolved measurements are obtained for direct comparison for example with numerical tools. The relation between the spectral radiance ($I(\lambda)$ in $W/m^2/sr/nm$) and the local spectral emission (spectral power density $\epsilon(\lambda)$ in $W/m^3/sr/nm$) can be expressed as:

$$\epsilon = -\frac{1}{\pi}\int_{r=y}^{r=r_p} \frac{dI_\sigma(y)}{dy}\frac{dy}{\sqrt{y^2-r^2}} \qquad (1)$$

with r_p being the jet radius.

Following the work of Deron [21], the integral of equation 1 was evaluated using cubic spline interpolation. The Abel inversion procedure was tested with a sinusoidal function as presented in Fig. 4. The inverted profile (c) is almost identical to the original intensity profile.

Treatment of the experimental spectra was necessary prior to conversion of local emission via equation 1. Firstly, the calibrated line-of-sight integrated data were spatially filtered at every spectral position

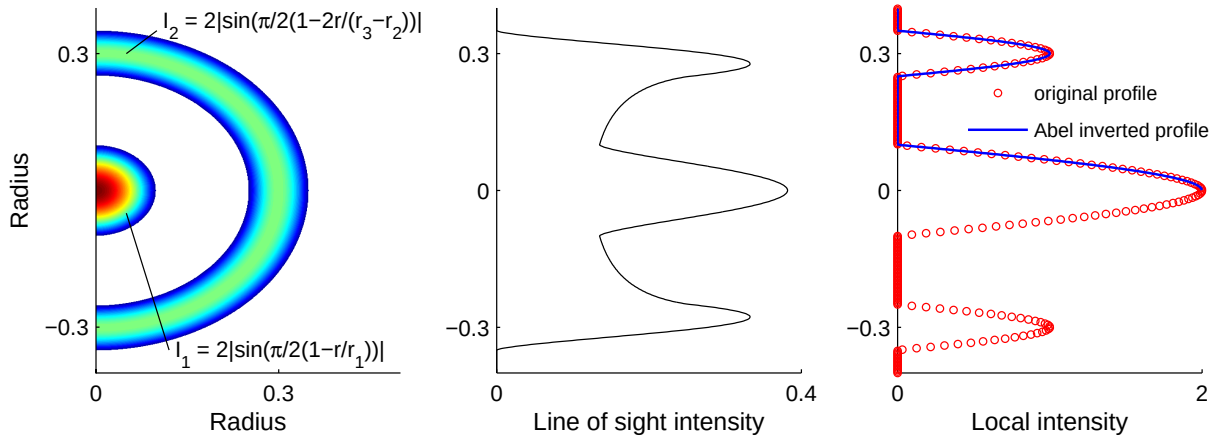

Figure 4: Validation of Abel inversion procedure: Raw emission intensity (left), and line integrated emission (middle); the Abel inversion carried out on the integrated profile compares well to the analytical solution (right).

(i.e. for every vertical profile). Secondly, the symmetry of vertical profiles was checked and averaged half-profiles were computed. Figure 5 shows the outcome of each step of the process: from the calibrated experimental data to smoothed and interpolated data to the radial emission results via Abel inversion.

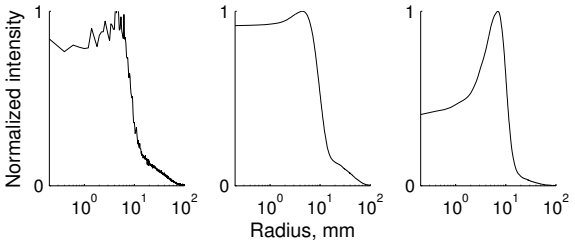

Figure 5: Data treatment: calibrated experimental data (left); smoothed and symmetized data (middle); Abel inverted data (right).

Local emission intensities, for example of CN violet or C_2 Swan, can then be compared to intensities coming from radiation models (Specair [22]) to obtain local ground state species concentrations. To do so, the emission of the molecular band of interest was integrated for species i and radial position r over a wavelength range λ_1 to λ_2 to capture all underlying radiation within the signal $S^r_{i,\lambda_1-\lambda_2}$. In the case of ablation in air, this signal is also a function of the time passed from sample injection.

$$S^r_{i,\lambda_1-\lambda_2}(t) = \int_{\lambda_1}^{\lambda_2} \epsilon_i(\lambda) d\lambda, \qquad [\mathrm{W/m^3/sr}] \qquad (2)$$

The $\Delta v = 0$ sequences of CN violet (370-390nm, see Fig. 9), and C_2 Swan (495-520 nm) were used for our study. The theoretical spectra computed with Specair were treated in the same way for comparison (section 4.1).

3.4. Effect of Self-absorption

The inverse Abel-transformation is only valid for optically thin media, i.e. light emitted within the hot boundary layer gas is not re-absorbed by the principal constituents of the gas itself as it travels through it. According to quantum mechanics, atoms and molecules can experience energy changes only within discrete energy levels, ruled by their individual electronic structure. As a consequence, absorption mainly occurs for the same species by which the light was emitted, so called self-absorption. Other species may also absorb light in the same wavelength range, if those are overlapped with the emitting species.

The effect of self-absorption can be determined from the number density of a species of interest, and hence, pressure, mole fraction and observed volume size have direct impact on the effect of self-absorption. The effect on the emission spectrum can be studied with Specair, if self-absorption is accounted for as illustrated in Fig. 6. Although emission spectra for $x_{CN} = 10^{-4}$ seem identical whether or not taking self-absorption into account, a mole fraction of 1 results in strong self-absorption. The difference compared to neglecting self-absorption is in the order of one magnitude. Absorption is strongest around the band-head at 388 nm.

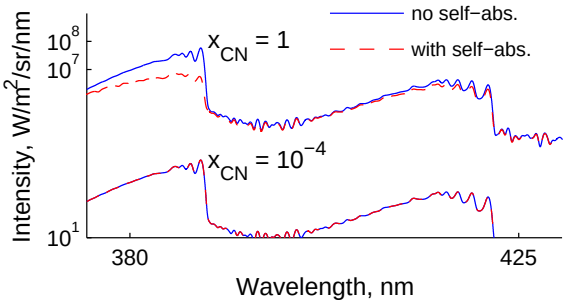

Figure 6: Difference between CN violet spectra computed with Specair accounting for self-absorption (dashed lines) and neglecting self-absorption (full lines) for mole fractions of $x_{CN} = 10^{-4}$ and 1.

To quantify the effect of reduced emission due to self-absorption we computed a database of CN violet spectra for mole fractions in the range of 10^{-5} to 1 for rotational and vibrational temperatures between 5000 and 10000 K at 100 hPa and a slab width of 1 cm. Each spectrum was computed accounting for self-absorption as well as assuming a thin medium (no absorption). The error between the two spectra was quantified by the Normalized Root Mean Squared Error (NRMSE)

$$NRMSE = \frac{1}{I_{thin,max} - I_{thin,min}} \sqrt{\frac{\sum_{i=1}^{k} (I_{thin}(i) - I_{abs}(i))^2}{k}} \qquad (3)$$

with I_{thin} being the spectrum computed neglecting absorption, and k the number of total spectral points (i) per computed spectrum. All spectra were convolved with a Gaussian function to reproduce the spectrometer's entrance slit.

From Fig. 7 (a) we can see the NRMSE evolution for mole fractions of $x_{CN} = 10^{-4} - 10^{-3}$ at increasing T_{rot} and T_{vib}, with a maximum NRMSE of 0.2%. Those data give an indication on the error made between the two spectra, but are somewhat expression-

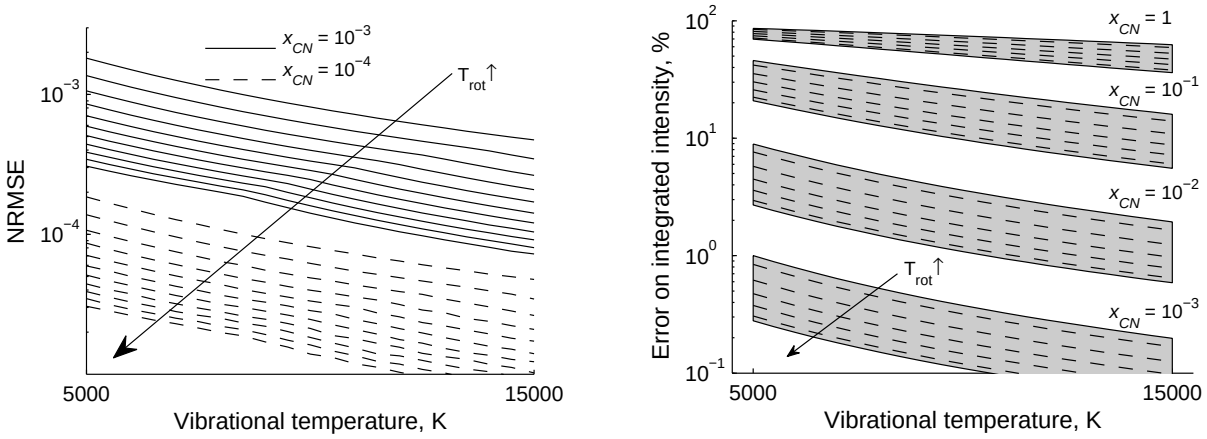

Figure 7: Effect of self-absorption on CN violet emission spectrum computed for different mole fractions at 100 hPa and a slab width of 1 cm: (a) Normalized RMSE between spectra neglecting and accounting for self-absorption for two mole fractions and changing T_{rot} and T_{vib}; (b) Error induced on spectrally integrated (375 to 390 nm) emission signal for rotational temperatures between 5000 and 10000 K (shaded areas); the error made for mole fractions below 0.001 is less than 1%.

less for our analysis.

We therefore applied equation 2 to both thin and self-absorbed spectra to identify directly the error made on the integrated emission, as presented in Fig. 7 (b). From this graph it is clear that self-absorption at low temperatures and high mole fractions (at 100 hPa and 1 cm slab width) can result in tremendous errors close to 100% for $x_{CN} = 1$, but drops below 1% for $x_{CN} = 10^-3$.

4. Numerical method for simulated emission intensities

4.1. Integrated spectral power density of CN violet as a function of mole fractions

We carried out an analysis of the integrated spectral power density of the CN violet and C_2 Swan systems with Specair 2.2, assuming a Boltzmann distribution of excited levels. Inputs for Specair are translational, rotational, vibrational, and electronic temperatures, as well as mole fraction of the species of interest, pressure and slab width. The slab width indicates the plasma column along the line of sight of a virtual spectrometer. The slab width will not be of importance in the following due to the treatment of locally resolved emission intensities. Those are obtained from Specair by division with the slab width ($W/m^2/sr/nm$ to $W/m^3/sr/nm$). Molar fractions of emitting species can hence be determined if temperatures and pressures are accessible. The spectra were simulated in the range of 5,000 to 15,000 K for rotational and vibrational temperatures, respectively. Molar fractions were set equal to 1 at a pressure of 15 hPa and a slab width of 1 cm. For optically thin spectra, the spectral radiance scales linearly with molar fraction and pressure, each of which simply in- or decreases the particle density N_i of species i in the simulated volume by

$$N_i = c_i N_A = x_i N_A \frac{\rho}{M} \tag{4}$$

with the Avogadro constant N_A and the average molar mass M. The upper (excited) states $n_{u,i}$ of species i and hence, their emission I_i, are directly related to N_i

$$I_i(\lambda) \sim n_{u,i} \sim N_i \tag{5}$$

It is therefore sufficient to compute spectra for varying T_{rot} and T_{vib} for only one pressure, mole fraction and slab width. This database can then be scaled with pressure and mole fractions of interest (oI), highly decreasing the computational costs

$$I_{oI} = \frac{I_{S\,pecair}}{p_{S\,pecair}} \times p_{oI} \times x_{oI} \tag{6}$$

All theoretical spectra were then convolved with a Gaussian function (0.5 nm Full-Width-Half-Maximum (FWHM)) to reproduce the spectrometer's entrance slit, and integrated in the same wavelength range as the experimental emission (eq. 2). The result of the whole procedure is illustrated in Figure 8 for a CN mole fraction of 10^{-5} at 15 hPa.

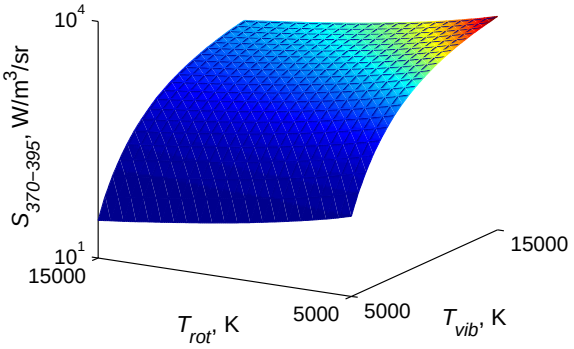

Figure 8: Integrated local emission intensity mapping of CN for $x_{CN} = 10^{-5}$ at 15 hPa as a function of T_{rot} and T_{vib}.

4.2. *Spectra fitting: rot. & vib. temperatures*

It is clear from section 4.1, that temperatures of the excited molecules are required for the estimation of their ground-state mole fractions. We used experimental spectra in the range 370 to 425 nm, including the CN violet $\Delta v = 0$ and $\Delta v = -1$ sequences, for comparison to simulated spectra in order to obtain temperatures of the excited molecule. A fitting procedure [23] was applied to SPECAIR to estimate translational-rotational temperatures T_{rot} and vibrational-electronic temperatures T_{vib}. The theoretical spectrum was convolved with a Gaussian function (0.5 nm FWHM) to reproduce the spectrometer's entrance slit.

A numerically fitted CN spectrum is presented in Fig. 9. Good agreement between the experimental and simulated spectra was obtained by varying T_{rot} and T_{vib}. The temperature bounds were based on an uncertainty of 10% on the spectrometer emission intensity, allowing the theoretical spectrum to vary within those limits for the fitting procedure.

Those temperatures are used in section 5 for estimation of CN mole fractions by comparing experimental emission intensities to those computed in the foregoing section.

5. Preliminary results

5.1. *Graphite ablation in nitrogen*

The procedure outlined in the previous sections was applied to graphite ablation tests in nitrogen plasma. Graphite consists only of carbon and leads to a strong CN violet emission spectrum in nitrogen plasmas due to nitridation and excitation transfer with molecular nitrogen [24].

$$C_s + N \rightarrow CN_g \qquad (7)$$

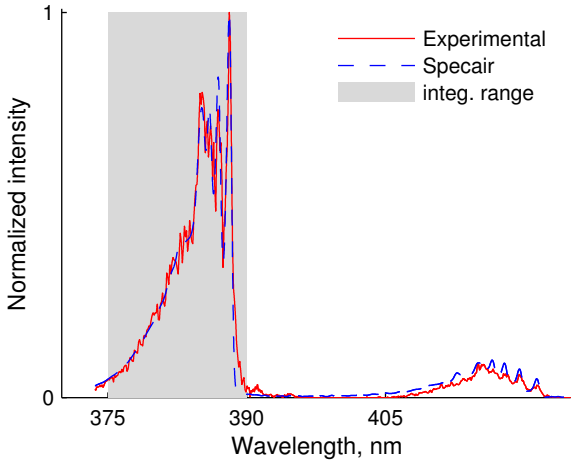

Figure 9: Experimental spectra of CN violet agree well with simulated, fitted spectra computed with Specair 2.2.
$T_{rot} = 6946\,\text{K} \pm 350\,\text{K}$, $T_{vib} = 8414\,\text{K} \pm 400\,\text{K}$.

Although the reactivity of carbon with nitrogen is low, the excited CN radical is a very strong emitter (for instance the CN violet with its second electronically excited state to ground state transition), and mole fractions in the order of 10^{-5} can easily be observed. But one can benefit from the low surface recession rate, and it is sufficient to record one averaged spectrum per ablation test, contrary to temporally resolved acquisition.

To assess the assumption of axisymmetry we integrated the Abel-inverted, locally resolved emission for each spectral position along the whole radius (vertical direction in Fig. 3) and compared the result to the originally recorded, line-of-sight emission at the centerline (row 512). The good agreement of the two curves is depicted in Figure 10. From this comparison we deduce that the assumption of axisymmetry is valid, as inhomogeneous surface ablation or boundary layer chemistry would result in different curves.

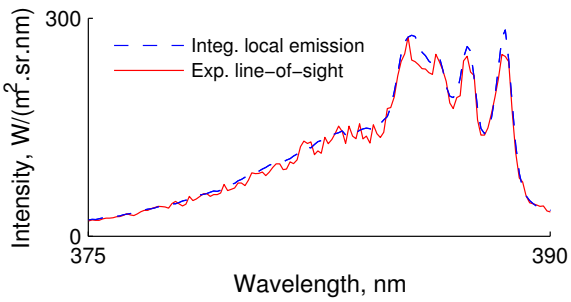

Figure 10: Check of axisymmetry assumption: Locally resolved emissions integrated over full radius (vertical direction) for each spectral position compares well to originally measured line-of-sight spectrum at centerline (pixel 512).

The radial emission profile of the CN violet bandhead at 388.3 nm is shown in Figure 11 for different heating conditions, at surface temperatures ranging from 1540 K to 2670 K. The profiles are almost identical for the four conditions, responding with an intensity increase with temperature. Emission was highest at the stagnation line, decreasing towards the sides. As expected, the maximum emission was observed for the highest surface temperature.

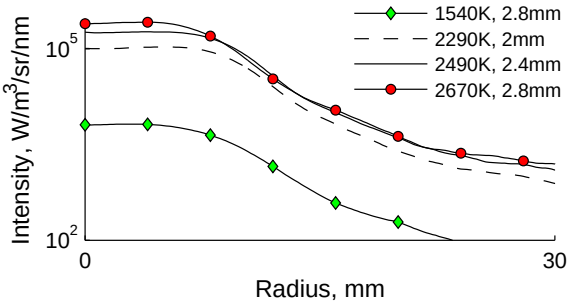

Figure 11: Locally resolved emission of the CN violet bandhead (388.3 nm) along the radius at different surface temperatures (distance from surface indicated).

On the basis of Fig. 11, it seems fair to suggest that the CN species density was highest towards the stagnation line. We assume that temperatures along a radius of 10 mm did not change significantly.

The procedure to obtain CN mole fractions including uncertainty bounds is outlined in Fig.12. T_{rot} and T_{vib} including their uncertainties are output of the fitting procedure described in section 4.2 and serve as input for the calculation of the presented curve of mole fractions vs. spectraly integrated radiance $S^0_{375-390}$, obtained from the numerical procedure of section 4.1. The experimental mole fraction was obtained by intersecting this curve with the measured intensity, including uncertainties on the fitting procedure (dash-dot lines) and the measured intensity ΔS (20 %).

CN mole fractions including uncertainties obtained from three graphite ablation cases are reported in table 1. The gathered data clearly suggests that a higher surface temperature led to higher CN mole fractions in the boundary layer. Next steps will be the comparison of these data to ablation models of carbon surfaces in air and nitrogen flows, for instance such as described in [25; 26]. Turchi et al. report CN mole fractions on a graphite surface in nitrogen flows in the order of 10^{-4} to 10^{-3} depending on the surface temperature and the assumed nitridation probability at the wall. Those results are in line with our experimental observations.

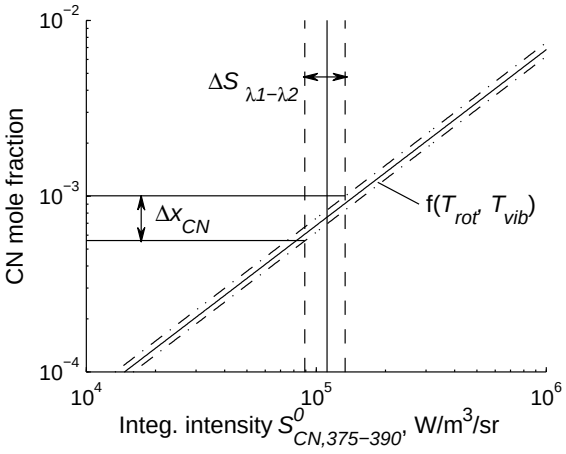

Figure 12: CN mole fraction determination: Mole fractions are plotted vs. integrated emission intensities computed with SPECAIR at T_{rot} and T_{vib}, intersection with the experimental integrated intensities provides x_{CN}; uncertainty is introduced by 20 % of exp. intensity and uncertainty on fitted temperatures (dash-dot lines).

Table 1: Estimated CN mole fractions: Three graphite test conditions indicating the recorded surface temperature, estimated T_{rot} and T_{vib} as well as integrated emission intensity for each condition; CN mole fractions increase with surface temperature.

T_S K	T_{rot} K	T_{vib} K	$S^0_{370-395}$ kW/m^3/sr	x_{CN} -	Δx_{CN} -
2290	6713	9462	107.2	7.2E-4	2.1E-4
2490	6857	9091	156.6	1.5E-3	4.4E-4
2630	6963	7698	200.7	3.9E-3	1.4E-3

5.2. Cork P50 ablation in air

We used ablation tests of P50 cork for observation of CN violet and C_2 Swan emission spectra in the presence of pyrolysis gases. Those experiments were carried out in the frame of the Qarman project at VKI and are closer discussed elsewhere [17]. The experiments were carried out in air plasma with a hemispherical test sample of 25 mm in diameter. P50 is made of cork granules agglomerated with special phenolic binders and a density of 480 kg/m^3.

The main difference of these experiments compared to those of graphite in nitrogen, are now the importance time-dependent phenomena. Firstly, pyrolysis of the phenolic filler is a transient process, resulting in strong outgassing just after test sample injection due to sudden increase of surface temperature. Secondly, ablation in air leads to surface recession due to consumption of the char layer by oxygen. As the spectrometer setup was not moved during each experiment, the distance of the surface from the collection

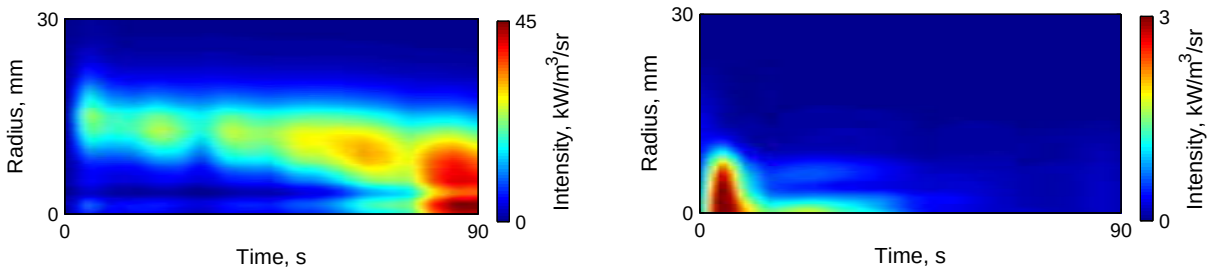

(a) CN (b) C_2

Figure 13: Mapping of integrated CN violet (375 to 390 nm) and C_2 Swan (495-520 nm) local emission over time and radius: CN responds with an intensity increase towards test end whilst C_2 strongly drops off after injection.

optics strongly influence the results and knowledge of the recession rate is required. The high-speed camera was used to obtain the location of the surface during each experiment.

Elementary reactions involving C_2 play an important role in hydrocarbon chemistry, and C_2 spectra are prominent in high-temperature processes such as combustion and gas-phase pyrolysis. Especially the two carbon atoms of the alkyne acetylene are bonded together in a strong triple bond, breaking up at higher temperatures into C_2 and H [27]:

$$C_2H_2 + M \rightleftharpoons C_2H + H + M \tag{8}$$

$$C_2H + M \rightleftharpoons C_2 + H + M \tag{9}$$

The C_2 Swan system was also identified by emission spectroscopy during ablation testing of the carbon-phenolic ablator PICA [28], MonA [20], and AQ60 [29].

An intensity map of the integrated local emission $S^r_{\lambda 1-\lambda 2}$ for CN violet (a) and C_2 Swan (b) over time and radius is given in Fig. 13. Differences between the two ejected species are clearly visible: Whilst CN intensity was increasing towards test end, C_2 was strongest at test start, followed by a strong drop and vanished after around 40 s into the experiment. The outgassing rate fell off as expected during the course of the experiment. The observation of an increasing CN signal is however surprising, but can be explained by a swelling cork sample during the experiment. In this case, surface recession is compensated, or rather overcome, by the expansion of the test sample due to its thermal response. The spectrometer was initially located 2 mm ahead of the test sample. During swelling, the sample surface came closer to the spectrometer collection optics, leading to an increase in CN violet emission. Extracted radial profiles of CN and C_2 are plotted in Fig. 14 to better point-out this observation.

Beside the temporal increase of the CN violet signal, the data suggests a radial shift of the emission from off-stagnation region ($\approx$ 15 mm) towards the stagnation line at 80-90 s.

Estimated mole fractions at test start and 5 s after

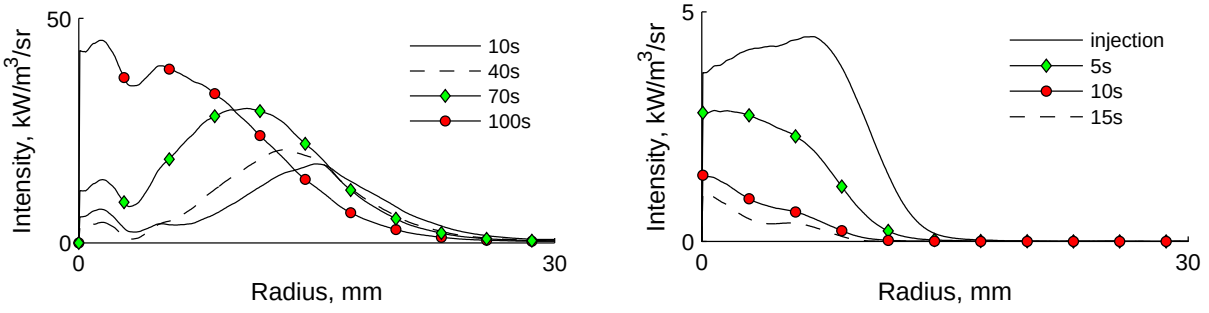

(a) CN (b) C_2

Figure 14: Radial profiles of integrated CN violet emission (375 to 390 nm) during cork ablation at different times throughout the test run portray shift of maxima towards centerline (100 hPa, 1 MW/m^2).

injection are listed in Table 2. The drop of C_2 concentration during the first 5 s is apparent, as well as the higher concentration off the stagnation line at a radial position of 100 mm. More processing of the experimental data is required for the future, as well as comparison to stagnation line models including the treatment of pyrolysis gas mixtures. This paper mainly serves as a documentation of the methodology and assessment of the underlying assumptions, such as axisymmetry and negligence of self-absorption.

Table 2: Estimated C_2 mole fractions: Cork P50 test at 1730 K surface temperature, time from injection and radius of estimated mole fractions are listed, as well as T_{rot} and T_{vib} and integrated emission intensity for each condition; C_2 mole fractions are highest at test start and off-stagnation line.

τ	r	T_{rot}	T_{vib}	$S^0_{\lambda 1-\lambda 2}$	x_{C_2}	Δx_{C_2}
s	mm	K	K	W/m^3/sr	-	-
0	2	5316	7887	3930	2.7E-5	7.8E-6
0	100	5361	7816	5230	5.1E-5	1.8E-5
5	2	5068	7816	1220	9.1E-6	4.5E-7

6. Conclusions

In the last few years, ablation research including assessment of the ablation products by emission spectroscopy became a new expertise at the von Karman Institute. Multiple spectrometers were dedicated in the past to record the line-of-sight integrated emission signature within the chemically active boundary layer. This work reports the extend of our experimental setup for ablation characterization in the VKI Plasmatron facility, including data treatment to obtain mole fractions of reaction products in the boundar layer. An intensified camera with a 2D CCD array connected to an Acton Series spectrograph recorded the full radial boundary layer emission profile. Under the assumption of axisymmetry and an optically thin medium, the inverse Abel transformation yielded locally resolved emission intensities (spectral power density) of carbon containing molecules such as CN and C_2.

Locally resolved emission integrated over the full radius for each spectral position compared well to originally measured line-of-sight spectra at the centerline. These results provide confirmatory evidence that axisymmetry can be assumed. We further found by comparison of spectra computed with Specair accounting for self-absorption, that the error made on the integrated emission is lower than 1 % for mole fractions below 10^{-3}. On these grounds and maximum CN mole fractions of $x_C = 0.004$, we can argue that self-absorption can be neglected for our conditions of interest.

Most of the report is dedicated to experimental and numerical data treatment in order to
1) obtain local emission intensities (spectral power densities) from the experimental data, including smoothing, averaging and Abel inversion procedures,
2) creating a look-up table of theoretical spectroscopic data produced with Specair for comparison to the experimental data. Temperatures of observed molecular spectra were estimated by a fitting procedure applied to Specair. The experimental data was then compared to the data set of theoretical emission intensities of CN violet and C_2 Swan to estimate mole fractions of both underlying species.

The data gathered in this study also portraits the temporal and spatial evolution of the observed species. CN violet emission was highest close to the centerline for ablation without pyrolysis blowing (graphite in nitrogen). But during cork ablation, highest CN emission was found $\approx$ 15 mm away from the stagnation region. C_2 Swan emission was highest during the injection of the cork sample, highly decreasing during the first 10 s and vanished half way through the experiment after 40 s. The latter finding lends support to the claim that C_2 is a product of the pyrolysis gases injected into the boundary layer by the material.

The CN mole fractions obtained within this work are in the order of 0.0005 to 0.005, for graphite surface temperatures between 2300 and 2700 K. C_2 mole fractions ranged close to 10^{-5} during air ablation at 1730 K surface temperature. All of those values are as anticipated and wait for comparison with numerical data. A current test campaign is dedicated to the nitridation and recombination effects of carbonic surfaces to nitrogen and new ablation models are in development. Implementation of appropriate tools to deal with the pyrolysis effects and their comparison to the data provided here will help putting forward the research on their effect on the surrounding boundary layer.

Acknowledgments

We acknowledge Mr. P. Collin for his valuable help as Plasmatron operator and warmly thank Dr. Damien Le Quang for his expertise in emission spectroscopy and fruitful discussions. We gratefully acknowledge Amorim Cork Composites for providing the P50 test

material. The research of B. H. is supported by a fellowship of the Agency for Innovation by Science and Technology (IWT, dossier #111529) in Flanders, and research of T.M. by the European Research Council Starting Grant #259354.

References

[1] B. Laub, E. Venkatapathy, Thermal Protection System Technology and Facility Needs for Demanding Future Planetary Missions, in: International Workshop on Planetary Probe Atmospheric Entry and Descent Trajectory Analysis and Science, Lisbon (Portugal), ESA SP-544, October, 2003, pp. 239 – 247.

[2] G. Duffa, Ablative Thermal Protection Systems Modeling, AIAA Education Series, 2013.

[3] G. Sutton, The Initial Development of Ablation Heat Protection: An Historical Perspective, J. Spacecraft Rock. 19 (1) (1982) 3–11. doi:10.2514/3.62196.

[4] L. Torre, J. Kenny, A. Maffezzoli, Degradation behaviour of a composite material for thermal protection systems Part I - Experimental characterization, J. Mater. Sci. 33 (1998) 3137–3143. doi:10.1023/A:1004399923891.

[5] H. K. Tran, Development of Lightweight Ceramic Ablators and Arc Jet Test Results, Tech. Rep. TM-108798, NASA Ames Research Center (1994).

[6] H. K. Tran, C. E. Johnson, D. J. Rasky, F. C. L. Hui, M. T. Hsu, T. Chen, Y. K. Chen, D. Paragas, L. Kobayashi, Phenolic Impregnated Carbon Ablators (PICA) as Thermal Protection Systems for Discovery Missions, Tech. Rep. TM 110440, NASA Ames Research Center (1997).

[7] H. Ritter, P. Portela, K. Keller, J.-M. Bouilly, S. Burnage, Development of a European Ablative Material for Heatshields of Sample Return Missions, in: 6th European Workshop on TPS and Hot structures, Stuttgart (Germany), 1-3 April 2009.

[8] M. Stackpoole, S. Sepka, I. Cozmuta, Post-Flight Evaluation of Stardust Sample Return Capsule Forebody Heatshield Material, in: 46th AIAA Aerospace Sciences Meeting and Exhibit, Reno (US-NV), AIAA 2008-1202, January, 2008. doi:10.2514/MASM08.

[9] K. T. Edquist, B. R. Hollis, C. O. Johnston, D. Bose, T. R. White, M. Mahzari, Mars Science Laboratory Heatshield Aerothermodynamics: Design and Reconstruction, in: 44th AIAA Thermophysics Conference, San Diego (US-CA), AIAA 2013-2781, June, 2013. doi:10.2514/MTP13.

[10] R. M. Kendall, E. P. Bartlett, R. A. Rindal, C. B. Moyer, An analysis of the coupled chemically reacting boundary layer and charring ablator: Part I, Tech. Rep. CR 1060, NASA (1968).

[11] F. S. Milos, Y.-K. Chen, Comprehensive model for multicomponent ablation thermochemistry, in: 35th Aerospace Sciences Meeting & Exhibit, AIAA 1997-0141, Reno (US-NV), January, 1997. doi:10.2514/MASM97.

[12] J. Lachaud, I. Cozmuta, N. Mansour, Multiscale approach to ablation modeling of phenolic impregnated carbon ablators, J. Spacecraft Rock. 47 (6) (2010) 910–921. doi:10.2514/1.42681.

[13] J. Lachaud, N. N. Mansour, Porous-Material Analysis Toolbox Based on OpenFOAM and Applications, J. Thermophys. Heat Transfer 28 (2) (2014) 191–202. doi:10.2514/1.T4262.

[14] B. Helber, O. Chazot, T. Magin, A. Hubin, Space and Time-Resolved Emission Spectroscopy of Carbon Phenolic Ablation in Air and Nitrogen Plasmas, in: AIAA paper 2013-2770, 2013. doi:10.2514/MTPHT14.

[15] B. Helber, O. Chazot, A. Hubin, T. Magin, Microstructure and gas-surface interaction studies of a low-density carbon-bonded carbon fiber composite in atmospheric entry plasmas, Composites Part Adoi:10.1016/j.compositesa.2015.02.004.

[16] B. Helber, A. Turchi, O. Chazot, A. Hubin, T. Magin, Gas/Surface Interaction Study of Low-Density Ablators in Sub- and Supersonic Plasmas, in: 11th AIAA/ASME Joint Thermophysics and Heat Transfer Conference (US-GA), AIAA 2014-2122, June, 2014. doi:10.2514/MTPHT14.

[17] I. Sakraker, In-flight Experiment Design and Ground Testing of a Re-EntryCubeSat, in: Review of the VKI Doctoral Research, von Karman Institute for Fluid Dynamics, 2015.

[18] Cozmuta, I. and Wright, M. J. and Willcockson, W. H., Defining Ablative Thermal Protection System Margins for Planetary Entry Vehicles, in: AIAA 2011-3757, 2011.

[19] B. Bottin, O. Chazot, M. Carbonaro, V. van der Haegen, S. Paris, The VKI Plasmatron Characteristics and Performance, in: RTO AVT Course on Measurement Techniques for High Enthalpy and Plasma Flows, Rhode-Saint-Genèse (Belgium), RTO EN-8, October, 1999, pp. 6–01 – 6–26.

[20] B. Helber, C. O. Asma, Y. Babou, A. Hubin, O. Chazot, T. E. Magin, Material response characterization of a low-density carbon composite ablator in high-enthalpy plasma flows, J. Mater. Sci. 49 (13) (2014) 4530 – 4543. doi:10.1007/s10853-014-8153-z.

[21] C. Deron, Rayonnement thermique des plasmas d'air et d'argon: modélisation des propriétés radiatives et étude expérimentale, Ph.D. thesis, Ecole centrale de Paris (2003).

[22] C. Laux, Radiation and Nonequilibrium Collisional-Radiative Models, in: Fletcher, D., Charbonnier, J.M., Sarma, G.S.R., and Magin, T. (Ed.), Physico-Chemical Modeling of High Enthalpy and Plasma Flows, von Karman Institute Lecture Series 2002-07, 2002.

[23] A. Cipullo, B. Helber, F. Panerai, L. Zeni, O. Chazot, Investigation of Freestream Plasma Flow Produced by Inductively Coupled Plasma Wind Tunnel, J. Thermophys. Heat Transfer 28 (3) (2014) 381–393. doi:10.2514/1.T4199.

[24] P. Boubert, P. Vervisch, CN spectroscopy and physicochemistry in the boundary layer of a C/SiC tile in a low pressure nitrogen/carbon dioxide plasma ow, J. Chem. Phys 112 (23) (2000) 10482–10490. doi:10.1063/1.481682.

[25] A. Turchi, B. Helber, A. Munafò, T. E. Magin, Development and Testing of an Ablation Model Based on Plasma Wind Tunnel Experiments, in: AIAA 2014-2125, Atlanta, USA, 2014.

[26] P. Schrooyen, Development of a Numerical Simulation Tool for the Aerothermal Flow through an Ablative Thermal Protection System for Atmospheric Entry, in: Review of the VKI Doctoral Research, von Karman Institute for Fluid Dynamics, 2015.

[27] T. Kruse, P. Roth, Kinetics of C_2 Reactions during High-Temperature Pyrolysis of Acetylene, J. Phys. Chem. 101 (1997) 2138–2146. doi:10.1021/jp963373o.

[28] J. Uhl, W. P. Owens, J. M. Meyers, D. G. Fletcher, Pyrolysis Simulation in an ICP Torch Facility, in: 42nd AIAA Thermophysics Conference, Honolulu (US-HI), AIAA 2011-3618, June, 2010. doi:10.2514/MTC11.

[29] R. Wernitz, C. Eichhorn, T. Marynowski, G. Herdrich, Plasma Wind Tunnel Investigation of European Ablators in Nitrogen/Methane Using Emission Spectroscopy, International Journal of Spectroscopy 2013 (2013) 1–9. doi:http://dx.doi.org/10.1155/2013/764321.

Development of a Numerical Simulation Tool for the Aerothermal Flow through an Ablative Thermal Protection System for Atmospheric Entry

Pierre Schrooyen

Aeronautics and Aerospace Department, von Karman Institute for Fluid Dynamics, Belgium, pierre.schrooyen@vki.ac.be

Supervisor: Thierry Magin

Associate Professor, Aeronautics and Aerospace Department, von Karman Institute for Fluid Dynamics, Belgium, magin@vki.ac.be

University Supervisor: Philippe Chatelain

Assistant Professor, Institute of Mechanics, Materials and Civil Engineering, Université Catholique de Louvain, philippe.chatelain@uclouvain.be

Abstract

The interaction between the flow in the free stream and the ablation is one of the phenomena that leads to difficulties in heat-flux prediction during atmospheric entries. This paper presents the computational tool based on a high-order discontinuous Galerkin method, that simulates and models both the flow and wall phenomena in a continuum approach. Numerical results to verify and validate the methodology are presented.

Keywords: atmospheric entry, thermal protection system, ablation, discontinuous Galerkin.

1. Introduction

The atmospheric entry of spacecrafts presents several challenges in simulating the response of the ablative Thermal Protection Systems (TPS). This thermal response strongly depends on the interaction between the ablative material of the heat shield and the high-enthalpy flow surrounding the capsule. Requirements concerning mass efficiency for missions with very high entry velocities have led to the development of new classes of light carbon composite ablators. Such materials are typically composed of carbon fibers impregnated with phenolic resin and their micro-structure is rather complex. Therefore, existing physico-chemical models and computational methods need to be upgraded or new ones have to be developed to study the material response of these new ablators in high enthalpy flows.

The components of these ablative materials are carbon fibers and a matrix of phenolic resin. During atmospheric entry, a part of the heat flux is transferred to the heat shield, involving a temperature gradient inside the material and its transformation. The phenolic resin will be pyrolysed leaving carbonized material and the carbon preform. The highly porous material close to the wall will react with the high enthalpy flow and this char layer material will be consumed by ablation. Depending on the flow conditions, oxidation of the carbon preform can occur mainly at the surface or the oxygen can diffuse through the porous matrix and react in-depth [1]. This work is mainly focus on this last phenomenon and our interest is dedicated to the ablation of the carbon fibers.

The common approaches for the macroscopic modeling of the TPS material are mainly of three different types. The first approach is based on the one- or multi-dimensional transient computation of the conduction inside the material [2]. A lot of complexity can be added to the modeling if the accurate resolution of the processes taking place inside the material is sought [3]. However, simplified boundary conditions are usually used for the gas–solid interface in this kind of approach [2]. For instance, inviscid boundary-layer edge conditions are taken from separate simplified flowfield simulations, and the surface conditions (i.e., temperature or convective heat flux) are obtained by means of semi–empirical relations. In the second approach, the surface ablation is treated using a dedi-

cated boundary condition in the CFD simulation of the flow field. This approach has been used extensively in a wide range of applications (i.e., heat shields, solid rocket nozzles, etc) giving satisfactory results. Studies on both charring and non-charring materials, using either equilibrium or finite-rate surface chemistry, have been carried out using this method [4; 5; 6; 7; 8]. The last, most complex approach, can be described in short as a combination of the previous two. It can be performed either by coupling together two distinct solvers designed to compute the solid- (first approach) and the gas-side (second approach) of the problem [9; 10], or by directly developing a unified numerical tool. This should be capable of computing the flow through and around the material accounting also for in-depth ablation of the material fibers [11; 12]. The use a unified tool is very promising for the study of highly porous materials for which, under certain conditions, the hypothesis of a mere surface ablation is not accurate enough. This unified methodology is the approach followed in this work and will be identified in the following as the *volumetric approach*.

This paper presents the methodology implemented and numerical test cases to verify it. The replication of an experiment carried on in the NASA Ames side arm facility is also presented and discussed. The interactions between the flow and the ablated geometry is studied and especially the competition between surface and volume ablation. Finally, the fidelity of the models is discussed and studied through a sensitivity analysis with respect to kinetics and transport properties.

2. Methodology

The multi-dimensional numerical tool is implemented within the research code Argo developed at Cenaero based on a high-order Discontinuous Galerkin Method (DGM). This type of discretization was introduced back in 1973 by Reed and Hill [13] to solve neutron transport problems. DGM cumulates the advantages of finite volume and finite element methods. The advantage lies in their accuracy on unstructured meshes, computational efficiency and scalability due to the locality of data and operations [14]. This type of discretization is a particular class of *Finite Elements Methods (FEM)*. Unlike within classical continuous Garlerkin formulation, DGM allows discontinuities in between elements. Additional terms in the discretization scheme can be considered as internal boundary conditions that couple an element with its neighbors. These are implemented in this code using an (approximate) Riemann solver for the convective problem, while for the diffusive part a Nitsche type weak Dirichlet condition is used [15]. The Argo CFD solver has already been extensively verified to solve incompressible and compressible flow problems [16]. Within this platform, a fully implicit method was developed to simulate multiphase reacting flows. The code has been coupled with the library Mutation^{++} developed at the von Karman Institute [17]. This library provides thermodynamic and transport properties as well as reaction rates within the fluid phase.

In order to treat a multiphase system, the volume averaging approach is used to derive continuum equations [18]. Each phase is described by field quantities which are continuous within this specific medium but discontinuous in the whole volume. Solving the equations for each phase separately requires to account for the microstructure of the porous medium which can be quite complex and computationally expensive. Using volume averaging theory, the equations describing one phase are averaged over a small elementary volume such that the volume averaged quantities are continuous in space. Within this work, the system is composed of two phases, the solid matrix and the fluid phase (see Fig. 1). The pores of the medium are filled

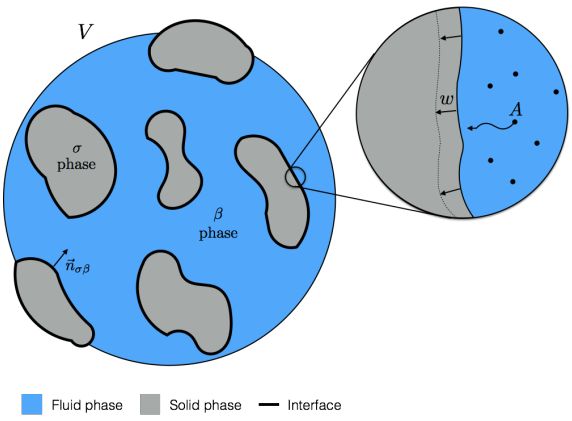

Figure 1: Volume averaging for the porous medium.

with a fluid phase β and subscript σ represents quantities related to the solid phase. An elementary volume V is therefore composed of V_β and V_σ, and the volume fraction of each phase is defined as

$$\epsilon_\beta = \frac{V_\beta}{V}, \epsilon_\sigma = \frac{V_\sigma}{V}, \tag{1}$$

where the volume fraction of the fluid phase ϵ_β is usually called the porosity or the void fraction. The su-

perficial average of a quantity α

$$\langle \alpha \rangle \;=\; \frac{1}{V} \int_{V_\gamma} \alpha \; dV, \tag{2}$$

has to be distinguished from the intrinsic average on a general phase γ,

$$\langle \alpha \rangle_\gamma = \frac{1}{V_\gamma} \int_{V_\gamma} \alpha \; dV. \tag{3}$$

The two averages are linked by the volume fraction:

$$\langle \alpha \rangle = \epsilon_\gamma \langle \alpha \rangle_\gamma. \tag{4}$$

To apply this method to a set of partial differential equations, the volume average of derivatives has to be related to the derivatives of volume averaged quantities. The theorem of local volume averaging detailed in many works [18; 19] is

$$\langle \nabla \cdot \alpha \rangle = \nabla \cdot (\langle \alpha \rangle) + \frac{1}{V} \oint_{\partial \Omega_\beta} \alpha \cdot n_{\beta\sigma} \; dS \;, \tag{5}$$

$$\langle \frac{\partial \alpha}{\partial t} \rangle = \frac{\partial \langle \alpha \rangle}{\partial t} - \frac{1}{V} \oint_{\partial \Omega_\beta} (\alpha w) \cdot n_{\beta\sigma} \; dS \;. \tag{6}$$

Applying the volume averaging theory to the Navier-Stokes equations, the set of equations (mass, momentum and energy conservation laws) describes the macroscopic flow through the porous medium. The following sections summarize the development of the Volume Averaged Navier-Stokes equations (VANS) for multi-species flows through a reactive porous medium. Detailed development can be found in many publications [18; 20; 21].

2.1. Mass Conservation Law

The mass conservation law is averaged for each species in the gaseous phase accounting for species diffusivity and heterogeneous reactions at the surface of the solid matrix. Applying the volume averaging theory, the mass conservation equation can be expressed as:

$$\begin{aligned} &\frac{\partial \langle \rho_i \rangle}{\partial t} + \nabla \cdot (\langle \rho_i u \rangle) \\ &\quad = \nabla \cdot \Big((D_{eff} + D_{disp}) \nabla \langle \rho_i \rangle_\beta \Big) + \dot{\omega}_{hom} + \dot{\omega}_{het}, \end{aligned} \tag{7}$$

where $\langle \rho_i \rangle$ is the superficial average over the small elementary volume ($\langle \rho_i \rangle = \epsilon_\beta \langle \rho_i \rangle_\beta$), $\dot{\omega}_{hom}$ is the homogeneous production term , $\dot{\omega}_{het}$ is the heterogeneous source term, D_{eff} is the effective diffusion coefficient and D_{disp} is the hydrodynamic dispersion. The effective diffusivity for an isotropic medium can be expressed as a function of the void fraction and the tortuosity (η) of the inner porous medium [22]

$$D_{eff} = \frac{\epsilon_\beta}{\eta} D_{ref}. \tag{8}$$

The dispersive effects will only be important if the Peclet number based on the pore size is larger than one [18]. According to Lachaud [23], for the ablation of carbon fibers, the Peclet number is often smaller than unity leading to negligible dispersive effects.

In the case of material recession, a mass balance for the solid phase is added to the system of equations to track the evolution of the porosity. The solid phase is assumed rigid and the mass loss will occur only at the surface of the solid matrix, the solid mass conservation is

$$\frac{\partial \left(\epsilon_\sigma \langle \rho \rangle_\sigma \right)}{\partial t} = \dot{\omega}_{het}, \tag{9}$$

where $\langle \rho \rangle_\sigma$ is the intrinsic solid density which is not changing. Equation 9 is therefore used to track the change in porosity. In this work, the porous matrix is composed of carbon fibers. Assuming an homogeneous distribution of these cylindrical fibers, as well as a uniform and radial recession of these, their radius can be computed based on the porosity [23]

$$\frac{r_0^2}{\epsilon_{\sigma,0}} = \frac{r^2}{\epsilon_\sigma}. \tag{10}$$

Finally, the heterogeneous reaction term in Eq. 7 and 9 can be expressed if one assumes an irreversible first order reaction between the solid phase and the fluid phase

$$\dot{\omega}_{het} = -S_f k_f \langle \rho_A \rangle_\beta, \tag{11}$$

where k_f is the forward reaction rate which is assumed constant on the surface of the fibers, and $\langle \rho_A \rangle_\beta$ is the intrinsic density of reactant. The specific surface (S_f) is defined as

$$S_f = \frac{A_w}{V_s}, \tag{12}$$

where A_w and V_s are respectively the contact surface of the solid matrix with the fluid phase and the control volume. For a fibrous porous medium, it can be expressed as

$$S_f = \frac{N 2\pi r L_f \epsilon_\sigma}{N \pi r^2 L_f} = \frac{2}{r_0} \sqrt{\epsilon_0 \epsilon_\sigma}. \tag{13}$$

2.2. Momemtum Conservation Law

The volume averaged momentum equation can be written as

$$\frac{\partial(\langle \rho u \rangle)}{\partial t} + \nabla \cdot (\epsilon_\beta \langle \rho \rangle_\beta \langle u \rangle_\beta \langle u \rangle_\beta) = -\epsilon_\beta \nabla \langle p \rangle_\beta + \nabla \cdot \langle \tau \rangle + F, \quad (14)$$

where $\langle p \rangle_\beta$ is the pressure inside the fluid phase, F is the drag force and Whitaker [18] has shown that it can be modeled by:

$$F = \frac{-\mu}{\kappa} \epsilon_\beta^2 \langle u \rangle_\beta. \quad (15)$$

In Eq. 14, it is assumed that the Reynolds number based on the length of a pore is sufficiently small such as the inertial term can be neglected. The correlation between deviations is also supposed negligible with respect to the drag force term [20]. Assuming incompressible flow, Darcy's law can be retrieved at steady state:

$$\nabla p = \frac{-\mu}{\kappa} \epsilon_\beta \langle u \rangle_\beta = \frac{-\mu}{\kappa} \langle u \rangle. \quad (16)$$

2.3. Energy Conservation Law

For the energy equation, thermal equilibrium between the two phases is assumed. Therefore only one equation is used for both phases:

$$\frac{\partial \langle \rho E_{tot} \rangle}{\partial t} + \nabla \cdot \left(\epsilon_\beta \langle \rho \rangle_\beta \langle H \rangle_\beta \langle u \rangle_\beta \right) = \nabla \cdot k_{eff} \nabla T + \nabla \cdot (\langle \tau \cdot u \rangle), \quad (17)$$

where the total energy is composed of the energy of the solid phase and the energy of the fluid phase

$$\langle \rho E_{tot} \rangle = \epsilon_\beta \left(\langle \rho \rangle_\beta (\langle e \rangle_\beta + 0.5 \langle u \rangle_\beta^2) \right) + \epsilon_\sigma \langle \rho \rangle_\sigma \langle e \rangle_\sigma, \quad (18)$$

with H being the enthalpy of the gaseous phase, τ is the stress tensor and k_{eff} is an effective conductivity inside the porous medium.

2.4. Modeling the Interface Area

The hypothesis made to derive this system of equations assumes that the porosity is constant in the small averaging volume. This is no longer valid in the interface region between a porous medium and a plain fluid domain. To treat this interface, the two existing main methods either use a jump condition to correct the approximation of the closure model in the interface region [20; 24] or use a variable permeability/porosity in a part of the domain [25; 26]. Futhermore, in the case of flow field over ablative material, this interface area will move due to recession. Therefore, an *interface tracking* or an *interface capturing* method has to be used to follow the moving boundary. The *interface tracking* technique presents many limitations for multidimensional problems, since the mesh movement can seriously degrade mesh quality in cases of non-uniform material recession. Remeshing can be time consuming and quite complex depending on the shape of the interface. Therefore, it is proposed to use an *interface capturing* technique, which does not require the meshes to follow the interface. For the ease of implementation, a diffuse approach is proposed. These techniques smooth the discontinuity over a transition region. Within this work, a normalized hyperbolic tangent function is used to smooth the initial solid volume fraction on the grid

$$H(\phi) = \tanh\left(\frac{\pi \phi}{\epsilon_\phi}\right), \quad (19)$$

where ϕ is the initial distance function from the porous medium and ϵ_ϕ is the double grid distance on which the quantity is regularized. Following the work of Pochet [27], in order to ensure stability of the scheme, the smoothing distance has to be at least equal to

$$\epsilon_\phi = 1.5 \frac{h}{p}, \quad (20)$$

h being the mesh size and p the interpolation order. Using a diffuse interface capturing method, it is natural to adopt a variable porosity approach. This porosity will vary from a constant value in the homogeneous porous medium to one in the plain fluid region.

The value for the porosity is used to determine the properties of the porous medium. For the permeability for instance, there is no general function of the porosity and usually these assume homogeneous porous medium. However, the model of Carman-Kozeny [28] will be used to link the local porosity and the permeability. This semi-heuristic model is based on the concept of hydraulic radius and leads to a permeability, κ, which depends on the porosity, the tortuosity and the specific surface area

$$\kappa^{-1} = \frac{S_{f,0}^2 (1 - \epsilon_\beta)^2 k_k}{\epsilon_\beta^3}, \quad (21)$$

where k_k is directly proportional to the tortuosity and the proportional constant depends on the shape of the solid matrix. Using this model, even in the heterogeneous interface region, the permeability will be adapted implicitly in case of recession.

Table 1: Shock characteristic quantities.

X [-]	P [Pa]	T [K]	v_s [m/s]
N_2/O_2	5.0	300	12300
0.79/0.21			

3. Verification Test Cases

To verify the developed tools two verification test cases are proposed. The first verifies the resolution of a multi-species reactive flow inside the Argo platform. The second example tests the solution of a problem involving fluid flow and porous media.

3.1. Shock Relaxation

This test case verifies the solution of the multi-species reactive Euler equations. Assuming steady state and 1D problem, it is possible to transform the system of partial derivative equations into a system of ordinary differential equations which can be solved easily [29]. The solution of this system was implemented in the shocking code provided in the Mutation^{++} suite which solves the chemical relaxation behind a strong shock. Typical values for a shock during an atmospheric entry are given in Table 1. In order to reduce the number of degrees of freedom only 5 species are considered (N, O, N_2, O_2, NO). Comparison with the results of Argo are shown in Fig. 2.

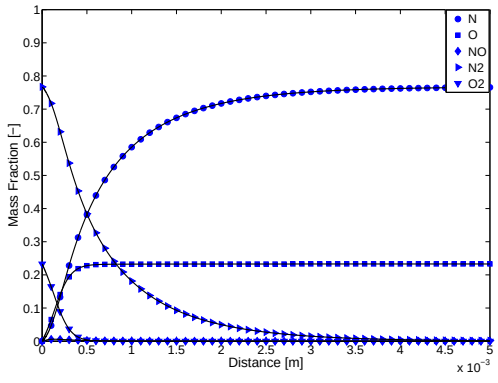

Figure 2: Chemical relaxation after a strong shock (see Table 1). The mass fractions at steady state are compared with the results of a one dimensional code (black solid lines).

3.2. Porous Plug

This test case is of particular importance regarding the numerical experiment discussed in Section 3.2. For this problem, a channel flow is forced to pass through a porous medium. The upper and lower boundaries are considered as non-slip walls, the pressure is imposed at the outlet while temperature and velocity profile are given at the inlet. The porosity of the medium is 0.7 and the permeability is defined using Darcy number: $Da = \kappa/H^2 = 1e^{-3}$. For this problem, the Poiseuille velocity profile is expected to become more uniform in the porous region (see Fig. 3). The numerical results in Fig. 4 for the pressure and velocity profile along the axis of symmetry are compared with the results of Betchen [30]. Since the flow is normal to the interface, the pressure gradient will be substantially higher in the porous region while the averaged velocity is expected to be of the same order of magnitude. A small discrepancy can be observed in the interface region which can be explained by the smoothing

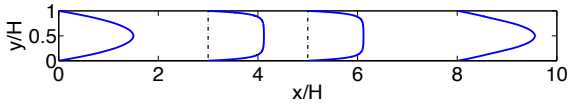

Figure 3: Velocity profile at several positions in the channel.

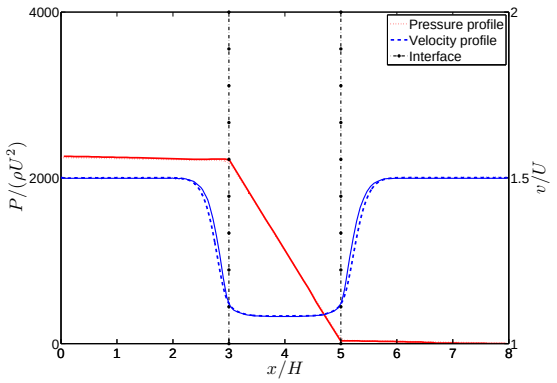

Figure 4: Non-dimensional pressure and velocity profile at the center of the channel for a the steady state flow with a porous plug ($Da = 1e-3$). Plain lines are the numerical results of Betchen [30].

Table 2: Experimental Setup [31].

Test ID	p_1 $[Pa]$	T $[K]$	t_{final} $[s]$	$\dot{m}$ $[mg/s]$
a4	1960	1000	3600	2.21
a6	1973	1200	3600	2.21

Table 3: Initial Material Properties [31].

Test ID	ϵ_0	$\rho_{C,0}$ $[kg/m^3]$	κ_0 $1e^{-9}$ $[m^2]$	r_0 $[\mu m]$	η_0
a4	0.85	1095.77	1.3720	5.5	1.15
a6	0.85	1038.67	1.3786	5.5	1.15

The computational tool is used to investigate numerically the oxidation of carbon preform in a set of experiments conducted inside the NASA flow tube reactor by Panerai et al.[31]. A cylindrical carbon preform sample of 25.4 $[mm]$ in length is inserted inside a 22 $[mm]$ diameter tube enclosed in a furnace. A low Reynolds number flow is forced to pass through the porous sample. The temperature is set by the furnace and remains constant during the experiment while the outlet pressure is not fixed to ensure constant inlet conditions. Different pressure and temperature conditions can be tested and this work focus on the replication of two tests. The experimental setup values are summarized in Table 2 and the properties of the material are given in Table 3.

The problem is treated as a 2D axisymmetric case. The surface of the tube are modeled as non-slip isothermal wall. For the boundary condition at the outlet, the pressure has to be specified hence a Proportional Integral (PI) controller is implemented in order to adjust the outlet pressure to keep the mass flux constant at the inlet. Furthermore, following the numerical work of Martin [11], re-radiation from the hot surface has to be accounted to simulate accurately the experiment. A radiation source term is applied in the interface region at both extremities of the sample $q_{rad} = F_{s,t}\xi\left(T_w - T_{inf}\right)^4$. The emissivity ($\xi$) is taken as 0.9 and the view factor ($F_{s,t}$) is computed depending on the geometry. The carbon preform sample will react with the incoming air. In this work, only the forward heterogeneous reaction $C_{(s)} + \frac{1}{2}O_2 \rightarrow CO$ is considered in a first attempt. The reference forward reaction rate is taken from Panerai et al [31] and is

Table 4: Comparison between experimental data (E_P), numerical results of Panerai et al. (N_P) and numerical results of this work (N_A).

Test ID	Work	Δx $[mm]$	$\Delta m/m_0$ $[\%]$	$p_{2,0}$ $[Pa]$	$p_{2,end}$ $[Pa]$
a4	E_P	3.8	23.3	1084	1125
	N_P	–	23.3	1087	1841
	N_A	0.3	23.9	1084	1315
a6	E_P	5.8	28.7	577	787
	N_P	–	28.5	595	1866
	N_A	0.4	37.1	595	1238

discussed in the following

$$k_f = 0.087 \exp\left(\frac{-42400}{RT}\right). \tag{22}$$

The temperature profile, mass fractions and solid density profile for test a4 are shown in Fig. 5 to 7 . Results at the final time are compared with experimental and numerical results of Panerai et al. [31] in Table 4.

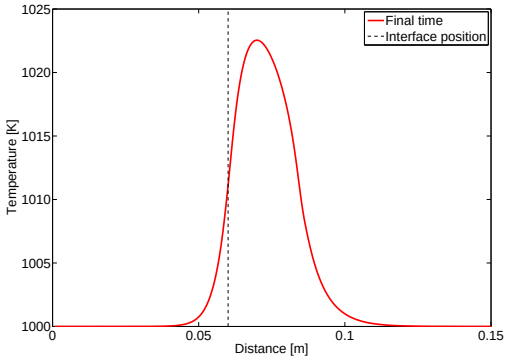

Figure 5: Temperature profile along the axis of the tube for test a4 at $t = 3600$ $[s]$.

Analysing the results, the mass loss computed with Argo is close to the experimental data but a discrepancy can be observed at higher temperature. It should be noted that the reaction rate given in Eq. 22 is fitted such that the mass loss computed numerically by Panerai et al.[31] corresponds to the experiments at different temperature.

The pressure drop across the sample evolves as expected; for higher mass loss, the permeability is lower leading to a reduced pressure difference. In addition, the model used to link the porosity and permeability

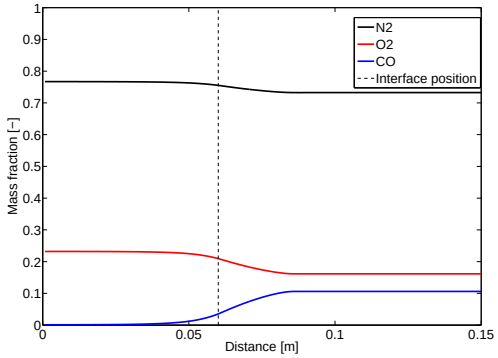

Figure 6: Mole fractions inside the tube for test a4 at $t = 3600$ $[s]$.

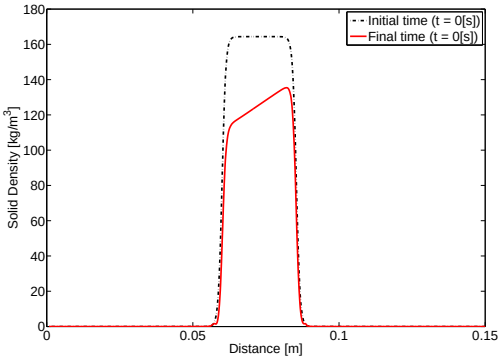

Figure 7: Comparison of the averaged solid density profile at the axis of the cylinder for test a4 at $t = 0$ and 3600 $[s]$.

(Eq. 21) gives a pressure difference closer to the experimental data than the one computed in the numerical work of [31].

Finally, as found by Panerai et al., the recession computed numerically is much lower than the one measured in the experiments. The competition between surface/volume ablation is not well captured with the current model implemented. Uncertainties on some material properties as well as physical phenomena neglected in the present model can explain this discrepancy. For instance, mechanical erosion (spallation) is not accounted for. A sensitivity analysis on transport and reaction parameters is carried on to investigate the competition between surface and volume ablation. This competition will be strongly influenced by the ratio between diffusion and reaction. This can be described by the Thiele number

$$\Phi = \frac{L}{\sqrt{D_{eff}/\left(S_f k_f\right)}}. \tag{23}$$

For high value of the Thiele number, the diffusion process is not fast enough and the oxygen in this case will be consumed at the surface of the sample (surface ablation). The competition between diffusion and reaction will drive whether the sample is ablated mainly at the surface or whether the mass is loss in-depth. For this sensitivity analysis, the effort is focused on the parameters involved in Eq. 23. In order to save computational time, the sensitivity analysis studies the effect after 20 $[min]$ of exposure and for the a4 test only.

3.3. Effective Diffusion

To compute the diffusion coefficients, several options are implemented. It is possible to specify a constant diffusion coefficient, a constant Lewis number or use the multi-components diffusion coefficients provided by Mutation^{++}. Using this last approach, the coefficients are computed based on collisional data and there is no reason to investigate uncertainties of these parameters. However, the tortuosity is a material parameter which has a direct influence on the evaluation of the effective diffusion coefficient (see Eq. 8). Changing the tortuosity factor up to 50% of its reference value leads to less than 0.1% in volume and mass change. Therefore, the underestimation of surface ablation can not be explained by uncertainties on the effective diffusion coefficients.

3.4. Reaction Rate

The Thiele number is directly dependent on the reaction rate; increasing k_f leads to a higher Thiele number and promotes surface ablation. In addition, as seen in Fig. 5, due to the exothermic heterogeneous reaction, there is a temperature gradient inside the sample. Therefore, the dependance of k_f with respect to temperature will also influence the effective rate at different depth. Discrepancies in the choice of the Arrhenius law among the literature show how sensitive the selection of the reaction rate might be. Both experimental conditions and material properties can explain this large range of reaction rate [11]. The present study does not aim to determine the actual reaction rate but tries to investigate the effect of such choice on the surface/volume ablation competition. For this analysis, two additional reaction rates are investigated and results are specified in Table 5. As expected, for higher reactivity, the ratio between the mass loss at the surface and in the volume becomes more favorable to surface ablation. However, it was not possible to find a law such that both this ratio is satisfied and total mass loss correspond to what was experimentally measured

Table 5: Study of the reactivity, the reaction rate is expressed as an Arrhenius law $k_f = AT^n \exp\left(\frac{E_a}{RT}\right)$. Mass and volume change are computed after 20 [min] of exposure.

A	n	E_a	Ref.	$\Delta m/m_0$	$\Delta V/V_0$
$[m/s]$		[kJ/mol]		[%]	[%]
$1e^2$	0.0	120.0	[3]	2.09	0.00
0.087	0.0	42.4	[31]	8.25	0.47
$2.2e^6$	0.0	180.03	[32]	22.1	30.4

at different temperature. The surface ablation is always underestimated comparing to volume ablation.

3.5. Permeability

The permeability appears in the drag term of the momentum equation 15 and, depending on the flow conditions, it can have an influence on the pressure gradient and the velocity field inside the porous medium. For the plug case, as shown in the verification test case (see Section 3.2), it affects mostly the pressure gradient. The initial value for this parameter is computed such that the initial back pressure ($p_{2,0}$) is the one measured experimentally. Considering a permeability a hundred times smaller than the one in Table 3, the recession length is found to be the same as in the reference case while the mass loss is slightly higher ($\pm 1\%$). Therefore, this suggests that the permeability is not a key parameter to explain the discrepancy between surface and volume ablation.

3.6. Surface of Reaction

The sensitivity analysis conducted on uncertainties of material parameters cannot explain the mismatch between surface and volume ablation observed numerically. Regarding the definition of the Thiele number, another key parameter is the effective surface reaction. The current model assumes that recession of the fibers is radial and uniform. This leads to a monotone reactive surface (S_f) decrease with respect to the fiber radius and porosity. However, it can be observed on micrographs of oxidized carbon preform a pitting phenomenon at low pressure [31] which results in a more complex function of S_f. Furthermore, an increase of the oxidation rate where gaseous oxidation products are released [33] can also influence the ratio between surface and volume ablation. Considering these, the heterogeneous reactions with fibers already eroded will be enhanced. Assuming that the reactive surface function can be expressed as $S_f = \gamma \frac{A_w}{V_s}$, and considering that eroded fibers are not cylindrical anymore but composed with holes of $1-2$ [μm], and these react twice as much as virgin fibers, a modified reactive surface evolution can be computed and is depicted on Fig. 8. The replication of test a4 with the reference rate and this $S_f(\epsilon)$ gives after 20 [min] a mass loss of 14.9 % while the volume change is 3.6 %. As expected, this has a direct influence on the ratio volume/mass loss. Therefore, a better knowledge of the evolution of fibers reactivity and geometry can help to define an accurate effective reaction rate in order to match both mass and volume loss.

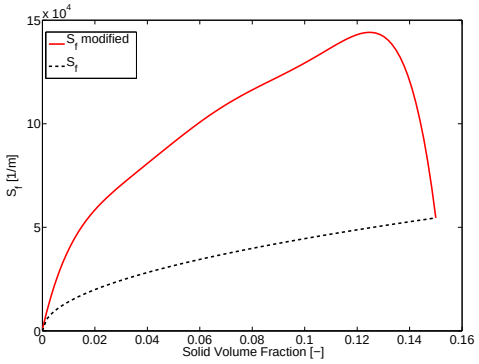

Figure 8: Reactive surface with respect to solid volume fraction.

4. Future work

This paper presents the methodology implemented to simulate both the porous medium and the fluid flow enabling to capture volume ablation phenomena. During the NASA Summer program in 2014, an effort together with A. Turchi has been dedicated to work on the second coupling approach.

Two tools, developed separately and able to handle two different aspects of the ablative material modeling: a stagnation-line code featuring an integrated ablative boundary condition[34], and a material code[35] have been coupled. The coupled algorithm allows for a time accurate solution for the thermal response of ablative material accounting for detailed surface chemistry, in-depth material behavior, and surface recession. The coupled tool was used to rebuild Plasmatron experiments conducted at the von Karman Institute showing good agreements with experimental data. The rebuilding of these experiments conducted by Helber in the VKI Plasmatron [36] was

considered as a suitable test to validate the implemented algorithms. The Plasmatron facility creates a high-enthalpy, highly dissociated subsonic gas flow which can be used to reproduce aero-thermodynamic environment of re-entry plasma flows [37]. The experimental test conditions of Helber [36], used as input for the computation, are summarized in Table 6. The free-stream conditions for the simulations were obtained from the test measurements through the standard procedure used at the VKI to rebuild the boundary-layer edge conditions by means of the VKI Rebuilding code [38]. The hemispherical sample of 2.5 $[cm]$ radius was made of Calcarb, a short fibers carbon preform [39] with a nominal density of 180 $[kg/m^3]$. During the Plasmatron experiments, data on surface quantities are provided by a two-color pyrometer (surface temperature) and by a high speed camera (recession).

Table 6: Plasmatron test conditions [36].

Test ID	Working gas	Cold wall heat flux, $[MW/m^2]$	Pressure $[Pa]$
P1	air	1.5	1500
P5	air	3.0	1500

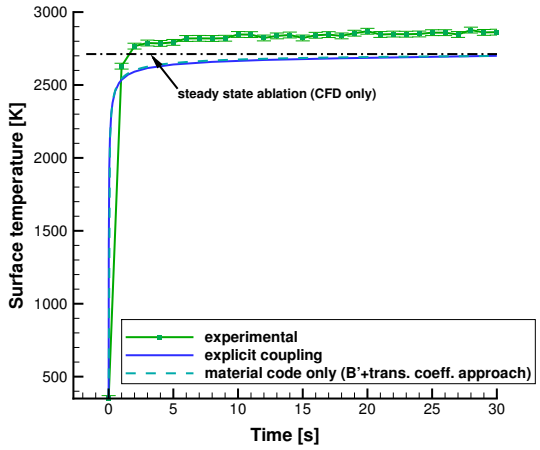

Figure 9: Comparison for the surface temperature between experimental data, material code only solution, CFD only solution and explicit coupling.

Figure 9 shows the comparison between the three

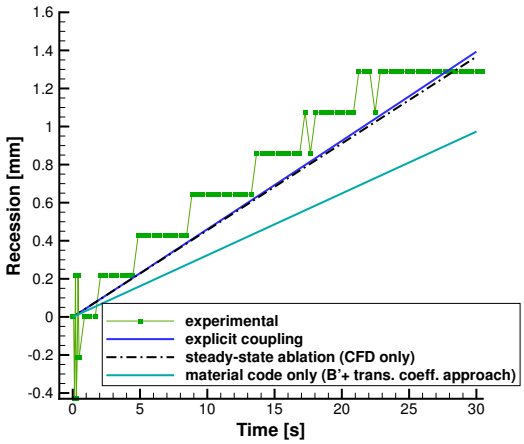

Figure 10: Comparison for the recession between experimental data, material code only solution, CFD only solution and explicit coupling.

different methods to rebuild the experiment: using the CFD code only, using the material code only, or performing the explicit coupling. The two transient solutions were computed either by using only the material code with the transfer coefficient approach or running a coupled CFD/material simulation. The steady-state solution was obtained by using the lone stagnation-line code with the steady-state ablation approximation. As seen, the wall temperature evolution computed by the material code using the transfer coefficient approach agrees well with that obtained using the coupled strategy. In Fig. 10, the total recession computed by the material code alone differs from the other two, which are closer to experimental data. Also, it is worth noting that, for this particular test case, the stagnation line code alone gives already satisfactory results. However, the critical drawback of this approach is that the transient or the material in-depth temperature field are not captured. It is proposed in future works to rebuild this Plasmatron experiment using the numerical tool presented in this paper in order to compare with the aforementioned methods.

5. Conclusion

The development of a numerical tool to simulate multi-species reactive flows with the presence of a porous medium has been verified against several test cases. The volume averaged Navier-Stokes equations

are used to model both phases in the same computational domain considering a single set of conservation laws. The porosity is itself a variable of the computation, allowing to take volumetric ablation into account through adequate source terms. The replication of an experiment conducted in the NASA Ames side arm facility has shown the limits of this code and current models to capture the competition between surface and volume ablation. In particular, the sensitivity analysis conducted has demonstrated the need for more information at the microstructure level to better characterize the ablation of carbon fibers. The evolution of the reactive surface has proved to be a key parameter to investigate.

Acknowledgments

P. Schrooyen is supported by a fellowship from the Fund for Research Training in Industry and Agriculture (FRIA). The first author would like to thank N. Mansour for hosting him during the last summer at NASA Ames and enhancing collaboration. The Argo team support from Cenaero is also gratefully acknowledged and especially K. Hillewaert. Interesting discussions with A. Turchi, B. Helber and J.B. Scoggins are also gratefully acknowledged. Collaborations with F. Panerai are also gratefully acknowledge for providing the data used to compare the results with experiments. Computational resources have been provided by the supercomputing facilities of the Université catholique de Louvain (CISM/UCL) and the Consortium des Equipements de Calcul Intensif en Fédération Wallonie Bruxelles (CECI) funded by the Fond de la Recherche Scientifique de Belgique (FRS-FNRS).

References

[1] J. Lachaud, N. Mansour, Microscopic Scale Simulation of the Ablation of Fibrous Materials, American Institute of Aeronautics and Astronautics, 2010. doi:10.2514/6.2010-984.

[2] E. P. Bartlett, R. M. Kendall, C. B. Moyer, R. A. Rindal, An analysis of the coupled chemically reacting boundary layer and charring ablator, Part 1 summary report, Contractor Report CR-1060, NASA (June 1968).

[3] J. Lachaud, I. Cozmuta, N. N. Mansour, Multiscale approach to ablation modeling of phenolic impregnated carbon ablators, Journal of Spacecraft and Rockets 47 (6) (2010) 910–921. doi:10.2514/1.42681.

[4] F. Milos, D. J. Rasky, Review of numerical procedures for computational surface thermochemistry, Journal of Thermophysics and Heat Transfer 8 (1) (1994) 24–34. doi:10.2514/3.497.

[5] Y. Chen, F. Milos, Navier-stokes solutions with finite rate ablation for planetary mission earth reentries, Journal of Spacecraft and Rockets 42 (6) (2005) 961–970. doi:10.2514/1.12248.

[6] D. Bianchi, F. Nasuti, E. Martelli, Navier-stokes simulations of hypersonic flows with coupled graphite ablation, Journal of Spacecraft and Rockets 47 (4) (2010) 554–562. doi:10.2514/1.47995.

[7] P. Thakre, V. Yang, Chemical erosion of carbon-carbon/graphite nozzles in solid-propellant rocket motors, Journal of Propulsion and Power 24 (4) (2008) 822–833. doi:10.2514/1.34946.

[8] A. Turchi, D. Bianchi, F. Nasuti, M. Onofri, A numerical approach for the study of the gas-surface interaction in carbon-phenolic solid rocket nozzles, Aerospace Science and Technology 27 (2013) 25–31. doi:10.1016/j.ast.2012.06.003.

[9] D. Bianchi, A. Turchi, M. O. F. Nasuti, Coupled CFD analysis of thermochemical erosion and unsteady heat conduction in solid rocket nozzles, no. 48th AIAA/ASME/SAE/ASEE Joint Propulsion Conference and Exhibit, Atlanta, GA, 2012.

[10] Y.-K. Chen, T. Gökçen, Implicit coupling approach for simulation of charring carbon ablators, Journal of Spacecraft and Rockets 51 (3) (2014) 779–788. doi:10.2514/1.A32753.

[11] A. Martin, Volume averaged modeling of the oxidation of porous carbon fiber material, American Institute of Aeronautics and Astronautics, 2013. doi:10.2514/6.2013-2636.

[12] P. Schrooyen and T.E. Magin and P. Chatelain , Development of a Numerical Simulation Tool for the Aerothermal Flow through an Ablative Thermal Protection System for Atmospheric Entry, no. VKI PhD Symposium, Sint-Genesius Rode, Belgium, 2014.

[13] W. Reed, T. Hill, Triangular mesh methods for the neutron transport equation, Contractor Report LA-UR-73-479, Los Alamos Scientific Laboratory (June 1973).

[14] B. Cockburn, G. Karniadakis, C.-W. Shu, The development of discontinuous Galerkin methods, in: B. Cockburn, G. E. Karniadakis, C.-W. Shu (Eds.), Discontinuous Galerkin Methods, Springer, 2000, pp. 3–50.

[15] D. Arnold, F. Brezzi, B. Cockburn, M. L.D., Unified analysis of discontinuous galerkin methods for elliptic problems, SIAM Journal Numerical Analysis 39(5) (2001) 1749–1779.

[16] K. Hillewaert, Development of the discontinuous Galerkin method for large scale/high-resolution CFD and acoustics in industrial geometries, Ph.D. thesis, Universite catholique de Louvain (2013).

[17] J.B. Scoggins and T.E. Magin, Development of Mutation^{++}: Multicomponent Thermodynamic and Transport Properties for Ionized Plasmas written in C^{++}, no. 11th AIAA/ASME Joint Thermophysics and Heat Transfer Conference., American Institute of Aeronautics and Astronautics, Atlanta,Ga, 2014. doi:10.2514/6.2014-2966.

[18] S. Whitaker, The Method of Volume Averaging, Kluwer Academic Publishers, Dordrecht, The Netherlands, 1999.

[19] W. Gray, P. Lee, On the theorems for local volume averaging of multiphase systems, International Journal of Multiphase Flow 3 (1977) 333–342.

[20] W. Breugem, The influence of wall permeability on laminar and turbulent flows, Ph.D. thesis, Technische Universiteit Delft (2005).

[21] S. Ganesan and D.R. Poirier, Conservation of Mass and Momentum for the Flow of Interdendritic Liquid during Solidification, Metallurgical transactions 21 (B) (1990) 173–181.

[22] M. Tomadakis, S. Sotirchos, Ordinary and transition regime diffusion in random fiber structures, AIChE Journal 39 (3) (1993) 397–412.

[23] J. Lachaud and N. M. Mansour and A. Ceballos and D. Pejakovic and L. Zhang and J. Marschall , Validation of a volume-averaged fiber-scale model for the oxidation of a carbon-fiber preform, no. 42nd AIAA Thermophysics Conference, Honolulu, Hawaii, 2011.

[24] M. Moesner and R. Radespiel , Numerical Simulation of Turbulent Flow over Porous Media, no. 21st AIAA Computational Fluid Dynamics Conference, San Diego, CA, 2013.

[25] M.Sahraoui and M. Kaviany, Slip and no-slip velocity boundary conditions at interface of porous, plain media, International Journal of Heat and Mass Transfer 35 (1992) 927–943.

[26] J.A. Ochoa-Tapia and S. Whitaker, Momentum transfer at the boundary between a porous medium and a homogeneous fluid-II. Comparison with experiment, International Journal of Heat and Mass Transfer 38 (1995) 2647–2655.

[27] F. Pochet and K. Hillewaert and P. Geuzaine and J.-F. Remacle and E. Marchandise, A 3D strongly coupled implicit discontinuous Galerkin level-set based method for modeling two-phase flows, Computers and Fluids 87 (25) (2013) 144–155.

[28] F. Dullien, Porous Media: Fluid Transport and Pore Structure, Academic Press, San Diego, 1991.

[29] T.E. Magin, A Model for Inductive Plasma Wind Tunnels, Ph.D. thesis, Université Libre de Bruxelles (2004).

[30] L. Betchen, A. G. Straatman, T. B. E., A nonequilibrium finite-volume model for conjugate fluid/porous/solid domains, Numerical Heat Transfer 49 (A) (2006) 543–565. doi:10.1080/10407780500430967.

[31] F. Panerai, A. Martin, N. N. Mansour, Numerical and experimental study of carbon fiber oxidation, American Institute of Aeronautics and Astronautics, 2014. doi:10.2514/6.2014-1208.

[32] H. K. Chelliah, A. Makino, I. Kato, N. Araki, C. Law, Modeling of graphite oxidation in a stagnation-point flow field using detailed homogeneous and semiglobal heterogeneous mechanisms with comparisons to experiments, Combustion and Flame 104 (4) (1996) 469–480. doi:10.1016/0010-2180(95)00151-4.

[33] K. Lee, H. M. Lee, H. Eun, W. R. Lee, S. Kim, D. Kim, The electronic structure of lattice vacancies on the stm image of a graphite surface, Surface Science 321 (3) (1994) 267–275. doi:10.1016/0039-6028(94)90192-9.

[34] A. Turchi, B. Helber, A. Munafò and T.E. Magin, Development and Testing of an Ablation Model Based on Plasma Wind Tunnel Experiments, no. 11th AIAA/ASME Joint Thermophysics and Heat Transfer Conference, Atlanta, GA, 2014.

[35] P. Schrooyen and K. Hillewaert and T.E. Magin and P. Chatelain, Discontinuous Galerkin discretization coupled with sharp interface method for ablative materials, in: 21st AIAA Computational Fluid Dynamics Conference, no. 2013-2457, San Diego, CA, 2013.

[36] B. Helber, A. Turchi, O. Chazot, T.E. Magin and A. Hubin, Gas/Surface Interaction Study of Low-Density Ablators in Sub-and Supersonic Plasmas, in: 11th AIAA/ASME Joint Thermophysics and Heat Transfer Conference, no. AIAA 2014-2122, Atlanta, GA, 2014.

[37] B. Bottin, O. Chazot, M. Carbonaro, V. van der Haegen, S. Paris, The VKI plasmatron characteristics and performance, Contractor Report RTO EN-8, Los Alamos Scientific Laboratory (June 1999).

[38] P. Barbante, O. Chazot, Flight extrapolation of plasma wind tunnel stagnation region flowfield, Journal of Thermophysics and Heat Transfer 20 (3) (2006) 493–499. doi:10.2514/1.17185.

[39] Mersen, Calcarb rigid carbon thermal insulation, Technical guide HT 29 GB 0121, Mersen (2011).

Fast Hybrid Statistical Narrow Band Model for Radiative Transfer in Atmospheric Entry Flows

James B. Scoggins

Aeronautics and Aerospace Department, james.scoggins@vki.ac.be

Supervisor and University Supervisor: Thierry Magin

Associate Professor, Aeronautics and Aerospace Department, magin@vki.ac.be.
Laboratoire d'Énergétique Moléculaire et Macroscopique, Combustion (EM2C), École Centrale Paris

Co-Supervisor: Anouar Soufiani

Research Head, Laboratoire d'Énergétique Moléculaire et Macroscopique, Combustion (EM2C), École Centrale Paris

Abstract

An adaptive spectral meshing algorithm is developed for atomic spectra when coupled with the hybrid statistical narrow band (HSNB) method developed at EM2C. The accuracy and CPU cost of the method is compared to full line-by-line (LBL) calculations for FIRE II flight conditions. It is shown that the adaptive HSNB algorithm can provide good estimates of the stagnation line radiative heat flux at significantly lower computational cost than with LBL.

Keywords: Radiative Heat Transfer, Hybrid Statistical Narrow Band, HSNB, Hypersonic Entry Vehicles

1. Introduction

Space exploration is one of the boldest and most exciting endeavors that humanity has undertaken, and it holds enormous promise for the future. After the successful manned missions to the Moon and many probe entries in the atmospheres of outer planets, our next challenges include bringing back samples to Earth by means of robotic missions and continuing manned exploration, which aims at sending human beings to Mars and returning them safely home.

Of the many design challenges associated with these goals is the difficult task of accurately predicting the heat-flux to the surface of the spacecraft thermal protection system (TPS) during planetary entry. An inaccurate prediction can be fatal for the crew or the success of robotic missions. Large safety factors are often added to vehicle TPS thicknesses to avoid such catastrophes at the expense of additional cost, weight, and reduced payload margins. The following complex phenomena that affect the surface heat-flux are considered as potential "mission killers:" 1) Radiation of the plasma in the shock layer, and 2) Complex surface chemistry on the thermal protection system material.

Current entry-vehicle design paradigms largely decouple the radiation and flow fields associated with hypersonic entry conditions due to numerical and modeling constraints, making it difficult to infer from current design tools the complex, coupled phenomena occurring for any given entry problem. Our poor understanding of the coupled mechanisms of flow and radiation leads to difficulties in an accurate heat flux prediction.

In order to make coupled calculations practical, Lamet *et al.* [1] developed an approximate radiative model for air plasmas based on the Statistical Narrow Band (SNB) formulation. Spectral band parameters have been computed for molecular electronic systems, bound-free, and free-free processes from the EM2C spectroscopic database [2–4] and have been tabulated according to translation-rotation and vibration-electronic-electron temperatures. When associated with a line-by-line (LBL) treatment of atomic radiation, this model is termed the Hybrid Statistical Narrow Band (HSNB) model.

A great deal of work has already been done to as-

sess and improve the accuracy of the SNB parameters for atmospheric entry applications [1]. In this respect, the treatment of atomic lines has largely been a secondary issue in the development of the HSNB model. However, as will be shown, when only atomic lines are treated with LBL, the general characteristics of the computed spectra vary greatly from that of spectra including molecular and continua contributions. Namely, atomic lines are generally few in number (typically a couple thousand) and can have large spaces in-between line centers as compared to the line half-widths. This fact allows for the development of a robust adaptive spectral mesh generation algorithm for the LBL treatment of atoms in the HSNB formulation.

In what follows, a brief description of the HSNB model is given in Section 2, followed by the development of an adaptive spectral mesh specifically for atomic lines in Section 3. Section 4 is then dedicated to comparing the adaptive scheme with full LBL solutions for the FIRE II flight conditions before presenting concluding remarks.

2. The Hybrid Statistical Narrow Band model

Consider an optical path in a non-scattering medium with an optical index of 1. The spectral radiative intensity for a wavenumber σ at an abscissa s is given by the radiative transfer equation (RTE) as

$$I_\sigma(s) = I_\sigma(0)\tau_\sigma(0,s) + \int_0^s \eta_\sigma(s')\tau_\sigma(s',s)ds', \quad (1)$$

where η_σ is the local emission coefficient of the medium. The transmissivity τ_σ between points s' and s is defined as

$$\tau_\sigma(s',s) = \exp\left(-\int_{s'}^{s} \kappa_\sigma(s'')ds''\right), \quad (2)$$

where κ_σ is the local absorption coefficient. We search for an expression of the averaged intensity over a narrow spectral band $\overline{I_\sigma(s)}^{\Delta\sigma}$. Radiative mechanisms are first grouped into different contributions, which are assumed to be statistically uncorrelated, allowing us to write

$$\overline{I_\sigma(s)}^{\Delta\sigma} = \overline{I_\sigma(0)}^{\Delta\sigma}\prod_k \overline{\tau_\sigma^k(0,s)}^{\Delta\sigma} + \sum_k \int_0^s \overline{\eta_\sigma^k(s')\tau_\sigma^k(s',s)}^{\Delta\sigma} \prod_{k'\neq k} \overline{\tau_\sigma^{k'}(s',s)}^{\Delta\sigma} ds', \quad (3)$$

where the index k refers to a radiative contribution. Lamet *et al.* [5, 1] proposed different strategies to evaluate $\overline{\eta_\sigma^k(s')\tau_\sigma^k(s',s)}^{\Delta\sigma}$, depending on the type of contribution k. The contributions are split into (i) optically thick molecular systems, (ii) optically thin molecular systems and continua, and (iii) atomic lines. The following splitting of the mean intensity is then introduced.

$$\overline{I_\sigma(s)}^{\Delta\sigma} = \overline{I_\sigma^0(s)}^{\Delta\sigma} + \overline{I_\sigma^{\text{thick}}(s)}^{\Delta\sigma} + \overline{I_\sigma^{\text{box}}(s)}^{\Delta\sigma} + \overline{I_\sigma^{\text{at}}(s)}^{\Delta\sigma}, \quad (4)$$

where $\overline{I_\sigma^0(s)}^{\Delta\sigma}$ is the boundary contribution. Note that the mean intensity at the starting point of the path ($s = 0$) is assumed to be uncorrelated with the total transmissivity.

2.1. Optically thick molecular systems

Discretizing the optical path into homogeneous cells of size $\Delta s_i = s_{i+1} - s_i$, the contribution of optically thick molecular systems to the mean intensity is written as

$$\overline{I_\sigma^{\text{thick}}(s_j)}^{\Delta\sigma} = \sum_{k\in\mathcal{M}}\sum_{i=0}^{j-1}\left(\overline{\tau_\sigma^k(s_{i+1},s_j)}^{\Delta\sigma} - \overline{\tau_\sigma^k(s_i,s_j)}^{\Delta\sigma}\right) \times \overline{\left.\frac{\eta_\sigma^k}{\kappa_\sigma^k}\right|_i}^{\Delta\sigma} \prod_{\substack{k'\in\mathcal{S}\\ k'\neq k}} \overline{\tau_\sigma^{k'}(s_i^*,s_j)}^{\Delta\sigma}, \quad (5)$$

where $\mathcal{M}$ is the set of optically thick molecular systems and $\mathcal{S}$ is the set of all the systems. Two points should be underlined: (i) the ratio $\eta_\sigma^k/\kappa_\sigma^k$ is assumed uncorrelated to the mean transmissivity τ_σ^k, and (ii) a mean equivalent point s_i^*, such that

$$\overline{\tau_\sigma^k(s_i^*,s_j)}^{\Delta\sigma} = \sqrt{\overline{\tau_\sigma^k(s_{i+1},s_j)}^{\Delta\sigma}\,\overline{\tau_\sigma^k(s_i,s_j)}^{\Delta\sigma}}, \quad (6)$$

has been introduced to allow a simple spatial integration between s_i and s_{i+1}.

The SNB model provides an expression for the mean transmissivity of a homogeneous column as a function of three band parameters: a mean absorption coefficient and two overlapping parameters related to Doppler and Lorentz broadening. For addressing nonhomogeneous optical paths, both the Curtis-Godson and the Lindquist-Simmons approximations [6] have been considered in [7] and it was found that the Lindquist-Simmons approximation provided significantly better agreement with LBL calculations, especially in the free stream.

2.2. Optically thin molecular systems and continua

The mean transmissivity of the set of optically thin molecular systems and continua, $\mathcal{B}$, is computed using the simple box model,

$$\overline{\tau_\sigma^k(s',s)}^{\Delta\sigma} = \exp\left(-\int_{s'}^{s} \overline{\kappa_\sigma^k(s'')}^{\Delta\sigma} ds''\right), \quad \forall\, k \in \mathcal{B}. \tag{7}$$

The contribution to the mean intensity is then written as

$$\overline{I_\sigma^{\text{box}}(s_j)}^{\Delta\sigma} = \sum_{k\in\mathcal{B}} \sum_{i=0}^{j-1} \overline{\eta_\sigma^k|_i}^{\Delta\sigma} \prod_{k'\in\mathcal{S}} \overline{\tau_\sigma^k(s_i^*,s_j)}^{\Delta\sigma} \Delta s_i. \tag{8}$$

2.3. Atomic lines

Unfortunately, the SNB model is not able to accurately reproduce atomic spectra due to the weak spectral density of atomic lines. Therefore, the contribution of atomic lines is written as

$$\overline{I_\sigma^{\text{at}}(s_j)}^{\Delta\sigma} = \sum_{i=0}^{j-1} \overline{\frac{\eta_\sigma^{\text{at}}}{\kappa_\sigma^{\text{at}}}\bigg|_i \left(\tau_\sigma^{\text{at}}(s_{i+1},s_j) - \tau_\sigma^{\text{at}}(s_i,s_j)\right)}^{\Delta\sigma} \times \prod_{\substack{k'\in\mathcal{S}\\ k'\neq\text{at}}} \overline{\tau_\sigma^{k'}(s_i^*,s_j)}^{\Delta\sigma} \tag{9}$$

where the average over the spectral band of the product $\eta_\sigma^{\text{at}}/\kappa_\sigma^{\text{at}} \times \tau_\sigma^{\text{at}}$ is obtained exactly from a LBL calculation.

3. Atomic Spectral Mesh

As described in the previous section, the HSNB method treats atomic lines with a full LBL approach, and molecular and continua contributions are modeled via the statistical narrow band formulation. In previous results presented with the HSNB model, the spectral mesh used for the atomic line spectra has generally been the same mesh as is used in the full LBL calculations for comparison. However, the size of a spectral mesh required to accurately resolve full LBL spectra is considered overkill for the HSNB formulation as there are typically only a few thousand atomics lines considered compared to several million lines typically modeled for molecular spectra. In the following subsections, the calculation of atomic spectra is quickly reviewed and then three spectral mesh generation techniques are described, including a high resolution mesh, and two adaptive techniques designed to significantly reduce the required mesh size.

3.1. Atomic line spectra

The spectral emission, η_σ, and absorption, κ_σ, coefficients for a given set of electronic transitions between upper and lower electronic energy levels, *ul*, are

$$\eta_\sigma = \sum_{ul} n_u \tfrac{A_{ul}}{4\pi} hc\sigma\, f_{ul}^{se}(\Delta\sigma_{ul}) \tag{10}$$

$$\kappa_\sigma = \sum_{ul} \left[n_l B_{lu} f_{ul}^{a}(\Delta\sigma_{ul}) - n_u B_{ul} f_{ul}^{ie}(\Delta\sigma_{ul})\right] h\sigma \tag{11}$$

where A_{ul}, B_{lu}, and B_{ul} are the Einstein coefficients for spontaneous emission, absorption, and induced emission, respectively. $\Delta\sigma_{ul} = \sigma - \sigma_{ul}$ is the distance from the line center, $\sigma_{ul} = E_u - E_l$, for each transition, *ul*. f_{ul}^{se}, f_{ul}^{a}, and f_{ul}^{ie} are the associated line profiles for spontaneous emission, absorption, and induced emission, respectively. The line shapes are related to one another to retrieve equilibrium

$$f_{ul}^{a} = f_{ul}^{se}(\Delta\sigma_{ul})\left(\tfrac{\sigma_{ul}}{\sigma}\right)^3 \tag{12}$$

$$f_{ul}^{ie} = f_{ul}^{se}(\Delta\sigma_{ul})\left(\tfrac{\sigma_{ul}}{\sigma}\right)^3 \exp\left(\tfrac{hc(\Delta\sigma_{ul})}{k_B T_{\text{elec}}}\right). \tag{13}$$

In this work, the convolution of both Lorentz and Doppler line shapes know as the Voigt profile is assumed for the spontaneous emission, where

$$f(x) = \tfrac{\gamma_L}{\gamma_D}\sqrt{\tfrac{\ln 2}{\pi^3}} \int_{-\infty}^{\infty} \tfrac{\exp\left(-(\xi-x)^2 \ln 2/\gamma_D^2\right)}{\xi^2+\gamma_L^2} d\xi, \tag{14}$$

and γ_L and γ_D are the half-widths at half-maximum for the Lorentz and Doppler profiles. Unfortunately, there is no analytical method to compute the Voigt profile in Eq. (14). There have been several methods developed to approximate the Voigt profile to various degrees of precision at a low CPU cost [8–10]. In this work, the method of [11] has been used.

When several atoms are considered, the sums in Eqs. (10) and (11) are taken over each electronic transition for every atom. An example absorption spectrum of N, O, N^+, and O^+ lines is given in Fig. 1 for conditions characteristic to a flow behind a shock wave for an atmospheric entry vehicle. The conditions were chosen to represent a case with a likely maximum amount of line broadening and overlap for the atomic lines. That is, the pressure and electronic temperature are near the high end of what is to be expected in atmospheric entry calculations. The high resolution spectral mesh used in the figure is described in the next section. As can be seen in the figure, the atomic lines are few and far between, especially at large wavenumbers. This fact is essential in developing a fast adaptive spectral meshing algorithm which

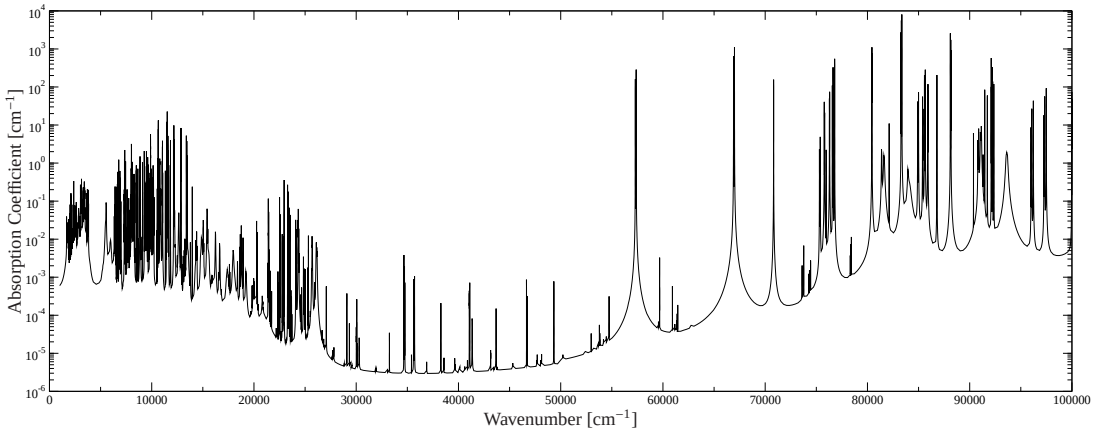

Figure 1: Absorption coefficient spectrum of N, O, N^+, and O^+ lines for the wavenumber range 1000 cm^{-1} to 100 000 cm^{-1} at 1 bar and 15 000 K. Mole fractions for N, O, N^+, O^+ are 0.67, 0.13, 0.08, and 0.02 respectively.

will remain accurate for a large range of cases and nonhomogeneity. Consider also that this is only the case because of the SNB treatment of molecular systems and continua.

3.2. High resolution spectral grid

A high resolution spectral mesh has been used in this work for both the LBL and HSNB calculations as a baseline for comparison of the adaptive spectral meshes detailed in the next sections. The grid has been designed to increase exponentially from a small spacing, $\Delta_{\min}$, at the minimum wavenumber, $\sigma_{\min}$, to a large spacing, $\Delta_{\max}$, at $\sigma_{\max}$. Specifically, the grid point σ_i is defined as

$$\sigma_i = (a+1)^{(i-1)}\left[\sigma_{\min} + \tfrac{\Delta_{\min}}{a}\right] - \tfrac{\Delta_{\min}}{a}$$

where $a = (\Delta_{\max} - \Delta_{\min})/\sigma_{\max}$ and $\Delta_{\min} < \Delta_{\max}$. In the results which follow throughout the remainder of this paper, the spacing 0.01 cm^{-1} to 0.12 cm^{-1} has been used for $\Delta_{\min}$ and $\Delta_{\max}$. The considered spectral range is taken to be 1000 cm^{-1} to 200 000 cm^{-1}. These parameters have been chosen based on previous experience with full LBL calculations for Air and are such that many points are guaranteed to be in every line. The total grid size using these parameters is found to be 4,420,667 points.

3.3. An 11 point stencil spectral grid

Da Silva [12] has developed fixed, 5, 7, 9, and 11 point stencils for approximating the Voigt line shape based on the estimated line center, line wing, and far wing regions of each line. For a given line, the estimated distance from the line center, to the line wing, $\Delta\sigma_W$, and far wing, $\Delta\sigma_{FW}$, boundaries are computed by

$$\{\Delta\sigma_W, \Delta\sigma_{FW}\} = \tfrac{2}{\pi}(1+\zeta)\,\gamma_L + \beta\gamma_D. \qquad (15)$$

For σ_W, the values of the $\{\zeta, \beta\}$ constants are taken to be $\{1, 1.8\}$, while for σ_{FW}, they are chosen as $\{2.6, 5.8\}$ based on an analysis of Lorentz and Doppler line profiles by Lino da Silva. The 11 point line stencil, which will be used in this work, is then taken to be $\sigma_{ul}, \sigma_{ul} \pm \Delta$ where Δ is the 5 point half-stencil

$$\Delta = \left\{\tfrac{1}{8}\gamma_V, \tfrac{1}{2}\gamma_V, \Delta\sigma_W, \Delta\sigma_{FW}, \tfrac{25}{2}\gamma_V\right\}.$$

$\gamma_V = \sqrt{\gamma_D^2 + \gamma_L^2}$ is the estimated Voigt half-width. For each atomic line, the 11 points above are added to the overall spectral mesh. It was shown that such a mesh provides a reasonably accurate resolution of line intensities for low pressure atmospheric entry conditions due to the low degree of line broadening in that regime [12]. This method will therefore be used as a benchmark for a slightly more detailed algorithm presented in the next section.

3.4. Augmenting with bisection

The fixed point method above is likely to work well in spectral regions with a high number of electronic transitions and with a large degree of line overlap because the majority of the points are distributed around the line centers. For areas in which there are large distances between neighboring line centers, the method is likely to provide poor estimates of spectral quantities due to the large error in interpolating the spectral values in the far line wing regions.

For this reason, the 11 point stencil in the previous section has been modified to ensure that the far line wing regions are correctly handled. To begin, the complete line list for atoms considered is first ordered by ascending line center values. Then, each region between two consecutive lines is considered. It is assumed that consecutive lines have little overlap, and thus the regions around each line center can be assumed to be well approximated by the line shape corresponding to that line alone, and not by other lines in the same vicinity. For each consecutive line pair, an adaptive mesh is then created based on the two corresponding line shapes. We will denote the left line shape properties with the superscript L, and the right properties with an R. First, the approximate "center" point between each line is defined simply as $\sigma_{LR} = (\sigma_{ul}^L + \sigma_{ul}^R)/2$. Next the following set of points are added to the mesh based on the 11 point stencil above, but ensuring that points added for each line do not overlap one another.

$$\sigma_{ul}^L + \Delta^L, \quad \forall\ \Delta^L < \sigma_{LR} - \sigma_{ul}^L$$

$$\sigma_{ul}^R - \Delta^R, \quad \forall\ \Delta^R < \sigma_{ul}^R - \sigma_{LR}$$

For lines which are sufficiently close, the above procedure will prevent unnecessary points from being added to the spectral grid. Note that it may easily be adapted to any other fixed point stencil based on line shape widths.

For lines which are very far apart in comparison to their line widths, the region around σ_{LR} will likely be poorly resolved. Therefore, the above set of points are augmented by adding points recursively to the center region by successively bisecting the two intervals closest to the last points added by the stencil above until the spacing between the outermost two stencil points for each line is at least half the size of the spacing between the outermost stencil point and the next point. In other words, two bisection fronts are propagated towards the line centers until the spacing between points matches that of the two outermost stencil points of each line.

Figs. 2 and 3 show both the absorption spectra and band averaged curves of growth for two spectral regions from Fig. 1 as obtained using the adaptive meshes compared to high resolution spectra. In the small wavenumber range 10 000 cm^{-1} to 12 000 cm^{-1} shown in Fig. 2, both adaptive methods work well. This is largely due to the fact that there are many spectral lines close to one another, and while some of them are very weak, they still contribute grid points in the wing regions of stronger lines. The differences

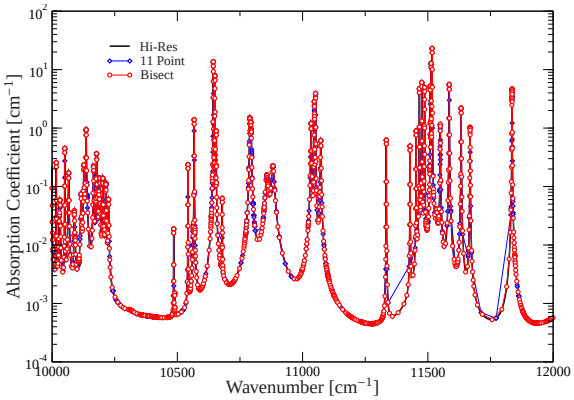

(a) Absorption coefficients.

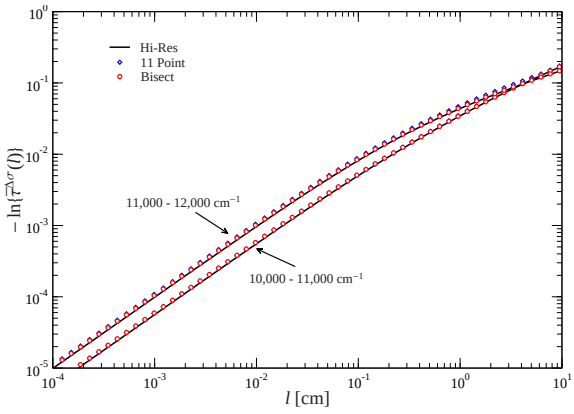

(b) Curves of growth.

Figure 2: Atomic absorption coefficients and curves of growth using adaptive spectral grids, compared to a high-resolution mesh, for the spectral range 10 000 cm^{-1} to 12 000 cm^{-1}. Same conditions as in Fig. 1.

become much more apparent in the larger wavenumber range 75 000 cm^{-1} to 77 000 cm^{-1} as in Fig. 3. Here, the atomic lines are far enough apart such that the 11 point stencil is not wide enough to encompass the far wing regions of some lines. Therefore, large interpolation errors are clearly visible in the absorption spectrum using only these points, while the points augmented with the bisection algorithm represent the true spectrum well. The affect this interpolation error has on the computed curves of growth are also clearly visible, with a significant error shown even at a slab length of 1 mm for both band regions.

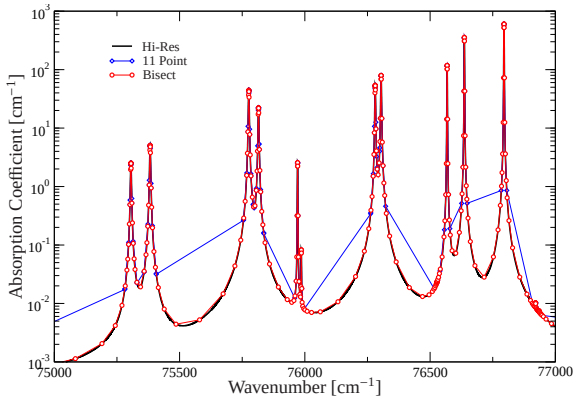

(a) Absorption coefficients.

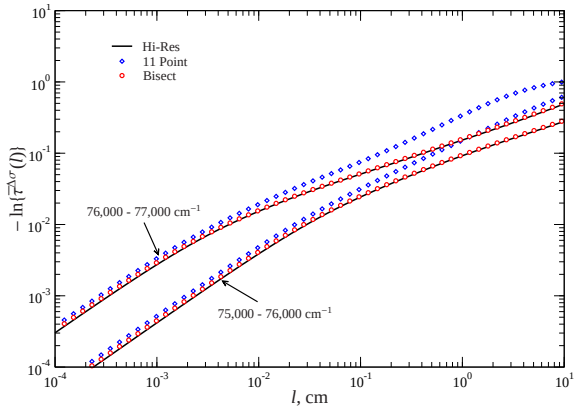

(b) Curves of growth.

Figure 3: Atomic absorption coefficients and curves of growth using adaptive spectral grids, compared to a high-resolution mesh, for the spectral range 75 000 cm^{-1} to 77 000 cm^{-1}. Same conditions as in Fig. 1.

4. Results for Fire-II Test Case

The FIRE II flight experiment [13, 14] has been widely used to validate and compare coupled and uncoupled flow/radiation simulations [1, 15, 16] for two primary reasons: (i) the flight conditions provide both strong thermochemical nonequilibrium and equilibrium conditions in the shock layer, and (ii) (perhaps more importantly) there is little other flight data to be used for such purposes. For these reasons, the FIRE II conditions will also be used here to compare the different adaptive methods presented above to LBL calculations on realistic flow fields. In this work, the 1634 s and 1645 s trajectory points have been considered for this work because they produce strong thermochemical nonequilibrium and equilbrium flow fields. The flight conditions at these trajectory points

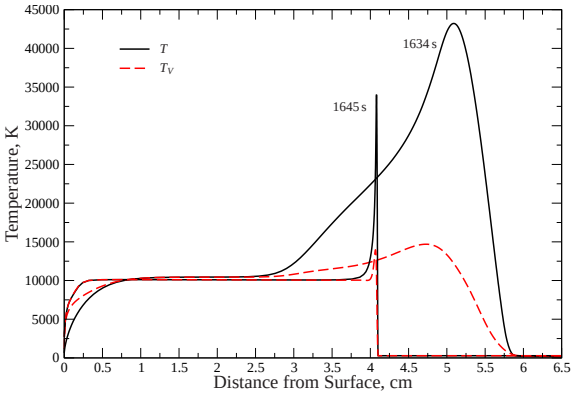

Figure 4: Simulated temperature profiles along the stagnation line of the Fire-II vehicle.

are given in Table 1.

4.1. Stagnation line flow

Flow field calculations have been performed using the Dimensionally-Reduced Navier-Stokes (DRNS) approximation of [17], implemented by [18] and applied to the two temperature, thermochemical nonequilibrium model detailed by [19]. This approximation leads to a quasi-one-dimensional set of governing equations for the flow along the stagnation-line of a blunt, spherical body. All thermodynamic and transport properties are provided by the Mutation^{++} library [20]. Chemical production rates are taken from [21].

The computed stagnation line temperature distribution for each trajectory point in Table 1 are shown in Fig. 4. It is clear from the figure that a significant thermochemical nonequilibrium exists at 1634 s in the shock and boundary layer regions due to the low free stream density. However, by 1645 s, the density has risen two orders of magnitude, causing the shock layer to be nearly in thermal equilibrium.

4.2. Results

Uncoupled radiative heat flux calculations have been performed using the flow fields computed for the trajectory points in Table 1 in order to assess the accuracy of grid adaptation methods from the previous section with full LBL calculations. The EM2C-HTGR database has been used for the calculation of spectral emission and absorption coefficients, both for the LBL and HSNB calculations. The contributions of 19 diatomic systems of N_2, N_2^+, NO, and O_2 have been included in the calculations, as well as atomic lines

Table 1: FIRE II trajectory points.

Time, s	Altitude,km	Velocity, km/s	Density, kg/m^3	Radius, cm	T_{wall}, K	T_∞, K
1634	76.42	11.36	3.72e-5	93.47	615	195
1645	48.4	9.83	1.32e-3	80.52	1520	285

Table 2: Summary of the radiative contributions considered is this work. Line-by-line data is provided by the EM2C-HTGR database [2, 3] and SNB parameters were computed in the work of Lamet et al [1].

Atomic lines	N, O, N^+, O^+	
Diatomic systems	N_2	Birge-Hopfield 1 & 2, Caroll-Yoshino, 1st & 2nd Positive, Worley, Worley-Jenkins
	NO	11 000 Å, Infrared, β, β', δ, ϵ, γ, γ'
	N_2^+	1st & 2nd Negative, Meinel
	O_2	Schumann Runge
Continua	Bremsstrahlung (N, O, N^+, O^+, N_2, O_2)	
	Photoionization (N, O, N_2, O_2, NO)	
	O_2 Photodissociation	

of N, O, N^+, O^+, and continuum processes. They are summarized in Table 2.

Fig. 5 shows a comparison of the radial and stagnation point heat fluxes for the 1634 s trajectory point. The radial heat flux profile appears as expected, with emission in the hot shock layer into the free stream and boundary layer. All of the HSNB results compare reasonable well with that of the LBL solution, but over-predict the heat flux at the stagnation point. The HSNB with high resolution and bisection grid results are essentially the same, showing better agreement with the full LBL solution than the HSNB 11 point fixed stencil mesh.

The spectral wall directed heat flux shown in Fig. 5 shows the contribution of the error in the total stagnation point radiative heat flux due to each wavenumber band. Note that a significant portion of the differences between the fixed stencil and the other methods occurs in the higher wavenumber region between 50 000 cm^{-1} to 100 000 cm^{-1}. This is likely due to two reasons. First, there are relatively few atomic lines bewteen 30 000 cm^{-1} to 50 000 cm^{-1}, thus the atomic lines contribute little to the total flux, and thus little to the error in this range (see Fig. 1). Second, the Doppler broadening increases proportionally to the wavenumber, which increases the relative contribution of the line wing regions to the overall flux field. With the fixed point stencil, the far line wing regions are not well resolved as previously discussed.

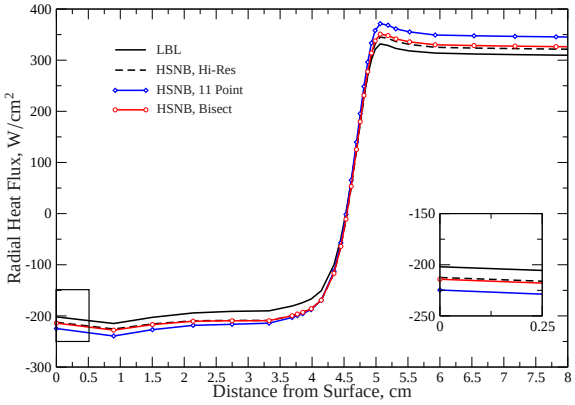

(a) Heat flux.

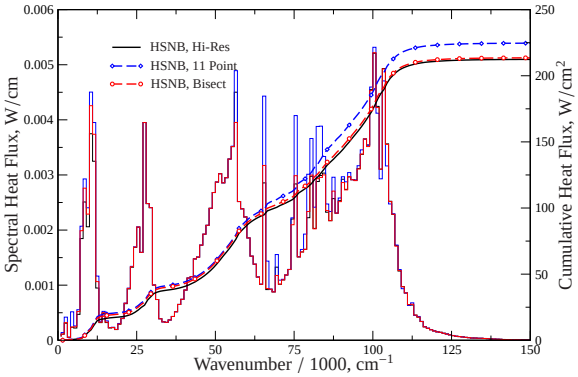

(b) Wall directed heat flux.

Figure 5: Comparison of radiative heat fluxes for the 1634 s case obtained using different methods.

The same comparison is made for the 1645 s trajectory point in Fig. 6. Note that the radial flux field has a slightly different behavior than in the 1634 s case due to the thin shock region. Again, the results obtained with HSNB using the high resolution spectral mesh and that obtained using the bisection algorithm have excellent agreement with the full LBL solution. However, the fixed point adaptive mesh yields significant errors in the radial flux field. The spectral flux obtained at the stagnation point shows why. Unlike the 1634 s case, which was at a relatively low pressure condition, the 1645 s has a significant Lorentz broadening of the atomic lines. Therefore, even at low wavenumbers, where the Doppler broadening is small,

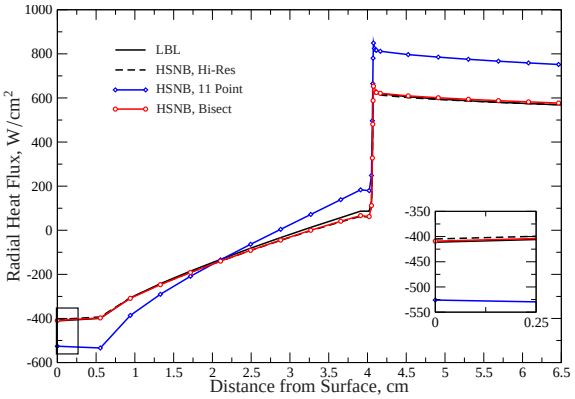

(a) Heat flux.

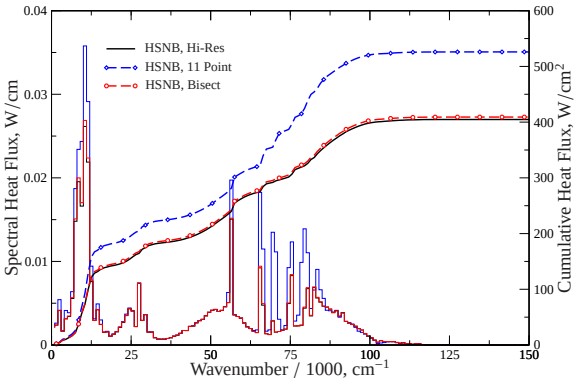

(b) Wall directed heat flux.

Figure 6: Comparison of radiative heat fluxes for the 1645 s case obtained using different methods.

the atomic line wings are poorly resolved, leading to significant errors in the cumulative heat flux.

Table 3 summarizes the results for each of the methods at each trajectory point in Table 1, including errors in the calculated wall heat flux, and the CPU time required to compute the radiative flux, relative to the time with the bisection method. The CPU time required for the full flux calculation is two orders of magnitude less for the adaptive HSNB methods compared to the LBL solution, while the high-resolution HSNB model allows a one order of magnitude reduction. In practice, the adaptive HSNB methods required between 60 s to 90 s for 30 spatial grid points, while the LBL solution was completed in about 2.5 h, running on a single core of an Intel(R) Core(TM) i7-4770K CPU. Differences in CPU times for the different trajectory points are caused primarily by the assigned spectral window for each atomic line which was taken to be $10000\gamma_V$ for these calculations. The 1645 s case has significantly more Lorentz broadening of the atomic lines, which increases the number of spectral grid points that the line shape of each atomic line must be computed over. This is reflected in the fact that the percentage of time required to compute the line spectra is proportionately more at 1645 s than at 1634 s.

It can also be seen in Table 3 that for the full LBL calculations, 99 % of the total CPU time is spent just generating the spectra, and only 1 % is spent performing the spatial, angular, and spectral integration. This is in large contrast to the HSNB methods which clearly tend to spend more time in the integration as the number of atomic spectral grid points is reduced. This is to be expected, when it is considered that the time required for the computation of the spectra is proportional to the product of the number of lines with the number of spectral and spatial grid points. The integration time, however, is proportional to the product of the spectral and spatial grid points only. Therefore, it is clear that since the number of lines considered is significantly lowered using the HSNB methodology (by a factor of $\approx$ 1000), a significant amount of the overall reduction in CPU time is due to the spectral property calculation. It should also be noted that the HSNB formulation does not permit the use of the E_3 exponential function to "analytically" perform the angular integration in the tangent slab formulation as is typically done in most RTE solvers. Therefore, there is an additional cost required to compute the angular integration included in the HSNB results. This additional complexity and cost is completely justified however, when the overall CPU cost requirements are considered.

Finally, the accuracy of the adaptive HSNB methods are compared to LBL. The relative percent difference of the stagnation point radiative heat flux between the HSNB solutions and that of the LBL calculations are given in the last column of Table 3. In all cases the high resolution HSNB result provides a very good estimate of the full LBL heat flux, with a maximum error of just 5.2 %. For the fixed point adaptive grid, the HSNB formulation provides a reasonable result for the 1634 s case with an 11.3 % difference from LBL results. However, there is a 27.9 % difference observed for 1645 s, which is likely not acceptable for most applications. When the fixed point mesh is augmented with the bisection method, this error is seen to disappear, and the adaptive mesh provides a flux estimate close to the high resolution HSNB formulation. Interestingly, this adaptive approach provides an even better estimate to the LBL solution than the high resolution spectral mesh for the 1645 s case. However,

Table 3: Timing and error statistics for the various spectral methods used for the test cases in Table 1. CPU times are relative to that obtained with the HSNB-Bisect method and were obtained using a single processor. The number of spectral grid points per atomic line is based on the total 3,333 atomic lines included in the database for N, O, N^+, and O^+, though not all lines fall within the considered spectral range of 1000 cm^{-1} to 200 000 cm^{-1}.

Trajectory Point	Method	Spectral Grid Size	Points per Atomic Line	Relative CPU Time	% Spectra	% Integration	$\frac{q_{r,\text{wall}}-q^{\text{LBL}}_{r,\text{wall}}}{q^{\text{LBL}}_{r,\text{wall}}}$, %
1634 s	LBL	4,420,667	-	146.7	99.0	1.0	-
	HSNB-HiRes	4,420,667	1,326.3	21.7	59.2	40.8	5.2
	HSNB-daSilva	33,735	10.1	0.96	14.9	85.1	11.3
	HSNB-Bisect	40,976	12.3	1.00	16.8	83.2	6.0
1645 s	LBL	4,420,667	-	131.6	99.0	1.0	-
	HSNB-HiRes	4,420,667	1,326.3	24.7	63.0	37.0	-1.6
	HSNB-daSilva	33,735	10.1	0.95	17.1	82.9	27.9
	HSNB-Bisect	41,669	12.5	1.00	19.3	80.7	-0.55

since the total error is less than 1 %, it is assumed that this was just a lucky outcome, and that the high resolution and adaptive HSNB methods should be considered to provide essentially the same results.

5. Concluding Remarks

The HSNB formulation has been shown to provide good estimates of the flux field for real hypersonic flight conditions, both in thermochemical nonequilibrium and equilibrium regimes. In this work, the CPU time of the atomic LBL calculation embedded in the HSNB method was addressed by developing an adaptive spectral mesh algorithm based on the fixed point spectral mesh provided by Lino da Silva, which attempts to augment the generated grid points in the far line wing regions through a recursive bisection algorithm. Comparisons of the HSNB method using the high resolution spectral mesh, as well as the two adaptive schemes, have been compared to full LBL solutions of the radial heat flux along the stagnation line of the FIRE II vehicle. The results show an excellent agreement of the adaptive HSNB formulation with LBL values with a two order of magnitude reduction in the overall CPU cost of the flux calculation.

The greatly reduced CPU cost requirement allows for fast estimate of radiative heat fluxes to the surface of hypersonic entry vehicles. Indeed, a stagnation line result can now be obtained in less than 90 s on a single processor to an accuracy within about 5 % of full LBL calculations. Furthermore, additional improvements may easily be envisaged as the HSNB formulation remains embarrassingly parallel and the current work does not account for weak atomic lines which do not contribute to the solution and can thus be ignored or modeled in a more simple way.

Acknowledgments

This research is funded through a Fellowship provided by the European Research Council Starting Grant #259354. J.S. would like to thank Laurent Soucasse from VKI and Philippe Riviere from EM2C for their help in this work.

References

[1] J.-M. Lamet, P. Rivière, M.-Y. Perrin, A. Soufiani, Narrow-band model for nonequilibrium air plasma radiation, Journal of Quantitative Spectroscopy and Radiative Transfer 111 (1) (2010) 87–104. doi:10.1016/j.jqsrt.2009.07.010.

[2] S. Chauveau, M. Perrin, Ph. Rivière, A. Soufiani, Contributions of diatomic molecular electronic systems to heated air radiation, Journal of Quantitative Spectroscopy and Radiative Transfer 72 (2002) 503–30.

[3] S. Chauveau, Ch. Deron, M. Perrin, Ph. Rivière, A. Soufiani, Radiative transfer in lte air plasmas for temperatures up to 15000 K, Journal of Quantitative Spectroscopy and Radiative Transfer 77 (2003) 113–130.

[4] Y. Babou, P. Rivière, M.-Y. Perrin, A. Soufiani, Spectroscopic data for the prediction of radiative transfer in CO2–n2 plasmas, Journal of Quantitative Spectroscopy and Radiative Transfer 110 (1-2) (2009) 89–108. doi:10.1016/j.jqsrt.2008.09.007.

[5] J. Lamet, Ph. Rivière, L. Tessé, A. Soufiani, M. Perrin, Radiation modelling of air plasma in nonequilibrium conditions: application to earth atmospheric re-entry, in: Proceedings of the 3rd International Workshop on Radiation of High Temperature Gases in Atmospheric Entry, Heraklion, Greece, 2008.

[6] P. Rivière, A. Soufiani, Generalized malkmus line intensity distribution for CO2 infrared radiation in doppler broadening regime, Journal of Quantitative Spectroscopy and Radiative Transfer 112 (3) (2011) 475–485. doi:10.1016/j.jqsrt.2010.09.010.

[7] L. Soucasse, J. B. Scoggins, T. Magin, P. Rivière, A. Soufiani, Radiation calculations along the stagnation line of atmospheric entry flows using a hybrid statistical narrow band model, in: Proceedings of the 6th International Workshop on Radiation of High Temperature Gases in Atmospheric Entry, St. Andrews, UK, 2014.

[8] J. Humlíček, Optimized computation of the voigt and complex probability functions, Journal of Quantitative Spectroscopy and Radiative Transfer 27 (4) (1982) 437–444. doi:10.1016/0022-4073(82)90078-4.

[9] K. L. Letchworth, D. C. Benner, Rapid and accurate calculation of the voigt function, Journal of Quantitative Spectroscopy and Radiative Transfer 107 (1) (2007) 173–192. doi:10.1016/j.jqsrt.2007.01.052.

[10] F. Schreier, Optimized implementations of rational approximations for the voigt and complex error function, Journal of Quantitative Spectroscopy and Radiative Transfer 112 (6) (2011) 1010–1025. doi:10.1016/j.jqsrt.2010.12.010.

[11] S. R. Drayson, Rapid computation of the voigt profile, Journal of Quantitative Spectroscopy and Radiative Transfer 16 (7) (1976) 611–614.

[12] M. Lino da Silva, An adaptive line-by-line statistical model for fast and accurate spectral simulations in low-pressure plasmas, Journal of Quantitative Spectroscopy and Radiative Transfer 108 (1) (2007) 106–125.

[13] E. S. Cornette, Forebody temperatures and calorimeter heating rates measured during project fire ii reentry at 11.35 kilometers per second, Tech. Rep. NASA TM X-1305 (November 1966).

[14] D. L. Cauchon, Radiative heating results from the fire ii flight experiment at a reentry velocity of 11.4 kilometers per second, Tech. Rep. NASA TM X-1402 (July 1967).

[15] G. E. Palmer, T. White, A. Pace, Direct coupling of the NEQAIR radiation and DPLR CFD codes, Journal of Spacecraft and Rockets 48 (5) (2011) 836–845.

[16] A. Soufiani, P. Rivière, M.-Y. Perrin, High temperature gas radiation (htgr) database and models, in: STO/AVT Lecture Series: Radiation and gas-surface interaction phenomena in high speed re-entry, STO-EN-AVT-218, 2013.

[17] A. Klomfass, S. Müller, Calculation of stagnation streamline quantities in hypersonic blunt body flows, Shock Waves 7 (1) (1997) 13–23.

[18] A. Munafò, T. Magin, Modeling of stagnation-line nonequilibrium flows by means of quantum based collisional models, Physics of Fluids 26 (2014) 097102.

[19] P. A. Gnoffo, R. N. Gupta, J. L. Shinn, Conservation equations and physical models for hypersonic air flows in thermal and chemical nonequilibrium, Technical Paper 2867, NASA (Feb. 1989).

[20] J. B. Scoggins, T. E. Magin, Development of mutation++: Multicomponent thermodynamic and transport properties for ionized plasmas written in c++, in: 11th AIAA/ASME Joint Thermophysics and Heat Transfer Conference, American Institute of Aeronautics and Astronautics, 2014. doi:10.2514/6.2014-2966.

[21] C. Park, R. L. Jaffe, H. Partridge, Chemical-kinetic parameters of hyperbolic earth entry, Journal of Thermophysics and Heat Transfer 15 (1) (2001) 76–90.

A Hybrid Method for Coupled Spallation-Radiation Physics for Ablating Heat Shields under Re-entry Conditions

Pedro Duarte Milheiro Santos

Aeronautics and Aerospace Department, von Karman Institute for Fluid Dynamics, Belgium, pedro.duarte.santos@vki.ac.be

Supervisor: Herman Deconinck

Professor, Aerodynamics Department, Faculty of Engineering Sciences, UniversitélibredeBruxelles, Belgium, herman.deconinck@ulb.ac.be)

Abstract

The PhD project will investigate the influence of spallation on the radiative-ablative fluid dynamics for Thermal Protection Systems (TPS) under space reentry conditions. We propose to study these phenomena using 1) A Monte Carlo solver for radiation heat transfer, 2) A Lagrangian formulation of the spalled particles and 3) A high-order flux reconstruction scheme for the flow equations. The solvers will work on both GPU's and CPU's and will be developed inside COOLFluiD, a world-class open-source framework for aerothermodynamics simulations.

Keywords: spallation, radiation, flux reconstruction, HPC, GPU, Monte Carlo, Euler-Lagrange, COOLFluiD

1. Introduction

The next challenges of the space exploration program will include bringing back samples to Earth by means of robotic missions and the manned missions to Mars. Those interplanetary missions will require increasingly higher atmospheric reentry speeds and with that, increased heating on the space probe, stretching the performance of the current generation of thermal protection systems (TPS) to the limit. The complex aerothermodynamics of high-speed space reentry vehicles poses, still nowadays, a challenging problem for the accurate characterization of the flow field, the chemical processes and radiative properties. Predicting an accurate heat flux is crucial for sizing the thermal protection system necessary to withstand the extreme environment of this regime. Under reentry speeds, three coupled physical processes occur and will need to be accurately modeled: 1) radiation, due to the high temperatures of the gas, 2) non-equilibrium chemistry, as the chemical reaction speeds are comparable to the flow velocity and 3) TPS ablation and the consequent contamination of the flow-field with ablative products [1]. A challenging, but still poorly understood phenomenon, called spallation, refers to the process depicted in Fig. 1 by which solid particles are ejected from an ablating heat shield into the surrounding medium. Those high enthalpy particles will influence 1) the radiative field by means of absorption, emission and scattering, 2) the chemical diffusion rates by promoting ablative processes outside the TPS walls and 3) the flow field, by disturbing the surrounding media. The goal of this project is to investigate spallation on ablative heat shields using highly accurate numerical solvers for the three processes. To cope with the very challenging computational workloads introduced by these methods, a substantial part of this project will be devoted to the design, implementation and validation of robust and general algorithms for modern heterogeneous computing, enabling fast computations on both CPU's and Graphical Processing Units (GPU's) on a cluster of computers. The modeling of the effects of the particles in the flow-field and radiative medium will be centered on four main themes: 1) particle dynamics solver; 2) radiation solver, 3) high-order HPC flow solver and 4) spallation and radiation physical modeling. The code base will be developed and released inside COOLFluiD [2; 3], a world-class open source software platform for multi-physics simulations. By doing so, the implementation will plug into an already established and fully functional software with most of the HPC performance issues addressed, namely, fully parallelized algorithms, load balancers, moving mesh capabilities,



Figure 1: Helber et al [1] Experimental studies of ablation on a chemical processes and radiative cork heat shield

particle tracking algorithms and concurrent simulation, where the various physical models can run simultaneously on different computing nodes. The computational effort will be thus devoted to expand, when needed, the capabilities of the existing software while implementing the aforementioned physical models, either from scratch or by interfacing to standard external libraries.

2. Particle dynamics solver

Various modeling approaches and numerical methods for dispersed two-phase flows have been developed in the past for different types of problems [7]. The most accurate way to simulate this phenomenon is to solve the conservation equations of mass, momentum and energy together with the constitutive equations of the phases and the interface conditions between the continuous and the particulate phase. The numerical techniques associated are computationally extremely costly, thus they can only be applied to problems where a relatively small number of dispersed entities is involved [4]. Apart from direct methods, two distinct approaches can be used in multiphase CFD, namely 1) The Eulerian-Eulerian model and 2) the Eulerian-Lagrangian model. The first, based on the work of Ishii [8] treats the two phase flow as inter-penetrating, non-mixing two-fluid continua. The second approach is to treat only the carrier phase in a continuous manner, while the dispersed entities are treated as particles and tracked individually, each one satisfying Newton's equation of motion [9]. The choice which method to apply depends on the specific physical problem. For dense mixtures, an Eulerian-Eulerian representation is more useful. For dilute dispersed two-phase flows with small entities, mostly the Eulerian-Lagrangian method is applied. Since spallation laced flows behave as a dilute two phase flow, the Eulerian-Lagrangian method will be used, through an algorithm named Combined Continuum and Discrete Model (CCDM) [10]. The implementation, while enabling more accurate physical models, is typically more computational involving than the two-fluid formulation. Reusing the HPC capabilities of COOLFluiD like particle tracking and load balancers greatly reduces the implementation effort necessary. Basing the new particle solver on the existing algorithms, the CCDM method will be implemented and validated. After an optimization effort, the algorithm will be extended to GPU computing and evaluated for a space reentry situation. Reviewing the Euler-Euler versus Lagrange-Euler choice, the results of those simulations will be used to access the possibility of a continuum assumption for the particle dynamics and, if affirmative, a closure equation for a two-fluid Euler-Euler model will be proposed.

3. Radiation solver

Different algorithms exist for solving the Radiative Transfer Equation (RTE), with different levels of accuracy and computational effort. Modest [11] identifies the four most relevant methods for aerothermodynamic applications, here ordered with increasing computational cost and decreasing solution error. First, the tangent slab approximation, reducing the problem to a one-dimensional radiation heat transfer formulation, for which an analytical solution exists. Second, the Spherical Harmonics (SD) method [12] that converts the RTE to a set of partial differential equations in 3D space by transforming the continuous directional dependence of radiative intensity into a series of spherical harmonics. Third, the Discrete Ordinances Method (DOM) [13], reducing the directional-dependent integrals of the RTE into a set of numerically solved quadratures with constant properties: this method converges to the exact solution with the increase of the number of quadratures. The last method is Monte Carlo [14]. In this case, the energy of the medium is divided into an integer number of particles, whose properties (e.g. wavelength, direction or position) are randomly assigned, biasing this choice for the most relevant ones. The method will approach exactness as the number of particles increases. Some authors also propose hybrid formulations, like the work of Bansal and Modest [15], combining the fast SH method with the accurate Monte

Carlo algorithm to attain higher computational efficiencies. Comparing the different methods discussed, the Monte Carlo incurs, by definition, no approximation and is of straightforward implementation. The treatment of scattering and reflection is considerably easier compared to the other methods. Its main disadvantage is probably the statistical nature of the convergence, although Veach [16] noted that this property can be favorably used by calculating the variance of the sample set and estimate the quality of the solution. Another advantage is the straightforward application to a domain-decomposition parallelization, where each processor keeps only a part of the computational grid; unlike other types of parallelization strategies, a domain decomposition formulation is proved to scale up to very large computational grids (>100M control points). Currently, a fully parallelized Monte Carlo solver for radiation heat transfer is implemented inside COOLFluiD [17] with a numerical result depicted in Fig. 2. To benefit from the optimizations and heterogeneous computing algorithms developed while designing and implementing a particle dynamics solver, the current Monte Carlo implementation will be moved to a CCDM formulation. Non-equilibrium flow radiation is currently treated in COOLFluiD by interfacing to ESA's library PARADE [18]. Previous numerical simulations have shown suboptimal performance of the library so alternatives will be explored, such as models from the Mutation++ database or the HPC-RAD library [19]. On the particle side, to account for scattering, a Von Mises model will be implemented based on the size and position of the particles. Its influence on the overall system will be estimated, first, by accessing whether the addition of scattering on the physical model considerably alters radiative field and second, if the model can be simplified by assuming independent scattering.

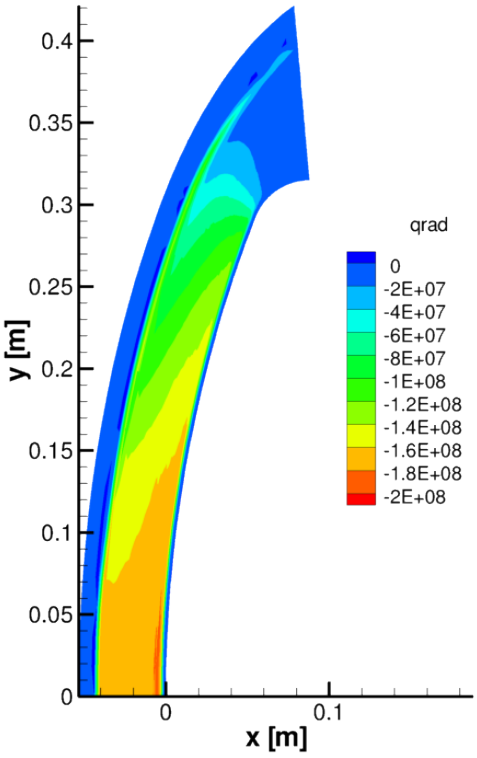

Figure 2: Volumetric radiative source term $[W/m^3]$ for the FireII capsule under peak heating conditions

4. Flow solver

Over the last decade, new methodologies have been developed to extend the order of accuracy of flow solvers beyond the classical second-order finite volume discretizations. Bridging Finite Volume (FVM) and Finite Element methods (FEM), Discontinuous Galerkin algorithms (DG) [22] allow for higher spatial resolution while using a finite element solution space which is discontinuous between the elements. Others, like spectral Differences Methods (SH) [23] impose global and periodic shape functions, enabling the system to be solved using a fast Fourier transform (FFT) algorithm. In the presence of shocks, no spectral shape function is currently known to be numerically stable so the focus is directed to the family of FEM methods. Recently, Huynh [24] unified a number of high order schemes, including DG and SD into a single framework called Flux Reconstruction (FR). The FR approach is an effort to address the disadvantages of high-order methods by attempting to make them simultaneously more robust, intuitive, and numerically efficient. Castonguay et al [25] derived a range of Vincent- Castonguay-Jameson-Huynh (VCJH) flux reconstruction schemes that proved to be stable for arbitrary orders of accuracy for linear fluxes in first order systems. Subsequent numerical studies with GPU computing showed speed-ups of up to 45x relative to a serial computation in a current generation CPU. While still not adopted by the industry, high order methods are emerging as important tools for novel turbulence models, LES simulations and overall simulations where high accuracy is required. High order flow solvers are advantageous to use not only due to increased accuracy, but also on enhanced computational efficiency: since most of the computations are local to the cell, this method proves to be better

suited to be used with GPU's than the usual FV. Moreover, as the shape functions need to be interpolated to retrieve the flux at the boundaries, this effort can be reused to efficiently and accurately compute the particle paths in the CCDM method. The VCJH FR numerical framework shows promising traits in being a common mathematical framework for high order methods and computational efficiency for accurate solutions. As an algorithmic optimization effort, the existing FVM and FEM codes inside COOLFluiD will be integrated under the VCJH FR numerical framework. Due to COOLFluiD's careful use of object-oriented design, the numerical solvers are decoupled from the rest of the code base, enabling a full reuse of the previous work in physical models and parallelization. With a working CPU implementation, a CUDA kernel will be written and validated.

5. Spallation physical modeling

The physical process to which particles are spalled is not completely understood. Park [26] identifies two probable causes; the first refers to the formation of soot during the process of pyrolysis. The second is due to fragmentation of the carbon fibers under heating. Three probable ejection mechanisms are also identified, namely 1) caused ejection of high pressure gas pockets inside the material due to pyrolysis, 2) deceleration of the re-entering vehicle or 3) by the Magnus effect, where the rotation of the particles inside the TPS causes a lift force directed outwards of the heat shield. Some modeling effort was already devoted to this problematic. Park et al. [27] developed an analytical model to explain the attenuation experienced when a laser beam crosses the shock layer. Wright et al [28], without knowing a priori the spallation rate, developed a sensitivity analysis with a Euler-Euler approach and a tangent slab method for radiation simulation. Nonetheless, a better understanding of this phenomenon can be attained through a particle method and an accurate radiation solver. For the re-entry flight of the Stardust capsule, whose TPS was made of a phenolic impregnated carbon ablator (PICA), the radiative heat flux due to particles has been predicted to account for 8% of the total heat flux at the stagnation point, with an estimated uncertainty margin of 150%. Considering the flow field alone, thermo-chemical non-equilibrium effects will also influence the modeling of radiation, as energy state population may not follow a Boltzmann distribution. The emission and absorption coefficients are deduced from the species composition and assuming a multi-temperature approach [29]. The extension to particulate media will alter the overall absorption and emission coefficients, as the spalled particles will both emit and absorb radiation onto the surrounding medium. A fundamental difference is the inclusion of scattering where the traveling radiation changes its direction by interacting with the spalled particles. Modest [13] identifies the three separate phenomena associated with scattering, namely, diffraction, reflection by the particle's surface and refraction inside the particle. The Mie scattering theory must be used if the size of the particles is too large to apply the Rayleigh theory, but too small to employ geometric optics [30]. When the distance between the particles are much larger than the wavelength of the incident radiation, the scattering is said to be independent, and the relations greatly simplify; from [27] it is suggested that particle spallation falls onto this regime. An empirical model will be made from wind tunnel testing, including measured data from the in-house VKI Plasmatron [31]. Park [27] also provides a solid foundation for an empirical model. The ejection rates, velocity and particle size will be determined and implemented as a flow field boundary condition. The spalled particles will be modeled as small spheres for which a kinetic equation validated with DNS simulations is known [32]. Moreover the influence of these particles on the chemical profile of the flow field will be determined by interfacing ablation chemistry models from the Mutation++ [33] database.

6. Applications

The direct application is an accurate prediction of the effects of spallation on ablative thermal protection systems (TPS). Because of that, a better sizing of the thickness of the protective layer on the re-entry capsule can be made. Empowered by efficient and accurate physical models and solvers, the industry can design such protection systems with increased confidence of the TPS design parameters. The subsequent reduction of the extra TPS weight due the necessity of lower safety factors will increase the space probe payload and thus, the economic revenue for a commercial capsule or the amount of scientific equipment aboard for a scientific endeavor. Future work could include using the FR scheme for subsonic plasma simulations and turbulence modeling, or the particle solver for Direct simulation Monte Carlo (DSMC) of rarefied media. The low diffusivity of the FR scheme, will

also benefit low-speed applications, such as aeroacoustic characterizations. The multi-phase methodology also directly benefits industrial applications outside the scope of aerothermodynamics. In particular, the Euler-Lagrange CCDM framework will be deliberately made general so that it can be easily adapted to a large range of applications and industries. Outside the academic word, some applications can be found:

- Plasma coating: In this type of applications, a powder material is injected and melted in a hot plasma stream. The gas flow carries the particles in the direction of the surface. On the surface the powder quickly solidifies, forming a top protective layer. The framework developed would accurately predict the quality of the coating and help design new coating methods.
- Filtration Devices: Some equipments are designed to remove particulates from an air, gas or liquid stream without filters, though a process named cyclonic separation. Accurate modeling of the multi-phase physics will lead to more efficient designs while increasing the equipment life span.
- Aerosol administration: Some drugs, like Asthma prescriptions, are targeted to the ventilatory system and orally administrated as aerosols. By using the multi-fluid approach of this work, important design choices on the aerosol particle size so that the majority of them are dispersed to the lungs.
- Soot deposition: The incomplete combustion process is characterized by the sublimation of carbon forming particles of amorphous carbon, called soot. The particles will be dispersed and adhere to the sorrowing walls. The CCDM method could help to better understand the dispersion process and allow for better designs of the combustion chamber and piping, avoiding the excessive deposition of soot.

In addition, other applications outside the scope of fluid dynamics can extend the particle methods developed, and exploit the HPC computing environment for the following specialized tasks:

- Molecular dynamics: This discipline deals with the description of the atomic and molecular interactions that govern microscopic and macroscopic behaviors of physical systems. With a classical mechanics formulation, the atoms are modeled as Lagrangian particles, following the Newton Law of motion and inter-molecular forces. A Molecular dynamics algorithm, implemented as a subset of the CCDM method, would help describe protein folding and pharmaceutical drugs behaviour.
- Planetary motion: Modeling the planets as particles with gravitational forces, the motion of complex celestial systems can be simulated, creating a better understanding of the formation of galaxies and the Solar system.

7. Conclusion

We propose an ambitious and multi-disciplinary project combining state-of-art solvers and high performance computing implementations. The final result will be a fast and efficient numerical framework capable of tackling spallation and general multi-phase flow with radiation. With the powerful tools developed, a better understanding of the influence of spallation on the surrounding media will be achieved. The algorithms will be kept as general as possible so that the software developed can directly benefit other research fields and applications.

References

[1] B. Helber, O. Chazot, T. Magin, A. Hubin. *Ablation of Carbon Preform In the VKI Plasmatron*. 43rd AIAA Thermophysics Conference, 2012

[2] A. Lani. *An Object Oriented and high performance platform for aerothermodynamics simulation*. Phd thesis, Universit e Libre de Bruxelles, 2008.

[3] Andrea Lani, Tiago Quintino, Dries Kimpe, Herman Deconinck. *The coolfluid framework - design solutions for high-performance object oriented scientific computing software*. International Conference Computational Science, 1: 281286, 2005.

[4] Rodney O. Fox. *Large-Eddy-Simulation Tools for Multiphase Flows*. Annual Review of Fluid Mechanics. 44:4776, 2012

[5] S. V. Apte, K. Mahesh, T. Lundgren. *An Eulerian-Lagrangian model to simulate two-phase/particulate flows*. Center for Turbulence Research. Annual Research Briefs 2003

[6] T. Nierhaus B. *Modeling and Simulation of Dispersed Two-Phase Flow Transport Phenomena in Electrochemical Processes*. PhD Thesis, RWTH Aachen

[7] S. Pannala, M. Syamlal,T. J. O'Brien. *Computational Gas-Solids Flows and Reacting Systems: Theory, Methods and Practice*. Advances in Chemical and Materials Engineering (ACME) Book Series.

[8] M. Ishii. *Thermo-fluid dynamic theory of two phase flow*. Eyrolles, Paris, France (1975). xi, 2, 3, 5, 14, 131

[9] N. A. Patankar , D. D. Joseph. *Lagrangian numerical simulation of particulate flows*.

[10] K. F. Malone, B. H. Xu, M. Fairweather. *The Combined-Continuum-and-Discrete-Model (CCDM) for simulation of liquid-particle flows*. 16th European Symposium on Computer Aided Process Engineering and 9th International Symposium on Process Systems Engineering, 2006

[11] Modest, M. F. *Radiative Heat Transfer, 2nd Edition*. Academic Press, 2003

[12] J. H. Jeans. *The equations of radiative transfer of energy*. Monthly Notices Royal Astronomical Society. 68:28-36, 1917

[13] E. H. Chui, G. D. Raithby. *Computation of Radiant Heat Transfer on a Non-Orthogonal Mesh Using the Finite-Volume Method*. Numerical Heat Transfer, Part B, 23:269-288, 1993.

[14] J R Howell. *The Monte Carlo method in radiative heat transfer. Journal of Heat Transfer*. 120(3):547560, 1998

[15] A. M. Feldick, A. Bansal, M. F. Modest. *Variance Reduction Techniques for Monte Carlo Solutions of Radiative Transfer in Hypersonic Flows: Hybrid P1-Monte Carlo*. 49th AIAA Aerospace Sciences Meeting. 2011

[16] Eric Veach. *Robust Monte Carlo methods for light transport simulation*. PhD thesis, Stanford University. 1997.

[17] Andrea Lani, Pedro D. Santos, Alessandro Sanna. *An efficient Monte Carlo method for radiation transport in aerothermodynamic simulations*. AIAA Fluid Dynamics and Co-located Conferences. 2013

[18] ESA PlasmA RAdiation Database (PARADE). Development history, status, current developments and future prospects. *Proceedings of the First International Workshop on Radiation of High Temperature Gases in Atmospheric Entry*. 8(10):26142623, 2003.

[19] Panesi, M. et al. *Analysis of the Fire II Flight Experiment by means of a Collisional Radiative Model*. Journal of Thermophysics and Transfer, 2009, 23, 236-248

[20] David M. Williams, Patrice Castonguay, Peter E. Vincent, Antony Jameson. *An Extension of Energy Stable Flux Reconstruction to Unsteady, Non-linear, Viscous Problems on Mixed Grids*. 20th AIAA Computational Fluid Dynamics Conference. 2011.

[21] J: Kim, P. Moin, R. Moser. *Turbulence statistics in fully developed channel flow at low Reynolds number*. J. Fluid Mech., Vol. 177, pp. 133-166 (1987). xii, 50, 51, 52

[22] D. Di Pietr, A. Ern. *Mathematical Aspects of Discontinuous Galerkin Methods*. Springer, 2012

[23] M. Z. Liu, Vinokur, J. Wang. *Discontinuous spectral difference method for conservation laws on unstructured grids*. Proceedings of the 3rd International Conference on Computational Fluid Dynamics, 2004

[24] Huynh, H., *A Flux Reconstruction Approach to High-Order Schemes Including Discontinuous Galerkin Methods*. 18th AIAA Computational Fluid Dynamics Conference. 2007.

[25] P. Castonguay , D. M. Williams , P. E. Vincent , M. Lopez , A. Lopez. *On the Development of a High-Order, Multi-GPU Enabled, Compressible Viscous Flow Solver for Mixed Unstructured Grids*. 20th AIAA Computational Fluid Dynamics Conference. 2011

[26] Chul Park. *Interaction of Spalled Particles with Shock Layer Flow*. Journal of Thermophysics and Heat Transfer, 13(4):441-449, 1999

[27] Chul Park, George A. Raiche, David M. Driver. *Radiation of Spalled Particles in Shock Layers*. Journal of Thermophysics and Heat Transfer, 18(4):519-526, 2004

[28] Michael J. Wright , Stephen M. Ruffin. *Investigation of Ablation and Spallation-Enhanced Radiative Heating Predictions using DPLR*. Final Report for NASA Grant #NNX09AI14A

[29] Chul Park. *Nonequilibrium Hypersonic Aerothermodynamics*. Wiley, 1990

[30] D. R. Yafaev, *Mathematical Scattering Theory: General Theory*. 1991

[31] Bottin, B. et al. *The VKI Plasmatron characteristics and performance*. RTO EN 8. 1999

[32] Zaichik LI, Alipchenkov VM, Sinaiski EG. *Particles in Turbulent Flows*. Weinheim: Wiley-VCHi 2008

[33] J.B. Scoggins. *Development of Mutation++: Multicomponent Thermodynamic and Transport Properties for Ionized Plasmas written in C++*. Applied Modeling & Simulation (AMS) Seminar Series. 2014

GROUND AND FLIGHT EXPERIMENTS

In-flight Experiment Design and Ground Testing of a Re-Entry CubeSat

Işıl Şakraker

Aeronautics and Aerospace Department, isil.sakraker@vki.ac.be

Supervisor: Olivier Chazot

Professor, Aeronautics and Aerospace Department, olivier.chazot@vki.ac.be.

University Supervisor: Gaëtan Kerschen

Professor , Department of Aerospace and Mechanical Engineering, University of Liege, g.kerschen@ulg.ac.be

Abstract

The conservative safety margins applied to the spacecraft thermal protection systems can be reduced by improving the numerical/experimental tools which is done through the validation with real flight data. A complete procedure from pre-flight analysis to flight measurements and finally a post-flight strategy is given in application to the test case of QARMAN mission. An accurate flight-to-ground extrapolation methodology is developed for unconventional geometries at plasma wind tunnels which is used to characterize its protective material Cork P50. Relevant aerothermodynamic in-flight experiments are designed and tested to collect real flight data and validate the proposed procedures.

Keywords: Atmospheric Entry, Plasma Flows, In-Flight Experiments, Experimental Aerothermodynamics, CubeSats

1. Introduction

Spacecraft, returning back to Earth, experience a very harsh environment during the encounter with the particles of the atmosphere. One of the major issues of atmospheric entry is the extreme aerothermodynamic heating and the exothermic chemical reactions due to the gas-surface interaction at hypersonic velocities. Hence, the spacecraft have to be protected by special shields that are called Thermal Protection Systems (TPS). When designing and sizing TPS, material engineers must be very conservative to ensure the safety of the crew or the payload since the aerothermochemical environment and its physics are complex to accurately predict.

The optimization of the TPS design is made through numerical and experimental simulations of hypersonic entry flows and material response. In this study, an effort is made to improve the high error margins of the ground testing methodologies by proposing a Flight-to-Ground Extrapolation methodology that duplicates the stagnation region aerothermochemistry and which is valid for all entry vehicle geometries [1].

The need of geometry independent methodology arose from an on-going VKI project called QARMAN [2]. It stands for Qubesat for Aerothermodynamic Research and Measurements on AblatioN and it is a triple unit (3U) CubeSat platform that is a rectangular prism [3] shown in Fig. 1. It weighs 4 kg with dimensions $34 \times 10 \times 10$ cm. Different from the generic CubeSats, QARMAN has a cork P50 ablative thermal protection material at the nose and silicon based ceramic material on the body. It will perform an atmospheric entry representative of bigger scale missions with 7.7 km/s at 120 km with a peak hot wall heat flux of 2.6 MW/m^2 [2]. It carries on board a number of in-flight experiments to collect real flight data that will be used to improve experimental and numerical tools for TPS design. The objectives of the in-flight experiments are to retrieve data on ablator efficiency (temperature, pressure, recession) and temperature/pressure/skin friction measurements for transition on the side panels. The stabilization and de-orbiting manoever will be performed by the open-

ing panels shown in Fig. 1. Overall, this challenging mission targets to contribute to atmospheric entry research with nano and pico satellite technology offering a very flexible system with good launch opportunities and reduced costs.

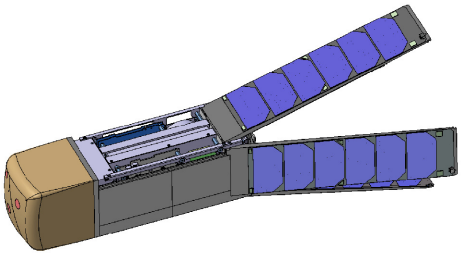

Figure 1: QARMAN vehicle overview with its cork based front TPS and ceramic based side TPS. The nose radius of curvature is 23 cm and the corner radius is 1.2 cm.

The following sections are divided as pre-flight, flight and post-flight analyses. The pre-flight section covers the details of the necessary simulation rules in a plasma wind tunnel and the associated measurement techniques as well as the numerical simulation procedures. It also includes a mission-tailored TPS material characterization campaign and understanding the expected behavior of the TPS during flight through engineering models. The flight section discusses the design of the aerothermodynamic measurements onboard QARMAN which will provide real flight data to be inserted in the models developed in the pre-flight analysis. Finally, the post-flight analysis includes the iteration and validation of the models, and analyses of the pre-flight assumptions with real flight data.

The study from Flight-to-Ground extrapolation approach to TPS characterization and in-flight experiment design is presented with the application to VKI Plasmatron plasma wind tunnel, QARMAN mission and its TPS. However, it should be noted that the whole procedure can be applied to any other subsonic plasma wind tunnel and any other entry vehicle regardless of its geometry and TPS material.

2. Pre-Flight Analysis I: Ground Testing Methodology

2.1. Local Heat Transfer Simulation

The stagnation point heating of a vehicle flying at hypersonic velocities (Fig. 2) can be approximated by a number of equations with certain assumptions. One of the most common expressions is Eq. 1 from Fay and Riddell [4]:

$$\dot{q}_w = 0.763 Pr^{-0.6} (\rho_e \mu_e)^{0.4} \left(\frac{du_e}{dx}\right)\Big|_{edge}^{1/2} (\rho_w \mu_w)^{0.1} \times (h_{0,e} - h_w)\left[1 + (Le^{\alpha} - 1)\left(\frac{h_{D,e}}{h_{0,e}}\right)\right] \quad (1)$$

This form of the equation is valid for fully dissociated air and where Prandtl number is not necessarily equal to 0.71. The exponent of Lewis number α is given 0.52 for an equilibrium boundary layer and 0.63 for a frozen boundary layer with fully catalytic wall. The latter is suggested as 2/3 by Lees [5]. Goulard [6] suggested a similar heat flux equation for frozen boundary layer with arbitrary catalytic efficiencies at the wall and at any degree of dissociation:

$$\dot{q}_w = 0.664 Pr^{-2/3} (\beta_e \rho_e \mu_e)^{1/2} h_{0,e} \times \left[1 + \left(Le^{2/3}\phi - 1\right)\left(\frac{h_{D,e} y_e}{h_{0,e}}\right)\right] \quad (2)$$

where y_e is the atom mass fraction at the boundary layer edge and ϕ introduces the catalytic efficiency at the wall.

When the above equations are examined, it is seen that there are four independent parameters, namely the density ρ, the velocity gradient $du/dx = \beta$, the total enthalpy h_0 and the composition at the boundary layer edge. If local thermochemical equilibrium (LTE) can be assumed, then the density and the composition can be expressed in terms of pressure and enthalpy, thus there are three independent parameters. This is expressed as local heat transfer simulation (LHTS) by Kolesnikov [7]. If these independent parameters at the boundary layer edge of a hypersonic vehicle are duplicated in a ground facility on a TPS, then the entire stagnation region aerothermochemistry is the same. A sketch of the LHTS logic is given in Fig. 2.

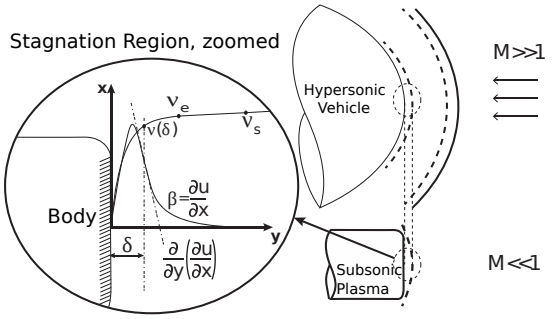

Figure 2: Local Heat Transfer Simulation (LHTS) approach.

2.2. Flight-to-Ground Extrapolation Procedure

Among the three parameters of LTE case, the velocity gradient β deserves a different attention since enthalpy and pressure are free stream characteristics. The velocity gradient is defined as the derivative of the velocity component normal to the stagnation line and it plays a major role on the chemistry in the boundary layer edge by changing the Damkohler number. A wide literature survey on velocity gradient was given in previous year [8]. The velocity gradient determination can be found in references [9; 10; 11; 12; 13; 14; 15; 16]. In all studies, β is given in the following form:

$$\beta = f\left(R_{eff,H}, p_\infty, p_e, \rho_e, \rho_\infty, ...\right) \tag{3}$$

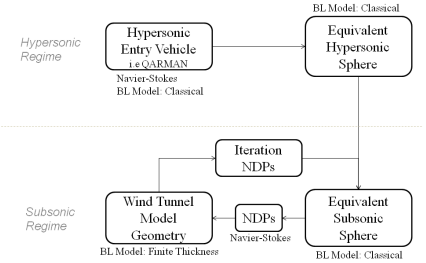

Figure 3: Flight-to-Ground extrapolation methodology.

The $R_{eff,H}$ is an *equivalent sphere* which has the same stagnation aerothermal profiles as the actual hypersonic vehicle. Its approximate computation can be found in the references given above for axisymmetric bodies with varying bluntness but mainly spherical noses. If the TPS of an axisymmetric and spherical nosed vehicle is to be characterized in the ground facility, the engineers can perform a Ground-to-Flight extrapolation with the above equation as described in [17]. Although in application of Ground-to-Flight extrapolation, the probe geometry can be easily determined, the velocity gradient term is often ignored since ESA standard probe geometry [18] is used in generic TPS characterization campaigns. Those testing conditions do not always apply to a spacecraft and its entry trajectory. This issue has been discussed by Panerai [19] for IXV vehicle.

The case of QARMAN the vehicle has a square cross section and a highly blunt nose, which makes the direct usage of the Eq. 3 impossible since there are two unknowns: β and $R_{eff,H}$. In order to close the equation, an iterative *Flight-to-Ground Extrapolation* procedure has been proposed. The steps of the procedure are depicted in Fig. 3 and are detailed in author's study in [8].

The procedure starts by computing the flight conditions of the vehicle along its atmospheric entry trajectory. An equivalent sphere flying at hypersonic velocities is defined by the stagnation line properties of the computed flight trajectory. The pick-up location is where the stagnation line temperature profile stops to be linear. Lunev [15] formulation is adopted as is used by Kolesnikov [7]. An equivalent *hypersonic* sphere changes along the trajectory together with the free stream parameters given in the above equations. Next, an equivalent *subsonic* sphere is defined for the subsonic plasma flow by equating the heat fluxes at hypersonic and subsonic flows as developed by [20] and [21]. It is found that the hypersonic and subsonic spheres differ only by a function of pressures. The dynamic pressure should be measured experimentally for the given static pressure-enthalpy flow condition. An experimental database is needed and built for this case which is discussed in Sec. 2.4. Using the equivalent subsonic sphere, the model geometry for the plasma wind tunnel conditions is determined. To do so, the boundary layer models used for computations are adapted according to the appropriate Reynolds number regime in the test facility. This step requires a database of numerical simulations of the test chamber to compute the non dimensional parameters (NDPs). The model geometry is related to the equivalent subsonic sphere through a function of NDPs computed for a given probe geometry and pressure-enthalpy test conditions. Finally an iterative process takes place for converging the computed ground test conditions and the model geometry found from the procedure.

The boundary layer temperature profiles of QARMAN vehicle, the equivalent hypersonic sphere and the ground facility probe geometry are given in Fig. 4 for trajectory point at 66 km altitude. It is interesting to note how the geometry changes from the vehicle all the way down to the sample geometry. The hypersonic QARMAN shape has dimensions of 100x100 mm with a nose radius of curvature 230 mm, while the equivalent hypersonic sphere has a radius of 124 mm and the sample size for ground facility is 10.52 mm.

A sensitivity analysis is conducted to quantify the change in the resultant probe geometry caused by various effects. The three main effects are found to be the pick-up location of β, the pressure measurement errors of the Plasmatron tests and the effect of facil-

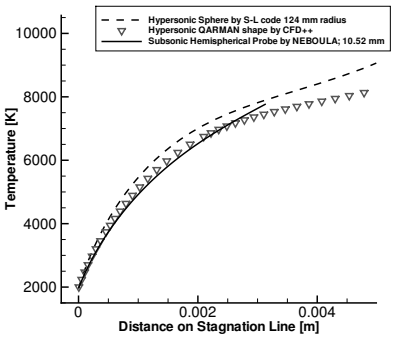

Figure 4: Temperature along stagnation line. Comparison of the squared hypersonic QARMAN CFD, the hypersonic equivalent sphere CFD and the hemispherical model in subsonic plasma for 66 km conditions.

ity power on the NDPs. The extreme conditions are given in Fig. 5 which results in an error margin of $R_m = 10.52 \pm 1.2$ mm.

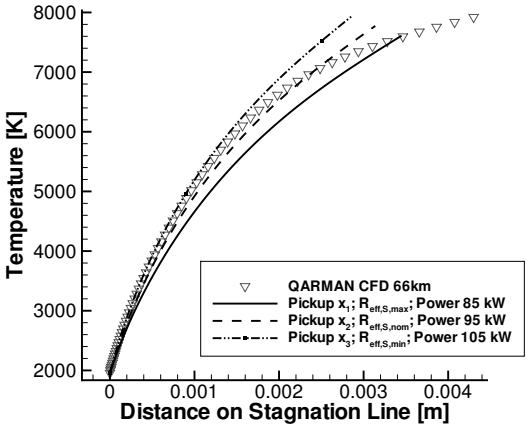

Figure 5: The combination of errors leading to cases where the temperature profiles showed the extreme low and high values. The lowest temperature case has $R_m = 11.68$ mm, the nominal case has $R_m = 10.52$ mm and the highest temperature case has $R_m = 9.45$ mm. The pick-up locations are depicted $x_1 = \overline{x}_\beta - 10\%$, $x_2 = \overline{x}$ and $x_3 = \overline{x}_\beta + 10\%$ for legend simplicity.

2.3. Enthalpy Determination Measurement Techniques

In the previous section, the LHTS approach is used under the LTE assumption, having three independent parameters, due to the fact that the enthalpy is so far always determined under the LTE assumption in VKI Plasmatron. The testing conditions discussed in this paper are considered to be in LTE based on the work of Le Quang [22] where the electron densities are measured and compared to the Griem threshold [23]. Therefore, the determination of enthalpy in non-equilibrium flow is not taken in consideration in this study.

At VKI Plasmatron, the enthalpy is often rebuilt by a numerical procedure, under LTE assumption, using the reference heat flux measured by a copper water cooled calorimeter, and the static and dynamic pressures. It also requires the a priori knowledge of the catalytic behavior of copper specific to the testing conditions. Together with the errors of heat flux and dynamic pressure measurements, the enthalpy at the boundary layer edge is determined with at least 7% or higher errors [24].

Two measurement techniques are introduced in order to have an independent means of enthalpy determination which also aims to determine the reference copper catalycity. The enthalpy probe and two methods of optical emission spectroscopy are presented in this section.

2.3.1. Enthalpy Probe

The "enthalpy probe" is a means of intrusive direct enthalpy measurement; a heat exchanger tube, surrounded by insulating cooling jacket, connected to a vacuum pump for plasma suction. The heat is only exchanged at the inner wall where the plasma is flowing with a pumping device. The enthalpy is determined iteratively from multiple acquisitions at different suction rates as depicted in Fig. 6. The detailed description and the working principles of the "enthalpy probe" were discussed previously in [8]. However it is found important to remind the assumptions in this section prior to present the results of the experimental campaign. The subsonic flow in VKI Plasmatron is a chemically reacting plasma and in order to relate the exchanged heat inside the probe to free stream enthalpy one has to make the following assumptions:

- The testing gas is a chemically reacting perfect gas mixture.
- The special case of local thermodynamic and chemical equilibrium is valid.
- The enthalpy is a function of two intensive state variables [12] which are chosen as temperature and pressure and is given as:

$$H_i(T,p) = h_i + (\Delta h_f)_i^\circ \quad (4)$$

$$h_i(T,p) = C_p(T,p)T \quad (5)$$

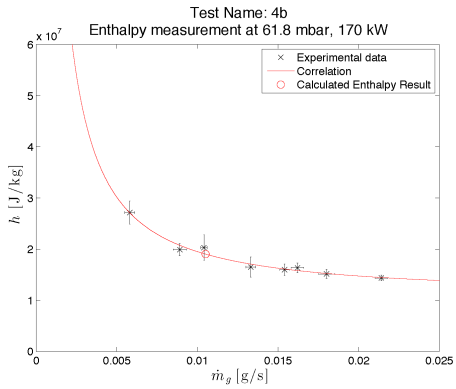

Figure 6: Correct suction rate computation of Case4b.

where $H_i = h_i$ are specific enthalpy (enthalpy per unit mass), C_p is the specific heat, T is temperature and p is pressure. (Note that the perfect gas state equation $pv = RT$ is also valid for chemically reacting perfect gases and specific volume, v, could be chosen instead of p.)

- The term corresponding to the heat of formation of each species i, $(\Delta h_f)_i^\circ$ is equal to zero.

A series of tests are performed with this technique and the test matrix is summarized in Tab. 1. The enthalpy probe is found to be operating only at pressures above 6100 Pa. This is due to the current vacuum system of the experimental setup. The plasma is sucked inside the heat exchanger of the probe by a vacuum pump. In between, there is a rotameter that adjusts the flow rate and also a small tank to damp the oscillations in order to keep the mass flow steady.

The results of the iterative mean enthalpy determination procedure are given in Table 1. A rudimentary Monte Carlo simulation is performed [25] with the input variables: P_{dyn}, $\dot{m}_{g_{read}}$, $\dot{m}_w$, T_2, T_1, and T_3. For each variable, a normal distribution was assumed with standard deviations. C_{p_a}, C_{p_w}, k_p, R, and the Mutation++ data [26] are considered exact and constant. For each case, 50 000 iterations are run. The uncertainties on the mean enthalpy are given in Table 2. A sensitivity analysis is also performed to investigate how the individual errors propagated but the results are not shown here.

2.3.2. *Optical Emission Spectroscopy*

The developed tool REDES (Real-time Enthalpy Determination with Emission Spectroscopy) uses a method adopted from Fletcher[27] for generic air plasma [28]. It considers the peaks and the integrated areas of N_2^+ first negative $\Delta v = 0$ and CN Violet $\Delta v = 0$ sequences. The theoretical spectrum for a given total pressure can be computed. Later the peak or the integral ratios are compared with preloaded 'theoretical ratio vs. temperature' curves and the temperature is retrieved. Using Mutation library of VKI, the temperature data is automatically converted to enthalpy assuming local thermal equilibrium. It has been shown later [29] that this method is over-predicting the enthalpy due to the plasma fluctuations having higher frequency than the integration time of the spectrometer.

In order to build the test conditions, another OES method is taken as reference. This time, the spectrum is acquired with a higher resolution spectrometer where the line of sight is placed at the predicted boundary layer edge by numerical simulation of the test chamber. The method consists of measuring the

Test name	Pressure p_s [Pa]	Power [kW]	Enthalpy [MJ/kg]
4b	6180	170	19.02
4bbis6	10000	150	18.37
4bbis	10000	170	20.42
4bbis4	10000	190	28.24
4bbis5	10000	210	28.01
5a	11967	150	12.62
5c	11967	190	23.60
6b	17143	170	18.10
6c	17143	190	23.39
7a	19815	150	13.75
7b	19815	170	13.09
7c	19815	190	17.07
8a	23482	150	14.87
8b	23482	170	17.91
8c	23482	190	21.12

Table 1: Enthalpy probe test conditions and measured mean enthalpies.

Test name	h [MJ/kg]	σ_h [MJ/kg]
4b	19.23	1.4037
4bbis5	28.06	1.5919
5c	23.81	2.0198
6c	24.24	5.3531
7b	13.21	2.3965
8b	18.71	6.8868

Table 2: Monte Carlo simulation results

spectral radiance of the excited oxygen triplet at 777 nm wavelength. The spectral emission is then rebuilt through Abel inversion and straightly related to a temperature assuming LTE [23]. Knowing the pressure and temperature, the thermodynamic properties of the gas mixture at equilibrium can be then computed including enthalpy. The applicability of LTE is limited by Plasmatron operating conditions. The accuracy of the measurements is calculated 7%. This method is chosen together with the enthalpy probe as reference over the numerical rebuilding procedure depending on the case whichever has a better accuracy for Flight-to-Ground extrapolation.

2.4. Building Testing Conditions

2.4.1. Experimental Database

An experimental database is needed to know at a given static pressure which power provides the enthalpy of the entry trajectory. Furthermore, the dynamic pressure values are needed at those points to perform the step of going from hypersonic to subsonic equivalent spheres.

A series of experiments is conducted at VKI Plasmatron facility based on the entry trajectory of QARMAN vehicle. Eight points along the trajectory are chosen for reference pressures. The power, as the driver parameter of the free stream enthalpy, is changed until the enthalpy is matched to the one of the trajectory at the given static pressure. The enthalpy is determined by the methods discussed in Sec. 2.3. The dynamic pressure values are measured at those points. The power is also a key parameter since the numerical simulation of the Plasmatron chamber has pressure and power as input.

The test matrix has pressures ranging from 2100 up to 23400 Pa and ICP powers from 60 to 110 kW. The results of the experimental campaign are given previously in [8] and will not be further discussed here.

2.4.2. Numerical Database

The numerical simulation of Plasmatron chamber is done with the in-house ICP code [30]. The testing conditions in terms of pressure and power are the inputs as well as the probe geometry. The code returns the stagnation line profiles that are used to determine the NDPs which provide the passage from the equivalent subsonic sphere to the model geometry that is equivalent to the hypersonic flying vehicle.

Since the model geometry prior to the Flight-to-Ground extrapolation is unknown, a numerical database of ICP computations is generated for a large number of free stream conditions and probe geometries. The conditions of the numerical database covers the conditions of the experimental database with probe geometries from 6 mm 57.5 mm radii hemispheres. Such database is specifically useful since the existing NDP regressions are only for changing powers for a fixed pressure and fixed probe geometry. Instead, the Flight-to-Ground extrapolation requires iteration on the probe geometry. 3D surface fits are done for the LHTS parameters being, enthalpy (or power), pressure and model radius (velocity gradient) for each NDP.

3. Pre-Flight Analysis II: TPS/Ablation Characterization Campaign

A TPS selection campaign has been conducted with three candidate materials and Cork P50 is chosen as the best fit for QARMAN mission profile. Thanks to the numerical and aerothermodynamic databases, the Flight-to-Ground extrapolation is performed along QARMAN's entry trajectory and the necessary probe geometries to be tested in VKI Plasmatron are defined.

Cork P50 consists of phenolic resin and high percentage of cork. It recesses and unlike many other ablators swells when exposed to plasma under certain conditions. The complicated pyrolysis behavior of the material makes the numerical simulation of the material response very difficult. It is the aim of this study to conduct an experimental campaign, including the atmospheric entry trajectory envelope of QARMAN spacecraft, in order to provide an engineering model based on experiments to assess the expected behavior during flight.

3.1. Experimental Setup and Test Matrix

A number of samples are exposed to plasma at VKI Plasmatron and the dependency on pressure, heat flux and different from generic TPS characterization campaigns, the dependency on the velocity gradient is investigated. This approach is in line with the LHTS and the Flight-to-Ground extrapolation methodology presented in Sec. 2.2. The heat flux equation form $\dot{q} = f(Pressure, Enthalpy, Velocity\ Gradient)$ becomes as follows for VKI Plasmatron operations:

$$\dot{q} = f(Pressure, Power, Sample\ Radius) \qquad (6)$$

Since each of the eight trajectory points required a number of test cases, the number of necessary tests increases exponentially which comes with high costs. Therefore, a reduced test matrix with 19 cases is built

paying attention to cover the testing envelope of Plasmatron and QARMAN entry trajectory. Keeping the heat load at 48000 $kW.s/m^2$ for all, the test matrix is summarized in Table 3.

The experimental setup consists of a number of measurement techniques. The surface temperature evolution during the plasma exposure are recorded with a two color pyrometer (independent of emissivity) and an infrared radiometer (function of emissivity). The comparison of the two measurements provides the evolution of surface emissivity The in-depth temperature of the samples are measured at 4, 8 and 12 mm away from the initial surface with type K and type E thermocouples. The mass change and char-pyrolysis layer thicknesses are determined for each case. A high speed camera is used to determine the swelling and recession rates of each sample. The optical emission spectroscopy is used to determine the species behavior (mainly CN and C2) at a vertical line in front of the sample. This tool is operated and reported by Bernd Helber [31].

3.2. Results

3.2.1. Surface Temperature and Emissivity

For all samples, the pyrometer and the radiometer were pointed at the stagnation point. Each surface temperature profile indicated a sudden increase shortly after plasma exposure and then showed a steady temperature. The steady surface temperatures are given in Figs. 7, 8 and 9.

Fig. 7 shows that the heat flux is the driving parameter for the surface temperature and it has a bigger effect than the pressure. On the other hand, in the Fig. 8 it is seen that for lower heat fluxes, the surface temperature is less affected by the changes in pressure. However for all the heat fluxes, mid pressures of 6180 Pa consistently showed a higher temperature. The Fig. 9 shows the effect of the last parameter given in Eq. (6). Having the same pressure and the reference heat flux suggests having the same enthalpy of the free stream. When the heat flux is increased by 7 times, the surface temperature shows an increase about 55%. At a fixed reference heat flux and sample radius, changing pressure from 1500 to 20000 Pa, the surface temperature changes by a 3.5% in average. The velocity gradient seems to affect almost as much as the pressure with a 4% change for a given pressure and reference heat flux. Apart from the reference heat flux, it is also interesting to see how the surface temperature changes with the "impinging" heat flux on each sample changing with the sample radius. The linear relation between the two is given in Fig. 10.

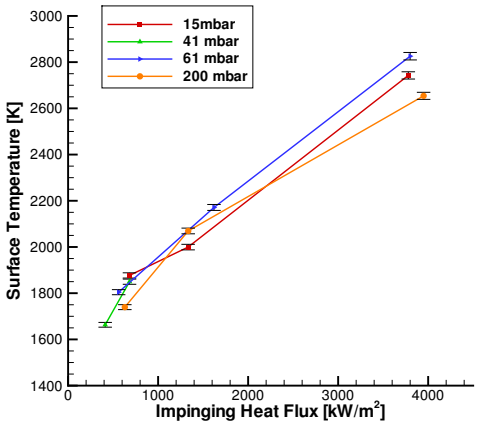

Figure 7: Change of surface temperature with increasing power, thus impinging and reference heat fluxes for cases with 15 mm radii. The reference cold wall heat fluxes are 280, 463, 1000 and 3000 kW/m^2 respectively.
$\dot{q} \nearrow = f\,(Pressure \leftrightarrow, Power \nearrow, Sample\,Radius \leftrightarrow)$

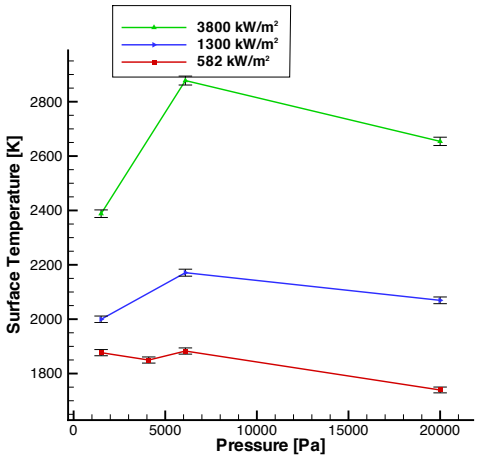

Figure 8: Change of surface temperature with pressure at a fixed reference heat flux.
$\dot{q} \leftrightarrow = f\,(Pressure \nearrow, Power \nearrow, Sample\,Radius \leftrightarrow)$

Table 3: Ablation characterization campaign test matrix and summary of the measurements.

Test Name	Radius	Pressure	Reference Heat Flux[a]	Duration	Steady Surface Temperature	Mass Loss Rate	Total Recession	Recession Slope	Swelling Slope
	mm	Pa	kW/m^2	s	K	$g/mm^2/s$	mm	mm/s	mm/s
13	15	1500	524.52	82	1876.87	1.64E-4	N/A	0.05	-0.13
14R	25	1500	1000.61	48	2088.14	1.07E-4	3.80	0.06	-0.22
15	15	1500	1025.64	37	1999.57	2.80E-4	-1.20	0.05	-0.18
16	11	1500	1029.26	27	2051.17	4.62E-4	0.00	0.28	-0.14
18RR	15	1500	2907.36	13	2742.61	8.65E-4	-2.70	0.12	-0.31
17	25	1500	3122.68	17	2556.66	2.11E-4	-0.50	N/A	N/A
22	11	4100	292.06	120	1740.38	1.23E-4	0.00	0.13	-0.23
21	15	4100	317.09	132	1663.23	1.04E-4	-1.35	0.12	-0.22
20	25	4100	364.11	171	1594.50	4.29E-5	1.60	0.04	-0.10
19	25	4100	520.80	103	1726.50	5.92E-5	1.20	0.03	-0.09
23	15	4100	525.00	82	1849.77	1.53E-4	-1.45	0.03	-0.10
3R	15	6180	432.02	82	1804.45	1.31E-4	0.00	0.04	-0.20
9R	25	6180	449.25	100	1753.92	5.75E-5	-0.22	0.05	-0.08
27	11	6180	474.02	60	1810.18	2.01E-4	N/A	0.12	-0.22
5	15	6180	1246.73	46	2171.08	2.24E-4	-0.90	0.05	-0.29
7R	15	6180	2923.00	13	2825.76	9.52E-4	-3.60	0.27	None
24	15	20000	484.70	82	1739.65	1.25E-4	-1.50	0.05	-0.14
25	15	20000	1026.60	37	2069.37	2.27E-4	-1.30	0.06	-0.22
26	15	20000	3038.02	13	2654.13	5.38E-4	-2.00	None	-0.31

[a] The cold wall heat flux measured by 25 mm radius hemispherical water cooled copper calorimeter.

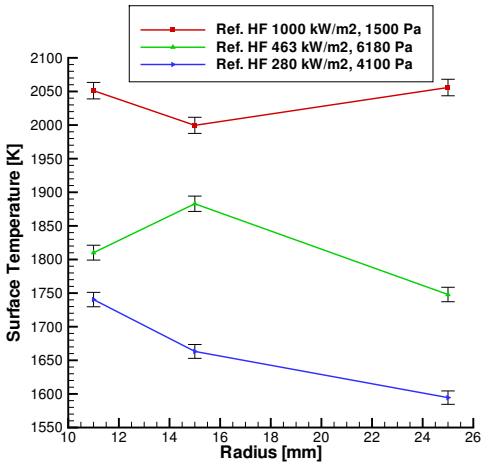

Figure 9: The effect of the velocity gradient when the samples are exposed to the same free stream conditions of pressure and reference heat flux.
$\dot{q} \leftrightarrow = f(Pressure \nearrow, Power \nearrow, Sample\,Radius \leftrightarrow)$

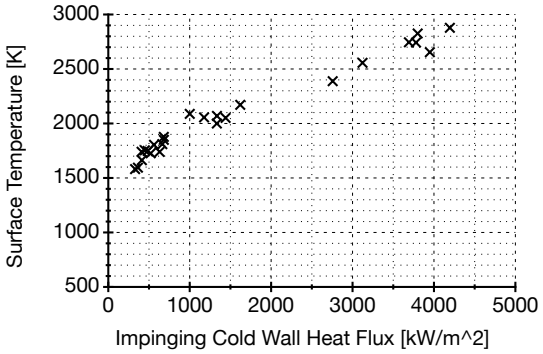

Figure 10: The surface temperatures and impinging cold wall heat flux.

The emissivity values are averaged at the steady state. Unfortunately, the field of view size of the radiometer was too large in some test cases, especially for the small radii samples. One can observe that for higher surface temperatures, the samples have a lower emissivity as shown in Fig. 11.

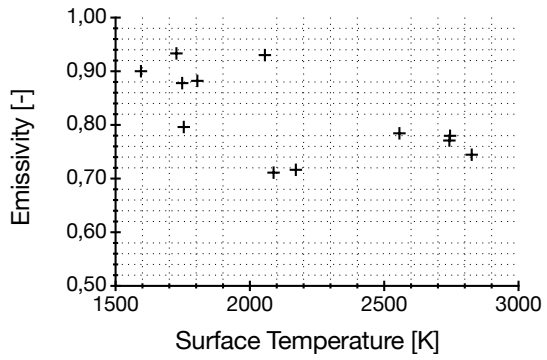

Figure 11: Steady state surface temperatures and emissivities.

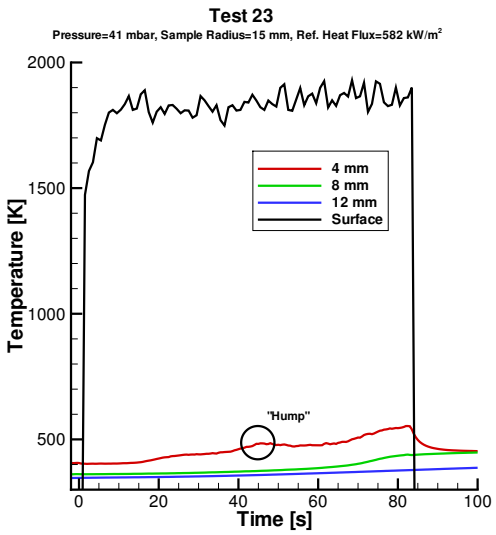

Figure 12: The ”hump” in 4 mm deep thermocouple data for Test 23.

3.2.2. *In-Depth Temperatures*

All samples were equipped with three in-depth thermocouples. As the samples swell or recess, the surface position changes and the thermocouples stay where they initially were since the extensions are fixed to the sample holder. Therefore throughout the test the thermocouple depths change with respect to the surface but in the plots presented in this study, they will be named after the initial positions.

Fig. 12 shows the surface and in-depth temperature profiles of Test 23 as an example. The first and although not very visible, the second thermocouple data show a ”hump” after certain time as if a heat wave occurs. This behavior has also been reported for other materials such as NASA’s PICA, Phenolic Impregnated Carbon Ablators [32]. The term ”hump” is also used by Milos and Chen [32] referring to the treatment of PICA data first in arcjet tests and later the real flight data from Mars Science Laboratory thermal plugs by Mahzari et al. [33].

The location and the timing of these humps are examined as the pressure and sample radii are changed. Fig. 13 show the 4 mm thermocouple data for two cases having the same sample radius but the same reference heat flux suggesting same surface temperatures. Regardless of the pressure, the three humps occurred almost at the same time. Similar behavior is seen when the reference heat flux (thus same surface temperature) is kept constant and the sample radius is changed.

3.2.3. *Swelling and Recession Profiles*

The swelling and recession profiles are captured with a high speed camera throughout the plasma exposure and the rates are given in Table 3. All the samples except Test 7 and 26 first swelled and then recessed. While Test 7 showed only a swelling behavior, Test 26 directly started recessing. Three recession profiles at a fixed pressure and sample radius are plotted in Fig. 14 for an increasing heat flux. It can be deduced that with an increasing heat flux, both selling and recession rates increase. Additionally, the swelling duration decreases with increasing heat flux.

When all the cases are analyzed, the trend seen for the surface temperatures also exists here. Table 4 shows two reference heat flux cases of 520 and 1000 kW/m^2. Regardless of the sample radius and pressure, if the reference heat flux is kept the same, the swelling and recession rates are in a good agreement.

3.2.4. *Mass Loss Rates*

The mass loss rates are given in Table 3. It is computed from the total change in mass before and after plasma exposure per unit exposure area per unit time. The time is different in each case in order to keep the heat load the same.

The only general trend for the mass loss rates is seen to be related to the steady surface temperatures. As the surface temperature increases, the mass loss rate also increases by an order of magnitude.

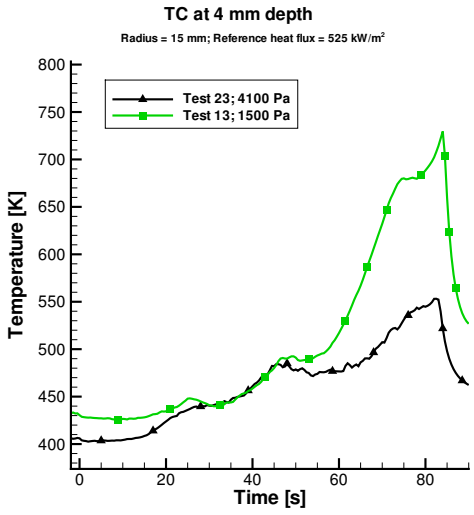

Figure 13: The "humps" in thermocouple data at 4 mm depth for two cases of different pressures but the same radius and the same reference heat flux.

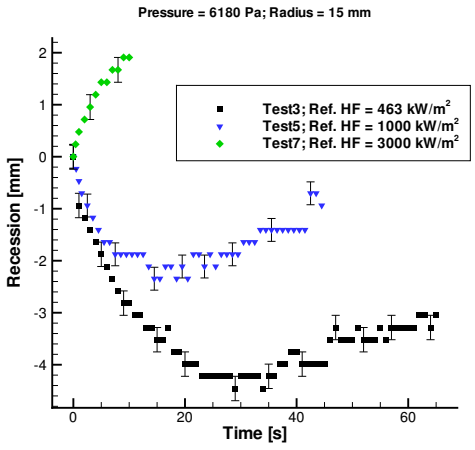

Figure 14: Swelling and recession profiles of three cases with the same radii but different reference heat fluxes. Positive values correspond to recession and negatives mean swelling.

Table 4: Emphasis on two reference heat fluxes.

Test Name	Radius	Pres.	Reference Heat Flux	Recess.	Swell.
	mm	*Pa*	kW/m^2	*mm/s*	*mm/s*
14R	25	1500	1000.61	0.06	-0.22
15	15	1500	1025.64	0.05	-0.18
25	15	20000	1026.60	0.06	-0.22
19	25	4100	520.80	0.03	-0.09
23	15	4100	525.00	0.03	-0.10

Although hard to deduce from the few data points, it is also seen that for a fixed sample radius and reference heat flux, the mass loss rate decreases as the pressure increases. However, at the highest heat fluxes of 3000 kW/m^2, the situation is the opposite. This result could be due to the much shorter duration of the high heat flux cases.

3.3. Discussion

The steady state surface temperature is primarily driven by the reference heat flux. The pressure and the sample radius affect the temperature only within a range of maximum 4%. Although not very precise a vague trend is seen for emissivity which decreases as the surface temperature increases. For a given reference heat flux, regardless of the pressure and the sample radius, a "hump" is seen almost at the same time in the in-depth thermocouple data. The swelling and recession rates are seen to increase with surface temperatures. Thus, the rates increase with reference heat flux and pressure/sample radius do not play a major role. For a given radius and pressure, as the reference heat flux increases, the swelling duration becomes shorter. In other words, the sample starts recessing earlier at higher reference heat fluxes. The mass loss rates are higher for increased surface temperatures by an order of magnitude.

4. Flight: QARMAN Mission and In-Flight Experiments

QARMAN mission is introduced in the Sec. 1. The in-flight experiments are given in Table 5 and were detailed in [8]. A short summary of XPL01 and XPL02 designs, being the in-flight experiments of the ablative TPS, is given here considering their direct relation to the Ablation Characterization Campaign presented in the previous section and the next one on post-flight analysis. The data of both XPL01 and 02 will be used for validating the Flight-to-Ground extrapolation methodology presented in Sec. 2.2.

4.1. XPL01

The objective of this payload is to measure the heating and the ablation of the front TPS, which is made of Cork P50. It can be done by simple temperature measurements thus a thermal plug concept is implemented. The measurement chain is designed and manufactured at VKI in collaboration with Akyol [34]. The thermal plugs are made of type K thermocouples with teflon insulation and are built in-house. The

Table 5: Overview of the Aerothermodynamic Payloads.

Payload	Objective	Parameter
XPL01	TPS Efficiency	Temperature
XPL02	TPS Pressure	Pressure
XPL03	Vehicle Stability	Pressure
XPL04	Laminar to Turbulence Transition	Pressure Temperature
XPL05	Side Panel Heating	Temperature
XPL06	Radiation	Species

thermal plugs and the electronics have been exposed to plasma in VKI Plasmatron and performed well. XPL01 will return the profile of in-depth temperature inside Cork P50 at three thermal plug locations by 12 thermocouples.

4.2. Flight Test on QB50p1 satellite

The measurement chain of XPL01, and XPL05, is sent to an orbit of 610 km altitude in June 2014 on board of both precursor missions of QB50 [35] QB50p1 and QB50p2. The payloads consisted of three XPL01 thermocouples and their measurement chains. The objective was to qualify the design even though the temperature measurement range will not be representative to an atmospheric entry flow. As a preliminary analysis, the measurement junction temperature and electronic board data are clean and the results show that the payload performed well in space environment and survived the launch loads without any damage.

4.3. XPL02

This payload consists of absolute pressure measurements in the front part of the vehicle to understand the aerothermodynamic environment in front of the TPS together with the XPL01. It will allow us to reconstruct the trajectory and will also act as input to understand the ablative material behavior and efficiency. The subject trades, sensor selection and measurement chain design were detailed previously in [8].

4.4. XPL01-XPL02 Qualification Tests in VKI Plasmatron

A sample that includes the payload heads and the electronics of the XPL01-02 payloads are put inside Plasmatron chamber for qualification. The objectives are to monitor the behavior of the thermal plug configuration with radial thermocouples; to check the pyrolysis inside the bare pressure port; to monitor the surface temperature next to the pressure port; to monitor the emissivity of the surface; to monitor the recession of the sample at the center and at the corners; to check the char and pyrolysis layer; to monitor the back cavity temperature for electronics' operational range; to monitor the noise behavior of the temperature and pressure data under strong electromagnetic field effects; and to investigate the circuit and component level stability in plasma environment.

4.4.1. Sample

The sample is 6/10 scaled QARMAN geometry made of Cork P50 as depicted in Figure 15. The upper part of the sample has one thermal plug with three thermocouples and one absolute pressure measurement station of a bare pressure port.

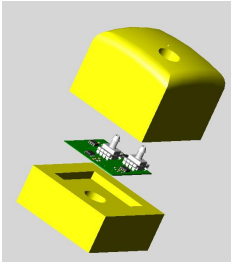

Figure 15: Qualification test model.

Three pre-made type K thermocouples with teflon insulation are used. The two wires are split and inserted to the thermal plug radially. The TC depths are 8, 15 and 22 mm away from the surface. The thermal plug has a diameter of 14 mm and its center is 13.51 mm away from the stagnation point in diagonal direction. A bare 2 mm diameter hole is opened where the pressure sensor tip is directly aligned and inserted at the back wall of the top part.

The PCB is designed based on the previous circuits and components that have been tested and qualified in plasma environment in the Breadboard testing campaign of June-September 2013. Smaller components have been used in order to fit in the small 4x4 cm PCB area. The remaining areas are covered with ground plane in order to increase the grounding and decrease the plasma triggered noise effects. The flight configuration is fit on a smaller scale PCB, therefore the hardware could be tested thoroughly. A simple code is written to pass the information over the UART(Universal asynchronous receiver/transmitter) bus. A UART to USB converter is used to pass the data to the PC. Data was logged using a standard terminal software.

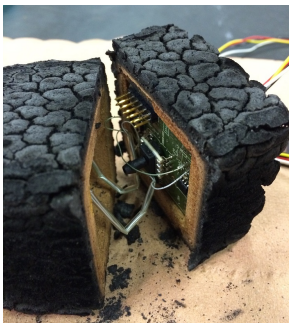

Figure 16: Inside the sample after the test.

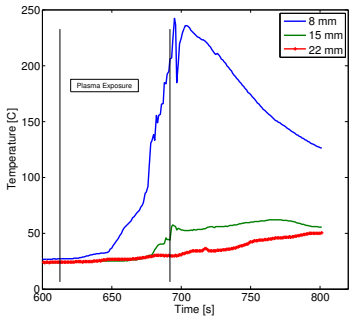

Figure 17: Thermal plug thermocouple data (top) and the electronics temperature (bottom).

4.4.2. Experimental Setup and Testing Conditions

The sample is mounted inside the cooled box in Plasmatron. The test sample is exposed to plasma at constant pressure of 10000 Pa and four staged reference cold wall heat fluxes of 708, 1250, 1500, 1640 kW/m^2 for 80 seconds in total. The measurement techniques used are identical to the ablation characterization campaign described in Sec. 3.1.

4.4.3. Results

When the sample is separated after the experiment, it was seen that the PCB and the cavity still sit in the virgin layer and they are in good shape. The view from both sides can be seen in Figure 16. The high speed camera revealed a total swelling of +1.6 mm at the stagnation point and a corner recession on the other hand of -8.43 mm. The surface temperatures by the pyrometer showed the expected increases at different heat fluxes around 1700, 2100, 2250 and 2350 K at the stagnation point. The thermocouple data are given in Figure 17. Not shown here but the temperatures in the back of the TPS did not exceed the operational range of the electronics.

The thicknesses of the char/pyrolysis/virgin layers are 5.7 mm, 0.24 mm and 42.16 mm respectively. It is important to state that the first thermocouple of the plug is placed at 8 mm from the surface and therefore all thermocouples are in the virgin layer which explains the not so high temperature data.

The pressure port seem not to char/have pyrolysis layer larger than the sample itself. No blockage due to ablation is observed along the pressure hole. The transducer is directly mounted in the back of the hole. The measurement frequency was 1 Hz and the data can be seen in Figure 18. The fluctuations on the measurements are of the order $\pm 30Pa$. However it is important to note that the chamber pressure is also fluctuation by $\pm 100Pa$ according to the static pressure sensor mounted in the chamber. The expected total pressure order of magnitude would be static pressure 10000 Pa + dynamic pressure 20 Pa. Considering the pressure drop in the chamber due to the vacuum pump operation during the test, the total pressure is in good agreement with Plasmatron sensor.

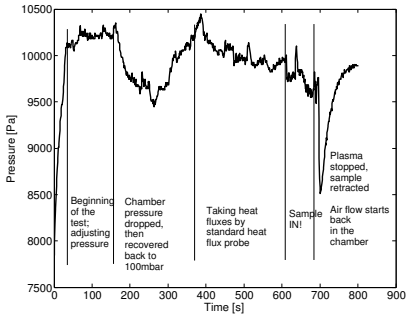

Figure 18: Pressure sensor measurement at the stagnation point. The plasma exposure is between t=617s - 698s.

5. Post-Flight Strategy

It is also the objective of this PhD research to propose a post-flight analysis once QARMAN is flown and successfully returned its flight data. It includes four main topics:

- Data reduction
- Ablation Model Implementation on XPL01
- Off-Nominal Trajectory Scenario
- Flight-to-Ground Extrapolation Method Validation

Data reduction includes the step where the flight data is cleaned up. The information will come in a

discrete time digital form at the available acquisition frequencies. The downlink is also at a tight budget on board QARMAN and it could potentially lead to missing intermediate data packages. Smoothing, filtering and interpolation methods will be applied at this stage. It should be noted that the thermal plug data from MSL entry did not need filtering [33]. The experiments performed with QARMAN DAQ system also showed quite smooth results.

The second item is the application of the ablative material response model to the flight data. It is previously stated that Cork P50 material is rather difficult to model, thus an extensive test matrix is covered for data collection. The experimental data presented in Sec. 3 is going to be used in the numerical engineering material response models to reconstruct the surface temperature, and later heat flux, of the Plasmatron experiments. One way to do this is to trim the thermal and chemical properties until the surface temperature and the recession rates (that are known for ground tests) are matched. This minimal approach is very useful for a preliminary analysis of the flight data from XPL01 and eventually for pressure and trajectory location from accelerometers, gyros and XPL02. More advance approaches can be used as studied extensively for MSL and Mars Pathfinder flight data such as "Inverse Methods". One thermocouple of the thermal plug is used as reference and the surface properties of the TPS are computed. This is mathematically an ill-posed problem and should be treated carefully. The approach and the details can be found in [36; 37] for MSL and in [38] for Mars Pathfinder mission.

The third analysis includes the behavior if QARMAN does not follow the nominal trajectory. Best and worst case scenarios are already being addressed within QARMAN mission design. For the aerothermodynamic in-flight experiments, the worst case scenarios are especially important for measurement ranges of the sensors and for the survival of the electronics. Sensor selection and measurement chain design are however made accordingly and QARMAN's "survival box" concept ensures for significant duration the survival of the electronic boards. Another aspect is the prediction of the surface properties from XPL01 and XPL02. That is already taken into account in the test matrix of the TPS experiments as discussed in Sec. 3.1.

All these items will iterate back on the validation process of the Flight-to-Ground Extrapolation method described in Sec. 2.2. If QARMAN follows an off-nominal trajectory that cannot be precisely matched to the test matrix in Table 3, additional experiments in VKI Plasmatron can be performed. New sample geometries can be computed for the new trajectory conditions and new experiments can be done where the developed material response model can be reapplied in order to match the new conditions.

6. Conclusion

A procedure from the pre-flight design phase of a spacecraft to post-flight data analysis is presented throughout the paper. First, a Flight-to-Ground extrapolation methodology is developed in order to correctly duplicate the flight aerothermodynamic conditions in a plasma wind tunnel for a spacecraft of arbitrary geometry. Secondly, the procedure is applied to the re-entry test vehicle QARMAN, which carries a number of aerothermodynamic in-flight experiments so that flight data can be returned for its validation. Its thermal protection material is characterized in VKI Plasmatron wind tunnel to provide experimental data both to the material response models for a safe vehicle design and a means for comparison with flight data. Later, the necessary in-flight experiments are designed and tested. A post-flight strategy is briefly introduced on how to make use of the flight data after the mission.

Although the entire procedure is presented on QARMAN, the step-by-step approach is applicable to any given mission of any spacecraft geometry, any trajectory and any mission whether to collect flight data or not.

Acknowledgments

The authors are thankful to Dr. Cem O. Asma, Dr. Damien Le Quang Huy, Thorsten Scholz, HyunWoo Krassilchikoff and Ertan Umit. The authors are grateful to Mr. Pascal Collin for his unique dedication to the operation of the VKI Plasmatron facility.

References

[1] I. Sakraker, O. Chazot, A flight-to-ground extrapolation methodology for subsonic plasma windtunnels and its validation by real flight experiment qarman, in: AIAA Aviation: 32nd AIAA Applied Aerodynamics Conference, no. AIAA 2014-2567, 2014.

[2] I. Sakraker, E. Umit, V. van der Haegen, O. Chazot, Atmospheric entry aerothermodynamics flight test on cubesat platform, in: 11th International Planetary Probe Workshop, Pasadena, CA, USA,, 2014.

[3] CalPoly, Cubesat design specification, revision 13, the cubesat program (issued 20.01.2014) [cited 10.02.2015].
URL www.cubesat.org
[4] J. A. Fay, F. R. Riddell, Theory of stagnation point heat transfer in dissociated air, in: VKI, An Introduction to Hypersonic Aerodynamics 13 p(SEE N 90-13334 05-02), 1958.
[5] L. Lees, Laminar heat transfer over blunt nosed bodies at hypersonic flight speeds, Jet Propulsion 26 (1958) 497–499.
[6] R. Goulard, On catalytic recombination rates in hypersonic stagnation heat transfer, Jet Propulsion 28 (11) (1958) 737–745.
[7] A. Kolesnikov, Extrapolation from high enthalpy tests to flight based on the concept of local heat transfer simulation, RTO AVT Course on "Measurement Techniques for High Enthalpy and Plasma Flows", Rhode-Saint-Genese, Belgium (October 1999).
[8] I. Sakraker, In-flight experiment design and ground testing of a re-entry cubesat, in: 5th Symposium of VKI PhD Research, 2014.
[9] J. Boison, A. Curtiss, An experimental investigation of blunt body stagnation point velocity gradient, ARS Journal (1959) 130–135.
[10] J. C. Ellison, Experimental stagnation point velocity gradients and heat transfer coefficients for a family of blunt bodies at mach 8 and angles of attack, Tech. Rep. TN D-5121, NASA Langley (1969).
[11] L. Lees, Recent developments in hypersonics, ARS Semi-Annual Meeting, San Francisco, California, 1957.
[12] J. Anderson, Hypersonic and High Temperature Gas Dynamics, McGraw-Hill, 1989.
[13] E. V. Zoby, E. M. Sullivan, Effects of corner radius on stagnation-point velocity gradients on blunt axisymmetric bodies, Tech. Rep. NASA-TM-X-1067, NASA (1965).
[14] H. Olivier, Influence of the velocity gradient on the stagnation point heating in hypersonic flow, Shock Waves 5 (1995) 205–216.
[15] V. Lunev, Hypersonic Aerodynamics, Mashinostroyeniye (in Russian), Moscow, Russia, 1975.
[16] L. Trimmer, E. Clark, Stagnation-point velocity gradients for spherical segments in hypersonic flow, AIAA Journal 7 (10).
[17] P. F. Barbante, O. Chazot, Flight extrapolation of plasma wind tunnel stagnation region flowfield, Journal of thermophysics and heat transfer 20.3 (2006) 493–499.
[18] A. Guelhan, B. Esser, A. D. Vecchio, S. Loehle, N. Sauvage, O. Chazot, C. Asma, Comparative heat flux measurements on standard models in plasma facilities, in: 13th International Space Planes Conference, no. AIAA 2005-3324, Capua, Italy, 2005.
[19] F. Panerai, Aerothermochemistry characterization of thermal protection systems, Ph.D. thesis, Universite degli Studi di Perugia and von Karman Institute for Fluid Dynamics (2012).
[20] E. V. Zoby, Empirical stagnation point heat transfer relation in several gas mixtures at high enthalpy levels, Tech. Rep. TN D-4799, NASA Langley (1968).
[21] O. Chazot, R. Regnier, A. G. Munoz, Simulation methodology in plasmatron facility and hypersonic wind tunnels, 12th International Conference on Method of Aerophysical Research, Akademgorodok, Novosibirsk, Russia, 2004.
[22] D. L. Q. Huy, Spectroscopic measurements of sub- and supersonic plasma flows for the investigation of atmospheric re-entry shock layer radiation, Ph.D. thesis, Universite Blaise Pascal and von Karman Institute for Fluid Dynamics (2014).
[23] H. R. Griem, Principles of Plasma Spectroscopy, isbn-9780511524578 Edition, Cambridge University Press, 1997.
[24] N. Villedieu, F. Panerai, O. Chazot, T. Magin, Uncertainty quantification for gas-surface interaction in plasmatron facility, in: 7th European Symposium on Aerothermodynamics, ESA SP-692, Brugge, Belgium, 9-12 May 2011.
[25] T. Rees, Development of an enthalpy probe for the plasmatron, Tech. Rep. SR 2014-44, von Karman Institute for Fluid Dynamics (2014).
[26] J. B. Scoggins, T. Magin, Development of mutation++: Multicomponent thermodynamics and transport properties for ionized gases library in c++, in: 11th AIAA/ASME Joint Thermophysics and Heat Transfer Conference, no. AIAA 2014-2966, Atlanta, GA, 16-20 June, 2014.
[27] D. G. Fletcher, Nonintrusive diagnostic strategies for arcjet stream characterization, RTO AVT Course on Measurement Techniques for High Enthalpy and Plasma Flows, Rhode-Saint-Genese, Belgium (October 1999).
[28] P. S. Lopez, Non-intrusive real time enthalpy determination in plasma flows, Tech. Rep. SR 2012-41, von Karman Institute for Fluid Dynamics (2012).
[29] J. P. P. Leite, Assessment of ground testing conditions for in-flight experiment development, Master's thesis, PR2013-08, von Karman Institute for Fluid Dynamics, Rhode-Saint-Genese (2013).
[30] G. Degrez, D. V. Abeele, P. Barbante, B. Bottin, Numerical simulation of inductively coupled plasma flows under chemical non-equilibrium, International Journal of Numerical Methods for Heat & Fluid Flow 14 (4) (2004) 538–558.
[31] B. Helber, Absolute radiation measurements of ablation products in the boundary layer of carbon based ablators, in: 6th Symposium of VKI PhD Research, 2015.
[32] F. Milos, Y. Chen, Ablation and thermal response property model validation for phenolic impregnated carbon ablator, in: 47th AIAA Aerospace Sciences Meeting Including The New Horizons Forum and Aerospace Exposition, Orlando, Florida, Vol. AIAA 2009-262, 2009.
[33] M. Mahzari, R. D. Braun, T. R. White, D. Bose, Preliminary analysis of the mars science laboratory's entry aerothermodynamic environment and thermal protection system performance, in: 51st AIAA Aerospace Sciences Meeting including the New Horizons Forum and Aerospace Exposition, Grapevine, Texas, Vol. AIAA 2013-0185, 2013.
[34] I. E. Akyol, Design of data acquisition subsystem of qarman payloads and validation in plasma facilities-hardware, Tech. rep., SR 2013-16, von Karman Institute for Fluid Dynamics (2013).
[35] Qb50 project, www.qb50.eu, last accessed: 10.02.2015.
[36] M. Mahzari, Inverse estimation methodology for the analysis of aeroheating and thermal protection system data, Ph.D. thesis, Department of Aerospace Engineering, Georgia Institute of Technology, Atlanta, GA (2013).
[37] S. R. Copeland, M. Mahzari, I. Cozmuta, J. J. Alonsox, A statistics-based material property analysis to support ablation simulation uq efforts, in: 53rd AIAA/ASME/ASCE/AHS/ASC Structures, Structural Dynamics and Materials Conference, Vol. AIAA 2012-1763, Honolulu, Hawaii, 2012.
[38] M. Mahzari, R. Braun, T. White, Reconstruction of mars pathfinder aerothermal heating and heatshield material response using inverse methods, in: AIAA-Paper 2012-2872, 2012.

Efficient Trajectory Simulation for Optimization of the Simultaneous Deployment of a Network of CubeSats

Thorsten Scholz

Aeronautics and Aerospace Department, von Karman Institute for Fluid Dynamics, Belgium, scholz@vki.ac.be

University Supervisor: Stefanos Fasoulas

Professor, Institut für Raumfahrtsyteme, Universität Stuttgart, Pfaffenwaldring 29, 70569 Stuttgart, fasoulas@irs.uni-stuttgart.de

Abstract

The on-going miniaturization of satellite systems and the increasing popularity of micro- and nano-satellites leads to new satellite networks for distributed science measurements in orbit. The low mass per satellite makes the simultaneous launch of the complete constellation feasible and more attractive due to the reduced complexity and launcher related costs for a dedicated single launch. To reduce the increasing complexity on the mission design and analysis, which is introduced by the simultaneous launch due to the variety of parameters related to the deployment, an orbit propagator coupled with an optimization software is developed to find the optimal parameter set for the collision risk reduction, best distribution in orbit after commissioning and other constraints.

Keywords: orbit propagation, trajectory simulation, optimization, atmospheric model

1. Introduction

All satellite constellations so far like the IRIDIUM network were brought into orbit using several launches lifting only one or two satellites with each flight due to the large mass of the satellite and the payload mass constraints of the used rocket. The on-going miniaturization of the satellite systems and components like electrical power systems, on-board computers or attitude determination and control systems leads to a boom of small-scale satellites using the CubeSat or similar nano or micro-satellite form factors. More and more science mission are continuing to emerge similar to the QB50 project using several micro-satellites for distributed measurements in Earth orbit employing the benefits of spatial and temporal resolution for the obtained dataset, shorter re-visiting times for specific locations on Earth or risk reduction by redundant satellites. Unlike larger satellites weighing above several hundreds of kilograms, small satellites with masses around or lower than $10\,kg$ can be launched and deployed together in the desired orbit using a single launch vehicle.

The deployment of the network using a single launcher however introduces further complexity to the mission design and analysis, especially the increased collision risk in the early phase of the mission after deployment is a complex problem due to the dependency on a large number of input parameters. Beside the target orbital parameter, the used deployment system (applied ΔV, directions) and performance parameters from the upper stage like attitude constraints play a major role for the deployment scenario as visualized in Figure 1 for the deployment direction. These pa-

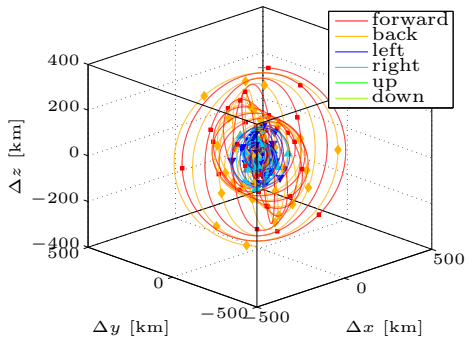

Figure 1: Influence of deployment direction on CubeSat spreading ($\Delta v = 1.5\,\frac{m}{s}$, $t = 1\,d$, rotating frame)

rameters related to the deployment of the satellites can be optimized to ensure a collision free deployment, science compatible dispersion of all satellites in orbit and beneficial communication windows with ground beside other mission depended constraints.

Most of the mission design and analysis tools like STK[1], ASTOS[2] or GMAT[3] support simulations of multiple satellite by interaction with a graphical user interface, but the large amount of input parameters require a detailed background knowledge about the impact of each parameter on several mission aspects. Hence a dedicated orbit propagation tool is developed in the framework of the thesis supporting all important required operations like thruster of satellites or upper stage, deployment of child object from parent objects, three and six degree of freedom attitude simulation, various gravitational and atmospheric models. The propagator is coupled with an optimization software using different order algorithms to minimize the specific goal in an efficient way as shown in Figure 2. Depending on the simulation time, different algorithms will be utilized like the zero-order evolutionary method for deployment collision risk studies over the first few orbits and first-order methods like algorithmic differentiation for the long-duration optimization with higher constraints on the computational costs.

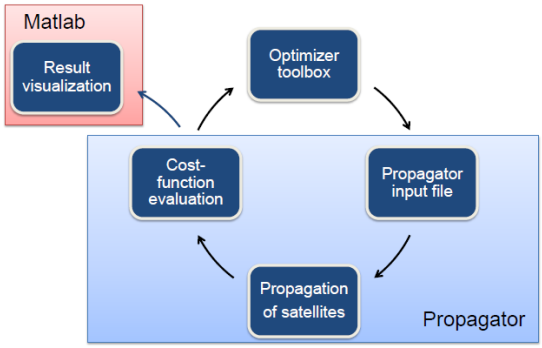

Figure 2: Schematic overview of propagator/optimizer interface

A typical use-case for the developed software is the QB50 project, where a network of 50 CubeSats will be launched to perform in-situ measurements of the spatial and temporal variation of atmospheric properties in the lower thermosphere at an altitude of 350 km to 150 km [4]. CubeSats are small nano-satellites with different form factors available. The smallest possible size is 10 x 10 x 10 cm. The CubeSats for QB50 will be 2U or 3U (units) with 20 or 30 cm length build by different universities from all over the world. The project will demonstrate the possibility of using the small satellites as efficient and low-cost technology demonstrators. QB50 will be the first simultaneously launched CubeSat network and helps in gaining a better understanding of such complex missions.

The choice for conducting measurements in the lower thermosphere is influenced by several factors and constraints. The atmospheric properties in this region and their relationship to Earth's climate and space-weather like sun storms are yet not well known [4]. This leads to larger uncertainties in lifetime and trajectory simulations, which the recently uncontrolled and not precise predictable re-entries of UARS, Rosat or Phobos-Grunt have shown. Another influence factor for the choice of orbit is the mitigation of space debris creation and fulfilment of the 25 year lifetime requirement.

The mission design of QB50 will be especially challenging in terms of mission design and includes several points to be looked at. First the development of a suitable deployment strategy for the 50 CubeSats is mandatory to reduce the collision risk to a minimum. The deployment also effects the spreading and therefore the global distribution of the satellites from which most of them have no on-board propulsion used to additional increase of the drift rate. Figure 1 shows the distance to the deployment origin after 1 day for different deployment directions relative to the flight direction. The deployment of the satellite and the in-orbit motion with its impact e.g. on the communication and power budget will be analyzed using the trajectory propagation tool. To increase the confidence in the simulations, the necessary input parameters, like the atmospheric environment or initial orbit (see Figure 3), have to be investigated and the associated uncertainties incorporated into the simulations.

2. Propagator

This section describes the development of the propagator including the various models used as input for the simulation of the satellite motion in orbit and during re-entry. A brief overview of the different models is given in Figure 3.

[1] Systems Tool Kit [1], Analytical Graphics, Inc.
[2] AeroSpace Trajectory Optimization Software [2], Astos Solutions GmbH
[3] General Mission Analysis Tool [3]

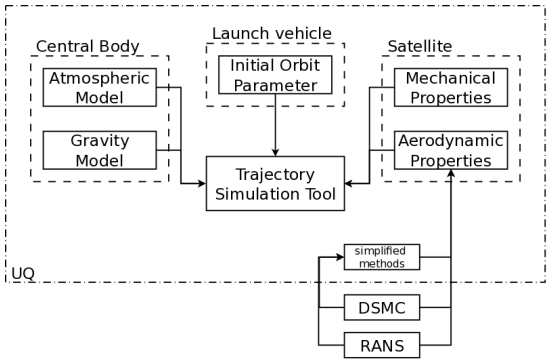

Figure 3: Schematic overview of the trajectory propagation tool

2.1. Satellite motion

The motion of a satellite can be approximately expressed by solving the two-body problem in an inertial reference frame. The only force acting on the satellite in this simplified case is the gravity attraction of the central body. Using Newton's law the differential equation for the motion of a spacecraft around Earth can be described as following

$$\ddot{\mathbf{r}} = \frac{\mu}{r^2}\mathbf{e}_r = \ddot{\mathbf{r}}_g, \tag{1}$$

where r is the distance between the two objects, μ the gravitational parameter of Earth and $\mathbf{e}_r$ the unity vector pointing from the Earth to the satellite. This equation is only valid for a spherical gravity field and as already mentioned, when no other forces are acting on the satellite. The solution to this problem can be expressed analytical as a Kepler orbit using the six orbital elements to describe the orientation of the orbit plane and the position inside the plane. It is well described and can be found in text books like [5].

However in reality, additional forces are acting on the satellite in orbit beside gravity. The contribution from these forces can be incorporated by introducing additional accelerations into equation 1 leading to the perturbed equation of motion.

$$\ddot{\mathbf{r}} = \ddot{\mathbf{r}}_g + \ddot{\mathbf{r}}_{pg} + \ddot{\mathbf{r}}_{tb} + \ddot{\mathbf{r}}_t + \ddot{\mathbf{r}}_a + \ddot{\mathbf{r}}_{srp} + \ddot{\mathbf{r}}_{other} \tag{2}$$

Depending on the orbit altitude some perturbations can be neglected due to their small contribution. The magnitudes of various perturbations are shown in Figure 4 for different altitudes. For low earth orbits (LEO) the most important contributions are due to gravity (spherical gravity field $\ddot{\mathbf{r}}_g$, inhomogeneous gravity field $\ddot{\mathbf{r}}_{pg}$) of the central body and aerodynamic forces ($\ddot{\mathbf{r}}_a$) introduced by the atmosphere. With increasing distance, the third body perturbations ($\ddot{\mathbf{r}}_{tb}$) from the Moon, Sun and other planetary objects are getting more and more important. The solar radiation pressure ($\ddot{\mathbf{r}}_{srp}$) is independent of the altitude but will vary along the orbit due to the changing angle of the spacecraft towards the Sun and eclipse periods. The influence on LEOs of the later mentioned perturbations can be regarded as small [6] and are therefore not currently implemented in the trajectory tool. However the integration of these models are planned for the future. Artificial disturbances like thrusting ($\ddot{\mathbf{r}}_t$) can be also considered in the equation of motion.

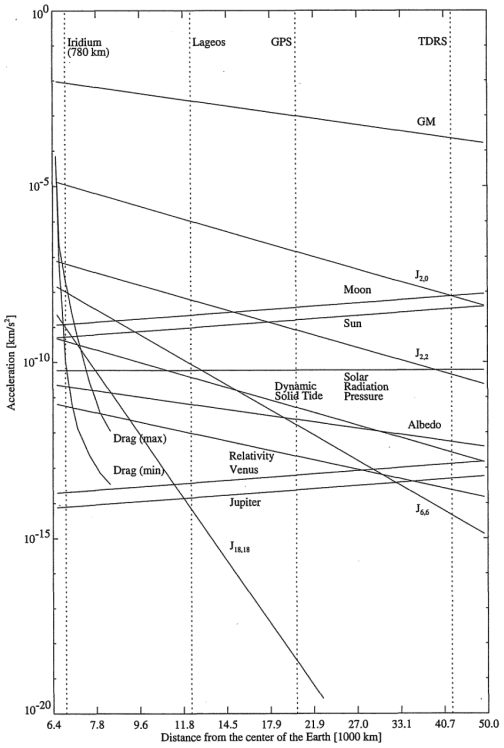

Figure 4: Order of magnitude of various perturbations of a satellite orbit [6]

It is necessary for the simulation of the satellite motion to model the perturbations and to evaluate the functions for the given position, velocity and attitude of the spacecraft, described by the state vector $\mathbf{s}$. Due to the complexity added by the perturbations, the problem is no longer analytically solvable. The ordinary differential equation can be solved using an initial state and approximate the solution using time-stepping schemes like Runge-Kutta methods [7][8].

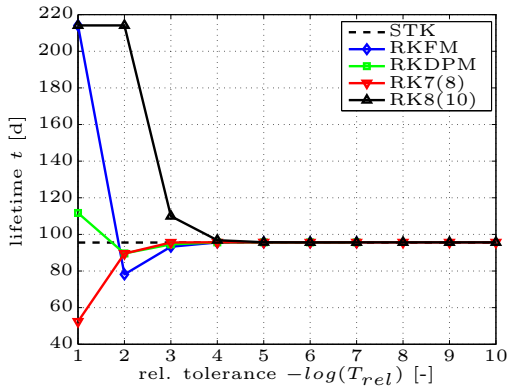

Figure 5: Influence of relative tolerance for different integration schemes ($T_{abs} = 1$, $\Delta t_{min} = 1\ s$)

2.2. Input parameters

An overview of the different input parameters and models for the trajectory simulation tool is given in Figure 3 and the preliminary results of the assessment performed so far will be presented in the following. For each simulation, the standard values for a 2U CubeSat have been used when not specified differently. The mass is $2\,kg$, drag coefficient $C_D = 2.3$, reference area $A_{ref} = 0.01\,m^2$ and the NRLMSISE00 atmospheric model [9] has been used with $F_{10.7} = F_{10.7A} = 133.0\,sfu$ and $A_p = 43\,nT$ as input parameters.

The initial Kepler elements in J2000 frame are:

- semi-major axis $a = 6699\,km$
- RAAN $\Omega = 40°$
- inclination $i = 70°$
- eccentricity $e = 0$
- true anomaly $\nu = 75°$

2.2.1. Simulation parameters

Different numeric integration schemes have been implemented in the trajectory tool using a single or multi-step approach with fixed or variable step size. The current schemes available in the tool are going up to 8th order allowing larger time steps with higher accuracy by performing more intermediate steps. The performance of the schemes, RK Fehlberg 4(5) , RK Dormand Prince 4(5), RK7(8) and RK8(10) [10][11][12][13], have been compared using a typical QB50 CubeSat orbit. The two numbers inside the name represent the two orders used in the scheme to calculate the integrated state and to estimate the truncation error. The local truncation error $\mathbf{e}$ for each step is estimated by comparing the results obtained for different orders, e.g for the Runge-Kutta Fehlberg method the result with 4th (state $\mathbf{s}_{i,l}$) and 5th (state $\mathbf{s}_{i,h}$) order can be obtained. The relative tolerance is multiplied by the maximum value of last and current state and compared with the truncation error, see equation 3. Figure 5 shows the calculated lifetime for different values of the relative tolerance T_{rel} for each step. Similar an absolute tolerance T_{abs} can be specified for the integration to restrict the time step further and in cases where the state variable is equal to zero. For the convergence study, the absolute tolerance was set to 1. The time step will be adjusted automatically each integration step to fulfill the tolerance requirements [7]. An upper and lower bound for the time step can be specified to limit the adjustment process.

$$\mathbf{e} = |\,\mathbf{s}_{i,h} - \mathbf{s}_{i,l}\,| \leq |\,T_{rel} \cdot max(\,\mathbf{s}_{i,l},\,\mathbf{s}_{i-1})\,| + T_{abs} \quad (3)$$

The required relative tolerance to obtain *good* simulation results depends on the used methods and on the precision demands of the result. With a relative tolerance of $T_{rel} = 10^{-5}$ the orbital lifetime matches the one obtained with STK. However the higher precision necessary for the deployment and collision analysis requires a lower relative and absolute tolerance.

The average time step distribution for the convergence study is shown in Figure 6 for the different schemes. The maximum and minimum time step for each simulation are given as dashed lines. Obeying the same relative tolerance, the possible time step for the high order schemes is approximately one magnitude larger compared to the 4th order schemes. The computation time for the high order methods is significantly shorter due to the larger time step despite the larger number of function calls to the model.

2.2.2. Atmospheric model

The knowledge of the neutral density along the orbit of a spacecraft is mandatory for the calculation of the aerodynamic forces and moments induced by the residual atmosphere of the Earth.

Nowadays a couple of atmospheric models based on orbital decay observations or experimental measurements exist who predict the composition, temperature and density for a given time and position. These models are based on relations between historic measurements of the atmosphere and the solar activity around the measurement time point as the main influencing parameter. With more and more data sources available the accuracy of these models advanced over time and typically an error less than 10-20 % for the neutral density can be expected nowadays [14], even

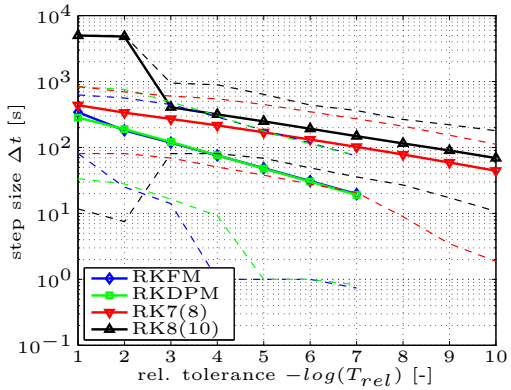

Figure 6: Minimum, average and maximum step size for different integration schemes ($T_{abs} = 1$, $\Delta t_{min} = 1\,s$)

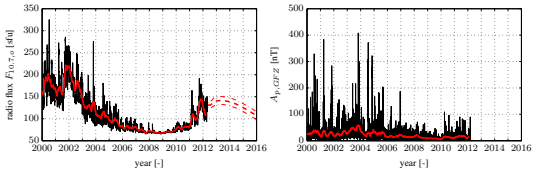

(a) solar radio flux [21][22] (b) geomagnetic index [23]

Figure 7: Historic values for solar activity indices

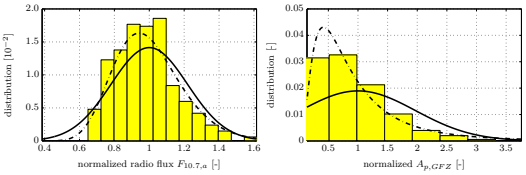

(a) solar radio flux (b) geomagnetic index

Figure 8: Distribution function for launch date equivalent year (2003)

with the models improving over the last few years due to measurements obtained by the GRACE and CHAMP mission [15]. However due to lack of proper understanding of all processes taking place in the atmosphere, the error can not be reduced significantly any further without additional data.

A second type of atmospheric models exists where the whole atmosphere is simulated to obtain the properties like composition, neutral density or temperature. These physical models are computational demanding compared to the models based on simple relations with experimental data. They are solving the mass, momentum and energy equations using a structured three dimensional grid for a large part of the atmosphere.

The performance of different models comprising both groups has been studied and the results in terms of neutral mass density compared. From the available experimental models, JB2006 [16], JB2008 [15], NRLMSISE00 [9], DTM2000 [17] and DTM2009 [18] have been choosen; from the physical models, GITM [19] and TIEGCM [20] have been selected.

The solar activity is the most important input parameter for all atmospheric models and is typically described by the solar radio flux $F_{10.7}$, which quantifies the solar radiation at an wavelength of 10.7 cm, an 81-day centered average value of the flux $F_{10.7A}$ and the geomagnetic index A_p. Recently additional parameters have been developed to include the solar radiation at different wavelength to improve further the accuracy of the models [15]. Figure 7 shows the solar activity for the last solar cycle of 11-years and, if available, predicted values for the next years. The predicted average value for the solar radio flux from [21] is given with uncertainties for different confidence levels, the 1 σ value is given as dashed lines in the figure. This uncertainty however does not represent the temporal variation of the flux itself. Therefore the distribution of both parameters for the launch year was obtained by analyzing the historic data for a representative year in the last solar cycle. Figure 8 shows the normalized results for the year 2003 including the fitted normal and log-normal distribution function.

With the distribution and prediction uncertainty, different cases can be constructed representing higher or lower solar activity for the launch year. A typically density distribution for one altitude level obtained by the NRLMSISE00 model is shown in Figure 9. The diurnal bulge due to the increased solar radiation and the continental effects are clearly visible.

For better comparison with the US76 standard atmosphere, the average of the density was taken for each calculated altitude level. The change in density over altitude for different models is shown in Figure 10. Density values obtained by measurements of satellite drag using accelerometers on the GRACE/CHAMP mission [24] are shown in black. The error bar shows the average (black cross); maximum and minimum value of the satellite data for the period of one day are given as upper and lower bound.

With increasing altitude the difference between the

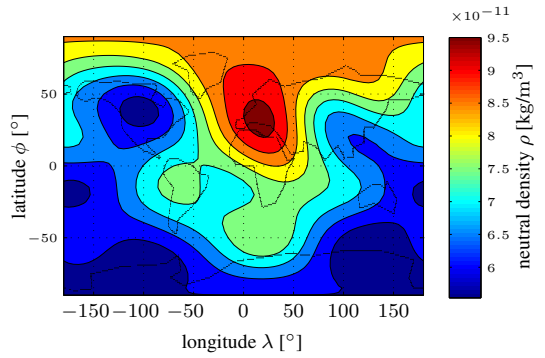

Figure 9: Neutral mass density for NRLMSISE00 at 250 *km* of altitude (1 Oct. 2014, UTC noon)

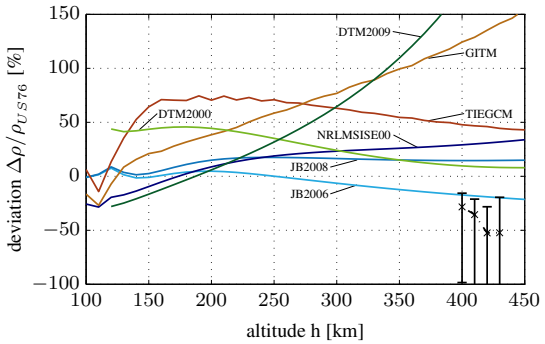

Figure 10: With US76 model normalized neutral density for different models

various models increases which shows clearly the need of QB50 to broaden the database of atmospheric measurements in this altitude region. The detailed assessment is given in [25]. However even with the comparable output from different models, not all recent developments and changes in the atmosphere are included in the underlying database for the models.

Therefore these models can not take into account recent changes in the atmosphere like the observed decrease in neutral density over the past years. These changes have to be quantified and included separately in the orbital dynamics simulation. As discussed in [26] and [27], the global neutral density can be obtained with the help of the derived drag value for near-Earth satellites. Seasonal variations and other included biases in the obtained measurement have to be removed and the resulting density can be compared to the density for different atmospheric models using the measured input parameters to describe the solar activity. It can be observed that the neutral density decreases more than the model with the observed solar activity predicted due to the increase in CO_2 concentration in the lower atmosphere [27]. The trend given in the paper represents a decrease of 3.55 % per decade and was obtained by a curve fit with the annual average values; the trend varies from -5 % for solar minimum and -2 % for solar maximum. Abnormalities like this are unpredictable and still not fully explainable today. Half of the decrease can be attributed to the lower solar radio flux and an increase of the CO_2 cooling [28] but the other half has still to be examined in more detail.

2.2.3. Initial orbit

The initial orbit elements have a strong impact on the propagation and the mission. The most important parameters are the semi-major axis, the longest diameter of the orbit ellipse, the inclination, the angle between the equatorial plane and orbital plane, and the true anomaly describing the position along the orbit. Only a circular orbit has been investigated for QB50 leaving the argument of periapsis undefined.

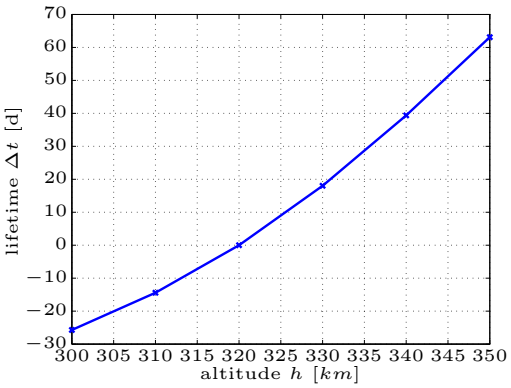

Figure 11: Influence of semi-major axis on lifetime

The variation in lifetime with change of semi-major axis or orbit altitude for circular orbits is shown in Figure 11 normalized with the initially planned QB50 orbit parameters (here 320 km altitude). The exponential increase of lifetime due to decrease in density with higher altitude is already visible for the small variations. An additional lifetime of 60 days could be achieved by lifting the orbit to 350 km still below ISS altitude.

The inclination has a similar effect on the lifetime which is shown in Figure 12. With increased inclination, the lifetime increases since the satellites passes more often and longer through the low density re-

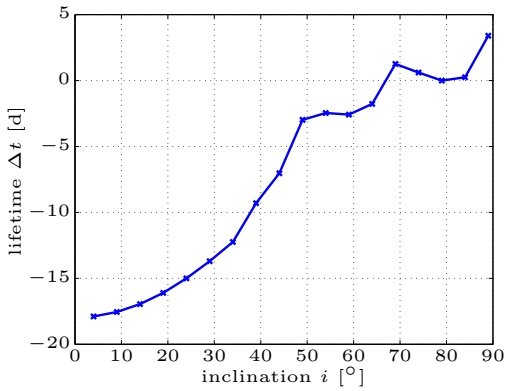

Figure 12: Influence of inclination on lifetime

gions. Through the non-regular shape of the Earth with the flattening on the poles, the density there is smaller compared to equatorial regions.

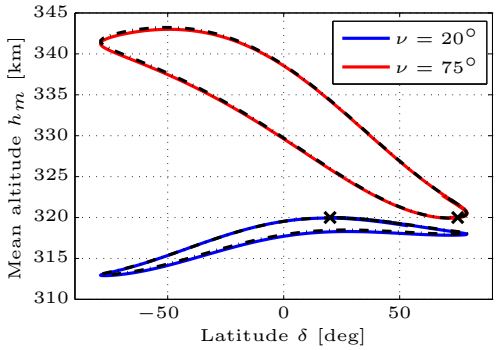

Figure 13: Altitude relative to mean Earth radius for first orbit shown for a true anomaly of 20° and 75° (STK black dashed line and trajectory simulation tool colored lines)

The influence of the true anomaly on the lifetime for a circular orbit is not as intuitive as for the other parameters. By changing the initial position along a orbit, one could expect that there is no effect on the lifetime. However due to the conversion from Kepler elements to Cartesian or other coordinates used in the propagation the irregularity of the shape of the Earth is introduced again into the problem. Figure 13 shows the first orbit for two different anomalies (blue $\nu = 20°$, red $\nu = 75°$) using the developed trajectory tool and STK for comparison. The initial position is marked in both cases with a black X at the correct initial altitude. Due to the fact, that the velocity in both points are the same, the orbit shape differs and the satellite is exposed to different neutral densities during it's lifetime. The impact of the true anomaly on the lifetime is shown in Figure 14. The increase in lifetime corresponds to the higher orbit altitude with less initial drag.

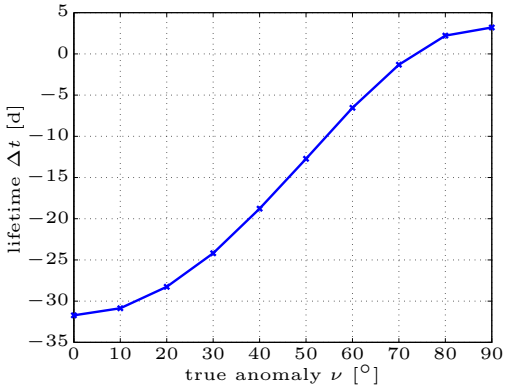

Figure 14: Influence of true anomaly on lifetime

2.2.4. Aerodynamic characterization

Detailed knowledge of the aerodynamic forces and moments is necessary to calculate the perturbations on the spacecraft induced by the residual atmosphere. The lift force is typically neglected when performing 3-DOF simulation to determine the satellite motion leaving the drag coefficient as the important parameter to be specified.

Different approaches can be found in the literature to estimate or calculate the drag coefficient. Oltrogge [29] used satellite observations and motion to predict the drag coefficient using an inverse approach. He analyzed the orbits of 47 CubeSats and calculated the coefficient for each satellite from the orbit decay. Since no detailed knowledge of the attitude, mass and exposed area is available for most CubeSats, the resulting values show a large scattering, which is shown in Figure 15. However the average value for the drag coefficient is approximately 2.3.

Sentman proposed already 1961 the free molecule flow theory (FMT) to calculate the exact forces and moments acting on the satellites exposed to rarefied environment [30]. The pressure distribution along the spacecraft could be obtained by calculating the angle between the free stream and each satellite surface. The drag coefficient is calculated by summarization of the forces in velocity direction. The FMT method has been implemented into the trajectory simulation tool to calculate on demand the aerodynamic coeffi-

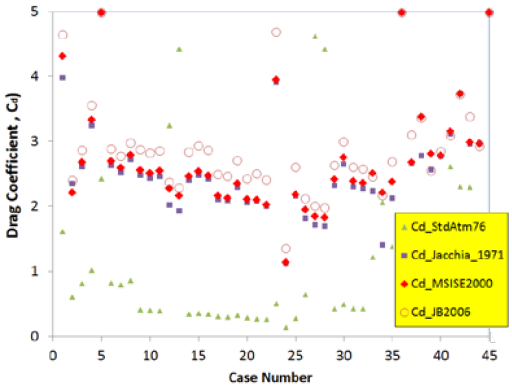

Figure 15: Best-fitting drag coefficient for different CubeSat Cases [29]

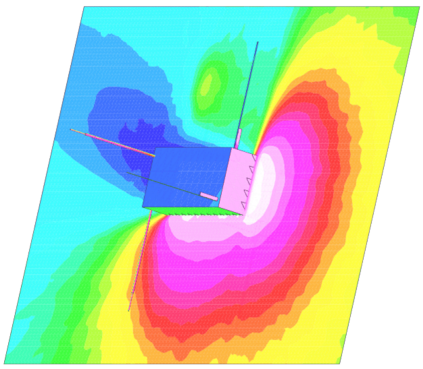

Figure 16: Visualization of the flow field around a 2U standard CubeSat with deployed antennas and Langmuir probes (ITAM)

Table 1: Drag coefficient for different geometries, angle of attack and side-slip angle at $h = 350\,km$

Geometry	α [°]	β [°]	C_D [-]
2U	0	0	2.8
2U	10	10	3.6
2U	90	45	6.0
3U	0	0	3.1
3U	10	10	4.5
3U	90	45	10.3
2UwA	0	0	3.35

cients beside the possibility to specify the coefficients directly.

For altitudes of $100\,km$ or above the atmosphere is so rarefied that the flow-field can not be calculated with the help of RANS solver; stochastic methods simulating each particle or a subset of them are mandatory to use. Due to the stochastic approach this method is more computational demanding than the FMT method based on the surface inclination. The computation time can be reduced by increasing the number of simulated particles resulting in higher memory consumption, however the duration is still orders of magnitudes above the simplified theory. Figure 16 shows the flow field for a 2U standard CubeSat with antennas using RGDAS. The Direct Simulation Monte Carlo (DSMC) tool RGDAS is available at VKI and has been used to generate a database with aerodynamic coefficients for the standard 2U and 3U CubeSat together with the Institute of Theoretical and Applied Mechanics (ITAM). The obtained values can be used to verify the results calculated with the FMT method.

A reduced set of obtained drag coefficients for the altitude of $350\,km$ are given in the Table 1 obtained by VKI and ITAM.

In the current implementation in the trajectory code, the difference between the FMT method and the DSMC results are in the order of 20 % for the drag and lift coefficient which is shown in Figure 18 for QARMAN, the re-entry CubeSat of VKI with deployed AeroSDS. The drag and lift coefficient results obtained with DSMC and FMT are given in Figure 17a. The large drag coefficient results from the increased exposed area due to the deployed panels. However for easier comparison the same reference area $A_{ref} = 0.01\,m^2$ as for standard CubeSats has been used for the calculation of the aerodynamic coefficients. The pitching momentum coefficient is shown in Figure 17b. The deviation between the two methods is again in the range of 20 %.

3. Optimization

Different optimization techniques employing zero and first-order methods [31] will be used for the optimization depending on the scenario and the computational costs associated with the propagation of the satellites. Here mainly two main scenarios can be distinguished.

For short time collision risk studies during the first few orbits after deployment with a simulation time of approximately 3 to 4 hours, less efficient zero-order methods can be employed for problems with a smaller amount of parameters. These methods require typically more iterations to convergence to the optimum

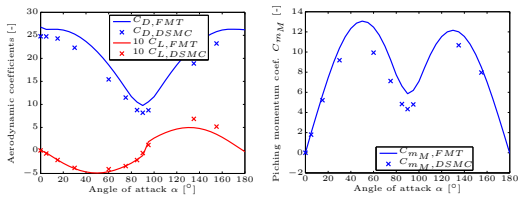

(a) drag and lift coef. (b) pitching moment coef.

Figure 17: DSMC and FMT results for QARMAN with AeroSDS at altitude $h = 320\,km$

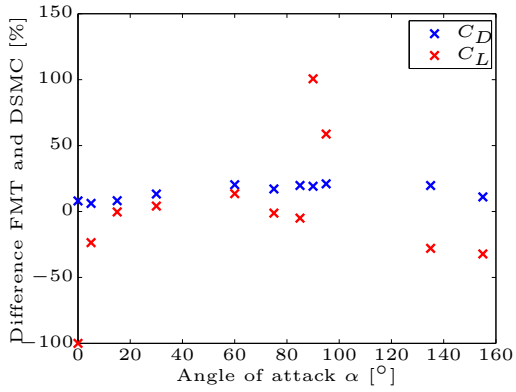

Figure 18: DSMC and FMT comparison for QARMAN with AeroSDS at altitude $h = 320\,km$

since they rely on no additional information like the gradient of the objective function. The major advantage of these derivative-free method is the lower complexity in the implementation and their insensitivity against discontinuous objective functions. An evolutionary algorithm [32][33] will be employed following the evolutionary process by using techniques like mutation, crossover and selection inside an initial population to find the optimal set of parameters or also called individual in the evolutionary methods. For each iteration, all individuals in the population will be analysed and their objective function or fitness determined. Depending on which algorithm is employed, the population will be altered for the next iteration. A popular choice for the strategy used for the selection and adaptation is the Genetic algorithm as described in [34].

For long-duration simulations with additional objectives like equal distribution of the satellite inside the orbital plane, less amount of conflicts between the satellites during ground station passes, similar lifetime in orbit and others, the complexity of the problem raises. The attitude and behaviour of the satellite in orbit (tumbling, aligned with velocity or other vector), which could be assumed to be constant during the short time period of propagation before, now plays a significant role in the spreading of the network and increases the complexity and number of parameters of the optimization. Beside that, the computational costs for complete lifetime simulations of satellites increases by a couple of magnitudes depending on the initial altitude of deployment and the connected duration in orbit. Therefore a first-order method will be likely implemented to improve the optimization performance and to assess the sensitivity of the objectives with respect to the inputs via the reverse mode of the algorithmic differentiation technique [35][36].

4. Conclusion

The current status of the trajectory propagation tool coupled with optimization software and the assessment of the input parameters for the simulation has been reported. The validation of the tool, mainly the 6 DOF simulation, continues and comparisons to other high precision simulation data [37] are planned for the future. The coupling with the optimization kit is currently on-going. Beside these efforts, further improvements will be incorporated like communication analysis, to be used as additional optimization object.

Acknowledgments

The research leading to these results has received funding from the European Community's Seventh Framework Programme ([FP7/2007-2016]) under grant agreement n° 284427 for the QB50 Project.

References

[1] Analytical Graphics, Inc., STK - Systems Tool Kit, `http://www.agi.com/STK`, online; accessed 11-Februar-2013 (2013).

[2] Astos Solutions GmbH, AeroSpace Trajectory Optimization Software, `http://www.astos.de/products/astos`, online; accessed 23-November-2012 (2012).

[3] NASA et al., General Mission Analysis Tool, `http://gmat.gsfc.nasa.gov/`, online; accessed 21-October-2014 (2014).

[4] J. Thoemel, F. Singarayar, T. Scholz, D. Masutti, P. Testani, C. Asma, R. Reinhard, J.-M. Muylaert, Status Of The QB50 Cubesat Constellation Mission, in: Proceedings of 65th International Astronautical Congress, IAF, Toronto, Canada., 2014.

[5] D. Vallado, W. McClain, Fundamentals of Astrodynamics and Applications, Space Technology Library, Springer, 2001.

[6] O. Montenbruck, E. Gill, Satellite orbits: models, methods and applications, 2005.
[7] E. Haier, S. Norsett, G. Wanner, Solving Ordinary Differential Equations I, Nonstiff Problems, Section III.
[8] D. Griffiths, D. Higham, Numerical Methods for Ordinary Differential Equations: Initial Value Problems, 2010.
[9] J. M. Picone, A. Hedin, D. Drob, A. Aikin, Nrlmsise-00 empirical model of the atmosphere: Statistical comparisons and scientific issues, Journal of Geophysical Research 107 (A12) (2002) 1–16.
[10] E. Fehlberg, Classical fifth-, sixth-, seventh-, and eighth-order Runge-Kutta formulas with stepsize control, October (October).
[11] P. Prince, J. Dormand, High order embedded Runge-Kutta formulae, Journal of Computational and Applied ....
[12] N. Zealand, History of Runge-Kutta methods, Applied Numerical Mathematics 20 (1996) 247–260.
[13] T. Feagin, A tenth-order Runge-Kutta method with error estimate, Proceedings of the IAENG Conf. on Scientific ... (4) (2007) 4–9.
[14] D. A. Vallado, D. Finkleman, A Critical Assessment of Satellite Drag and Atmospheric Density Modeling, Specialist (2008) 1–31.
[15] B. R. Bowman, W. K. Tobiska, F. A. Marcos, C. Y. Huang, C. S. Lin, W. J. Burke, A New Empirical Thermospheric Density Model JB2008 Using New Solar and Geomagnetic Indices, Direct (August).
[16] B. R. Bowman, W. K. Tobiska, F. A. Marcos, A new empirical thermospheric density model JB2006 using new solar indices, in: AIAA, 2006.
[17] S. Bruinsma, G. Thuillier, F. Barlier, The DTM-2000 empirical thermosphere model with new data assimilation and constraints at lower boundary: accuracy and properties, Journal of atmospheric and solar-terrestrial physics 65 (2003) 1053–1070. doi:10.1016/S1364-6826(03)00137-8.
[18] S. Bruinsma, D. Tamagnan, R. Biancale, Atmospheric densities derived from CHAMP / STAR accelerometer observations, Planetary and Space Science 52 (2004) 297 – 312. doi:10.1016/j.pss.2003.11.004.
[19] A. J. Ridley, Y. Deng, G. Tóth, The global ionosphere thermosphere model, Journal of Atmospheric and Solar-Terrestrial Physics 68 (2006) 839–864. doi:10.1016/j.jastp.2006.01.008.
[20] R. G. Roble, E. C. Ridley, A. D. Richmond, R. E. Dickinson, A coupled thermosphere/ionosphere general circulation model 15 (1988) 1325–1328.
[21] National Oceanic and Atmospheric Administration - National Geophysical Data Center, Solar Radio Flux, ftp://ftp.ngdc.noaa.gov/stp/solar_data/solar_radio/flux, online; accessed 15-October-2012 (2012).
[22] National Oceanic and Atmospheric Administration - Space Weather Prediction Center, Solar Radio Flux predictions, http://www.swpc.noaa.gov/ftpdir/weekly/Predict.txt, online; accessed 15-October-2012 (2012).
[23] Deutsches GeoForschungsZentrum, Helmholtz-Zentrum Potsdam, Geomagnetic index, http://www.geomag.bgs.ac.uk/cgi-bin/apindex, online; accessed 15-October-2012 (2012).
[24] E. Doornbos, F. Matthias, B. Fritsche, T. V. Helleputte, J. V. D. Ijssel, D. Rees, P. Visser, M. Kern, L. Hermann, Air Density Models Derived from Multi-Satellite Drag Observations, Data Processing.
[25] T. Scholz, C. Asma, A. Aruliah, Recommended Set of Models and Input Parameters for the Simulations of Orbital Dynamics of the QB50 CubeSats, no. 5th ICATT 2012, International Conference on Astrodynamics Tools and Techniques, ESA, The Netherlands, 2012.
[26] J. Emmert, Thermospheric Density Trends Derived from Satellite Drag, in: 4th IAGA/ICMA/CAWSES Workshop on Long-Term Changes and Trends in the Atmosphere, no. September, 2006.
[27] J. T. Emmert, J. M. Picone, R. R. Meier, Thermospheric global average density trends, 1967–2007, derived from orbits of 5000 near-Earth objects, Geophysical Research Letters 35 (L05101). doi:10.1029/2007GL032809.
[28] J. T. Emmert, J. L. Lean, J. M. Picone, Record-low thermospheric density during the 2008 solar minimum, Geophysical Research Letters 37 (L12102). doi:10.1029/2010GL043671.
[29] D. Oltrogge, An Evaluation of CubeSat Orbital Decay, in: Conference on Small Satellite, 2011.
[30] L. Sentman, L. Missiles, S. Company, Free Molecule Flow Theory and Its Application to the Determination of Aerodynamic Forces, LMSC-448514, Lockheed Missiles & Space Company, a division of Lockheed Aircraft Corporation, 1961.
[31] T. Verstraete, Introduction to Optimization and Multidisciplinary Design, VKI Lecture Series, Von Karman Institute for Fluid Dynamics, Belgium, 2014.
[32] J. H. Holland, Adaptation in Natural and Artificial Systems, MIT Press, Cambridge, MA, USA, 1992.
[33] I. Rechenberg, Evolutionsstrategie: Optimierung technischer Systeme nach Prinzipien der biologischen Evolution, Problemata, 15, Frommann-Holzboog, 1973.
[34] K. Deb, S. Agrawal, A. Pratap, T. Meyarivan, A fast elitist non-dominated sorting genetic algorithm for multi-objective optimization: Nsga-ii, in: M. Schoenauer, K. Deb, G. Rudolph, X. Yao, E. Lutton, J. Merelo, H.-P. Schwefel (Eds.), Parallel Problem Solving from Nature PPSN VI, Vol. 1917 of Lecture Notes in Computer Science, Springer Berlin Heidelberg, 2000, pp. 849–858. doi:10.1007_3-540-45356-3_83.
URL http://dx.doi.org/10.1007/3-540-45356-3_83
[35] A. Griewank, Evaluating Derivatives: Principles and Techniques of Algorithmic Differentiation, no. 19 in Frontiers in Appl. Math., SIAM, Philadelphia, PA, 2000.
[36] L. B. Rall, Automatic differentiation: Techniques and applications, ZAMM - Journal of Applied Mathematics and Mechanics / Zeitschrift fr Angewandte Mathematik und Mechanik 62 (7) (1982) 355–355. doi:10.1002/zamm.19820620735.
URL http://dx.doi.org/10.1002/zamm.19820620735
[37] D. A. Vallado, An Analysis of State Vector Propagation Using Differing Flight Dynamics Programs, Tech. Rep. 1996 (1999).

Simulation and Reconstruction Tools for Atmospheric Entry Probes to Mars

Bart Van Hove

Royal Observatory of Belgium, Ringlaan 3 Ukkel 1180, o.karatekin@observatory.be

Supervisor: Olivier Chazot

Professor, Aeronautics and Aerospace Department, von Karman Institute for Fluid Dynamics, Belgium, chazot@vki.ac.be

Supervisor: Özgür Karatekin

Royal Observatory of Belgium, Ringlaan 3 Ukkel 1180, o.karatekin@observatory.be

University Supervisor: Chris Lacor

Professor, VUB Dept. Mechanical Engineering, Triomflaan 43 Brussel 1050, chris.lacor@vub.ac.be

Abstract

Entry, descent, and landing (EDL) on other planets is challenging and expensive. Therefore EDL flight data must be fully exploited to gain insight in both vehicle behavior and the planetary environment. In support of the 2016 ExoMars mission, we develop tools to reconstruct the atmospheric environment from flight data. We consider conventional accelerometers & gyroscopes as well as heat shield pressure sensors. The reconstruction tools were successfully applied to flight data from the 2008 Phoenix mission. We also extended our in-house atmospheric entry simulator to support multi-body parachute descent.

Keywords: Entry, Descent, and Landing, EDL, flight data, reconstruction, atmospheric profiles, atmospheric density, wind estimation, Flush Air Data Systems, FADS, ExoMars EDL Demonstrator Module, EDM

1. Introduction

The ExoMars (ESA/Roscosmos) mission will attempt Europe's first successful landing on the surface of Mars [1]. ExoMars involves an orbiter and landed platform in 2016, followed by a rover in 2018. The 2016 lander is named EDM for Entry, Descent, and Landing (EDL) Demonstrator Module. EDM will record flight data along its atmospheric entry trajectory. From this flight data, atmospheric profiles of temperature, density, pressure and potentially winds and dust concentrations can be derived.

We develop tools to reconstruct the atmospheric environment from flight data recorded by atmospheric entry probes. VKI and ROB (Royal Observatory of Belgium) are members of the AMELIA team responsible for the scientific investigation of flight data collected by ExoMars EDM [2]. Atmospheric reconstruction requires a versatile set of tools that supports different types of flight sensors, and provides uncertainty bounds on reconstructed variables. Flight simulation is used to generate synthetic data, for the purpose of code validation, investigating different atmospheric scenarios, and uncertainty quantification. Main developments in 2014 involved the following projects:

- **Kalman filter reconstruction (IMU data)** sensor noise characterization, fast estimation of reconstruction uncertainty, application to flight data from the Phoenix lander.
- **Reconstruct density from stagnation pressure** fast 1-D flow model to analyze heat shield pressure measurements.
- **Multi-body simulation of parachute descent** code verification and validation, application to Phoenix parachute descent phase.

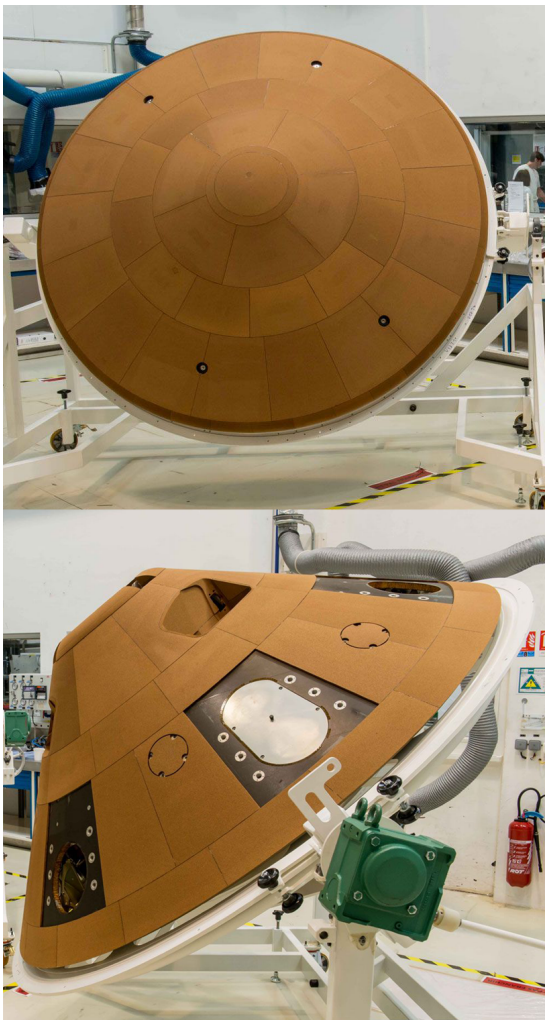

Figure 1: ExoMars 2016 EDM: heat shield (top) and back shell (bottom) from Airbus Defence & Space

2. Kalman filter for accelerometer and gyroscope (IMU) flight data

2.1. Objectives

Flight instrumentation typically includes accelerometers and gyroscopes that record translational and rotational rates. The flight trajectory can be derived by numerically integrating these rates over time. Atmospheric density, pressure, and temperature along the trajectory can be estimated by assuming values for the aerodynamic drag coefficient of the vehicle [3].

We compared two different implementations of this reconstruction methodology. One is a simple step-by-step implementation of the conventional reconstruction method [3]. In this case, uncertainty quantification (UQ) requires running the program many times, i.e. Monte Carlo sampling. The other method is a Bayesian estimator called a Kalman filter that performs reconstruction and UQ simultaneously, but is significantly more complex. The Kalman filter has some advantages over the step-by-step approach, such as much faster UQ and the ability to blend multiple types of flight data into a single lowest uncertainty reconstruction.

Trajectories and atmospheric profiles derived from flight data must be accompanied by uncertainty estimates. Uncertainty arises from unknown modeling and measurement errors. The type and amount of sensor noise is indicative of measurement error, and must be characterized or modeled to quantify uncertainty of reconstructed atmospheric profiles. Kalman filters usually support only Gaussian white noise representations. Our objectives are to accurately characterize sensor noise, and establish sensor noise modeling requirements in support of atmospheric profile reconstruction UQ. Only accelerometer and gyroscope data was considered at this stage.

2.2. Progress and results

We characterized sensor noise in accelerometer and gyroscope flight data recorded by the 2008 Phoenix lander [4]. Figures 2 and 3 show how two typical simplifying assumptions about sensor noise are not exactly satisfied for this flight data. These are zero cross-correlation (noise from different sensors is unrelated) and white noise (equal amounts of noise at all frequencies). Complete statistical descriptions of sensor noise were stored for three-axis accelerometer and three-axis gyroscope data, for later use in UQ:

- **UQ in the step-by-step reconstruction** involves running the program many times and analyzing the resulting reconstructions statistically. This is referred to as Monte Carlo sampling where samples are drawn from a stochastic data noise generator. Monte Carlo sampling poses no limitations on the type or details of data noise generators. In many applications, uncorrelated Gaussian (normal distribution) white noise is assumed.

- **UQ in the Kalman Filter** is performed during a single reconstruction. This performance advantage over sampling methods is achieved by propagating simple analytical uncertainty descriptions that are limited to uncorrelated Gaussian white noise.

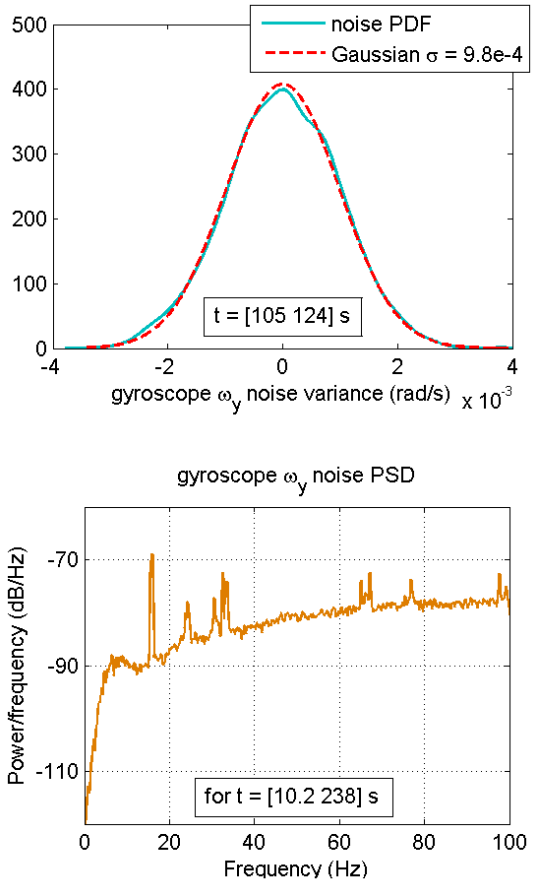

Figure 2: Phoenix accelerometer and gyroscope sensor noise: distributed normally (top), frequency spectrum is not white (bottom)

Detailed sensor noise characteristics such as cross-correlation and frequency spectrum cannot be modeled in the current Kalman filter implementation. First, we verified the Kalman filter code by assuming Gaussian white noise for both the filter and the Monte Carlo approach. Similar results indicated correct implementation of the filter. Second, detailed noise descriptions were used in Monte Carlo to assess the importance of non-zero cross-correlation and a colored frequency spectrum. We found that cross-correlations between data noise from different sensors had negligible impact on the reconstruction uncertainty. On the other hand, assuming a white frequency spectrum was found to overestimate reconstruction uncertainty for the trajectory. That for atmospheric profiles was not affected significantly. The study concludes that white noise assumptions can work but must be justified and used very carefully, since they can result in overestimated uncertainty bounds on reconstruction results.

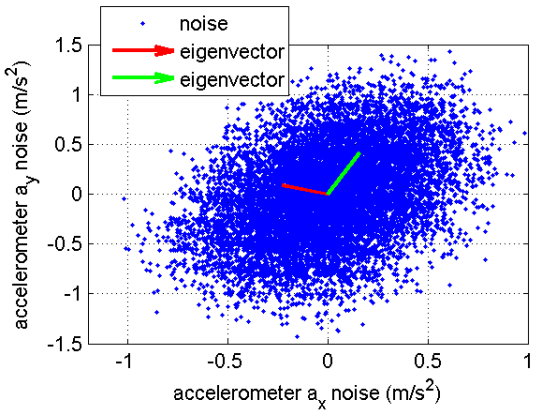

Figure 3: Phoenix accelerometer and gyroscope sensor noise: cross-correlation is not zero (right)

2.3. Perspectives

The Kalman filter will be validated and developed further. Additional types of flight data (e.g. from heat shield pressure sensors, Doppler altimeters...) can be blended with accelerometer and gyroscope data. Common assumptions of uncorrelated white noise must be evaluated at every step, and if necessary the filter may be extended to model additional sensor noise characteristic such as frequency spectrum or probability distribution.

3. Flow solver for heat shield pressure data

3.1. Objectives

The ExoMars EDM heat shield is instrumented with four surface pressure sensors. Figure 4 illustrates a flow field on the larger but geometrically similar Mars Science Laboratory (MSL) heat shield, with EDM pressure sensor locations indicated.

Predictions of the surface pressure distribution on the heat shield are required to reconstruct atmospheric conditions and flow angles from flight data. Stagnation (maximum) pressure is a strong function of airspeed and atmospheric density, while relative differences between off-stagnation pressures can be correlated with flow incidence angles. EDM will fly a ballistic trajectory at approximately zero angle of attack, so the central pressure sensor will measure stagnation pressure almost directly. Atmospheric density can be derived from this pressure using known values for the stagnation pressure coefficient C_{pt2}. We thus need predictions of C_{pt2} for the trajectory conditions relevant to atmospheric entry probes on Mars, to reconstruct atmospheric density from heat shield flight data.

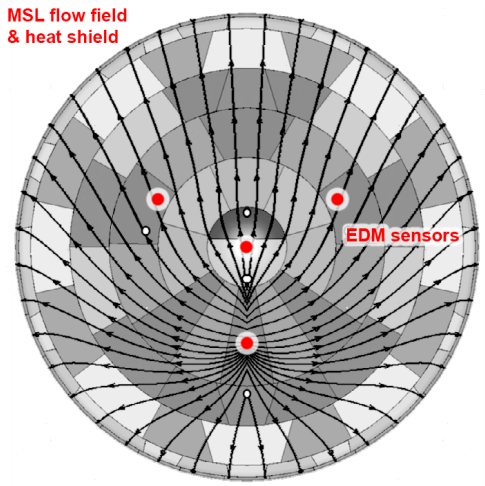

Figure 4: Flow field on MSL heat shield with EDM pressure sensors [5] (stagnation point about 15 deg below centerline)

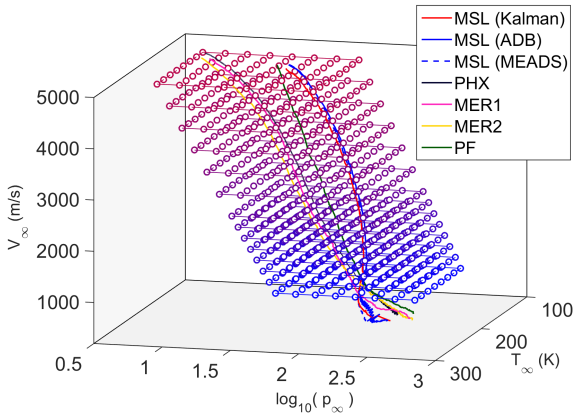

Figure 5: Flow solver input conditions covering a range of trajectory conditions encountered by previous atmospheric entry probes to Mars (above 1 km/s)

3.2. Progress and results

We used a 1-D flow model that solves adiabatic conservation equations across the shock wave ahead of the heat shield. An iterative Newton solver finds stagnation conditions as a function of the selected atmospheric free stream conditions. Stagnation pressure coefficients can then be derived for use in atmospheric profile reconstruction. High temperatures in the shock layer flow require accurate thermodynamic and transport parameters for the Martian atmosphere. These were provided by the Mutation library [6] developed at the von Karman Institute (VKI). A gas mixture composed of CO_2, Ar, N_2, and O_2 was used to represent the Martian atmosphere. The resulting flow solver is much faster than finite element computational fluid dynamics (CFD), but is limited to the stagnation line and operates under the assumptions of an inviscid fluid and isentropic flow in the shock layer.

Figure 5 shows over one thousand sets of flow solver inputs that cover most trajectory conditions encountered by previous entry probes to Mars. The inputs are air speed V_∞, atmospheric pressure p_∞, and atmospheric temperature T_∞. Velocities below 1 km/s will be considered at a later stage. The resulting database of normalized pressure coefficients will be used for atmospheric density reconstruction from stagnation pressure flight data.

Stagnation pressure coefficients were calculated for every set of input conditions. C_{pt2} varies more strongly with air speed than with atmospheric inputs, and was interpolated by high order polynomials as a function of air speed. These can be evaluated quickly and inexpensively during atmospheric density reconstruction.

3.3. Perspectives

The general 1-D flow solver will be extended to lower velocities, down to parachute deployment / heat shield jettison. Reconstruction of flow angles and potentially in-situ winds requires more complex flow field models dedicated to ExoMars EDM. These can be provided by additional CFD and wind tunnel testing.

4. Multi-body parachute descent simulation

4.1. Objectives

We extended our flight simulator to include the parachute descent phase of atmospheric entry probes. In the planetary boundary layer, atmospheric dynamics affect the motion of parachute descent systems. This includes turbulent and convective motions as well as winds. Given accurate aerodynamic characterization of the parachute payload system, atmospheric motion could be derived from parachute motion observed in flight. The final objective is to assess the feasibility of estimating atmospheric variables from a reconstructed lander (parachute payload) trajectory.

4.2. Progress and results

The parachute payload system is modeled by two rigid bodies connected by a single or a network of linear spring dampers. Figure 6 shows a typical Mars parachute system, with the same key components as

the ExoMars EDM parachute system. Our simulator models the canopy and suspension lines as a single rigid body, and the riser and bridle lines as linear spring dampers. Aerodynamic forces and moments are specified for the parachute body as well as a mass distribution. The spring damper dynamics are calculated by an iterative Newton solver, and were found to pose strong restrictions on the simulations time step size in some cases. The parachute simulator can be configured to represent a wind tunnel setup, to make eventual comparison with wind tunnel testing possible.

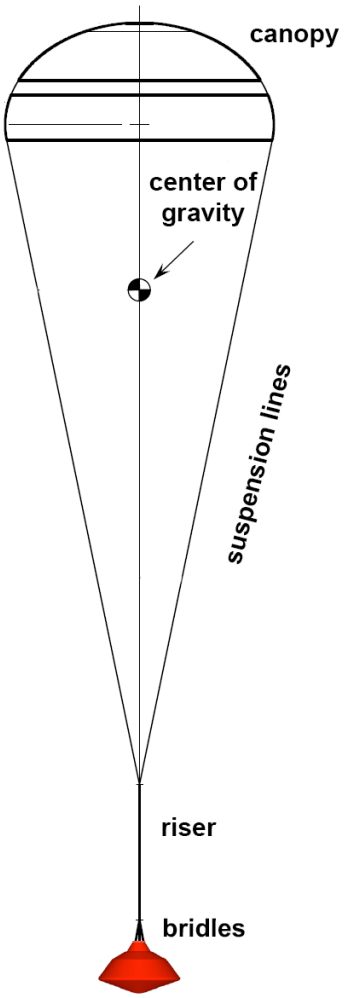

Figure 6: Typical Mars lander parachute system [7]. In the simulator, riser and bridle lines are modeled as linear spring dampers, canopy and suspension lines are modeled as a single rigid body

Preliminary validation included simplified cases such as vertical drops and wind tunnel scenarios for which analytical solutions can be derived. Results of a similar approach employed for the NASA POST II multi-body simulator are available in the literature [8]. We are in the process of reproducing these results in a first cross-simulator validation. Figure 7 shows good agreement for a test case involving a simplified parachute payload system, falling vertically from an initial rest position, with initially 1 cm of slack in the riser line.

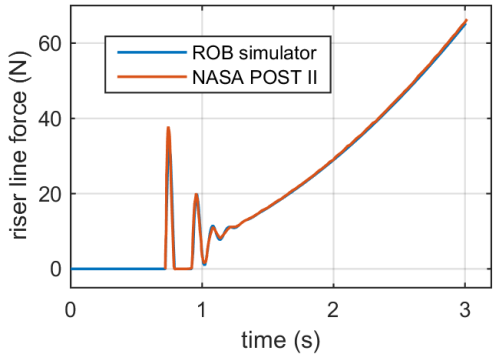

Figure 7: Comparison of tension force in riser line (spring damper) predicted by ROB and NASA POST II simulators for a simplified parachute system.

Simulations of the Phoenix descent trajectory were performed but with approximate inputs, since complete descriptions of the Phoenix parachute mass distribution and aerodynamics are not available to us. Figure 8 shows that our simulated vertical descent velocity is in relatively good agreement with the flight data reconstruction. Other trajectory variables such as Phoenix angle of attack could not be reproduced as accurately, likely due to approximate or missing simulation inputs.

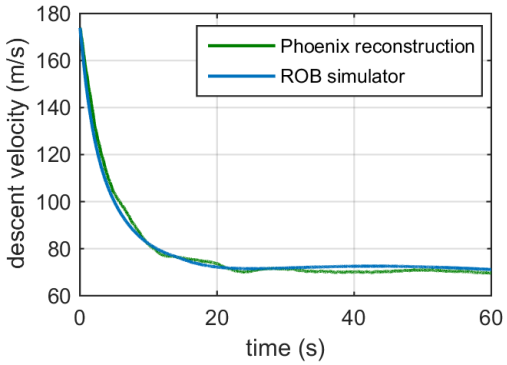

Figure 8: Phoenix vertical descent velocity predicted by simulator compared to flight data reconstruction

4.3. Perspectives

We eventually wish to validate against flight data from existing missions. This is challenging due to the limited availability and accuracy of parachute modeling parameters. Further cross-validation between simulators using real or hypothetical descent scenarios can bridge the gap to direct flight validation. We have initiated contacts with ESA, and with a private company named Vorticity, that designed the parachutes for the Huygens and ExoMars missions. We are currently working on simulating the ExoMars EDM parachute descent and will compare those results with an independent ESA simulation.

In a next step, simulated parachute descent trajectories will be subjected to sensitivity and uncertainty analysis to determine the feasibility of reconstructing atmospheric variables from observed payload (lander) trajectories.

5. Conclusion

Development of the Kalman filter will focus on validation before blending complementary flight data such as heat shield pressure data with conventional accelerometer and gyroscope data. The Kalman uncertainty models may need to be refined to represent the frequency spectrum of noisy flight data. We showed that assuming white noise may lead to overestimation of reconstruction uncertainty.

A general but approximate 1-D flow solver was used to model the stagnation line flow for Mars entry probes. Efforts are ongoing to extend the heat shield pressure model to off-stagnation locations. This will improve stagnation point localization and enable flow angle reconstruction. Very accurate flow angle estimates are required for atmospheric wind estimation.

The atmospheric entry flight simulator is now sufficiently mature and validated to be used with complete confidence for ballistic 6-DOF entry scenarios. The addition of the multi-body parachute model will continue to be validated, before being used to assess the impact of atmospheric motion on parachute-payload motion. Collaborations between ROB and VKI outside of the scope of this document are producing further additions to the simulator, i.e. support for thrust vectoring and flight control algorithms.

Acknowledgments

This work is supported by the Royal Observatory of Belgium to develop reconstruction tools for the 2016 ExoMars mission. ROB and VKI are members of the AMELIA team responsible for the scientific investigation of flight data from the ExoMars EDM entry probe.

References

[1] L. V. Lorenzoni, ExoMars 2016 Entry Descent and Landing Demonstrator Module EDL overview, in: IPPW-10 in San jose State University, CA, 2013.

[2] F. Ferri et al., ExoMars Atmospheric Mars Entry and Landing Investigations and Analysis (AMELIA), in: IPPW-9 in Toulouse, France, 2012.

[3] B. Van Hove & O. Karatekin, Mars Atmosphere Reconstruction using a Flush Air Data System on the ExoMars Entry, Descent and Landing Demonstratore Module, in: IPPW-10 in San Jose State University, CA, 2013.

[4] B. Van Hove & O. Karatekin, Mars Entry, Descent, and Landing reconstruction from Flight Data: Uncertainty Quantification, in: IPPW-11 in Pasadena State University, CA, 2013.

[5] C. D. Karlgaard et al., Mars Entry Atmospheric Data System Trajectory Reconstruction Algorithms and Flight Results, in: 51st AIAA Aerospace Sciences Meeting, Grapevine, Texas, 2013.

[6] J. B. Scoggins, Development of MUTATION++: Multicomponent Thermodynamics And Transport properties for IONized gases library in C++, in: Rev. of the VKI Doctoral Research 2012-2013, 2013.

[7] J. R. Cruz et al., Parachute Models Used in the Mars Science Laboratory Entry, Descent, and Landing Simulation, in: AIAA Aerodynamic Decelerator Systems (ADS) Conference, Daytona Beach, Florida, 2013.

[8] B. Raiszadeh et al., Validation of Multibody Program to Optimize Simulated Trajectories II Parachute Simulation With Interacting Forces, Technical Publication NASA/TP2009-215765, NASA (2009).

WHO’S WHO

Who's who



Mohamed Hassanine
Aissa



Alejandro
Alvarez Laguna



Georgios
Bellas Chatzigeorgios



Aurélie
Bellemans



Christopher
Chahine



Julien
Clinckemaille



Nicolas
De Cock



Cis
De Maesschalck



Giulia
Dell'Era



Bruno Ricardo
Dias Barros



Jorge
Fernandes Lopes de Sousa



Clara
García Sánchez



Sara
González Ruiz



Gian Luca
Gori



Gabriele
Grasso



Koen
Groot



Daniel
Guariglia



Bernd
Helber



Imre
Horváth



Ugur
Karban



Aude
Lahalle



Miguel Alonso
Mendez



Lasse
Müller

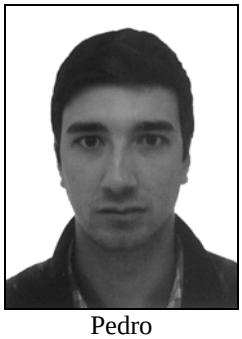

Pedro
Santos Duarte



Işil
Şakraker



Sebastian
Scholl



Torsten
Scholz



Pierre-Louis
Schrooyen



James B.
Scoggins



Alessia
Simonini



Nikolaos
Stergiannis



Orkun
Temel



Roberto
Tomasssini



Stefano
Vagnoli



Bart
Van Hove



Alan
Viladegut



Augustin
Villa Ortiz

PhD candidates who have not presented a paper at the symposium



Gilles
Bailet



Francesco
Baldani



Stefano
D'Angelo



Leandro
Dantas De Santana



Guéric
De Crombrugghe



Lamberto
Dell'elce



Jësus
Garicano Mena



Guillaume
Grossir



Alejandro
Huertas Martinez



Silvânia
Lopes



Gennaro
Serino



Jérôme
Sans



Jorge
Pinho



Chiara
Spaccapaniccia



Erik
Torres



Martin
Vymazal